
This item was submitted to [Loughborough's Research Repository](#) by the author.
Items in Figshare are protected by copyright, with all rights reserved, unless otherwise indicated.

The aerodynamic behaviour of an annular S-shaped duct

PLEASE CITE THE PUBLISHED VERSION

PUBLISHER

© K.M. Britchford

LICENCE

CC BY-NC-ND 4.0

REPOSITORY RECORD

Britchford, Kevin M.. 2010. "The Aerodynamic Behaviour of an Annular S-shaped Duct". figshare.
<https://hdl.handle.net/2134/6877>.

This item was submitted to Loughborough University as a PhD thesis by the author and is made available in the Institutional Repository (<https://dspace.lboro.ac.uk/>) under the following Creative Commons Licence conditions.



Attribution-NonCommercial-NoDerivs 2.5

You are free:

- to copy, distribute, display, and perform the work

Under the following conditions:

 **Attribution.** You must attribute the work in the manner specified by the author or licensor.

 **Noncommercial.** You may not use this work for commercial purposes.

 **No Derivative Works.** You may not alter, transform, or build upon this work.

- For any reuse or distribution, you must make clear to others the license terms of this work.
- Any of these conditions can be waived if you get permission from the copyright holder.

Your fair use and other rights are in no way affected by the above.

This is a human-readable summary of the [Legal Code \(the full license\)](#).

[Disclaimer](#) 

For the full text of this licence, please go to:
<http://creativecommons.org/licenses/by-nc-nd/2.5/>



Pilkington Library

Author/Filing Title BRITCHFORD, K.M.

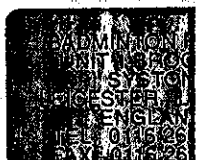
Accession/Copy No.

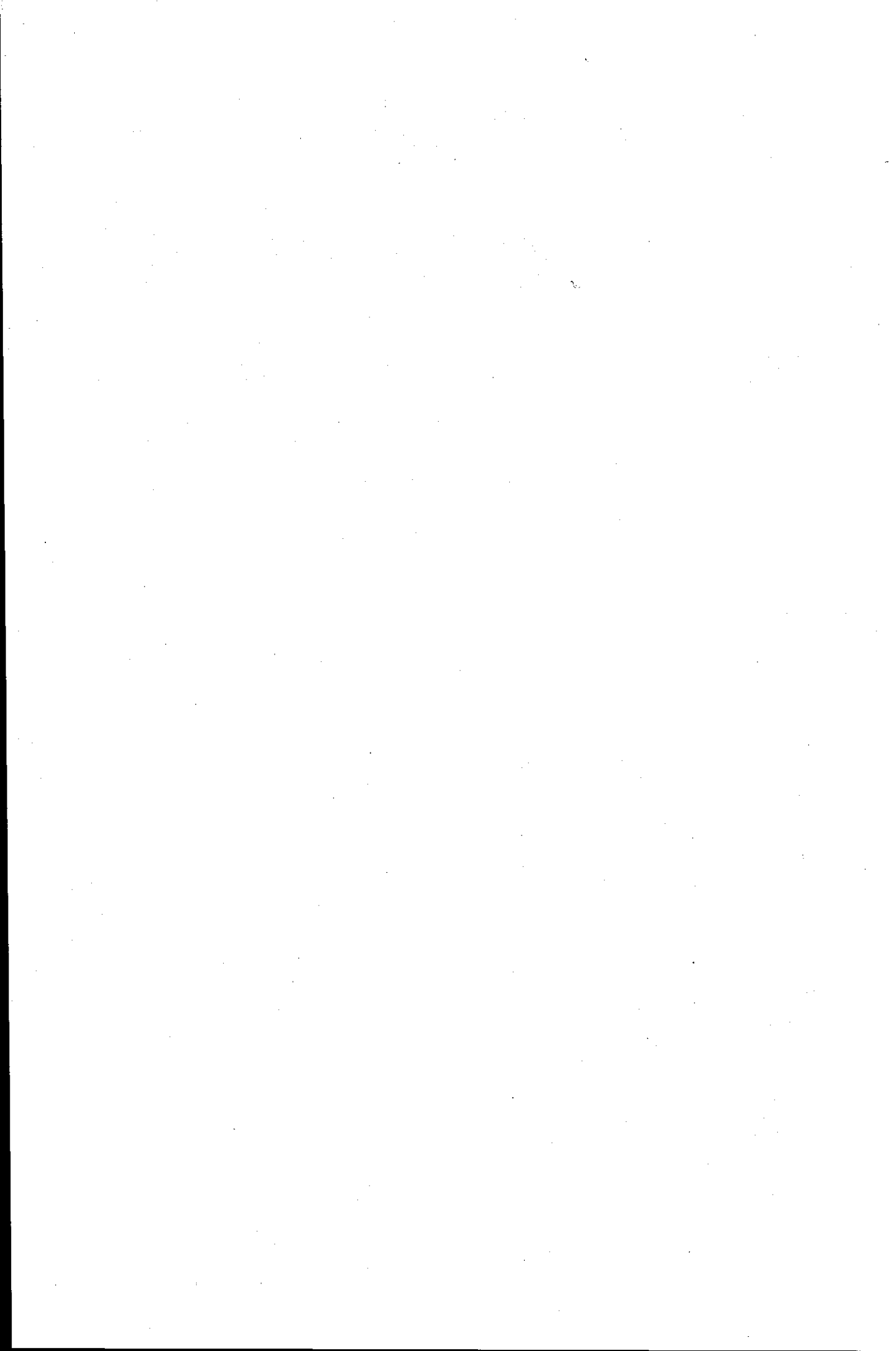
Vol. No.	Class Mark
---------------	------------------

ARCHIVES
copy

FOR REFERENCE ONLY

040166144X





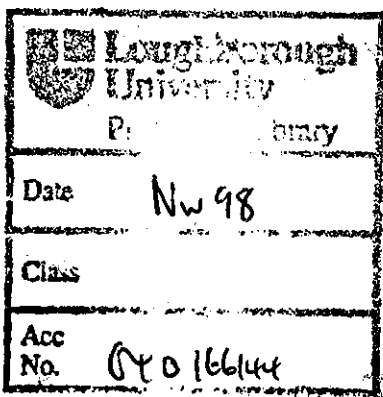
The Aerodynamic Behaviour of an Annular S-shaped Duct

by

K. M. Britchford

Doctoral Thesis

Submitted in partial fulfilment of the requirements
for the award of
Doctor of Philosophy of Loughborough University
June, 1998



SUMMARY

In this thesis, a detailed investigation into the aerodynamic behaviour of an annular S-shaped duct is reported. One of the main objectives of this work was to acquire experimental data on the flow field within an S-shaped duct, which, with reducing mean radius, was representative of that used to connect the compressor spools of a gas turbine engine. A new test rig was designed and constructed, and a data acquisition system developed, to allow measurements to be obtained across the passage at a series of traverse locations. To generate engine representative inlet conditions, a single stage axial compressor could be located upstream of the S-shaped duct, but, although data was obtained in this configuration, the results presented mainly relate to the axisymmetric flow obtained without the compressor. With a parallel inlet section upstream, the flow through the S-shaped duct consisted of well-established turbulent boundary layers, which remained attached to the walls and isolated by an irrotational core region throughout the rig.

As well as using conventional five hole probe techniques, detailed measurements of the turbulent flow were obtained with a 3-component Laser Doppler Anemometry (LDA) system. The mean velocity and turbulence data show that the flow within the S-shaped duct is complex, with the rapidly varying streamwise pressure gradients and streamline curvature having a significant effect on the flow behaviour. In this thesis, these various effects are examined in detail, and the physical mechanisms responsible for the observed behaviour are explained. Most importantly, the extra strain rate due to curvature was seen to affect the Reynolds shear stress distribution, which, together with the pressure gradient, affected the mean velocity distribution. Whilst the strong adverse pressure gradient along the inner wall reduced the wall shear stress, boundary layer separation did not occur. Moreover, the overall total pressure loss through the duct was relatively low, and some regions of increasing total pressure were observed.

In addition to the experimental investigation, Computational Fluid Dynamics (CFD) methods were used to predict the axisymmetric flow through the S-shaped duct. Using standard $k-\epsilon$ and Reynolds stress transport equation turbulence models, solutions of the Reynolds-averaged Navier-Stokes equations have been compared with the experimental data. In order to predict the physical behaviour of flow adequately, it is clear from the results that the Reynolds stresses must be obtained from transport equations, and not from an eddy-viscosity model. Even then, the modelling assumptions contained in the Reynolds stress transport equations, particularly the pressure-strain model, limit the accuracy of the prediction.

ACKNOWLEDGEMENTS

I would like to express my thanks to Rolls-Royce plc for sponsoring this research, and giving me the opportunity to work at Loughborough University for four years, and also to SERC for their contribution to the cost of the project.

I also wish to thank my supervisors at Loughborough: Stan Stevens and Jim McGuirk for directing the research; Paul Wray for his help in designing the rig and data acquisition system; Jon Carrotte for his assistance with the LDA measurements and Andy Manners for his guidance with the CFD predictions.

Additional thanks to Jon Carrotte, Paul Wray and Jim McGuirk for proof-reading this thesis, and for their constructive criticism.

I would also like to thank the Airflow Laboratory technicians, Roy Marson, Dave Glover, Les Monk and Bill Niven, for their help in the construction of the test rig, and all the other departmental technicians who have been involved.

Thanks also to the other members of staff within the department with whom I have had many interesting and useful discussions; especially my research colleagues, Jon Carrotte, Martin Passmore, Clive Marsh, Andrew Little, Adrian Spencer, Paul Denman and David Bailey.

Special thanks to Andy Manners for the many hours we spent playing squash, and for all that I have learnt from him over the years.

Finally, and most sincerely, I would like to thank my wife, Diane, and my children, Danielle, Emily and Kristina, for their love and support throughout this work, for enduring the many hours and late nights I have spent working on this project and, above all, for encouraging me to complete this thesis. They deserve a Ph.D. for their patience.

DEDICATION

To those who think, and achieve understanding.

To those who do, and reach their objective.

To those who assist, and constructively advise.

To those who support, and those who care.

LIST OF CONTENTS

	Page
Summary	ii
Acknowledgements	iii
Dedication	iv
List of Contents	v
List of Tables	ix
List of Figures	x
List of Photographs	xv
Nomenclature	xvi
Chapter 1 Introduction	1
1.1 Annular S-shaped Ducts	2
1.1.1 The Gas Turbine Application	2
1.1.2 Duct Geometry	3
1.2 Flow in Annular S-shaped Ducts	5
1.2.1 Ideal Behaviour	6
1.2.2 Actual Behaviour	9
1.3 Review of Related Work	13
1.3.1 Turbulent Boundary Layers	14
1.3.2 The Effect of Pressure Gradient on Turbulent Boundary Layers	16
1.3.3 The Effect of Curvature on Turbulent Boundary Layers	20
1.3.4 Combined Effects of Pressure Gradient and Curvature	27
1.3.5 Inlet Conditions	30
1.3.6 Conclusions from the Review	31
1.4 Objectives of the Present Investigation	32
1.4.1 Contents of the Thesis	34
Chapter 2 Experimental Equipment	35
2.1 Test Rig	36
2.1.1 Preliminary Aerodynamic Design	36

List of Contents

2.1.2 Mechanical Design and Construction	39
2.1.3 Annular S-shaped Duct	42
2.1.4 Single Stage Compressor	46
2.1.5 Inlet and Exit Sections	47
2.1.6 Facility	48
2.2 Data Acquisition	49
2.2.1 Practical Considerations	49
2.2.2 Basic Instrumentation	54
2.2.3 Data Acquisition System	57
2.2.4 Laser Doppler Anemometer	61
Chapter 3 Data Analysis	70
3.1 Reduction of Measured Data	72
3.1.1 Co-ordinate Systems	72
3.1.2 Five Hole Probe Measurements	76
3.1.3 LDA Measurements	80
3.2 Derived Quantities	89
3.2.1 Determining the Potential Velocity Distribution	89
3.2.2 Integral Parameters	91
3.2.3 Boundary Layer Parameters	95
3.2.4 Determining the Wall Shear Stress	97
3.2.5 Spatial Gradients	100
3.3 Errors and Accuracy	102
3.3.1 Hardware	102
3.3.2 Five Hole Probe	103
3.3.3 Laser Doppler Anemometer	105
3.3.4 Overall Parameters	109
Chapter 4 Experimental Results	111
4.1 Rig Commissioning Tests	112
4.1.1 General Considerations	112
4.1.2 Axial Compressor Performance	113
4.1.3 Operating Conditions	114
4.2 Axisymmetric Flow Without the Compressor	115
4.2.1 Presentation of the Results	116
4.2.2 Mean Flow Quantities	116
4.2.3 Turbulence Data	131
4.2.4 Derived Data	141
4.3 Flow With the Compressor Installed	155

List of Contents

4.3.1 Mean Flow Quantities	155
4.3.2 Turbulence Data	161
4.4 Concluding Remarks	163
Chapter 5 Computational Approach	164
5.1 Introduction	165
5.1.1 Review of Related Work	166
5.1.2 Scope and Aims of the Present CFD Calculations	172
5.2 Turbulence Models	172
5.2.1 Eddy-viscosity Models	173
5.2.2 Reynolds Stress Transport Equation Turbulence Models	175
5.3 Calculations Undertaken	179
5.3.1 Solution Technique	179
5.3.2 Geometry and Grid	181
5.3.3 Boundary Conditions	182
5.3.4 Post-processing and Presentation of Results	183
Chapter 6 Discussion	185
6.1 Comparison of the Predictions with the Experimental Data	186
6.1.1 Overall Parameters	186
6.1.2 Mean Velocities	187
6.1.3 Reynolds Stresses	189
6.2 Reynolds Stress Production in 2D Curvilinear Co-ordinates	192
6.2.1 The Production Terms	193
6.2.2 Effects on Reynolds Stress Production	194
6.2.3 Assessment of the Effects	197
6.3 The Behaviour of the Modelled Reynolds Stress Equations	201
6.3.1 Simplified Modelled Equations	202
6.3.2 Limitations of the Modelled Equations	206
Conclusions	215
Recommendations	216
References	217
Tables	232
Figures	247
Photographs	398

List of Contents

Appendix 1 Single Stage Axial Compressor Design	407
Appendix 2 Ideal Behaviour of a Curved Flow	410
A2.1 The Exact Inviscid Behaviour	410
A2.2 Derivation of an Approximate Velocity Distribution	412
Appendix 3 The Exact Equations of Motion	414
A3.1 Continuity Equation	414
A3.2 Momentum Equations	414
A3.3 Mean Energy Equation	415
A3.4 Reynolds Stress Transport Equations	415
A3.5 Turbulent Kinetic Energy Transport Equation	416
A3.6 Turbulent Kinetic Energy Dissipation Rate Equation	417
Appendix 4 Transformation of the Equations of Motion to Curvilinear and Polar Co-ordinates	418
A4.1 Method of Transformation	418
A4.1.1 Curvilinear (s-n-z) Co-ordinates	418
A4.1.2 Polar (x-r-θ) Co-ordinates	422
A4.2 Comparison of the Equations of Motion in Cartesian (x-y-z), Curvilinear (s-n-z) and Polar (x-r-θ) Co-ordinates	424
A4.2.1 Continuity Equation	424
A4.2.2 Momentum Equations	425
A4.2.3 Mean Energy Equation	431
A4.2.4 Reynolds Stress Transport Equations	432

LIST OF TABLES

	Page
1 S-shaped Duct Geometry	233
2 Traverse Geometry	234
3 Rotor Aerodynamic Parameters	235
4 Rotor Profile Parameters	236
5 Stator Aerodynamic Parameters	237
6 Stator Profile Parameters	238
7 Optical Configuration	239
8 Boundary Layer Integral Properties	240
9 Wall Pressure Gradient	241
10 Wall Geometrical Curvature	242
11 Shape Parameters	243
12 Effective Curvature and Wall Potential Velocity	244
13 Wall Shear Stress	245
14 Wall Shear Stress based on Wall Potential Velocity	246

LIST OF FIGURES

	Page
1 Gas Turbine Schematic	252
2 Rig General Arrangement	253
3 Working Section and Traverse Locations	254
4 LDA Optical Arrangement	255
5 Five Hole Probe Calibration	256
6 Compressor Characteristics	257
7 Wall Static Pressure Distribution	258
8 Static Pressure Distribution	259
9 Streamwise Velocity Distribution	260
10 Velocity Vectors throughout S-shaped Duct	261
11 Flow Streamlines	262
12 Distribution of Streamwise Velocity Ratio vs. Height - 5HP Data with Boundary Layer Thickness Indicated	263
13 Distribution of Streamwise Velocity Ratio vs. Stream Function - 5HP Data with Boundary Layer Thickness Indicated	264
14 Streamwise Velocity Distribution - Comparison of LDA and 5HP Data	265
15 Cross-stream Velocity Distribution - Comparison of LDA and 5HP Data	266
16 Circumferential Velocity Distribution - Comparison of LDA and 5HP Data	267
17 Radial Velocity Distribution - Comparison of LDA and 5HP Data	268
18 Potential velocity Distribution - Comparison of LDA and 5HP Data	269
19 Streamwise Velocity Ratio Distribution - Comparison of LDA and 5HP Data	270
20 Axial Variation of Mean Pressure Coefficient	271
21 Axial Variation of Kinetic Energy Flux Coefficient	272
22 Axial Variation of Displacement Thickness - Experiment (LDA & 5HP) Clean	273
23 Axial Variation of Momentum Thickness - Experiment (LDA & 5HP) Clean	274
24 Axial Variation of Boundary Layer Shape Parameter - Experiment (LDA & 5HP) Clean	275
25 Axial Variation of Friction Velocity - Experiment (LDA & 5HP) Clean	276
26 Axial Variation of Wall Potential Velocity - Experiment (LDA & 5HP) Clean vs. Inviscid Calculation	277

27	Axial Variation of Boundary Layer Thickness (δ^* , θ)	278
28	Axial Variation of Boundary Layer Thickness (δ^* , θ)	279
29	Axial Variation of Boundary Layer Shape Parameter	280
30	Axial Variation of Skin Friction Coefficient	281
31	Skin Friction vs. Reynolds Number - (Up _w based)	282
32	Axial Variation of Skin Friction Coefficient - Experiment vs. Ludwieg-Tillmann	283
33	Skin Friction Coefficient vs. Shape Parameter - Experiment vs. Ludwieg-Tillmann	284
34	Pressure Gradient Parameter vs. Wall Curvature Parameter	285
35	Clauser Parameter vs. Pressure Gradient Parameter	286
36	Clauser Parameter vs. Wall Curvature Parameter	287
37	Shape Parameter vs. Pressure Gradient Parameter	288
38	Skin Friction Coefficient vs. Pressure Gradient Parameter	289
39	Variation of Streamwise Normal Stress (\overline{uu})	290
40	Variation of Cross-stream Normal Stress (\overline{vv})	291
41	Variation of Circumferential Normal Stress (\overline{ww})	292
42	Variation of Reynolds Shear Stress (\overline{uv})	293
43	Variation of Reynolds Shear Stress (\overline{uw})	294
44	Variation of Reynolds Shear Stress (\overline{vw})	295
45	Variation of Turbulent Kinetic Energy	296
46	Variation of Shear Stress Correlation Coefficient	297
47	Variation of Reynolds Stress Ratio ($\overline{vv}/\overline{uu}$)	298
48	Variation of Reynolds Stress Ratio ($\overline{uv}/\overline{uu}$)	299
49	Variation of Reynolds Stress Ratio ($\overline{uv}/\overline{vv}$)	300
50	Variation of Reynolds Stress Ratio (\overline{uv}/k)	301
51	Variation of Reynolds Stress Ratio (\overline{uu}/k)	302
52	Variation of Reynolds Stress Ratio (\overline{vv}/k)	303
53	Variation of Reynolds Stress Ratio (\overline{ww}/k)	304
54	Measured Reynolds Stress Anisotropy	305
55	Variation of Triple Velocity Correlation (\overline{uuu})	306
56	Variation of Triple Velocity Correlation (\overline{uuv})	307
57	Variation of Triple Velocity Correlation (\overline{uuw})	308
58	Variation of Triple Velocity Correlation (\overline{uvv})	309
59	Variation of Triple Velocity Correlation (\overline{uvw})	310
60	Variation of Triple Velocity Correlation (\overline{uvw})	311
61	Variation of Triple Velocity Correlation (\overline{vvv})	312
62	Variation of Triple Velocity Correlation (\overline{vww})	313

List of Figures

63	Variation of Triple Velocity Correlation (\overline{vww})	314
64	Variation of Triple Velocity Correlation (\overline{www})	315
65	Variation of Triple Velocity Correlation ($\overline{q^2u}$)	316
66	Variation of Triple Velocity Correlation ($\overline{q^2v}$)	317
67	Turbulent Kinetic Energy Transport Velocity (V_q)	318
68	Variation of U-skewness	319
69	Variation of V-skewness	320
70	Variation of W-skewness	321
71	Variation of U-intermittency	322
72	Variation of V-intermittency	323
73	Variation of W-intermittency	324
74	Measured Inner Wall Streamwise Velocity - Log-law Co-ordinates	325
75	Measured Outer Wall Streamwise Velocity - Log-law Co-ordinates	326
76	Measured Reynolds Shear Stress Profiles - Inner Wall - (Non-dimensionalised by Local Parameters)	327
77	Measured Reynolds Shear Stress Profiles - Outer Wall - (Non-dimensionalised by Local Parameters)	328
78	Mean Strain Rate Distribution	329
79	Strain Rate and Vorticity Distribution	330
80	Cross-Stream Gradient of Streamwise Velocity	331
81	Measured Reynolds Shear Stress Profiles with 'Best Fit' Interpretation and Wall Values	332
82	Total Shear Stress Distribution vs. Height - 'Best Fit' Interpretation of Measured Reynolds Shear Stress Profiles	333
83	Total Shear Stress Distribution vs. Stream Function - 'Best Fit' Interpretation of Measured Reynolds Shear Stress Profiles	334
84	Variation of Shear Stress Gradient ($\partial\overline{uv}/\partial n$) vs. Stream Function	335
85	Variation of Shear Stress Gradient ($U\partial\overline{uv}/\partial n$) vs. Height	336
86	Regions of Positive and Negative Shear Stress Gradient	337
87	Comparison of Measured and Derived Total Pressure	338
88	Axial Variation of Loss Coefficient - Experiment (5HP) vs. Shear Stress Derived Value (LDA)	339
89	Variation of Turbulent Kinetic Energy Production	340
90	Mean Energy Redistribution and Loss	341
91	Variation of Streamwise Pressure Gradient (cf. Shear Stress Gradient)	342
92	Streamwise Acceleration (cf. Stress Gradient minus Pressure Gradient)	343
93	Streamwise Velocity Profiles vs. Height - (Clean Inlet - 5HP)	344
94	Streamwise Velocity Profiles vs. Stream Function - (Clean Inlet - 5HP)	345

List of Figures

95	Total Pressure Distribution vs. Height - (Clean Inlet - 5HP)	346
96	Total Pressure Distribution vs. Stream Function - (Clean Inlet - 5HP)	347
97	Total Pressure Distribution vs. Fractional Distance from Wall - (Clean Inlet - 5HP)	348
98	Total Pressure Distribution vs. Fractional Mass Flow from Wall - (Clean Inlet - 5HP)	349
99	Total Pressure Distribution vs. Fractional Distance from Wall - (Clean Inlet - Derived from LDA $\bar{u}\bar{v}$ Measurements)	350
100	Total Pressure Distribution vs. Fractional Mass Flow from Wall - (Clean Inlet - Derived from LDA $\bar{u}\bar{v}$ Measurements)	351
101	Experimental Measurement Mesh	352
102	Contours of Streamwise Velocity (S-duct Inlet - $x/L = 0.0$)	353
103	Contours of Radial Velocity (S-duct Inlet - $x/L = 0.0$)	354
104	Contours of Circumferential Velocity (S-duct Inlet - $x/L = 0.0$)	355
105	Secondary Velocity Vectors (S-duct Inlet - $x/L = 0.0$)	356
106	Contours of Total Pressure Coefficient (S-duct Inlet - $x/L = 0.0$)	357
107	Measured Contours of Total Pressure Coefficient	358
108	Mean and Wall Static Pressure Distribution With the Compressor	359
109	Comparison of the Static Pressure Distribution With and Without the Compressor - (Pitch-averaged 5HP Measurements)	360
110	Comparison of Streamwise Velocity Profiles With and Without the Compressor - (Pitch-averaged 5HP Measurements)	361
111	Streamwise Velocity Profiles vs. Height - (Compressor at Inlet - 5HP)	362
112	Streamwise Velocity Profiles vs. Stream Function - (Compressor at Inlet - 5HP)	363
113	Total Pressure Distribution vs. Height - (Compressor at Inlet - 5HP)	364
114	Total Pressure Distribution vs. Stream Function - (Compressor at Inlet - 5HP)	365
115	Axial Variation of Boundary Layer Shape Parameter With and Without the Compressor	366
116	Secondary Velocity Vectors ($x/L = 0.25$)	367
117	Contours of Turbulent Kinetic Energy (S-duct Inlet - $x/L = 0.02$)	368
118	Contours of $\bar{u}\bar{u}$ Normal Stress (S-duct Inlet - $x/L = 0.02$)	369
119	Contours of $\bar{v}\bar{v}$ Normal Stress (S-duct Inlet - $x/L = 0.02$)	370
120	Contours of $\bar{w}\bar{w}$ Normal Stress (S-duct Inlet - $x/L = 0.02$)	371
121	Contours of $\bar{u}\bar{w}$ Shear Stress (S-duct Inlet - $x/L = 0.02$)	372
122	Contours of $\bar{v}\bar{w}$ Shear Stress (S-duct Inlet - $x/L = 0.02$)	373
123	Contours of $\bar{u}\bar{v}$ Shear Stress (S-duct Inlet - $x/L = 0.02$)	374

List of Figures

124 CFD Calculation Grid	375
125 Axial Variation of Boundary Layer Displacement Thickness - (CFD vs. Experiment)	376
126 Axial Variation of Boundary Layer Momentum Thickness - (CFD vs. Experiment)	377
127 Axial Variation of Boundary Layer Shape Parameter - (CFD vs. Experiment)	378
128 Axial Variation of Friction Velocity - (CFD vs. Experiment)	379
129 Comparison of Measured (LDA) and Predicted Streamwise Velocity Profiles	380
130 Comparison of Measured (5HP) and Predicted Streamwise Velocity Profiles	381
131 Comparison of Measured (LDA) and Predicted Radial Velocity Profiles	382
132 Comparison of Measured (5HP) and Predicted Radial Velocity Profiles	383
133 Comparison of Measured and Predicted Streamwise Normal Stress Profiles (\overline{uu})	384
134 Comparison of Measured and Predicted Cross-stream Normal Stress Profiles (\overline{vv})	385
135 Comparison of Measured and Predicted Circumferential Normal Stress Profiles (\overline{ww})	386
136 Comparison of Measured and Predicted Reynolds Shear Stress Profiles (\overline{uv})	387
137 Comparison of Measured and Predicted Turbulent Kinetic Energy Profiles	388
138 Predicted Turbulent Kinetic Energy Dissipation Rate Profiles	389
139 Comparison of Measured and Predicted Normal Stress Ratio ($\overline{vv}/\overline{uu}$)	390
140 Comparison of Measured and Predicted Anisotropy Tensor Component a_{11}	391
141 Comparison of Measured and Predicted Anisotropy Tensor Component a_{22}	392
142 Comparison of Measured and Predicted Anisotropy Tensor Component a_{33}	393
143 Comparison of Measured and Predicted Anisotropy Tensor Component a_{12}	394
144 Predicted Reynolds Stresses in Core Region	395
145 Predicted Turbulent Kinetic Energy in Core Region	396
146 Predicted Shear Stress in Core Region	397

LIST OF PHOTOGRAPHS

	Page
1 Overall View of Test Rig	399
2 Rig Inner Wall	400
3 Air Intake	401
4 Compressor Rotor	402
5 Compressor Stator	403
6 Test Section	404
7 LDA Optical Arrangement and Traverse	405
8 Laser and Data Acquisition System	406

NOMENCLATURE

x, y, z	Cartesian co-ordinates
s, n, z	plane curvilinear co-ordinates
x, r, θ	cylindrical polar co-ordinates
x_i	general orthogonal co-ordinate directions
$\underline{i}, \underline{j}, \underline{k}$	unit vectors in the general orthogonal co-ordinate directions
U, V, W	velocity components in x, y, z directions
U_s, V_n, W_z	velocity components in s, n, z directions
V_a, V_r, V_θ	velocity components x, r, θ directions
U_e, V_e, W_e	velocity components in any local orthogonal co-ordinate system
U_i	components of the mean velocity vector \underline{U} in x_i direction
u_i	fluctuating velocity components
U_i	instantaneous velocity components [= $U_i + u_i$]
p	mean static pressure
p'	fluctuating static pressure
p	instantaneous static pressure [= $p + p'$]
Ω_i	components of the mean vorticity vector
$\overline{u_i u_j}$	components of the kinematic Reynolds stress tensor
$\overline{u_i u_j u_k}$	components of the triple velocity correlation tensor
$\overline{q^2}$	sum of the normal stresses [= $\overline{u_k u_k}$]
α	kinetic energy flux coefficient
β	pressure gradient parameter [= $(\delta^*/\tau_w)(\partial p/\partial s)$]
χ	pressure gradient parameter [= $(v/\rho U_\tau^3)(\partial p/\partial s)$]
δ	boundary layer thickness
δ^*	boundary layer displacement thickness
δ^{**}	boundary layer momentum deficit thickness
δ_{ij}	Kronecker delta [= 1 when $i=j$, = 0 when $i \neq j$]
ε_{ij}	dissipation rate tensor

Nomenclature

ε	dissipation rate of turbulent kinetic energy [$= \frac{1}{2} \varepsilon_{kk}$]
ϕ	angle of s relative to x
κ	Von Kármán constant (0.41)
ν	kinematic viscosity [$= \mu/\rho$]
μ	molecular viscosity
ν_t	turbulent viscosity [e.g. $= C_\mu k^2/\varepsilon$]
θ	boundary layer momentum thickness [$= \delta^{**} - \delta^*$]
θ	angle of r relative to y
ρ	air density [$= p/Rt$] (1.225 kg/m ³ on a standard day)
τ	shear stress [$= \mu \partial U / \partial n - \rho \bar{uv}$]
τ_w	wall shear stress [$= \mu (\partial U / \partial n)_w$]
ψ	stream function [$= \int dm / \dot{m}$]
ζ	fractional area [$= \int dA / A$]
h	fractional height [$= (n - n_i) / h$]
Δ	universal boundary layer thickness
a_{ij}	anisotropy tensor [$= (\bar{u}_i u_j / k) - \frac{2}{3} \delta_{ij}$]
b_{ij}	anisotropy tensor [$= \frac{1}{2} a_{ij}$]
c_p	specific heat at constant pressure (1004.4 Nm/kgK for air at 288.15 K)
h	passage height [$= n_o - n_i$]
k	turbulent kinetic energy [$= \frac{1}{2} \bar{u}_k u_k$]
n	cross-stream distance
\dot{m}	mass flow rate
p_a	atmospheric pressure (101325.4 N/m ² on a standard day)
r	radius
s	streamwise distance
t	time
t	static temperature
t_a	atmospheric temperature (288.15 K on a standard day)
\dot{v}	volume flow rate
x	distance in x direction (axial distance)
y	distance in y direction

Nomenclature

z	distance in z direction
A	area [$= 2\pi r_m h$]
B	blockage [$= 1 - \bar{U}/\bar{U}_p$]
C_f	skin friction coefficient [$= 2(U_\tau/U_{Mean})^2$]
C'_f	skin friction coefficient [$= 2(U_\tau/U_{p_w})^2$]
C_p	pressure coefficient [$= (p - \tilde{p}_{in})/(\tilde{P}_{in} - \tilde{p}_{in})$]
G	universal boundary layer shape parameter
H	boundary layer shape parameter [$= \delta^*/\theta$]
Π	second invariant of the anisotropy tensor [$= \frac{1}{2} b_{lm} b_{ml}$]
K_{eff}	effective curvature [$= 1/R_{eff}$]
L	S-shaped duct axial length [$= x_{m_{ex}} - x_{m_{in}}$]
N	rotational speed of compressor (rpm)
P	total pressure [$= p + Q$]
Q	dynamic pressure [$= \frac{1}{2}\rho U_{tot}^2$]
R	geometric radius of curvature [$= \partial\phi/\partial s$]
R	gas constant (287.05 Nm/kgK for pure air)
R	Reynolds number
R_θ	Reynolds number based on θ and U_{Mean}
R'_θ	Reynolds number based on θ and U_{p_w}
R_t	turbulent Reynolds number [$= k^2/v\varepsilon$]
R_{uv}	shear stress correlation coefficient [$= \bar{uv}/(\bar{uu}\bar{vv})^{1/2}$]
T	total temperature
U_τ	friction velocity [$= (\tau_w/\rho)^{1/2}$]
U_{blade}	compressor blade speed
U_{Mean}	reference mean velocity at inlet [$= \bar{U}_{in}$]
U_p	potential velocity
U_{tot}	magnitude of the velocity vector [$= \sqrt{U_k^2}$]
P_{ij}	Reynolds stress production tensor
P	production of turbulent kinetic energy [$= \frac{1}{2} P_{kk}$]

Subscripts

i	inner wall ($\hbar = 0.0$)
m	mid-height ($\hbar = 0.5$)
o	outer wall ($\hbar = 1.0$)
in	S-shaped duct inlet ($x/L = 0.0$)
ex	S-shaped duct exit ($x/L = 1.0$)
w	wall value
c	core region

Superscripts

—	time average [$= \frac{1}{T} \int_T dt$]
~	area-weighted spatial average [$= \frac{1}{A} \int_A dA$]
~	mass-weighted spatial average [$= \frac{1}{m} \int_A dm$]
+	non-dimensional quantities based on wall U_t and v
*	non-dimensional quantities based on U_{Mean} and h_{in}

Tensor Notation

Indices are used as shorthand to represent a particular quantity in each co-ordinate direction in turn. Thus, U_i represents the three components of the velocity vector, $\overline{u_i u_j}$ represents the nine components of the Reynolds stress tensor (of which 6 are independent) and $\overline{u_i u_j u_k}$ represents the 27 components of the triple velocity correlation tensor (of which 10 are independent). When equations are written in tensor notation, indices that occur only once per term take a particular value for that equation. For all indices that occur more than once in any term, however, a summation is implied for the components represented by the repeated indices.

CHAPTER 1 INTRODUCTION

	Page
1.1 Annular S-shaped Ducts	2
1.1.1 The Gas Turbine Application	2
1.1.2 Duct Geometry	3
1.1.2.1 Annulus Parameters	3
1.1.2.2 S-shaped Duct Parameters	4
1.2 Flow in Annular S-shaped Ducts	5
1.2.1 Ideal Behaviour	6
1.2.1.1 The Pressure Field	6
1.2.1.2 Velocity Field	8
1.2.2 Actual Behaviour	9
1.2.2.1 Wall Boundary Layers	10
1.2.2.2 Inlet Conditions	11
1.3 Review of Related Work	13
1.3.1 Turbulent Boundary Layers	14
1.3.2 The Effect of Pressure Gradient on Turbulent Boundary Layers	16
1.3.2.1 Favourable Pressure Gradient	16
1.3.2.2 Adverse Pressure Gradient and Separation	17
1.3.2.3 Alternating Pressure Gradient	19
1.3.3 The Effect of Curvature on Turbulent Boundary Layers	20
1.3.3.1 Mild Curvature	21
1.3.3.2 Strong Curvature	24
1.3.4 Combined Effects of Pressure Gradient and Curvature	27
1.3.4.1 Related Investigations	28
1.3.4.2 S-shaped Ducts	29
1.3.5 Inlet Conditions	30
1.3.6 Conclusions from the Review	31
1.4 Objectives of the Present Investigation	32
1.4.1 Contents of the Thesis	34

A prerequisite for the successful design of any aerodynamic device is a fundamental physical understanding of the flow behaviour. In this thesis, the flow through an annular S-shaped duct is studied thoroughly, in order to obtain such knowledge. As well as providing aerodynamic conditions of academic interest, S-shaped ducts are of practical significance to the gas turbine industry, which needs to be able to design the 'optimum' duct for a particular application. Nowadays, the aerodynamic design process can be guided greatly by the use of Computational Fluid Dynamics (CFD) methods, but the accuracy of such methods will be unknown unless the predictions are compared with good quality experimental data. The primary objective of this investigation, therefore, was to acquire comprehensive data in a representative annular S-shaped duct, enabling the physical behaviour of the flow to be understood. Furthermore, by predicting the flow using standard CFD techniques, this thesis also aims to provide useful information on the performance of the various models employed to solve the equations governing the flow. Before considering the details of the experimental investigation, however, and before examining the results and predictions, it is necessary to build up a basic understanding of the problem. In this chapter, therefore, the most significant features will be identified by reference to previous experience.

1.1 Annular S-shaped Ducts

An annular S-shaped duct is an aerodynamic passage, used to redirect a fluid from one radial position to another without significantly altering the flow direction. To achieve this, the duct must firstly turn the fluid away from the original direction and then turn it back again, giving rise to the S-shape.

1.1.1 The Gas Turbine Application

The present investigation is concerned with S-shaped ducts found within aircraft gas turbine engine compression systems (Fig. 1). Current large civil engine designs employ high pressure ratios, typically in the range 30 to 40, which can only be generated by the use of many axial compressor stages. However, these high pressure ratios cannot be achieved using a single spool compressor, since it becomes aerodynamically unstable when operating significantly below its design speed, due to positive incidence stalling of the front stages. To avoid this problem, it is usual to split the compression process between several spools, which, together with other techniques, reduces the incidence seen by the front stages of each compressor at part speed.

In multi-spool gas turbine engines, optimisation of the compression system leads to a reduction in the mean diameter of each successive spool. Whilst employing the

maximum achievable stage loading ($C_p \Delta T / U_{blade}^2$), the highest possible blade speed is required in order to maximise the work input per stage; thereby minimising the number of stages and engine weight. In addition, reducing the hub-tip ratio has a beneficial effect on stage efficiency, which, since the required flow area (A) is fixed, can be achieved by reducing the mean diameter. In order to obtain the required blade speed, therefore, the rotational speed of the compressor (N) must increase. Furthermore, in order to maintain the flow coefficient (V_a / U_{blade}) consistent with an efficient design, the annulus area decreases through the engine as the air density increases. However, with mechanical stress proportional to AN^2 , a reduction in mean diameter can only be tolerated at the high pressure end of the compressor, where the reduced area allows higher rotational speeds to be achieved without stress limits being exceeded. In addition, for flow stability reasons, the mean diameter of a particular spool remains nearly constant. Consequently, the reduction in diameter tends to occur between the spools, giving rise to the need for an annular S-shaped duct to connect the compressors.

Although the compressor interconnecting duct application is the main focus of the present investigation, similar ducts can also be found in other parts of gas turbine engines. For example, they are used between the turbine spools, where the mean diameter increases, and also within the combustion chamber, where they are used to channel air to the annuli surrounding the flametube. In many gas turbine applications streamlined struts pass through the S-shaped duct, and these are often used to carry mechanical loads from the core of the engine to the outer structure, as well as allowing oil and air feeds and mechanical drives to pass through the engine. Although struts are important, they were not considered as part of the present investigation.

1.1.2 Duct Geometry

Several parameters are used to define the geometry of an annular S-shaped duct. These describe the size of the annulus through which the flow passes, and characterise the overall changes that occur between inlet and exit.

1.1.2.1 Annulus Parameters

The following parameters can be used to describe the annular flow path, which has an inner radius (r_i) and outer radius (r_o), relative to the engine centreline.

Mean radius (r_m) is defined as,

$$r_m = (r_i + r_o) / 2 \quad 1.1$$

Annulus height (h) is defined as,

$$h = r_o - r_i \quad \dots\dots 1.2$$

Annulus area (A) is given by,

$$A = \pi(r_o^2 - r_i^2) = 2\pi r_m h \quad \dots\dots 1.3$$

In addition, hub-tip ratio (HTR) is a non-dimensional parameter describing the ratio of the inner and outer radii, i.e.,

$$HTR = r_i/r_o \quad \dots\dots 1.4$$

1.1.2.2 S-shaped Duct Parameters

There are three basic characteristics which need to be described. These are the change in radius, the change in area and the length (L) of the duct. Using subscripts 'in' and 'ex' to denote the inlet and the exit, respectively, mean radius ratio (MRR) is defined as,

$$MRR = \frac{(r_m)_{ex}}{(r_m)_{in}} = \frac{(r_i + r_o)_{ex}}{(r_i + r_o)_{in}} \quad \dots\dots 1.5$$

Area ratio (AR) is defined as,

$$AR = \frac{A_{ex}}{A_{in}} = MRR \frac{h_{ex}}{h_{in}} \quad \dots\dots 1.6$$

and non-dimensional length (NDL) as,

$$NDL = L/h_{in} \quad \dots\dots 1.7$$

Furthermore, in order to obtain a smooth and continuous flow path, there is a need to align the ends of the duct with the direction of the upstream and downstream passages (see Fig. 1). Consequently, the duct has a characteristic S-shape as the radius varies along its length, and the geometrical curvature of the two bends will be of a similar magnitude but of opposite sense.

The shape of the duct can be described by any mathematical function which relates the radius of the mean line (r_m) to an axial position (x). Within each bend, the maximum radius of curvature of this line can be calculated. For example, the mean line could be defined by a cubic spline, with four constraints of position and zero slope at each end. In this case, the maximum radius of curvature (R) of the line, which occurs at the ends, can be calculated in terms of MRR, NDL and HTR_{in} , and non-dimensionalised by the

inlet height (h_{in}), to give an equation for estimating the geometric curvature (h_{in}/R) of the duct, i.e.,

$$\frac{h_{in}}{R} = 3 \frac{(1 - MRR)}{(NDL)^2} \frac{(1 + HTR_{in})}{(1 - HTR_{in})} \quad \dots\dots 1.8$$

This shows that, for a given inlet geometry (HTR_{in} fixed), the curvature of the mean line is proportional to $(1 - MRR)/(NDL)^2$.

The position of the inner and outer annulus walls is fixed by any two of the ‘annulus’ parameters (described in Section 1.1.2.1). Since all of these can vary from inlet to exit of the duct, the shape of the annulus walls can be specified as a variation of these along the length of the duct; for example, an area distribution along a mean line. Alternatively, the inner and outer annulus walls can be specified as individual functions, i.e.,

$$r_i = f_i(x_i) \quad \text{and} \quad r_o = f_o(x_o) \quad \dots\dots 1.9$$

In this case, the functions (f_i and f_o) must ensure that the annulus walls pass through the four ‘corner points’, which are determined to give the required MRR, AR and NDL for a given HTR and inlet height. To avoid any sharp corners in the duct, the functions must be continuous and constrained to ensure that their first derivatives match that of the upstream and downstream annulus walls, which would again give rise to an S-shape. With reducing radius, the inner wall will be convex in the first part of the duct, followed by a concave region, whereas the outer wall will be initially concave, and then convex in the latter part of the duct.

1.2 Flow in Annular S-shaped Ducts

Having described the basic shape of the duct, it is necessary to consider its basic aerodynamic properties, and identify the features that are likely to be important. In order to establish the underlying behaviour, the ideal situation is considered first, which, although over-simplistic, provides a basic level of understanding prior to examining the actual flow behaviour in more detail. By way of introduction, the most important features of the flow, such as the presence of turbulent boundary layers along the annulus walls, are identified. The behaviour of the turbulent flow within these boundary layers, when subjected to the conditions found within an S-shaped duct, not only determines the main subject area of the subsequent literature review, but of the experimental and theoretical investigation as a whole.

1.2.1 Ideal Behaviour

By assuming that the flow is inviscid, it is possible to establish how it would behave under ideal conditions. By neglecting viscosity, the equations governing the motion of the fluid are much simplified, and, with further constraints, simple relationships linking the static pressure and the streamwise velocity can be obtained.

1.2.1.1 The Pressure Field

In order to turn a flow, there must be a modification of static pressure (p). For inviscid flow, moving with velocity (U) in a circular path of radius (R), the radial pressure gradient ($\partial p / \partial r$) necessary to maintain the flow in radial equilibrium is given by,

$$\frac{1}{\rho} \frac{\partial p}{\partial r} = \frac{U^2}{R} \quad \dots\dots 1.10$$

Note that the co-ordinate r , used here by way of example, is not the same as the true radius (r). Also, the radius of curvature (R) is a particular value of r in the example only, and is not the same as the geometric radius of curvature (R), relating to the s-n co-ordinate system used later in this thesis.

To generate the centripetal acceleration associated with circular motion, it is apparent from Eq. 1.10 that there will be a pressure gradient in the r -direction. Although the flow within the bends of an annular S-shaped duct will not be truly circular, it is clear that the pressure must increase from the convex to the concave side of each bend. Within the first bend, therefore, the pressure increases from the inner wall to the outer wall. Since the flow is nominally returned to the axial direction by the second bend, the pressure gradient across this part of the duct is reversed, such that the inner wall pressure will be higher than that of the outer wall.

Assuming that, for irrotational flow, U is given by Eq. 1.18 (see Sect. 1.2.1.2), the variation of pressure with r can be obtained by integrating Eq. 1.10, i.e.,

$$C_p = 1 - (R_m/r)^2 \quad \dots\dots 1.11$$

where the pressure coefficient (C_p) is defined as,

$$C_p = \frac{p - p_m}{\frac{1}{2} \rho U_m^2} \quad \dots\dots 1.12$$

and pressure (p_m) and velocity (U_m) occur at $r = R_m$.

Across a duct of height (h), the difference in C_p between the inner and outer walls ($\Delta C_p = C_{p_o} - C_{p_i}$) can be obtained by assuming that the flow rotates about a common centre, at a distance R_m from the mid-height position of the duct. In this way, it can be assumed that the radius of curvature of the flow at the nominal position of each wall is given by, $r_i = R_m - h/2$ and $r_o = R_m + h/2$. With these, Eq. 1.11 can be used to obtain the C_p at each wall, and, therefore, the difference across the duct,

$$\Delta C_p = \frac{32(h/R_m)}{(4 - (h/R_m)^2)^2} \quad \dots\dots 1.13$$

Moreover, for small h/R_m (< 0.2), $\Delta C_p \approx 2(h/R_m)$.

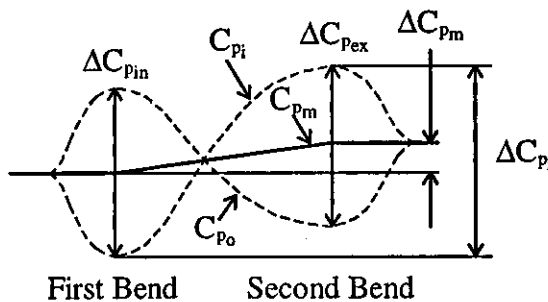
Across each bend, therefore, the pressure difference depends on the non-dimensional curvature of the flow (h/R_m), which is related, but not equal, to the geometric curvature of the duct. However, by assuming that R_m is equal to the mid-height geometric curvature, which itself can be estimated from Eq. 1.8, it is possible to obtain an approximate ΔC_p across a given duct.

As well as the pressure variation due to curvature, the mean pressure can vary along the duct if the area changes. For inviscid flow, the ideal change in C_p from duct inlet to exit (ΔC_{p_m}) is given by,

$$\Delta C_{p_m} = 1 - (AR)^{-2} \quad \dots\dots 1.14$$

With increasing area ($AR > 1.0$), therefore, the pressure will increase, whilst it will reduce when $AR < 1.0$.

By way of example, the diagram below shows the streamwise pressure gradients that result in an S-shaped duct of increasing area, where the reversal of the cross-stream pressure gradient combines with an increase in the mean pressure.



Pressure Distribution

Along the inner wall, for example, the pressure (C_{pi}) will increase from inlet to exit, unless the area reduces by a substantial amount. An estimate of this change in pressure (ΔC_{pi}) can be obtained by combining $\frac{1}{2} \Delta C_{pin} + \frac{1}{2} \Delta C_{pex} + \Delta C_{pm}$ (remembering that ΔC_{pex} across the second bend is non-dimensionalised by $(\frac{1}{2} \rho U_m^2)_{ex}$ and needs to be multiplied by $(AR)^{-2}$ to make it compatible with ΔC_{pin} and ΔC_{pm}). Using the simple expressions for the various contributions results in,

$$\Delta C_{pi} = [h/R_m]_{in} + [1 - (AR)^{-2}] + [h/R_m]_{ex} (AR)^{-2} \quad 1.15$$

which is non-dimensionalised with respect to the inlet dynamic pressure $(\frac{1}{2} \rho U_m^2)_{in}$. This expression provides a very simple means of assessing the static pressure rise along the inner wall which, as will become apparent, has a very important effect on the flow. This simple method, together with the assumption that the flow curvature is directly related to the geometric curvature (e.g., Eq. 1.8), can be used to assess the affect of varying the basic geometric parameters of the S-shaped duct. Increasing the curvature, by reducing the length (NDL^2) or by increasing the change in radius ($1 - MRR$), will increase the pressure rise. By specifying a maximum ΔC_{pi} , which is known to produce satisfactory operation, it is possible to design a minimum length duct (for a given MRR) to meet this requirement. This approach, which forms the basis of the design methods used by industry, was used to specify the basic geometry of the annular S-shaped duct used in the present experimental investigation, as described in Chapter 2 (Sect. 2.1.3).

1.2.1.2 Velocity Field

By assuming that the flow is inviscid, it is possible to establish an ideal velocity distribution within the curved flow region. For this simple approach, it is assumed that the inlet velocity is constant across the duct so that the flow can be considered to be irrotational. Thus, for zero vorticity,

$$\frac{1}{r} \frac{\partial(rU)}{\partial r} = 0 \quad 1.16$$

Across the flow, therefore, the variation of velocity in the r -direction can be obtained by integrating Eq. 1.16, i.e.,

$$rU = constant \quad 1.17$$

For irrotational (free-vortex) flow, therefore, U is inversely proportional to r , and, with $U = U_m$ when $r = R_m$, the velocity distribution is given by,

$$U = \frac{R_m U_m}{r} \quad 1.18$$

However, even for inviscid irrotational flow through an annular S-shaped duct, this is an oversimplification. A full solution of the governing (Euler) equations, with an irrotational inlet condition, would lead to a different result. The reason for this is that the flow is constrained by the duct walls, which determine the curvature of the bounding streamlines. In addition, within the duct the streamlines are dependent on the actual velocity distribution, which is related to the pressure field, which, in turn, is related to the curvature of the streamlines. As a result of this coupling between the flow variables (described by the simultaneous partial differential equations), the flow in each bend will not rotate about a common point and, therefore, the radius of curvature of any streamline in the flow cannot be described by a simple linear function of the cross-stream co-ordinate (i.e., r itself).

In addition, the curvature of the flow will be less than that suggested by the geometric curvature of the duct. This effect can be understood by considering the streamline dividing the mass flow in half. Since the velocity increases over the convex surfaces and reduces near the concave, the dividing streamline will be relatively closer to the convex side of each bend, in comparison to a line dividing the flow area in half, and consequently will be less curved. Therefore, the pressure difference across the bends of the duct, and the pressure rise along the inner wall, will be somewhat less than that suggested by the geometrical radius of curvature (Eq. 1.13). Given this important inviscid effect, obtained without consideration of the actual behaviour, it is clearly necessary to predict the flow, at the very least with an inviscid method, to obtain the pressure variation within the duct.

1.2.2 Actual Behaviour

In reality, the most important influence on the flow behaviour arises from its viscosity. The most fundamental effect of viscosity, which can be considered to be a homogeneous fluid property, is to ensure that the flow has zero velocity when it is in contact with a solid surface. Thus, above a surface, the streamwise velocity (U) must take on a sheared distribution, as it increases up to the velocity of the main stream. In general, the rate of change of any velocity component (U_i) with distance in any direction (x_j) is the shear strain rate $\partial U_i / \partial x_j$, and, above a surface, the predominant strain rate relates to the variation of U in the direction perpendicular to the surface (n), i.e., $\partial U / \partial n$. The shear layer adjacent to a surface, in which $\partial U / \partial n$ is finite, is referred to as a boundary layer.

1.2.2.1 Wall Boundary Layers

Along the solid walls of the annular S-shaped duct, boundary layers will be present in the flow. However, the extent to which this is important depends on the size of the affected region in comparison to the rest of the flow, and also on the state of the boundary layer. Depending on the Reynolds number, as determined by a characteristic velocity and length scale in relation to the viscosity, the boundary layer can be either laminar or, above a critical value, turbulent. Within a boundary layer, the shear strain rate gives rise to shear stress. This arises both due to the viscosity of the fluid and, when the boundary layer is turbulent, due to the correlation between the fluctuating velocity components of the turbulent motion ($\bar{u_i} \bar{u_j}$), which are known as Reynolds stresses. Note that $\rho \bar{u_i} \bar{u_j}$ strictly has the dimensions of stress, but, for incompressible flow, it is more convenient to refer to the corresponding kinematic quantities as stresses; a convention adopted throughout this thesis. For a simple turbulent boundary layer, the viscous stress ($\nu \partial U / \partial n$) and Reynolds stress (\bar{uv}) both exist. At high Reynolds numbers, the Reynolds stress is much larger than the viscous stress, except in a small region close to the wall known as the viscous sub-layer. As the wall is approached, the Reynolds stress reduces, becoming zero at the wall, and the viscous stress increases, due to the rapidly increasing strain rate. At the wall, therefore, there is a finite shear stress, due entirely to viscosity, which is known as the wall shear stress. As the Reynolds number reduces, the size of the viscous sub-layer increases, and at a sufficiently low Reynolds number, there will be no significant turbulent motion, i.e., the shear stress will arise only from the viscosity, and the boundary layer will be laminar.

In setting up an experiment to represent a real gas turbine flow, the Reynolds number needs to be as representative as possible. For a gas turbine, the Reynolds number based on passage height and mean flow velocity will be of order 10^6 , but it is virtually impossible to achieve such values in laboratory experiments. Even so, at practicable levels of order 10^5 , the boundary layer will effectively be the same. Even though the viscous sub-layer will be an order of magnitude thicker in the experimental flow, at these relatively high values of Reynolds number the viscous sub-layer will be so small, in comparison to the overall thickness, that it will have a relatively small influence on the behaviour of the turbulent boundary layer.

In measuring the detailed behaviour of a boundary layer, it would be desirable to obtain data in, or at least close to, the viscous sub-layer. Most instrumentation, however, can only obtain measurements within a finite distance of the wall, and so it is desirable for the viscous sub-layer to be as large as possible. This could be achieved by using a large experimental facility, such that, at a given Reynolds number, the size of the boundary layer increases in proportion to the size of the facility. Usually, however, the size is

limited by the space available within an existing university laboratory, and by the large cost involved. Alternatively, within these constraints, the size of the sub-layer can be increased by reducing the Reynolds number, but, if this is reduced too much, detailed measurements will be obtained in an unrepresentative boundary layer. In a laboratory experiment, therefore, the practical limitation on Reynolds number does have the advantage of allowing measurements to be made closer to the viscous sub-layer, but care must be taken to ensure that the overall behaviour is not affected significantly.

For an annular S-shaped duct, the overall effectiveness will be dependent on the behaviour of the turbulent boundary layers. Since streamwise pressure gradients are present, it is necessary to consider the influence of these on the boundary layers. In particular, regions of increasing pressure tend to decelerate the flow, and in a boundary layer where the velocity adjacent to the wall is already low, the adverse pressure gradient may cause the near-wall flow to reverse, thus separating the boundary layer from the wall. In the gas turbine application, this is of concern since the velocity distribution across the passage would become very distorted, and, as a consequence, might adversely affect the performance of the downstream compressor. It is essential, therefore, that the flow within the annular S-shaped duct remains attached. Clearly, turbulent boundary layers can flow against adverse pressure gradients without separating, but, if the magnitude of the pressure gradient is severe, separation might occur. In order to design an annular S-shaped duct which reduces the mean radius in the shortest possible distance, it is necessary to increase the severity of the pressure gradients, without incurring flow separation. To do this successfully, however, requires the behaviour of turbulent boundary layers to be well-understood and, more importantly, that this can be predicted accurately by CFD methods.

1.2.2.2 Inlet Conditions

In considering the flow in annular S-shaped ducts, it is necessary to examine the nature of the inlet flow. In the gas turbine application, the most obvious influence on the inlet flow is the presence of an axial compressor upstream of the duct. An axial compressor is formed by combining rotating blade rows with stationary rows, the purpose of which is to increase the total pressure of the flow. The rotor adds energy to the flow, increasing its total temperature, but not all of the available energy is converted into total pressure, so the compressor is less than 100% efficient. The origin of much of this inefficiency is the loss of total pressure within the blade surface boundary layers, which merge at the trailing edge to form wakes. Every blade, whether rotating or stationary, will produce a wake in the flow, and, hence, introduce an aerodynamic loss.

The complexity of the flow will depend on the number of upstream compressor stages, with each stage producing rotating and stationary wakes. As the flow from one row moves downstream, the wakes will decay, and the circumferential variation of velocity will reduce. However, although the rotating blades cut through the stationary wakes, and vice versa, the wakes remain visible as they pass through the subsequent rows. In addition, the annulus wall boundary layers and the blade wakes interact, giving rise to an even more complicated situation, and there is a distinct possibility of flow separation occurring within the corner region between the annulus walls and the suction surface of the blades. Over a range of operating conditions, the efficiency of a real multistage compressor will vary. At lower speeds, in particular, it becomes increasingly difficult to operate the compressor efficiently, as the amount of flow separation increases, and, at some point, a particular blade row will stall and lead to a complete breakdown of the flow through the whole compressor (i.e., surge).

To investigate the flow through an annular S-shaped duct, therefore, it is necessary to create experimental conditions which are representative of the complex environment of a real gas turbine. This is difficult to achieve within the constraints of a university laboratory, but, as a minimum requirement, the experimental test rig ought to have a single stage compressor upstream of the duct. Although more stages would be desirable, the three-dimensional (3D) flow produced by a single stage axial compressor would be sufficiently complex to be representative of a real gas turbine, whilst maintaining the academic quality of providing a test case for 3D CFD predictions. Within the S-shaped duct, in particular, the combined behaviour of the stator blade wakes and the annulus wall boundary layers can be studied more easily. In addition, the rotating wakes from the rotor can be considered as a steady (time-average) phenomena, tending to increase the level of 'pseudo' turbulence within the flow, and so it ought to be possible to compare the measured behaviour with steady 3D predictions; provided that the inlet conditions to the calculation are sufficiently well-defined.

Without a compressor stage present, the flow in an annular S-shaped duct would be circumferentially uniform and, therefore, two-dimensional (2D). Often, this is referred to as 2D axisymmetric, to distinguish it from a 2D rectangular flow, in which the test section is rectangular with a reasonably large aspect ratio. As far as inlet conditions are concerned, the only relevant consideration in the 2D axisymmetric case is the thickness of the wall boundary layers, in comparison to the height of the annular passage. To enable detailed measurements to be made, the boundary layers need to be as large as possible at inlet to the duct. Using a parallel duct upstream of the test section, the thickness of the incoming boundary layers can be increased, and, if sufficient length is provided, these would meet in the middle and eventually become fully developed.

However, by ensuring that the wall boundary layers remain isolated by an inviscid irrotational core region, it is easier to understand their behaviour within the S-shaped duct, which will be very different along each wall. Moreover, the resultant flow would be ideally suited for the testing of CFD methods, where it would only be necessary to carry out a 2D calculation. On comparing the predicted behaviour of the annulus wall boundary layers with the experimental data, it would be possible to assess, in some detail, the various models used in solving the equations governing the flow.

In considering inlet conditions, the possibility of having swirl within the flow cannot be overlooked. Certainly, it must be remembered that a 2D axisymmetric flow can have a component of velocity in the circumferential direction, and this too would be of interest for CFD validation. As a starting point, however, the present investigation is concerned only with swirl free flow, as this provides a datum against which any future swirling flow investigation can be compared. In addition, the majority of gas turbine annular S-shaped ducts operate with zero swirl since, traditionally, axial compressors were designed with zero swirl between each stage. Also, from a practical point of view, it is very difficult to generate swirling inlet conditions which are truly 2D, since the swirl has to be produced by rotating or stationary blades, whereas it is relatively simple to create swirl free inlet flow.

1.3 Review of Related Work

In annular S-shaped ducts, the flow will be influenced by the combined effect of pressure gradient and curvature. Already, it is clear that the geometry of the duct gives rise to streamwise pressure gradients, both adverse and favourable, which will influence the development of the annulus wall boundary layers. In addition, however, it will be seen that streamwise curvature has a significant effect on turbulent flow. Although these effects have been mainly studied in isolation, a significant understanding can be gained from these investigations. In the following literature review, therefore, the properties of turbulent boundary layers are examined, particularly the way in which they are influenced by streamwise pressure gradients. In addition, the effect of curvature is considered, especially the differing effects of convex and concave surface curvature, of varying magnitude, on turbulent boundary layers. Although some studies have involved the combined effects of pressure gradient and curvature, none of them are similar to the present annular S-shaped duct investigation.

In this review, many experimental investigations are cited. These have been grouped according to their subject area, and, for each, a brief description and summary of the relevant conclusions is given. Although undoubtedly incomplete, this review is

nonetheless comprehensive. As well as providing a useful overview, and lead into the vast amount of available information, it allows a good understanding of the relevant flow situations to be gained. Note that a separate review of the work related to the numerical prediction of turbulent flow is given in Chapter 5 (Sect. 5.1.1).

1.3.1 Turbulent Boundary Layers

A good introduction and general overview of turbulent boundary layers can be obtained from Schlichting^[135], Rotta^[132], Townsend^[175], Cebeci and Bradshaw^[31] and Hinze^[68]. However, the following sections provide a more detailed selection of material relevant to the present investigation.

Because of its simplicity, many investigations have studied the flow over a flat surface. For example, mean velocity and turbulence measurements were made in a turbulent boundary layer ($R_\theta \approx 6000$) with zero pressure gradient by Klebanoff^[84], who found that the mean velocity distribution could be divided into three regions; a viscous region extending to $y^+ \approx 30$, an intermediate region with log-linear behaviour extending to $y/\delta \approx 0.2$ and an outer intermittent region. The total shear stress was found to increase from zero at the edge of the boundary layer up to a finite value at the wall, where the distribution attained zero slope. In addition, the turbulence intensities were found to increase towards the wall, but these were highly anisotropic. Very close to the wall, the largest component ($\overline{uu}^{\frac{1}{2}}$) was seen to increase rapidly, whereas the smallest component ($\overline{vv}^{\frac{1}{2}}$) reduced, and this region was shown to be extremely important for both the production and dissipation of turbulent energy.

Clauser^[37] investigated the mean velocity distribution of equilibrium turbulent boundary layers with zero, moderate and strong adverse pressure gradients. By arranging for constant values of pressure gradient parameter (β), with magnitudes 0, 2 and 7 respectively, the boundary layers were maintained in equilibrium throughout their development. In each case, the boundary layer was found to develop with a universal velocity distribution [$(U - U_e)/U_\tau$ vs. y/δ]; with universal thicknesses (Δ/δ) of 3.6, 6.4 and 12.0 and shape parameter (G) of 6.1, 10.1 and 19.3 respectively. In addition, the 'Clauser chart' method for determining skin friction coefficient (C_f) was originated, in which the mean velocity profile is plotted as U/U_e vs. $\log(y U_e/v)$ on to a chart which shows lines of constant C_f [$= 2(U_\tau/U_e)^2$] obtained from the universal law-of-the-wall, or log-law, i.e., $U/U_\tau = 5.6 \log(y U_\tau/v) + 4.9$. Similarly, Coles^[38] showed that the mean velocity in the outer 'wake' region of a turbulent boundary layer could be represented by a simple universal function. When used in conjunction with the log-law, this function,

scaled by a wake strength parameter (Π), was found to describe reasonably the mean velocity distribution in a number of turbulent boundary layer flows.

Again for equilibrium turbulent boundary layers, Bradshaw^[16] made measurements of the mean velocity and turbulence, including the triple velocity correlations pertaining to the transport of turbulent kinetic energy, allowing a better understanding of the energy balance to be established. For the zero, moderate and strong adverse pressure gradient cases investigated, it was found that the distribution of parameters such as turbulent viscosity, mixing length and \bar{uv}/q^2 were similar. In addition, detailed mean flow and turbulence measurements in zero pressure gradient turbulent boundary layers were performed by Murlis et al.^[110], over a range of low Reynolds numbers. These showed that there was a significant variation in both the shape of the mean velocity profile and the turbulence structure up to a R_θ of about 5000. At low Reynolds number the mean velocity had a smaller 'wake', consistent with an increased skin friction coefficient. Further, the Reynolds stresses were shown to vary significantly with Reynolds number, as was the ratio \bar{uu}/\bar{vv} which reduced rapidly with reducing R_θ ; but the triple velocity correlations were found to remain fairly constant. Using data from a direct numerical simulation of turbulent boundary layer flow at $R_\theta=225$ and 1410, Spalart^[156] showed that the normal stresses \bar{uu} and \bar{ww} (normalised by U_τ and v) increased with increasing Reynolds number in the near-wall region (unlike U and \bar{uv}), in broad agreement with experimental data.

It is now widely accepted that the velocity in the near-wall region of a turbulent boundary layer is proportional to the wall friction velocity (U_τ), for a wide range of flows, and has a linear distribution when plotted against $\log(y U_\tau/v)$. However, in a recent critique, Bradshaw and Huang^[23] showed that in many situations the basic assumptions made in deriving the log-law are invalidated, casting doubt on its universality.

Very close to solid surfaces, the turbulence in a boundary layer is affected by the presence of the wall. Although direct numerical simulation is now able to provide detailed information, several experimental investigations have also concentrated on obtaining data in this region. For example, Johansson and Karlsson^[75] used their laser anemometry data to calculate the magnitude of the terms in the turbulent kinetic energy transport equation, and showed good agreement with the direct numerical simulation data of Spalart^[156]. In addition, in the near-wall region of a turbulent boundary layer, Karlsson^[82] determined the constants in the asymptotic expressions for the near-wall Reynolds stresses.

Using large-eddy simulation, with the unresolved sub-grid scale turbulence obtained using an eddy-viscosity model, Moin and Kim^[107] were able to predict fully developed channel flow ($R = 13,800$) in great detail, and showed that the computed statistics were in good agreement with experimental data. By obtaining the magnitude of the various terms in the Reynolds stress transport equations, they observed a ‘splatting’ effect in the near-wall pressure-strain which was responsible for transferring turbulent energy from the normal to the horizontal components. In addition, Kim et al.^[83] carried out a direct numerical simulation of fully developed turbulent channel flow ($R = 3300$), which was in good agreement with experimental measurements. This was used by Mansour et al.^[102] to calculate the magnitude of the terms in the Reynolds stress and dissipation rate transport equations, which showed that all the terms became important close to wall, and that existing Reynolds stress transport equation turbulence models were unable to reproduce the exact behaviour; and needed to be improved.

1.3.2 The Effect of Pressure Gradient on Turbulent Boundary Layers

In practical flows, the static pressure rarely remains constant in the streamwise direction. When the pressure is decreasing, the favourable pressure gradient will influence a turbulent boundary layer; but with no serious consequence. When the pressure is increasing, however, the adverse pressure gradient may cause a turbulent boundary layer to separate from the surface, often with serious consequences. The behaviour of boundary layers under the influence of pressure gradients, particularly adverse ones, has been researched in great detail.

1.3.2.1 Favourable Pressure Gradient

In the presence of a strong favourable pressure gradient, Patel^[115] found that the mean velocity profile deviated substantially from the log-law, which was confirmed by Patel and Head^[118]. This was thought to be associated with a tendency to revert to a laminar state, and it was suggested that the distribution of shear stress was an important factor in initiating this reverse transition. Similarly, Blackwelder and Kovasznay^[14] subjected a turbulent boundary layer to a strong favourable pressure gradient and found that the measured mean velocity profiles differed from the log-law. In this case, the Reynolds stresses were measured, and were found to remain approximately constant along mean streamlines in the outer layer, but to increase near the wall. However, when non-dimensionalised by the increasing local free stream velocity, the Reynolds stresses were effectively reduced. The concept of ‘relaminarization’ in highly accelerated flows was examined by Narasimha and Screenivasan^[112], who concluded that this was essentially due to the dominance of the pressure forces over the slowly responding

Reynolds stresses. This gave rise to a ‘quasi-laminar’ flow, in which the Reynolds stresses had no significant effect on the mean flow. In addition, Spalart^[155] carried out a direct numerical simulation of a turbulent boundary layer for several values of an acceleration parameter (K). The favourable pressure gradient was found to increase the extent of the log-law region and alter the energy balance of the turbulence near the edge of the boundary layer, and relaminarization was found to occur at $K=3\times10^{-6}$, with a corresponding $R_\theta = 330$.

1.3.2.2 Adverse Pressure Gradient and Separation

When a boundary layer is subjected to an adverse pressure gradient, the streamwise velocity will reduce. Unlike a laminar flow, a turbulent boundary layer can flow against the increasing pressure, to a limited extent, due to the turbulent transport of momentum towards the wall. However, when the pressure gradient is too severe, or sustained for too long, separation of the flow will occur. Schubauer and Klebanoff^[137] measured the shear stress in a turbulent boundary layer subjected to an adverse pressure gradient, and found that it increased with increasing distance from the wall, reaching a maximum away from the wall, before falling to zero at the edge of the boundary layer. In the near-wall region, the shear stress gradient normal to the wall counteracted the streamwise pressure gradient and reduced the deceleration, such that the velocity adjacent to the surface remained positive for some distance before separation eventually occurred. However, adverse pressure gradients do not always lead to separation. For example, Clauser^[37] and Bradshaw^[16] established equilibrium adverse pressure gradient flow by achieving a constant pressure gradient parameter. Although the flow was decelerating, the resultant shear stress distribution was able to preserve a ‘similar’ non-dimensional velocity distribution throughout, ensuring that flow reversal did not occur.

Whilst some workers (e.g., Townsend^[174]) theoretically investigated turbulent boundary layers near separation, others took a more pragmatic approach. For example, Kline et al.^[87] correlated existing experimental data to provide an improved understanding of their integral properties at incipient detachment ($H=2.2$, $C_f>0$), full detachment ($H=4.0$, $C_f=0$) and other states. In addition, Sovran and Klomp^[154] assessed the performance of different length and area ratio annular diffusers to determine whether, or not, the strength of the resulting adverse pressure gradient was sufficient to produce partial or total separation of the flow (diffuser stall).

To obtain a better physical understanding of turbulent boundary layers under adverse pressure gradient conditions, much detailed experimental data has been obtained. For example, Goldberg^[64] measured the mean velocity and turbulence in cylindrical annulus

wall turbulent boundary layers with a number of different pressure distributions which were externally imposed (zero, reducing adverse, linear and increasingly adverse pressure gradients). Within these non-equilibrium boundary layers, it was found that the shear stress was not uniquely related to the mean velocity, but was dependant upon the 'upstream history' of the flow. For rapidly growing boundary layers, the streamwise normal stress gradients were shown to be important in the momentum balance.

For separating turbulent boundary layers, a detailed understanding of the physics of separation has been obtained. For example, Simpson et al.^[144] found that the normal Reynolds stresses made a significant contribution to the momentum and Reynolds stress transport equations. Using laser anemometry, Simpson et al.^[145] investigated the back flow region, where it was found that the turbulent velocity fluctuation were large whilst the turbulent shear stress was insignificant. In this region, the log-law was shown to be inapplicable and mixing length theory and eddy-viscosity models meaningless. Shiloh et al.^[139] found that the turbulence intensity in the transverse direction was equal to the component normal to the wall over the outer 90% of the shear layer, and Simpson et al.^[146] found that there was little turbulent kinetic energy production in the back flow region; the energy being supplied by turbulent transport from the outer region, which was found to become increasingly important as separation was approached.

Turbulent boundary layer separation, produced by a strong adverse pressure gradient, was also investigated experimentally by Dianat and Castro^[46, 47]. From their comprehensive mean flow and turbulence measurements, they found that the separating shear layer, bounding the highly turbulent reverse flow region, was quite different from either a plane mixing-layer or a wall boundary layer. In this shear layer, significant turbulent and pressure transport was present, and the normal stresses were found to be important in the production of turbulent energy. Since the individual Reynolds stresses exhibited different behaviour, it was felt that the only way of predicting separation successfully was through the use of Reynolds stress turbulence models; and, even then, the turbulent and pressure transport would not be treated accurately by the usual gradient diffusion models. A similar conclusion was reached by Driver^[49], who also provided 3D laser anemometry data in an adverse pressure gradient turbulent boundary layer with and without separation. Since the flow is not in equilibrium, and turbulent transport is important, turbulence models which rely on the eddy-viscosity assumption, such as mixing length and $k-\epsilon$ models, are poor at predicting separation; whereas Reynolds stress transport models are much better.

Another relevant investigation was performed by Samuel and Joubert^[134], who subjected a turbulent boundary layer to an increasingly adverse pressure gradient. They found that

all the mean velocity profiles exhibited linear log-law behaviour, with the corresponding wall shear stress in agreement with Preston tube and floating element measurements. These were also in agreement with the measured shear stress distribution, whose gradient at the wall was equal to the wall pressure gradient. In addition, Dengel and Fernholz^[45] investigated three turbulent boundary layer flows in which the minimum C_f remained positive, was equal to zero or went negative. The mean flow and turbulence data showed characteristic behaviour as separation was approached; decreasing C_f and a more rapid growth of δ and δ^* than θ as the mean velocity lost fullness. In addition, the decrease in $\partial U/\partial y$ at the wall led to a reduction in the Reynolds stresses, by reducing their production rate, whilst away from the wall a new local maximum in $\partial U/\partial y$ gave rise to local maxima in the Reynolds stresses and their production; which moved away from the wall in the downstream direction. The occurrence of the first reverse flow events ($H \approx 2$) coincided with a vanishing log-law region and $\partial U/\partial y = 0$, which implied a change in the nature of the near-wall flow; and with 50% reverse flow, and zero average skin friction, H was found to be 2.85.

1.3.2.3 Alternating Pressure Gradient

Of some relevance to the present investigation are studies which have considered the effect, on flat surface turbulent boundary layers, of alternating the sign of the streamwise pressure gradient. One such experimental investigation was carried out by Tsuji and Morikawa^[176], with a twice alternating adverse to favourable pressure gradient cycle, who found that the boundary layer increasingly departed from equilibrium. As the flow progressed downstream, the peak in the shear stress distribution, created by the first adverse pressure gradient, broadened and moved away from the surface; whilst a new peak was created by the favourable pressure gradient and moved away from the surface by the subsequent adverse pressure gradient. This increasingly complex shear stress distribution, containing a ‘knee point’, was created by the interaction between the turbulence and the mean strain; which itself was affected by the variation, across the boundary layer, of the streamwise pressure gradient and cross-stream shear stress gradient.

For turbulent boundary layer flow subjected to favourable followed by adverse pressure gradient, Spalart and Watmuff^[157] produced a carefully controlled comparison between direct numerical simulation and experimental data. To validate the simulation data, mean velocity and Reynolds averaged data were compared, and shown to be in good agreement. Although the low Reynolds number makes it difficult to apply the results quantitatively to higher Reynolds number flows, the extensive nature of the data provides an invaluable contribution to the understanding of turbulent flow behaviour.

1.3.3 The Effect of Curvature on Turbulent Boundary Layers

The effect of streamline curvature on turbulent flow has been widely investigated. Of direct relevance to the present investigation are those which relate to turbulent boundary layer flow over curved surfaces. In this review, the various investigations have been grouped according to the strength and nature of the curvature, and most of the related references are included and summarised.

In the 1930s, Prandtl and his co-workers performed several experimental investigations into the effect of curvature on turbulent boundary layers. Wilcken^[180] made mean flow measurements in the flow over the convex and concave walls of a mildly curved channel, from which the Reynolds shear stress and apparent mixing length were deduced, and concluded that the turbulence was greatly reduced over the convex wall and increased over the concave. Similarly, in the boundary layer over a convex surface, Schmidbauer^[136] showed that skin friction was reduced and that the Reynolds number at which transition (from laminar to turbulent flow) occurred was increased. In addition, Wattendorf^[178] compared the fully developed flow in two curved channels with that of a straight channel. Measurements of the mean velocity, together with Stanton tube measurements of the wall shear stress, were used to estimate the variation of shear stress, turbulent viscosity and mixing length across the channel. Relative to the straight channel, large increases and decreases were observed on the concave and convex side of the curved channel respectively. Further, the position at which zero shear stress occurred across the channel did not coincide with either the maximum velocity, zero strain or zero vorticity position, and, when compared on a log-linear basis, the mean velocity profiles showed a pronounced curvature effect.

Curvature has an effect on the boundary layer turbulence in accordance with the stability criterion proposed by Rayleigh^[124]. According to this criterion, the motion of a fluid, with mean velocity U and streamline radius of curvature r , is stable if $\partial(rU)/\partial r$ is positive and unstable if it is negative. Thus, the turbulent motion would be stabilised in the case of a turbulent boundary layer flow over a convex surface, and destabilised over a concave surface. In addition, Von Kármán^[177] (cited by Bradshaw^[18]) qualitatively explained the effect of curvature by considering the motion of a disturbed element of fluid. In essence, for any curved flow, there must exist a gradient of pressure to produce the centripetal acceleration. For a convex surface, if a fluid element is displaced away from the centre of curvature, such that its velocity is less than that of the surrounding fluid, then the pressure gradient at this point will be greater than that required to support its circular motion, and therefore it will be returned to its original radius. Conversely, for a concave surface, if the fluid element is displaced away from the centre of

curvature, such that its velocity is now greater than that of the surrounding fluid, then the pressure gradient at this point will not be sufficient to support its circular motion, and therefore the fluid particle will continue to move away from the centre of curvature.

In the 1950s, Eskinazi and Yeh^[54] measured the turbulence in a fully developed curved channel flow for the first time. Using hot wire anemometry, they found an increase in turbulence intensity on the concave side, and a reduction on the convex, which was most pronounced at low frequencies. The linear shear stress distribution was zero at a position closer to the convex wall, but this position did not coincide with the position of maximum velocity, zero vorticity or zero strain rate. In addition, the curvature effects were shown to result from the extra production terms arising in the Reynolds stress transport equations.

It was not until much later that interest in the effects of curvature intensified. Bradshaw^[17] studied the analogy between streamline curvature and buoyancy effects, and developed a formula for modifying the mixing length in a curved flow, i.e., $\ell = \ell_0(1 - \beta R_c)$, which could be used to improve simple CFD predictions. This was based on a curvature Richardson number [$R_c = 2S(1 + S)$, where $S = (U/R)/(\partial U/\partial y)$] for which positive R_c implied a stabilising effect. The constant β was inferred to be of order 10, and, moreover, it was shown that a 10% change in mixing length could result for curvatures as small as $|\delta/R| \approx 1/300$. In addition, Bradshaw^[18] provides an excellent review of work prior to 1973, which laid the foundations for subsequent research. He pointed out that curvature was one of a number of distortions, “extra rates of strain”, which produce unexpectedly large effects on turbulent shear flows; even for flows with a streamline radius of curvature of order 100 times the boundary layer thickness. In another review, Bradshaw^[22] discusses complex strain fields and their effect on turbulent flow.

1.3.3.1 Mild Curvature

Convex

Over a mildly curved convex surface, Gibson et al.^[62] carried out mean velocity and turbulence measurements in a turbulent boundary layer, in comparison to an equivalent flat surface flow. At the start of curvature, the turbulence reduced rapidly due to the imposition of the extra strain rate, which had a much larger effect on the shear stress (\bar{uv}) than on the normal stresses. The turbulent kinetic energy was found to reduce mainly as a result of the lower \bar{uv} , rather than the extra strain, affecting its production rate, such that, as k fell, the ratio \bar{vv}/\bar{uu} remained constant. Since the effect of extra strain rate was felt mainly in the outer layer (where $\partial U/\partial y$ is small), the shear stress

reduction was greatest in this region. This led to an increase in $\partial\bar{v}/\partial y$ close to the wall, giving rise to the observed reduction in the near-wall velocity and increase in H . In addition, the triple velocity correlations were found to be reduced by the curvature, but it was shown that these changes were adequately represented by gradient diffusion processes in which the diffusion coefficient was scaled by $\bar{v}v$ (i.e., $C\bar{v}v k/\epsilon$).

Similarly, Muck et al.^[109] investigated a mildly curved convex turbulent boundary layer, as an extension of the work of Meroney and Bradshaw^[106] (see also Hoffmann et al.^[69]). From extensive measurements of the mean velocity and turbulence they concluded that the effects of convex (stabilising) and concave (destabilising) curvature were totally different, and showed that mild convex curvature tended to attenuate the pre-existing turbulence. The shear stress in the boundary layer was significantly reduced, but not annihilated as in strong convex curvature flows, and this was found to occur very rapidly at the start of the curvature. In addition, gradient diffusion coefficients used in turbulent transport models, such as the eddy-viscosity, were found to be affected by curvature.

Flow visualisation of turbulent boundary layer flow over flat and convex surfaces was carried out by Chiwanga and Ramaprian^[34]. They saw that the large-scale structures, present in the flat surface boundary layer, vanished in the convex region; confirming the conclusions drawn by many workers from conventional measurements. In addition, along a flat surface downstream of the convex curvature, the large scale structures only started to reappear after some considerable distance.

Concave

Within concave boundary layers, Tani^[170] discovered the existence of streamwise vortices. A spanwise variation was observed in velocity measurements, taken within laminar and turbulent boundary layers, and it was proposed that a centrifugal instability, which gives rise to Görtler vortices in laminar boundary layers, was producing an analogous effect in the turbulent boundary layer.

Hoffmann et al.^[69] investigated a mildly curved concave turbulent boundary layer, as an extension of the work of Meroney and Bradshaw^[106] (see also Muck et al.^[109]). Based on extensive measurements of the mean velocity and turbulence, they concluded that the effects of convex (stabilising) and concave (destabilising) curvature on boundary layers were totally different. Mild concave curvature resulted in the quasi-inviscid generation of streamwise vortices, which were maintained at a fixed spatial location by vortex generators far upstream, together with significant changes in the turbulence structure induced primarily by the curvature and indirectly by the vortices. The mean velocity

profiles were found to scale on the increased wall shear stress, and display linear log-law behaviour in the near-wall region, with a reduced wake strength and shape parameter. In addition, the turbulence intensity, shear stress and turbulent transport were all found to be increased across the boundary layer.

Convex and Concave

In curved channels, the effect of convex and concave curvature can be investigated simultaneously. Ellis and Joubert^[53] measured the discrete turbulent boundary layers on the convex and concave walls of various curved channels. The mean velocity profiles all displayed a linear log-law region, but its extent was reduced on the convex and increased on the concave side. In addition, the wall shear stress on the convex side was lower than that on the concave, and this difference was found to become larger as the duct curvature was increased. Similarly, Hunt and Joubert^[71] compared the boundary layer development in long straight and mildly curved channels at three Reynolds numbers. By the end of the channel, the initially flat profile had fully developed and the velocity profiles on both sides of the curved channel, and the straight channel, displayed similarity in log-law co-ordinates. The near-wall turbulence intensities also appeared to scale on the wall shear stress, which was lower on the convex side than on the concave.

Over surfaces with prolonged mild convex and concave curvature, Meroney and Bradshaw^[106] measured the mean velocity and turbulence. The turbulence was suppressed by the stabilising influence of the convex curvature, and the shear stress reduced rapidly away from the wall, falling to zero at about 0.88δ , and there was a 10% drop in wall shear stress. The mean velocity in the near-wall region scaled on the reduced wall friction, giving a linear log-law region and a slight increase in H, and the growth rate of the boundary layer was substantially reduced. In contrast, over the concave surface there was a significant lateral variation of properties, indicating the presence of stable streamwise vortices. As a result of the increased mixing, promoted by the destabilising influence of the concave curvature, there was an increase in the turbulent kinetic energy and shear stress, and a reduction in H.

For turbulent boundary layers, Ramaprian and Shivaprasad^[120] found that the mean velocity profile was affected by curvature; especially in the outer 'wake' region. Over both convex and concave surfaces, the near wall velocity was found to scale on the friction velocity (U_τ), producing a linear log-law region. The convex curvature reduced U_τ , increased the wake strength and reduced the extent of the linear log-law region ($n^+ = 250$); with a correspondingly higher H. In contrast, the concave curvature increased U_τ , produced a shallow wake and increased the linear region ($n^+ = 700$); with a reduction in H. With subsequent turbulence measurements, Shivaprasad and

Ramaprian^[142] showed that convex curvature decreased both the length and velocity scales of the turbulent motion; whereas concave curvature had the opposite effect, but to a lesser extent. Considering the small magnitude of the curvature, a surprisingly large change was seen in the shear stress and, to a lesser extent, the turbulent kinetic energy.

Continuing the investigation, Ramaprian and Shivaprasad^[121] found that convex curvature reduced the production of turbulent kinetic energy, and confined it to a reduced region near the wall, whereas concave curvature had an opposite effect. In addition, turbulent transport was significantly affected by curvature; with convex curvature suppressing, and concave curvature increasing, the transport of turbulence away from the wall. Analysis of the u and v velocity signals showed that convex curvature suppressed large scale motion such that the remaining shear stress was due, almost entirely, to the higher frequency, smaller scales; whereas concave curvature increased the low frequency motion. Near the wall, Ramaprian and Shivaprasad^[122] analysed the turbulent fluctuations and showed that the mechanism of turbulent production was not affected by mild streamline curvature.

A detailed understanding of curved turbulent flow, albeit at low Reynolds number, has been obtained by direct numerical simulation. In a mildly curved channel with fully developed flow, Moser and Moin^[108] found that the shear stress was significantly different between the convex and concave sides. In addition, stationary Taylor-Görtler vortices were present on the concave side, and found to significantly contribute to the shear stress. By computing the magnitude of the terms in the Reynolds stress transport equations, they were able to show that the most significant differences between the convex and concave sides occur in the shear stress equation.

1.3.3.2 Strong Curvature

Convex

Over the convex wall of a 90° rectangular duct, Patel^[116] investigated the turbulent boundary layer. Despite large secondary flows, and streamwise pressure gradients introduced by the highly curved duct, the measurements showed that curvature had a marked influence on the mean velocity profiles, which were found to have higher H values than suggested by existing boundary layer calculation methods. Consequently, a more general momentum integral equation was derived, which was better able to predict the momentum thickness, and, with a large variation of velocity (U_p) in the irrotational region above boundary layer, a new definition for δ^* and θ was suggested, which used the U_p distribution as a reference against which to judge the actual velocity profile.

In a highly curved turbulent boundary layer over a convex surface, So and Mellor^[151] found that the shear stress was reduced dramatically. From turbulence measurements, they found that the shear stress fell to zero at 0.4δ , and, also, that the turbulent kinetic energy was reduced. In the near-wall region, the mean velocity was found to scale on the reduced wall shear stress, giving a linear log-law region, and, in the outer layer, the 'wake' strength was increased. Relative to a flat surface boundary layer, therefore, the mean velocity profile had a higher H value; despite the initial reduction due to the favourable pressure gradient at the start of the curvature. In addition, with the Reynolds shear stress layer confined to the inner half of the velocity defect layer, the boundary layer thickness remained virtually constant.

Similarly, Gillis and Johnston^[63] measured the mean velocity and shear stress in a turbulent boundary layer over a convexly curved surface. By adjusting the opposite wall of the channel, they were able to achieve virtually constant pressure along the test surface. Following the introduction of curvature, the shear stress in the outer layer was sharply diminished, as was the turbulent length scale, and the wall shear stress also reduced. When the wall became flat again, however, the shear stress was found to recover very slowly. In addition, the shear stress distributions (\overline{uv}/U_τ^2), taken from several experiments with different levels of curvature, were found to be similar when the distance from the wall (n) was non-dimensionalised by the radius of curvature (R), i.e., n/R , which seemed to suggest that an asymptotic state was reached for $\delta/R > 0.05$. Moreover, once the active shear layer had collapsed (to a thickness less than the velocity defect layer), it continued to grow at a rate characteristic of its reduced thickness. In the near-wall region, the mean velocity profiles over the curved surface displayed linear log-law behaviour (up to $n^+ \approx 100$), and the mixing length remained proportional to distance from the wall, suggesting that curvature effects were weak in this region.

On a flat surface downstream of strong convex curvature, Alving et al.^[2] found that the recovery of the mean flow and the turbulence were different. The mean velocity and wall shear stress recovered fairly rapidly at first, becoming asymptotic to flat surface conditions, but the turbulence relaxation was more complicated and occurred over a much longer distance. A stress 'bore', initially generated adjacent to the wall, thickened and eventually filled the whole boundary layer, giving rise to shear stress levels above that of a flat surface layer, before finally declining. Although convex curvature caused a reduction in the shear stress in the outer layer, the large shear stress gradient near the wall (combined with an adverse pressure gradient) reduced the near-wall velocity (and wall shear stress). As a result, the mean shear strain rate increased above the surface, and, once the stabilising influence was removed, produced elevated levels of shear stress in this region.

Concave

In a highly curved concave turbulent boundary layer, So and Mellor^[152] found a lateral variation in the mean velocity. This was thought to be an indication of stable streamwise vortices in the flow, but further downstream the coherence degenerated as the turbulence level increased. There was also a lateral variation in the Reynolds stresses which, on average, were substantially increased, and the existence of finite \bar{uw} and \bar{vw} was seen as a further indication of the presence of discrete vortices. When scaled on the increased wall shear stress, there was only a very limited linear log-law region in the mean velocity profile.

Using flow visualisation and laser anemometry, Barlow and Johnston^[10] also investigated the effect of concave curvature on turbulent boundary layers in a curved water channel. Unlike previous investigations, however, they found no distinct streamwise vortices and there were no significant spanwise variations in the mean flow properties. Instead, the flow was found to be dominated by random large scale structures which on average produced an increase in the mixing across the boundary layer, with fluctuations normal to the wall being affected the most. Increases in turbulent energy and shear stress in the outer layer were due, almost entirely, to these low frequency large scale fluctuations. The higher momentum fluid transported to the wall increased the wall shear stress, but, when this was used to scale the Reynolds averaged statistics, the near-wall behaviour was found to be similar to that of a flat surface. In addition, higher order statistics were measured and found to be increased significantly by concave curvature. Barlow and Johnston^[11] continued to investigate the large scale structures in the boundary layer over a concave surface. By using vortex generators to organise these structures, which otherwise occur randomly in the flow, it was possible to obtain a stationary pattern. In addition, because of the relatively low Reynolds number, reliable measurements could be made down into the viscous sublayer (as close as $n^+ \approx 10$), and these were used to assess the Reynolds averaged turbulence structure in the near-wall region.

Shizawa and Homani^[143] made mean flow and turbulence measurements in a turbulent boundary layer over a flat to concave surface, in which the opposite wall of the channel was adjusted to give zero pressure gradient. Due to the curvature, there was a rapid increase in shear stress (\bar{uv}) and the cross-stream normal stress (\bar{vv}), which was explained by examining the inter-relationship between these stresses which occurs within the production terms of the Reynolds stress transport equations. Moreover, the effective streamline curvature of the flow was shown to increase before the start of the geometric curvature, such that some adjustment of the flow had already occurred upstream, making the changes seem all the more rapid.

Convex and Concave

As an extension of earlier work, Patel^[117] measured the turbulent boundary layer flow on both surfaces of a 180° rectangular duct, which was designed to produce long zero pressure gradient regions. Unfortunately, after some attempts were made to reduce the large secondary flows in the duct, it was concluded that a larger aspect ratio (>10) was needed in order to produce a reasonable 2D flow. However, streamwise vortices were observed in the concave wall boundary layer.

In highly curved turbulent boundary layers over prolonged convex and concave surfaces, So and Mellor^[150] made extensive mean flow and turbulence measurements. Over the convex surface, turbulent mixing was very much reduced but the log-law held (see So and Mellor^[151]) and, over the concave surface, mixing was enhanced and a system of streamwise vortices was found (see So and Mellor^[152]). In addition to the zero pressure gradient measurements, an adverse pressure gradient was imposed on the convex surface boundary layer, which resulted in separation. Interestingly, this was believed to have occurred earlier than for a plane boundary layer under the influence of a similar pressure distribution.

On the flat surface downstream of short sections of strong convex and concave curvature, Smits et al.^[147] investigated the recovery behaviour of turbulent boundary layers. In the concave case, the flow was complicated by large spanwise variations, but it was shown that the decay of the high turbulence intensity, generated within the concave bend, was non-monotonic in that the Reynolds stresses in the outer layer collapsed to levels well below those at inlet. Through the convex bend, the shear stress was reduced to zero in the outer layer. Downstream of the bend, however, a large peak was generated near the wall, which moved away from the wall eventually increasing the shear stress across the entire boundary layer (stress ‘bore’). In both cases, this behaviour was due to an interaction between the shear stress and the mean strain rate.

1.3.4 Combined Effects of Pressure Gradient and Curvature

Investigations into the behaviour of turbulent boundary layers under the combined influence of pressure gradient and curvature are rare; especially in annular S-shaped duct geometries. Of course, several of the curved flow experiments, already described, have also involved pressure gradients. Usually these were present at the beginning and end of the curved region, especially for the highly curved experiments, and have influenced the behaviour of the turbulent boundary layer. Apparently, as in the flat surface experiments, the pressure gradient alters the mean strain rate, initially close to the wall, such that turbulence production is affected; which then changes the magnitude

of the Reynolds stresses, affecting the mean velocities and so on. This cycle of events is most apparent in the recovery downstream of a short curved region, where a wave in the Reynolds stress has been observed.

Of particular interest to the present investigation are situations in which the curvature changes sign. When this occurs within a short distance, severe pressure gradients arise naturally, which vary in sign along the length of the duct. In this section, therefore, several related investigations are described, before considering those that have involved S-shaped ducts.

1.3.4.1 Related Investigations

Strangely, the flow over a curved hill is very closely related to the present investigation, because of a similarity between their curvature and pressure gradient variations. In such a situation, Baskaran et al.^[12] found that an ‘internal layer’ formed at the concave-to-convex transition, in a region of strong favourable pressure gradient, and showed that the behaviour of this layer was identical to that of a turbulent boundary layer over a bi-convex wing section with the same profile as the convex part of the hill. The mean flow and turbulence data showed a strong curvature effect in the outer layer, with large changes in the Reynolds stresses, but the effect of curvature on the internal layer, and wing boundary layer, was found to be small. In addition, the wall shear stress and the eventual separation on the leeward side were determined mainly by the pressure gradient.

Further, Baskaran et al.^[13] analysed the effect of curvature and pressure gradient on the turbulence over the same curved hill. By considering the transport equations for shear stress and turbulent kinetic energy, the influence of extra strain rates was examined, and found to be different in each equation. For example, the extra strain due to curvature had a greater influence on shear stress than on turbulent kinetic energy, due to the anisotropy of the turbulence, whilst the extra strain due to acceleration only affected turbulent kinetic energy. In a concave region, where the flow was also accelerating, the tendency for turbulent kinetic energy to increase due to destabilising curvature, was thought to be offset by a negative contribution due to the acceleration. Moreover, at the exit from the concave bend, the reduction of shear stress and turbulent kinetic energy over the convex surface was assisted by a substantial reduction in the main strain rate; directly reducing their production.

Experimentally, Nakayama^[11] investigated the effect of streamline curvature and pressure gradient on a wake. As the defect velocity was small, the extra strain rates due to curvature and pressure gradient were large in comparison to the main shear strain. By

deflecting the wake in two different pressure gradient environments, the separate effects of pressure gradient and curvature could be identified. The Reynolds stresses, particularly the shear stress, were found to be strongly influenced by both effects, but the defect velocity was not strongly influenced by curvature. Examination of the magnitude of the terms in the turbulent kinetic energy transport equation showed that production responded rapidly to the extra strain, but the rates of response of the turbulent transport and dissipation were slower. Overall, the flow was far from equilibrium and, as such, could not be described by simple turbulence models, and, in addition, gradient diffusion models for momentum and Reynolds stress transport were shown to be inappropriate.

1.3.4.2 S-shaped Ducts

Before describing the few related investigations, it is worth noting that there are several examples of flow in S-shaped ducts which are simply not relevant because they involve circular or low aspect ratio rectangular ducts, as sometimes found in aircraft intakes. For example, Bansod and Bradshaw^[9] showed that a complex secondary flow pattern arose within a circular S-shaped duct, and that strong counter-rotating vortices were generated near the outside of the second bend, which expelled boundary layer fluid into the free stream, thereby creating a region of low total pressure in the exit plane.

Considering the enormous amount of development carried out by gas turbine engine manufacturers, there are very few examples of annular S-shaped duct work reported in the open literature. Although Rolls-Royce^[130] had developed a design method, based on a wall diffusion loading parameter (calculated from simple geometrical and aerodynamic rules), no detailed information existed on the aerodynamic behaviour of annular S-shaped ducts. However, basic testing and water analogy were used to establish a maximum level for this loading parameter, such that it could be used to estimate the minimum duct length for a given change of radius. In addition, Burrill and Barnes^[26] discussed the future need for a large radius change, and indicated that existing (conservative) design rules would lead to excessively long ducts.

Those examples that are available have mainly concentrated on overall performance. For example, Sucharov^[168] made pressure measurements at inlet and exit of a compressor interconnecting duct, Amann et al.^[3] evaluated the performance of a turbine interstage S-shaped diffuser, and Thayer^[172] measured the pressure recovery of various annular S-shaped exhaust diffusers, along with wall static pressure distributions, showing the performance to be similar to equivalent straight ducts. In the same way, Japikse and Pampreen^[73] found that the performance of turbine interconnecting ducts and curved exhaust diffusers were comparable with similar straight walled diffusers,

and, more recently, Dominy and Kirkham^[48] have made measurements in a turbine interstage duct.

Of some relevance, however, was an investigation carried out by Bandyopadhyay and Ahmed^[8]. By measuring the mean flow in an S-shaped rectangular duct, they were able to examine pressure gradient and curvature effects. Through the variation of the boundary layer integral parameters, and the wall shear stress, they demonstrated the complex nature of the flow, and it was found that the concave-convex curvature sequence produced a sustained lower wall friction in the recovery region, downstream of the duct, than the convex-concave curvature sequence. In addition, Md. Abdalla^[104] obtained mean velocity and Reynolds stress data on the boundary layer growth along a highly loaded annular S-shaped duct. Although this investigation was mainly concerned with the effects of swirl, the Reynolds stresses in the zero swirl case reduced over the convex surfaces, and increased over concave surfaces. Interestingly, the swirl was thought to eliminate a short region of separation along the inner wall, although, because the swirl was produced by vanes which were not present in the zero swirl case, the vane wakes are likely to have had a strong influence.

Also of relevance, Stevens and Eccleston^[162] made pressure measurements to assess the performance of a 40° outwardly canted annular diffuser with fully developed flow. Since the diffuser was located between axial inlet and exit sections, the whole arrangement was S-shaped. In this diffuser, it was found that the pressure recovery was comparable with that of a similar non-canted design, but the total pressure loss was much higher. Subsequent turbulence measurements, reported by Stevens and Fry^[163], suggested that the higher loss was due to the increased turbulent mixing after the first bend. In addition, it was found that the shear stress was reduced by the convex curvature at diffuser inlet, and that the concave curvature of the exit bend reduced the distortion of the mean velocity profile.

1.3.5 Inlet Conditions

With a compressor stage upstream of the S-shaped duct, the inlet conditions to the duct are significantly more complicated. The effect of inlet conditions on conical diffuser performance has been reviewed by Klein^[85], who concluded that increasing inlet blockage, whilst initially reducing diffuser performance, could increase performance due to the high turbulence intensity. Similarly, based on measurements of annular diffuser performance, Stevens and Williams^[164, 165] showed that increasing the turbulence intensity at diffuser inlet led to a marked improvement in the stability of the outlet flow and increased the pressure recovery, with only a small increase in total pressure loss. In

addition, Evans^[56] examined the effect of free stream turbulence on turbulent boundary layers, and found that the ‘fullness’ of the mean velocity profile increased with increasing free stream turbulence, giving rise to a higher wall shear stress.

Downstream of an axial compressor, Adenubi^[1] investigated the performance of annular diffusers, and found that the higher turbulence intensity led to an increase in the pressure recovery performance of the diffuser. For an outwardly curved combustor pre-diffuser, operating downstream of an axial compressor stage, Stevens and Wray^[166] also showed that the stator blade wakes re-energise the diffuser wall boundary layers, reducing the distortion of the outlet velocity profile. Similarly, for a turbine interconnecting duct, Japikse and Pampreen^[73] found that flow separation, seen in a ‘clean’ model test, disappeared when the same duct was tested downstream of a turbine stage.

1.3.6 Conclusions from the Review

Overall, this literature review has considered the behaviour of turbulent boundary layers. Since an annular S-shaped duct will give rise to both pressure gradients and curvature, these effects have been examined in detail, and, although these have been considered in isolation, this information is applicable to the present investigation. Although there are some examples where the combined effects are present, it is apparent that annular S-shaped ducts have not been investigated in great detail, and certainly not with compressor generated inlet conditions.

As far as pressure gradient is concerned, the review has shown that turbulent boundary layers are affected significantly. Adverse pressure gradient may lead to separation, but the mechanism which ensures that this does not always occur is the modification of the shear strain rate, which leads to an increase in the shear stress, such that its gradient close to the wall reduces the deceleration. Favourable pressure gradient can lead to the disappearance of the linear log-law region in the mean velocity profile, and also may result in relaminarization. When the pressure gradient alternates rapidly in sign, a complex non-equilibrium flow is always produced.

The effect of curvature on turbulent boundary layers was significant, even for mild curvature, with convex curvature tending to reduce, and concave curvature increasing, the turbulent motion in the flow. In the present investigation, the curvature effect is strong, with $\delta/R = 0.1$. From the literature, it is clear that this level of convex curvature would be sufficient to totally eliminate the shear stress in the outer regions of the boundary layer. For highly curved concave surfaces, the shear stress would be significantly increased, with the possibility of discrete streamwise vortices appearing in

the flow. Within a curved flow, it is the appearance of the extra strain rate (U/R) that gives rise to this behaviour since it changes the production rate of the Reynolds stresses; affecting the shear stress more than the normal stresses.

The flow in the present investigation, however, will be influenced by the combined effects of pressure gradient and curvature which, in addition, will alternate in sign along the length of the duct. Several of the investigations covered by the review have indicated that the effect of such changes will be complex, involving the interaction of the mean velocities and Reynolds stresses; leading to a highly non-equilibrium flow. In this situation, therefore, where the conditions (i.e., $\partial p/\partial s$ and U/R) are changing, the overall behaviour will be determined by the differing rates of response of the momentum and Reynolds stress transport equations. Typically, there is a lag in the response of the shear stress. For example, as the pressure gradient changes, the shear stress will, initially at least, remain the same and the velocity will increase or decrease accordingly. As it does so, the strain rate ($\partial U/\partial n$) will change, thereby affecting the rate of production of the shear stress. Since this alters the rate of change of the shear stress in the streamwise direction, its magnitude will change over some distance. Thus, only after some delay, will the cross-stream shear stress gradient have changed sufficiently to influence the velocity. In the mean time the pressure gradient, itself, may have changed, giving rise to a situation where the flow variables are all out of phase with each other. When this is combined with the effect of curvature, the rate of production of the shear stress is affected further, by the appearance of U/R , and the situation becomes more complex.

The investigations into the effect of inlet conditions have shown that increasing the turbulence level of the flow, by whatever means, has a beneficial effect on turbulent boundary layers in adverse pressure gradient situations. Thus, the addition of a single stage compressor upstream of the annular S-shaped duct is likely to have an important influence on the flow.

1.4 Objectives of the Present Investigation

In order to design an annular S-shaped duct effectively, it is necessary to be able to predict the flow through such a device accurately. However, the methods best suited to this are, to some extent, still under development and information on their accuracy, under known conditions, is essential to continue this process. The main objective of the present investigation, therefore, was to acquire detailed experimental data within a representative annular S-shaped duct, so as to provide the means by which prediction methods could be assessed. For this a new rig was required, which was capable of

incorporating an axial compressor stage in order to provide inlet conditions representative of a real gas turbine. In addition, the S-shaped duct had to produce the most severe conditions possible, without causing the flow to separate. Within the constraints of the laboratory, it had to be as large as possible, to facilitate accurate measurements, and pass sufficient flow so that a realistic Reynolds number was generated. The initial objective, therefore, was to design, build and commission the rig, and associated equipment, necessary for obtaining the experimental data.

Without the compressor installed, it would be possible to obtain data in a 2D axisymmetric flow. In this case, with the inlet flow consisting of well-established, but isolated, turbulent boundary layers, the objective was to measure the behaviour of these boundary layers under the combined effects of strong pressure gradient and curvature. From the literature, it is clear that these effects will be pronounced, but, although there is a large amount of information on these separate effects, it is not obvious how they will combine to affect the behaviour of the turbulent boundary layers in an annular S-shaped duct. In addition, since both the pressure gradient and curvature change sign within a short distance, the flow will not be in equilibrium. Although limited, the available literature suggests that the behaviour will be dependent on the interaction of the mean flow and turbulence, which react in different ways and at different rates to the changing conditions. In short, the behaviour can only be understood and, more importantly, predicted by considering the Reynolds stress transport equations in conjunction with the mean momentum equations.

Since there is no detailed experimental data available for annular S-shaped duct flows, in particular with an axial compressor stage upstream, it was not known whether available prediction methods would be able to capture the complex flow behaviour. Certainly, only methods involving the Reynolds stress transport equations were likely to be successful, but, even then, it was unknown if the modelling assumptions involved would return an adequate solution. In the case with the compressor generated inlet conditions, the need to carry out a 3D prediction would present an even more severe test for the present models, since the number of grid points required to adequately resolve the flow would undoubtedly lie beyond the present capacity of the available computers.

To provide the data necessary for turbulence model development, it was essential that information on the turbulence was obtained. Fortunately, a 3-component Laser Doppler Anemometry (LDA) system was available during the investigation, which could measure all the mean velocities, Reynolds stresses and triple velocity correlations. In addition, a conventional 5-hole pressure probe (5HP) could be used to obtain data on the static pressure, as well as the mean velocity components. It was essential, therefore, that

the experimental facility was capable of obtaining these measurements throughout the annular S-shaped duct, and in sufficient detail that the streamwise, as well as the cross-stream, variation of the flow parameters could be determined.

Once the new rig and instrumentation were available the aims of the investigation were to:

- (i) Calibrate the rig and axial compressor.
- (ii) Obtain 5HP data on the mean flow, with and without the compressor stage present, and assess the basic performance of the duct in each case.
- (iii) Use the 3-component LDA to obtain more detailed measurements, without the compressor stage, so that the behaviour of this 2D axisymmetric flow can be understood.
- (iv) Assess the ability of the standard $k-\epsilon$ and Reynolds stress transport equation turbulence models to predict the 2D axisymmetric flow, using measured data to define the inlet conditions.
- (v) Obtain time-averaged turbulence data in the stator exit flow, in order to define the inlet conditions for 3D CFD predictions.

1.4.1 Contents of the Thesis

The present investigation has been concerned with both the measurement and the prediction of flow within an annular S-shaped duct. In Chapter 2, the equipment necessary to carry out the experimental part of the investigation is described, giving details of the design and construction of the test rig and instrumentation, and Chapter 3 gives details of the experimental procedures and data reduction techniques used. Chapter 4 is devoted to presenting the experimental results, concentrating on the 2D axisymmetric case, and discusses the physical behaviour of the flow indicated by this comprehensive and detailed data, which relates to both the mean and the turbulent flow fields. Chapter 5 is concerned with numerical prediction techniques, reviewing the relevant literature and giving details of the turbulence models used to predict the flow. Chapter 6 considers the predicted results in comparison to the measured data, and discusses several points related to the behaviour of the flow and the modelled Reynolds stress transport equations. Finally, conclusions and recommendations for future work are given.

CHAPTER 2 EXPERIMENTAL EQUIPMENT

	Page
2.1 Test Rig	36
2.1.1 Preliminary Aerodynamic Design	36
2.1.2 Mechanical Design and Construction	39
2.1.3 Annular S-shaped Duct	42
2.1.4 Single Stage Compressor	46
2.1.5 Inlet and Exit Sections	47
2.1.6 Facility	48
2.2 Data Acquisition	49
2.2.1 Practical Considerations	49
2.2.1.1 Location of Measurements	49
2.2.1.2 Traverse Arrangements	50
2.2.1.3 Rig Operating Conditions	52
2.2.1.4 Correction of Measured Data to Standard Conditions	54
2.2.2 Basic Instrumentation	54
2.2.2.1 Five Hole Probes	55
2.2.2.2 Pressure Transducers	56
2.2.2.3 Wall Static Pressure Taps	56
2.2.2.4 Thermocouples	57
2.2.3 Data Acquisition System	57
2.2.3.1 Description	57
2.2.3.2 Software	58
2.2.3.3 Traversing	59
2.2.3.4 Test Procedure	59
2.2.4 Laser Doppler Anemometer	61
2.2.4.1 Equipment	61
2.2.4.2 Optical Arrangement	62
2.2.4.3 Signal Processing	65
2.2.4.4 LDA Operation and Experimental Technique	67

This chapter considers the equipment required to carry out a detailed experimental investigation into the aerodynamic behaviour of an annular S-shaped duct. One of the most important aspects of this, of course, is the test rig, which had to be designed and built. Of particular significance during the design phase was the need to incorporate a single stage axial compressor upstream of the annular S-shaped duct. As well as specifying the geometry of the S-shaped duct, therefore, the compressor blades had to be designed, along with the other components of the rig and facility. Furthermore, an automated data acquisition and test management system was developed. Whilst the rig was operated at the required condition, a 5-hole pressure probe was used to acquire mean flow data throughout the S-shaped duct. As well as this basic system, however, a 3-component LDA system was used to measure turbulence quantities, and various techniques were developed to allow this equipment to be used on the rig.

2.1 Test Rig

The test rig (Fig. 2 and Photo. 1) had to enable detailed measurements of the flow behaviour to be made within a representative annular S-shaped duct geometry. Although it was desirable to make the annular rig as large as possible, space limitations and the available power to drive the compressor provided considerable constraints. For the mechanical design of the rig, the main concern was the arrangement of a structure sufficient to support the compressor and allow it to rotate. By using simple design rules which would ensure satisfactory operation without flow separation, an S-shaped duct of minimum acceptable length was designed with a typical radius ratio and constant passage area. As well as the S-shaped duct, the geometry of the compressor was specified, such that it would operate efficiently at the required aerodynamic conditions, and the geometry of the remaining aerodynamic passages was determined. The wood and perspex construction of the rig allowed relatively easy access for instrumentation, including pressure probes and optical access for the LDA system.

2.1.1 Preliminary Aerodynamic Design

To determine the maximum diameter of the axial compressor, it is possible to perform a simple analysis of the power required. An electric motor was considered the only practical means of driving the compressor, and it was desirable to locate this below the rig such that a direct coupling onto the compressor drive shaft was possible. For a given motor speed and power, a trade-off between compressor diameter and loading can be established, allowing the diameter to be determined for a typical aerodynamic loading.

Experimental Equipment

The power (P) absorbed by a compressor is dependant on the mass flow (\dot{m}) that passes through it and the total temperature rise (ΔT) it produces, i.e.,

$$P = \dot{m} c_p \Delta T \quad \dots \dots 2.1$$

For a given axial velocity (V_a), passing through an annulus of area (A), \dot{m} is given by,

$$\dot{m} = \rho A V_a \quad \dots \dots 2.2$$

where A can be calculated from the mean radius (r_m) and hub-to-tip radius ratio (HTR) using,

$$A = 4\pi r_m^2 \left\{ \frac{(1 - \text{HTR})}{(1 + \text{HTR})} \right\} \quad \dots \dots 2.3$$

When the compressor blade speed (U_{blade}), which is related to the rotational speed ($\dot{\theta}$) by $U_{\text{blade}} = \dot{\theta} r_m$, is used to non-dimensionalise V_a and $c_p \Delta T$, the above can be combined to give,

$$P = 4\pi \rho \left(\frac{V_a}{U_{\text{blade}}} \right) \left(\frac{c_p \Delta T}{U_{\text{blade}}^2} \right) \left\{ \frac{(1 - \text{HTR})}{(1 + \text{HTR})} \right\} \dot{\theta}^3 r_m^5 \quad \dots \dots 2.4$$

A HTR of 0.8 was chosen, which is typical of the middle stages of a gas turbine compressor, and, since the air passing through the rig would be at near atmospheric conditions, a density of 1.225 kg/m^3 was assumed. Thus,

$$P = 1.710 \left(\frac{V_a}{U_{\text{blade}}} \right) \left(\frac{c_p \Delta T}{U_{\text{blade}}^2} \right) \dot{\theta}^3 r_m^5 \quad \dots \dots 2.5$$

For a given non-dimensional compressor operating condition, therefore, the power required increases with the cube of the rotational speed and the fifth power of the mean radius.

An electric motor was found to drive the compressor, which was rated at 43 kW at its maximum rotational speed of 3050 rpm. With the compressor design speed set at 285.6 rad/s ($N_D = 2727.3 \text{ rpm}$), so that it could be driven at speeds up to 110% N_D if required, the motor power was used to determine a relationship between aerodynamic loading and mean radius, i.e.,

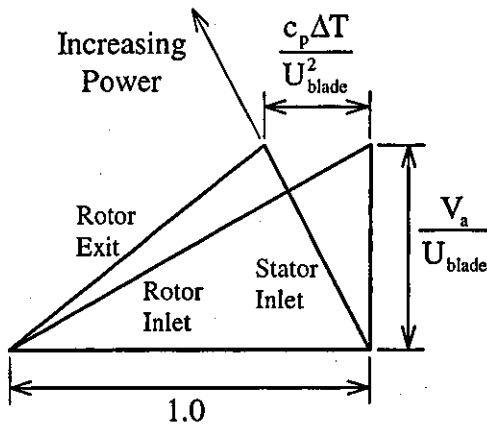
$$\left[r_m^5 \left(\frac{V_a}{U_{\text{blade}}} \right) \left(\frac{c_p \Delta T}{U_{\text{blade}}^2} \right) \right]_{\max} = 0.00108 \quad \dots \dots 2.6$$

Experimental Equipment

As the size of the compressor is increased, therefore, the maximum permissible aerodynamic loading is reduced. For example,

r_m (m)	0.20	0.25	0.30	0.35	0.40
$\left(\frac{V_a}{U_{blade}} \right) \left(\frac{c_p \Delta T}{U_{blade}^2} \right)$	3.372	1.105	0.444	0.205	0.105

For a compressor, the loading parameters V_a/U_{blade} and $c_p \Delta T/U_{blade}^2$ determine the shape of the velocity triangles (Cohen et al.^[39]), i.e.,



Velocity Triangles

From the velocity triangles, the inverse tangent of the reciprocal of V_a/U_{blade} determines the rotor inlet angle, and of the ratio of $c_p \Delta T/U_{blade}^2$ to V_a/U_{blade} determines the stator inlet angle. To be representative of typical intermediate pressure compressors (Rolls-Royce^[130]), V_a/U_{blade} should be greater than about 0.5, avoiding an excessively large rotor stagger angle, and the ratio of $c_p \Delta T/U_{blade}^2$ to V_a/U_{blade} should also be about 0.5. The following parameters were therefore selected,

V_a/U_{blade}	0.560
$c_p \Delta T/U_{blade}^2$	0.285

These have a product of 0.16, and from Eq. 2.6 the largest mean radius possible would be 0.368 m. However, to allow for a margin of error and electrical/mechanical losses, it was decided to base the mean radius on half the available power, allowing a mean radius of 0.32 m to be used. At this size it would be possible, if required in the future, to design a more highly loaded compressor; although the noise generated by the present compressor was already substantial.

To specify the annulus, the outer wall radius (r_o) is given by,

$$r_o = r_m \left\{ \frac{2}{(1+HTR)} \right\} \quad \dots\dots 2.7$$

and the inner wall radius (r_i) by,

$$r_i = HTR r_o \quad \dots\dots 2.8$$

With $HTR = 0.8$, this gives,

r_i	0.2845 m
r_o	0.3556 m

with a corresponding mean radius, annulus height (h) and area of,

r_m	0.32005 m
h	0.0711 m
A	0.142977 m ²

With a mid-height compressor blade speed (U_{blade}) of 91.4 m/s, the chosen loading parameters give an axial velocity (V_a) of 51.2 m/s ($m = 8.96 \text{ kg/s}$) and a temperature rise (ΔT) of 2.37 K. Assuming a compressor efficiency of 90% gives an estimated pressure rise of 2640 N/m² (270 mm H₂O) or pressure ratio of 1.026. Moreover, for these loading parameters, the compressor mid-height flow angles relative to the blades are found to be,

α_0	0.0	(inlet)
α_1	60.8	(rotor inlet)
α_2	51.9°	(rotor exit)
α_3	27.0°	(stator inlet)
α_4	0.0°	(stator exit)

2.1.2 Mechanical Design and Construction

The mechanical design of the rig was dominated by the need to include the axial compressor stage, and the only practical way of driving this was via a shaft through the centre of the rig (Fig. 2). By using a vertical configuration, an approach which has been used successfully before (Wray et al.^[183]), the necessary support for the rotating machinery can be kept clear of the main aerodynamic passages.

With the air passing through the rig from top to bottom, the main rig support could be floor mounted. Within a lower plenum box, a large cast aluminium platform was supported by four steel pillars about 1.0 m above the ground. The purpose of this platform was to carry the central support tube for the drive shaft, locating the compressor about 0.8 m above the platform. In addition, the platform allowed an electric motor to be hung from its underside, which, since it was aligned with the rig centreline, could be attached directly to the drive shaft with a flexible coupling. The platform also served to support the inner and outer casings, which form the aerodynamic passage. Since the platform had internal spokes, air could pass through it into the lower plenum and, by ensuring that the spokes were as long as possible, the annular passage downstream of the compressor could be located at any radial position.

The drive shaft and bearing support tube were made of steel. The drive shaft was fabricated from a steel tube and solid ends, which were welded and turned to size. The shaft was supported by bearings at each end, and held in position by a steel support tube which had welded flanges. To facilitate assembly, separate bearing housings were machined and bolted to the support tube. The axial location of the compressor was guaranteed by arranging the bearings such that the upper deep groove ball bearing was pre-loaded. This was achieved by using a disc spring to apply a force to the stationary part of the lower bearing, which was free to slide in its housing. The axial load generated by the compressor, therefore, was carried by the upper bearing alone, and, since this load was vertically upwards, it was necessary for the spring to apply an upward force sufficient to overcome the weight of the shaft and compressor disc. Although there was little radial load on the bearings, under normal operation, they provided accurate radial location of the shaft and compressor.

The compressor rotor blades were carried in a ring, connected to the shaft via a disk. The ring and disk were cast in aluminium and turned to size, and to facilitate easy assembly they were bolted together, as well as to the end of the shaft. The staggered platform of the compressor rotor blades were pinned into a recess in the carrier ring, and, as an assembly, the tip of the rotor blades were turned to the required diameter. One important feature of the compressor design was the use of an aluminium outer casing surrounding the rotor. Since aluminium has a large coefficient of expansion, any change in temperature will alter the diameter of the rotor. By using an aluminium outer casing, the tip clearance (between the rotor blades and the casing) could be maintained, since the casing responded to changes in temperature in the same way as the disk. In addition, since the tip clearance reduces with speed, the static clearance was carefully set up during rig commissioning to give a minimum clearance at high speed.

The aerodynamic passages were made of perspex. Each casing was manufactured from sheet perspex by forming it into a cylinder and, with flanges attached, turning it to size. Casings were bolted together using spigotted joints to ensure a smooth, continuous aerodynamic surface. The parallel inlet duct was made in several sections of varying length, so that a range of overall lengths could be achieved between 0.4 and 1.0 m, in steps of 0.1 m. To ensure concentricity with the rotor, the weight of the inner part of the inlet duct was carried by a small bearing on the end of the compressor shaft.

The air intake, which accelerates the air from an upper plenum into the inlet duct, was made of hardwood, constructed in sections and turned to size (Photo. 3). The inner part was an elliptical bullet and the outer part was a casing of reducing diameter, which together formed a symmetrical contraction. Above this was a parallel section, housing a honeycomb layer, and an intake scroll. The inner and outer parts of the intake were joined by four thin struts, which held the inlet casings concentric, and also provided a means of routing pneumatic pressure tubing from inside to out.

The S-shaped duct was also manufactured from perspex. Due to its complex shape, however, each casing had to be built up from a series of eight segments, which were individually formed and cut to size prior to being finally cemented together. With flanges attached, each casing was turned to the required shape, ensuring that the aerodynamic surface was smooth and axisymmetric. An overall view of the working section can be seen in Photograph 6.

The compressor rotor and stator blades were injection moulded using ABS plastic. A mould for each blade was created from a master blade, which was CNC machined from solid brass using a digital specification of the blade geometry. Each blade was hand finished to remove burs to ensure a smooth finish. The rotor blades (Photo. 4) were attached to an aluminium ring, that bolted to the disc. The stator blades (Photo. 5) were assembled in a row between two perspex carrier rings, such that there was no hub or tip clearance. The stator assembly, therefore, could be located in the rig in such a way that it was free to move circumferentially, and the position of the stator blades was determined by a flexible steel cable and a winch. For the tests without the compressor, dummy wooden sections were used in place of the compressor stage (Photo. 2), which, for both the inner and outer surfaces, provided a smooth continuation of the parallel inlet section up to the start of the S-shaped duct.

2.1.3 Annular S-shaped Duct

A simple method, developed by Rolls-Royce^[130], was used to specify the geometry of the annular S-shaped duct. This method uses an analytical function to specify the shape of the inner wall, meeting certain geometrical constraints, and then calculates the outer wall shape to give a linear variation of passage area between inlet and exit. Assuming the flow to be inviscid and irrotational, and that all streamlines rotate about a common point, it was shown in Chapter 1 (Eq. 1.13) that the pressure difference (ΔC_p) across a curved duct can be related to the non-dimensional curvature (h/R_m). The premise of the design method is that ΔC_p should be of similar magnitude across each bend of an S-shaped duct, and therefore,

$$\left(\frac{h}{R_m}\right)_{in} = \left(\frac{h}{R_m}\right)_{ex} \quad \dots\dots 2.9$$

However, the passage height can vary between inlet and exit as a function of both area ratio (AR) and mean radius ratio (MRR), i.e.,

$$\frac{h_{in}}{h_{ex}} = \frac{AR}{MRR} \quad \dots\dots 2.10$$

and therefore the mid-height radius of curvature (R_m) must change accordingly.

The design method assumes that the variation of inner wall radius (r_i) with non-dimensional axial position (x/L) is given by,

$$r_i = a_1 + a_2 \cos\left\{\pi \frac{x}{L}\right\} - a_3 \sin^2\left\{\pi \frac{x}{L}\right\} \quad \dots\dots 2.11$$

so that,

$$r'_i = \frac{dr_i}{dx} = \tan(\phi) = -a_2\left(\frac{\pi}{L}\right) \sin\left\{\pi \frac{x}{L}\right\} - a_3\left(\frac{\pi}{L}\right) \sin\left\{2\pi \frac{x}{L}\right\} \quad \dots\dots 2.12$$

and,

$$r''_i = \frac{d^2 r_i}{dx^2} = \frac{1}{R_i} = -a_2\left(\frac{\pi}{L}\right)^2 \cos\left\{\pi \frac{x}{L}\right\} - 2a_3\left(\frac{\pi}{L}\right)^2 \cos\left\{2\pi \frac{x}{L}\right\} \quad \dots\dots 2.13$$

Thus at $x/L = 0.0$, $r_i = r_{i_{in}} = a_1 + a_2$, $r'_i = 0.0$ and,

$$r''_i = \frac{1}{R_{i_{in}}} = \left(\frac{\pi}{L}\right)^2 (-a_2 - 2a_3) \quad \dots\dots 2.14$$

Experimental Equipment

and at $x/L = 1.0$, $r_i = r_{i_{ex}} = a_1 - a_2$, $r'_i = 0.0$ and,

$$r''_i = \frac{1}{R_{i_{ex}}} = \left(\frac{\pi}{L}\right)^2 (a_2 - 2a_3) \quad \dots\dots 2.15$$

Therefore, Eq. 2.11 defines an inner wall which varies from $r_{i_{in}}$ at inlet to $r_{i_{ex}}$ at exit, with zero slope at each end. The variation is almost cosinusoidal but, with the inclusion of the sine squared (a_3) term, it is possible to have a different curvature at each end. Note that for $a_2 > 0$, the geometrical radius of curvature (R) is negative at inlet and positive at exit, whereas R is always positive.

Thus the coefficients of Eq. 2.11 (a_1 , a_2 , a_3) can be determined from the end conditions. Clearly, a_1 and a_2 are related to $r_{i_{in}}$ and $r_{i_{ex}}$, i.e.,

$$a_1 = (r_{i_{in}} + r_{i_{ex}})/2 \quad \dots\dots 2.16$$

$$a_2 = (r_{i_{in}} - r_{i_{ex}})/2 \quad \dots\dots 2.17$$

In addition, these can be written in terms of MRR, AR, HTR_{in} and h_{in}, since these determine the relationship between $r_{i_{in}}$ and $r_{i_{ex}}$, i.e.,

$$a_1 = \frac{h_{in}}{4} \left[(1 + MRR) \frac{(1 + HTR_{in})}{(1 - HTR_{in})} - \frac{AR}{MRR} - 1 \right] \quad \dots\dots 2.18$$

$$a_2 = \frac{h_{in}}{4} \left[(1 - MRR) \frac{(1 + HTR_{in})}{(1 - HTR_{in})} + \frac{AR}{MRR} - 1 \right] \quad \dots\dots 2.19$$

By assuming that the curvature of the inner wall can be related simply to the curvature at mid-height (i.e., $R_{m_{in}} = R_{i_{in}} + h_{in}/2$ and $R_{m_{ex}} = R_{i_{ex}} - h_{ex}/2$), it is possible, with the use of Eqs. 2.9 and 2.10, to obtain expressions for $R_{i_{in}}$ ($= -R_{i_{in}}$) and $R_{i_{ex}}$ ($= R_{i_{ex}}$) in terms of $h_{in}/R_{m_{in}}$, i.e.,

$$\frac{R_{i_{in}}}{h_{in}} = -\left(\frac{R_{m_{in}}}{h_{in}} - \frac{1}{2} \right) \quad \dots\dots 2.20$$

and,

$$\frac{R_{i_{ex}}}{h_{in}} = \frac{AR}{MRR} \left(\frac{R_{m_{in}}}{h_{in}} + \frac{1}{2} \right) \quad \dots\dots 2.21$$

Experimental Equipment

The sum and difference of Eqs. 2.14 and 2.15 can be used to give the coefficients a_2 and a_3 in terms of the non-dimensional length (NDL), i.e.,

$$a_2 = h_{in} \frac{NDL^2}{2\pi^2} \left[-\frac{h_{in}}{R_{i_{in}}} + \frac{h_{in}}{R_{i_{ex}}} \right] \quad \dots\dots 2.22$$

and,

$$a_3 = h_{in} \frac{NDL^2}{4\pi^2} \left[-\frac{h_{in}}{R_{i_{in}}} - \frac{h_{in}}{R_{i_{ex}}} \right] \quad \dots\dots 2.23$$

which are related by,

$$a_3 = \frac{a_2}{2} \frac{(R_{i_{ex}} + R_{i_{in}})}{(R_{i_{ex}} - R_{i_{in}})} \quad \dots\dots 2.24$$

To determine the geometry of the S-shaped duct, it was necessary to assess the effect of various configurations on the estimated pressure rise along the inner wall (ΔC_{pi}). The preliminary compressor study had fixed the dimensions of the inlet annulus (i.e., h_{in} and HTR_{in}), so there were three remaining parameters to be determined; AR, MRR and NDL. Firstly, the area ratio was set equal to 1.0, such that the constant area would give an approximately equal, but opposite, pressure variation along each wall. Since the pressure gradients then exist purely to turn the flow, and not as a result of area change, the aerodynamic behaviour will represent the most generic case of S-shaped flow for a given MRR and NDL.

The remaining two parameters, in combination, affect the pressure rise along the inner wall of the duct (ΔC_{pi}). Reducing either one of them will increase ΔC_{pi} ; NDL more so than MRR. Using the above method, it is possible to calculate the duct length that will produce a particular pressure rise, for a chosen mean radius ratio. With h_{in} , HTR_{in} and AR fixed, the chosen MRR can be used to calculate a_1 and a_2 (Eqs. 2.18 and 2.19). With $AR = 1.0$ and the same ΔC_p across each bend, ΔC_{pi} is equal to ΔC_{pin} , which can be calculated from $h_{in}/R_{m_{in}}$ using Eq. 1.13. In addition, $h_{in}/R_{m_{in}}$ can be used to calculate $h_{in}/R_{i_{in}}$ (Eq. 2.20) and, using the chosen MRR, $h_{in}/R_{i_{ex}}$ (Eq. 2.21). These, together with a_2 , can be used to calculate NDL (Eq. 2.22) and, if required, a_3 (Eq. 2.23).

Using this approach, therefore, it was possible to assess various combinations of parameters. In particular, three levels of loading were chosen and the NDL calculated for a range of MRR, e.g.,

Experimental Equipment

$h_{in}/R_{m_{in}}$	ΔC_{pi}	MRR	NDL
0.343	0.728	0.9	2.71
		0.8	3.95
		0.7	4.99
0.450	0.999	0.9	2.34
		0.8	3.40
		0.7	4.29
0.584	1.396	0.9	2.01
		0.8	2.92
		0.7	3.68

For the present investigation, the annular S-shaped duct had to be representative of a modern gas turbine engine application, where a severe change of radius is required in a short length. As the severity is increased, however, the curvature and pressure gradients increase, eventually leading to flow separation within the duct. Based on the experience of Rolls-Royce^[130], a suitable limit on the inner wall pressure rise coefficient was established to be $\Delta C_{pi} \leq 1.0$. Whilst this was believed to be conservative, the need to guarantee separation-free operation was paramount. With $\Delta C_{pi} = 1.0$ ($h_{in}/R_{m_{in}} = 0.45$), the MRR had to be chosen to be representative; but as MRR reduces, the required length increases. Although, from a practical point of view, it would be easier to incorporate instrumentation into a long working section, axial space was limited on the rig due to the nature of the overhung bearing support for the compressor. In addition, reducing MRR leads to low HTR values at duct exit, as the duct height has to be increased (by $1/MRR$) to maintain the area. Since this gives rise to a small inner wall radius at exit, it was necessary to ensure that this did not fall below a practical minimum radius. With all this in mind, MRR = 0.8 was chosen.

In summary, then, the selected overall parameters describing the shape of the annular S-shaped duct are,

AR	1.0
MRR	0.8
NDL	3.4

and, to define the inner wall, the corresponding coefficients of Eq. 2.11 are,

a ₁	0.24805
a ₂	0.03645
a ₃	0.00598

The radius, slope and curvature distribution of both walls are given in Table 1. Since AR = 1.0, the position of the outer wall was determined such that the passage area ($2\pi r_m h$) was constant. This was calculated at a series of stations which were perpendicular to, and uniformly spaced along, the mid-height line of the duct, which, of course, was an iterative process since the mid-height line was unknown until the outer wall was defined. Note that the datum (x = 0) axial position was at S-shaped duct inlet.

The inlet and exit geometry of the annular S-shaped duct is also summarised below,

	Inlet	Exit	Ratio
x _m (m)	0.00000	0.24174	—
r _i (m)	0.28450	0.21160	0.74376
r _o (m)	0.35560	0.30050	0.84505
r _m (m)	0.32005	0.25605	0.80003
h (m)	0.07110	0.08890	1.25035
A (m ²)	0.142977	0.143023	1.00032
HTR	0.80006	0.70416	0.88013

2.1.4 Single Stage Compressor

During the preliminary design phase, the mid-height operating conditions of the compressor had been established. At a rotational speed of 285.6 rad/s, the compressor has to pass a mass flow of 8.96 kg/s and generate an overall pressure ratio of about 1.026, whilst producing zero swirl at exit from the stator. Corresponding to this design point, the compressor will have a non-dimensional loading of approximately $V_a/U_{blade} = 0.560$ and $c_p \Delta T / U_{blade}^2 = 0.285$. The compressor was designed to meet these requirements using a standard technique, outlined in Appendix 1, which allowed the radial distribution of the aerodynamic conditions to be estimated prior to determining a suitable blade geometry. For the rotor, the aerodynamic conditions are given in Table 3, and the geometry of the 43 'DCA' blades was generated using the parameters given in Table 4. Similarly, for the stator, Table 5 gives the aerodynamic and Table 6 the geometric parameters used to specify the 62 'C4' blades.

2.1.5 Inlet and Exit Sections

Although one of the primary considerations in the rig design has been the incorporation of a single stage compressor, it was essential that the behaviour of the S-shaped duct was established without this present. In Chapter 1, it was recognised that, within the S-shaped duct, the behaviour of the turbulent boundary layers under the combined influence of pressure gradients and curvature would be of interest, and so the inlet duct needed to generate reasonably thick turbulent boundary layers. Although the inlet duct was limited to a maximum length of 1 m, since an inlet plenum was already available within the laboratory, this was satisfactory. Over a distance of 1 m, assuming transition has already occurred, a turbulent boundary layer with zero pressure gradient will grow to a thickness of about 0.018 m (based on $\delta/x = 0.37/R_x^{1/5}$, given by Schlichting^[135]). Each boundary layer, therefore, would occupy about one quarter of the annulus height at S-shaped duct inlet, with an inviscid core region in between.

To allow the air to flow smoothly into the parallel inlet duct, an intake and symmetrical contraction were used. The inner part of the contraction was a half-ellipse shaped bullet, of aspect ratio 1.5, and the outer part of the contraction was designed such that the flow area was the same on either side of the mid-area radius (0.3220 m). As such, the parallel section above the contraction had a radius of 0.4554 m, giving an area contraction ratio of 4.557. This housed a 0.1 m layer of honeycomb with hexagonal cells about 10 mm across, used to straighten the air, and above this was a scroll, with steadily increasing radius of curvature, used to accelerate the air smoothly into the intake from the surrounding plenum.

One further important feature of the inlet design, was the use of boundary layer trips. Their purpose was to ensure that transition occurred in the same way, and at the same axial position, at all circumferential locations around the annulus. Due to the flow acceleration within the contraction, the boundary layers probably would have remained laminar up, and possibly beyond, the end of the contraction. The subsequent free transition would not only have delayed the start of the turbulent boundary layer growth but, more importantly, it might have occurred in a non-uniform manner around the annulus. Therefore, a 0.5 mm diameter wire was attached, with very thin wire loops, to both sides of the contraction, close to the start of the inlet length. These trips were sufficiently large to guarantee transition, but small enough not to artificially increase the size of the boundary layer.

The purpose of the exit duct was to allow the flow to recovery freely from the effects of the second bend, without additional disturbance. The pressure variation across the duct was expected to become uniform within about one duct height downstream of the exit,

and so this was the absolute minimum required exit length. Having reviewed the literature, it was realised that the recovery of the velocity, and particularly the Reynolds stresses, would occur over some considerable distance, but there was insufficient space downstream of the duct for this to be investigated properly. Given the position of the S-shaped duct above the platform, the parallel exit duct was as long as it could be (~0.4 m). From the end of the annular duct, the air passed into the lower plenum, with no attempt made to recover the dynamic pressure of the air.

2.1.6 Facility

The annular S-shaped duct rig was located inside a laser proof room, in one of three available sites supported by a common inlet plenum and exhaust system. With the other sites blanked off, two centrifugal fans were used to provide the pressure rise necessary to draw air through the rig, but these could be bypassed when the rig's own axial compressor was in use.

Air was drawn directly into the inlet plenum through its top surface, which was covered with a coarse wire mesh and a layer of filter material. This removed dust particles from the air and, due to its relatively large surface area ($\approx 4 \text{ m}^2$), provided a uniform low velocity ($\approx 2 \text{ m/s}$) air supply with a minimal loss of pressure. The intake was located centrally within the inlet plenum, which had a square cross-section and a volume of $\sim 6 \text{ m}^3$, with the scroll about 0.6 m above the bottom surface. From the rig, the air was collected by a plenum surrounding the support platform and compressor drive motor. After freely expanding into the plenum, the air flowed into the exhaust through a variable area opening, which was used to control the flow rate through the rig. Along with a 0.2 m^2 opening, which could be manually blanked off in stages to give a coarse adjustment, a remotely operated sliding door could be moved across a square hole of area 0.15 m^2 to provide fine control.

Between the inlet and exit of the entire system, the loss of pressure has to be matched by a pressure rise generated by the axial compressor or centrifugal fans. The pressure loss (ΔP) is proportional to volume flow rate (\dot{V}) squared, such that the operating line is described by $\Delta P = C \dot{V}^2$, where C is a constant. In order to operate at the design point of the single stage compressor, which generates a pressure rise of about 2640 N/m^2 at $\dot{V} \approx 7.3 \text{ m}^3/\text{s}$, the value of C needed to be ~ 50 . This was made up of several individual contributions, the most significant of which were the rig, which gave $C \approx 32$ mainly due to the pressure loss associated with the free expansion into the lower plenum, and the exhaust duct ($C \approx 6$). The remaining contribution was due to the throttle, which was necessary to control the flow. Since this gave $C \approx 1.4/A^2$, based on actual throttle area

(A), a value of $C \approx 12$ was obtained with the maximum available throttle area (0.35 m^2), giving a marginally acceptable maximum flow operating line (see Fig. 6).

The two centrifugal fans were driven by electric motors which were individually controlled, but the speed of the motors could only be changed in finite steps. At their maximum speed, the maximum flow capacity of the two fans running in parallel was about $5 \text{ m}^3/\text{s}$, but with $C \approx 50$ they produced a volume flow rate of $\sim 4 \text{ m}^3/\text{s}$. This gave a mean velocity of about 28 m/s , compared with 51 m/s with the rig compressor installed.

The axial compressor was driven by a DC motor, which was connected to a thyristor based speed control unit. Once set, the speed of the motor was held constant by the feedback of a tachometer voltage to the control unit, where it was compared to a voltage across a variable potentiometer. Although the control unit had a built-in speed control and digital speed display, a remote control was built to make operating the compressor more convenient. By using a ten-turn potentiometer, it was possible to set the speed to within 1 rpm of the required speed, and, in addition, a voltage output proportional to speed was provided (610 rpm/Volt). In order to avoid stalling the compressor during start-up, the control unit limited the maximum acceleration to 50 rpm/s.

2.2 Data Acquisition

This section considers the various techniques used to acquire the experimental data. After covering the practical considerations, the basic instrumentation is outlined. This is followed by a description of the data acquisition system used to log the data, traverse the probe and monitor the rig operation. It then discusses the three-component Laser Doppler Anemometry (LDA) system.

2.2.1 Practical Considerations

At the desired traverse locations, it is necessary to position the probe automatically using a mechanism driven by a computer. Furthermore, it is necessary to control, or at least monitor and manually control, the rig operating conditions during testing, enabling the measured data to be corrected for changes in the atmospheric conditions.

2.2.1.1 Location of Measurements

Since the aerodynamic properties within the S-shaped duct can vary in the streamwise direction, it was desirable to have a large number of traverse stations. Moreover, since the flow direction changes significantly through the duct, it was more appropriate to

angle each traverse line such that it was approximately perpendicular to the streamwise direction. Between inlet ($x/L=0$) and exit ($x/L=1$), nine traverse lines were equally spaced along the mid-height line of the duct, to which they were perpendicular. These are shown in Figure 3 and fully defined by their mid-height position (x_m, r_m) and the traverse angle (ϕ) in Table 2, which also gives the nominal intersection of the traverse and each wall. (Note that ϕ is the angle between the traverse line and the radial direction.)

In addition, several traverses were located upstream and downstream of the S-shaped duct (Table 2). The two inlet traverses (W1 and W2) were located at the end of the inlet duct, some distance upstream of the inlet plane ($x/L=0$) to avoid the axial compressor location. Similarly, the two downstream traverses (A7 and A8) were some distance from the exit plane ($x/L=1$). In this case, they were specified to be approximately one and two exit duct heights away from the exit plane in order to study, to a limited extent, the behaviour of the flow as it recovered from the S-shaped duct.

At the majority of traverse locations, only a single circumferential position was required. This was because circumferential variations were determined by moving the stator blades circumferentially around the rig, over a finite number of blade passages, relative to the fixed probe position. Unfortunately, however, it was not possible to have all the traverses in line with each other along the length of the rig, so the B1, B2 and B3 traverses were located at a slightly different circumferential position around the annulus. Since the A and B traverses were just over a blade passage apart, it was possible to re-set the same stator blade with respect to both, ensuring that all the measurements were made in the wake of the same blade. In order to assess the symmetry of the flow, however, additional traverse were placed around the rig. At positions W2 and A6, four traverses were equally spaced around the circumference.

2.2.1.2 Traverse Arrangements

By traversing across the passage, it was possible to obtain a good definition of the annulus wall turbulent boundary layers. To enable a large quantity of data to be collected in a reasonable time, a traverse mechanism was required that could be driven, and positioned accurately, under computer control. This was achieved by using a stepper motor to drive the traverse mechanism. Typically, a motor speed of 1 rev/sec was used, which was sufficiently quick to allow the traverse to move over its full range in a reasonable time, whilst still providing reliable movement.

For pressure probe measurements, it was necessary for the probe to pass through the outer wall into the passage. To gain access to the rig, the probe body passed through a

small central hole (\varnothing 3 mm) in a bung, which was then inserted into a larger diameter hole (\varnothing 20 mm) in the side of the rig, allowing the probe to move across the passage along the required traverse line. A solid bung was used to blank off the access holes when they were not in use, and, to maintain the smooth continuous wall shape, the ends of both sets of bungs were contoured to the surface geometry. In Photograph 6, the blanking bungs for each traverse can be seen passing through a large perspex block on the side of the rig, which was used to support the traverse mechanism.

The traverse mechanism used for the 5HP measurements consisted of a rack and pinion, driven by a stepper motor through a gear box. The mechanism, supported on a perspex block and attached to the side of the rig in line with each traverse, produced a linear movement of 1 mm for one revolution of the motor, which consisted of 96 half-steps. With one half-step equivalent to 0.01 mm, the probe could be moved very precisely, although the positional accuracy was probably slightly worse (~0.1 mm), due to the small amount of backlash in the mechanism and the nature of the setting up procedure.

For the LDA measurements, the optical probes were moved by a lead-screw directly connected to a stepper motor (Photo. 7). With a pitch of 2 mm and 200 steps per motor revolution, the probe could be moved precisely 0.01 mm in one step. In addition, since an optical technique was developed (see Sect. 2.2.4.4) to enable the wall positions to be found, and with virtually no backlash in the mechanism, the accuracy with which the probe could be positioned was nearly as good (~0.05 mm).

When the compressor was present, circumferential traversing was achieved by moving the stator blades, relative to the fixed circumferential location of the probe. The traverse mechanism consisted of a steel cable and winch (Fig. 3), driven by a stepper motor via a reduction worm-gear box, which pulled against the aerodynamic load on the stators, with counterbalance weights used to offset the large load at high compressor speeds. Although a high precision was achieved per step, the use of a cable meant that there was some uncertainty in the circumferential position, but this could be minimised by moving the stator blades to the required position from the same direction (over a given distance against the load). In this way, the stator blades could be moved to an absolute position with an accuracy of approximately 0.1% of the blade circumferential space (θ_s).

In practice, traversing was performed in a number of different ways. For the 5HP measurements, the probe was simply traversed from the inner to outer wall. However, due to the relative difficulty of obtaining data close to the annulus walls, the LDA measurements were taken from mid-height to inner, then mid-height to outer, with a final point back at mid-height. Circumferential traversing was carried out in the positive θ -direction, which was in the same direction as the compressor rotation, i.e., clockwise

Experimental Equipment

when viewed from upstream. Effectively, for the probe to move in this direction, the stator blades had to be moved in the opposite direction, against their aerodynamic load. When the compressor was present, area traversing was carried out over one blade sector, from mid-passage to mid-passage. For the 5HP measurements, the probe was moved primarily in the cross-passage direction, with the stator blades incremented on completion of each traverse. However, the LDA area traverse was carried out the other way round, with movement primarily in the circumferential direction. Without the compressor, it was possible to reduce the uncertainty in the data by repeating the traverse several times. With the 5HP, each traverse was carried out six times and, at every position across the passage, the data was averaged to define a single profile. The LDA data was taken twice, as individual traverses, one run after the other with some points taken at different positions. In this case, there was no attempt to merge or average the two traverses, rather they will be presented alongside each other to give an increased confidence in the indicated flow behaviour.

One important feature of the present investigation was that the measurements were taken at the same non-dimensional positions at each traverse location. As a result, the data was collected on a structured mesh, like a CFD calculation, allowing the streamwise variations in the flow properties to be easily determined. For example, the 5-hole probe data was obtained at the following fraction heights at every location, with the points becoming more closely spaced towards the wall,

Pt.	1	2	3	4	5	6	7	8	9	10	11	12	13	14	15	16	17	18	19	20	21	22	23
h (%)	2	4	7	10	13	16	20	24	28	34	42	50	58	66	72	76	80	84	87	90	93	96	98

Similarly, when traversing downstream of the compressor, a common circumferential distribution was used. In this case, the angular position (θ), relative to the stator blade mid-passage datum position, was used to define the position of the probe (even though the stator blades were actually moved), and the same positions, non-dimensionalised by the stator spacing ($\theta_s = 2\pi/62$ rad.), were used at every location, with the points more closely space in the wake, e.g.,

Pt.	1	2	3	4	5	6	7	8	9	10	11	12	13	14	15	16	17	18	19	20	21
θ/θ_s (%)	0	10	18	24	29	34	38	42	45	48	50	52	55	58	62	66	71	76	82	90	100

2.2.1.3 Rig Operating Conditions

While acquiring test data, it was important that the rig was operated at the same condition during the individual runs, which occurred over a number of days. However,

since the atmospheric pressure (p_α) and temperature (t_α) would vary over this period, the operating conditions were described by non-dimensional parameters involving p_α and t_α . The air flow rate was described by the flow function ($\dot{m}\sqrt{t}/A p$) and, when the axial compressor was installed, N/\sqrt{t} was used for compressor speed. (Note that these quantities are not strictly non-dimensional, since several dimensional constants have been removed for convenience, but, in the gas turbine industry, it is common practice to refer to them as the 'non-dimensional' flow and speed; a convention followed here.)

The mass flow rate (\dot{m}) could be obtained by measuring the change in static pressure across the inlet contraction (Δp). Assuming 1D inviscid flow, the mass flow is given by,

$$\dot{m} = C \sqrt{\rho \Delta p} \quad \dots\dots 2.25$$

where, C is a function of the upstream area ($A_1=0.651532 \text{ m}^2$) and the downstream area ($A_2=0.142977 \text{ m}^2$), i.e.,

$$C = \left(\frac{2 A_1^2 A_2^2}{A_1^2 - A_2^2} \right)^{\frac{1}{2}} = 0.207 \quad \dots\dots 2.26$$

In reality, the actual numerical value of C will differ slightly from this ideal value and should be obtained by calibration (i.e., a discharge coefficient should be obtained for the flow meter). Unfortunately, a full calibration could not be undertaken as there was no readily available facility on which this could be carried out. However, the mass flow rate obtained by integrating the mean velocity profile measured at the end of the parallel inlet duct was found to be in good agreement with the value obtained from Eq. 2.25, suggesting that the well designed inlet had a discharge coefficient close to 1.0.

Along with Δp , it was necessary to measure the atmospheric pressure and temperature in order to determine the mass flow rate from Eq. 2.25. As well as determining the air density (ρ) from,

$$\rho = \frac{p_\alpha}{R t_\alpha} \quad \dots\dots 2.27$$

these were also required in order to calculate the 'non-dimensional' flow and speed. To measure p_α , a Druck absolute pressure transducer (PDCR 910) with a 1 Bar range was used, which produced an output proportional to absolute pressure ($1.111 \times 10^6 \text{ N/m}^2$ per Volt with a 9 V power supply). In addition, atmospheric temperature was measured by a K-type thermocouple placed in the intake.

In order to determine the compressor speed, the output voltage signal from the remote speed control unit was measured.

2.2.1.4 Correction of Measured Data to Standard Conditions

By running the rig at constant 'non-dimensional' operating conditions ($m\sqrt{t}/Ap$ and N/\sqrt{t}), it was possible to apply a simple correction to the raw data, before it was recorded, to correct it to standard atmospheric conditions ($p_\alpha = 101325.4 \text{ N/m}^2$ and $t_\alpha = 288.15 \text{ K}$). The flow function ($m\sqrt{t}/Ap$) is proportional to the mean Mach number of the flow ($\hat{U}/\sqrt{\gamma R t}$) and, similarly, N/\sqrt{t} is proportional to the blade speed Mach number ($U_{\text{blade}}/\sqrt{\gamma R t}$).

Therefore, the correction applied to measured velocities (U_{meas}), obtained directly from LDA for example, simply uses the fact that the Mach number of the corrected velocity, based on standard conditions, will be the same as that of the measured velocity, based on the actual conditions, i.e.,

$$U_{\text{corrected}} = U_{\text{meas}} \times \left(\frac{288.15}{t_{\alpha \text{meas}}} \right)^{\frac{1}{2}} \quad \dots \dots 2.28$$

Further, given that pressures would be measured relative to a suitable reference pressure in the rig, the measured pressure difference (Δp_{meas}) will be proportional to the mean dynamic pressure of the flow, i.e., $\propto \rho \hat{U}^2$. Therefore, since \hat{U}^2/t_α would be the same for both the measured and corrected data, the correction that has to be applied to measured pressures, obtained from a 5HP for example, becomes,

$$\Delta p_{\text{corrected}} = \Delta p_{\text{meas}} \times \left(\frac{101325.4}{p_{\alpha \text{meas}}} \right) \quad \dots \dots 2.29$$

Note that velocities obtained from corrected pressure data (e.g., from the analysis of corrected 5HP measurements) correspond to standard conditions, and do not need to be corrected with Eq. 2.28 as well.

2.2.2 Basic Instrumentation

During the present investigation, a 5-hole probe (5HP) was used to measure the mean flow behaviour. Due to the relative ease with which this could be used, measurements were taken at every station, with and without the compressor present. In using a 5HP, differential pressure transducers were needed to convert the measured pressures into

voltage signals, so that they could be read by the data acquisition system. To provide additional data, wall static pressure taps and thermocouples were also used.

2.2.2.1 Five Hole Probes

By measuring five pressures with this specially constructed probe, it was possible to fully define the mean flow, i.e., three velocity components and static pressure. The head of the probe was manufactured from five hypodermic tubes, soldered together, and was approximately 1.6 mm across. The four side tubes, surrounding the centre tube, were chamfered at approximately 45° , producing a faceted appearance at the tip of the probe. At a distance of 10 mm from the end, the tubes were bent through 90° , before passing into the probe body about 40 mm further along. The body was simply a 3 mm diameter tube, carrying the five pressure tubes and giving the probe strength.

The magnitude of the pressure sensed by each of the holes varies according to the velocity and direction of the flow, relative to the probe head. Since it was not practical to determine the flow direction by automatically varying the orientation of the probe until the pressures sensed by opposite side holes were equal, the probe was used in a non-nulled mode. Consequently, it was necessary to calibrate the probe to determine the way in which the five pressures varied with flow direction. The calibration involved placing the probe in a flow of known conditions, over a range of pitch and yaw angles, for which a free-jet and gimbal mechanism were used. The air jet was produced by a centrifugal blower discharging through a circular nozzle, which had a flat velocity profile in the core of the jet. The stepper motor driven gimbal allowed the probe to be rotated in two directions at once, presenting a compound flow angle onto the probe head. Using differential pressure transducers, the five pressure were measured relative to the ambient static pressure, along with a reference Pitot pressure, and data was acquired automatically over a range of angles using the data acquisition system. The method by which the calibration data is processed and then used to obtain meaningful quantities from the actual pressure measurements is described in Chapter 3 (Sect. 3.1.2).

One important aspect of the 5HP measurements was the need to allow a finite time for the reading to settle. After the probe has been moved to a new location, such that the holes sense a different pressure, it takes some time for the pressure to adjust in the relatively large volume of each tube, connecting the probe to the transducer, since the necessary transfer of air occurs through the very small diameter hypodermic tube within the probe. By examining the response of the indicated pressures when the probe was moved within the flow of interest, a suitable waiting period was determined beforehand, so that a fixed period (typically ten seconds) could be applied before reading the probe at each measurement position.

2.2.2.2 Pressure Transducers

Apart from the absolute ambient pressure transducer, all pressures were measured relative to a reference pressure using Furness transducers. Depending on the type, these were able to operate with differential pressures in the range ± 5000 , ± 1000 or $\pm 250 \text{ N/m}^2$, although all types produced a $\pm 1 \text{ V}$ output. Several sets of similar transducers were available, such that a set could be used to measure the five pressures of a 5HP at the same time.

To convert the voltage signal into pressure, it was necessary to determine the exact calibration of each transducer. This was achieved by measuring the output voltage when a series of known pressures, read from a Betz water manometer, were applied across the transducer. Since the response was exactly linear, it was possible to use a single calibration constant, obtained as the slope of a least-square straight line fit through the calibration data, providing the transducer output was zero when both sides of the transducer were at the same pressure. Prior to use, therefore, each transducer was manually adjusted to give zero output. This was important since the output of the transducers drifted slowly over time, even though they were kept at their operating temperature by leaving them switched on in between tests. In addition, after completion of a test the transducer outputs were checked, and if their zero readings were greater than $\pm 1 \text{ mV}$ the test was invalidated and the data rejected. However, for the majority of tests the drift was typically less than $\pm 0.2 \text{ mV}$.

2.2.2.3 Wall Static Pressure Taps

Many static pressure taps were incorporated into the annulus walls of the rig. These were used to obtain additional data, as well as providing a choice of reference pressures, relative to which probe measurements could be made. They were mainly positioned in line with the traverses, although additional taps were closely spaced along the length of the S-shaped duct, on a helical line to avoid creating any aerodynamic disturbance between adjacent holes. The taps were 0.5 mm diameter holes drilled directly into the perspex walls, with extreme care being taken to ensure that the edge of the hole was not damaged. Upstream of the compressor, the inner wall taps were connected to the outside of the rig via steel tubes running through the four struts in the intake, whereas, downstream, the flexible tubes ran into the lower plenum, where they were connected to steel tubes which passed into the laboratory through the side of the plenum.

As already outlined, the mass flow rate could be determined by measuring the change in static pressure across the inlet contraction. For this, four static pressure taps were placed around the cylindrical part of the scroll intake, between the honeycomb flow

straightener and contraction, and four pairs of taps, opposite each other on the inner and outer parts, were located very close to the end of the contraction, mid-way between the struts. To obtain a consistent mass flow, one upstream and one downstream outer wall tap were used throughout the testing.

2.2.2.4 Thermocouples

Temperature was measured using standard K-type thermocouples. These were made by joining thin wires, of the appropriate metals, at one end, and, at the other end, a standard connector was used so that the thermocouple could be plugged directly into the data acquisition system. Of primary interest was the measurement of ambient temperature, for which the end of a single thermocouple was placed in the inlet flow, through a hole drilled in the intake just upstream of the honeycomb. In addition, compressor shaft bearing temperatures were monitored using thermocouples embedded in their housings.

During rig commissioning, the temperature rise of the compressor was very crudely measured, along with the static pressure rise, to assess its performance. For this, thermocouple probes were used, with the junction placed at the tip of a probe, and inserted into the rig in the same way as pressure probes. Two probes were fixed in position at mid-height, one upstream and the other downstream of the compressor at mid-stator passage. In this way, simultaneous static pressure and temperature measurements could be taken, over a range of operating conditions.

2.2.3 Data Acquisition System

In order to record the experimental data from the test rig, a PC based data acquisition system was used. As well as the main task of digitising the signals from a variety of sources, the system could control the position of the stepper motor driven traverse mechanism and ensure that the rig was operating at the correct condition.

2.2.3.1 Description

To allow a degree of flexibility when setting up a particular experiment, a CIL Alpha modular system was purchased. With this system, a variety of different blocks could be used within a single rack, with an additional power supply block also present. The rack was connected to a standard PC, using an Alpha03 card inside the computer. Of use during the present tests were the 'A' block for analogue voltage input, the 'K' block for thermocouple input and the 'S' block for providing stepper motor drive logic; although the fast response 'F' block was also used during the development of the system. The various blocks were linked by a parallel bus and cable to the Alpha03 card, which, as

well as controlling the operation of all the blocks, contained a 2.5 kHz, 16 bit ADC, used to digitise analogue signals from the 'A' and 'K' blocks.

The 'A' block was a multiplexer, with eight analogue (differential) voltage input channels accepting signals in the range of ± 5.0 V, ± 2.5 V, ± 1.0 V or ± 0.1 V. To obtain a reading, the required channel was selected and the input range specified. With the 16 bit ADC, an integer in the range $\pm 32,768$ was returned. This value could be a single reading or the average of a specified number of samples, each sample taking 0.4 ms to acquire. When more than one channel was in use, the readings could not be taken at the same time and had to be sequenced by the software.

Similarly, the 'K' block was a multiplexer, with six thermocouple input channels. A linearised and cold junction compensated integer output was returned, which could be converted into temperature with a resolution of 0.1°C . Again, the reading could be the average of any number of samples, acquired at a rate of 2.5 kHz, with only one channel read at a time.

The 'S' block was used to drive a stepper motor, by alternately energising the four coils of the motor in the correct sequence. With appropriate power supply, the 'S' block could have been directly connected to the motor, but, in order to drive large (2 A per phase) stepper motors, it was necessary to use a separate McLennan stepper motor drive unit to provide the power. This unit was controlled using the step, direction and enable logic (TTL) generated by the 'S' block. For a given direction, the square wave signal ensures that the motor moves a specified number of steps and, in addition, the speed of the motor can be controlled by varying the step rate.

Typically, the data acquisition system used during the present investigation comprised; two 'A' blocks, to measure the five 5HP pressures, additional reference pressures and rig operating conditions (ambient pressure, mass flow and compressor speed); a 'K' block, for ambient and bearing temperatures; and two 'S' blocks, one for the probe traverse and one for the circumferential traverse.

2.2.3.2 Software

To simplify the use of the CIL equipment, a suite of generalised routines was written to control and acquire data from each of the blocks. Using the software driver supplied, a separate routine was used for each block, which was designed to simply return the required readings, in relevant units, or drive the stepper motor to a specified position. All parameters controlling the operation of the blocks were stored in a set-up file, such that they could be modified to reflect the requirements of a particular test.

Along with the basic parameters, the set-up file allowed the number of samples of each channel to be specified. On taking a reading, the samples were always averaged to give a single value for each channel, but, for a particular selection of channels, the sequence in which the samples were taken could be varied. With the hardware, it was possible to specify the number of samples in any one reading. However, since a large number of samples were required to obtain a reasonably steady reading, a finite time would elapse before the next channel could be read. On measuring the five pressures of a 5HP, for example, this was not acceptable since each pressure would be obtained at a different time, between which the conditions at the probe may have altered, however slightly and for whatever reason. When reading more than one channel, therefore, it was possible to reduce the number of hardware samples per reading and repeatedly read the channels, in sequence, a specified number of times. In this way, the software could calculate an overall average for each channel, which would include data obtained throughout the overall sampling period. Typically, the data was obtained from the average of 1000 samples, with 50 samples per hardware reading and 20 sequentially repeated readings.

2.2.3.3 Traversing

During a test, data was obtained at a series of traverse positions, which were specified in a traverse file to allow them to be altered easily. Using information contained in the set-up file, which specified the steps-per-revolution and the number of revolutions required to move a physical distance, the traverse control software could move to the required positions, so long as its datum position was known. At the start of a test, therefore, it was necessary to move the probe to a known position, using the annulus walls as a reference. By touching the probe very carefully onto each wall, it was possible to move half way between them and specify the mid-height position as the datum. In addition, on accounting for the size of the probe, the distance between the two walls could be determined accurately and, by assuming the mid-height position to be correct, the actual wall positions obtained.

2.2.3.4 Test Procedure

With the appropriate set-up and traverse files, the data acquisition program was used to control the test. After measuring the atmospheric conditions, an output file for the data was opened containing the initial information about the traverse location and test conditions. At the required 'non-dimensional' operating conditions, the probe was moved to each successive position and, after a period of waiting to allow the probe to settle, data was taken and written to the output file.

To ensure that the rig operated at the same condition throughout each test, the mass flow (\dot{m}), compressor speed (N) and the atmospheric conditions (p_a and t_a) were measured before each point, and used to calculate the 'non-dimensional' operating conditions (N/\sqrt{t} and $\dot{m}\sqrt{t}/Ap$). When these were outside a given tolerance, due to a change in the atmospheric conditions for example, the discrepancy was indicated and data acquisition could not proceed until the speed or throttle setting had been adjusted to correct the situation. In addition, when the compressor was in operation, the shaft bearing temperatures were measured, so that a warning could be given when they exceeded their predetermined normal operating temperature, thereby indicating potential mechanical problems.

With the rig compressor installed, the monitoring of flow was not necessary. Provided the non-dimensional behaviour of the compressor and facility operating line did not change, the correct $\dot{m}\sqrt{t}/Ap$ would be achieved simply by maintaining the correct N/\sqrt{t} , i.e., there was no need to adjust the throttle. Therefore, the speed was checked using a tight tolerance, typically ensuring that it was within 0.1% of the required value. However, without the rig compressor, it was necessary to adjust the throttle to maintain the desired $\dot{m}\sqrt{t}/Ap$, as the flow fans could only be set in discrete intervals due to the nature of their control units. Therefore, as the flow fans did not operate at constant N/\sqrt{t} , the throttle had to be adjusted to achieve the desired flow. In this case, when the flow function was checked, a 0.2% tolerance was typically applied.

As an additional check on the rig operating conditions, a pitot probe was used. This was located upstream of the S-shaped duct, at mid-height, and was measured relative to a nearby wall static pressure, at the same time as the actual data, using another differential pressure transducer. In a similar way to the flow meter, the square root of this pressure difference was proportional to the flow rate, and could be used to account for minor discrepancies in the operating conditions. In addition, without the compressor, the five pressures of the 5HP were measured relative to the same static pressure, which itself was measured relative to the inlet total pressure, obtained from a static pressure tap in the centre of the inlet bullet. Since the total pressure remains constant within the potential core, between the annulus wall boundary layers, both reference pressures were equivalent. During the subsequent analysis, therefore, pressures could be referenced to the inlet total pressure, which was more meaningful than using the wall static pressure. When the compressor was installed, a static pressure in the parallel exit section was used to reference the 5HP measurements, and, in order to monitor the compressor operation, this was measured relative to an upstream static pressure.

2.2.4 Laser Doppler Anemometer

To obtain a better understanding of the flow behaviour, Laser Doppler Anemometry (LDA) was used to measure the turbulent flow within the annular S-shaped duct. With this well established non-intrusive technique, it was possible to obtain good spatial and temporal resolution of flow velocity, with no calibration of the equipment necessary. In addition, by simultaneously measuring in three different directions, using a 3-component system, three mutually orthogonal velocity components could be derived. From the many coincident samples at each point, it was possible to obtain all the time-averaged velocity data, including all the Reynolds stresses and higher order velocity correlations.

Techniques had to be developed to allow the LDA system to be used on the test rig. By mounting the optical probes on a traverse, data could be obtained across the passage, and with the transmitted light and the reflected signals passing through thin windows in the outer casing, the three measurement volumes remained coexistent at every position. Using several curved windows, measurements were obtained at the same streamwise locations as the 5HP data, even though optical access was severely restricted and the measured velocity components were highly non-orthogonal. In addition, by using off-axis detection and avoiding stray reflections, data could be obtained in close proximity to the surfaces of the annular passage.

2.2.4.1 Equipment

Measurements were obtained using a Dantec 3-component LDA system, incorporating the 60X FibreFlow series of optical elements (Photo. 8). Light produced by a Coherent 5 watt Argon Ion laser was separated into the green, blue and violet wavelengths within a transmitter box, mounted in line with the laser on a rigid bench. For each of the different colour components, two coherent laser beams were required in order to create interference fringes in the measurement volume, formed by the intersection of the beams, using optics to focus the light in this very small region. Further, by using a Bragg cell to shift the frequency of one of the beams by 40 MHz, the fringes were made to move across the volume such that slow moving or reverse flow could be detected.

To give maximum flexibility, the optical probes were connected to the system using fibre optic cables. For each probe, a distribution box was used to link the probe to both the laser light source, via fibre optic manipulators attached to the transmitter box, and to a photomultiplier. To obtain 3-component measurements, two probes were used simultaneously; a 1D probe for the violet light and a 2D probe for the other two components. The basic probes were small, with a focal length of 50 mm. In order to acquire data across the entire annular passage, therefore, beam expanders were needed

to increase the focal length; although this also increased the probe head diameter to 28 mm, making it more difficult to hold and manoeuvre them on the rig. Along with the transmitting optics, each probe incorporated receiving optics to allow light signals to be detected and transmitted back along the multi-mode fibre to the photomultipliers, and, for each channel, optical filters were used to ensure that the photomultiplier detected only light of the appropriate frequency.

In order to obtain a signal, it was necessary to seed the flow. By introducing small particles that follow the flow, a burst of light was scattered by each particle as it passed through the measurement volume. Seeding was provided by a TSI Six-jet atomiser using a relatively low viscosity oil, which was driven by the laboratory compressed air supply. The resulting particles of approximately 1 μm diameter were injected by a single radial pipe, with multiple outlet holes, located in the plenum directly upstream of the measurement position.

For each channel, the voltage signal from the photomultiplier was processed by a 57N10 Burst Spectrum Analyser (BSA). As a result of the Doppler effect, the burst of scattered light from a particle crossing the interference fringes in the measurement volume was frequency modulated. By processing this Doppler burst in the frequency domain, the BSAs can determine the frequency of the burst, and hence a velocity component of the particle, which is assumed to be following the flow. To ensure synchronous operation and simultaneous detection of bursts the BSAs were linked together, and, in addition, they were linked via an IEEE 488 interface to a stand-alone PC, running "Burstware" (V3.0). As well as controlling the mode of operation and set-up of the BSAs, this software allowed the raw data to be acquired and stored on the hard-disk of the computer, in a relatively easy manner, for later analysis.

2.2.4.2 Optical Arrangement

At the focal point of a probe, the interference fringes can be thought of as regularly spaced light and dark regions within the measurement volume (Dantec^[42]). For a known laser light frequency (λ), the fringe spacing (C) is determined by the included angle between a pair of intersecting beams (θ), i.e.,

$$C = \frac{\lambda}{2 \sin(\theta/2)} \quad 2.30$$

As a particle crosses the fringes, the scattered light intensity will increase and decrease at a frequency which is dependant on C, and the velocity normal to the fringes. By

Experimental Equipment

measuring the Doppler frequency (f_D), therefore, the velocity (U_{BSA}) of the particle can be determined from C, which is referred to as the calibration factor, i.e.,

$$U_{BSA} = C f_D \quad 2.31$$

During the present investigation, the beam separation at the front lens was 16 mm, and the receiving optics aperture was 22 mm in diameter. A focal length of 120 mm was used for the majority of the measurements, although 100 mm was used at the upstream station, giving rise to various calibration factors,

Calibration Factor (m/s per MHz)				
Focal Length (mm)	θ (°)	Green ($\lambda = 0.5145 \mu\text{m}$)	Blue ($\lambda = 0.4880 \mu\text{m}$)	Violet ($\lambda = 0.4765 \mu\text{m}$)
100.0	9.1478	2.9876	3.0597	3.2259
120.0	7.6281	3.5817	3.6681	3.8673

On the test rig, the transmitted light and the reflected signals had to pass through the outer casing, with optical access provided by several curved perspex windows. Each window was made to follow the local surface curvature of the outer casing, thereby leading to windows of complex geometry within the S-shaped duct. Although each beam was refracted by a different amount as it passed through the window, the coexistence of the three measurement volumes could be maintained, at all positions across the passage and at all traverse locations, by limiting the window thickness to 1 mm. Five windows were used on the rig, to cover the traverse stations defined for the 5HP measurements. These were located at various circumferential positions around the rig, and each covered a number of traverse locations, i.e., window 1 - W1; window 2 - N1, A2, A3; window 3 - B1, A4; window 4 - B2, A5, B3, A6; window 5 - A7, A8, defined in Table 2. Note that the upstream position W1 was used due to the limited space available for the laser window, whereas W2 had been used to acquire the 5HP data, and, similarly, it was necessary to use position N1, slightly downstream of the probe traverse position A1, due to the difficulty of obtaining optical access to the duct close to the compressor location. Each window was manufactured with a frame supporting the thin, highly polished optical region, and slotted into holes cut into the outer casing, producing a smooth continuous surface.

At each location, the traverse mechanism was attached to a large perspex plate on the side of the rig (Photo. 7), and also to the frame of the window so that the whole assembly could be removed from the rig. The probes were rigidly mounted onto a perspex probe support plate, attached to the traverse, which allowed them to be set at

any of a number of angular positions, rotating about a virtual centre corresponding to the nominal focal point of the probes. In addition, each probe was held within a perspex block, which allowed it to be set at any angle of rotation about its own axis, whilst being able to slide along its axis under the action of a fine precision screw.

While measuring the three velocity components, it was essential that the measurement volumes were coexistent. To achieve initial alignment the probes were removed from the test rig along with the window, while mounted on the support plate and attached to the traverse mechanism. In this way, alignment could be achieved on an optical set-up bench, and could be guaranteed when the whole arrangement was returned to the rig. On the bench, all six beams were projected through the window and made to pass simultaneously through a 50 µm diameter pin hole. With the probe angles determined by the chosen mounting position on the support plate, this was achieved through minor adjustment of the probe positions along their own axes, and by allowing one probe to rotate very slightly about an axis in the axial-radial plane perpendicular to the probe axis. In addition, the pin hole was also used to track the path of each beam which allowed the probe angles, defined in Figure 4 relative to the traverse direction, to be determined to within $\pm 0.2^\circ$. The actual probe angles used at each traverse location are given in Table 7. These angles were required to determine the value of the terms in the optical transformation matrix, used to convert the measured velocity components into mutually orthogonal components (see Sect 3.1.3.1).

To minimise errors associated with the derived velocity data, the probes were mounted on the support plate with the included angle between them as large as possible. Unfortunately, this was limited by the size of the access window and the distance to be traversed across the annulus and, with typical included angles of about 42.5° , this resulted in a noticeable error in the cross-stream Reynolds normal stress. At the majority of the traverse locations, the error in the Reynolds shear stress was negligible, since the probes were set on either side of the traverse line such that their average angle was as small as possible. At S-shaped duct inlet, however, both probes had to be set on the same side of the traverse line due to the limited optical access downstream of the compressor location, resulting in a large average angle and a noticeable error in the derived shear stress. These errors are discussed further in Chapter 3 (Sect. 3.1.3.3), where it is shown that they result from the finite resolution, to which the processor can determine velocity, and the optical transformation process.

Off-axis detection was used to reduce the length of the measurement volume, with the 1D probe being used to detect signals from the blue, green velocity components and vice-versa. For each probe, a pair of intersecting beams give a measurement volume of

approximately $0.1 \times 0.1 \times 1.5$ mm in size. However, the volume of intersection between two probes at different angles is much smaller, with only part of each volume seen by the other probe. For the typical included angles used, the measurement volume was reduced to an effective size of $0.1 \times 0.1 \times 0.3$ mm. In addition, several techniques were used to prevent stray reflections entering the receiving optics. To cut out beams reflected from the outer surface of the optical window, a beam-stop was positioned between the probes, and the 1D probe was always at a larger angle than the 2D probe to prevent violet light, reflected from the inner wall, from entering the 2D probe at some point across the passage. Similarly, the 2D probe was rotated through 45° so that the reflected green and blue beams would not reach the 1D probe, and, in addition, the inner surface was coated with matt black paint to minimise the reflected light level. With the aid of all these techniques, data could be obtained as close as 0.4 mm to each surface.

2.2.4.3 Signal Processing

The signals from the photomultipliers were processed using BSAs (Dantec^[42]). As a particle passes through the measurement volume, the Doppler burst is detected and processed, within the hardware of the BSA, using a Discrete Fourier Transform (DFT) technique to determine its frequency. Upon detection, the continuous voltage signal is sampled at a frequency (f_s), and a finite number of samples (N) are used by the DFT to determine the frequency of the signal (f_D). To avoid aliasing problems, f_s must be at least twice f_D , which would severely limit the operating range of the processor. Therefore, the input signal is mixed with a sinusoidal signal which has a frequency equal to the centre frequency (f_C) of the measurements (i.e., f_C is equivalent to the mean velocity detected by the relevant channel). With additional filtering, the compound signal has a frequency no greater than half the bandwidth (B) of the measurements (i.e., B is equivalent to the maximum minus minimum velocity of the turbulent motion that can be detected by the channel). In this way, the processor can sample the signal at a much reduced frequency, dependent only on B . In fact, a sampling frequency of three times the maximum frequency ($B/2$) is used, i.e.,

$$f_s = 1.5B \quad 2.32$$

The BSA could operate at discrete bandwidths (in multiples of $2^n \times 32$ MHz), up to a maximum B of 32 MHz (equivalent to about 100 m/s for the present values of C) determined by its maximum sampling frequency of 48 MHz. A wide range of centre frequencies were also available, depending on the choice of B and whether frequency shift was selected. Without frequency shift, negative velocities could not be detected, allowing f_C to be set in steps of $0.125B$ between $0.625B$ and $2B$. With frequency shift,

Experimental Equipment

however, f_C could be set between $-2B$ and $2B$, in steps of $0.125B$, for $B \leq 8$ MHz, but above this the range of f_C was constrained slightly.

On determining the frequency of the burst, the DFT produces a frequency spectrum containing a series of discrete values. The position of the global maximum of the spectrum is used to determine f_D . However, the finite interval between the discrete values in the spectrum is effectively the resolution to which f_D can be determined, and, according to Fourier transform theory, is given by f_s/N . Note that the reciprocal of this is also the record interval (R_I), the period of time over which the burst is sampled, i.e.,

$$R_I = \frac{N}{f_s} \quad \dots\dots 2.33$$

To improve the resolution of f_D , the BSA uses two techniques. Firstly, zeros are added to the sampled time signal in between the actual values, before the DFT is performed, which doubles the number of discrete values in the Fourier spectrum, without affecting the frequency. Secondly, a sinc curve ($\sin(\pi(f - f_D)R_I)/\pi(f - f_D)R_I$), representing the Fourier transform of a time-limited complex exponential (which is similar to the actual signal sampled over R_I), is fitted to the largest discrete value and its two neighbours in the Fourier spectrum, which are $1/2R_I$ apart due to the zero-filling. In this way, a frequency resolution of about $1/16R_I$ is obtained, and, by including the calibration factor, the velocity resolution (ΔU_{BSA}) can be determined, i.e.,

$$\Delta U_{BSA} = \frac{C}{16 R_I} \quad \dots\dots 2.34$$

Thus the value of R_I determines the processor resolution, and Eq. 2.34 suggests that R_I should be as large as possible. However, there is a limit to which R_I can be increased, since, for too large a value, the signal would be sampled beyond the duration of the burst. With some of the samples wasted, the resultant frequency spectrum would be poorly defined, due to the reduced signal-to-noise ratio (SNR), and, if validated, would increase ΔU_{BSA} . Therefore, for the present investigation, a record interval of $1.333 \mu s$ was used, since, for the measured velocity components, this was about half the time taken by the fastest particle to cross the measurement volume. In addition, the same value of R_I has to be used on all three processors. With this fixed, a further constraint is placed on the selection of B , since from the definition of R_I and f_s it is easily shown that $B = N/2$ for the required R_I , and N is limited to 8, 16, 32 or 64 by the processor.

To ensure that each sample of the three velocity components was associated with the same particle passing through the control volume, all measurements were performed with hardware coincidence filtering. This meant that the incoming signals were only

processed when bursts were detected simultaneously by all three BSAs. Detection is performed by filtering the signal to extract the pedestal and envelope of the Doppler burst, and when both these have crossed a threshold level, in all three BSAs, sampling begins and the arrival time is recorded. Furthermore, if the level of these signals continues to rise above other predetermined levels, the arrival time is amended and sampling is restarted to ensure that the largest amplitude part of the burst is used for frequency determination.

After simultaneous detection, some bursts were rejected by the internal validation tests conducted by each processor. Oversize particles, which give rise to a large pedestal, were immediately rejected by the burst detector, and signals which gave rise to a poorly defined spectrum (largest discrete value in the fourier spectrum value less than 4 times the next highest local maximum) were rejected after processing. This latter criterion meant that poor quality bursts, with a low SNR, were rejected. Unfortunately, due to the properties of the Argon-Ion laser, which produces lower light power levels in the blue (60%) and, to a greater extent, the violet channels (20%) in comparison to the green (100%), the proportion of data validated by each processor during acquisition was different. Typically, only 50% of the bursts were validated for the violet channel and 75% for the blue, in comparison with 100% for the green, which suggests that these channels were operating with a poorer SNR. In addition, those bursts that are validated by the blue and, in particular, the violet channels will produce a poorer quality spectrum, such that ΔU_{BSA} is larger than that indicated by Eq. 2.34. On assessing the Reynolds stress errors produced by the finite resolution and the optical transformation process (Sect. 3.1.3.3), ΔU_{BSA} was found to correspond fairly well with Eq. 2.34 for the green channel, whereas for the violet channel ΔU_{BSA} was twice as large.

2.2.4.4 LDA Operation and Experimental Technique

During the LDA tests, the rig operation and traversing was controlled by a separate PC to that used to acquire the data. In effect, the data acquisition software used for the 5HP measurements was used to monitor the rig operating conditions and drive the traverse mechanism, but not for the LDA data acquisition. Having moved to the required position, the operating conditions were checked in the usual way before handing over to the LDA. On completion of the data acquisition, movement of the traverse to the next point was signalled manually to the rig control program. With the rig operating at constant 'non-dimensional' conditions, the constant Mach number meant that the actual velocities were dependant on temperature. Although it was not possible to correct the measured velocities on-line, Eq. 2.28 could have been used after the tests were completed. However, this was found to be unnecessary, since the correction would have

had an insignificant effect on the velocities due to the fact that the temperature remained fairly constant, at ~288 K, during the measurements.

With the rig on-condition and the seeding turned on, the BSAs settings were adjusted to reflect the particular conditions at each point. With a live display of the velocity on each BSA, as it detected and processed the Doppler bursts, the centre frequency and bandwidth were adjusted to match the incoming data. In addition, while the data was being acquired, Burstware provided a display of the measured velocities in the form of a histogram. Having completed the acquisition, it was possible to adjust the settings and repeat the process if part of the histogram was outside the selected range.

Although 10,000 bursts were detected at each point, some were rejected by the BSAs. If any one channel failed to validate a burst, the data recorded by the other two channels could not be used. When analysing the data, therefore, it was necessary to filter the data and extract only those samples that were coincident in time. In practice, a finite coincidence window of 2 μ s was used, based on the estimated time taken for a particle to cross the control volume, and the data was accepted if the arrival time recorded by all three channel samples was within this period. Typically, about 5,000 coincident samples remained after filtering.

To maximise the number of coincident samples, which was dependent on the channel with the poorest validation, it was necessary to adjust the gain setting of each BSA. The incoming signals from the photomultipliers were amplified by the BSAs, so that the bursts could be detected and sampled to determine their frequency. For an individual BSA, operating in private, the rate at which bursts were detected could be increased by increasing the gain, but, due to amplification of noise in the signal, the proportion of bursts validated started to reduce beyond a certain point. As such, an optimum gain was selected, which gave the highest possible data rate consistent with a high validation. However, with the BSAs linked together to detect the same burst at the same time, it was more difficult to determine the optimum gain settings, which were very dependent on the violet channel. Whilst data acquisition rates that were as high as 5 kHz in the potential core region, it was sometimes necessary to accept a lower data rate in order to keep the proportion of validated data high. Close to solid surfaces, in particular, where the SNR was reduced by reflected light contaminating the signal, data rates as low as 100 Hz were typical.

Whilst the majority of data could be acquired reasonable quickly, the continual adjustment of the BSA settings meant that the acquisition of LDA data was a relatively slow process, with a typical traverse at one location taking several hours to complete. Occasionally, also, oil from the seeding would form droplets on the laser window and

interfere with the light signals, especially when the compressor was installed. When this occurred, it was necessary to shutdown the rig so that the window could be wiped clean.

In order to move the measurement volume to a known position at the start of a test, an optical technique was developed and used. With the optical probes mounted on the rig, their position was found by moving the traverse and monitoring the light power detected by one particular receiving optic, using a photo-diode in place of the photomultiplier. Utilising one channel only, and with off-axis detection, the output signal from the photo-diode reached a maximum when the centre of the control volume passed through the surfaces of the inner and outer walls. Having determined the wall positions to within 50 μm , the measurement volume was positioned at mid-height.

For the LDA tests, different traverse positions were used in comparison to 5HP measurements. Since it was more difficult to obtain data near to the wall, the traverse was started at mid-height so that as the walls were approached it became increasingly difficult to obtain data until, at some point, it was lost altogether. In addition, the number of positions was increased to improve the definition of the derived quantities and, for the measurements without the compressor, the traverse was repeated with alternative positions used to add data in between the original points within the boundary layer. Typically, the following basic positions were used,

Pt.	1	2	3	4	5	6	7	8	9	10	11	12	13	14	15	16	17	18	19	
\hbar (%)	50	42	34	28	24	20	16	13	11	9	7	5	3	2	1.5	1.0	0.8	0.6	0.4	
Pt.	20	21	22	23	24	25	26	27	28	29	30	31	32	33	34	35	36	37	38	39
\hbar (%)	50	58	66	72	76	80	84	87	89	91	93	95	97	98	98.5	99.0	99.2	99.4	99.6	50

At a particular location, and at each point in the traverse, the instantaneous velocities of the measured (non-orthogonal) components were sampled, over a period of time, and the validated data recorded. The reduction of the measured velocities into orthogonal components, and the derivation of the time-averaged velocity data is described in detail in Chapter 3 (Sect. 3.1.3).

CHAPTER 3 DATA ANALYSIS

	Page
3.1 Reduction of Measured Data	72
3.1.1 Co-ordinate Systems	72
3.1.1.1 Cartesian (x-y-z) Co-ordinates	73
3.1.1.2 Curvilinear (s-n-z) Co-ordinates	73
3.1.1.3 Polar (x-r-θ) Co-ordinates	73
3.1.1.4 Traverse Geometry and Co-ordinates	73
3.1.1.5 Curvature Definitions	75
3.1.2 Five Hole Probe Measurements	76
3.1.2.1 Five Hole Probe Theory	76
3.1.2.2 Calibration	78
3.1.2.3 Data Analysis	79
3.1.3 LDA Measurements	80
3.1.3.1 Coincident Orthogonal Velocity Components	80
3.1.3.2 Time-averaged Quantities	82
3.1.3.3 Reynolds Stress Errors	83
3.1.3.4 Additional Turbulence Data	88
3.2 Derived Quantities	89
3.2.1 Determining the Potential Velocity Distribution	89
3.2.1.1 Using Mean Velocity and Static Pressure	89
3.2.1.2 Using Mean Velocity Alone	90
3.2.2 Integral Parameters	91
3.2.2.1 Passage Height	91
3.2.2.2 Passage Area	91
3.2.2.3 Mass flow	92
3.2.2.4 Mass-weighted Pressures	92
3.2.2.5 Kinetic Energy Flux Coefficient	93
3.2.3 Boundary Layer Parameters	95
3.2.3.1 Displacement Thickness	95
3.2.3.2 Momentum Deficit Thickness	95
3.2.3.3 Momentum Thickness	96
3.2.3.4 Universal Thickness	96
3.2.3.5 Shape Parameters	96
3.2.4 Determining the Wall Shear Stress	97
3.2.4.1 The Law of the Wall	97

Data Analysis

3.2.4.2 Single Point Method	98
3.2.4.3 Multiple Point Method	99
3.2.5 Spatial Gradients	100
3.3 Errors and Accuracy	102
3.3.1 Hardware	102
3.3.2 Five Hole Probe	103
3.3.3 Laser Doppler Anemometer	105
3.3.3.1 Mean Velocity	105
3.3.3.2 Reynolds Stress	107
3.3.3.3 Triple Velocity Correlations	108
3.3.4 Overall Parameters	109

The techniques used to analyse the experimental data are considered in this chapter. At each position, static pressure and mean velocity components were obtained from the 5-hole probe (5HP), in a local co-ordinate system aligned with the traverse, and Laser Doppler Anemometry (LDA) measurements were used to derive time-averaged turbulence data. In addition, to characterise the overall behaviour of the flow, various parameters were derived by integrating across the passage, including those relating to the boundary layer. Finally, the experimental errors and accuracy of the data are assessed.

3.1 Reduction of Measured Data

At each traverse location, the geometry of the traverse and the orientation of the measured velocity components can be related to the principal co-ordinate systems. Moreover, analysis techniques were required to reduce the measured quantities into meaningful data. The five pressures obtained from the 5HP were converted into static pressure and three orthogonal velocity components using a probe calibration, and the coincident velocities measured using the LDA system were transformed into orthogonal velocity components before being time-averaged.

3.1.1 Co-ordinate Systems

For an annular S-shaped duct, there is no simple co-ordinate system to describe both the geometry and the flow. The governing flow equations are described most easily in a Cartesian co-ordinate system (Appendix 3). However, since the flow follows a curved path, it is also convenient to describe the behaviour with respect to the mean flow direction. The equations of motion can be transformed into a curvilinear co-ordinate system, in which the co-ordinates follow a curved line (Appendix 4, Sect. A4.1.1). Since the rig is annular, the overall geometry is readily described by a polar co-ordinate system, into which the flow equations can also be transformed (Appendix 4, Sect. A4.1.2). Clearly, an appropriate combination of curvilinear and polar co-ordinates is useful for describing the geometry and the flow.

For the case without the compressor at inlet, the flow under consideration is both axisymmetric and has zero mean velocity in the circumferential direction. (Note that these are two distinct conditions; axisymmetric means that the time-averaged flow properties do not vary in the circumferential direction, such that their derivatives are zero in this direction, and zero mean circumferential velocity is an additional simplification.)

3.1.1.1 Cartesian (x-y-z) Co-ordinates

This co-ordinate system needs no explanation other than to give its orientation with respect to the rig. The ordinate x is aligned with the rig centre line, in the streamwise direction, and the ordinate y is aligned with the radial direction, at any given circumferential location. The ordinate z is perpendicular to $x-y$ forming a right handed system. Distances measured in the axial direction (x) are relative to S-shaped duct inlet, which was chosen to be the datum axial position of the co-ordinates. The velocity components in the x , y and z directions are designated U , V and W .

3.1.1.2 Curvilinear (s-n-z) Co-ordinates

This co-ordinate system is defined relative to a curved line (S), which lies in the $x-y$ plane. At any point, the ordinate s is aligned with S , in the streamwise direction, and is at an angle (ϕ) with respect to the x direction. The ordinate n is perpendicular to s in the $x-y$ plane. At a given point, the rate of change of ϕ with distance (s) along S ($\partial\phi/\partial s$) is equal to the curvature of S ($1/R$). The third ordinate z (equivalent to the Cartesian z) is perpendicular to the $s-n$ plane forming a right handed system. The velocity components in the s , n and z directions are U_s , V_n and W_z .

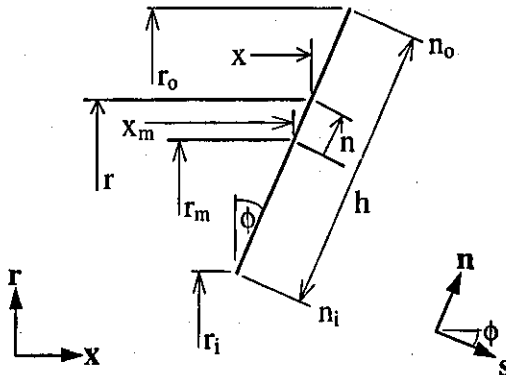
Note that S can be any curved line in the flow but, for convenience, is often chosen to be approximately aligned with the flow such that V_n is then small compared to U_s . Moreover, when S follows an actual streamline, V_n is zero along S by definition.

3.1.1.3 Polar (x-r-θ) Co-ordinates

This co-ordinate system is naturally suited to an annular rig. The ordinate x is aligned with the rig centre line, in the streamwise direction. The ordinate r is radially outward from the centre and rotates about x such that it is at an angle (θ) relative to a datum circumferential position. With y aligned to this position, θ is the angle between r and y . At a given circumferential position, the third ordinate θ is perpendicular to $x-r$, forming a right handed system. At a given radius (r), distance in the θ direction (S_θ) is given by $r\theta$, so that the rate of change of θ with S_θ ($\partial\theta/\partial S_\theta$) is equal to the curvature ($1/r$). The velocity components in the x , r and θ directions are V_a , V_r and V_θ .

3.1.1.4 Traverse Geometry and Co-ordinates

In the present investigation, measurements have been made along lines that were perpendicular to the mean line of the S-shaped duct, in the $x-r$ plane.



Traverse Line

For each traverse, the $s-n$ co-ordinates were aligned such that s was perpendicular, and n parallel, to the traverse line. The position of the traverse line was defined by its mid-height location in $x-r$ space (i.e., x_m and r_m), and its orientation by the angle ϕ between the traverse line and r , which is also the angle between s and x . The angle ϕ was zero in the inlet and exit sections, and negative within the S-shaped duct (Table 2).

The distance along the traverse line (n) was defined with respect to the mid-height location (i.e., $n = 0$ at $r = r_m$). Thus at any position (n), the corresponding axial position (x) and radius (r) can be obtained from,

$$x = x_m - n \sin \phi \quad \dots\dots 3.1$$

$$r = r_m + n \cos \phi \quad \dots\dots 3.2$$

For 3D flow, in which the various aerodynamic properties vary in the circumferential direction (e.g., downstream of the compressor stage), measurements were also made at a number of θ locations. Thus for a given r and θ , the corresponding position in Cartesian space is given by,

$$y = r \cos \theta \quad \dots\dots 3.3$$

$$z = r \sin \theta \quad \dots\dots 3.4$$

Note that the rotation of the compressor was clockwise, viewed from upstream (looking in the positive x -direction), which corresponds to the positive θ -direction. Thus, the swirl velocity (V_θ) was positive between the rotor and stator and, since the design intention of the stator was to produce zero swirl at exit, positive V_θ downstream of the stator corresponds to an under-turning of the air, and negative V_θ to an over-turning.

To distinguish the measured velocity components, which can be obtained in any local co-ordinate system (ℓ), they are referred to as U_ℓ , V_ℓ and W_ℓ . However, when ℓ is aligned with the traverse, it is apparent that $U_\ell \equiv U_s$ and $V_\ell \equiv V_n$. In addition, for a given traverse angle (ϕ), polar velocity components can be obtained from,

$$\begin{Bmatrix} V_a \\ V_r \\ V_\theta \end{Bmatrix} = \begin{bmatrix} \cos \phi & -\sin \phi & 0 \\ \sin \phi & \cos \phi & 0 \\ 0 & 0 & 1 \end{bmatrix} \begin{Bmatrix} U_\ell \\ V_\ell \\ W_\ell \end{Bmatrix} \quad \dots \dots 3.5$$

and, for a given circumferential angle (θ), these can be converted to Cartesian velocity components using,

$$\begin{Bmatrix} U \\ V \\ W \end{Bmatrix} = \begin{bmatrix} 1 & 0 & 0 \\ 0 & \cos \theta & -\sin \theta \\ 0 & \sin \theta & \cos \theta \end{bmatrix} \begin{Bmatrix} V_a \\ V_r \\ V_\theta \end{Bmatrix} \quad \dots \dots 3.6$$

Note that for the 2D (axisymmetric) case, for which $\theta = 0$, the Cartesian and polar velocities are equivalent and that $W = V_\theta = W_\ell \equiv W_z$.

3.1.1.5 Curvature Definitions

Along the curved line (S) defining the s-n co-ordinate system (Sect. 3.1.1.2), the curvature ($1/R$) is,

$$\frac{1}{R} = \frac{\partial \phi}{\partial s} \quad \dots \dots 3.7$$

where ϕ is the angle between the s and x directions. Since this is based on the mathematical definition for the curvature of a line, it is referred to as the geometric curvature. Note, however, that $1/R$ is not necessarily the curvature of the geometry, since it could refer to the curvature of the flow if S were a streamline. For the present S-shaped duct, where ϕ becomes increasingly negative in the first bend ($\partial \phi / \partial s < 0$) and is returned back to zero in the second ($\partial \phi / \partial s > 0$), the geometric curvature is negative in the first bend and positive in the second.

The effective curvature (K_{eff}) is defined as,

$$K_{eff} = 1/R_{eff} \quad \dots \dots 3.8$$

where R_{eff} is the effective radius of curvature of a streamline passing through mid-height ($n = 0$), and is taken as positive when in the same direction as n . For the present S-duct, where n increases from the inner wall to the outer wall, the effective curvature is

positive in the first bend and negative in the second. It follows, then, that the geometric radius of curvature at mid-height (R_m) is equal to $-R_{eff}$.

Within the present S-shaped duct, the signs of the geometric and effective curvatures are as follows,

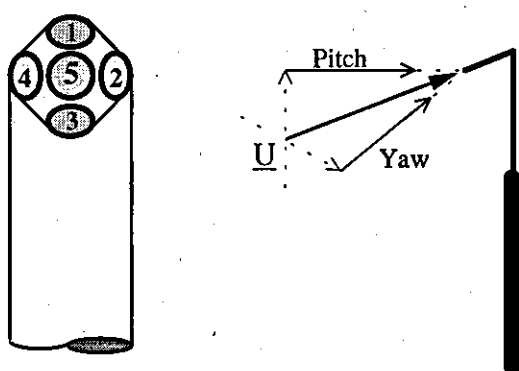
			Sign of Curvature	
Bend	Wall	Curvature	Geometric	Effective
First	Inner	Convex	negative	positive
First	Outer	Concave	negative	positive
Second	Inner	Concave	positive	negative
Second	Outer	Convex	positive	negative

3.1.2 Five Hole Probe Measurements

By using the 5-hole probe (5HP) measurement technique, the mean flow could be resolved completely. Although it was necessary to calibrate the 5HP, this provided the required information to convert the five measured pressures, obtained from the test rig, into static pressure and three orthogonal velocity components.

3.1.2.1 Five Hole Probe Theory

In order to understand the calibration and analysis procedure, the theory behind the 5HP technique (Wray^[182]) is given below. The convention used for hole numbering and the pitch and yaw directions are shown in the following diagram.



Five Hole Probe

In a flow with orthogonal velocity components U_ℓ , V_ℓ and W_ℓ , the magnitude of the velocity vector (U_{tot}) is given by,

$$U_{\text{tot}} = \sqrt{U_\ell^2 + V_\ell^2 + W_\ell^2} \quad \dots\dots 3.9$$

and the dynamic pressure (Q) by,

$$Q = \frac{1}{2} \rho U_{\text{tot}}^2 \quad \dots\dots 3.10$$

Each hole of a 5-hole probe will register a pressure (p_n) which will be some proportion (k_n) of Q above the local static pressure (p). Thus,

$$p_n = p + k_n Q \quad \dots\dots 3.11$$

Mach number and Reynolds number effects can be considered negligible in the present application, and thus the values of k_n are dependent only on the flow direction. This is used as the basis for defining the pitch parameter (X), the yaw parameter (Y), the dynamic pressure parameter (D_p) and the stagnation pressure parameter (S_p), as discussed below.

Note that there is a limit to the angle at which the flow can approach the probe head. As the angle is increased, the pressure sensed by the leeward hole will reduce. This pressure can fall well below p , but at some point flow separation from the centre hole will mean that the pressure variation with angle will no longer be well behaved. In practice, therefore, the probe cannot be reliably used beyond this point, known as the cone acceptance angle. Although this angle will be different for each probe, it is typically between 30° and 40° .

Using Eq. 3.11, the difference between the pressure sensed by the centre hole and any of the other four is given by,

$$(p_s - p_n) = (k_s - k_n) Q \quad \dots\dots 3.12$$

Thus, for a given flow direction, $(p_s - p_n)$ is a function of Q . By non-dimensionalising $(p_s - p_n)$ by Q , the D_p parameter is defined, i.e.,

$$D_p = \frac{p_s - p_i}{Q} \quad \dots\dots 3.13$$

Since $D_p = k_s - k_i$, it is a function of flow direction only. Note that n has been replaced by i since, in practice, only holes 2 or 4 are used to determine D_p .

The difference in pressure sensed by opposite side holes is uniquely related to the flow direction; $(p_1 - p_3)$ to pitch angle and $(p_2 - p_4)$ to yaw angle. For a given flow direction, Eq. 3.11 shows that these are functions of Q and, when non-dimensionalised by $(p_5 - p_i)$, are used to define the X and Y parameters, i.e.,

$$X = \frac{p_1 - p_3}{p_5 - p_i} \quad \dots\dots 3.14$$

$$Y = \frac{p_2 - p_4}{p_5 - p_i} \quad \dots\dots 3.15$$

Since $X = (k_1 - k_3)/D_p$ and $Y = (k_2 - k_4)/D_p$, X and Y are functions only of flow direction, and, therefore, for any particular flow direction there will be a unique X , Y pair. In order to avoid dividing by zero when $p_i = p_5$, and excessively large values of X and Y when they are similar, the particular hole denoted by subscript i is chosen to give the largest value of $(p_5 - p_i)$, which effectively means that p_i is taken from the leeward side of the probe.

The difference between the total pressure (P) and the centre hole pressure can be obtained from,

$$(P - p_5) = (p + Q) - (p + k_5 Q) = (1 - k_5)Q \quad \dots\dots 3.16$$

By non-dimensionalising $(P - p_5)$ by $(p_5 - p_i)$, the S_p parameter is defined, i.e.,

$$S_p = \frac{P - p_5}{p_5 - p_i} \quad \dots\dots 3.17$$

which is again dependant only on flow direction, i.e., $S_p = (1 - k_5)/D_p$.

In principle, therefore, a 5HP probe can be used to determine the mean flow properties through measurement of five pressures. In practice, however, this can be achieved only through calibration, which, due to subtle differences in probe geometry, is necessary for every probe.

3.1.2.2 Calibration

The calibration procedure involved placing the probe in an air stream of known conditions, and measuring the variation of the non-dimensional parameters (X , Y , D_p and S_p) over a range of pitch and yaw angles. A calibration traverse mechanism rotated the probe in two directions, in order to present a compound flow angle onto the probe head. Due to the mechanical arrangement of the symbol mechanism, a range of true

yaw (λ_{tr}) and pseudo pitch (ϕ_{ps}) angles (defined in the diagram below) were possible. For a typical calibration, these ranged from -25° to $+25^\circ$, in increments of 2.5° ; more than covering the variation encountered during use.

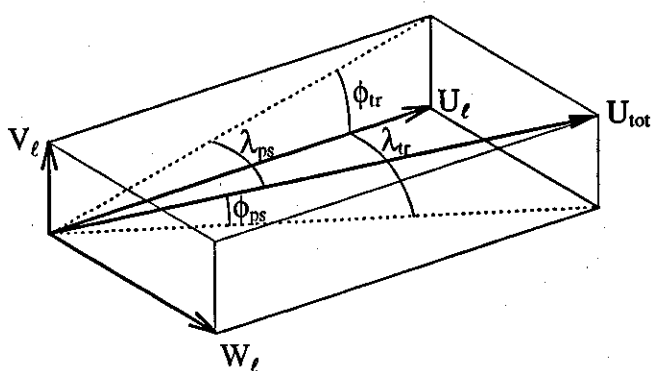
During a calibration, the five pressures from the 5HP were recorded, along with a total pressure (P) from an adjacent Pitot probe; all measured relative to a reference pressure (p_{ref}). A free-jet flow was used and, since the static pressure within the flow was atmospheric (p_α), the dynamic pressure of the flow could be obtained from P, since $p_{ref} = p_\alpha$ was used (i.e., $Q = P$).

The calibration procedure was automated, using the PC based data acquisition system to drive the probe and acquire the data, over the range of angles required, in the same way that actual data would be taken on the test rig. A typical calibration (Fig. 5) contained 441 data points, consisting of ϕ_{ps} , λ_{tr} , D_p and S_p for each X, Y pair.

3.1.2.3 Data Analysis

With data acquired from the test rig, in the form of five measured pressures at any number of positions, the static pressure and orthogonal velocity components were derived for each data point. The analysis procedure recognised the fact that the probe had a finite size and, whenever possible, interpolated the measured side hole pressures at the centre hole position before calculating X and Y. To obtain the corresponding values of ϕ_{ps} , λ_{tr} , D_p and S_p from the calibration file, a least square bi-quadratic surface was fitted to each of the four parameter arrays, using the closest surrounding 25 points.

Having derived Q from D_p (Eq. 3.13), the magnitude of the velocity vector (U_{tot}) was obtained and used to calculate the velocity components. In a local co-ordinate system aligned with the probe, corresponding with that used to calibrate the probe, these are related to U_{tot} through the yaw and pitch angles, i.e.,



Velocity Components

Thus, given the true yaw (λ_{tr}) and pseudo pitch (ϕ_{ps}) angles, the velocity components were obtained from,

$$U_t = U_{tot} \cos(\phi_{ps}) \cos(\lambda_{tr}) \quad 3.18$$

$$V_t = U_{tot} \sin(\phi_{ps}) \quad 3.19$$

$$W_t = U_{tot} \cos(\phi_{ps}) \sin(\lambda_{tr}) \quad 3.20$$

and, if necessary, the true pitch angle (ϕ_{tr}) could be calculated from,

$$\tan(\phi_{tr}) = \frac{V_t}{U_t} = \frac{\tan(\phi_{ps})}{\cos(\lambda_{tr})} \quad 3.21$$

In addition, having derived P from S_p (Eq. 3.17), the static pressure was also obtained.

3.1.3 LDA Measurements

From the LDA measurements, it was possible to derive time-averaged velocity data, including Reynolds stresses and triple velocity correlations. These were calculated statistically from the coincident orthogonal velocities, obtained for each sample by transforming the measured components. In addition, systematic errors arising in the derived Reynolds stresses were determined and removed from the data.

3.1.3.1 Coincident Orthogonal Velocity Components

During the experiment, the velocity components measured by the LDA system were highly non-orthogonal. Their actual directions were determined by the alignment of the optical probe heads, since the velocity detected was in the plane of the relevant pair of beams and perpendicular to the probe centreline. The 1D (violet) and 2D (green, blue) probes were mounted in the axial-radial plane at angles of α and β to the traverse direction respectively. In addition, the violet beams were constrained to lie in this plane, whereas the planes containing the green and blue beams were rotated about the 2D probe axis by angles γ_g and γ_b . All the angles and associated sign conventions are defined in Figure 4, and the actual angles used during the present investigation are given in Table 7.

For any set of angles, it was possible to determine the optical transformation relating the measured velocity components to the orthogonal velocities U_t , V_t and W_t , in a local co-ordinate system aligned with the traverse. The 2D probe, measuring U_{BSA_1} (green)

and U_{BSA_2} (blue), was sensitive to W_t and U_{2D} , a component perpendicular to the 2D probe in the axial-radial plane, i.e.,

$$U_{BSA_1} = \cos(\gamma_g) U_{2D} + \sin(\gamma_g) W_t \quad \dots\dots 3.22$$

$$U_{BSA_2} = \cos(\gamma_b) U_{2D} + \sin(\gamma_b) W_t \quad \dots\dots 3.23$$

and the 1D probe, measuring U_{BSA_3} (violet), was sensitive to U_t and V_t , i.e.,

$$U_{BSA_3} = \cos(\alpha) U_t + \sin(\alpha) V_t \quad \dots\dots 3.24$$

Similarly, U_{2D} is related to U_t and V_t by,

$$U_{2D} = \cos(\beta) U_t + \sin(\beta) V_t \quad \dots\dots 3.25$$

Thus, by solving these equations for U_t , V_t and W_t , it is possible to determine the optical transformation,

$$\begin{Bmatrix} U_t \\ V_t \\ W_t \end{Bmatrix} = \begin{bmatrix} a_{11} & a_{12} & a_{13} \\ a_{21} & a_{22} & a_{23} \\ a_{31} & a_{32} & a_{33} \end{bmatrix} \begin{Bmatrix} U_{BSA1} \\ U_{BSA2} \\ U_{BSA3} \end{Bmatrix} \quad \dots\dots 3.26$$

for which the terms in the matrix (a_{ij}) are given by,

$$a_{11} = -\frac{\sin(\alpha) \sin(\gamma_b)}{\sin(\alpha - \beta) \sin(\gamma_g - \gamma_b)} \quad \dots\dots 3.27a$$

$$a_{12} = \frac{\sin(\alpha) \sin(\gamma_g)}{\sin(\alpha - \beta) \sin(\gamma_g - \gamma_b)} \quad \dots\dots 3.27b$$

$$a_{13} = -\frac{\sin(\beta)}{\sin(\alpha - \beta)} \quad \dots\dots 3.27c$$

$$a_{21} = \frac{\cos(\alpha) \sin(\gamma_b)}{\sin(\alpha - \beta) \sin(\gamma_g - \gamma_b)} \quad \dots\dots 3.27d$$

$$a_{22} = -\frac{\cos(\alpha) \sin(\gamma_g)}{\sin(\alpha - \beta) \sin(\gamma_g - \gamma_b)} \quad \dots\dots 3.27e$$

$$a_{23} = \frac{\cos(\beta)}{\sin(\alpha - \beta)} \quad \dots\dots 3.27f$$

$$a_{31} = \frac{\cos(\gamma_b)}{\sin(\gamma_g - \gamma_b)} \quad \dots \dots 3.27g$$

$$a_{32} = -\frac{\cos(\gamma_g)}{\sin(\gamma_g - \gamma_b)} \quad \dots \dots 3.27h$$

$$a_{33} = 0 \quad \dots \dots 3.27i$$

For each coincident sample, Eq. 3.26 was used to calculate the instantaneous orthogonal velocities from the measured components.

3.1.3.2 Time-averaged Quantities

At each measurement position, the instantaneous values of the orthogonal velocities were used to derive the mean velocity components, the Reynolds stresses and other statistical quantities. The temporal variation of the velocity was defined in terms of three randomly sampled time histories (i.e., the samples were not at regular time intervals), with the orthogonal components in each sample being coincident in time.

For each of the three orthogonal components, the mean velocity (U_i) was calculated from,

$$U_i = \overline{U_i} = \frac{1}{T} \int_T U_i dt = \frac{1}{N} \sum_{n=1}^N (U_i)_n \quad \dots \dots 3.28$$

and used to derive the instantaneous fluctuating velocity (u_i), defined as,

$$u_i = U_i - \overline{U_i} \quad \dots \dots 3.29$$

Subsequently, the six independent Reynolds stresses ($\overline{u_i u_j}$) were calculated from,

$$\overline{u_i u_j} = \frac{1}{T} \int_T u_i u_j dt = \frac{1}{N} \sum_{n=1}^N (u_i u_j)_n \quad \dots \dots 3.30$$

and, similarly, the ten independent triple velocity correlations ($\overline{u_i u_j u_k}$) from,

$$\overline{u_i u_j u_k} = \frac{1}{T} \int_T u_i u_j u_k dt = \frac{1}{N} \sum_{n=1}^N (u_i u_j u_k)_n \quad \dots \dots 3.31$$

In addition, for each component, the variance (V_i), skewness (S_i) and flatness (F_i) of the velocity distribution were calculated from,

$$V_i = \frac{1}{N} \sum_{n=1}^N (u_i^2)_n \quad [= \overline{u_i u_i}] \quad 3.32$$

and,

$$S_i = \frac{1}{N} \sum_{n=1}^N (u_i^3)_n \Big/ V_i^{\frac{3}{2}} \quad 3.33$$

and,

$$F_i = \frac{1}{N} \sum_{n=1}^N (u_i^4)_n \Big/ V_i^2 \quad 3.34$$

3.1.3.3 Reynolds Stress Errors

Due to the finite resolution to which each velocity sample can be determined, errors can arise in the derived Reynolds stresses, but not in the mean velocities. In addition, these errors are dependent on the optical transformation, used to convert the measured velocities into orthogonal components. As a result of various factors, the direction of the measured velocity components can be highly non-orthogonal, and this can influence the Reynolds stress errors significantly. Errors in the derived velocity components will occur if the terms in the transformation matrix (a_{ij}) are not of the correct magnitude, and systematic errors of this type are a function of the accuracy to which the probe angles (α , β , γ_g and γ_b) can be measured. However, systematic errors in the Reynolds stresses arise for other very different reasons, and can be analysed by rewriting the optical transformation (Eq. 3.26) as,

$$U_i = a_{ij} c_j \quad 3.35$$

where, the i th. component of velocity (U_e , V_e or W_e) is obtained by summing over the measured velocities. (Note that c_j used here is equivalent to U_{BSA_j} .)

In converting each Doppler burst into a velocity measurement, therefore, the finite resolution (Δc_i) of the processor means that c_i can only be determined to within $\pm \Delta c_i$ of its true value. Hence, each derived orthogonal velocity also will be subject to a finite resolution (Δu_i), but this is of different magnitude to that determined by each processor and is given by,

$$\Delta u_i = \frac{\partial u_i}{\partial c_1} \Delta c_1 + \frac{\partial u_i}{\partial c_2} \Delta c_2 + \frac{\partial u_i}{\partial c_3} \Delta c_3 \quad 3.36$$

But $\partial u_i / \partial c_j = a_{ij}$ and therefore,

$$\Delta u_i = a_{ij} \Delta c_j \quad \dots \dots 3.37$$

Since the resolution error of each processor is random, it will have no effect on the mean orthogonal velocities (U_i), obtained from averaging a number of samples, as $\Delta c_i = 0$. However, all the measured Reynolds stresses ($\bar{u}_i u_j$) will contain errors ($\Delta \bar{u}_i u_j$), which are given by the product $\Delta u_i \Delta u_j$. On substituting Eq. 3.37, $\Delta \bar{u}_i u_j$ can be obtained by assuming that $\Delta c_i \Delta c_j = 0$ for $i \neq j$, and since $(\Delta c_i)^2 \neq 0$ this leads to,

$$\Delta \bar{u}_i u_j = a_{ik} a_{jk} (\Delta c_k)^2 \quad \left[\sum_{k=1}^3 \right] \quad \dots \dots 3.38$$

For example, the \bar{uv} error ($\Delta \bar{uv}$) is given by,

$$\Delta \bar{uv} = (a_{11} a_{21}) (\Delta c_1)^2 + (a_{12} a_{22}) (\Delta c_2)^2 + (a_{13} a_{23}) (\Delta c_3)^2 \quad \dots \dots 3.39$$

and the \bar{vv} error ($\Delta \bar{vv}$) is given by,

$$\Delta \bar{vv} = (a_{21})^2 (\Delta c_1)^2 + (a_{22})^2 (\Delta c_2)^2 + (a_{23})^2 (\Delta c_3)^2 \quad \dots \dots 3.40$$

The resolution is a function of the type of processor and the signal-to-noise ratio (SNR) associated with a given measurement. In addition, however, the Reynolds stress errors ($\Delta \bar{u}_i u_j$) are determined by the magnitude of the terms in the transformation matrix (a_{ij}). Thus, although errors in the variance of each measured component will occur due to the finite processor resolution, the transformation process can give rise to errors in all the derived Reynolds stress components, which may be amplified to much higher levels. The amplification is dependant upon the optical transformation and can be significantly larger for one Reynolds stress component compared with others. Further, Eq. 3.38 shows that the derived normal stresses are always greater than their true values, whereas the shear stresses may be subjected to errors of either sign.

The relative magnitude of the error in each of the Reynolds stresses was investigated (see Carrotte and Brinchford^[28] for further details) by assuming that the resolution of each processor ($\Delta U_{BSA_k} \equiv \Delta c_k$) was of unity magnitude (i.e., 1 m/s). This assumption is not realistic, but allows the relative size of the errors, rather than their absolute values, to be assessed for different angle combinations. By including the actual terms of the transformation (Eqs. 3.27) in Eq. 3.38, it was possible to calculate $\Delta \bar{u}_i u_j$ for a wide range of probe angles (α, β), which were defined in terms of the included angle between the probes ($\alpha - \beta$) and the average angle made by the probes with respect to the traverse direction $0.5(\alpha + \beta)$. Further, it was assumed that the green and blue fringe angles (γ_g, γ_b) were at 45° and -45° respectively, as was approximately the case in the experimental measurements. If transformation was not necessary, an error of 1.0 would

be obtained for the normal stress components, while the error in the shear stresses would be zero. Due to transformation, however, certain angle combinations will give rise to error values much greater than these, indicating a significant amplification of the errors resulting from the finite processor resolution. For the case described, only the Reynolds stress errors $\Delta\bar{u}u$, $\Delta\bar{v}v$ and $\Delta\bar{u}v$ vary with α , β ($\Delta\bar{w}w = 1$ and $\Delta\bar{u}w = \Delta\bar{v}w = 0$ for all α , β).

Although errors can be predicted for a large number of angle combinations, in reality the choice is restricted by the nature of a fully annular facility, where optical access is gained through windows in the outer casing, so that large differences occur between the measured velocity components and the traverse direction. As a result, the error in the cross-stream normal stress component ($\bar{v}v$) tends to be much larger in comparison to the error in the streamwise component ($\bar{u}u$). For example, at zero average angle and an included angle of 20° , the error in $\bar{v}v$ is 16.6 (for unity resolution) compared with 0.52 for $\bar{u}u$. However, halving the included angle to 10° will increase the $\bar{v}v$ error value to 65.8, whereas it will reduce to 4.27 if the included angle is doubled. Thus the error in cross-stream normal stress is mainly a function of the included angle between the probes, and can be reduced by increasing the included angle; thereby more closely aligning the measured components with the traverse direction. For the streamwise normal stress ($\bar{u}u$) and the shear stress ($\bar{u}v$), the average angle of the probes, as well as the included angle, can influence the error magnitudes. For $\bar{u}v$ in particular, the error arises only when the average angle of the probes is finite, and can be of either positive or negative magnitude. For example, at an average angle of 30° the $\bar{u}v$ error is 7.0 with an included angle of 20° , but reduces to 1.6 when the included angle is doubled. In this case, the error for a wide range of included angles can be minimised by having the probe heads symmetrically located about the traverse direction. Although the above analysis is useful for deciding, within the constraints, the best angle combination (α , β , γ_g , γ_b) to use to minimise errors, an estimate of the resolution of each processor is needed to determine the actual magnitude of each Reynolds stress error.

Without the compressor, a potential core region existed throughout the S-shaped duct, between the annulus wall boundary layers. At every traverse location in this region, the measured normal stresses were unequal, with the magnitude of the cross-stream component ($\bar{v}v$) much larger than the streamwise ($\bar{u}u$) and circumferential ($\bar{w}w$) values. In addition, although the measured shear stress ($\bar{u}v$) in the core region was zero at most locations, non-zero values were measured at $x/L = 0.02$. Undoubtedly, the turbulence in the core region would have been isotropic, with equal normal stress components ($\bar{u}u = \bar{v}v = \bar{w}w$) and zero shear stress components ($\bar{u}v = \bar{u}w = \bar{v}w = 0$), and, therefore, the measured Reynolds stresses were in error by differing amounts.

Fortunately, however, it was apparent that the differences were systematically related to the transformation errors, arising as a result of a relatively small included angle between the probes and, at $x/L = 0.02$, the use of a relatively large average angle.

Using the measured data in the core region, therefore, the actual resolution of each BSA processor could be estimated. At each location, with the transformation coefficients (Eqs. 3.27) determined by the actual probe angles (Table 7), the error in each Reynolds stress ($\Delta \bar{u_i u_j}$) could be calculated from Eq. 3.38, with the resolution of each processor (ΔU_{BSA_k}) supplied. At every position across the passage, therefore, the same value of $\Delta \bar{u_i u_j}$ was used to correct the measured data using,

$$\overline{(\mathbf{u}_i \mathbf{u}_j)}_{\text{corrected}} = \overline{(\mathbf{u}_i \mathbf{u}_j)}_{\text{meas}} - \Delta \overline{\mathbf{u}_i \mathbf{u}_j} \quad 3.41$$

In this way, therefore, the ΔU_{BSA_k} values could be adjusted until, in the core region, the normal stresses were approximately equal and the shear stress was zero. Different ΔU_{BSA_k} values were obtained at each traverse location, but it was evident that each processor was typically operating with a different resolution, since the difference between the three ΔU_{BSA_k} values was always larger than the variation in the various values obtained for any one processor. Typically, for all the measurements, resolutions of approximately 0.14 m/s, 0.21 m/s and 0.28 m/s were indicated for ΔU_{BSA_1} , ΔU_{BSA_2} and ΔU_{BSA_3} , respectively.

The resolution of each BSA is a function of the record interval (R_I), this being the period over which a Doppler burst is sampled. Due to the various signal analysis techniques used by the BSA, it was shown in Chapter 2 (Sect. 2.2.4.3) that the accuracy to which a particular measurement can be resolved (ΔU_{BSA}) is a function of the R_I (Eq. 2.34). Although R_I must be the same for all BSAs when making 3-component measurements, ΔU_{BSA} may be different for each since the SNR also affects the resolution. With a record interval of 1.333 μ s, and the appropriate calibration factor, the resolution of the green component (BSA_1) typically suggested by the measurements corresponds to that given by Eq. 2.34. The poorer resolution obtained for the other BSAs, however, appears to indicate that they are operating at a lower SNR, since ΔU_{BSA} is expected to increase as SNR reduces. This is in good agreement with the fact that the proportion of data validated by the blue and, to a greater extent, the violet channels was lower, since, without doubt, this is affected by reduced SNR. As BSA_1 operates with near perfect validation, and therefore a good SNR, Eq. 2.34 provides a reasonable estimate of the best resolution that can be achieved.

In regions of low turbulence the Reynolds stress errors are of greatest significance since they are of similar magnitude to the actual stress levels. For example, the magnitude of

the isotropic normal stresses was approximately $0.04 \text{ m}^2/\text{s}^2$ (equivalent to a turbulence intensity of 0.7% with $U_{\text{Mean}} = 28.3 \text{ m/s}$), whereas the errors are typically 0.03 for \overline{ww} , between 0.03 - 0.05 for \overline{uu} and, for \overline{vv} , between $0.20 - 0.25 \text{ m}^2/\text{s}^2$. In addition, for \overline{uv} , the errors were typically less than ~ 0.03 in magnitude, except at $x/L = 0.02$, where the error was $\sim 0.08 \text{ m}^2/\text{s}^2$. Within each boundary layer, therefore, these errors would be relatively insignificant because of the higher Reynolds stress levels.

The fact that observed differences in the measurements can be explained, seems to justify the above understanding and the analysis techniques used. With estimated processor resolutions, the errors arising from the transformation adequately account for differences between the measured Reynolds stresses and, in the core region, those of isotropic turbulence. In addition, the magnitude of the resolution agrees with that expected for each BSA. As further confirmation of the technique, however, an additional traverse was carried out at $x/L = 1.4$ using an increased included angle between the probes. Although data could not be obtained close to the inner wall, lower \overline{vv} levels were measured across a large proportion of the passage when the included angle was increased from 40° to 68° . With the processors operating at approximately the same resolution, the observed reduction in \overline{vv} was in good agreement with that expected for the different transformation.

Although the error magnitude may increase due to changes in the processor resolution, particularly close to solid surfaces, the Reynolds stresses presented in Chapter 4 have been corrected using the same resolution values for all data taken during the same traverse. These values were obtained separately for each traverse, with reference to the measurements in the core region, although they did not vary by much. Clearly, applying a constant correction to each Reynolds stress, across the passage, is not ideal as the resolution may vary at each point. However, by careful selection of the signal gain on each BSA, it was possible to maintain the proportion of data validated by each channel about the same for all points across the traverse, such that, with the SNR remaining approximately constant, each BSA operated with similar resolution throughout. For the present situation, therefore, correction of the data in this way removed most of the systematic errors. In regions of low turbulence intensity, across the core and within the outer part of the boundary layer for example, the accuracy of the Reynolds stresses increases significantly, also leading to more accurate Reynolds stress ratios, such as $\overline{vv}/\overline{uu}$ in particular.

3.1.3.4 Additional Turbulence Data

Having obtained the Reynolds stresses ($\overline{u_i u_j}$) at each position, several additional turbulence parameters were calculated. The most important of these is the turbulent kinetic energy (k), which is defined as half the sum of the normal stresses, i.e.,

$$k = \frac{1}{2} \overline{u_k u_k} \quad \dots\dots 3.42$$

Turbulent kinetic energy is a scalar quantity and, therefore, invariant with co-ordinate system rotation. As such, k is used to non-dimensionalise the Reynolds stresses, giving the Reynolds stress ratios ($\overline{u_i u_j}/k$). Note that the ratio involving the primary shear stress (\overline{uv}/k) is often referred to as the structure coefficient. In addition, the components of the anisotropy tensor (a_{ij}) were determined as,

$$a_{ij} = \left(\overline{u_i u_j}/k \right) - \frac{2}{3} \delta_{ij} \quad \dots\dots 3.43$$

where δ_{ij} is the Kronecker delta, or, alternatively, as b_{ij} ($= \frac{1}{2} a_{ij}$). Clearly, the first invariant of the anisotropy tensor (b_{kk}) is zero, unlike the stress tensor which has a first invariant of $2k$. However, the overall amount of anisotropy present in the turbulence can be characterised by the second invariant (Π), i.e.,

$$\Pi = \frac{1}{2} b_{lm} b_{ml} \quad \dots\dots 3.44$$

As well as the structure coefficient, the correlation coefficient ($R_{\overline{uv}}$) can be calculated from the primary shear stress, i.e.,

$$R_{\overline{uv}} = \frac{\overline{uv}}{\left(\overline{uu} \overline{vv} \right)^{\frac{1}{2}}} \quad \dots\dots 3.45$$

Together, these parameters are used to describe the state of the turbulence and, in particular, the relative magnitudes of the Reynolds stress components.

The triple velocity correlations ($\overline{u_i u_j u_k}$) were combined to give the triple correlations relating to $\overline{q^2}$ ($= 2k$), i.e.,

$$\overline{q^2 u_i} = \overline{u_k u_k u_i} \quad \dots\dots 3.46$$

and the $\overline{q^2 v}$ term was divided by $\overline{q^2}$ to produce a quantity referred to as the turbulent kinetic energy transport velocity (V_q).

In addition, an intermittency parameter ($3/F_i$) was calculated from the flatness (F_i). For a normally distributed signal, the skewness (S_i) is zero whereas F_i is equal to three.

Therefore, in the intermittent region at the edge of a turbulent boundary layer, where F_i increases above three, the quantity $3/F_i$ reduces, like intermittency, below one.

3.2 Derived Quantities

Having established the spatial variation of the aerodynamic properties throughout the S-shaped duct, by reducing the measured data into meaningful parameters, it was then possible to derive further quantities which characterise the overall behaviour. In this section the various methods for obtaining these are described. Since many of them are derived with respect to a potential velocity distribution, the methods by which this can be determined are also presented. Mostly, the derived quantities are obtained by averaging across the passage or, with the compressor installed, a sector of the annulus, and can be used to quantify the overall performance of the duct. Moreover, various parameters relating to the annulus wall boundary layers can be obtained, which, for the axisymmetric case in particular, give an indication of the overall changes that occur in the mean velocity profile along the length of the duct. In addition, various methods for determining the wall shear stress are presented, and an indication is given as to the way by which spatial gradients were obtained from the experimental data.

3.2.1 Determining the Potential Velocity Distribution

In the present investigation, the flow passes through a parallel annular passage before entering the S-shaped duct. At the end of the inlet section, the annulus wall turbulent boundary layers occupy about a quarter of the passage each and, therefore, are separated by a significant core region. The core flow, despite containing the decaying turbulence generated by the honeycomb flow straightener, can be considered to be inviscid and irrotational. The behaviour of the flow in this region is described in Appendix 2, and the presence of a core region is particularly useful for determining the potential velocity distribution across the whole of the passage.

3.2.1.1 Using Mean Velocity and Static Pressure

Provided that the inlet total pressure variation is known, static pressure and mean velocity are sufficient to determine the exact potential velocity distribution. At the start of the parallel inlet section, the total pressure will be constant across the passage, since the scroll intake is fed from a large plenum, and the air only passes through a uniform honeycomb layer (at low velocity) before being accelerated by the inlet contraction. As the flow passes through the rig, the total pressure in the core region will not change, whereas total pressure will be lost within the annulus wall boundary layers. At any

streamwise location, therefore, the total pressure distribution will have a constant maximum level in the core region (P_c), and will reduce across each boundary layer to reach the static pressure level at the wall. From the actual distribution of total pressure, P_c can be determined by searching for this maximum level, but, when analysing experimental data, it is necessary to ensure that P_c is obtained from the average of as many data as possible within the core region, and not just a single maximum value.

For non-swirling flow ($W = 0$) and $V \ll U$, the total pressure (P) is related to the static pressure (p) and mean streamwise velocity (U) by $P = p + \frac{1}{2}\rho U^2$. Having obtained the P distribution from p and U , P_c can be determined, and, by assuming that P_c exists across the whole passage, the potential velocity distribution can then be determined from the static pressure, i.e.,

$$U_p = \sqrt{\frac{2(P_c - p)}{\rho}} \quad \dots\dots 3.47$$

When the inlet total pressure is not constant, it is necessary to use a slightly different approach. Since total pressure remains constant along streamlines in an ideal flow, the variation of total pressure with mass flow ratio (ψ) will not change. Thus, if this variation can be determined in a region relatively unaffected by the growth of the wall boundary layers, it can be used at any streamwise location, along with the actual static pressure distribution, to determine the potential velocity.

3.2.1.2 Using Mean Velocity Alone

In curved flow, it is particularly difficult to determine the potential velocity distribution from mean velocity data alone, as obtained by LDA for example. Without the associated static pressure information, it is necessary to approximate the cross-stream variation of streamline radius of curvature in some way. In Appendix 2 (Sect. A2.2) a potential velocity distribution for inviscid irrotational flow rotating about a common point is derived (Eq. A2.15), which can be used to estimate the variation of U_p across a curved duct. Providing a reasonable core region exists, an effective curvature can be chosen to model the actual behaviour in the core region, which then can be used to define U_p across the boundary layers. Although only approximate, this approach is reasonable for duct flow in which an inviscid irrotational core exists. However, for more complex flows in which the core region has disappeared, such as fully developed flow or downstream of a compressor stage, it is inappropriate.

In the core region, a numerical optimisation technique was used to determine the best fit of the function $U_p = U_m / (1 + n K_{eff})$ to the actual mean velocity data $U = f(n)$. Using

this technique, the values of U_m and K_{eff} are varied automatically until the minimum (root-mean-square) difference between the function and the data is obtained. In fact, K_{eff} can be determined directly from the mean velocity and its cross-stream gradient at mid-height ($n = 0$) since, from Eq. A2.10,

$$\left. \frac{\partial U}{\partial n} \right|_m = -U_m K_{eff} \quad 3.48$$

but, for the analysis of experimental data in particular, this approach is limited by the accuracy to which the derivative can be determined. Nevertheless, it does provide a reasonable estimate of K_{eff} (and the U_p distribution), which can be used to ascertain exactly which data lie within the core region prior to curve fitting, and, in addition, an initial guess for the optimisation procedure is obtained, which helps to improve its rate of convergence.

3.2.2 Integral Parameters

For a given traverse, various parameters can be defined by integrating along the traverse line between the inner wall position (n_i) and the outer wall position (n_o). For an annular duct, $dA = 2\pi r dn$ and so the radius (r) is required as a function of position (n), i.e.,

$$r = r_m + n \cos \phi \quad 3.49$$

where, ϕ is the traverse angle and r_m is the mean radius ($= \frac{1}{2}(r_i + r_o)$).

3.2.2.1 Passage Height

The passage height (h) is given by,

$$h = \int_A dn = \int_{n_i}^{n_o} dn = (n_o - n_i) \quad 3.50$$

Thus, $n_i = -h/2$ and $n_o = h/2$, since $(n_i + n_o) = 0$ by definition.

Similarly, fractional height (\bar{h}) at any position (n) is given by,

$$\bar{h} = \frac{1}{h} \int_{n_i}^n dn = \frac{(n - n_i)}{h} \quad 3.51$$

3.2.2.2 Passage Area

The area (A) of the annular passage is given by,

$$A = \int_A dA = \int_{n_i}^{n_o} 2\pi r dn = 2\pi r_m h \quad 3.52$$

and fractional area (ζ) at any position (n) is given by,

$$\zeta = \frac{1}{A} \int_{n_i}^n dA = \frac{1}{r_m h} \int_{n_i}^n r dn = \int_{n_i}^n \frac{r}{r_m} d\bar{n} \quad 3.53$$

3.2.2.3 Mass flow

The mass flow rate (\dot{m}) is given by,

$$\dot{m} = \int_A dm = \int_A \rho U_\ell dA = \int_{n_i}^{n_o} \rho U_\ell 2\pi r dn \quad 3.54$$

where, U_ℓ is the mean velocity in the streamwise direction, normal to the traverse line.

By defining mean velocity (\hat{U}) such that,

$$\dot{m} = \rho A \hat{U} = \rho 2\pi r_m h \hat{U} \quad 3.55$$

means that \hat{U} is given by,

$$\hat{U} = \frac{1}{A} \int_A U_\ell dA = \int_A U_\ell d\zeta \quad 3.56$$

or,

$$\hat{U} = \frac{1}{r_m h} \int_{n_i}^{n_o} U_\ell r dn = \int_{n_i}^{n_o} U_\ell \frac{r}{r_m} d\bar{n} \quad 3.57$$

Similarly, fractional mass flow (or stream function) at any position (n) is given by,

$$\psi = \frac{1}{\dot{m}} \int_{A_n} dm = \frac{1}{A} \int_{A_n} \frac{U_\ell}{\hat{U}} dA = \int_{A_n} \frac{U_\ell}{\hat{U}} d\zeta \quad 3.58$$

or,

$$\psi = \frac{1}{h} \int_{n_i}^n \frac{U_\ell}{\hat{U}} \frac{r}{r_m} dn = \int_{n_i}^n \frac{U_\ell}{\hat{U}} \frac{r}{r_m} d\bar{n} \quad 3.59$$

3.2.2.4 Mass-weighted Pressures

At any location in the flow, the total pressure (P) is given by sum of static pressure (p) and dynamic pressure (Q), i.e., $P = p + Q$, where,

$$Q = \frac{1}{2} \rho (U_t^2 + V_t^2 + W_t^2) \quad \dots \dots 3.60$$

For the flow as a whole, mass-weighted average total (\tilde{P}), static (\tilde{p}) and dynamic pressures (\tilde{Q}) can be obtained from,

$$\tilde{P} = \frac{1}{\dot{m}} \int_A P dm, \quad \tilde{p} = \frac{1}{\dot{m}} \int_A p dm \text{ and } \tilde{Q} = \frac{1}{\dot{m}} \int_A Q dm \quad \dots \dots 3.61$$

or,

$$\tilde{P} = \frac{1}{A\bar{U}} \int_A PU_t dA, \quad \tilde{p} = \frac{1}{A\bar{U}} \int_A pU_t dA \text{ and } \tilde{Q} = \frac{1}{A\bar{U}} \int_A QU_t dA \quad \dots \dots 3.62$$

Thus,

$$\tilde{P} = \tilde{p} + \tilde{Q} \quad \dots \dots 3.63$$

3.2.2.5 Kinetic Energy Flux Coefficient

The kinetic energy flux coefficient (α) is defined as the ratio of the actual kinetic energy flux ($= \frac{1}{A} \int_A QU_t dA$) to the kinetic energy flux of a flat ($U_t = \bar{U} = \text{constant}$) profile ($= \frac{1}{2} \rho \bar{U}^3$), i.e.,

$$\alpha = \frac{\frac{1}{A} \int_A QU_t dA}{\frac{1}{2} \rho \bar{U}^3} \quad \dots \dots 3.64$$

From the definition of \tilde{Q} (Eq. 3.62) and assuming that V_t and W_t are small in comparison to U_t so that $Q \approx \frac{1}{2} \rho U_t^2$,

$$\frac{1}{A} \int_A QU_t dA = \tilde{Q} \bar{U} = \frac{1}{A} \int_A \frac{1}{2} \rho U_t^3 dA \quad \dots \dots 3.65$$

giving,

$$\alpha = \frac{\tilde{Q}}{\frac{1}{2} \rho \bar{U}^2} = \frac{\int_A U_t^3 dA}{A \bar{U}^3} \quad \dots \dots 3.66$$

Thus,

$$\tilde{P} = \tilde{p} + \alpha \frac{1}{2} \rho \bar{U}^2 \quad \dots \dots 3.67$$

Curved Flow

The kinetic energy flux coefficient of the potential velocity (U_p) distribution is,

$$\alpha_p = \frac{\int_A U_p^3 dA}{A \bar{U}_p^3} \quad \dots \dots 3.68$$

where,

$$\bar{U}_p = \frac{1}{A} \int_A U_p dA \quad \dots \dots 3.69$$

In curved flow, in which U_p is not constant across the passage, $\alpha_p > 1.0$. Since the kinetic energy flux coefficient is conventionally used to characterise the degree of distortion of the velocity profile due to viscous effects, it is necessary to find an alternative definition. However, defining α_n as the ratio of the actual kinetic flux to the kinetic energy flux of the potential velocity profile, i.e.,

$$\alpha_n = \frac{\int_A U_\ell^3 dA}{\int_A U_p^3 dA} \quad \dots \dots 3.70$$

leads to $\alpha_n < 1.0$, since the mass flow of the two profiles is different, although the mean velocities \bar{U} and \bar{U}_p are related by the blockage (B) where,

$$B = \frac{\bar{U}_p - \bar{U}}{\bar{U}_p} = 1 - \frac{\bar{U}}{\bar{U}_p} \quad \dots \dots 3.71$$

which implies that, $\bar{U}/\bar{U}_p = (1 - B)$.

Taking the product of α_p (Eq. 3.68) and α_n (Eq. 3.70) gives,

$$\alpha_p \alpha_n = \frac{1}{A \bar{U}_p^3} \int_A U_\ell^3 dA = \frac{(1-B)^3}{A \bar{U}^3} \int_A U_\ell^3 dA = \alpha (1-B)^3 \quad \dots \dots 3.72$$

which implies that, $\alpha = \alpha_p \alpha_n / (1 - B)^3$.

Thus, a curved flow kinetic energy flux coefficient (α_c) can be defined as the ratio of the actual kinetic energy flux to the kinetic energy flux of a pseudo potential velocity profile (U'_p) which is scaled from U_p as $U'_p = (1 - B)U_p$ such that $\bar{U}'_p = (1 - B)\bar{U}_p = \bar{U}$ giving,

$$\alpha_c = \frac{\int_A U_\ell^3 dA}{\int_A U'_p^3 dA} = \frac{1}{(1-B)^3} \frac{\int_A U_\ell^3 dA}{\int_A U_p^3 dA} = \frac{\bar{U}_p^3}{\bar{U}^3} \frac{\alpha A \bar{U}^3}{\alpha_p A \bar{U}_p^3} = \frac{\alpha}{\alpha_p} \quad \dots \dots 3.73$$

which implies that, $\alpha = \alpha_p \alpha_c$.

3.2.3 Boundary Layer Parameters

To determine the integral boundary layer parameters, it is necessary to compare the actual mean velocity distribution ($U(n)$) to the ideal behaviour of the flow, described by the potential velocity distribution ($U_p(n)$). Above the boundary layer the flow is effectively inviscid, and the edge of the boundary layer is defined as the position (n_δ) at which $U = 0.995 U_p$. The boundary layer thickness (δ) is therefore given by,

$$\delta = n_\delta - n_w \quad \dots\dots 3.74$$

3.2.3.1 Displacement Thickness

The displacement (or mass deficit) thickness (δ^*) represents the mass flow deficit of $U(n)$ relative to $U_p(n)$. At a distance δ^* away from the wall, the position n_{δ^*} is defined such that the mass flow associated with $U_p(n)$ between n_{δ^*} and n_δ is the same as the mass flow of $U(n)$ between n_w and n_δ , i.e.,

$$\int_{n_{\delta^*}}^{n_\delta} U_p dA = \int_{n_w}^{n_\delta} U dA \quad \dots\dots 3.75$$

For axisymmetric flow, $dA = 2\pi r dn$, and by assuming that $U_p = U_{p_w} = constant$ for $n_w \leq n \leq n_{\delta^*}$ and that the area between n_w and n_{δ^*} (A_{δ^*}) is approximately equal to $2\pi r_w \delta^*$, the following expression is obtained,

$$\delta^* = \frac{1}{r_w U_{p_w}} \int_{n_w}^{n_\delta} (U_p - U) r dn \quad \dots\dots 3.76$$

3.2.3.2 Momentum Deficit Thickness

The momentum deficit thickness (δ^{**}) represents the momentum deficit of $U(n)$ relative to $U_p(n)$. At a distance δ^{**} away from the wall, the position $n_{\delta^{**}}$ is defined such that the momentum associated with $U_p(n)$ between $n_{\delta^{**}}$ and n_δ is the same as the momentum of $U(n)$ between n_w and n_δ , i.e.,

$$\int_{n_{\delta^{**}}}^{n_\delta} U_p^2 dA = \int_{n_w}^{n_\delta} U^2 dA \quad \dots\dots 3.77$$

For axisymmetric flow, $dA = 2\pi r dn$, and by assuming that $U_p = U_{p_w} = constant$ for $n_w \leq n \leq n_{\delta^{**}}$ and that the area between n_w and $n_{\delta^{**}}$ ($A_{\delta^{**}}$) is approximately equal to $2\pi r_w \delta^{**}$, the following expression is obtained,

$$\delta^{**} = \frac{1}{r_w U_{p_w}^2} \int_{n_w}^{n_\delta} (U_p^2 - U^2) r dn \quad \dots\dots 3.78$$

3.2.3.3 Momentum Thickness

The momentum thickness (θ) is defined as the difference between δ^{**} and δ^* , i.e.,

$$\theta = \delta^{**} - \delta^* = n_{\delta^{**}} - n_{\delta^*} \quad \dots\dots 3.79$$

From the derivation of δ^* and δ^{**} , it is possible to obtain the following expression for θ , which applies to axisymmetric flow,

$$\theta = \frac{1}{r_w U_{p_w}^2} \int_{n_w}^{n_{\delta}} U(U_p - U) r dn \quad \dots\dots 3.80$$

3.2.3.4 Universal Thickness

For equilibrium boundary layers subjected to a constant pressure gradient parameter (β), Clauser^[37] found that the mean velocity exhibited universal behaviour in terms of $(U_p - U)/U_\tau$ vs. $(n - n_w)/\delta$, where the friction velocity (U_τ) is defined by Eq. 3.89 below. Thus δ^* , δ^{**} and θ depend on U_τ/U_{p_w} ($\equiv \sqrt{C_f/2}$) which varies as the boundary layer develops (δ increasing) and so are dependant on Reynolds number. Given this and the difficulty of determining δ itself, Clauser^[37] defined a thickness (Δ) based on the universal velocity profile, which in the present notation is written as,

$$A_\Delta = \int_{n_w}^{n_{\delta}} \frac{(U_p - U)}{U_\tau} dA \quad \dots\dots 3.81$$

where A_Δ is the area between n_w and n_Δ and $\Delta = n_\Delta - n_w$. Thus for a given β , the integral and therefore Δ/δ remains constant (N.B. for $\beta = 0$, $\Delta/\delta = 3.6$).

In addition, since $\int_{n_w}^{n_{\delta}} (U_p - U) dA = A_\delta \cdot U_{p_w}$, the relationship between Δ and δ^* is,

$$\Delta = \frac{U_{p_w}}{U_\tau} \delta^* \quad \dots\dots 3.82$$

3.2.3.5 Shape Parameters

The most frequently used shape parameter (H) is defined as the ratio of displacement thickness to momentum thickness,

$$H = \frac{\delta^*}{\theta} \quad \dots\dots 3.83$$

Clauser^[37] defined an alternative shape parameter (G) based on the first and second moments of the universal velocity profile about zero, i.e.,

$$G = \frac{\int_{n_w}^{n_s} \left(\frac{U_p - U}{U_\tau} \right)^2 dA}{\int_{n_w}^{n_s} \left(\frac{U_p - U}{U_\tau} \right) dA} \quad 3.84$$

which can be simplified to,

$$G = \frac{U_{p_w}}{U_\tau} \left(2 - \frac{\delta^{**}}{\delta^*} \right) = \frac{U_{p_w}}{U_\tau} \left(\frac{H-1}{H} \right) \quad 3.85$$

3.2.4 Determining the Wall Shear Stress

In the present investigation, no direct measurements of wall shear stress were made, using such devices as floating surface elements, thin film gauges or Preston tubes. Therefore, methods based on the law of the wall (log-law) were used, in which the wall shear stress is determined from the mean velocity profile.

3.2.4.1 The Law of the Wall

In a zero pressure gradient laminar boundary layer, in which the shear strain gives rise to shear stress (τ) purely through the action of molecular viscosity, it can be shown (e.g., Schlichting^[135]) that the velocity profile is described by,

$$U^+ = n^+ \quad 3.86$$

where,

$$U^+ = \frac{U}{U_\tau} \quad 3.87$$

and,

$$n^+ = \frac{nU_\tau}{V} \quad 3.88$$

In these expressions, n is the distance from the wall and $U = U(n)$, and the velocity scale (U_τ), often referred to as the friction velocity, is based on the wall shear stress, i.e.,

$$U_\tau = \sqrt{\frac{\tau_w}{\rho}} \quad 3.89$$

The Log-law

In a zero pressure gradient turbulent boundary layer, Eq. 3.86 only applies in a very small region adjacent to the wall, known as the viscous sub-layer, which extends up to $n^+ \approx 5$. Beyond this, the Reynolds shear stress begins to contribute to the total stress, affecting the mean velocity. By $n^+ \approx 25$, the Reynolds stress contributes 90% of the total shear stress, and the change over to fully turbulent behaviour is virtually complete. Above this 'buffer' region, the behaviour of the mean velocity is observed to follow a log-law behaviour,

$$U^+ = \frac{1}{\kappa} \ln(n^+) + A \quad \dots \dots 3.90$$

where κ is the Von Kármán constant and the constant of integration (A) has to be determined experimentally. There is some debate as to the appropriate value of this constant, which is known to vary with surface roughness (see Rotta^[132]) and increase at low Reynolds number (Spalart^[156]). In the present investigation, a value of $A = 2/\kappa$ was used (from Clauser^[37]).

Thus, the mean velocity profile is expected to exhibit a region of linear behaviour in log-linear co-ordinates. The extent of this region, known as the inner-layer, varies, but an upper limit of several hundred n^+ ($n/\delta \approx 0.2$) is typical. Despite the simple assumptions in its derivation, the log-law has been found to hold over a wide range of flows (Bradshaw and Huang^[23]), and is often used as a means of determining the wall shear stress. In the literature review, however, it was shown that the extent of the log-law region may be somewhat reduced over convex surfaces, or under adverse pressure gradient, and may disappear altogether in highly accelerated boundary layers.

3.2.4.2 Single Point Method

For a given mean velocity U_1 , at a distance n_1 from the wall, a value of U_τ can be determined from the log-law (Eq. 3.90) which satisfies these values. Unfortunately, this cannot be determined explicitly, and must be found implicitly using a iterative method. Using a Newton-Raphson method, U_τ was obtained from,

$$U_{\tau(n+1)} = U_{\tau(n)} - \frac{\left\{ U_{\tau(n)} \left[\frac{1}{\kappa} \ln \left(\frac{n_1 U_{\tau(n)}}{v} \right) + A \right] - U_1 \right\}}{\left\{ \frac{1}{\kappa} \left[1 + \ln \left(\frac{n_1 U_{\tau(n)}}{v} \right) \right] + A \right\}} \quad \dots \dots 3.91$$

Starting with any reasonable guess (say, $U_{\tau(1)} \approx 0.04 U_{p_w}$), the scheme converges to a tolerance of $|U_{\tau(n+1)} - U_{\tau(n)}| < 10^{-5} \times U_{\tau}$ within a few iterations.

3.2.4.3 Multiple Point Method

The problem with using the single point method, to determine U_{τ} , is deciding which data point to use, and whether this data point is appropriate. To overcome this, and thereby increase the accuracy of U_{τ} , a multi-point method was devised. In the present investigation, the Reynolds number was sufficiently high to guarantee that data could not be obtained within the sub-layer or buffer regions; although the LDA was able to get fairly close. The 5-hole probe was not able to get as close, but still n^+ values as small as 100 could be achieved. The first data point from the wall, therefore, would seem an obvious choice for use with the single point method, but there are several concerns in making this assumption. Without first plotting all the data in log-linear co-ordinates, there is no way of knowing whether, and to what extent, a linear log-law region exists. Thus, in a computerised single point analysis, it is not known if the first data point is within the log-law region. In addition, experimental data measured close to a surface tends to be less accurate, and blind use of the data next to the wall may yield unrepresentative results. Away from the wall, the data may be more accurate but will still suffer from some degree of scatter, associated with the measurement precision, and, even if these data all lie in a linear log-law region, a single point may not be representative of the overall trend. What is required, therefore, is a way of using all the measurements within the inner layer, so that an 'average' U_{τ} value can be determined.

One such possible method was developed, in which a value of U_{τ} is determined for each data point in the mean velocity profile, using the single point method (Eq. 3.91). Now, if a log-law region exists, the U_{τ} values will tend towards a constant value in the near-wall region. Visually, it is easy to see if the actual data has several points with near constant U_{τ} , and determine a sensible average value, but this is not so easy to do within a computerised method.

In an attempt to automate this procedure, therefore, a curve fit method was used. The parabolic curve,

$$U_{\tau} = a_1 + a_2 \{ \ln(n^+) - 3 \}^2 \quad \dots \dots 3.92$$

can be used to represent the behaviour of U_{τ} as it tends towards a constant at $\ln(n^+) = 3$. By fitting this curve to the actual U_{τ} values in the range $3 < \ln(n^+) < 6$, using a least square fit method to determine the constants (a_1 and a_2), the most representative U_{τ} is given by the numerical value of a_1 . Thus, any scatter in the experimental data is

averaged out and, for actual data that does not exhibit constant U_r behaviour, an estimate of the behaviour at $\ln(n^+) \approx 3$ is obtained.

3.2.5 Spatial Gradients

In contrast to the integral approach used to obtain overall quantities, various parameters were differentiated to determine their spatial gradients. These quantities appear in the differential equations of motion, and are of use in describing the physical behaviour of the flow. Of primary importance are the pressure, mean velocity and Reynolds stress gradients appearing in the momentum equations, since they represent the forces and accelerations present in the flow.

In order to obtain spatial gradients from the experimental data, a finite difference technique was used. Since data was obtained on traverse lines across the duct (j -lines), it was possible to determine the cross-stream gradient ($\partial\phi/\partial n$), for any parameter (ϕ), using the central difference formula,

$$\left. \frac{\partial\phi}{\partial n} \right|_{ijk} = \frac{1}{2} \left(\frac{\phi_{j+1} - \phi_j}{n_{j+1} - n_j} + \frac{\phi_j - \phi_{j-1}}{n_j - n_{j-1}} \right) \quad 3.93$$

On the walls, of course, a one-sided difference was used.

In the streamwise direction, a similar approach was applied wherever possible. For the 5HP pressures and velocities, the data were obtained at the same number of positions, each of which was at the same non-dimensional height (h), and, therefore, streamwise gradients could be obtained using,

$$\left. \frac{\partial\phi}{\partial s} \right|_{ijk} = \frac{1}{2} \left(\frac{\phi_{i+1} - \phi_i}{s_{i+1} - s_i} + \frac{\phi_i - \phi_{i-1}}{s_i - s_{i-1}} \right) \quad 3.94$$

Although one sided differences again were used at the most upstream and downstream locations, the values at $x/L = 0.0$ and $x/L = 1.0$ also were difficult to obtain accurately, since the variation upstream and downstream of the S-shaped duct was poorly defined due to the relatively long distance to the next traverse location.

As well as the static pressure gradients ($\partial p/\partial s$, $\partial p/\partial n$), finite differencing was used to obtain the mean strain rates from the 5HP data. In a $s-n$ co-ordinate system in which the curved line (S) is taken to be a line of constant h (i -line), corresponding to the measurement positions, the mean strain rates equivalent to the Cartesian strains in the $x-y$ plane are,

$$\frac{\partial U}{\partial x} \equiv \frac{\partial U_t}{\partial s} - \frac{V_t}{R} \quad \dots\dots 3.95$$

$$\frac{\partial U}{\partial y} \equiv \frac{\partial U_t}{\partial n} \quad \dots\dots 3.96$$

$$\frac{\partial V}{\partial x} \equiv \frac{\partial V_t}{\partial s} + \frac{U_t}{R} \quad \dots\dots 3.97$$

$$\frac{\partial V}{\partial y} \equiv \frac{\partial V_t}{\partial n} \quad \dots\dots 3.98$$

In calculating the mean strain rates, therefore, it was necessary to find the geometric curvature ($1/R$) of S . This was achieved using the central difference formula,

$$\frac{1}{R} = \frac{\tan^{-1}\left(\frac{y_{i+1} - y_i}{x_{i+1} - x_i}\right) - \tan^{-1}\left(\frac{y_i - y_{i-1}}{x_i - x_{i-1}}\right)}{\frac{1}{2}(s_{i+1} - s_{i-1})} \quad \dots\dots 3.99$$

From the LDA data, it was more difficult to obtain spatial gradients. The main problem was that data did not exist at all points on a structured grid, due to difficulties in obtaining measurements at some positions (close to surfaces in particular), and streamwise gradients could not be obtained directly from the data. Whilst the mean strain rate $\partial U_t / \partial n$ could be obtained directly from the mean velocity data, cross-stream gradients of the Reynolds stresses, taken along the traverse lines, were subject to a relatively large error due to the scatter in the Reynolds stresses.

Of all the Reynolds stress gradients, the cross-stream shear stress gradient ($\partial \bar{u}\bar{v} / \partial n$) was by far the most important to determine accurately. With the scatter in the Reynolds stress data affecting the finite difference gradients, therefore, a smooth curve was fitted through the measured $\bar{u}\bar{v}$ data at each traverse location. A piecewise linear curve was used, and the points were adjusted (manually) until a good fit was obtained. In addition, each wall value was set equal to the shear stress obtained from the log-law, and the point adjacent to the wall (at a distance of $0.005h$ from the wall) was set such that the gradient between this and the wall value was equal, and opposite, to the streamwise pressure gradient ($\partial p / \partial s$). Using this interpretation of the shear stress, $\partial \bar{u}\bar{v} / \partial n$ could be obtained easily and accurately.

In order to calculate products of the Reynolds stresses and mean strain rates, it was necessary to interpolate the LDA data on to the 5HP measurement positions. This was achieved using a piecewise linear interpolation of the Reynolds stresses, along each traverse line. In this way, it was possible to calculate many quantities containing both

mean velocity and turbulence data, from which gradients could be obtained if necessary. Most importantly, however, it allowed the turbulent kinetic energy production rate (P) to be obtained from,

$$P = -\bar{uv} \left(\frac{\partial U}{\partial n} + \frac{\partial V}{\partial s} + \frac{U}{R} \right) - \bar{uu} \left(\frac{\partial U}{\partial s} - \frac{V}{R} \right) - \bar{vv} \left(\frac{\partial V}{\partial n} \right) \quad \dots\dots 3.100$$

3.3 Errors and Accuracy

In obtaining and analysing experimental data, errors will be present in the results. Inevitably, the overall accuracy of each parameter will depend on a combination of factors, and therefore is difficult to quantify. However, the errors which contribute to the accuracy can be identified, and to some extent these can be estimated. Generally, in this investigation, the errors have been kept to a very low level and the data obtained is of the highest quality, which can be judged by examining the repeatability and smoothness of variation of the data. Whilst there is some uncertainty in the higher order turbulence data, particularly in the outer wall boundary layer, the mean velocities and, to a large extent, the Reynolds stresses exhibit very little scatter.

3.3.1 Hardware

The experimental test rig was manufactured as far as possible to the specified geometry. Since this could never be exact, the actual geometry was established by measuring the position of the annulus walls. The general accuracy of rig dimensions was typically about 0.1 mm, although, due to the difficulty in manufacturing the more complex shape, the error between the actual and nominal geometry increased to a maximum difference of about 0.4 mm within the annular S-shaped duct. This was established by measuring the annulus height, at each traverse location, using the probe (5HP or LDA). This could determine the wall position to within ~0.05 mm, relative to the mid-height position, which was assumed to be correct. The spatial resolution of the traverse equipment is discussed in more detail in Chapter 2 (Sect. 2.2.1.2), which effectively defines the accuracy to which the probe could be positioned within the flow.

As a consequence of the geometrical differences, the duct area varies by up to 1%, relative to the nominally constant area design intention. Naturally, the actual geometry was used when deriving spatially average quantities from the mean velocity data. In presenting the data, however, the mean velocities are non-dimensionalised by a single mean reference velocity (equivalent to the mean velocity through a nominal area duct at the operating mass flow), and, therefore, will vary according to the actual area. In

addition, the measurements were made at different circumferential positions, especially with the LDA because of the window locations, and small difference in the local flow behaviour may have resulted from the geometrical variation around the rig.

3.3.2 Five Hole Probe

In any pressure measurement system, the absolute accuracy is dependent on the calibration of the pressure transducers, and on the data acquisition system used to digitise the transducer output voltages. The calibration of each transducer was determined using to a Betz manometer, which was used to measure the pressure applied across the differential pressure transducers to within $\pm 2.5 \text{ N/m}^2$, whilst the output voltage was logged by the data acquisition system, over a range of $\pm 2500 \text{ N/m}^2$. The accuracy of the analogue voltage channels ('A' block and ADC) was determined by applying a very accurate DC voltage source, over a range of values, and recording the system output. Although the ADC used 16 bits, the accuracy was only about $\pm 0.1\%$. The accuracy of the transducer calibration, therefore, was about $\pm 0.2\%$.

When measuring pressures from the rig, the finite accuracy of the voltage measurement combined with the transducer calibration accuracy gives an overall pressure measurement accuracy of $\pm 0.3\%$. However, this applies only at the maximum pressure difference, and, as a percentage, will increase when the pressures are lower. Typically, for the tests without the compressor, the measured pressures were between a third to a half of the $\pm 1000 \text{ N/m}^2$ transducers, resulting in an accuracy of about $\pm 1\%$. In addition, the precision of the pressure measurements was obtained experimentally. By repeatedly measuring a number of pressures, obtained from a fixed probe and wall static taps, while operating the rig at constant conditions, the standard deviation of the samples was found to be about 0.3% in all cases. Each reading was taken in the normal way, from an average of 1000 samples, and, assuming a normal distribution, this suggests that 99% of the pressure measurements are within $\pm 1\%$ of the average reading that would result if a very large number of samples had been taken at each point. The random scatter in the readings, therefore, is of a similar magnitude to the estimated overall accuracy.

In terms of velocity, the overall accuracy can be estimated. The total velocity of the flow is obtained from the dynamic pressure (Q), which is obtained from the measured 5HP pressures using the calibration. If Q was obtained with an accuracy similar to that of the individual pressures, and with Q proportional to velocity squared, the velocity error would be half that of the pressure data, i.e., $\pm 0.5\%$. However, the 5HP was calibrated using the same data acquisition system and, therefore, the calibration coefficients also were measured to a finite accuracy. Unfortunately, these errors are

difficult to quantify, but will be of a similar order of magnitude to the pressure measurement accuracy. When in use, therefore, the absolute accuracy of a 5HP measurement may be worse than $\pm 1\%$. What is more important, however, as far as determining the flow behaviour is concerned, is the repeatability of the measurements from one point to the next, and from one traverse to the next. This is dependant on the precision of the pressure data, not the accuracy, and, providing the rig non-dimensional operating conditions are maintained and the data corrected appropriately (Chapter 2, Sect. 2.2.1.4), the velocity will repeat to within about $\pm 0.5\%$ at every point.

In general, there are several points worth noting about the 5HP method. The calibration was carried out at approximately same velocity as encountered in the rig to avoid Reynolds number effects, and for incompressible flow there were no Mach number effects to be considered. In addition, the calibration procedure was rigorous, and, apart from the pressure measurement error already discussed, the angles used were set within $\pm 0.1^\circ$ of the required value; although it had to be assumed that the calibration jet was aligned with the nozzle, relative to which the probe angles were set. When in use in the rig, however, probe alignment was more difficult. Whilst pitch angle was determined by the probe head geometry, as calibrated, the yaw angle of the probe had to be aligned with the rig for each traverse, which only could be achieved within about $\pm 1^\circ$. Overall, however, the procedure adopted led to errors in the circumferential velocity (W_θ) of a similar magnitude at each traverse location, in comparison to the LDA data, equivalent to about $+3^\circ$ of yaw. This suggests that, for whatever reason, there was a systematic misalignment between the probe calibration and its use on the rig.

Furthermore, the 5HP data may be affected by the presence of nearby solid surfaces. Certainly, it is apparent that the data taken closest to each wall, at a distance of $0.02h$ from the surface, was influenced, since the static pressure and cross-stream velocity (V_θ) are, in some cases, inconsistent with the rest of the data. This may be due to a local change in the pressure sensed by the hole closest to the wall, or, alternatively, could be due to the large strain rate present in this region. Since the probe has a finite size, the pressure sensed by each hole will be influenced by velocity gradients. For the majority of the data this is taken into account, since the variation in each pressure, as determined by the adjacent points, is used to interpolate the measured side hole pressures at the centre hole location. For data adjacent to solid surfaces, however, errors will arise in this process which will affect the accuracy of the data.

3.3.3 Laser Doppler Anemometer

Whilst the accuracy of each velocity sample can be guaranteed, there are several sources of error which affect the results. Since a finite number of samples were collected, statistical errors will occur in the time-average flow quantities, and systematic errors associated with the measurement technique will affect the overall accuracy.

3.3.3.1 Mean Velocity

Statistical

By calculating the average from a finite number of samples, the mean value may be in error, relative to the true mean obtained from an infinite number of samples. Theory suggests that for a normally distributed signal with variance (V), the mean value obtained from a finite number of samples (N) will, with a certain level of confidence, lie within $\pm \epsilon$ of the true mean. For 99% confidence,

$$\epsilon = 2.58 \sqrt{\frac{V}{N}} \quad \dots\dots 3.101$$

For each velocity component, V is equivalent to the normal stress of that component, which increases through the boundary layer from the low isotropic level of $\sim 0.04 \text{ m}^2/\text{s}^2$ in the core region up to values between about $2\text{-}8 \text{ m}^2/\text{s}^2$ adjacent to the wall, depending upon the component and the location. Within the core region, the low turbulence levels and the large number of samples ($\sim 5,000$) meant that the mean velocity error was negligible. Adjacent to the surface, where the turbulence levels were highest, fewer samples were obtained (~ 500). In this extreme case, the mean velocity obtained for each component lies within 0.3 m/s ($0.01 U_{\text{Mean}}$) of the true value, with 99% confidence. Over most of the boundary layer, however, a minimum of 2000 samples were obtained at each point, and with lower normal stresses, the error was more typically less than $\pm 0.1 \text{ m/s}$.

When obtaining an average, it is important that the samples are statistically independent. In a turbulent flow, the velocity signal will correlate with itself over a finite time, and this can be estimated by obtaining an autocorrelation curve, from which the integral time scale can be derived. For the present data, however, this was not possible, and so an alternative approach was adopted. If the turbulent flow is conceived as a series of eddies passing the measurement position, it can be argued that data obtained from the same eddy would be correlated, and, therefore, not statistically independent. Using this approach, a time scale (T_e) was calculated using the mean velocity (U) and a typical eddy size as described by the mixing length (ℓ). Data obtained at a rate greater than the

typical eddy passing frequency ($1/T_\ell$) will not be independent. The mixing length, itself, was estimated from Prandtl's mixing length hypothesis, using the measured shear stress (\bar{uv}) and the mean strain rate ($\partial U/\partial n$) to give the turbulent viscosity, and therefore ℓ . As expected, ℓ increased with increasing distance from the surface, at a rate roughly equal to k , before reaching a fairly constant maximum over the outer layer of the boundary layer. Due to the effect of curvature, however, the mixing length in the outer layer, and therefore T_ℓ , was very much larger in the concave regions in comparison to the convex, but, for the majority of the data, the time scale estimated from the above analysis was less than 0.1 ms. With mean data rates no higher than 5 kHz, and even allowing for the fact that peak data rates might be higher than this, most of the samples obtained were statistically independent. However, in the outer layer of the outer wall boundary layer downstream of the concave bend, the larger time scale may have meant that some of the data in this region was obtained too rapidly, reducing the number of valid samples.

Systematic

Errors in the derived velocity components will occur if the terms in the transformation matrix (a_{ij}) are not of the correct magnitude. Systematic errors of this type are a function of the accuracy to which the probe angles (α , β , γ_g and γ_b) can be measured. With knowledge of the limits to which laser beam alignment can be determined, the effect on the mean orthogonal velocities (U_ℓ , V_ℓ , W_ℓ) can be evaluated by varying a_{ij} to correspond with these limits. For example, with the probe angle accuracy estimated to be $\pm 0.2^\circ$, U_ℓ , V_ℓ and W_ℓ would be in error by no more than ± 0.1 m/s (less than $\pm 0.5\%$ of U_{Mean}) due to this effect.

As indicated by Edwards^[51], the arrival rate of the particles is not independent of flow velocity, and so a simple numerical average can be biased. It was suggested by Edwards that the magnitude of the error is related to the square of the turbulence intensity, and, therefore, the bias error (ΔU_i) can be assessed using, for example,

$$\frac{\Delta U_i}{U_{Mean}} \approx \frac{k}{U_{Mean}^2} \quad 3.102$$

This suggests that the error will be of greatest significance close to the solid surfaces where the turbulent kinetic energy (k) is largest. As such an error of about 1% might be expected in the near-wall region, but over the majority of the annulus the error will be very much less. There are several methods that can be used to reduce velocity bias, mainly using a weighted average to determine the time-average quantities. However, due to the relative insignificance of the error, no bias correction was attempted.

Another possible error might arise due to the finite size of the measurement volume. In regions of high mean velocity and Reynolds stress gradients, the velocity of a seeding particle could vary as it passes through the volume. In this case, differences may arise between the actual velocity of the particle, at the centre of the volume, and that obtained from the frequency spectrum of the burst, which will be broader due to the slight variation of frequency at which each fringe is crossed. With an effective measurement volume size of less than 0.1 mm in the flow direction, it is unlikely that errors of any significance arise due to this effect. More importantly, however, the effective measurement volume is approximately 0.3 mm long in the cross-stream direction, even when off-axis detection is used. In regions of high strain rate, therefore, each end of the measurement region will be detecting particles that are in regions of different mean velocity. By averaging all the samples obtained across the entire length of the volume, this may give rise to errors in the mean velocity, and also in the variance of the signal, but it has not been possible to quantify their magnitude.

3.3.3.2 Reynolds Stress

Statistical

The statistical error associated with the calculated variance (V) can be derived using the Chi-squared distribution (χ^2). To obtain the 99% confidence limits, χ^2 is obtained at probabilities of 0.005 and 0.995 based on the number of samples (N), i.e.,

$$\frac{N V}{\chi^2_{0.005}(N)} < V_{\text{true}} < \frac{N V}{\chi^2_{0.995}(N)} \quad \dots\dots 3.103$$

Using this, the uncertainty in the variance reduces as the number of samples increases. For example, with $N=500$ the true variance will lie within $0.85V < V_{\text{true}} < 1.18V$, whereas with $N=5000$, $0.95V < V_{\text{true}} < 1.05V$. Since the variance of each velocity signal is equivalent to the normal stress, the accuracy of the measured normal stresses (\bar{uu} , \bar{vv} , \bar{ww}) can be estimated. At the majority of positions, approximately 5000 statistically independent samples were collected, and typically, with 99% confidence, the normal stresses will be within $\pm 5\%$ of their true values. However, at some points only 2000 samples were obtained, and here the error in normal stresses will be $\pm 8\%$. The error associated with the shear stress (\bar{uv}) could not be estimated in this way, but is believed to be of a very similar magnitude to the normal stress errors. In addition, since these statistical errors occurs randomly, they will only affect the amount of scatter in the Reynolds stresses, and not the accuracy of the overall trend indicated by several adjacent points.

Furthermore, it should be noted that the increased scatter in the Reynolds stresses, obtained in the outer wall boundary layer, is probably due to a reduction in the number of statistically independent samples. This may have resulted from sampling the velocity too rapidly, in regions where large scale turbulent motion, produced by the concave curvature, gives rise to long times scales. At some points, a noticeable difference was observed in the variance of the on-line histogram when the data acquisition was repeated a number of times. Whilst it was realised that a larger sample, taken over a longer period of time, would have been desirable, the configuration of the experiment would not allow this to be done at the time, and so judgement was applied in choosing the most representative collection of samples to store for subsequent analysis.

Systematic

The Reynolds stress errors, arising from the finite processor resolution and the optical transformation process, were discussed in Section 3.1.3.3. Using a theoretical analysis, it was possible to estimate the magnitude of the errors and remove them from the data. For this, it was necessary to estimate the magnitude of the processor resolution, which was possible in the central core region of the flow, where the turbulence was isotropic. The resolutions obtained were in good agreement with those expected for the processor, taking into account the processing technique and the effect of signal-to-noise ratio (SNR), and were assumed to apply within the boundary layers as well. After correction in this way, the accuracy of the Reynolds stresses was substantially improved, especially in the core region, and although the errors may increase slightly as the surface is approached, due to the lower SNR, the error remaining after correction would be insignificant in comparison to the Reynolds stress levels.

It is worth noting that all types of LDA signal processing equipment, commercially available, will operate with a finite resolute, and, therefore, give rise to errors in the derived Reynolds stresses. Fortunately, during the present investigation, the signal processors used were spectrum analysers, which, it is generally believed, give the best resolution, in comparison to other types of processing equipment, due to the way that they determine velocity using a fourier transformation technique.

3.3.3.3 Triple Velocity Correlations

Whilst it has not been possible to quantify formally the uncertainty associated with the triple velocity correlations, it is clear that these errors are somewhat larger than for the Reynolds stresses. Since the triple correlations are obtained from a finite number of samples, there will be a statistical error associated with the value. For the same number of samples, this will be larger than that associated with the double velocity correlations,

simple due to the increased order of the correlation. Since this error is random, however, the larger uncertainty will lead to an increase in the scatter of the data, but, providing a trend can be ascertained from the surrounding data, the magnitude of the triple correlations will be reasonable accurate.

Furthermore, it was found that systematic errors do not result from the finite processor resolution. In contrast to the errors arising in the Reynolds stresses, the odd number of velocities means that the time average of the random error associated with any one processor is zero, i.e., $\overline{(\Delta c_i)^3} = 0$, and, likewise, the errors arising in different processors are not correlated.

3.3.4 Overall Parameters

A thorough analysis of the errors associated with the overall parameters has not been performed, but there are several points worth noting. In obtaining the various integral parameters, it was necessary to integrate the data numerically in order to obtain the spatial averages. To minimise the numerical errors associated with using Simpson's rule on a finite number of data, additional points were first interpolated using a cubic B-spline. In addition, for the mean velocities, the region between the wall and the first data point was represented by a log-law velocity distribution, calculated from the first point and its distance from the wall, so that the interpolation was well behaved in the critical end regions of the data. By carrying out tests on an idealised velocity profile, it was found that, by using the log-law in this way, the accuracy of the boundary layer parameters, such as δ^* , θ and H , was improved, since they were highly sensitive to the velocity distribution in the near-wall region.

At the majority of positions, the wall shear stress (τ_w) could be obtained to within about $\pm 5\%$, from the mean velocity profile using the log-law techniques previously outlined. In the region of strong acceleration adjacent to the outer wall, however, there was no linear log-law region, and the value of friction velocity (U_τ) calculated for each point in the velocity profile increased towards the surface. Hence, in such regions, τ_w could be only broadly estimated ($\pm 10\%$). Overall, however, it should be noted that there was good agreement between the wall shear stress values derived from the mean velocity data and those indicated by extrapolation of the measured shear stress (\bar{uv}) distribution, making use of the wall pressure gradient to determine the shear stress gradient close to the wall. Indeed, in the region of strong acceleration, this additional information allowed τ_w to be estimated more accurately ($\pm 5\%$), and, since the values in this region were above those obtained from the mean velocity profiles, it is apparent that there was virtually no linear log-law region between the closest measurement and the wall.

Of all the integral parameters, the calculated mass flow can be used to judge the overall quality of the experiment. Whilst it is impossible to assess the overall accuracy, the variation in the mass flow derived by integrating the velocity profile at each traverse location can give an indication of the repeatability of the overall experimental procedure. This covers all aspects of the experiment, including the setting of the rig operating conditions, the individual measurements and the analysis procedure, all of which can lead to errors in the derived mass flow. Without the compressor present, analysis of the 2D axisymmetric data gave mass flows that were within $\pm 0.5\%$ of the nominal value, which is extremely good. However, with the compressor installed, the increased complexity of the flow, including the compressor wakes, led to a larger variation ($\sim 2\%$) of mass flow.

CHAPTER 4 EXPERIMENTAL RESULTS

	Page
4.1 Rig Commissioning Tests	112
4.1.1 General Considerations	112
4.1.2 Axial Compressor Performance	113
4.1.3 Operating Conditions	114
4.2 Axisymmetric Flow Without the Compressor	115
4.2.1 Presentation of the Results	116
4.2.2 Mean Flow Quantities	116
4.2.2.1 Static Pressure Distribution	117
4.2.2.2 Streamwise Velocity and Stream Function	117
4.2.2.3 Comparison of 5HP and LDA Velocities	121
4.2.2.4 Overall Parameters	123
4.2.2.5 Wall Pressure Gradient and Curvature	129
4.2.3 Turbulence Data	131
4.2.3.1 Reynolds Stresses	131
4.2.3.2 Structure Parameters	135
4.2.3.3 Higher Order Velocity Correlations	138
4.2.4 Derived Data	141
4.2.4.1 Log-law Co-ordinates	142
4.2.4.2 Mean Strain Rates	143
4.2.4.3 Shear Stress Gradient and Total Pressure Loss	147
4.2.4.4 Turbulent Kinetic Energy Production	151
4.2.4.5 Streamwise Acceleration	153
4.3 Flow With the Compressor Installed	155
4.3.1 Mean Flow Quantities	155
4.3.1.1 S-shaped Duct Inlet Conditions	156
4.3.1.2 Pressure and Velocity Distribution	157
4.3.1.3 Circumferentially Averaged Profiles	159
4.3.1.4 Overall Parameters	160
4.3.2 Turbulence Data	161
4.3.2.1 S-shaped Duct Inlet Conditions	161
4.4 Concluding Remarks	163

The experimental results are presented in this chapter. Mainly, these are taken from the axisymmetric flow, without the compressor, and give a comprehensive description of the flow behaviour in an annular S-shaped duct. Along with the 5-hole probe (5HP) data, which defines the mean flow, 3-component LDA measurements are presented. As well as confirming the 5HP mean velocities, the LDA data completely defines the time-average turbulence, including all the Reynolds stress components and the higher order velocity correlations. With the compressor installed, the 3D flow including the stator blade wakes was surveyed, using the 5HP at every station and the LDA at stator exit. Some of the results from this are presented, in order to show the main features of the more complex flow, but the primary aim of this thesis is to describe and understand the physical behaviour of the 2D axisymmetric flow under the combined influence of pressure gradient and curvature effects.

4.1 Rig Commissioning Tests

Before presenting the main results, the tests used to confirm the satisfactory operation of the rig are described briefly. Upon completion of the new experimental facility, it was essential that the quality of the flow through the rig was assessed. In particular, the inlet flow was confirmed as being axisymmetric, which was crucial since any distortion present in the inlet flow would have made it difficult to interpret the results. In addition, the axial compressor performance was measured, allowing a suitable rig operating condition to be established close to its design point. Without the compressor, the mass flow rate through the rig was lower, but a satisfactory Reynolds number could still be obtained.

4.1.1 General Considerations

Of primary concern when assessing the new rig was the quality of the inlet flow. Upstream of the rig, air entered the centrally mounted intake from within a large square section plenum, which itself drew air through a filter on the upper surface. Even though the geometry of the inlet system was symmetrical, it was necessary to check that the intake was well behaved, and gave rise to axisymmetric conditions within the parallel annular inlet duct. In order to demonstrate that the flow was axisymmetric, measurements were made at four equally spaced circumferential positions. Primarily, these were taken at the upstream location W2 (see Fig. 3) and at S-shaped duct exit (A6), where the inner and outer wall static pressures were shown to be reasonably uniform around the annulus. In addition, a Pitot probe was used to obtain the total pressure distribution across the annulus at the four W2 locations. Excellent agreement

was found between the four profiles, with a similar loss of total pressure associated with the boundary layers at each position. As will be seen, the velocity distribution was very similar across each annulus wall boundary layer, suggesting that the symmetrical area contraction through the intake was having much the same effect on both the inner and outer wall flows, prior to the boundary layer development along the parallel inlet length. In the central region of the flow, as expected, there was no loss of total pressure between the inlet plenum and each measurement location. Within experimental error, therefore, the circumferential uniformity of the total and static pressure confirmed that the flow was axisymmetric. Furthermore, the subsequent 5HP and LDA measurements, taken at one circumferential position, showed that the inlet flow had zero swirl.

As part of the rig commissioning, the data acquisition system was checked very carefully. Since the system was new, every part of the equipment and experimental procedure was examined thoroughly. For the 5HP technique in particular, it was necessary to ensure that the data was correct, which was achieved by back analysing calibration data. Also during this investigation, the LDA system was newly acquired, and, therefore, extreme care was taken to ensure that the data obtained was meaningful. The first LDA measurements were taken at the upstream location (W1), at the end of the parallel inlet duct, since the annulus wall boundary layers had developed under simple zero pressure gradient conditions. By comparing the mean and turbulent properties obtained at W1 (see Carrotte et al.^[27]) with well establish data on equilibrium turbulent boundary layers (e.g., Klebanoff^[84]), high confidence was obtained in the LDA system. Moreover, the thorough error analysis presented in Chapter 3 (Sect. 3.3.3), has shown the accuracy of the LDA data to be extremely good.

4.1.2 Axial Compressor Performance

In order to assess the operation of the single stage axial compressor, some performance measurements were made, which are presented in Figure 6. For a range of speeds and flows, the overall pressure rise generated by the compressor was of particular interest, but the temperature rise was also measured to allow the efficiency to be estimated. For a compressor, it is usual to obtain the performance characteristics at constant speed, while adjusting the throttle to vary the flow. However, because of the relative ease with which the operating speed could be set, data was obtained along constant throttle lines, at predetermined speeds, such that the constant speed characteristics could be extracted. In addition, the stall limit of the compressor was obtained at several speeds. In this case the throttle was gradually closed, and data was recorded up to the point at which stall was detected. As there was a possibility of breaking the compressor blades during a stall event, the stall line was not obtained at high speed.

The pressure rise was obtained by recording the static pressure sensed by several taps upstream and downstream of the compressor. Since the static pressure varied through the S-shaped duct, the average of the inner and outer wall static pressure in the parallel sections at inlet (W2) and exit (A8) were used to obtain the pressure rise (Δp). Since the annulus area was the same, the static pressure rise was approximately equal to the increase in total pressure across the compressor, and, therefore, Δp was used to obtain the compressor pressure ratio. Although this includes the loss of total pressure associated with the S-shaped duct, Figure 6 shows the approximate pressure ratio against the flow function ($m\sqrt{t}/Ap$), with operating characteristics obtained at several speeds, which are indicated as a proportion of the design speed ($N/\sqrt{t} = 160.7$). The maximum flow was obtained with the throttle fully open, and was therefore limited by the facility, and, at the other extreme, the minimum flow at a given speed was limited by compressor stall. In addition, the operating line shown in Figure 6 was used to set the flow during the tests with the compressor, which, at the design speed, gave a pressure ratio and flow close to the design values.

The temperature rise of the compressor was obtained by measuring the total temperature at mid-height only. With a thermocouple fixed in position, upstream (W2) and downstream of the compressor (A1), this was a very crude measure of the temperature rise (ΔT), and with only a small ΔT generated by the compressor, it was difficult to obtain ΔT accurately. In Figure 6, however, this has been used to calculate the loading coefficient ($c_p \Delta T / U_{blade}^2$), using the blade speed at mid-height, which has been plotted against the flow coefficient (V_a / U_{blade}), based on the mean velocity obtained from the measured mass flow. In addition, the pressure rise coefficient ($2\Delta p / \rho U_{blade}^2$) is shown. For a low speed compressor, both the pressure rise and loading coefficients are unique characteristics against flow coefficient, independent of speed, as is broadly the case for the present compressor. Along the operating line, therefore, the flow coefficient remained nearly constant (≈ 0.545), and the compressor operated with a loading coefficient of approximately 0.32 and a pressure rise coefficient of approximately 0.59. With the pressure rise data providing a good description of the overall compressor performance, and the temperature rise measurements giving a rough indication of the loading, it could be confirmed that the compressor was operating with the intended conditions into the stator, such that its exit flow was representative of a real compressor.

4.1.3 Operating Conditions

Without the compressor present, the rig was operated at a constant flow function of $m\sqrt{t}/Ap = 0.0058$. On a standard day ($p_\alpha = 101325.4 \text{ N/m}^2$, $t_\alpha = 288.15 \text{ K}$), this gives a mass flow (m) of 4.95 kg/s and a mean velocity within the constant area duct

($A = 0.142977 \text{ m}^2$) of 28.3 m/s. After correction to standard day conditions, this velocity was used to non-dimensionalise the data, and is referred to as U_{Mean} throughout. Along with this velocity scale, the passage height at annular S-shaped duct inlet (h_{in}) was used as the reference length scale. With $U_{\text{Mean}} = 28.3 \text{ m/s}$ and $h_{\text{in}} = 0.0711 \text{ m}$, the reference Reynolds number was 1.4×10^5 . All the data presented for the 2D axisymmetric flow, for both the 5HP and LDA measurements, were obtained with the rig operating at this condition.

When the compressor was present, it was mostly driven at its design speed, given by $N/\sqrt{t} = 160.7$. During each test this remained constant, and the compressor was throttled to operate with a flow function of $\dot{m}\sqrt{t}/Ap = 0.0102$, which also was held constant. Having obtained the compressor performance (Fig. 6), these conditions were chosen so that the compressor was operating near to its design point and, therefore, at peak efficiency. At this condition, the stator blades will operate without any regions of flow separation, and the wakes will be relatively thin. On a standard day, the rig operating conditions correspond to a mass flow of 8.71 kg/s and $U_{\text{Mean}} = 49.7 \text{ m/s}$, giving a reference Reynolds number of 2.4×10^5 , based on h_{in} . During this investigation, measurements with the compressor present were made mainly using the 5HP. However, LDA data was obtained immediately downstream of the compressor, but, in order to reduce the magnitude of the velocities being measured by the LDA system, the compressor was driven at 80% of its design speed (i.e., $N/\sqrt{t} = 128.56$). To ensure that the stator exit conditions were effectively the same, non-dimensionally, the flow was also reduced to a value of $\dot{m}\sqrt{t}/Ap = 0.0080$, this being on the same operating line. To prove that the stator performance was not affected by reducing the Reynolds number, 5HP measurements of the stator exit conditions were also obtained with the compressor operating at 50% speed (i.e., $N/\sqrt{t} = 80.35$) and at a flow function of $\dot{m}\sqrt{t}/Ap = 0.0050$. Even at this condition, no change in the non-dimensional exit conditions could be detected, and, although the blade chord Reynolds number was only about 1.0×10^5 (cf. 2.0×10^5 at design), the presence of rotating wakes emanating from the upstream rotor blades was sufficient to avoid the possibility of laminar separation from the stator blades.

4.2 Axisymmetric Flow Without the Compressor

Without the compressor, the flow in the annular S-shaped duct was found to be axisymmetric (see Sect. 4.1.1). Since the time-average properties were constant in the circumferential direction (i.e., $\partial/\partial\theta = 0$), the measurements were made at a single circumferential position, by traversing across the passage at several streamwise

locations. In addition, the flow was further simplified since, as will be seen, the circumferential component of velocity was very small throughout the duct. The results presented in this section describe, in detail, the complex behaviour of the 2D axisymmetric, zero swirl flow through the annular S-shaped duct.

4.2.1 Presentation of the Results

In this thesis, the majority of the results are presented in a common format. For any parameter, the data at each traverse location is shown on the same graph, with each line offset by a fixed amount. Mainly, the data has been plotted against fractional height (\bar{h}), where \bar{h} is referred to as 'Passage Height', although, in some cases, the fractional mass flow (ψ) has been used, and is referred to as 'Stream Function'. Each line is labelled according to the mid-height traverse location (x/L), and it should be noted that W2 ($x/L = -0.55$) was used for the 5HP measurements, whereas W1 ($x/L = -0.75$) was used for the LDA. In presenting the data for each parameter at each location, there is one line for the 5HP data, representing the average of six individual traverses, whereas two LDA profiles are shown, each taken during a different run. Consistently, throughout the text, the word 'location' is used to describe the streamwise location of interest, e.g., the location of a particular traverse line, whereas the word 'position' is used to describe the cross-passage position, e.g., the position along a traverse line.

In addition, the majority of the data presented has been non-dimensionalised using a reference velocity and length scale. These were taken at S-shaped duct inlet, and based on the mean inlet velocity (U_{Mean}) and the inlet passage height (h_{in}), but, since the area is constant, U_{Mean} is actually the mean velocity throughout the duct. Although the data has been non-dimensionalised in this way, in the text the variables are generally referred to in their dimensional form (i.e., U , \overline{uv} , etc.). In addition, the so called Reynolds stresses ($\overline{u_i u_j}$) are strictly kinematic Reynolds stresses, with the units of m^2/s^2 . Also, although pressures and stresses are often non-dimensionalised by ρU_{Mean}^2 , it should be noted that various coefficients (e.g., C_p and C_f) are based upon the dynamic pressure ($\frac{1}{2} \rho U_{Mean}^2$), which scales their value by a factor of two.

4.2.2 Mean Flow Quantities

To begin describing the flow behaviour of an annular S-shaped duct, quantities relating to the mean flow are presented in this section. Along with wall static pressure data, the mean flow was defined by both the 5HP and the LDA, and, in addition, various parameters have been determined which describe the overall behaviour of the flow.

4.2.2.1 Static Pressure Distribution

Since the development of the flow is affected significantly by the static pressure, Figure 7 shows its variation along the duct walls, and Figure 8 gives a more complete description by showing the cross-passage variation at each traverse location. This data is expressed in terms of a pressure coefficient (C_p), which is defined using the mass-weighted average total and static pressures at inlet to the duct ($x/L=0.0$). On extrapolating the 5HP data to the wall, it can be seen that these measurements are in good agreement with those obtained directly from the wall static pressure taps (Fig. 7).

Within the duct, the pressure field adjusts in order to turn the flow. At a given location, the static pressure gradient across the duct gives rise to the centripetal acceleration associated with the curved flow path. Thus, within the first bend the outer wall pressure is higher than the inner, but this situation is reversed within the second bend as the flow is returned to the axial direction. As a result of the turning, therefore, significant streamwise pressure gradients also occur within the duct. Along the inner wall, C_p initially falls and then rises from -0.34 to +0.22 along approximately 75% of the duct length, before finally decreasing. Consequently, the inner wall flow is subjected to a predominantly positive (i.e., adverse) gradient. In contrast, the pressure gradient along the outer wall is mostly negative (i.e., favourable), with C_p reducing from +0.20 to -0.28 along a similar length. As the flow passes through the constant area duct, the average static pressure level reduces steadily, consistent with a continual reduction in the total pressure.

Although the static pressure variation across the duct (Fig. 8) is smooth, it is interesting to note that, within the bends, the cross-stream gradient steadily increases from the concave to the convex side of the duct. This behaviour results from the fact that the streamline curvature of the flow does not vary linearly across the passage, and it will be seen in Section 4.2.2.3 that the potential velocity distribution derived using an effective curvature differs from that obtained using the static pressure.

4.2.2.2 Streamwise Velocity and Stream Function

Using the 5HP, three orthogonal velocity components were obtained at a number of positions throughout the duct, of which the streamwise component (U_ℓ) is of primary importance. Figure 9 shows the cross-passage variation of U_ℓ at each traverse location, and, to obtain a visual representation of the flow behaviour, velocity vectors in the $x-r$ plane have been plotted in Figure 10. Although the cross-stream component (V_ℓ) is small, the vectors have been obtained from both U_ℓ and V_ℓ , measured relative to the traverse, such that they show the true magnitude and direction of the flow at each point.

It is clear that the flow direction alters significantly as the flow passes around the first bend, and then returns to the axial direction within the second bend. In addition, the vector plot provides an overview of the large variation of velocity that occurs, although, of course, the magnitude can be obtained better from the U_ℓ profiles (Fig. 9).

Before describing the velocity variation within the duct, it is worth considering the inlet conditions in more detail. The velocity distribution at the end of the parallel annular inlet duct is given in Figure 9 ($x/L = -0.55$), where it can be seen that the velocity increases from zero at each wall up to a value greater than the spatial-average velocity ($\bar{U} \equiv U_{\text{Mean}}$) across the central portion of passage. Adjacent to each surface, the velocity varies rapidly across the turbulent boundary layers, which have grown along the walls of the inlet duct (~1m long) to occupy 24% of the passage height each. In the core region between the boundary layers, the velocity is constant ($\sim 1.07 \times U_{\text{Mean}}$) and, since the static pressure is constant across the inlet passage (Fig. 8), so is the total pressure. This value of total pressure must correspond to that in the inlet plenum (P_∞), whereas the mass-weighted average value (\tilde{P}) will be lower due to the pressure loss within the boundary layers. This loss of pressure ($\tilde{P} - P_\infty$) was measured to be -0.111 of the inlet dynamic pressure ($\frac{1}{2}\rho\bar{U}^2$) at the first traverse location, and the mass-weighted average static pressure (\tilde{p}), equal to the constant static pressure level, was $\alpha \frac{1}{2}\rho\bar{U}^2$ below \tilde{P} , where α was found to be 1.037 (Eq. 3.66). In addition, as described in Chapter 3 (Sect. 3.2.3), the integral properties of the boundary layers were obtained (Table 8) by integrating the velocity profile across each boundary layer, and, for Station 1, were found to be the same on both sides of the passage. With a Reynolds number $R_e = 3510$, based on U_{Mean} and momentum thickness (θ), the derived shape parameter ($H = 1.33$) and skin friction coefficient ($C_f = 0.00384$), obtained from the mean velocity profile using the log-law, are typical of equilibrium turbulent boundary layers developing in a zero pressure gradient.

For the S-shaped duct, the mean velocity variation can be considered separately for the boundary layers and the core region. In this latter region, the flow is both inviscid, because there are no significant viscous or Reynolds stress gradients present, and irrotational, because the total pressure is constant. Consequently, this flow can be described by the Euler equations, which, as shown in Appendix 2 (Sect. A2.1), means that the velocity in a curved flow will increase towards the centre of rotation. (Since the total pressure is constant, the velocity must increase as the static pressure reduces.) Within the first bend, therefore, the velocity in the core region increases towards the inner wall, whereas, in the second bend the velocity increases towards the outer wall. Interestingly, within the core region, there are significant velocity gradients across the passage at duct inlet ($x/L = 0.0$) and exit ($x/L = 1.0$), and these are consistent with the

Experimental Results

observed static pressure gradient. This implies that the flow is turning in the parallel sections just upstream and downstream of the S-shaped duct.

Within the annulus wall boundary layers, the behaviour of the velocity is more complex. As described by the Reynolds-averaged Navier-Stokes equations, the pressure gradients, the Reynolds stress gradients and, very close to the wall, the viscous stress gradients all influence the velocity distribution within the turbulent boundary layers. Although the pressure gradients are of primary significance, the Reynolds stress gradients have an important influence in the present investigation, and the distribution of the measured Reynolds stresses will be considered in more detail later (Sect. 4.2.3). Along the inner wall, after an initial acceleration, the strong adverse pressure gradient leads to a significant reduction in the streamwise velocity adjacent to the surface. Due to the action of the Reynolds shear stress, however, the velocity remains positive, and separation does not occur before the favourable pressure gradient in the latter part of the duct re-accelerates the flow. In contrast, along most of the outer wall, a strong favourable pressure gradient accelerates the flow, whilst adverse pressure gradients before and after this region have the effect of reducing the velocity adjacent to the surface. By the end of the duct, the final velocity profile ($x/L = 1.8$) shows that the boundary layers have increased in size to occupy 32% of the passage height each. More importantly, the velocity distribution on each side of the passage is very different, indicating that the Reynolds stresses have affected each boundary layer in a different way. In Section 4.2.4.5, it will be seen that these differences can be attributed to the behaviour of the Reynolds shear stress.

From the streamwise velocity distribution, it was possible to calculate the mass flow rate and its distribution throughout the duct. By integrating the U_ℓ profile according to Eq. 3.59, the mass flow ratio (ψ) at any point could be obtained by calculating the fraction of the total mass flow rate passing between the point and the inner wall. Since the passage is annular, a greater mass flow passes through the outer half of the duct (i.e., $\hbar > 0.5$), than the inner half, mainly because the area is larger ($\zeta = 0.472$ at $\hbar = 0.5$, or $\zeta = 0.5$ at $\hbar = 0.527$). In addition, however, since the velocity varies throughout the duct, and especially within the boundary layers, the relative position (in terms of \hbar) of a given ψ value changes at each location. In order to show the ψ variation, contours of constant ψ have been plotted in the $x-r$ plane (Fig. 11), which, in effect, represent a series of streamlines (or strictly stream-surfaces) within the flow. Since the underlying grid lines on this plot show the position of the measurements, which were obtained at the same \hbar values at each location, it can be seen that the streamlines deviate significantly from the constant \hbar -lines. It is apparent, therefore, that the effective curvature of the flow (represented by the streamlines) is less than the geometric curvature (represented by the

\hbar -lines). This is especially true along the inner wall, where the higher velocity over the first bend tends to move the streamlines toward the wall whereas the lower velocity in the latter part of the duct, associated with both the inviscid effect and the boundary layer growth, tends to move the streamlines away from the wall. Since the effective curvature of the flow determines the cross-stream pressure gradient, and therefore the streamwise pressure gradients, it is important to account properly for this effect when analysing the flow. Of course, like the experimental measurements, Navier-Stokes methods inherently include this effect. Unfortunately, however, Euler solvers miss out the effect of the growing boundary layer, although this can be partly offset through the use of a coupled integral boundary layer calculation, and methods based simply on the geometric curvature, like the simple method used to design the duct, described in Chapter 2 (Sect. 2.1.3), will overestimate the pressure gradients.

In order to show more clearly the way in which the boundary layer velocity changes from one location to the next, a streamwise velocity ratio has been calculated. As described in Chapter 3 (Sect. 3.2.1.1), it is possible to determine an exact potential velocity (U_p) distribution, at each location, using the 5HP measured velocities and static pressure (Eq. 3.47), which can be used to non-dimensionalise U_t . As such, the velocity ratio (U_t/U_p) is always unity in the central core region, and reduces across the boundary layers to reach zero at the walls. Figure 12 shows the cross-passage variation of U_t/U_p at each traverse location, along with an approximate indication of where the edge of each boundary layer lies. The reduction in velocity, and the increase in boundary layer thickness, due to the inner wall adverse pressure gradient is now clearly apparent, with the velocity ratio at the first measurement position falling to a value of 0.4 at $x/L=0.75$. Downstream of this position, however, the velocity ratio adjacent to the inner wall recovers to a value similar to that at inlet, although a lower value is present over a greater proportion of the flow. At the measurement position closest to the outer wall, the velocity ratio initial decreases, then steadily increases to a value of 0.8 and, finally, is reduced by the downstream adverse pressure gradient. The same data has also been plotted against ψ (Fig. 13), so that the change in velocity along a streamline (at a constant ψ) can be seen. Even though the boundary layer thickness varies significantly, the mass flow rate in each boundary layer increases steadily along the length of the duct; although its rate of increase reduces over the convex walls and increases over the concave. In addition, it is now apparent that there are several regions, adjacent to the walls in particular, where the velocity ratio increases along a streamline, which implies that the total pressure must be increasing. Thus, although in general the total pressure decreases along streamlines within a shear layer, the total pressure in the present flow can increase, and it will be seen in Section 4.2.4.3 that the Reynolds shear stress distribution is responsible for this behaviour.

4.2.2.3 Comparison of 5HP and LDA Velocities

In this section, all the mean velocity components are presented, both to define the overall mean flow behaviour and, also, to allow a comparison to be made between the 5HP and LDA measurement techniques. In Figure 14, the streamwise velocity component (U_ℓ) measured by the LDA is compared to the 5HP data, previously discussed. It can be seen that, in general, there is good agreement between the LDA data, for which there were two individual traverses made at each location, and the 5HP data. However, there are some differences apparent in the data, especially along the outer wall. Although it might be possible to explain some of the differences in terms of measurement error, it has been shown in Chapter 3 (Sect. 3.3) that the accuracy of both techniques is good, and, indeed, it is clear from the two separate LDA profiles, taken at each location, that the measurements are repeatable with a high degree of precision. Since the observed discrepancies occur mainly along the outer wall, at several traverse locations that otherwise show excellent agreement across the remainder of the passage, it is suggested that the differences arise due to the fact that the measurements were taken at various circumferential locations, where local differences in the geometric shape of the S-shaped duct may have altered the flow behaviour. Due to nature of the manufacture, the inner and outer wall shapes were the same everywhere around the circumference, but it is possible that the laser windows in the outer casing may not have conformed exactly to the surface shape. Although such differences were very small and, at the time of manufacture, were considered to be acceptable, it may be possible that these affected the flow adjacent to the LDA windows in comparison to that measured by the 5HP.

Figure 15 shows the cross-passage variation of the measured cross-stream velocity (V_ℓ) at each traverse location, where it can be seen that it varies significantly throughout the duct. Since velocity was measured along traverse lines approximately perpendicular to the mean flow direction, the magnitude of V_ℓ is always less than $0.1 \times U_{\text{Mean}}$. Whilst at most positions V_ℓ is positive, negative values were obtained at duct inlet ($x/L = 0.0$) and exit ($x/L = 1.0$) due to the fact the flow was moving radially inwards relative to these radial traverse lines, which correspond to the geometric start and end of the duct. Since V_ℓ is dependent on the orientation of the traverse, it is sometimes better to consider the radial velocity component (V_r), which is defined in a consistent way throughout the duct. The cross-passage variation of V_r at each traverse location is shown in Figure 17, where the magnitude of V_r can be seen to increase within the first part of the duct, reaching a maximum negative value of $\sim 0.4 \times U_{\text{Mean}}$ at $x/L = 0.5$, before reducing and returning to zero downstream of duct exit.

There are several factors which contribute to the observed differences between the 5HP and LDA data, and these need to be described individually. During the experiment, it was found that the 5HP and LDA traverse lines were at slightly different angles. At worst the difference was about one degree, but this does mean that the measured V_ℓ values (Fig. 15) are not entirely consistent. As mentioned, this error can be removed by comparing V_r values, which were calculated using the actual traverse angles. However, further differences can be seen in the V_r data (Fig. 17). Ignoring for a moment the data at $x/L = 0.375$ (B1), $x/L = 0.5$ (A4) and $x/L = 0.625$ (B2), it can be seen that the 5HP data is consistently higher than the LDA (by about $0.02\text{-}0.04 \times U_{Mean}$). This difference is believed to be the result of a systematic error in the 5HP measurement technique, whereby it is not possible to ensure that the probe angles in the rig relate exactly to those used during calibration. For the most part, therefore, the V_ℓ values measured by the LDA are more accurate, as reflected in the fact that near zero values were obtained at the upstream and downstream locations. However, at the three locations mentioned (B1, A4 & B2) the LDA data appears to be in error, but, unfortunately, it has not been possible to find a rational explanation. Allowing for the consistent 5HP error, the LDA V_r values at these locations are $\sim 0.04 \times U_{Mean}$ too low. One possible explanation for an error in V_ℓ , as measured by the LDA, lies in the optical arrangement of the LDA probes required to be used on the rig. Orthogonal velocity components are obtained by transforming the three measured velocities, but, in the case of V_ℓ , the arrangement dictates that V_ℓ is obtained as the difference between two relatively large values. Thus, in comparison to the other components, V_ℓ is more sensitive to any errors in the coefficients of the transformation matrix. However, these coefficients were determined in the same way at every location, by measuring the laser beam angles, and it seems unlikely that this would lead to the observed errors.

As an additional check, the 5HP measured flow vectors (Fig. 10) were overlaid onto the flow streamlines (Fig. 11) at a large scale. At all positions, the vectors were aligned consistently with the streamlines (allowing for the slight systematic error in the 5HP data), which, since $V_n = 0$ in an s-n co-ordinate system following a streamline, should be the case. Thus, as far as V_ℓ and V_r are concerned, the 5HP data appears to be consistent throughout the duct, despite the small systematic error. In contrast, the LDA appears to be more accurate, but, for an unexplained reason, the LDA data seems to be inconsistent at three locations. Although it has not been possible to understand this fully, it might be possible that the flow behaviour differs slightly at each of the circumferential locations used for the LDA measurements.

For the present 2D axisymmetric flow, without the compressor, the circumferential velocity (W_ℓ) was measured and found to be zero. Figure 16 shows the cross-passage

variation of W_ℓ at each traverse location, obtained using the 5HP and LDA, where it can be seen that the LDA data is effectively zero everywhere. However, this is not true of the 5HP data, which appears to show a finite W_ℓ ($\sim 0.06 \times U_{\text{Mean}}$) throughout the duct. This is believed to be due to a systematic probe setting error, because if there had been swirl present at inlet to the S-shaped duct W_ℓ would have increased as the radius reduced, to conserve angular momentum. Like the error in V_ℓ previously mentioned, it is difficult to align the probe inside the rig such that it is consistent with its calibration, but, for W_ℓ , the error ($\sim 4^\circ$) appears to be much worse. It is fortunate, therefore, that the LDA data has been able to show that the flow has zero swirl, as the 5HP data alone may have led to some concerns over the symmetry of the inlet flow.

Whilst the potential velocity (U_p) could be derived directly from the 5HP data, an effective curvature (K_{eff}) was used to determine U_p (Eq. A2.15) for the LDA measurements, as described in Chapter 3 (Sect. 3.2.1.2). The actual values of K_{eff} and mid-height velocity (U_m) obtained from the analysis are given in Table 12, and effectively define a U_p distribution at each location. Although there is good overall agreement between this approximation and the exact 5HP U_p distribution (Fig. 18), especially in the core region, there are some differences in the regions of greatest curvature. Contrary to the assumption used to derive Eq. A2.15, this suggests that the flow at each streamwise location does not rotate about a single point, and that the streamline curvature varies in a more complex way. It has already been noted that the static pressure takes on a complex distribution, and, of course, this is due to the fact the streamline curvature determines the local cross-stream static pressure gradient. Within the convex boundary layers, therefore, the curvature tends to increase relative to the simple approximation, whereas the opposite is true within the concave boundary layers. Thus, the resulting static pressure distribution, ensures that the exact U_p values are always above the approximate distribution within the boundary layers. However, when the derived streamwise velocity ratios are compared (Fig. 19), it is apparent that these subtle differences have little effect, since there is excellent agreement between the various data. As such, the combination of both sets of results only serves to increase the reliability of the data, allowing the detailed behaviour of the mean flow to be observed.

4.2.2.4 Overall Parameters

In order to simplify the description of the flow behaviour, the values of several overall parameters have been calculated. In general, these were obtained by integrating across the passage, at each traverse location, to obtain a streamwise variation of the parameter. In all cases, the data has been plotted against axial location. For whole passage parameters, the mid-height axial location of the traverse line (x_m) has been taken, whilst

for boundary layer parameters, the intersection of the traverse line and the wall (x_i or x_o) has been used (as given in Table 2). In addition, the wall friction velocity (U_w) is discussed in this section, since, although it is not an integral boundary layer parameter, it provides an overall description of the state of the near-wall flow.

Using the 5HP data, mass-weighted average total (\tilde{P}) and static (\tilde{p}) pressures have been derived. By integrating the cross-passage distribution of total and static pressure (Eq. 3.62), at each traverse location, the streamwise variations of \tilde{P} and \tilde{p} were obtained. In Figure 20, this data has been referenced to the mass-weighted average static pressure at S-shaped duct inlet (\tilde{p}_{in}) and non-dimensionalised by the mass-weighted average dynamic pressure ($\tilde{P}_{in} - \tilde{p}_{in}$), consistent with the earlier static pressure coefficients (Figs. 7 & 8). Although there is a small amount of scatter, the total pressure coefficient can be seen to fall gradually along the length of the rig. Despite the strong adverse pressure gradients that occur, there is no apparent increase in the rate at which pressure is lost within the S-shaped duct, but, as will be confirmed later (Sect. 4.2.4.3), it does appear that the rate of reduction of \tilde{P} is slightly less in the downstream parallel duct. Between duct inlet and exit, the total pressure coefficient falls by about 0.022, which is very similar to, if not less than, the loss which occurs over a similar length of the parallel inlet duct. Note that, although this loss coefficient may seem to be very small, it will be seen in Section 4.2.4.3 that the LDA shear stress data can be used to derive a loss coefficient, and that the value obtained in this way is in very close agreement with the value obtained directly from the 5HP pressure measurements.

With regard to the static pressure coefficient, it can be seen that there are two dips in the streamwise distribution. These occur within each bend, and are superimposed on a steady reduction that occurs along the length of the rig. Given that the flow area remains approximately constant throughout (i.e., $\bar{U} \approx constant$), the mass-weighted average dynamic pressure ($\tilde{Q} = \alpha \frac{1}{2} \rho \bar{U}^2$) depends only on the kinetic energy flux coefficient (α), and, since $\tilde{Q} = \tilde{P} - \tilde{p}$, α must increase to give rise to the lower \tilde{p} values. Indeed, the streamwise variation of α (Fig. 21) has two pronounced peaks, the first at $x/L=0.125$ reaching ~ 1.07 and the second at $x/L=0.75$ reaching ~ 1.10 . Upstream of the S-shaped duct, at the end of the inlet length, the value of α is 1.037, and, despite the rapid changes that occur within the duct, the value of α recovers to a value of 1.046 soon after duct exit; only slightly higher than at inlet.

The kinetic energy flux coefficient is described in detail in Chapter 3 (Sect. 3.2.2.5), where the conventional definition (Eq. 3.66) was extended to take account of curved flow. For plane channel flow, the magnitude of α depends on the amount of distortion present in the velocity profile, with $\alpha > 1$ when the viscous effects in the boundary layers

generate a velocity variation across the passage. In a curved channel, however, even inviscid flow will produce $\alpha > 1$, as the velocity will adjust as the flow turns. Thus in a real curved flow, in which viscous effects also distort the velocity profile, the magnitude of α cannot be used to judge the severity of the distortion without first accounting for the inviscid effects. Using the measured data, therefore, the potential kinetic energy flux coefficient (α_p) was calculated (Eq. 3.68), and is shown in Figure 21; these values being obtained from the LDA U_p profiles based on K_{eff} . In comparison, it can be seen that α_p makes a significant contribution to the overall α value, reaching a peak of ~ 1.015 in each of the bends. As a means of judging the viscous effects, a new curved flow kinetic energy flux coefficient (α_c) was proposed (Eq. 3.73), which, with $\alpha_c = \alpha/\alpha_p$, has a value of 1.0 when the velocity is undistorted by viscous effects. In the present S-shaped duct flow, therefore, it is interesting to note that α_c also increases within each bend (Fig. 21). This shows that there is a significant distortion of the velocity profile, in particular within the second bend, which is attributable to the velocity changes occurring within the boundary layers as a result of streamwise pressure gradients and curvature effects. However, despite the large changes that occur within the S-shaped duct, the distortion of the velocity profile can decrease as well as increase, such that there is very little change overall.

In order to quantify the behaviour of the annulus wall turbulent boundary layers, the usual integral parameters have been calculated. Unlike the conventional definitions, however, for curved flow it is necessary to determine the displacement thickness (δ^*) and the momentum thickness (θ) with respect to the potential velocity (U_p), as described in detail in Chapter 3 (Sect. 3.2.3). At each traverse location, therefore, the streamwise velocity (U_t) obtained from both the 5HP and LDA was integrated from the wall to the edge of each boundary layer to give δ^* (Eq. 3.76) and θ (Eq. 3.80), and, in addition, the ratio of these (δ^*/θ) was calculated to give the shape parameter (H). For each boundary layer, the streamwise variation of these parameters is presented; δ^* (Fig. 22), θ (Fig. 23) and H (Fig. 24).

In Figure 22, it can be seen that δ^* behaves very differently along each wall. Starting from a value of $0.0338 \times h_{in}$ at the upstream location, δ^* initially reduces along the inner wall, before increasing rapidly in response to the adverse pressure gradient. Having reached a peak value of $\sim 0.1 \times h_{in}$, the change of sign of the pressure gradient appears to reduce the inner wall δ^* substantially over the latter part of the duct, before eventually settling down to a steady rate of increase in the parallel exit duct. In contrast, along the outer wall δ^* initially increases, then decreases over most of the length of the duct, before finally increasing. Although by $x/L = 1.4$ the inner and outer wall values are similar, it is interesting to note that the outer wall value is slightly lower than that of the

Experimental Results

inner. Also, it must be remembered that part of the boundary layer thickness increase arises because of the reduction in mean radius, and if δ^* was non-dimensionalised with respect to the local passage height (rather than h_{in}) the overall increase through the duct would appear to be less. In Figure 23, it can be seen that the variation of θ follows a similar trend to that of δ^* . In this case, θ enters the S-shaped duct with a value of $0.0254 \times h_{in}$, and reaches a maximum value of $\sim 0.06 \times h_{in}$ along the inner wall.

The state of a boundary layer can be judged by the value of the shape parameter (H), and the variation of H along both walls of the S-shaped duct can be seen in Figure 24. At the end of the parallel inlet duct, the inner and outer wall boundary layers are identical, and, with $H = 1.33$, are typical of zero pressure gradient turbulent boundary layers developed over a similar length. On entering the S-shaped duct, the inner wall boundary layer H shows a small reduction before the strong adverse pressure gradient causes a rapid increase, up to a maximum value of 1.66. Since the near-wall streamwise velocity remains positive throughout, it is no surprise that H remains much lower than the values associated with a separating turbulent boundary layer; i.e., values in excess of 2.2 (see Chapter 1, Sect. 1.3.2.2). Downstream of the S-shaped duct, it is remarkable that the value of H returns to the same level as at inlet. However, this in no way indicates that the downstream boundary layer is the same as at inlet, since, as already noted, the velocity profiles are very different and, as will be seen, the turbulence is substantially modified. Along the outer wall, the variation of H is exactly opposite to that of the inner. Following an initial increase, H falls to a minimum value of 1.22 before recovering. Although the pressure variation is essentially equal and opposite along each wall, there is a much smaller variation in the magnitude of H along the outer wall, and the fairly low maximum values reached suggest that it is much further away from separation than the inner wall.

On comparing the 5HP and LDA data, it can be seen that there is excellent agreement between the two independent LDA traverses at all locations, and that this is in good agreement with the 5HP data in most cases. Along the inner wall, however, the 5HP data suggests that δ^* and θ increase by a slightly smaller amount, such that both boundary layers have similar values at exit. Since, in effect, δ^* and θ are based on the streamwise velocity ratio, closer examination of its distribution (Fig. 19) shows that there are small differences in the inner wall profiles, which would give rise to the higher LDA values. Despite the δ^* and θ differences, however, it would appear (Fig. 24) that the 5HP and LDA shape parameters are in excellent agreement.

During the present investigation, wall shear stress was not measured directly. However, by assuming that the mean velocity close to the wall has a linear variation in log-linear

co-ordinates, it is possible to use the log-law to determine the wall friction velocity (U_τ), as described in Chapter 3 (Sect. 3.2.4). In fact, U_τ was determined from the 5HP data using the single point method (Sect. 3.2.4.2), and from LDA data using the slightly more sophisticated multi-point method (Sect. 3.2.4.3). For each wall, the axial variation of U_τ is shown in Figure 25. Along the inner wall, the initial acceleration increases U_τ , but the subsequent adverse pressure gradient causes U_τ to reduce. If separation was to occur, the wall shear stress would fall to zero, but, since U_τ reaches a minimum value of $0.022 \times U_{\text{Mean}}$, it is again clear that the boundary layer is a long way from separation. Over the latter part of the S-shaped duct, U_τ increases again as the favourable pressure re-accelerates the near-wall flow, and rapidly returns to a similar level to that at inlet. Along the outer wall, following an initial fall, U_τ increases in response to the strong favourable pressure gradient, before reducing again. Downstream of the duct, U_τ is again very similar to the inlet level, but has a slightly lower value than the inner wall. On comparing the 5HP and LDA data, there is good agreement throughout. However, as will be seen in Section 4.2.4.1, there is no log-law region present in the highly accelerated outer wall flow, and therefore it was more difficult to determine the true wall shear stress. Fortunately, as discussed in Section 4.2.4.3, knowledge of the shear stress distribution and the wall pressure gradient has enabled more realistic U_τ values to be determined, which, when used to non-dimensionalise the streamwise velocity, produce believable velocity distributions in log-law co-ordinates (see Sect. 4.2.4.1).

To obtain a skin friction coefficient (C_f), it is possible to use either U_{Mean} or the wall potential velocity (U_{p_w}) to non-dimensionalise the U_τ values. In Figure 26, therefore, the axial variation U_{p_w} is shown for both the 5HP and LDA data, which is taken from cross-passage distributions (Fig. 18). In addition, the results of a simple flow calculation are shown, in which a streamline curvature method (Rolls-Royce^[130]) was used to solve the Euler equations (as described in Section A2.1), in the annular S-shaped duct geometry which, through the use of a coupled integral boundary layer method, was modified to account for the boundary layer displacement thickness (δ^*). Although there appears to be reasonable agreement between the data and this simple prediction, which was much better than a purely inviscid calculation (not shown), it is evident that the simple prediction has not fully captured the reduction in the curvature and, hence, the pressure variation which occur within the duct. For example, along the inner wall, the actual pressure coefficient increases by 0.56, whereas a value of 0.69 is obtained from the inviscid calculation with coupled integral boundary layer. Worse still, a value of 0.79 was obtained from the Euler solution, for which the coefficient is based on U_{Mean} (even though the inlet inviscid velocity was equal to that in the core region, i.e., $-1.07 \times U_{\text{Mean}}$).

Finally, in order to provide a concise statement of the results, the overall parameter data obtained from the experiment has been interpreted. Using all the available information, the most likely smooth variation has been determined for each parameter. For the boundary layer thicknesses, this was biased towards the LDA data, but in such a way that the δ^*/θ ratio of the interpretation remained consistent with the actual H data. In addition, as already noted, the measured shear stress distribution was used to aid the interpretation of the U_t data. Although the interpretation has been shown on each of the parameter plots, it also has been tabulated (Tables 8, 13 & 14) and re-plotted. In Figure 27, δ^* and θ are shown together with δ , so that their relative magnitudes are apparent, and, in Figure 28, only δ^* and θ are shown in order to provide a clear comparison. To complete the integral parameters, H is shown in Figure 29.

The interpreted U_t data has been converted into skin friction coefficients, based on both U_{Mean} (Table 13) and U_{p_w} (Table 14), and plotted in various ways. The simple non-dimensionalisation of U_t using the reference velocity (U_{Mean}) gives the skin friction coefficient (C_f), which has been plotted in Figure 30, and provides an indication of the axial variation of the wall shear stress. However, since the velocity at the edge of the boundary layer is sometimes used as a reference velocity, the skin friction coefficient (C'_f) has been calculated based on the local value of U_{p_w} , which was obtained from the effective curvature potential velocity distribution (Table 12). For zero pressure gradient turbulent boundary layers, it is well known that the magnitude of C'_f depends on Reynolds number. For example, Schlichting^[135] gives $C'_f = 0.0256 R'_\theta^{-0.25}$, where R'_θ is a Reynolds number based on momentum thickness (θ) and the boundary layer edge velocity. For the present data, therefore, the local value of R'_θ was calculated using U_{p_w} , and in Figure 31 the variation of C'_f with R'_θ is shown along with the Schlichting relationship. At the end of the parallel inlet ($R'_\theta = 3760$), the C'_f value is in good agreement, but, as expected, within the S-shaped duct large differences are apparent. Nevertheless, the equilibrium relationship serves to highlight the large, and very different, excursions the two boundary layers take about this line. Much of the variation is brought about by the streamwise pressure gradients, which tend to reduce C'_f when adverse and increase it when favourable. For equilibrium turbulent boundary layers subject to pressure gradient, the Ludwieg-Tillmann (LT) relationship, cited by Rotta^[132], ($C'_f = 0.246 R'_\theta^{-0.268} 10^{-0.678H}$) attempts to incorporate the effect of pressure gradient by relating C'_f to the shape parameter (H). On comparing the C'_f values obtained from this relationship with the actual values (Fig. 32), it is clear that the LT formula provides the correct trend, but underestimates the size of the variation. The actual relationship between C'_f and H is shown in Figure 33, along with lines of constant R'_θ obtained from the LT formula, where it can be seen that the two quantities are broadly related; remembering that there is a variation of R'_θ in the data. However, for the second bend

in particular, it is clear that the actual behaviour is different from the LT formula, which is based on equilibrium boundary layers, and suggests that the present flow cannot be predicted from simple formulae. As the flow approaches separation, it is interesting to note that the actual data is tending toward zero C_f' at $H \approx 2.2$, but, at the worst point, is a long way from reaching this condition.

4.2.2.5 Wall Pressure Gradient and Curvature

In this section, the variation of pressure gradient and curvature are discussed, as is their influence on several overall parameters. The magnitude of the streamwise pressure gradient ($\partial p/\partial s$) was obtained by differencing the wall static pressures such that, on applying a degree of manual smoothing, the values shown in Table 9 were obtained. In addition, two commonly used non-dimensional pressure gradient parameters have been derived; $\beta (= (\delta^*/\tau_w)(\partial p/\partial s))$ and $\chi (= (v/\rho U_\infty^3)(\partial p/\partial s))$. The magnitude of the wall geometric curvature ($1/R$) is shown in Table 10. This was obtained as $\partial \phi / \partial s$ by differencing the wall angle (ϕ), and, in addition, has been non-dimensionalised by the boundary layer thickness (δ) to obtain the curvature parameter (δ/R).

In order to describe the variation of pressure gradient and curvature, Figure 34 shows β plotted against δ/R for each wall. Note that 'wall curvature' has been used, so that both convex surfaces have positive curvature, and both concave surfaces have negative curvature. This is identical to the geometric curvature along the outer wall, but along the inner wall is of opposite sign. Obviously, positive β implies an adverse pressure gradient. Along the inner wall, therefore, it can be seen that δ/R reaches a maximum of ~ 0.10 , at the point where β changes from positive to negative. Subsequently, β reaches a maximum of ~ -14 , but this occurs after the curvature has turned concave since, even though $\partial p/\partial s$ has already started to reduce, δ^* is still increasing and τ_w reducing in this region. In the concave region, δ/R reaches a maximum negative value of ~ -0.12 , before returning to zero whilst β is negative. Along the outer wall, $\delta/R \approx -0.08$ is reached after a short region of positive β , then, whilst $\beta < 0$, the curvature turns convex. Having reached a maximum of ~ -0.09 , another short region of positive β returns both parameters to zero again. Even though the magnitude of $\partial p/\partial s$ is similar along the outer wall, the magnitude of β is very much less than the inner wall over the entire length of the duct, mainly because δ^* and τ_w act to reduce β in the region of the favourable pressure gradient. According to the literature review, presented in Chapter 1 (Sect. 1.3), this data suggests that the boundary layers are being subjected to both 'strong' pressure gradient and 'strong' curvature, which not only change sign but vary rapidly in different ways along each wall.

Given the importance of pressure gradient and curvature, the variation of other parameters with respect to these can be examined. For example, Clauser^[37] found a virtually unique relationship between the 'Clauser' shape parameter (G) and β . In that work, however, the pressure gradient was carefully controlled so that equilibrium boundary layers were established, for which β remained constant and the mean velocity profile (non-dimensionalised by U_τ and plotted against y/Δ) was similar along the length of the flat plate. In order to compare the present data with that of Clauser, G has been calculated (Eq. 3.85), and is shown in Table 11 along with the shape parameter (H) and U_τ/U_{P_w} . On plotting G against β (Fig. 35), it is clear that the flow is not in equilibrium. As opposed to the unique relationship, the data displays a sort of hysteresis about the equilibrium line, with G lagging behind the changes in β . Since G depends on U_τ , the highest value of G (~18) occurs along the inner wall, due to the low wall shear stress, at the same point where β reaches a maximum (~14). Although each wall has its own G - β relationship, they both exhibit the same trend. When β is positive and increasing, G tends to increase, but as β starts to reduce, G does not change very much until β has become negative. While β is negative, G tends to decrease, and does not increase again until β becomes positive. Although both boundary layers deviate significantly from equilibrium through the S-shaped duct, the downstream conditions are similar to those at inlet.

It is interesting to speculate that this rapid recovery, like that of all the overall parameters, occurs by virtue of the flow undergoing a complete pressure gradient cycle. In contrast to a single bend, where only half a cycle will occur, the complete pressure gradient cycle 'forces' a return to the starting condition. In a single bend, however, the boundary layer will be perturbed, but then left to recover naturally. For example, Alving et al.^[2] and Smits et al.^[147] measured the recovery of the flow downstream of a single bend, and, in contrast to the present data, showed a relatively slow recovery of the mean velocity parameters. However, in contrast to the mean parameters, it will be seen later that the Reynolds stresses downstream of the S-shaped duct recover slowly, in agreement with the other investigations.

As well as β , G has been plotted against curvature (Fig. 36). Although there is no unique relationship, there is a clear correlation between the two parameters, with the lowest values of G occurring over the convex surfaces, and the highest over the concave. However, this merely reflects the fact that the curvature primarily gives rise to the streamwise pressure gradients, and, therefore, it is not possible to ascertain the extent to which the curvature is influencing the overall parameters. In reviewing the literature, however, it was seen that curvature alone could significantly influence the mean velocity (e.g., Meroney and Bradshaw^[106] and Ramaprian and Shivaprasad^[120]);

with convex curvature tending to reduce the wall shear stress and increase H , whereas concave curvature had the opposite effect.

To determine the affect of pressure gradient on the key overall parameters, the shape parameter (H) and the skin friction coefficient (C'_f) have been plotted against β . In Figure 37, although H increases along the inner wall while β is increasing, the possibility of boundary layer separation appears to be removed once β begins to reduces. Even though β is still positive, H does not increase any further, and, when the favourable pressure gradient exerts its influence, H reduces rapidly again. Similarly, Figure 38 shows that C'_f falls under the influence of the adverse pressure gradient, to a minimum value of ~ 0.001 , but ceases to fall any further once β reduces. At the point of separation ($C'_f = 0$), Townsend^[173] found that, even though β tends to infinity, the product $\beta C'_f$ reaches a limiting value of ~ 0.022 , and $H=2.28$. In the present case, the inner wall reaches a $\beta C'_f$ value of ~ 0.014 at station 7 ($x/L=0.625$), where C'_f is also at its minimum, and a maximum H value of 1.66 at station 8 ($x/L=0.75$), providing clear confirmation that the boundary layer is far from separation.

4.2.3 Turbulence Data

Using the 3-component LDA, it was possible to obtain a complete description of the time-average turbulence in the annular S-shaped duct flow. Of utmost importance are the Reynolds stresses, all of which were obtained at a series of positions across the duct at every measurement location, and, in addition, various structure parameters have been obtained. Finally, the higher order velocity correlations are presented.

4.2.3.1 Reynolds Stresses

Within the S-shaped duct, the Reynolds stresses significantly affect the development of the flow. In general, the spatial gradients of the Reynolds stresses ($\partial \bar{u}_i \bar{u}_j / \partial x_j$) appear in the momentum equations, representing the turbulent transport of U_i , and the relevant terms influence the rate of change of a particular mean velocity component within the flow field. For the axisymmetric flow with zero swirl, in particular, the $\bar{u}\bar{v}$ shear stress component is of primary interest, since its cross-stream gradient affects the streamwise velocity. Each Reynolds stress has been obtained from the LDA data using Eq. 3.30, and, as described in Chapter 3 (Sect. 3.1.3.3), has been corrected (Eq. 3.41) for the small error that arises from the finite processor resolution. In addition, the turbulent kinetic energy (k) has been obtained from the normal stresses (Eq. 3.42). In this section, each Reynolds stress is presented separately; $\bar{u}\bar{u}$ (Fig. 39), $\bar{v}\bar{v}$ (Fig. 40), $\bar{w}\bar{w}$ (Fig. 41), $\bar{u}\bar{v}$ (Fig. 42), $\bar{u}\bar{w}$ (Fig. 43), $\bar{v}\bar{w}$ (Fig. 44) and k (Fig. 45). Each figure is a combined plot

showing the cross-passage variation at each traverse location, and they have all been drawn to the same scale. Since the LDA data was taken during two separate runs, the data from each run is distinguished using hollow foreground symbols for one and solid background symbols for the other. In addition, alternate traverse locations have been plotted using a different symbol, so as to minimise confusion when the profiles become closely spaced.

Before examining the variation of the Reynolds stresses within the duct, it is worth considering the inlet conditions in more detail. At the end of the parallel annular inlet duct, the annulus wall turbulent boundary layers each occupy 24% of the passage, and are separated by a potential core region. At this location, the distribution of the Reynolds stresses can be seen in each of the figures ($x/L = -0.75$). Within the potential core region, the turbulence is of low intensity and isotropic. Although it cannot be determined from the figures, the magnitude of each normal stress is $\sim 0.00005 U_{\text{Mean}}^2$ (i.e., $0.04 \text{ m}^2/\text{s}^2$) giving a turbulence intensity of $0.007 U_{\text{Mean}}$, and, of course, k will be 1.5 times larger. As expected, all the shear stresses were zero in the core region. Within each boundary layer, the normal stresses and the \bar{uv} shear stress are in good agreement with zero pressure gradient turbulent boundary layer data (e.g., Klebanoff^[84], or the recent DNS data of Spalart^[156]). Of the normal stresses, \bar{uu} has the largest magnitude. From its peak value of $\sim 0.009 U_{\text{Mean}}^2$, which occurs very close to the wall, \bar{uu} reduces across the boundary layer until the core is reached. In contrast, \bar{vv} is the smallest of the normal stresses, with a peak value of $\sim 0.0025 U_{\text{Mean}}^2$. In the near-wall region, there is a detectable reduction in \bar{vv} , such that the peak occurs a small distance away from the wall. The third normal stress (\bar{ww}), in the circumferential direction, can be seen to lie between the other two. Like \bar{uu} , the peak value of \bar{ww} ($\sim 0.004 U_{\text{Mean}}^2$) occurs very close to the wall, but is of lower magnitude, and, although larger than \bar{vv} over most of the boundary layer, \bar{ww} has a similar magnitude to \bar{vv} towards the outer edge. Unlike the normal stresses, which are always positive, the \bar{uv} shear stress is negative through the inner wall boundary layer, where $\partial U / \partial n$ is positive. The magnitude of \bar{uv} increases, in a near linear way, from zero at the edge of the boundary layer up to a maximum value close to the wall. Like all the Reynolds stresses, \bar{uv} is actually zero at the wall, but, since the Reynolds number is reasonably high, the changes that occur through the viscous sublayer could not be measured; although the first data point next to the wall was often very close to the sublayer (see Figs. 74&75, described in Section 4.2.4.1, for the lowest n^+ values reached at each location). Of course, at the wall there is a finite shear stress ($v \partial U / \partial n$), due to viscosity, which is effectively equal to the \bar{uv} distribution extrapolated to the wall. At the upstream location, the \bar{uv} profile is in good agreement with the value of wall shear stress (i.e., $C_f/2 = 0.00192$) obtained from the mean velocity profile using the log-law.

Experimental Results

Since the flow is axisymmetric with zero swirl, two of the six Reynolds stresses are zero throughout the duct. Nevertheless, \bar{uv} and \bar{vw} were obtained from the measurements in exactly the same way as the other stresses, and the fact that they are zero gives a good indication of the data quality. As is inevitable, though, there is a small amount of scatter in these results, which is worst close to the walls where fewer samples were obtained (due to the reduced SNR). In general, however, the magnitude of the scatter is remarkably small.

Within the S-shaped duct, the Reynolds stress variation is complex. On examining the normal stresses, and half their sum (k), it can be seen that each component behaves in a similar way. Along the inner wall, there is an initial reduction in the magnitude of normal stresses across most of the outer part of the boundary layer, such that the stresses rise rapidly towards the wall. By $x/L=0.5$, a clear peak has formed in the normal stresses, with a visible reduction between the peak and the wall, and, in the region outside of the peak, the stresses are no longer changing in the streamwise direction. As the flow progresses downstream, however, the peak moves away from the wall, and at the same time broadens, filling a greater proportion of the boundary layer. At duct exit ($x/L=1.0$), the outer edge of the peak has blended into the outer part of the boundary layer, leading to a profile which increases steadily from the core region up to the peak. Downstream of the S-shaped duct, the original peak gradually fades away, spreading and reducing in size. Close to the wall, however, a new peak is visible, with the normal stresses increasing towards the wall, and this new peak spreads and reduces in magnitude along the parallel exit duct.

In comparison to the inner wall, it can be seen that the outer wall normal stress distributions across each boundary layer are different, at all but the upstream location. Initially, there is an increase in their magnitude, except near the wall, giving rise to a peak in the distribution. As the flow progress downstream, this peak moves further from the wall and decreases in magnitude, but, at the same time, a new peak forms adjacent to the wall. Within the latter part of the duct, the normal stresses in the outer part of the boundary layer reduce, whilst the near-wall peak, whose level remains relatively high, broadens and becomes ever more visible. Finally, downstream of the S-shaped duct, the region of increased normal stress adjacent to the wall gradually becomes less pronounced, but, at the last measurement location, a kink is still visible in the profiles.

The variation of the \bar{uv} shear stress through the S-shaped duct is most spectacular (Fig. 42). Along the inner wall, there is a dramatic reduction in \bar{uv} over most of the boundary layer, and by $x/L=0.25$ \bar{uv} has virtually disappeared. This is directly

Experimental Results

attributable to the convex curvature, and is discussed in more detail in Chapter 6 (Sect. 6.2.3). Although \bar{uv} must reduce to zero at the wall, the total shear stress (τ) attains a finite value (i.e., $\tau_w = \mu \partial U / \partial n$) and, in addition, the cross-stream shear stress gradient equals the streamwise pressure gradient (i.e., at the wall $\partial \tau / \partial n = \partial p / \partial s$). Since the Reynolds number is reasonable high, however, the extent of the viscous sublayer is very small (~0.2-0.6 mm, depending on U_t) and, therefore, with $-\tau/p$ equal to \bar{uv} over most of the boundary layer, the measured \bar{uv} profile will appear to extend to the wall shear stress. At duct inlet, therefore, where the flow is subjected to a favourable pressure gradient, the shear stress must increase towards the wall, and reach a higher value than at the upstream location. Thus, although the magnitude of \bar{uv} has reduced in the outer layer, the shear stress increases rapidly towards the wall, over a short distance (which is not visible in the data at $x/L=0.02$, but does become apparent further downstream). By $x/L=0.25$, the streamwise pressure gradient has become adverse, and the wall shear stress has started to reduce, such that the shear stress must now peak away from the wall. Although the reduction on the wall side of the peak is not visible in the data, as it is still too close to the wall, the magnitude of \bar{uv} can be seen clearly to increase from the low level in the outer layer up to the peak. The deceleration of the flow adjacent to the wall, as a result of the adverse pressure gradient, leads to a continual reduction in the near-wall velocity and, therefore, the wall shear stress. The negative $\partial \bar{uv} / \partial n$ gradient between the wall and the peak (negative) \bar{uv} , however, offsets the positive pressure gradient and reduces the deceleration in this region, thereby delaying separation. On the other side of the peak, the positive $\partial \bar{uv} / \partial n$ gradient tends to increase the deceleration rate, and, as will be seen, leads to a region of increased strain rate in the mean velocity which is responsible for the outward movement of the \bar{uv} peak. Eventually, therefore, the peak in the \bar{uv} becomes clearly visible, and, in addition, can be seen to broaden as it moves away from the wall. Even though the curvature in the latter half of the duct is concave, there is very little change in the outer layer \bar{uv} until the outer edge of the peak has had an affect. By $x/L=1.0$, though, most of the outer part of the boundary layer has been affected by the outward moving peak, giving rise to a \bar{uv} distribution that increases, from the core region up to the top of the peak, without a visible kink in the profile. At the same time, the streamwise pressure gradient becomes favourable, so that the shear stress must now increase towards the wall, reaching a new maximum level. The formation of this new peak, along with the decaying remnants of the original peak, can be seen at $x/L=1.4$, but by the last measurement location these have decayed to an almost constant \bar{uv} level over the inner 15% of the passage.

Along the outer wall, the \bar{uv} shear stress variation is also interesting. As with the normal stresses, there is a marked difference in the \bar{uv} distribution when comparing the

inner and outer wall boundary layers at all but the upstream location. In contrast to the inner wall, there is an initial large increase in \bar{uv} over most of the boundary layer, which is attributable to the concave curvature. Close to the wall, however, the adverse pressure gradient reduces the near-wall velocity and hence the wall shear stress. By $x/L=0.125$, where the pressure gradient is changing sign, there is a clearly defined peak in the distribution, and the negative $\partial\bar{uv}/\partial n$ gradient between the wall and the peak tends to accelerate the flow, whereas the positive gradient across the rest of the boundary layer decelerates the flow. The resultant changes to the strain rate of the mean velocity, again leads to an outward movement and broadening of the peak. At the same time, the strong favourable pressure gradient increases the near-wall velocity, and, therefore, the shear stress distribution must increase towards the wall to balance the pressure gradient and reach the increased wall shear stress. Although the development of this second peak adjacent to the wall is not at first visible in the data, it can clearly be seen by $x/L=0.875$. By this point, however, the convex curvature has reduced \bar{uv} substantially over the outer part of the boundary layer, leading to the almost complete destruction of the shear stress and the disappearance of the original peak. Over the last part of the duct, the pressure gradient again turns adverse, and the reduction in the wall shear stress means that the peak moves away from the wall. Downstream of the S-shaped duct, the peak is clearly visible as a small region of the elevated shear stress, which moves slowly outward while reducing in magnitude. Over the rest of the boundary layer, \bar{uv} remains relatively low, with very little change in the streamwise direction.

Within the central core region, it was impossible to detect any variation in the measured Reynolds stresses. However, by examining the Reynolds stress transport equations, it is clear that the normal stresses must reduce in magnitude, since dissipation is the only non-zero term, and, as described in more detail in Chapter 6 (Sect. 6.2.3.3), streamline curvature will give rise to finite Reynolds stress production, which alters the rate of decay of the normal stresses (differently in each component) and leads to finite \bar{uv} shear stress. Indeed, the CFD prediction, described in Chapter 5 (Sect. 5.3), using a Reynolds stress transport equation turbulence model, was able to show the variation in each component (Fig. 144), but, given the low level of turbulence in the inlet flow, the magnitude of these changes is very small, and well below the precision of LDA technique.

4.2.3.2 Structure Parameters

To examine more thoroughly the nature of the turbulent flow in an annular S-shaped duct, several additional parameters have been derived from the Reynolds stress data. By

obtaining the ratio of one Reynolds stress relative to another, it is possible to determine more easily if the structure of the turbulence is modified within the duct. As well as assessing the size of \bar{uv} in relation to the normal stresses, it is possible to determine the relative contribution of each normal stress to the turbulent kinetic energy, and to see whether any of these structure parameters are modified by the rapidly varying pressure gradient and curvature.

One parameter commonly used to describe turbulent flow is the shear stress correlation coefficient (R_{uv}), defined in Section 3.1.3.4 (Eq. 3.45). In Figure 46, it can be seen that the magnitude of R_{uv} is approximately constant (~0.45) across the boundary layers at the end of the parallel inlet duct, but within the S-shaped duct there is a significant variation. Along the inner wall, the convex curvature causes R_{uv} to reduce to almost zero by $x/L = 0.125$, but, unlike \bar{uv} itself, there is a rapid recovery to a near constant value across the boundary layer. This occurs in a wave like manner, starting near the wall and moving outwards, and is complete by $x/L = 0.875$. In this concave curvature region, the magnitude of R_{uv} is slightly higher than the inlet value (~0.55). Close to the wall, however, there is a fall-off in the magnitude, suggesting that \bar{uv} falls more rapidly than the normal stresses in this adverse pressure gradient dominated region. Downstream of the S-shaped duct, the magnitude and distribution of R_{uv} at the last measurement location appears to be very similar to that at inlet. Along the outer wall, R_{uv} remains constant through the concave region, except for a slight reduction close to the wall, with its magnitude slightly above the upstream value. Through the convex region, however, the magnitude of R_{uv} falls dramatically, reaching a minimum at $x/L = 1.0$. In a similar way to the inner wall, there is a wave like recovery downstream of the S-shaped duct, but, by the last measurement location, it is evident that R_{uv} is still below the upstream value across most of the boundary layer. In the core region, of course, R_{uv} is zero, but, due to very low normal stresses, the actual data tends to be a little scattered.

Several ratios of the various Reynolds stress components have also been plotted. The ratio \bar{vv}/\bar{uu} (Fig. 47) is fairly constant (~0.35) across the turbulent boundary layers at the end of the parallel inlet length, except that as the wall is approached \bar{vv} reduces before \bar{uu} such that the ratio decreases, and in the core region \bar{vv}/\bar{uu} should be 1.0 since the turbulence is isotropic. Within the S-shaped duct, the distribution of \bar{vv}/\bar{uu} remains similar at each measurement location; although it is apparent that, within the boundary layers, the magnitude of the ratio changes along the length of the duct, and in a different way for each boundary layer. Over the first half of the duct, for example, the inner wall value remains fairly constant, whilst there is a slight increase along the outer wall, up to a value of ~0.55 at $x/L = 0.375$. In the latter half of the duct, however, as

Experimental Results

well as a change in the magnitude of $\overline{vv}/\overline{uu}$, there is also a slight change in the distribution across the boundary layers. By duct exit ($x/L = 1.0$), the inner wall ratio has increased, by varying amounts at different positions across the boundary layer, whereas the outer wall has returned to its initial value and distribution. Downstream, the inner wall boundary layer slowly returns to its upstream state, but this does not appear to be complete by the last measurement location.

When the \overline{uv} shear stress is involved, there is much larger variation in the magnitude of the Reynolds stress ratios. Both $\overline{uv}/\overline{uu}$ (Fig. 48) and $\overline{uv}/\overline{vv}$ (Fig. 49) vary significantly throughout the S-shaped duct, with the data suggesting that \overline{uv} changes much more dramatically than either \overline{uu} or \overline{vv} . At the end of the parallel inlet section, both these ratios are approximately constant across the inner and outer wall boundary layers, but, of course, their magnitudes are very different. Much like R_{uv} , the ratios are reduced over the convex inner wall surface, due to the low \overline{uv} , which then increase in the latter part of the duct, in a wave like manner, to reach a near-constant distributions by duct exit. Along the outer wall, there is some increase in the concave region, but, again, the most significant change occurs over convex surface.

Since they are the most commonly used structure parameters, the ratio of each Reynolds stress with the turbulent kinetic energy has been obtained. In equilibrium turbulent boundary layers, it is well established (e.g., Bradshaw^[16]) that the structure parameters attain near constant magnitude, and this fact provides a useful means of determining the Reynolds stresses from the turbulent kinetic energy. However, within complex flows in which there are rapidly varying pressure gradients and strong curvature, it is apparent that the structure parameters do not remain constant. As expected from the preceding data, \overline{uv}/k (Fig. 50) undergoes the most significant changes. Starting with a value of ~ 0.3 , \overline{uv}/k initially reduces along the inner wall, falling below ~ 0.1 across most of the boundary layer by $x/L = 0.25$, whereas there is a slight increase to ~ 0.4 along the outer wall. Further downstream along the inner wall, \overline{uv}/k quickly returns to ~ 0.3 , this recovery initiating close to the wall and then moving out into the boundary layer, although, at duct exit, the value close to the wall appears to fall below the constant value across the rest of the boundary layer. Along the outer wall, in the latter part of the duct, \overline{uv}/k reduces substantially, and remains suppressed at the last measurement location.

In contrast, the structure of the normal stresses remains fairly consistent throughout the duct. Since \overline{uu}/k (Fig. 51), \overline{vv}/k (Fig. 52) and \overline{ww}/k (Fig. 53) describe the distribution of energy amongst the individual normal stress components, an increase (or decrease) in one component must be accompanied by a corresponding decrease (or increase) in the other two. In broad terms, \overline{uu} remains approximately equal to k ,

whereas the other two components together equal k . In more detail, there are subtle changes taking place in the energy distribution, between different components in different regions. For example, whereas in general \overline{vv}/k tends to reduce adjacent to the wall, and \overline{uu}/k increase, there is an apparent reduction, or even reversal, of this trend in the adverse pressure gradient regions. Further, in the outer parts of the boundary layers, \overline{vv}/k remains relatively constant whilst there appears to be changes taking place in the other two components, with increases in \overline{ww}/k occurring at the same place as reductions in \overline{uu}/k , and vice versa. In the core region, of course, \overline{uv}/k should be zero and all three normal stress structure parameters should be ~ 0.667 , since the turbulence is isotropic. However, due to the low value of k in this region, the data is more scattered than across the boundary layers.

Finally, the Reynolds stress anisotropy (Π) has been obtained (Eq. 3.44), and is plotted in Figure 54. Although Π is dependant on \overline{uv} , and consequently reduces in the inner wall convex boundary layer, it is interesting to note that, in contrast to all the other parameters involving \overline{uv} , Π does not reduce in the outer wall convex region. Whereas the suppressed turbulence in the first convex bend becomes virtually isotropic, the increase in anisotropy in the outer wall concave bend appears to affect Π in the subsequent convex bend. Similarly, along the inner wall, the anisotropy increases downstream of the convex bend, but, in contrast to the outer wall, the concave bend does not lead to enhanced levels of anisotropy. At the last measurement location, the anisotropy in both boundary layers appears to be similar to the upstream flow.

4.2.3.3 Higher Order Velocity Correlations

Within the S-shaped duct, the variation of the higher order velocity correlations are of interest. In general, the spatial gradients of the triple velocity correlations ($\partial \overline{u_i u_j u_k} / \partial x_k$) appear in the Reynolds stress transport equations, representing the turbulent transport of $\overline{u_i u_j}$, and the relevant terms influence the rate of change of a particular Reynolds stress component within the flow field. The ten independent triple velocity correlations have been obtained from the LDA data using Eq. 3.31, and the variation of each is presented separately; \overline{uuu} (Fig. 55), \overline{uuv} (Fig. 56), \overline{uuw} (Fig. 57), \overline{uvv} (Fig. 58), \overline{uvw} (Fig. 59), \overline{uww} (Fig. 60), \overline{vvv} (Fig. 61), \overline{vww} (Fig. 62), \overline{vww} (Fig. 63), \overline{www} (Fig. 64). For axisymmetric flow with zero swirl, the terms involving an odd number of w 's are expected to be zero, but, nonetheless, have been included. In addition, the non-zero triple velocity correlations relating to the transport of turbulent kinetic energy have been obtained (Eq. 3.46), and are presented; $\overline{q^2 u}$ (Fig. 65), $\overline{q^2 v}$ (Fig. 66). One further parameter, referred to as the turbulent kinetic energy transport velocity (V_q), has also been obtained (Fig. 67) by dividing $\overline{q^2 v}$ by $\overline{q^2}$ ($= 2k$). It was not

possible to draw a best fit line through the data (other than by hand), and the need to show each triple velocity correlation on the same scale has meant that the ones with a large variation are slightly confusing at first. Nevertheless, with some effort, it is possible to extract relevant information from the data, and although any one measurement may be imprecise, due to the statistical error associated with extracting triple moments from a finite number of data, discussed in Chapter 3 (Sect. 3.3.3.3), the accuracy of the profiles is reasonable.

For axisymmetric flow with zero swirl, \overline{uuw} (Fig. 57), \overline{uvw} (Fig. 59), \overline{vww} (Fig. 62) and \overline{www} (Fig. 64) are expected to be zero. As such, these results provide a clear indication of the associated scatter, which is worst for \overline{www} . Furthermore, the amount of scatter tends to increase towards the wall, due to the lower number of samples obtained in this region (as a result of the reduced SNR), and it is also clear that the scatter becomes worse in the concave regions. This is because of the longer time scale associated with the large scale motion present in the concave boundary layers, which requires data to be taken over a longer time period to increase the number of statistically independent samples.

Within a turbulent flow, turbulent transport has a small but significant influence on the magnitude of the Reynolds stresses. As with the turbulent transport of momentum, it is possible to assume that turbulent transport can be modelled as a diffusive process, i.e., proportional to the spatial gradients of the quantity in question. For Reynolds stress transport, then, the triple velocity correlations can be assumed to be proportional to spatial gradients of the Reynolds stresses, with an appropriate diffusion coefficient. For a boundary layer, therefore, where the Reynolds stresses increase towards the wall, Reynolds stress turbulent transport would be away from the wall, down the gradients, thereby tending to reduce the peaks and increase the Reynolds stresses towards the outer edge of the boundary layer. As a diffusive process, therefore, the triple velocity correlations would tend to reach a peak mid-way across the boundary layer, such that their cross-stream gradient changes sign across the boundary layer. At the end of the parallel inlet duct, in particular, all the non-zero correlations at the first measurement location are distributed in this way, simply because the turbulent diffusion concept is reasonable in slowly varying (equilibrium) turbulent boundary layers.

Without describing every detail, it is worth making some pertinent observations about the behaviour of the triple velocity correlations within the S-shaped duct. As described above, the magnitude of a particular correlation can be related to the Reynolds stress gradients, but, when considering the effect of the correlations, it is the spatial gradients of triple velocity correlations that relate to the loss or gain of a particular Reynolds

stress. Moreover, although there are some fairly significant streamwise gradients present, it is the triple velocity correlation cross-stream gradients that are responsible for most of the Reynolds stress turbulent transport. Over the outer part of the boundary layer, for example, the observed cross-stream gradients (regardless of the actual sign) tend to increase the magnitude of the Reynolds stresses in the streamwise direction, providing the mechanism for boundary layer growth. Of particular interest are \overline{uvv} (Fig. 56), \overline{vvv} (Fig. 61), \overline{vww} (Fig. 63), and their sum $\overline{q^2v}$ (Fig. 66), whose cross-stream gradients are responsible for the turbulent transport of the normal stresses (\overline{uu} , \overline{vv} , \overline{ww}) and $\overline{q^2}$, respectively, and \overline{uvw} (Fig. 58), whose cross-stream gradient is responsible for \overline{uv} turbulent transport. In all these cases, it can be seen that the behaviour of the triple correlations is similar, and that there are several distinctive features occurring within the measured profiles. For example, there are large differences between the convex and concave regions, and very large variations associated with the inner wall adverse pressure gradient region. Curvature affects the triple velocity correlations in much the same way as the Reynolds stresses, with a significant reduction occurring in the convex regions and much higher values within the concave regions. In the convex boundary layers, therefore, this means that there is very little outward transport of the Reynolds stresses, such that boundary layer growth is suppressed, whereas in the concave regions turbulent transport is increased. Along the inner wall, the large variation in the triple correlation profiles is associated with the appearance of a peak in the Reynolds stress profiles. It was seen earlier that this peak forms very close to the wall, at the beginning of the adverse pressure gradient region, and moves further from the wall downstream. The triple correlations show that the Reynolds stresses are increased at the outer edge of the elevated region, whilst removing energy from the peak itself, and, therefore, turbulent transport aids the outward propagation of the peak. Adjacent to the wall, it can be seen that the triple correlations have a cross-stream gradient of the same sign as the outer region, indicating that turbulent transport also tends to increases the magnitude of the Reynolds stresses close to the wall. In the adverse pressure gradient region, in particular, this inward turbulent transport helps to prevent separation by supplying energy to the near-wall flow.

For completeness, the skewness (S) and flatness (F) of the turbulent velocity signals have been obtained. Like the variance of the fluctuating velocity, which is equivalent to the normal stress, S (Eq. 3.33) and F (Eq. 3.34) describe the shape of the probability density function (PDF) of the signal, and are based on the normal triple and quadruple velocity correlations, non-dimensionalised by an appropriate function of the variance. For each component, the skewness has been plotted in the usual way; S_u (Fig. 68), S_v (Fig. 69), S_w (Fig. 70), and, since $F=3$ for a normally distributed signal, $3/F$ was used to present the flatness data; $3/F_u$ (Fig. 71), $3/F_v$ (Fig. 72), $3/F_w$ (Fig. 73). In an

axisymmetric turbulent boundary layer with zero swirl, the u and v components will be skewed, whilst $S_w=0$. For example, S_u is predominantly negative, which reflects the fact that the negative tail of the PDF is larger than the positive tail. For a particular signal, this indicates that some of the slower velocities have a relatively large perturbation from the mean, since the slower velocities come from a region of higher turbulence, whereas the perturbation of the faster velocities is much less. In addition, the sign of S_v indicates that the cross-stream velocity away from the wall has a larger perturbation than towards the wall. When these two distributions are correlated, it is the slower streamwise velocities moving away from the wall that give rise to the \bar{uv} shear stress. Within the S-shaped duct, the skewness profiles vary significantly. For example, in the inner wall adverse pressure gradient region there is a local increase in S_u , which follows the outward moving edge of the Reynolds stress peak, and the appearance of positive skewness where there is inward turbulent transport. Furthermore, in comparison to S_u , S_v is affected much more by curvature, with lower skewness values in the convex regions compared to the concave. With regard to the flatness data, it can be seen that $3/F$ is approximately equal to 1.0 over the inner part of both boundary layers at all locations, and in the core region, but reduces over the outer part of the boundary layer. At the interface between the turbulent boundary layer and the free stream, the measured velocity intermittently changes between that of the free stream and the lower values associated with bursts of turbulent activity being transported towards the edge of the boundary layer. This intermittency gives rise to a very flat PDF, with a much broader spread of velocities than in the inner region, giving rise to high F and therefore lower values of $3/F$, which can be thought of as a measure of the intermittency. Although there is very little change in the $3/F$ profiles throughout the duct, $3/F_u$ does appear to be affected (like S_u) at the outer edge of the elevated Reynolds stress region, formed as a result of the adverse pressure gradient.

4.2.4 Derived Data

From the results presented so far, some additional data has been derived to provide further insight into the behaviour of the flow. Of particular interest are the streamwise velocity and \bar{uv} shear stress, which are presented in log-law co-ordinates. In addition, the mean strain rates have been derived from the mean velocities, and also the cross-stream shear stress gradient has been obtained from careful interpretation of the measured data. Most importantly, it has been possible to derive the total pressure variation from this shear stress gradient, which is shown to be in excellent agreement with the directly measured 5HP data. By combining the mean strain rates and Reynolds stresses, the turbulent kinetic energy production rate can be derived, and related to the

loss of mean flow energy. Finally, the cross-stream shear stress gradient is compared to the streamwise pressure gradient, which together affect the streamwise acceleration of the flow and, consequently, the primary shear strain rate. Together with the extra strain due to curvature, these changes affect the production of turbulence, giving rise to the observed behaviour of the Reynolds stresses.

4.2.4.1 Log-law Co-ordinates

From the mean velocity profiles, it was possible to estimate the wall shear stress using the log-law. However, the wall friction velocity (U_τ) values determined automatically by the methods described in Chapter 3 (Sect. 3.2.4) were manually adjusted, since they were inconsistent with the additional information provided by the measured \bar{uv} shear stress and wall static pressure distributions (see Sect. 4.2.4.3). While modifying U_τ , it was necessary to ensure that the non-dimensional mean velocity (U^+) profiles, plotted against $\ln(n^+)$, were consistent with each other, and, although not always matching exactly, were at least tending towards the log-law. As can be seen from the inner wall (Fig. 74) and outer wall (Fig. 75) mean velocity profiles, based on the U_τ values already presented in Section 4.2.2.4, some of the profiles exhibit large linear regions, whilst others do not. At the end of the parallel inlet section, both boundary layers exhibit typical profiles, with the linear portion extending up to $n^+ \approx 400$, followed by an outer 'wake' region slightly above the linear log-law.

Within the S-shaped duct, however, there is a significant variation in the mean velocity profiles. Although the velocity in the near-wall region scales with U_τ , mainly in agreement with the log-law, the large variation in U_τ gives rise to large differences in the outer part of the boundary layer. Along the inner wall, it can be seen that the profile initially falls below the log-law, before increasing significantly above it due to the low U_τ values resulting from the adverse pressure gradient. Although the extent of the linear behaviour is reduced in this region, the fact that the n^+ values are also relatively smaller ensures that the linear part of the profile is clearly defined. Further downstream, the wake reduces again due to the subsequent increase in U_τ , but the profile now exhibits a more complex shape. At the last measurement location, it appears as though the slope of the linear portion has changed, making it impossible to match the profile to the log-law. Even with the other available information, it was difficult to determine a suitable U_τ value, but it may be possible that a higher value should have been used. Without measurements even closer to the wall, it is impossible to be sure, but it would seem that the log-law is no longer applicable.

Along the outer wall, following an initial increase, the profile in the outer part of the boundary layer falls below the log-law. As a result of the strong favourable pressure

gradient, which increases U_τ , the measured profile does not match the log-law within the range of the measurements. Along with the other information, however, the chosen U_τ values give rise to profiles that consistently tend towards the log-law at much lower n^+ values, but the slope of these profiles differ significantly from that of the log-law itself. It would appear, therefore, that the log-law does not apply in regions of strong acceleration, and cannot be used to obtain the wall shear stress. Only by obtaining data close to the wall, within the viscous sublayer, would it be possible to determine U_τ accurately. It is believed, however, that the values used give a reasonable indication of the behaviour. Further downstream, the outer part of the mean velocity again increases above the log-law, but, as with the inner wall, the profile shape becomes more complex. Although there is some indication that the profile again matches the log-law, there is no conclusive evidence, and at the last measurement location it is again not clear whether a suitable U_τ has been found.

As well as the mean velocity, the \bar{uv} shear stress has been non-dimensionalised by U_τ . Since \bar{uv} is effectively equal to the total shear stress (τ/ρ), over all but the very thin viscous sublayer, and since τ/ρ is equal to U_τ^2 at the wall, \bar{uv}/U_τ^2 tends towards 1.0 at the wall, everywhere. In this case, the data has been plotted against non-dimensional distance across the boundary layer (n/δ), separately for the inner wall (Fig. 76) and the outer wall (Fig. 77) boundary layers. In both cases, however, it is clear that a limited amount of information can be extracted, since there is a large variation in the profiles brought about by the U_τ variation. For example, along the inner wall a peak value of ~ 6 is reached at stn. 8 ($x/L = 0.75$), since the shear stress is large in comparison to the low U_τ value, whereas at stn. 4 ($x/L = 0.25$) the wall shear stress is very high in comparison to the low \bar{uv} across the rest of the boundary layer, giving rise to very low \bar{uv}/U_τ^2 values. For the outer wall, the situation is similar, but, with the data plotted to the same scale as for the inner wall, it is clear that there is less variation in this case. In the present flow, therefore, normalisation of \bar{uv} by the wall shear stress is unsatisfactory, and suggests that, at a given location, the behaviour of the shear stress in the outer part of the boundary layer is unrelated to the wall behaviour. This is no surprise, of course, because the wall shear stress reacts quickly to the rapidly changing pressure gradient, whereas in the outer part of the boundary layer the shear stress, although affected directly by the curvature, reacts more slowly to the pressure gradient.

4.2.4.2 Mean Strain Rates

Using the measured mean velocities, it was possible to derive the mean strain rates. In general, for axisymmetric flow with zero swirl, in which there is also a significant radial velocity (V_r) component due to a change in radius (r), five out of the nine components of

the strain rate tensor are non-zero. Within the S-shaped duct, the measured velocity components were not Cartesian, and so it was necessary to account properly for the streamwise gradients, including the curvature terms that arise in an $s\text{-}n$ co-ordinate system, and the method used to obtain these spatial gradients is described in Chapter 3 (Sect. 3.2.5). The strain rates obtained from the 5HP mean velocities in this way are shown in Figure 78, as a combined plot of the cross-passage variation at each traverse location. The remaining strain rate, equivalent to $\partial W/\partial z$ in Cartesian co-ordinates, is given by Johnson and Hancock^[76], for example, as $(U_s \sin \phi + V_n \cos \phi)/r$, and exists because of lateral divergence (or, in this case, convergence) of the flow. Since the numerator in this expression is equal to V_r (Eq. 3.5), the lateral strain rate is simply given by V_r/r . Whilst V_r is zero upstream and downstream of the S-shaped duct, it can be seen from Figure 17 that the magnitude of V_r increases within the duct, reaching a maximum negative value of $\sim -0.4 \times U_{\text{Mean}}$. In this region, where the radius is $\sim 4 \times h_{\text{in}}$, V_r/r has a non-dimensional value of ~ -0.1 . Having obtained the magnitude of the lateral strain rate, its minor effect on the present flow is discussed below.

In Figure 78, it can be seen that $\partial U/\partial n$ (labelled as $i=1, j=2$) is the most significant strain rate. Adjacent to the wall, $\partial U/\partial n$ is very large, reaching non-dimensional values of order 100 within the viscous sublayer, and, therefore, to allow the behaviour of the strain rates across the rest of the flow to be seen more easily, the near-wall data has been neglected. Within the core region of the S-shaped duct, $\partial U/\partial n$ is non-zero (negative in the first bend and positive in the second) due to the cross passage variation of the streamwise velocity (see Fig. 9). From the core region, the magnitude of $\partial U/\partial n$ generally increases within the boundary layers, and it can be seen that there is a significant variation throughout the duct. Along the inner wall, for example, the initial acceleration leads to an increased strain rate adjacent to the wall, which moves away from the wall and becomes visible around $x/L = 0.5$. In the adverse pressure gradient region, there is a reduction in the strain rate between this local peak and the wall, which can be seen clearly at $x/L = 0.875$. Although the strain rate in the viscous region is not shown, the adverse pressure gradient along the inner wall leads to a reduction in the near-wall velocity. By differentiating the log-law (Eq. 3.90), the reduced wall shear stress can be used to estimate that the strain rate in the sublayer reduces from an upstream value of ~ 260 to a minimum of ~ 70 at $x/L = 0.625$. Along the outer wall, there is a noticeable reduction in $\partial U/\partial n$ across most of the boundary layer, which occurs first adjacent to the wall, as a result of the initial adverse pressure gradient, but becomes increasingly apparent downstream. Within the viscous sublayer, the strain rate increases due to the strong acceleration, reaching a maximum non-dimensional value of ~ 620 , but above the sublayer there is a noticeable dip in the strain rate. In the latter half of the duct, the strain rate in the outer part of the boundary layer is very low, in comparison to

upstream, and remains so downstream. However, although $\partial U / \partial n$ reduces in the sublayer as a result of the final adverse pressure gradient, there is an increase in the strain rate close to the wall, which appears to move away from the wall as the flow progresses downstream. In Section 4.2.4.5 it will be seen that the variation of streamwise acceleration across the duct, resulting from the pressure and shear stress gradients, is important in determining the $\partial U / \partial n$ distribution.

Although it was not possible to determine all the strain rates from the LDA data, $\partial U / \partial n$ was obtained (Fig. 80). In comparison to the 5HP data, it was possible to make LDA measurements much closer to the walls of the duct, providing increased resolution of the rapidly varying streamwise velocity in this region, and hence $\partial U / \partial n$. Thus, with higher values adjacent to the wall, it was necessary to change the scale of the plot, and in so doing emphasise the regions of increased strain rate. In particular, along the inner wall, it can be seen that a region of high strain rate appears, part way along the duct, and moves away from the wall, leaving a local minimum between this peak and the rapidly increasing strain rate adjacent to the wall. Further downstream, it can be seen that the region of increased strain rate slowly reduces, and eventually disappears.

Since the flow follows a curved path, there is a significant extra strain rate due to curvature ($\partial V / \partial s + U/R$). Since this was obtained along lines of constant height (i.e., along the measurement grid), and not true streamlines, $\partial V / \partial s$ is finite, but small in comparison to U/R . Within the first bend, therefore, where the curvature ($1/R$) is negative, the extra strain (labelled as $i=2, j=1$ in Fig. 78) is negative, reaching -0.25 at $x/L = 0.125$, whereas it is positive in the second bend, reaching ~ 0.20 at $x/L = 0.75$. In comparison to $\partial U / \partial n$, Figure 78 shows that the extra strain is relatively constant across the passage, but, apart from the variation of U , the magnitude changes due to the fact that the curvature varies across the duct, which is most pronounced within the first bend, where it increases towards the inner wall. One way of comparing the magnitudes of the extra strain and the main shear strain rates would have been to obtain the ratio of these at every point, but, since both these strain rates are zero somewhere in the flow, infinite values would be obtained whichever way round the ratio is taken. As such, it is better to show the two strain rates on the same plot (Fig. 78). In this way, it can be seen that the extra strain in each of the bends is of the same order of magnitude as $\partial U / \partial n$ over the outer part of the boundary layer, and only becomes insignificant close to the wall. Within the core region, the extra strain is the same as $\partial U / \partial n$. Since the difference between these two strain rates is the vorticity and their sum is the total strain rate, these quantities have been obtained separately, and are shown in Figure 79. Whereas the flow in the core region is irrotational throughout the S-shaped duct, the total strain rate ($\partial U / \partial n + \partial V / \partial s + U/R$) is finite in each bend. In Section 4.2.4.4 it will be seen that the

total strain rate, interacting with the shear stress, is mainly responsible for the production of turbulent kinetic energy. The fact, therefore, that the total strain rate distribution in two bends crosses through zero on the convex side of the duct, means that the production rate is much lower there, whereas it is increased on the concave side.

The normal strain rates $\partial U / \partial s - V/R$ and $\partial V / \partial n$ are also shown in Figure 78. Over most of the flow, their magnitude is small in comparison to $\partial U / \partial n$, but halfway along the S-shaped duct they become reasonably significant, as does V_r/r ; although their magnitudes are small in comparison to the maximum extra strain rate due to curvature obtained in the bends of the duct. Basically, due to the variation of the streamwise pressure gradient within this region of the duct, $\partial U / \partial s - V/R$ (labelled as $i=1, j=1$ in Fig. 78) is negative over the inner half of the duct and positive over the outer, becoming increasingly significant towards the wall and reaching a non-dimensional magnitude of ~ 0.2 . With $V_r/r \approx -0.1$ in this region, $\partial V / \partial n$ is positive over the inner half of duct (~ 0.3) and negative over the outer (~ -0.1). Since the normal strain rates must sum to zero to satisfy continuity, it is reassuring that, despite the various difficulties in obtaining the data, the sum of the two normal strain rates shown in Figure 78 is broadly equal and opposite to the estimated lateral strain rate.

Although in present flow the magnitude of V_r/r is small in comparison to the other strain rates, it must be recognised that lateral divergence can sometimes have a significant effect on the flow. For example, Johnson and Hancock^[76] investigated two free shear layers subjected to (stabilising) concave curvature and lateral divergence, which tended to resist the suppression of the shear stress arising due to curvature. They showed that shear stress production was increased by lateral divergence ($\bar{u}vV_r/r$), offsetting the reduction due to curvature, and that, although the magnitude of the normal stresses was largely controlled by the shear stress magnitude (through the shear stress based production terms), all the normal strains were large enough to significantly affect the normal stresses (through the normal stress based production terms). Smits et al.^[148] also investigated the effect of destabilising lateral divergence in a turbulent boundary layer downstream of a short region of concave curvature. In comparison to a plane 2D flow subject to the same curvature, in which there was a sudden collapse of the shear stress downstream of the curved region (as a result of a reduction in the shear strain rate), the shear stress downstream of the axisymmetric bend remained large since it was being generated by the lateral strain rate. In the present flow, by contrast, the lateral strain rate is of the opposite sense, and therefore will always tend to reduce shear stress. Moreover, in comparison to $\partial U / \partial n$, it is only of significant magnitude near the edge of the boundary layer. In Chapter 6 (Sect. 6.2), the effect of extra strain rates on Reynolds stress production is examined using a 2D planar s-n-z co-ordinate system, in which the

effects of lateral divergence are not present. Although this is a simplification, it does show (Eq. 6.18) that the extra strain due to curvature is amplified by a factor $2(\overline{uu}/\overline{vv}) - 1$ ($\approx 3-4$), increasing its significance relative to $\partial U/\partial n$. In comparison, since the lateral divergence shear stress production term is $\overline{uv} V_r/r$, the effect of V_r/r is dependant on the ratio $(\overline{uv}/\overline{vv})$, which is always less than 1.0 in the present flow (Fig. 49). In the curved regions, therefore, the lateral stain rate will have a small effect in comparison to the curvature. Moreover, halfway along the duct where the curvature strain rate is zero, the lateral stain rate will still only have a small influence on the turbulence because the shear strain rate is much larger than the lateral strain over all but the outer edge of the boundary layer (see Fig. 78). Finally, it is worth noting that the CFD predictions in this thesis take proper account for the axisymmetric effects, and, as such, the effect of lateral divergence is present in the results. For example, in Figure 144 the variation of the normal stresses along the mid-height grid line, where the lateral strain is predominantly balanced by $\partial V/\partial n$, shows that \overline{ww} is slightly increased and \overline{vv} slightly reduced, whereas \overline{uu} is basically unaffected, by the lateral strain.

4.2.4.3 Shear Stress Gradient and Total Pressure Loss

In this section, the cross-stream shear stress gradient is obtained, and used to derive the total pressure loss. In order to obtain this gradient accurately, it was first necessary to interpret the measured \overline{uv} shear stress data, which, for each traverse location, mainly involved fitting a smooth line through the \overline{uv} data. Furthermore, it was possible to determine the magnitude and slope of this line at each wall by taking into account the wall shear stress and streamwise pressure gradient. Although \overline{uv} reduces to zero at the wall, the total shear stress (τ) attains a finite value ($= \rho U_\tau^2$) and, in addition, the cross-stream shear stress gradient equals the streamwise pressure gradient (i.e., at the wall $\partial \tau / \partial n = \partial p / \partial s$). Since the extent of the viscous sublayer is very small, the \overline{uv} data was effectively equal to $-\tau/\rho$ everywhere, and, therefore, the line of best fit had to extrapolate to the wall shear stress, with a known gradient, over a small region adjacent to the wall. While interpreting the shear stress data, however, although the log-law was used to estimate the wall shear stress, it was necessary to adjust some of the wall values so that they could be reached at the correct gradient. Using $\partial p / \partial s$ values determined manually from the wall static pressure distribution (Table 9), the points defining the interpretation were moved manually until a smooth distribution was achieved at each location, meeting all the requirements, and, in addition, varying smoothly in the streamwise direction. As a result, a smooth U_τ distribution was obtained for each wall (Fig. 25), which gave consistent non-dimensional mean velocity profiles in log-law co-ordinates (Figs. 74&75). In Figure 81, then, the interpretation and final wall values are shown in comparison to the measured data (first presented in Fig. 42, but now drawn

to a different scale), and, for reference, the interpretation has been plotted against height (Fig. 82) and stream function (Fig. 83).

Having obtained a good representation of the measured shear stress, the cross-stream shear stress gradient was derived. Since the interpretation was defined via a series points, more closely spaced than the measured data, $\partial\bar{u}\bar{v}/\partial n$ was obtained by differencing the interpreted points, as described in Chapter 3 (Sect. 3.2.5), and, since the interpreted distribution was well defined close to the wall, the gradient could be obtained relatively accurately across the whole passage. In addition, however, the measured Reynolds stresses were interpolated at the 5HP measurement positions, which, since the LDA data was not obtained on a structured measurement grid, was necessary in order to calculate products of mean quantities and Reynolds stresses. Thus, it was also possible to use the interpolated $\bar{u}\bar{v}$ values to obtain $\partial\bar{u}\bar{v}/\partial n$, although, of course, this was not very accurate close to the wall. In Figure 84, therefore, $\partial\bar{u}\bar{v}/\partial n$ obtained from both the interpreted and interpolated data is shown, along with the wall values equivalent to $-\partial p/\partial s$. Note that the data has been plotted against stream function, since, as will be seen presently, the variation of $\partial\bar{u}\bar{v}/\partial n$ along a streamline basically determines the total pressure variation. In addition, by calculating the mean energy loss term ($U\partial\bar{u}\bar{v}/\partial n$), which is zero on the wall, Figure 85 shows more clearly the behaviour of the shear stress gradient throughout the duct. Again, both interpreted and interpolated data are shown, between which there is good overall agreement. Relative to the upstream boundary layers, across which the magnitude of the shear stress gradient gradually increases and decreases whilst remaining positive, the variation within the S-shaped duct is much more exaggerated. Along the inner wall, for example, there is an initial reduction over the outer part of the boundary layer, but, adjacent to the wall, a large positive region exists. As the flow progresses downstream, this moves away from the wall, and a pronounced negative region appears. In contrast, along the outer wall, there is an initial increase in the shear stress gradient over the outer part of the boundary layer, but, adjacent to the wall, a negative region forms which persists as the flow progress downstream. Within the second bend, however, both the original positive and negative regions reduce, and a new large positive region appears adjacent to the wall, which also moves away from the wall.

From the shear stress gradient, it was possible to derive the total pressure variation within the S-shaped duct. Along a streamline, the mean energy equation (Appendix 4, Sect. A4.2.3) shows that the streamwise total pressure gradient is effectively equal to the cross-stream shear stress gradient (i.e., $\partial P/\partial s = \partial\tau/\partial n$), since V_n is zero and the radius and curvature terms are small. Using this, therefore, the variation of $\partial\bar{u}\bar{v}/\partial n$ (in effect equal to $-\partial\tau/\partial n$) along a series of streamlines was obtained from the interpreted data,

by interpolating at the required ψ values, so that the change in total pressure between any two points on the streamlines could be determined. For each streamline, this was achieved by numerically integrating the $\partial \bar{u}v / \partial n$ variation, between the upstream location and another point along the streamline, which, in turn, was taken to be each of the traverse locations. At each location, therefore, a cross-stream total pressure distribution was derived, by applying the total pressure change to the inlet total pressure profile. Typically, the shear stress gradient leads to a reduction in the total pressure, with the rate at which it is lost varying significantly throughout the duct. Furthermore, in the present flow, there are several regions of increasing total pressure (Fig. 86), corresponding to the regions of negative $\partial \bar{u}v / \partial n$.

In Figure 87, the derived total pressure distribution is compared to the directly measured 5HP profiles, with the data shown relative to the rig inlet total pressure (P_∞) and non-dimensionalised by $\frac{1}{2}\rho U_{\text{Mean}}^2$. Overall, it can be seen that there is excellent agreement between the measured and derived values, which shows that the 5HP and LDA measurements are mutually consistent, and provides a high degree of confidence in the data. Moreover, this approach has enabled the physical mechanism responsible for the total pressure loss to be understood, and traced to particular regions within the flow. Along the inner wall, for example, the majority of the loss arises on the outer edge of the region of elevated shear stress. In the first bend, this occurs close to the wall, but, by the second bend, this has moved away from the wall, and a region of increasing total pressure occurs adjacent to the wall. In addition, because of the significant reduction in the shear stress over the outer part of the boundary layer, due to the initial convex curvature, there is very little total pressure loss in this region throughout the duct. In contrast, along the outer wall, most of the loss occurs in the outer part of the boundary layer, due to the increased shear stress which results from the initial concave curvature, although this reduces within the second bend due to the convex curvature. Closer to the wall, there is a region of increasing total pressure, which moves away from the wall, offsetting some of the earlier reduction, but, towards the end of the second bend, the region of elevated shear stress adjacent to the wall causes the total pressure to reduce. As a result, therefore, the total pressure distribution at duct exit is very different on each side of the passage, with the inner wall profile having a relatively low region in the middle of the boundary layer, whereas the outer wall profile has relatively low total pressure in the outer and inner regions.

By integrating the total pressure profiles, the mass-weighted average total pressure (\tilde{P}) variation through the duct was derived. According to the definition, given in Chapter 3 (Sect. 3.2.2.4), \tilde{P} can be obtained by integrating the pressure with respect to the stream function (i.e., $\int P d\psi$), and by using the non-dimensional pressure, a loss coefficient was

Experimental Results

obtained directly. In addition, as well as considering the whole passage, the loss associated with each boundary layer was found, by integrating across each half of the passage in turn. The results obtained are shown in Figure 88, plotted against mid-height axial position, and, since the loss coefficient will be zero at the beginning of the parallel inlet duct (at $x/L \approx -4.2$), the scale of the plot was chosen to include the inlet length, such that the data at stn. 1 represents the loss associated with the zero pressure gradient turbulent boundary layers. In deriving the total pressure from the shear stress, the 5HP total pressure distribution at $x/L = -0.55$ was used as the datum profile, but, since the LDA measurements were taken further upstream, it was necessary to assume that this profile was obtained at $x/L = -0.75$. Despite this slight discrepancy, there is good overall agreement between the measured and derived data, and, although there is some scatter in the experimental data, both show the same trends. In fact, over the length of the S-shaped duct, both data show that the loss coefficient is ~ 0.022 , which, remarkably, is lower than over the same length of inlet duct. Based on the shear stress distribution at the end of the inlet duct, the rate of increase of loss was calculated to be 0.024 per L, and, although this rate will vary along the length of the duct, this is in good agreement with the total loss of the inlet duct (~ 0.111), which is $\sim 4.2L$ long. In addition, it is clear that the rate of increase of loss is lower downstream of the S-shaped duct. Based on the shear stress distribution at the last measurement location in the exit duct (A8), the rate of increase of loss was calculated to be 0.016 per L, which is 65% of the upstream value. However, it must be remembered that the total surface area of the exit duct is also lower (it being 80% of the inlet value), and, therefore, the rate of loss increase would be expected to be less. Nevertheless, the actual reduction is still significant.

When the split between the inner and outer walls is considered, it can be seen that the loss associated with the inner wall boundary layer is much lower than the outer. However, this is also associated with the fact that the surface area of the inner wall is less than that of the outer. In the inlet duct, for example, even though the two boundary layers are identical in terms of their velocity and shear stress distributions with respect to passage height, the fact that the passage is annular means that a greater mass flow passes through the outer half of the duct and, therefore, the profiles are not the same with respect to stream function. Given that the hub-to-tip radius ratio of the inlet duct is 0.8, with a corresponding difference in the surface area, the mass-weighted loss of the inner wall boundary layer should be 80% of the outer. Although the derived loss presented in Figure 88 was based only on $\partial\bar{v}/\partial n$, by including the radius term \bar{v}/r in the analysis of the inlet boundary layers, it was possible to show that this was the case. Based on the shear stress at the end of the inlet duct, the rate of increase of loss was 0.0134 per L for the outer wall and 0.0110 per L for the inner wall, which is 82% of the outer wall value. (N.B., this was 86% without including the extra term.) In addition,

based on the shear stress at A8, the rate of increase of loss was 0.0084 per L for the outer wall and 0.0075 per L for the inner wall. For the inner wall, therefore, the rate of increase of loss at exit is 68%, whilst the surface area is 74.4%, of the inlet value, whereas for the outer wall the loss is 62% compared to 84.5% for the area. The S-shaped duct, therefore, appears to be able to lower the rate at which total pressure is lost in the downstream duct, and this beneficial effect mainly occurs in the outer wall boundary layer, as a result of the lower shear stress levels which arise because of the convex curvature in the final bend.

To provide further understanding, the total pressure data is presented in an alternative way. For this, the measured and derived total pressure has been plotted with passage height (h), or stream function (ψ), on the y-axis, such that the profiles for each traverse location, which are offset along the x-axis, are shown from left to right across the page. In addition, the profiles on each side of the passage have been compared, by plotting against fractional distance, or fractional mass flow, from each wall (i.e., for the inner wall, this means simply h , or ψ , but, for the outer wall, this is equivalent to $1-h$, or $1-\psi$). Of interest in this section, then, are the 5HP measured total pressure profiles, which have been plotted against h (Fig. 95), ψ (Fig. 96), fractional distance from the wall (Fig. 97) and fractional mass flow from the wall (Fig. 98), and, for comparison, the total pressure profiles derived from the shear stress data, which have been plotted against fractional distance from the wall (Fig. 99) and fractional mass flow from the wall (Fig. 100). From the comparison of profiles on each side of the passage, in particular, it is clear that the inner and outer wall boundary layers behave very differently. As previously described, the total pressure increases, as well as falls, within the S-shaped duct, and the profiles along each wall help to show where this occurs.

4.2.4.4 Turbulent Kinetic Energy Production

Since the energy lost by the mean flow is transferred to the turbulence, the turbulent kinetic energy production rate (P) was derived. According to the mean energy equation, the flow loses energy at a rate which is determined by the mean velocity and the Reynolds stress gradients (i.e., $-U_i \partial \bar{u}_i \bar{u}_j / \partial x_j$, in Cartesian tensor notation). However, this can be rewritten as $-\partial \bar{U}_i \bar{u}_i \bar{u}_j / \partial x_j + \bar{u}_i \bar{u}_j \partial \bar{U}_i / \partial x_j$, where the first term represents a redistribution of the mean energy (since its volume integral is zero) and the second term represents an energy loss (since its volume integral is equal to the net flux of total pressure through the surface of the volume, which is effectively the mass-weighted average total pressure loss across the volume). In the turbulent kinetic energy transport equation, the production term ($-\bar{u}_i \bar{u}_j \partial \bar{U}_i / \partial x_j$) is equal and opposite to the mean energy loss term, and so the energy lost by the mean flow is gained by the turbulence. In

addition, it can be seen that \mathbf{P} arises due to the Reynolds stresses working against the mean strain rates, and to derive \mathbf{P} it is necessary to evaluate various stress×strain products at a given point in the flow. Moreover, for the present axisymmetric data, \mathbf{P} was obtained using Eq. 3.100, in $s-n$ co-ordinates, and, since the LDA data was not obtained on a structured measurement grid, the Reynolds stresses were interpolated at the 5HP measurement points. The data derived in this way is presented in Figure 89, where the cross-stream distribution of \mathbf{P} can be seen at each traverse location. At inlet, \mathbf{P} increases across the boundary layer, reaching a peak adjacent to the wall due to the high strain rate (although this is not shown, so that the behaviour across the outer part of the boundary layer can be seen more easily). Although \mathbf{P} was calculated fully, its behaviour is dominated by the total strain rate (discussed in Section 4.2.4.2) which, together with the shear stress, gives rise to a significant variation of \mathbf{P} throughout the duct. Along the inner wall, for example, \mathbf{P} virtually disappears in the first bend, due to both the reduced total strain rate and the low shear stress. As will be seen in Chapter 6 (Sect. 6.2.3), the shear stress also falls because its production rate is reduced, more so than \mathbf{P} , by the extra strain rate (U/R) and lower $\bar{v}v$. Since \mathbf{P} basically affects the rate of change of k in the streamwise direction, the magnitude of k will fall as a result of the reduced production rate (see Fig. 45). Further along the inner wall, in the region dominated by the adverse pressure gradient, there is a pronounced increase in \mathbf{P} as a result of the increased strain rate (see Fig. 78), which forms adjacent to the wall and subsequently moves away from the wall, giving rise to the peak in the k distribution. In contrast, along the outer wall, \mathbf{P} increases in the first bend due to both the increased total strain rate and the increased shear stress (which occurs as a result of its production rate being increased by U/R and $\bar{v}v$), giving rise to the observed increase in the magnitude of k . Although $\bar{u}v$ remains relatively high downstream of the concave bend, there is a dip in the total strain rate which leads to a significant reduction in \mathbf{P} , across most of the boundary layer. Further along, through the convex bend, $\bar{u}v$ also reduces, so that \mathbf{P} remains low downstream of the S-shaped duct, except for a small increase adjacent to the wall.

As mentioned, the energy lost by the mean flow eventually goes into turbulent kinetic energy production. In Figure 90, therefore, the main redistribution term ($\partial \bar{U}v\bar{v}/\partial n$) has been evaluated, and presented along with the main loss term ($-\bar{u}\bar{v}\partial U/\partial n$) since their sum should equal the shear stress gradient ($U\partial \bar{v}/\partial n$), already presented (Fig. 85). In general, the shear stress gradient results in a loss of mean energy (total pressure) over the outer part of the boundary layer, which is then redistributed to the near-wall region, where it is lost to the turbulence. Although it is not impossible for turbulent kinetic energy to be transferred back to the mean flow, and indeed negative k -production does occur in a small region at the edge of the convex boundary layer, it is generally the case

that the energy lost adjacent to the wall can never be recovered by the mean flow. (Within the turbulence, of course, the energy is mostly dissipated as heat, but some of the energy is transported away from the wall, increasing in the turbulent energy in the outer part of the boundary layer, resulting in its growth.) During redistribution, however, not all the mean energy transferred towards the wall is lost to the turbulence. As already seen, there are several regions of negative $U\partial\bar{v}/\partial n$, where the total pressure increases, and from Figure 90 it is clear that, in these regions, negative redistribution exceeds the positive loss. Although the data close to the wall has been omitted, it is clear that the mean energy loss (turbulent kinetic energy production) is large, but, since this is matched by a large (negative) redistribution, the net effect on the mean flow is relatively small in this region.

4.2.4.5 Streamwise Acceleration

To understand further the physical behaviour of the S-shaped duct flow, the streamwise acceleration has been derived. Since the streamwise pressure gradient ($\partial p/\partial s$) and cross-stream shear stress gradient ($\partial \tau/\partial n$) are mainly responsible for the streamwise acceleration, $\partial p/\partial s$ has been obtained, and compared to $-\partial \tau/\partial n$ (Fig. 91). The streamwise pressure gradient was derived from the 5HP static pressure data (Fig. 8), as described in Chapter 3 (Sect. 3.2.5), by differencing the data in the streamwise direction along the measurement grid, and the cross-stream shear stress gradient was obtained from the interpreted shear stress distribution, as previously described (Sect. 4.2.4.3). At the furthest upstream and downstream locations, the data obtained by differencing was not reliable and has been omitted, but, clearly, in the parallel inlet and exit ducts $\partial p/\partial s$ is very small in comparison to the values attained within the S-shaped duct. In Figure 91, it can be seen that there is a substantial variation in $\partial p/\partial s$ throughout the S-shaped duct. At inlet ($x/L=0.0$), $\partial p/\partial s$ is negative over the inner half of the duct and positive over the outer, and, since it varies smoothly across the passage, its strength is greatest adjacent to the wall. Over a short distance, however, $\partial p/\partial s$ changes sign, passing through zero at $x/L=0.125$, becoming positive over the inner half of the duct and negative over the outer. Through the middle portion of the duct, there is relatively little change, but towards exit there is another rapid reversal of the pressure gradient, passing through zero part way between $x/L=0.75$ and 0.875 . At duct exit, therefore, $\partial p/\partial s$ is negative over the inner half and positive over the outer, but this soon reduces to near zero in the downstream passage.

In comparison to the pressure gradient, the magnitude of the shear stress gradient is relatively small throughout the duct; although at the wall, of course, $-\partial \tau/\partial n$ is equal and opposite to $\partial p/\partial s$. In combination with the pressure gradient, however, the

variation of the shear stress gradient has an important influence on the streamwise acceleration, which is shown in Figure 92. For this, the acceleration ($U\partial U/\partial s$) was obtained directly from the 5HP mean velocity data, and also from $\partial\tau/\partial n - \partial p/\partial s$. Although the latter is only an approximation, there is good overall agreement between the two sets of data, and, more importantly, by deriving the acceleration in this way it is possible to understand the way the shear stress gradient influences the behaviour of the flow. Along the inner wall, for example, the initial favourable pressure gradient gives rise to a shear stress distribution that increases rapidly towards the wall, reducing the magnitude of the acceleration in the near-wall region. Subsequently, however, whilst the pressure gradient rapidly reduces to zero, and then changes sign, the shear stress distribution remains substantially the same, except at the wall where its gradient falls, and then changes sign, in accordance with the pressure gradient. In addition, in the outer part of the boundary layer, the extra strain associated with the convex curvature leads to a dramatic reduction in the shear stress, which tends to exaggerate the shear stress increase adjacent to the wall. Thus, whilst the shear stress gradient across the outer part of the boundary layer is reduced, the gradient close to the wall is increased. As the pressure gradient changes, therefore, although the acceleration is zero on the wall, and at $x/L=0.125$ zero across most of the boundary layer, there is a thin region adjacent to the wall where the flow is being strongly decelerated. Further downstream, where the pressure gradient is positive, the peak in the shear stress distribution moves away from the wall, but, for some distance, there is a clearly defined local increase in the magnitude of the deceleration.

Within the flow, the distribution of the streamwise acceleration across the duct affects the primary strain rate and shear stress distributions. Since there is a variation in the streamwise acceleration across the duct, the strain rate ($\partial U/\partial n$) will be affected because the velocity at one position will change more than at another, and, in turn, this affects the rate at which the Reynolds stress are produced. Along the inner wall, for example, the region of strong deceleration, which arises close to the wall in the first bend, is responsible for producing the peak in the shear stress distribution, and moving it away from the wall. With a small region of relatively high deceleration, there will be an increase in the strain rate between the position of maximum deceleration and the edge of the boundary layer, and a reduction towards the wall, as previously described in Section 4.2.4.2. Together with the extra strain rate due to curvature, the modified strain rate then affects the turbulent kinetic energy production rate (as seen in Section 4.2.4.4) and, similarly, the shear stress production rate, which affect the rate at which the Reynolds stresses change in the streamwise direction. Since the strain rate is increased at the outer edge of the shear stress peak, and decreased across the top of the peak, it moves away from the wall in the downstream direction, and it would appear that this

whole cycle of events is triggered by the rapid reversal of the pressure gradient, within the first bend, in comparison to the more gradual change in the shear stress distribution. Along the outer wall, the flow behaviour is controlled by a similar mechanism, but in this case the rapid change in the pressure gradient, from adverse to favourable, in combination with the more slowly varying shear stress, results in a region of increased acceleration, which subsequently moves away from the wall. This has the effect of reducing the strain rate across the outer part of the boundary layer, most noticeably near to the peak in the acceleration, which, by reducing their production rate, tends to reduce the magnitude of the turbulent kinetic energy and shear stress.

4.3 Flow With the Compressor Installed

Although the main emphasis within this thesis has been placed on the 2D axisymmetric flow, a significant amount of experimental data was obtained with the single stage axial compressor installed upstream of the annular S-shaped duct. At every traverse location within the duct, a 5-hole probe (5HP) was used to measure the behaviour of the 3D mean flow, with the stator blade wakes present. Although there was insufficient time available to gather an equivalent set of turbulence data, the LDA system was used to measure the distributions of all six Reynolds stresses at S-shaped duct inlet, which are important for defining the inlet conditions for future CFD calculations of the wake development. In this section, therefore, the main results are presented for reference, but a detailed analysis and interpretation of them is beyond the scope of this thesis. Note that, following the completion of the measurements reported here, further LDA data within the S-shaped duct downstream of the compressor have been obtained (Bailey et al.^[4]), and, with the stator blades removed, a complete set of data in the swirling flow downstream of the rotor has also been acquired (Bailey and Carrotte^[5]).

4.3.1 Mean Flow Quantities

Downstream of the single stage compressor, the flow contains the wakes shed by the rotor and stator blades. In the stationary frame, however, only the stator blade wakes will be detected by the 5HP, since the pressure variation associated with the rotating wakes will be averaged by the probe and, in addition, the large number of pressure readings taken over a finite period of time were numerically averaged. It was assumed that the flow downstream of each of the 62 stator blades was the same, and measurements were made over a sector of the annulus equivalent to one stator blade space ($\theta_s = 0.10134$ rads). With the compressor operating at a constant non-dimensional

speed and flow, data was obtained at each traverse location in turn, thereby defining a complete experimental measurement mesh (Fig. 101).

4.3.1.1 S-shaped Duct Inlet Conditions

At S-shaped duct inlet (stator exit), the velocities obtained from the 5HP measurements are presented as contours of constant velocity for each component; U_ℓ (Fig. 102), V_ℓ (Fig. 103) and W_ℓ (Fig. 104). In Figure 102, the stator wake is clearly visible, as a thin region of reduced velocity running across the passage, and at each end the streamwise velocity reduces through the annulus wall boundary layer. In the core region, between the stator wakes and the wall boundary layers, the streamwise velocity also varies because of the streamline curvature. As the stator wake is thin, the stator is operating near minimum loss, and the small region of lower velocity, adjacent to the suction surface at each end of the blade, is a typical feature of compressor blades associated with secondary flow within the blade passage. At this location, 15 mm downstream of the stator trailing edge, the wake has already decayed substantially, with the minimum velocity in the wake well above zero ($\sim 0.9 U_{\text{Mean}}$ at mid-height).

Compared to the streamwise velocity, the magnitude of the other two components is small. Figure 103 shows that V_ℓ (which is equivalent to the radial velocity (V_r) at this location) is mostly negative, as the flow is already turning into the first bend of the S-shaped duct, but, within the wake, the magnitude of V_ℓ is slightly larger. This is because the radial pressure gradient, which exists to turn the mean flow, is able to accelerate the slower moving wake fluid inwards by a greater amount than the surrounding flow. Although the stator blade was designed to deliver zero swirl, Figure 104 shows that W_ℓ is slightly positive, suggesting that the blade is under-turning (by $\sim 2^\circ$ at mid-height). Towards the outer wall, the amount of swirl increases slightly (around 80-90% height), before reducing and becoming negative. This over-turning arises because the pressure gradient across the stator blade passage, which exists to turn the flow within the stator and reduce the rotor generated swirl, is able to accelerate the slower moving boundary layer fluid in the circumferential direction by a greater amount relative to the rest of the flow. Towards the inner wall, the flow adjacent to the wall is strongly accelerated, and, therefore, only the swirl increase (around 4% height) can be seen. The behaviour of the radial and circumferential velocity components can be seen more clearly by plotting the secondary flow vectors (Fig. 105), at every data point throughout the sector. As these are the vector sum of the in-plane components (i.e., V_ℓ and W_ℓ), the inward movement and the under-turning are obvious.

Finally, at inlet, the total pressure variation is shown in Figure 106. In this case, the data is presented as a total pressure coefficient, defined with respect to the mass-weighted

average total and static pressure, i.e., $(P - \tilde{p}_{in}) / (\tilde{P}_{in} - \tilde{p}_{in})$. Since the compressor was designed to deliver constant total pressure, there is relatively little variation across the core region; unlike the streamwise velocity, which is higher towards the inner wall because the static pressure is lower. Relative to the total pressure level in the core, therefore, it can be seen that the wake represents a region of total pressure loss. Although the total pressure reduces towards each wall, this deficit is not all due to the stator, nor for that matter the rotor, since the flow at inlet to the compressor was developed along the parallel inlet duct. In non-dimensional terms, the conditions at compressor inlet were identical to the 2D axisymmetric case without the compressor, with turbulent boundary layers occupying 24% of the passage and a potential core region in between.

4.3.1.2 Pressure and Velocity Distribution

Of all the 5HP data within the S-shaped duct, only the total pressure variation has been included in this thesis. Figure 107 shows the total pressure coefficient at each traverse location, which is defined relative to the mass-weighted pressures at duct inlet. Note that the data at inlet has already been seen in more detail (Fig. 106). As the flow develops along the duct, the stator blade wake decays (i.e., its depth reduces, whilst its width increases), but its structure is visible right up to the last measurement location. At first the wake decays rapidly, with the minimum pressure coefficient at mid-height already up to ~0.7 at duct inlet, and above 1.0 by $x/L = 0.375$, but in the latter part of the duct, the rate of decay is much less. In addition, because there is a small amount of swirl in the flow, which varies slightly across the duct, the wake does not remain straight, with each end moving further around the annulus than at mid-height. Along each wall, the boundary layer development is influenced strongly by the streamwise pressure gradients. Although there is a circumferential variation of total pressure within the boundary layers, due to the presence of the wake, it can be seen that the region of total pressure deficit increases along the inner wall, due the adverse pressure gradient, whereas it reduces along the outer wall. As in the 2D axisymmetric case, it can be seen that there are regions where the total pressure increases, offsetting some of the loss elsewhere. The total pressure in the core region, between the wakes and the boundary layers, remains virtually constant (apart from the mixing out of the rotor wakes), but, in comparison to the 2D axisymmetric case, the core region is quite small at the last measurement location.

Figure 108 shows the wall static pressure distribution, in comparison to the overall mass-weighted average total and static pressures, and Figure 109 shows the cross-passage variation at each traverse location, obtained by averaging the 5HP

Experimental Results

measured static pressures in the circumferential direction. To provide additional wall static pressure data, these profiles were extrapolated to the wall, and found to be in good agreement with the directly measured values from the static pressure taps. Along the inner wall, after an initial reduction, the static pressure increases along most of its length (from $C_p \approx -0.30$ to $+0.22$), before finally decreasing, whereas, along the outer wall the pressure mainly reduces (from $C_p \approx +0.24$ to -0.28). Despite this large variation, the overall average static pressure (Fig. 108) remains virtually constant, since the passage area is constant, apart from a gradually reduction due to the loss of total pressure. Relative to S-shaped duct inlet, which already includes the deficit associated with the stator blade wake, the overall average total pressure only falls by $\sim 2\%$ over the length of the duct. Even allowing for an increased experimental error, in obtaining and averaging data downstream of the compressor, this loss is similar to the 2D axisymmetric case. It suggests that the wake has little effect on the boundary layer loss, and that most of the wake mixing loss has already occurred between the stator blade trailing edge and the first measurement location. Indeed, Stevens and Wray^[166] found that stator blade wakes decay rapidly, even in an adverse pressure gradient.

In comparison, the static variation in the S-shaped duct downstream of the compressor is similar, but not identical, to the 2D axisymmetric case. In Figure 109, it is clear that the cross-passage pressure gradient ($\partial p / \partial n$), necessary to turn the flow, is virtually the same for both cases over the central portion of the flow, but is different across the boundary layers; especially near the inner wall in the first bend. This results in a noticeable increase in the minimum wall static pressure in the first bend, which changes the appearance of the wall static pressure distribution (Fig. 108 cf. Fig. 7), and gives rise to a slightly reduced adverse pressure gradient along the inner wall. In broad terms, the changes to $\partial p / \partial n$ must occur because of a modified velocity distribution, which, along with changes to the streamline curvature determined by the mass flow distribution, will affect the magnitude of the centripetal acceleration.

In order to compare more easily with the 2D axisymmetric case, the velocity distribution downstream of the compressor has been circumferentially averaged. Although there is a significant circumferential variation through the stator wakes, especially at S-shaped duct inlet, the mass-weighted average streamwise velocity profiles can be used to give an indication of the overall behaviour. In Figure 110, therefore, the cross-passage variation of streamwise velocity at each traverse location is shown for both cases, where it can be seen that there are significant differences. Throughout the duct, the velocity profiles downstream of the compressor are skewed relative to the 2D axisymmetric flow, with lower velocities over the inner half of the duct and higher over the outer. As well as the overall skewing of the profiles, Figure 110 shows that the velocity through

the inner wall boundary layer is very different to the 2D axisymmetric case, with a pronounced kink in the distribution at S-shaped duct inlet which persists to a lesser extent downstream. Thus, although the velocity over the outer part of the boundary layer is lower, the velocity adjacent to the inner wall is virtually the same. In contrast, the velocity distribution through the outer wall boundary layer is much more rounded, with a higher velocity adjacent to the wall. Without doubt, these differences are produced by the rotor, where secondary flow at the inner end of the blade tends to increase the pressure rise adjacent to the wall, whilst reducing it further outboard, whereas at the outer end of the blade the tip clearance flow will dominate, and cause the total pressure to reduce steadily across the tip region.

4.3.1.3 Circumferentially Averaged Profiles

For further comparison, some circumferentially averaged profiles downstream of the compressor have been presented in an alternative way. For this, the data has been plotted with passage height (\hbar), or stream function (ψ), on the y-axis, such that the profiles for each traverse location, which are offset along the x-axis, are shown from left to right across the page. The mass-weighted average streamwise velocity profiles have been plotted against \hbar (Fig. 111) and ψ (Fig. 112), and the mass-weighted average total pressure distribution has been plotted against \hbar (Fig. 113) and ψ (Fig. 114). These can be compared to the 2D axisymmetric streamwise velocity profiles measured by the 5HP, which have been plotted against \hbar (Fig. 93) and ψ (Fig. 94), and, similarly, the total pressure profiles are plotted against \hbar (Fig. 95) and ψ (Fig. 96).

Of particular interest are the total pressure profiles, which give a good indication of the compressor and duct performance. Across the central part of the passage, at S-shaped duct inlet in particular, it can be seen that the compressor produces a slightly higher total pressure towards the outer wall. Although these profiles are circumferentially averaged, it is known that the total pressure varies in a similar way across the passage in the core region, mid-way between the wakes. In between the boundary layers, therefore, there is an approximately constant difference between the maximum and the mean pressure profiles, such that the pressure deficit associated with the wake is nearly constant. As described in Appendix 1, the compressor was designed to deliver a constant total pressure ratio, but, as noted above, this has not quite been achieved. Although the actual deviation (between the exit air and blade angle) may be different than that assumed in the design, a more likely explanation for this behaviour is that the blade shape changes while it is running; which was not considered during the design. Given the flexibility of the plastic (ABS) blades, it is possible that the aerodynamic and mechanical loads on the blade were able to reduce the stagger of the rotor, towards the

tip, such that, by running at incidence, it was able to turn the air more and generate a larger pressure rise.

In Figures 113 & 114, the profiles have been shown relative to the maximum total pressure in the core region (i.e., at the outer edge of the core). Since this remains approximately constant along the length of the duct, the negative values in the central region give an indication of the loss associated with the wake ($\sim 5\%$ of $\frac{1}{2}\rho U_{Mean}^2$), which appears not to change very much either. Towards each wall, the total pressure reduces by an even greater amount, showing the deficit associated with the boundary layers, and, when plotted against stream function, the profiles can be integrated directly to obtain an overall total pressure deficit. At duct inlet (stn. 2), for example, a value of -0.16 is obtained, whereas at duct exit (stn. 10) this becomes -0.18 , again showing an overall total pressure loss of $\sim 2\%$ over the length of the duct.

4.3.1.4 Overall Parameters

From the circumferentially averaged streamwise velocity profiles, it is possible to derive various boundary layer parameters. However, because of the difficulty in defining a suitable potential velocity distribution against which to assess the profile, and because the profile itself only gives an indication of the true behaviour, such parameters are of limited use. Nevertheless, the shape parameter (H) variation for each boundary layer has been compared to the more meaningful distributions obtained from the 2D axisymmetric flow (Fig. 115). In deriving the potential velocity, it was assumed that the total pressure was constant across the passage, which, since this is nearly the case, has a minor affect on the derived H distribution. More importantly, as already seen (Fig. 110), the streamwise velocity profiles for the two cases are completely different, making it difficult to compare the H values. Along the inner wall, for example, it appears that the maximum value of H (~ 1.47) is significantly less than for the 2D axisymmetric flow, but some of this difference is due to the fact that the velocity at compressor exit is relatively high adjacent to the wall, with lower values away from the wall. Similarly, along the outer wall, the velocity adjacent to the wall is higher, giving rise to lower H values.

Despite the limitations, the lower H values obtained along the inner wall of the S-shaped duct downstream of the compressor may be highly significant. As a simple measure of the state of the boundary layer, it can be concluded that the presence of the compressor blade wakes has a beneficial effect on the flow, reducing the likelihood of separation occurring along the inner wall. This has significant implications for the design of gas turbine S-shaped ducts, since, in comparison to an acceptable design with axisymmetric flow, it means that a more highly loaded duct can be operated successfully. Along with

the differences in the velocity profiles, and the lower inner wall $\partial p / \partial s$, it is interesting to note that some of the beneficial effect associated with the presence of the compressor may be due to momentum transport within the stator blade wake. By examining the secondary velocity vectors at $x/L = 0.25$ (Fig. 116), it can be seen that there is a relatively large movement of fluid towards the inner wall within the wake, due to the fact that the cross-passage pressure gradient within the first bend, which exists to turn the mean flow, is able to accelerate the slower moving wake fluid inwards by a greater amount than the surrounding flow. Although there is a total pressure deficit in the wake, its streamwise velocity is higher than that in the boundary layer adjacent to the wall and, in moving towards the wall, will add energy to the near-wall flow.

4.3.2 Turbulence Data

Downstream of the single stage compressor, the 3-component LDA system was used to measure the Reynolds stresses at S-shaped duct inlet.

4.3.2.1 S-shaped Duct Inlet Conditions

At each point in the area traverse, the Reynolds stresses were obtained statistically from the temporal variation of orthogonal velocity components. Since some of the velocity variation was due to the periodic passing of the rotor wakes, together with the turbulent fluctuations, the double velocity correlations obtained are best described as pseudo Reynolds stresses, describing the pseudo steady behaviour of what is really an unsteady flow. As the LDA was able to measure the instantaneous velocity, the samples obtained randomly over a finite period of time contained information relating to the rotor. For each sample, however, the relative position of the rotor was unknown, and no attempt was made to obtain the circumferential variation of velocity in the rotating frame of reference.

To begin describing the Reynolds stresses, the variation of turbulent kinetic energy (k) has been obtained. In Figure 117, it can be seen that k is lowest within the core region, between the wakes and boundary layers, with a fairly constant value of $\sim 0.0012 U_{\text{Mean}}^2$, corresponding to a turbulence intensity of $\sim 0.035 U_{\text{Mean}}$. Due to the periodic rotor wakes, however, this is much larger than the turbulence level associated with the core region at compressor inlet ($\sim 0.7\%$). Across the passage, the stator blade wake is clearly visible as a region of elevated k , reaching $\sim 0.010 U_{\text{Mean}}^2$ in the centre of the wake at mid-height. Adjacent to the inner wall, the level of k in the wake is above that of the annulus wall boundary layer, which, between the wakes, has a similar radial distribution to the 2D axisymmetric case (Fig. 45). In contrast, adjacent to the outer wall, the level

of k within the wake is very high, and, in between, the level across the boundary layer is much higher than in the 2D axisymmetric flow. Undoubtedly, the rotor tip clearance is responsible for this behaviour, in which the highly turbulent flow produced by leakage over the tip of the rotor blade results in a high level of k in the corner of the stator blade passage, between the suction surface and the outer wall, which reaches a peak value of $\sim 0.032 U_{\text{Mean}}^2$.

For the Reynolds stresses, the variation of each component is different, and has been presented separately; \overline{uu} (Fig. 118), \overline{vv} (Fig. 119), \overline{ww} (Fig. 120), \overline{uw} (Fig. 121), \overline{vw} (Fig. 122) and \overline{uv} (Fig. 123). In Figures 118-120, the relative contribution of the three normal stresses to the turbulent kinetic energy can be seen. In the core region, the three components are of similar magnitude ($\approx 0.0008 U_{\text{Mean}}^2$, ± 0.0002), with $\overline{uu} \approx \overline{ww} > \overline{vv}$. As with k , the normal stresses increase within the boundary layers and, to a greater extent, the wake. Furthermore, the relative magnitude of the normal stresses varies considerably within these regions. In between the wakes, for example, the magnitude and distribution of the normal stresses are similar across the inner wall boundary layer. Thus, although k was similar to the 2D axisymmetric case, the normal stresses are much more nearly isotropic, with $\overline{uu} \approx \overline{ww} > \overline{vv}$. In contrast, for the outer wall boundary layer, the magnitude of each normal stress is very different, with $\overline{uu} > \overline{ww} > \overline{vv}$. Within the wake, the normal stresses all increase, especially towards the outer wall. Along with differences in the magnitude of the peak stress, it is clear that the position of the peak is also different for each component, as is the distribution through the wake. For example, \overline{uu} appears to increase on either side of the wake, whereas the other two components show only a single peak.

In Figures 121-123, it can be seen that \overline{uw} is most significant in the wake region, \overline{uv} is most important in the boundary layers, and, although the magnitude of \overline{vw} is relatively small, it is by no means constant. Unlike the normal stresses, however, all three shear stress components are effectively zero within the core region. Through the wake, the streamwise velocity varies in the circumferential direction, and, like $-\partial U / \partial \theta$, \overline{uw} is positive on the side of the wake originating from the pressure surface of the stator blade, and negative on the other, reaching $\pm 0.004 U_{\text{Mean}}^2$ at mid-height. Closer to the outer wall, in the region where the normal stresses are very high, the variation of \overline{uw} is even larger ($\pm 0.01 U_{\text{Mean}}^2$). Although smaller, and therefore not apparent in the contour plots, the other two shear stresses exist within the wake, between the boundary layers, with \overline{uv} positive on either side of the wake and reducing in the middle, and \overline{vw} becoming negative only on the suction side of the wake. Similarly, all three shear stresses exist within the boundary layers. Adjacent to the inner wall, between the wakes, the magnitude of \overline{uv} is similar to the 2D axisymmetric case (Fig. 42), which is starting to

reduce due to the convex curvature, but, like $-\partial U/\partial n$, the distribution of \bar{uv} does not increase steadily towards the wall. Across the inner wall boundary layer, the other two shear stresses are much smaller, but they do exist and are predominantly positive, with a quite complicated variation. In contrast, within the outer wall boundary layer between the wakes, all three shear stresses are important, due to a combination of the concave curvature and the rotor tip clearance flow. Midway between the wakes, \bar{uv} reaches a peak of $-0.006 U_{\text{Mean}}^2$ adjacent to the wall, more than twice that of the 2D axisymmetric case, and the other two components both reach about half this value, having been negative over the outer part of the boundary layer.

4.4 Concluding Remarks

The experimental results discussed in this chapter provide a detailed understanding of the physical behaviour of the flow through an annular S-shaped duct. It was seen that the strong adverse pressure gradient along the inner wall reduced the wall shear stress, but boundary layer separation did not occur (Sect. 4.2.2.4). The axisymmetric flow was complex, with the rapidly varying streamwise pressure gradients and streamline curvature having a significant effect on the flow. Along with the primary shear strain rate, the extra strain rate due to streamline curvature affects Reynolds stress production (Sect. 4.2.4.4), and, together with the pressure gradient, the resultant shear stress distribution affects the mean velocity (Sect. 4.2.4.5). In addition, the total pressure variation was derived from the shear stress gradient, and found to be in excellent agreement with the directly measured data (Sect. 4.2.4.3). The overall total pressure loss through the duct was relatively low, and some regions of increasing total pressure were observed. Moreover, the rate at which the total pressure reduces in the streamwise direction was found to be lower downstream of the S-shaped duct.

With a single stage compressor upstream of the S-shaped duct, the presence of the blade wakes had a beneficial effect on the flow (Sect. 4.3.1.4). Within the first bend, there was a relatively large movement of wake fluid towards the inner wall, which, together with other factors, helped prevent the boundary layer from separating. Moreover, the total pressure loss within the boundary layers was not increased substantially by the wakes.

Having presented the measurements obtained in a representative S-shaped duct, the main objective of the investigation has been satisfied. However, since the detailed and comprehensive data is of use as a test case for CFD methods, the remaining chapters in this thesis describe work that was undertaken to assess the accuracy of standard prediction techniques.

CHAPTER 5 COMPUTATIONAL APPROACH

	Page
5.1 Introduction	165
5.1.1 Review of Related Work	166
5.1.1.1 Turbulence Model Development	166
5.1.1.2 Relevant Example Predictions	169
5.1.1.3 Conclusions from the Review	171
5.1.2 Scope and Aims of the Present CFD Calculations	172
5.2 Turbulence Models	172
5.2.1 Eddy-viscosity Models	173
5.2.1.1 The $k-\epsilon$ Turbulence Model	174
5.2.2 Reynolds Stress Transport Equation Turbulence Models	175
5.2.2.1 Description of the Terms	175
5.2.2.2 Summary of Model and Constants Used	178
5.3 Calculations Undertaken	179
5.3.1 Solution Technique	179
5.3.2 Geometry and Grid	181
5.3.3 Boundary Conditions	182
5.3.4 Post-processing and Presentation of Results	183

The methods used to predict the turbulent flow studied experimentally are considered in this chapter. Computational fluid dynamic (CFD) methods are commonly used nowadays to predict flow behaviour and, therefore, current state-of-the-art CFD techniques have been used to calculate the flow in the present annular S-shaped duct. The steady-state behaviour of incompressible turbulent flow can be predicted by solving the Reynolds-averaged Navier-Stokes equations, but, since these do not form a closed set, a turbulence model is required in order to obtain the unknown Reynolds stresses. As part of the present investigation, the 2D axisymmetric flow through the S-shaped duct has been predicted using standard $k-\epsilon$ and Reynolds stress transport equation turbulence models, and the equations were solved using a finite volume method and a structured curvilinear grid. In general, errors can arise due to the numerical approximations used in the computational procedure, but, for the 2D calculations reported here, it is the turbulence model which dictates the overall accuracy since grid-independent solutions could be obtained. The work reported in this thesis has concentrated on establishing the turbulence model performance in the axisymmetric case, and no attempt has been made to extend the predictions to the 3D flow arising with the more realistic inlet conditions.

5.1 Introduction

Over recent years computers have grown larger and more powerful, allowing CFD to be used to solve many aerodynamic problems. With the increase in computing capacity, it has been possible to solve ever more complex problems, and rapid developments have enabled industry to benefit from the use of CFD in the aerodynamic design of practical components. Although the ultimate proof of a new design is still the experimental rig or engine test, the growing use of CFD has dramatically reduced the cost of developing the product. As the accuracy of the methods increases, and as confidence in their use grows, so the benefits will continue to be realised.

The detailed measurements in a representative S-shaped duct obtained during this investigation provide a suitable test case for assessing the accuracy of CFD methods. The experimental results presented in Chapter 4 show that even the 2D axisymmetric flow behaviour is complex, with the combined influence of the rapidly varying pressure gradient and the streamline curvature greatly affecting the flow. Most significantly, the Reynolds stresses were seen to exhibit a complex behaviour. Since these are provided by the turbulence model, an accurate prediction of the flow is only likely to result from a model which properly captures the physical behaviour of the Reynolds stresses.

5.1.1 Review of Related Work

In order to predict the behaviour of viscous flow, it is necessary to solve the Navier-Stokes equations. The world's most powerful computers are able to obtain an exact solution of these equations, using a technique known as Direct Numerical Simulation (DNS). This allows the instantaneous motion of a particular flow to be studied in detail, and the statistical (time-average) information extracted from such simulations has provided hitherto unavailable information on turbulent flow, particularly in the near-wall region. However, the huge computational effort involved presently limits the simulations to relatively simple geometries and fairly low Reynolds numbers (e.g., Spalart^[156], Kim et al.^[83], Moser and Moin^[108]). An alternative approach to DNS is Large Eddy Simulation (LES), which solves for the unsteady behaviour of the large eddies only. By using a model to represent the behaviour of the sub-grid scale turbulence, the most significant part of the turbulent motion can be resolved on the finest meshes affordable on commonly available computers. Whilst reasonably high Reynolds number flows can be computed, the technique is still restricted to relatively simple geometries.

Whilst DNS and LES are excellent tools for turbulence research, the prediction of practical engineering flows requires yet another approach. For incompressible turbulent flow, it is common practice to time-average the Navier-Stokes equations, such that only the steady-state behaviour is described. However, because of the appearance of the double fluctuating velocity correlations known as the Reynolds stresses ($\overline{u_i u_j}$), it is then not possible to solve these equations without the use of a turbulence model.

In this brief review, turbulence models relevant to the prediction of the flow in an annular S-shaped duct are considered. Following an examination of the main developments that have occurred, various relevant example predictions are discussed, in which the models have been used to predict similar flow features to those found in the present investigation.

5.1.1.1 Turbulence Model Development

Over the years there have been many publications relating to the development of turbulence models. Although a detailed review of this literature is unnecessary for the present investigation, it is worth citing several of the most pertinent examples. Reynolds^[125] has provided a general overview of CFD and turbulence modelling, and Bradshaw^[19] assessed the predictive capability for various complex flow situations. With a particular emphasis on compressible flow, Marvin^[103] considered external aerodynamics, and gave many examples of such predictions. In overviews of the

present state of second-moment closure, Launder^[88, 89] advocated this approach over eddy-viscosity based models, demonstrating the superior accuracy of predictions that included allowance for Reynolds stress transport. Moreover, Launder^[90] pointed out that the main advantage of second-moment closure was that the stress-strain intercoupling occurring in the exact production terms was able to account for the sensitivity of the turbulence to secondary (or extra) strain rates (which is of significance for S-shaped duct flows). Whilst Leschziner^[95] again emphasised that second-moment closure was able to capture the strong response of the turbulence to streamline curvature, it was noted that several defects were still present in the existing models. In addition, Speziale^[159] and Hanjalic^[65] have reviewed transport equation turbulence models in some detail. (Note that a precise definition of the terminology involved here is given in Section 5.2.)

The simplest approach to turbulence modelling is to use Prandtl's mixing-length hypothesis. This involves only an algebraic relationship for the turbulent (or eddy) viscosity (v_t), and, for example, was used by Cebeci and Smith^[30] and Baldwin and Lomax^[6]. Unfortunately, Stock and Haase^[167] showed that serious discrepancies exist between these two models, with the latter over-predicting the shear stress for mild adverse pressure gradient and under-predicting it near separation, which indicates the lack of universality which is inevitable in a purely algebraic turbulence model. With such models, the difficulty of properly accounting for streamline curvature effects has been widely considered. For example, Rastogi and Whitelaw^[123] used a curvature dependent mixing-length turbulence model to predict the flow over 2D curved surfaces. Although some success was achieved, in general it is not possible to capture curvature effects adequately with simple algebraic turbulence models.

Some improvement in predictive accuracy can be obtained by introducing transport effects (i.e., convection and diffusion) into the turbulence model. For example, Bradshaw et al.^[15] developed a method based on a single transport equation for the Reynolds shear stress (\bar{uv}) which was obtained from the turbulent kinetic energy (k) equation using empirical functions. Using this, it was then possible to predict boundary layer flows with a wide range of applied pressure gradients. A similar approach was developed by Johnson and King^[77], who used an ordinary differential equation (derived from the k -equation) to describe the streamwise development of the maximum shear stress. Since the outer layer turbulent viscosity was obtained from this, a significant improvement over simple algebraic models was achieved, for adverse pressure gradient flows in particular, without the cost of solving additional partial differential equations. As another alternative, Baldwin and Barth^[7] used one transport equation for the

turbulent Reynolds number ($k^2/v\epsilon$), which was derived from simplified forms of the standard k and ϵ transport equations.

An increased influence of turbulent transport effects can be gained by solving two extra equations to give the velocity and length scales of the turbulence. This is the basis of the k - ϵ turbulence model, described in Section 5.2.1, which uses the turbulent viscosity ($C_\mu k^2/\epsilon$) to obtain the Reynolds stresses from the eddy-viscosity assumption. Although the approach originally developed by Jones and Launder^[78] is still widely used, there have been many attempts to overcome its weakness in relation to the prediction of curved flow. For example, Chung et al.^[36] developed a curvature dependant model for the turbulent transport of k , using a simple isotropic gradient diffusion model with a composite time scale, based on k/ϵ and a curvature time scale. Similarly, Launder et al.^[91] proposed a curvature dependant modification to the dissipation equation based on a turbulent (time scale based) Richardson number. Indeed, many examples of Richardson number based curvature correction can be found, e.g., Park and Chung^[113], Cheng and Farokhi^[33] and Sung et al.^[169].

As an alternative to all these approaches, the eddy-viscosity assumption can be avoided altogether and the Reynolds stresses obtained from their respective transport equations. Even before adequate computing power was available, Reynolds stress turbulence models had been suggested (e.g., Chou^[35], Davidov^[43] and Rotta^[131]), but the most significant developments occurred in the 1970s (e.g., Daly and Harlow^[41], Shir^[141], Hanjalic and Launder^[66], Launder et al.^[92] and Gibson and Launder^[59]). Although the modelling assumptions involved in these turbulence models still limits their applicability, solving transport equations for the Reynolds stresses does give a substantial improvement over eddy-viscosity models, especially for complex flows.

Much work has been undertaken to develop and improve the models used for individual terms in the Reynolds stress transport equations, and by far the most important area of development has been the pressure-strain (ϕ_{ij}) model. For example, Hong and Murthy^[70] considered the behaviour of ϕ_{ij} in curved wall boundary layer flows, and Shih and Lumley^[138] examined various models for ϕ_{ij} in the light of DNS data obtained for homogeneous free shear flow (although these findings were disputed by Speziale and Gatski^[161]). Speziale et al.^[160] developed a non-linear model for ϕ_{ij} , which was assessed in homogeneous turbulence, Fu et al.^[57] proposed a cubic model, and Johansson and Hallbäck^[74] developed a model using rapid distortion theory. For the near-wall ϕ_{ij} component, Craft and Launder^[40] proposed a modified model which overcame the deficiency of the Gibson and Launder^[59] wall correction model in impinging flows, and

Launder and Tselepidakis^[94] tried to reduce the dependency of wall correction models on the distance from the wall.

5.1.1.2 Relevant Example Predictions

In order to assess the accuracy of turbulence models, predictions have often been compared with experimental data. Since some of the example predictions available in the literature have investigated flows involving pressure gradient and/or curvature, they are relevant to the present investigation. The need to provide suitable test cases for the assessment of CFD methods was established long ago (e.g., Kline et al.^[86]), and when different techniques are used to predict the same experimental test case (e.g., Ryhming et al.^[133]) the limitations of the various turbulence models can be detected.

Eghlima and Kleinstreuer^[52] predicted turbulent boundary layer flow over 2D bodies with a mixing-length model, and found that the inclusion of the cross-stream momentum equation (usually neglected for boundary layer calculations) was essential for the accurate prediction of curved flow. In various 2D flows, Wheeler and Johnston^[179] assessed zero and one-equation turbulence models, and found that the magnitude of the shear stress implied by the mixing-length model was less accurate than that of the transport equation model. On comparing various models under adverse pressure gradient conditions, Menter^[105] obtained good results from all but the algebraic model. The best overall agreement with the experimental test cases was obtained from the Johnson and King^[77] model, which was in agreement with the findings of Leung and Squire^[96]. Using a curvature dependant algebraic shear stress model to close the curved flow momentum equations, So and Mellor^[153] obtained good agreement with their own experimental data obtained in a highly curved convex flow, but the method only produced a fair prediction of the spanwise average flow field over the concave wall.

Several relevant investigations have been undertaken using the k- ϵ turbulence model. For example, both Jones and Launder^[79] and Launder and Spalding^[93] predicted various flows to demonstrate its general applicability, in comparison to mixing-length models, and obtained some agreement with experimental data. When predicting curved flow, Rodi and Scheuerer^[128] found that the standard model, and also three versions extended to account for the effects of streamline curvature, were not as good as the algebraic stress model of Gibson^[58], and, with adverse pressure gradient, Rodi and Scheuerer^[129] found that the performance of the k- ϵ model was also poor. Similarly, De Henau et al.^[44] examined flows with strong curvature and pressure gradient. In comparison to the standard k- ϵ model, they found that the modified model of Hanjalic and Launder^[67], with the dissipation rate equation sensitised to the normal stresses, performed well in plane adverse pressure gradient flow leading to separation, but, because of the

fundamental inadequacy of the turbulent viscosity formulation, both models performed poorly in a curved flow. In addition, Richmond and Patel^[127] predicted curved flow using standard and curvature sensitive models, including the two-layer approach of Chen and Patel^[32]. They found that all the models over-predicted the convex wall shear stress, and under-predicted the concave, and that the curvature sensitive models only produced a slight improvement over the standard model.

In order to demonstrate the improved accuracy of Reynolds stress models, many relevant investigations have been reported in the literature. In complex flows involving pressure gradient and curvature, it is clear that the main limitation of the simpler models is the use of the eddy-viscosity assumption itself. This was demonstrated theoretically by Eskinazi and Erian^[55], who showed that this assumption was invalid in curved flow because it could not account for the negative turbulent kinetic energy production that must occur between the position of zero shear stress and position of zero total strain. Furthermore, Irwin and Arnot Smith^[72] demonstrated that curvature effects were captured by a Reynolds stress turbulence model because of the extra curvature terms in the Reynolds stress transport equations, and that the same model was relatively insensitive to streamwise acceleration.

Using the Gibson and Launder^[59] Reynolds stress model, Gibson et al.^[60] predicted convex curved wall boundary layer flow. They found that this model consistently exaggerated the effect of strong curvature by predicting a sign reversal in the shear stress over the outer part of the boundary layer, which was thought to be due to the slow response of the ϵ -equation, in comparison to that of the Reynolds stresses, to changes produced by the mean strain rate. With the same model, Gibson and Rodi^[61] predicted a highly curved mixing layer, and found that it successfully reproduced the main features of the flow.

Similarly, Jones and Manners^[81] used the Gibson and Launder^[59] model to predict the fully developed flow through a 40° outwardly canted annular diffuser with axial inlet and exit. In comparison to k- ϵ , the Reynolds stress transport equation turbulence model accurately reproduced the observed features of the flow, including pressure gradient and curvature effects, which could not be adequately represented by the eddy-viscosity model. The stress transport model was least accurate in the diffusing section of the flow, which, it was thought, was due to the use of wall functions and/or the wall component of the pressure strain model.

5.1.1.3 Conclusions from the Review

Overall, this literature review has concentrated on turbulence modelling. It has identified the various approaches taken to close the Navier-Stokes equations, and covered the main developments that have taken place in the relevant areas. Moreover, the application of these various models to the prediction of related flow situations has been examined, and conclusions about their performance drawn.

From the review, it is clear that zero and one equation turbulence models are widely used because of their simplicity and robustness. However, their reliance on a prescribed length scale limits their use to simple geometries with wall bounded shear layers, so that they cannot easily be applied to more complex geometries and flows with free shear layers present. In general, they perform badly in non-equilibrium flow situations, but, with curvature correction of the length scale, zero and one equation models can predict the effects of mild streamline curvature.

Much attention in the literature has focused on the $k-\epsilon$ turbulence model, which is the most general eddy-viscosity model. Since it does not rely on an arbitrary length scale, its main advantage over simpler models is that it can be used to predict the flow in any geometry, with any kind of shear layer present. By accounting for the transport of k and ϵ , the turbulent viscosity tends to be predicted reasonable well, but the model is limited by the eddy-viscosity assumption. In many situations, and especially when streamline curvature is present, the Reynolds stresses cannot be related directly to the mean strain rates, and, in these situations, inaccurate Reynolds stresses result from the eddy-viscosity model. Since the $k-\epsilon$ turbulence model provides a relatively simple and cost effective prediction of turbulent flow, much effort has been put into overcoming this limitation. For example, the prediction of curved flow can be improved by correcting the turbulent viscosity depending on the curvature.

In general, however, the most accurate prediction of turbulent flow is obtained by using a Reynolds stress transport equation turbulence model. Whilst this involves increased numerical complexity and computational effort, it is clear from the literature that these models are better placed to predict the physical effects of curvature and pressure gradient, particularly when the flow is not in equilibrium. Since the transport of the individual Reynolds stresses is being considered and, most importantly, the Reynolds stress production term is exact, such predictions tend to be more accurate than eddy-viscosity models. In solving the Reynolds stress transport equations, however, it is necessary to model various terms, and, although these are at a higher order, these models can limit the accuracy. In highly curved flows, for example, the standard pressure-strain and turbulent transport models may be inappropriate, and the dissipation

rate equation too simplistic, although there have been recent developments to overcome the limitations.

Although industry would probably beg to differ, the overriding view of the research community is that the benefits of using Reynolds stress transport equation models now significantly outweigh the cost of their use.

5.1.2 Scope and Aims of the Present CFD Calculations

Having obtained comprehensive and detailed measurements describing the 2D axisymmetric turbulent flow through a representative annular S-shaped duct, the objective was to use standard CFD techniques to predict the same flow. It was clear from the above review that a Reynolds stress transport equation turbulence model was likely to provide the most accurate prediction, but, in order to provide an objective assessment, it was decided to use the $k-\epsilon$ model to provide a comparison and demonstrate the anticipated weakness of the eddy-viscosity assumption.

In assessing these turbulence models, it is important to obtain good quality predictions for comparison with experimental data. It was necessary, therefore, to ensure that numerical error was insignificant, which would be relatively easy to achieve since it was decided to perform only 2D calculations. Unlike 3D calculations, it would be possible to ensure that the results were grid independent within the bounds of available computer memory. In addition, to ensure that the predictions could be compared with the experimental results, it was important to use measured data to define the inlet conditions. Although ϵ could only be inferred, all the mean velocity and Reynolds stress components were obtained upstream of the S-shaped duct, and so the calculations could be run with these defined at inlet to the computational domain.

At the time the present investigation was undertaken, a suitable code, written by Manners^[100] for Rolls-Royce, was available with the necessary turbulence models. Based on the work of Jones and Manners^[81], it was decided to compare the Gibson and Launder^[59] Reynolds stress transport equation model with the standard Jones and Launder^[78] $k-\epsilon$ model.

5.2 Turbulence Models

In order to solve the momentum equations (Eq. A3.2), a turbulence model is required to obtain the unknown Reynolds stresses ($\overline{u_i u_j}$). One way of achieving this is to relate $\overline{u_i u_j}$ directly to the mean flow using an eddy-viscosity model. Although the turbulent

velocity and length scales used to evaluate the turbulent viscosity (v_t) can be obtained in a number of ways, the most common approach is to use the turbulent kinetic energy (k) and its dissipation rate (ϵ). In the k - ϵ turbulence model, k and ϵ are obtained by solving modelled transport equations for these properties.

Alternatively, $\overline{u_i u_j}$ can be obtained by solving all the Reynolds stress transport equations; an approach often referred to as second-moment closure. Although it is still necessary to model various terms in the exact transport equations, the production term can be obtained exactly. Moreover, since the transport of the individual Reynolds stresses is being considered, stress transport models can provide a better prediction of the behaviour of Reynolds stresses in complex flows, in which significant changes to the mean strain rates occur. As will become apparent, the generation and suppression of the Reynolds stresses due to streamline curvature is captured naturally by this approach. Along with transport equations for the Reynolds stresses, it is also necessary to solve a transport equation for the dissipation rate of turbulent kinetic energy.

In the following sections, the k - ϵ and Reynolds stress transport equation turbulence models are presented, and the modelling assumptions contained in these are outlined. For a more complete review of these and other models see, for example, Speziale^[159], Launder^[90] or Hanjalic^[65].

5.2.1 Eddy-viscosity Models

The assumption underlying all models of this kind is that the Reynolds stresses can be directly related to the mean strain rates. A simple linear eddy-viscosity model, first suggested by Boussinesq, was developed by analogy to the viscous stress in the diffusion term of Eq. A3.2, with the addition of an extra term to ensure that the sum of the normal stresses was equal to $2k$, i.e.,

$$\overline{u_i u_j} = -v_t \left(\frac{\partial U_i}{\partial x_j} + \frac{\partial U_j}{\partial x_i} \right) + \frac{2}{3} k \delta_{ij} \quad 5.1$$

In this way it is assumed that the turbulent transport of momentum can be modelled as a diffusion process, in a similar way to the viscous diffusion of momentum, and the turbulent viscosity (v_t) is used as an isotropic diffusion coefficient. Unlike molecular viscosity (v), which is a fluid property, v_t will vary throughout a turbulent flow, and needs to be determined if Eq. 5.1 is to be used to close the momentum equations. Like v , v_t has the dimensions of length \times velocity, which can be thought of as the length and velocity scale of the turbulent motion.

5.2.1.1 The k- ϵ Turbulence Model

In the k- ϵ turbulence model, the turbulent viscosity (v_t) required for Eq. 5.1 is obtained from the turbulent kinetic energy (k) and its dissipation rate (ϵ), i.e.,

$$v_t = C_\mu \frac{k^2}{\epsilon} \quad \dots\dots 5.2$$

This equation is derived from dimensional analysis, where $k^{1/2}$ is the velocity scale and $k^{1/2}/\epsilon$ is the length scale of the turbulence, and C_μ is a constant. In order that turbulent viscosity can respond to changes in the mean flow, transport equations are used to determine both k and ϵ , overcoming the limitations of simpler eddy-viscosity models. In this way also, there is no reliance on a prescribed length scale distribution, creating a truly general turbulence model which can be applied in any flow situation.

To solve the exact transport equations for k (Eq. A3.7) and ϵ (Eq. A3.8), it is necessary to replace various terms with models relating to known quantities. In the k-equation, for example, the Reynolds stresses appearing in the production term are replaced by those given by Eq. 5.1. The remaining modelling assumptions, provided by Jones and Launder^[78], give rise to the standard k and ϵ transport equations for high Reynolds number flows,

$$\frac{\partial}{\partial x_i} (U_i k) = P - \epsilon + \frac{\partial}{\partial x_i} \left(\left\{ v + \frac{v_t}{\sigma_k} \right\} \frac{\partial k}{\partial x_i} \right) \quad \dots\dots 5.3$$

and,

$$\frac{\partial}{\partial x_i} (U_i \epsilon) = \frac{\epsilon}{k} (C_{\epsilon 1} P - C_{\epsilon 2} \epsilon) + \frac{\partial}{\partial x_i} \left(\left\{ v + \frac{v_t}{\sigma_\epsilon} \right\} \frac{\partial \epsilon}{\partial x_i} \right) \quad \dots\dots 5.4$$

where,

$$P = v_t \left(\frac{\partial U_i}{\partial x_j} + \frac{\partial U_j}{\partial x_i} \right) \frac{\partial U_i}{\partial x_j} \quad \dots\dots 5.5$$

The standard model constants, given by Launder and Spalding^[93], were used for k- ϵ predictions reported in this thesis, i.e.,

$$C_\mu = 0.09, \quad C_{\epsilon 1} = 1.44, \quad C_{\epsilon 2} = 1.92, \quad \sigma_k = 1.0, \quad \sigma_\epsilon = 1.3.$$

The Launder and Spalding^[93] wall function approach was used in the near-wall region, as described by Manners^[100].

5.2.2 Reynolds Stress Transport Equation Turbulence Models

The fundamental weakness of eddy-viscosity models is the assumption that the Reynolds stresses are directly related to the mean strain rates. For complex flows, in which significant changes to the mean strain rates occur and, in particular, for rapidly varying conditions, the actual Reynolds stress will not respond in this way. Rather, as suggested by the exact transport equations (Eq. A3.6), the various strain rates, interacting with the existing Reynolds stresses, will affect the rate at which the Reynolds stresses are produced, and thereby affect their rate of change.

To solve the Reynolds stress transport equations, it is necessary to replace some of the exact terms with models relating to known quantities. The Reynolds stresses, therefore, are obtained from their respective modelled transport equations, which can be written as,

$$C_{ij} = P_{ij} + T_{ij} + V_{ij} + \Pi_{ij} + \epsilon_{ij} \quad \dots\dots 5.6$$

For the Reynolds stress calculations reported in this thesis, the Gibson and Launder^[59] modelled form of the transport equations were used.

5.2.2.1 Description of the Terms

Convection

$$C_{ij} = \frac{\partial}{\partial x_k} (U_k \overline{u_i u_j}) \quad \dots\dots 5.7$$

This term requires no modelling.

Production

$$P_{ij} = - \left(\overline{u_i u_k} \frac{\partial U_j}{\partial x_k} + \overline{u_j u_k} \frac{\partial U_i}{\partial x_k} \right) \quad \dots\dots 5.8$$

This term requires no modelling.

Turbulent Transport

$$T_{ij} = - \frac{\partial}{\partial x_k} (\overline{u_i u_j u_k}) \quad \dots\dots 5.9$$

This term has to be modelled, and there are several models available. They are all based on the gradient diffusion hypothesis, which assumes that the triple velocity correlations

are directly related to gradients of the Reynolds stresses. A simple gradient diffusion model, proposed by Shir^[14], with an isotropic turbulent diffusion coefficient was used,

$$T_{ij} = \frac{\partial}{\partial x_k} \left(C_s \frac{k^2}{\varepsilon} \frac{\partial \bar{u}_i u_j}{\partial x_k} \right) \quad \dots \dots 5.10$$

Viscous Diffusion

$$V_{ij} = \frac{\partial}{\partial x_k} \left(\nu \frac{\partial \bar{u}_i u_j}{\partial x_k} \right) \quad \dots \dots 5.11$$

This term requires no modelling, and is often neglected at high Reynolds number since it is small.

Velocity Pressure Gradient Interaction

$$\Pi_{ij} = -\frac{1}{\rho} \left(\bar{u}_i \frac{\partial p'}{\partial x_j} + \bar{u}_j \frac{\partial p'}{\partial x_i} \right) \quad \dots \dots 5.12$$

This term has to be modelled. The model is derived by partitioning the exact term into two components,

$$\Pi_{ij} = \underbrace{\frac{1}{\rho} \left(p' \frac{\partial \bar{u}_i}{\partial x_j} + p' \frac{\partial \bar{u}_j}{\partial x_i} \right)}_{\text{pressure-strain}} - \underbrace{\frac{1}{\rho} \left(\frac{\partial p' \bar{u}_i}{\partial x_j} + \frac{\partial p' \bar{u}_j}{\partial x_i} \right)}_{\text{pressure-transport}} \quad \dots \dots 5.13$$

The pressure transport component is usually considered to be adequately represented by the turbulent transport model (i.e., Eq. 5.10). However, the pressure-strain correlation (ϕ_{ij}) is of crucial importance and needs further explanation. For incompressible flow, ϕ_{ij} is traceless (i.e., $\phi_{kk}=0$) and therefore acts to redistribute the Reynolds stresses.

The exact expression for pressure-strain, derived by Chou^[35], shows that ϕ_{ij} can be split into three components, each reflecting a different physical process, i.e.,

$$\phi_{ij} = \phi_{ij}^{(1)} + \phi_{ij}^{(2)} + \phi_{ij}^{(w)} \quad \dots \dots 5.14$$

A simple model for the 'return-to-isotropy' term ($\phi_{ij}^{(1)}$) was proposed Rotta^[131],

$$\phi_{ij}^{(1)} = -C_1 \frac{\varepsilon}{k} \left(\bar{u}_i \bar{u}_j - \frac{2}{3} \delta_{ij} k \right) \quad \dots \dots 5.15$$

This model acts to equalise the normal stress components and reduce the shear stresses to zero on the basis that non-isotropic homogeneous turbulence, in a free stream with

negligible mean strain rate, will decay to the statistically more probable isotropic state. The rate at which this return-to-isotropy occurs is determined by a characteristic time scale of the turbulence (k/ε) and C_1 , which is taken to be a constant.

For the 'mean strain' component ($\phi_{ij}^{(2)}$), Gibson and Launder^[59] proposed,

$$\phi_{ij}^{(2)} = -C_2 \left(P_{ij} - \frac{2}{3} \delta_{ij} P \right) \quad \dots \dots 5.16$$

This was based on the dominant first term of a model first suggested by Launder et al.^[92], and recognises the influence of the mean strain rate on the redistribution of turbulent energy.

In the proximity of a solid surface, a near-wall model ($\phi_{ij}^{(w)}$) is necessary to account for the modification that occurs in the redistribution of turbulent energy between the components. In general, the fluctuations perpendicular to the surface, which would otherwise receive energy from the streamwise component, tend to reduce in magnitude. To produce a model for $\phi_{ij}^{(w)}$, Gibson and Launder^[59] further developed a model proposed by Shir^[141] as a near-wall addition to $\phi_{ij}^{(1)}$ by applying the same reasoning to $\phi_{ij}^{(2)}$,

$$\begin{aligned} \phi_{ij}^{(w)} = & \left\{ C'_1 \frac{\varepsilon}{k} \left[\overline{u_k u_l} n_k n_l \delta_{ij} - \frac{3}{2} \left(\overline{u_i u_k} n_j n_k + \overline{u_j u_k} n_i n_k \right) \right] \right. \\ & \left. + C'_2 \left[\phi_{kl}^{(2)} n_k n_l \delta_{ij} - \frac{3}{2} \left(\phi_{ik}^{(2)} n_j n_k + \phi_{jk}^{(2)} n_i n_k \right) \right] \right\} \left(\frac{k^{\frac{1}{2}} a^{\frac{1}{2}}}{\varepsilon} \frac{1}{d^{(w)}} \right) \end{aligned} \quad \dots \dots 5.17$$

In this model, n_i are the components of a unit vector (\underline{n}) normal to the surface, and, in order to apply this wall-correction in near-wall regions only, it uses the ratio of the turbulent length scale ($\ell = k^{\frac{1}{2}}/\varepsilon$) to the normal distance from the wall ($d^{(w)}$), which reduces to zero away from the wall. To produce a function which is unity in the wall region, this ratio is divided by its near-wall equilibrium ($P = \varepsilon$) value, equal to $\kappa/a^{\frac{1}{2}}$, where 'a' is a constant equal to the shear stress to turbulent kinetic energy ratio ($|\overline{uv}|/k$) in this region.

Dissipation

$$\varepsilon_{ij} = -2\nu \frac{\partial u_i}{\partial x_k} \frac{\partial u_j}{\partial x_k} \quad \dots \dots 5.18$$

This term is modelled by assuming that the dissipation is isotropic, i.e.,

$$\varepsilon_{ij} = -\frac{2}{3} \delta_{ij} \varepsilon \quad \dots \dots 5.19$$

The dissipation rate of turbulent kinetic energy (ϵ) is obtained from a modelled form of its exact transport equation (Eq. A3.8), developed by Hanjalic and Launder^[66],

$$\frac{\partial}{\partial x_i} (U_i \epsilon) = \frac{\epsilon}{k} (C_{\epsilon 1} P - C_{\epsilon 2} \epsilon) + \frac{\partial}{\partial x_i} \left(C_\epsilon \frac{k^2}{\epsilon} \frac{\partial \epsilon}{\partial x_i} \right) \quad \dots \dots 5.20$$

As in the Reynolds stress transport equations, a simple gradient diffusion model was used for the turbulent transport term in the ϵ -equation.

5.2.2.2 Summary of Model and Constants Used

$$\begin{aligned} \frac{\partial}{\partial x_k} (U_k \overline{u_i u_j}) &= P_{ij} - \frac{2}{3} \delta_{ij} \epsilon + \frac{\partial}{\partial x_k} \left(C_s \frac{k^2}{\epsilon} \frac{\partial \overline{u_i u_j}}{\partial x_k} \right) \\ &\quad - C_1 \frac{\epsilon}{k} \left(\overline{u_i u_j} - \frac{2}{3} \delta_{ij} k \right) - C_2 \left(P_{ij} - \frac{2}{3} \delta_{ij} P \right) + \phi_{ij}^{(w)} \end{aligned} \quad \dots \dots 5.21$$

and,

$$\frac{\partial}{\partial x_i} (U_i \epsilon) = \frac{\epsilon}{k} (C_{\epsilon 1} P - C_{\epsilon 2} \epsilon) + \frac{\partial}{\partial x_i} \left(C_\epsilon \frac{k^2}{\epsilon} \frac{\partial \epsilon}{\partial x_i} \right) \quad \dots \dots 5.22$$

where $k = \frac{1}{2} \overline{u_k u_k}$ and $P = \frac{1}{2} \overline{P_{kk}}$ where,

$$P_{ij} = - \left(\overline{u_i u_k} \frac{\partial U_j}{\partial x_k} + \overline{u_j u_k} \frac{\partial U_i}{\partial x_k} \right)$$

and,

$$\begin{aligned} \phi_{ij}^{(w)} &= \left\{ C'_1 \frac{\epsilon}{k} \left[\overline{u_k u_l} n_k n_l \delta_{ij} - \frac{3}{2} (\overline{u_i u_k} n_j n_k + \overline{u_j u_k} n_i n_k) \right] \right. \\ &\quad \left. + C'_2 \left[\phi_{kl}^{(2)} n_k n_l \delta_{ij} - \frac{3}{2} (\phi_{ik}^{(2)} n_j n_k + \phi_{jk}^{(2)} n_i n_k) \right] \right\} \left(\frac{k^{\frac{1}{2}}}{\epsilon} \frac{a^{\frac{3}{2}}}{\kappa} \frac{1}{d^{(w)}} \right) \end{aligned} \quad \dots \dots 5.23$$

The constants used in the pressure-strain model were $C_1 = 1.8$ and $C_2 = 0.6$, and the constants in the near-wall correction were $C'_1 = 0.5$ and $C'_2 = 0.3$, with $a^{\frac{3}{2}}/\kappa = 0.314$. The dissipation rate equation constants used were $C_{\epsilon 1} = 1.45$ and $C_{\epsilon 2} = 1.90$, and the turbulent transport model constants were $C_s = 0.058$ and $C_\epsilon = 0.044$. Wall functions were used in the near-wall region, as described by Manners^[100].

5.3 Calculations Undertaken

As part of the present investigation, the 2D axisymmetric flow through the S-shaped duct has been predicted using the k- ϵ and Reynolds stress transport equation turbulence models described above. The equations were solved using a finite volume method, utilising implicit hybrid differencing and a time-dependent pressure-correction scheme. A boundary-conforming orthogonal curvilinear co-ordinate system was used with grid-oriented velocities and Reynolds stresses, which were staggered to avoid decoupling. Wall functions were used on the solid boundaries, and conditions measured upstream of the S-shaped duct were used to define the inlet conditions.

5.3.1 Solution Technique

In order to solve the transport equations, a finite volume method was used. This was a 3D CFD code written by Manners^[100], which, if required, could also perform 2D axisymmetric calculations. In this particular code, the complete axisymmetric form of each transport equation was transformed to a curvilinear orthogonal co-ordinate system, before being discretised using finite differences taken over a structured grid defining the local co-ordinate directions. Although this approach is complicated by the additional terms arising in the transformed equations, a curvilinear grid has the advantage that it can be made to conform to an arbitrary boundary, provided it is reasonably smooth, and that the boundary treatment is straightforward.

Since the code was used for the calculation of incompressible flow, the numerical solution of the equations was achieved using a pressure-correction method. As the variation of temperature and density are small at low Mach numbers, the pressure, which is important in the momentum balance, cannot be obtained from the equation of state without small numerical errors in the calculated temperature and density having a relatively large effect on the velocity. To avoid this, therefore, pressure-correction methods are used to provide a means of updating the pressure and velocity fields, in such a way that continuity is imposed. Having solved the momentum equations with old pressure values, a pressure correction (δp) is determined from the velocity field, using a pressure correction equation obtained by combining the linearised continuity and momentum equations. As well as updating the pressure, δp is used to determine a velocity correction (δU_i), which allows the velocity field to be updated. So long as the pressure correction equation increments the pressure and velocity fields towards a final solution, the approximations involved in its derivation are not important, since δp tends to zero as the calculation converges.

Although the commonly used SIMPLE pressure correction algorithm (Patankar and Spalding^[114]) was available within the code, the AVPI time-dependent method of Jones and Marquis^[80] was used for the calculations reported in this thesis. By using the time-dependent form of the linearised equations, the pressure correction equation can be formulated in terms of a time step (Δt), such that the conditions at the next time level are obtained from the previous values. Since relaxation is included naturally through the time derivative term, convergence towards a steady-state solution can be guaranteed by choosing a sufficiently small time step; however if Δt is too small an excessive number of time steps are required to reach convergence. For the calculations, a $\Delta t = 0.0005$ s was used (which was ~3% of the time taken for a fluid particle to pass through the computational domain), and convergence was achieved in approximately 500 steps.

In solving the discretised equations, an implicit formulation was adopted with central differencing used for all but the convection terms. The linearised equations were solved sequentially using a line Gauss-Seidel method, for which diagonal dominance of the coefficient matrix is a necessary and sufficient condition for convergence. Although there is no stability restriction with a fully implicit approach, a central difference representation of the convection term can give rise to problems when the cell Peclet number (P_Δ) exceeds two. Since P_Δ is a Reynolds number based on the mean velocity and the cell size in the direction of the velocity component, P_Δ will be much larger than two in the streamwise direction of a high Reynolds number flow. To overcome this problem, Spalding^[158] proposed the hybrid differencing approach, in which central differencing is only used for the convection term when $P_\Delta < 2$. To maintain stability when $P_\Delta > 2$, upwind differencing is used for the convection term and the true diffusion is neglected. Unfortunately, however, this reduces the formal accuracy of the scheme, and effectively introduces numerical diffusion via the first-order truncation error.

For the calculations reported in this thesis, hybrid differencing was used for the convection terms without any significant numerical diffusion. In the present geometry, the use of a curvilinear orthogonal co-ordinate system ensures that the grid and the flow are almost aligned. Although upwind differencing would have been used in the streamwise direction, numerical diffusion was negligible due to the relatively small streamwise gradients and the sufficiently fine grid. Furthermore, in the cross-stream direction where physical diffusion was important, central differences were used by the hybrid scheme because of the low cross-stream velocity (i.e., $P_\Delta < 2$), again ensuring that numerical diffusion was insignificant. In the Reynolds stress transport equations, the source terms were approximated by standard central differences, and no special stabilising techniques were used.

To prevent decoupling, staggered storage locations were used. When all the solution variables are stored at the grid nodes, a central difference evaluation of the pressure gradient term in the momentum equations does not include the value of the pressure at the node itself. Since the pressure can take any value without affecting the velocity, the pressure and velocity fields can decouple, giving rise to a 'checker-board' effect. Whilst this can be prevented by a pressure smoothing technique (e.g., Rhie and Chow^[126]), the approach adopted in the code was to stagger the velocities, to lie half way between the grid points, in the direction of the particular component. Similarly, the Reynolds shear stresses were staggered to prevent them decoupling from the velocity field. As with pressure, a central difference evaluation of the shear stress gradients in the momentum equations, may lead to decoupling, although, because the Reynolds stresses are interrelated, an indirect mechanism for preventing this exists. Nevertheless, whilst the normal stresses, as well as k and ϵ , were stored at the nodes, the shear stresses were staggered twice, once in each direction.

5.3.2 Geometry and Grid

For the method described, a structured boundary-conforming orthogonal curvilinear grid was required. The $x-r$ co-ordinates of this 2D grid (shown in Figure 124) were generated from the S-shaped duct geometry (Table 1). As in the rig, parallel ducts were extended upstream and downstream of the S-shaped duct, but, for the calculations, the inlet plane was set at $x/L = -0.385$ and the exit plane at $x/L = 1.758$. Having chosen the required number of grid lines in the axial and radial directions, a simple algebraic grid was calculated so that, with this as an initial guess, the orthogonal grid could be generated by solving a Laplace equation (e.g., Manners and King^[101]). The points on the boundary were allowed to move along continuous functions, which passed through the discrete points defining the geometry, and the grid points inside the boundary also redistributed themselves until the streamwise and cross-stream grid lines were as orthogonal as possible throughout the entire grid.

For the calculations reported, the grid had 81 (streamwise) \times 101 (cross-stream) points. To ensure that the results were grid-independent, the number of cross-stream grid lines was halved by removing every other line. Whilst it was recognised that changing the distance of the first grid line from the wall could influence the comparison, the solutions obtained with the two grids were almost identical.

5.3.3 Boundary Conditions

To enable the predictions to be compared to the experimental data, the inlet conditions for the calculations were based on the measurements taken upstream of S-shaped duct. However, because of the scatter in the experimental data, and the need to ensure a self-consistent set of conditions, the inlet conditions were actually obtained by running additional calculations in a geometry equivalent to the parallel annular inlet duct. Starting with constant conditions, the boundary layer growth along the walls of the parallel duct was predicted, using both turbulence models. A 2 m long duct with 101x101 grid points was used, so that, at an appropriate point along the duct, the distribution of all the solution variables could be extracted and used directly as the S-shaped duct inlet conditions.

At inlet to the parallel duct, the streamwise velocity was 28.3 m/s, the other two components were set to zero, and the inlet static pressure was assumed to be zero, relative to atmospheric pressure. Although the $\bar{u}\bar{v}$ shear stress could be set to zero, the normal stresses ($\bar{u}_i\bar{u}_i$), the turbulent kinetic energy (k) and its dissipation rate (ϵ) were specified by considering their variation within the core region of the duct. Since the normal stresses were measured at the end of the parallel duct, it was necessary to set the upstream conditions to achieve the measured values. In the core region, k and ϵ decay according to their respective transport equations, which reduce to,

$$U \frac{\partial k}{\partial x} = -\epsilon \quad \dots\dots 5.24$$

and,

$$U \frac{\partial \epsilon}{\partial x} = -C_{\epsilon 2} \frac{\epsilon^2}{k} \quad \dots\dots 5.25$$

These can be solved analytically, and over a distance of 1 m, assuming a constant U of 30 m/s and with $C_{\epsilon 2}=1.92$, the magnitude of k and ϵ depend only on their starting values (k_0 and ϵ_0), i.e., $k = k_0(1+0.031\epsilon_0/k_0)^{-0.09}$ and $\epsilon = \epsilon_0(1+0.031\epsilon_0/k_0)^{-2.09}$. To achieve $k=0.06 \text{ m}^2/\text{s}^2$, it is clear that different combinations of k_0 and ϵ_0 can be used, leading to different ϵ values, e.g.,

$k (\text{m}^2/\text{s}^2)$	$k_0 (\text{m}^2/\text{s}^2)$	$\epsilon_0 (\text{m}^2/\text{s}^3)$	$\epsilon (\text{m}^2/\text{s}^3)$
0.06	0.085	1	0.525
	0.180	10	1.253
	0.504	100	1.677

Since ε was not measured, it was necessary to select k_0 and ε_0 values that were, in some way, reasonably representative. Based on the size of the honeycomb flow conditioner, $k_0 = 0.180$ and $\varepsilon_0 = 10$ were used because these gave a turbulence length scale ($k^{1/2}/\varepsilon$) of 0.0076 m. Although the length scale for the $\varepsilon_0 = 100$ case was also reasonable, the rate of decay of k at the end of the parallel duct was much larger than the measurements of k within the core region of the S-shaped duct suggested. Finally, to achieve the measured $\overline{u_i u_j} = 0.04 \text{ m}^2/\text{s}^2$, the normal stresses at inlet to the parallel duct Reynolds stress calculation were set to $0.120 \text{ m}^2/\text{s}^2$. For both predictions, the converged solutions were examined to determine the most representative position at which to extract the inlet conditions for the S-shaped duct. As expected, the predicted mean velocity profiles, and the turbulence quantities, were in good agreement with the measured data approximately 1 m from the start of the duct.

For all calculations, a simple zero gradient condition was imposed at exit, and, as already mentioned, wall functions were used on the solid boundaries.

5.3.4 Post-processing and Presentation of Results

In order to present results from the calculations, it was necessary to extract the required data from the solution files. Since the objective was to compare the predictions with the experimental data, it was necessary to obtain the cross-passage variation of the various parameters at a series of locations equivalent to the experimental traverse lines. Although the grid lines were curvilinear, it was possible to select lines which were sufficiently close to each of the traverses, i.e.,

traverse	-	0.0	0.02	0.125	0.25	0.375	0.5	0.625	0.75	0.875	1.0	1.39
grid line	1	16	17	21	26	31	36	41	46	51	56	68

Note that no attempt was made to interpolate the results onto the true traverse lines, so that the CFD data presented actually represents the variation along the relevant grid line.

Since the solution variables were staggered, proper account was taken of their respective positions. For the node-based variables, such as the pressure, turbulent kinetic energy and the normal stresses, the grid positions were already defined, but the effective positions of the mean velocities and \overline{uv} shear stress were calculated accordingly.

Several additional parameters were derived from the solution variables. Since grid-oriented velocities were used by the code, the Cartesian velocity components were also extracted from the converged solutions. In addition, for the $k-\varepsilon$ calculation, the \overline{uv} shear stress was derived from the mean strain rates using the eddy-viscosity assumption

(Eq. 5.1). In both cases, these were obtained at the grid nodes. Having extracted streamwise velocity profiles from the solutions, several overall parameters were also calculated. Using the same analysis procedure used for the experimental data, described in Chapter 3, the profiles were integrated to obtain the boundary layer parameters (Sect. 3.2.3), and, in addition, the wall friction velocity (U_τ) was determined using the single point method (Sect. 3.2.4.2).

The results obtained from the predictions are presented in Chapter 6. In the same way as the experimental data, all parameters have been non-dimensionalised by U_{Mean} and h_{in} , as appropriate, enabling them to be compared with the measurements.

CHAPTER 6 DISCUSSION

	Page
6.1 Comparison of the Predictions with the Experimental Data	186
6.1.1 Overall Parameters	186
6.1.2 Mean Velocities	187
6.1.3 Reynolds Stresses	189
6.2 Reynolds Stress Production in 2D Curvilinear Co-ordinates	192
6.2.1 The Production Terms	193
6.2.1.1 Normal Stresses	193
6.2.1.2 Turbulent Kinetic Energy	194
6.2.1.3 Shear Stresses	194
6.2.2 Effects on Reynolds Stress Production	194
6.2.2.1 Streamline Curvature	195
6.2.2.2 Streamwise Acceleration	196
6.2.3 Assessment of the Effects	197
6.2.3.1 Convex Curvature	197
6.2.3.2 Concave Curvature	199
6.2.3.3 Irrotational Core Region	200
6.2.3.4 Acceleration/Deceleration	201
6.2.3.5 Summary of the Effects	201
6.3 The Behaviour of the Modelled Reynolds Stress Equations	201
6.3.1 Simplified Modelled Equations	202
6.3.1.1 Free Shear Layer	202
6.3.1.2 The Near-wall Region	204
6.3.2 Limitations of the Modelled Equations	206
6.3.2.1 Assessment of the Model Constants	206
6.3.2.2 Response of the Modelled Equations	208
6.3.2.3 Wall Functions	209
6.3.2.4 Turbulent Transport	210
6.3.2.5 Overcoming the Limitations	213

The 2D axisymmetric flow through the S-shaped duct has been predicted using standard turbulence models, and in this chapter the results from these CFD calculations are compared to the measured data. In addition, by examining the production terms in the Reynolds stress transport equations, the significant effect that streamline curvature has on turbulent flow is explained thoroughly. Furthermore, the behaviour of the modelled Reynolds stress transport equations is discussed, showing that various features of the existing models give rise to the observed differences between the measurements and predictions.

6.1 Comparison of the Predictions with the Experimental Data

As described in Chapter 5, the 2D axisymmetric flow through the S-shaped duct was predicted using a standard Jones and Launder^[78] k- ϵ turbulence model (Sect. 5.2.1.1) and a Gibson and Launder^[59] Reynolds stress transport equation turbulence model (Sect. 5.2.2.2). In this section, these predictions are compared with the experimental data presented in Chapter 4, and, starting with some derived overall parameters followed by mean velocities and then Reynolds stresses, these comparisons are discussed.

6.1.1 Overall Parameters

To begin the assessment of the predictions, several overall parameters have been derived. By integrating the predicted mean velocity profiles at a series of locations along the duct, the streamwise variations of the integral boundary layer parameters (δ^* , θ and H) have been obtained. In addition, the wall friction velocity (U_t) was derived by assuming the log-law was applicable at the first point away from the wall. Although the grid lines used to obtain the velocity profiles mainly correspond to the measurement locations, several additional lines were used to obtain the overall parameters so that the streamwise variation just upstream and downstream of the S-shaped duct could be seen. The experimental results have already been discussed in Section 4.2.2.4, and the best interpretation of the 5HP and LDA data (Tables 8 & 13) has been used for comparison with the predictions.

On considering the boundary layer parameters, several observations can be made about the accuracy of the predictions. Along both walls, the predicted displacement thickness (δ^*) distributions (Fig. 125) are very similar. However, although the outer wall δ^* is in good agreement with the experimental data, the increase in δ^* due to the adverse pressure gradient along the inner wall is under-predicted by both models. Whilst the same may be said of the momentum thickness (θ) distributions (Fig. 126), the shape parameter (H) seems to be more sensitive to differences between the two predictions. In

Figure 127, it can be seen that the H distribution obtained using the Reynolds stress model is much closer to the measured behaviour than that of the $k-\epsilon$ model. Whilst both predictions are in general agreement with the experimental data, there are important differences along the inner wall. For example, in comparison to the peak experimental value of 1.66, the $k-\epsilon$ prediction only reaches 1.50, whereas the Reynolds stress model achieves a value of 1.58, which, although not perfect, is in much better agreement with the actual behaviour. Since it is highly desirable to be able to predict the peak value of H , in order to judge how near the flow is to separating, this provides a good initial indication that the Reynolds stress model has performed better than the $k-\epsilon$ model.

To assess the wall shear stress, the friction velocity (U_τ) has been plotted in Figure 128. For both predictions, the U_τ values were obtained from the streamwise velocity at the first grid point, using the log-law method described in Chapter 3 (Sect. 3.2.4.2), and, although the Reynolds stress model values are marginally better, the distributions are similar. At each point, this implies that the predicted velocities adjacent to the wall are similar, which suggests that the wall functions, despite being implemented differently in each model, are having almost the same effect on the predicted flow behaviour. In comparison to the experimental data, however, the predicted U_τ values along the inner wall are too high in the adverse pressure gradient region. Although the log-law was found to apply in this region (see Sect. 4.2.4.1), the wall functions are probably limiting the accuracy of the predictions by preventing the velocity from reducing sufficiently under the influence of the adverse pressure gradient. Interestingly, the U_τ distribution along the outer wall is in good agreement with the values obtained from the measured velocity profiles, but this is below the ‘interpreted’ distribution obtained by careful consideration of the measured shear stress distribution and streamwise pressure gradients (see Sect. 4.2.4.3).

6.1.2 Mean Velocities

Of fundamental interest when assessing the accuracy of the CFD methods are the mean velocities. In this section, the predicted velocities are compared to the measured 5HP and LDA data (discussed in Section 4.2.2.3). To simplify the comparisons, the predicted streamwise velocity (U_s) has been compared separately to the LDA data (Fig. 129) and the 5HP data (Fig. 130), and, although two sets of LDA data were obtained, only one of these is shown. Note that the x/L labels on the plots correspond to the locations at which the predicted profiles were obtained. At the first station, therefore, although the measurements were taken further upstream (LDA at $x/L = -0.75$ and 5HP at $x/L = -0.55$), it has been assumed that the same profiles would have been obtained at $x/L = -0.4$; which is thought to be reasonable. Furthermore, at S-shaped duct

Discussion

inlet, the predicted profiles were obtained at the LDA measurement location ($x/L=0.02$), so there is slight discrepancy when comparing these to the 5HP data, obtained at $x/L=0.0$.

Upstream of the S-shaped duct, the inlet conditions were deliberately matched to the experimental data, as described in Section 5.3.3. Whilst there are small differences between the two predictions, near the edge of the boundary layer, it can be seen that the velocity profiles at $x/L=-0.4$ are effectively identical to the experimental data. With this in mind, any discrepancies between the predicted and measured behaviour through the S-shaped duct can be attributed to the accuracy of the turbulence models.

Within the S-shaped duct, the mean velocity profiles predicted by the Reynolds stress model are generally more accurate than those of the $k-\epsilon$ model. Within the first bend, the predicted profiles are remarkably similar, and in close agreement with the measured data. Further downstream, however, differences between the two models start to become apparent. Along the inner wall, for example, the shape of the velocity profiles predicted by the Reynolds stress model contain a pronounced change of gradient, like the measured profiles, which is not present in the more rounded profiles from the $k-\epsilon$ model (e.g., $x/L=0.625$). In this region, the velocity adjacent to the wall is being reduced by the adverse pressure gradient, and, to be able to judge how close the flow is to separating, an accurate prediction of the velocity is essential. Although both models return near-wall velocities above the experimental values, probably due to the wall functions, the fact that the $k-\epsilon$ model is not able to capture the subtleties of the true behaviour suggests that this turbulence model is unsuitable in the present situation. Along the outer wall, also, the Reynolds stress model is generally in better agreement with the experimental data than the $k-\epsilon$ model. However, towards the end of the duct, the Reynolds stress model is clearly over-exaggerating the behaviour of the mean velocity (e.g., $x/L=0.875$), which, as will be seen, is related to problems with the predicted shear stress distribution. Interestingly, despite prior errors on both sides of the passage, the velocity distribution predicted by the Reynolds stress model downstream of the S-shaped duct ($x/L=1.4$) is in good agreement with the experimental data, with a different profile on one side of the passage compared to the other, whereas the $k-\epsilon$ velocity profiles on each side are much more similar.

Since grid-oriented velocity components were used, the predicted cross-stream velocity (V_n) depends on the local orientation of the curvilinear grid line. Although the lines used correspond to the measurement locations, the fact that they are not straight means that the V_n cannot be compared to the measured cross-stream component (V_ℓ). For both calculations, therefore, the radial velocity (V_r) was calculated, by the code, and has been

compared to the V_r distributions obtained from the LDA data (Fig. 131) and 5HP data (Fig. 132). In the figures, it can be seen that there is very little difference between the predicted V_r profiles, and, allowing for the differences between the 5HP and LDA data discussed in Section 4.2.2.3, these are in good agreement with the experimental results.

6.1.3 Reynolds Stresses

In this section, the predicted Reynolds stresses are compared to the experimental data (discussed in Section 4.2.3.1). With the Reynolds stress model, all the stresses are predicted directly, but, with the k-e model, the Reynolds stresses are obtained from the eddy-viscosity assumption, using the predicted k and ϵ values to determine the turbulent viscosity. In this assessment, each Reynolds stress component has been plotted separately; \overline{uu} (Fig. 133), \overline{vv} (Fig. 134), \overline{ww} (Fig. 135) and \overline{uv} (Fig. 136). For the normal stresses, only the Reynolds stress model results are shown, but, for \overline{uv} , the effective k-e values have been included along with the stress model distributions, which have finite values on each wall consistent with the U_τ values plotted in Figure 128. For the predictions, the Reynolds stress distributions at $x/L = -0.4$ were obtained from the separate parallel annular duct calculations (see Sect. 5.3.3), and it can be seen that these are in good agreement with the experimental data.

On comparing the normal stresses, it can be seen that the distributions are quite well predicted. For \overline{uu} , the inner wall values are particularly good, but along the outer wall there are some discrepancies. At $x/L = 0.625$ and $x/L = 0.875$, in particular, there are significant differences, which, since these are not present at $x/L = 0.75$, suggest the experimental data may be at fault. As discussed in Chapter 3 (Sect. 3.3.3), the large scale turbulent motion produced by the concave curvature can lead to statistical errors, which, while generally increasing the scatter in the outer part of the boundary layer, seem to have increased the \overline{uu} level at these two locations. On allowing for this, however, it can be seen that there is still an under-prediction of the \overline{uu} level, at the point where the distribution reaches a peak, which, starting at $x/L = 0.02$ near the wall, remains low as the peak moves away from the wall along the length of the duct. However, the fact that the shape of the profiles has been well-predicted provides a good indication that the Reynolds stress model is capturing the complex physical behaviour of the flow. For \overline{vv} , the predicted distributions are consistently lower than the LDA data. In particular, the model fails to predict the peak levels observed in the adverse pressure gradient regions of both walls. As will be seen in Section 6.3.1.2, the constants in the pressure-strain model essentially determine the \overline{vv} level in the near-wall region, and the present data suggests that the values used are responsible for this under-prediction.

Finally, for $\overline{w w}$, it can be seen that the predicted distributions are in excellent agreement with the LDA data.

Since the $\overline{u v}$ shear stress is of utmost importance in determining the behaviour of the flow, the overall quality of the calculation depends on the accuracy of the $\overline{u v}$ prediction. In Figure 136, the predicted $\overline{u v}$ distributions are compared to the experimental data, where it can be seen that the Reynolds stress model is generally much more successful at capturing the complex behaviour of $\overline{u v}$ within the S-shaped duct. Along the inner wall, it can be seen that the stress model predicts the significant reduction of $\overline{u v}$ due to the convex curvature (e.g., $x/L=0.125$), which then remains low in the outer part of the boundary layer further downstream, whereas the magnitude of $\overline{u v}$ returned by the $k-\epsilon$ model is generally too large (e.g., $x/L=0.375$). Moreover, the stress model correctly predicts the region of elevated shear stress adjacent to the wall (e.g., $x/L=0.625$), as it grows and moves away from the wall, which the $k-\epsilon$ model only partly reproduces (e.g., $x/L=0.875$). Similarly, along the outer wall, the stress model predicts the increase in $\overline{u v}$, due to the initial adverse pressure gradient and concave curvature (e.g., $x/L=0.125$), and then captures its slow decay as it moves away from the wall (e.g., $x/L=0.375$), whilst at the same time a new region of elevated $\overline{u v}$ forms adjacent to the wall (e.g., $x/L=0.625$). Although the $k-\epsilon$ model reproduces some of this complex behaviour, it always tends to smooth-out the distribution. In general, the $k-\epsilon$ model is unable to respond correctly to the curvature and pressure gradient effects because it obtains $\overline{u v}$ from the eddy-viscosity assumption, whereas the Reynolds stress model is able to capture all the physical effects by accounting for the transport of $\overline{u v}$ through an equation in which the production term is exact. However, the modelling assumptions used in this transport equation appear to be leading to an over-exaggerated behaviour in the convex bends, especially along the outer wall (e.g., $x/L=1.0$), and this weakness of the model is discussed further in Section 6.3.2.2.

In both predictions, the transport of turbulent kinetic energy is accounted for properly, so the resulting k behaviour should be in reasonable agreement with the LDA data (Fig. 137). With the Reynolds stress model, k is not obtained directly, but it behaves as if it were calculated from its own equation, since it is derived from the normal stresses. As such, the Reynolds stress model prediction of k is in excellent agreement with the data. Along the inner wall, the complex behaviour is captured correctly, including the suppression of k through the convex bend, and the appearance and movement of the elevated region adjacent to the wall. Similarly, the complex behaviour is reproduced along the outer wall, although the peak of the distribution appears to be under-predicted, particularly close to the wall at S-shaped duct inlet. With the $k-\epsilon$ model, the predicted k distribution is also fairly good. Even though the Reynolds stresses given by the

eddy-viscosity assumption are used to calculate the k -production, the varying magnitude of k has been broadly captured. However, it can be seen that the shape of the distribution is not predicted correctly by the model, the problem being that the clearly defined kinks in the actual behaviour are tending to be smeared, and this is indicative of the fact that the mean velocity is not responding correctly to the rapidly varying conditions, in such a way that the shear strain rate does not vary sufficiently across the passage. The same behaviour is reflected in the predicted dissipation rate (Fig. 138). Whilst broad overall agreement would be expected, since the ϵ -equation is similar in both models, the more complicated distribution predicted by the Reynolds stress model again indicates that the strain rate is able to vary across the passage in a reasonably correct way.

To provide a further insight into the accuracy of the predicted Reynolds stresses, various structure parameters have been compared. In Figure 139, the normal stress ratio ($\overline{vv}/\overline{uu}$) is shown against the LDA data discussed in Section 4.2.3.2, and, in addition, the Reynolds stress anisotropy (a_{ij}), defined by Eq. 3.43, is presented; a_{11} (Fig. 140), a_{22} (Fig. 141), a_{33} (Fig. 142), a_{12} (Fig. 143). Although the experimental results were not previously shown in this form, the a_{ij} distributions are effectively the same as the Reynolds stress to turbulent kinetic energy ratios. Whilst the Reynolds stress model is predicting the turbulent kinetic energy correctly, it is incorrectly distributing the energy amongst the normal stress components, giving, in general, too much anisotropy. As already seen, \overline{vv} is generally too low, and this is reflected in the $\overline{vv}/\overline{uu}$ and a_{22} values, particularly in the adverse pressure gradient regions along both walls. To compensate, a_{11} is over-predicted in these regions, especially towards the end of the duct in the inner wall boundary layer. Since the predicted and measured \overline{ww} are in excellent agreement, the differences seen in the a_{33} comparison, especially towards the end of the duct in the outer wall boundary layer, are related to differences in the turbulent kinetic energy. As with \overline{uv} , a_{12} has been plotted for both predictions, and good agreement is obtained in both concave regions. However, in the convex flow, the $k-\epsilon$ model does not predict the significant reduction in a_{12} , whereas the Reynolds stress model overreacts.

In the core region, further limitations of the $k-\epsilon$ turbulence model are revealed. In comparison to the Reynolds stresses predicted by the transport equation model along the mid-line of the grid (Fig. 144), Figure 145 shows that the turbulent kinetic energy predicted by the $k-\epsilon$ model increases significantly within each bend and Figure 146 shows that the \overline{uv} returned by this model has a relatively large magnitude and changes sign along the length duct. As will be seen in Section 6.2.3.3, the extra strain due to curvature leads to finite Reynolds stress production within the core region, and, since the production terms are exact, the expected behaviour is predicted by the transport

equation model. In the $k-\epsilon$ turbulence model, however, the Reynolds stresses are modelled using the eddy-viscosity model (Eq. 5.1). Since this is used to obtain the turbulent kinetic energy production (P), the resultant term (Eq. 5.5) is always positive. For example, in 2D flow ($\partial/\partial z = 0$), and with $W = 0$, Eq. 5.5 reduces to,

$$P = v_t \left(4 \left\{ \frac{\partial U}{\partial x} \right\}^2 + \left\{ \frac{\partial U}{\partial y} + \frac{\partial V}{\partial x} \right\}^2 \right) \quad \dots\dots 6.1$$

In the irrotational core region, the total strain rate ($\partial U/\partial y + \partial V/\partial x$) is negative within the first bend and positive in the second (see Sect. 4.2.4.2), but, since the strain rate terms are 'squared', P is always positive, leading to a continual increase of the turbulent kinetic energy. In addition, according to the eddy-viscosity assumption, the shear stress is given by,

$$\overline{uv} = -v_t \left(\frac{\partial U}{\partial y} + \frac{\partial V}{\partial x} \right) \quad \dots\dots 6.2$$

Since \overline{uv} is directly related to the total strain rate, the observed variation occurs along the duct. Both the above responses of the eddy-viscosity model are physically incorrect and not supported by the experimental data.

6.2 Reynolds Stress Production in 2D Curvilinear Co-ordinates

In the present investigation, the effects of streamline curvature on turbulent flow are of particular interest. By examining the modified production terms in the Reynolds stress transport equations, which include the extra strain due to curvature (U/R), these effects can be understood. Furthermore, as noted by Bradshaw^[18], the experimentally observed changes to the Reynolds stresses are an order of magnitude different to those suggested by the explicit extra terms, which can be explained by the fact that the Reynolds stresses are interrelated through their production terms. Thus a change in a particular Reynolds stress, as a direct result of the extra strain on its production, affects the other stresses whose production depend on that stress, and, in turn, this affects the production of the original stress, thereby creating a spiralling effect. As described by Launder^[90], this stress-strain intercoupling within the Reynolds stress production terms makes the turbulence extremely sensitive to extra rates of strain.

In addition to curvature, streamwise acceleration can be considered as an extra strain rate. The streamwise pressure gradients in the S-shaped duct both accelerate and

decelerate the flow, and the direct effect of these extra strains on Reynolds stress production can be examined in a similar way.

6.2.1 The Production Terms

The exact Reynolds stress transport equations in 2D curvilinear (**s-n-z**) co-ordinates (Appendix 4) contain extra terms, relative to their Cartesian form, which relate to the curvature ($1/R$) of the line (S) to which the co-ordinates are aligned. Considering the case when $W=0$, the Reynolds stress production terms for 2D ($\partial/\partial z=0$) flow are given below. Included in these expressions are the extra terms arising from the transformation of the convection terms, since they represent a pseudo production arising from the rotation of the co-ordinate system.

6.2.1.1 Normal Stresses

The production of streamwise normal stress (\overline{uu}) is given by,

$$P_{(\overline{uu}/2)} = - \left\{ \overline{uu} \frac{\partial U}{\partial s} + \overline{uv} \frac{\partial U}{\partial n} \right\} \underbrace{+ \overline{uu} \frac{V}{R}}_{\text{curvature}} \quad \underbrace{+ \overline{uv} \frac{U}{R}}_{\text{co-ordinate rotation}} \quad \dots\dots 6.3$$

which can be rewritten as,

$$P_{(\overline{uu}/2)} = \left(-\overline{uv} \right) \left[\frac{\partial U}{\partial n} - \frac{U}{R} \right] - \left(\overline{uu} \right) \left[\frac{\partial U}{\partial s} - \frac{V}{R} \right] \quad \dots\dots 6.4$$

The production of cross-stream normal stress (\overline{vv}) is given by,

$$P_{(\overline{vv}/2)} = - \left\{ \overline{uv} \frac{\partial V}{\partial s} + \overline{vv} \frac{\partial V}{\partial n} \right\} \underbrace{- \overline{uv} \frac{U}{R}}_{\text{curvature}} \quad \underbrace{- \overline{uv} \frac{U}{R}}_{\text{co-ordinate rotation}} \quad \dots\dots 6.5$$

which, with the use of the continuity equation, can be rewritten as,

$$P_{(\overline{vv}/2)} = \left(-\overline{uv} \right) \left[\frac{\partial V}{\partial s} + 2 \frac{U}{R} \right] + \left(\overline{vv} \right) \left[\frac{\partial U}{\partial s} - \frac{V}{R} \right] \quad \dots\dots 6.6$$

When $W=0$, there is no production of normal stress (\overline{ww}), i.e.,

$$P_{\overline{ww}} = 0 \quad \dots\dots 6.7$$

6.2.1.2 Turbulent Kinetic Energy

The production of turbulent kinetic energy is obtained from the sum of the production terms of the individual normal stresses, i.e.,

$$P_{(k)} = - \left\{ \overline{uu} \frac{\partial U}{\partial s} + \overline{uv} \left[\frac{\partial U}{\partial n} + \frac{\partial V}{\partial s} \right] + \overline{vv} \frac{\partial V}{\partial n} \right\} + \underbrace{\overline{uu} \frac{U}{R} - \overline{uv} \frac{V}{R}}_{\text{curvature}} \quad \dots \dots 6.8$$

which, with the use of the continuity equation, can be rewritten as,

$$P_{(k)} = (-\overline{uv}) \left[\frac{\partial U}{\partial n} + \frac{\partial V}{\partial s} + \frac{U}{R} \right] - (\overline{uu} - \overline{vv}) \left[\frac{\partial U}{\partial s} - \frac{V}{R} \right] \quad \dots \dots 6.9$$

6.2.1.3 Shear Stresses

The production of shear stress (\overline{uv}) is given by,

$$P_{(\overline{uv})} = - \left\{ \overline{uu} \frac{\partial V}{\partial s} + \overline{vv} \frac{\partial U}{\partial n} \right\} - \underbrace{\overline{uu} \frac{U}{R}}_{\text{curvature}} - \underbrace{-(\overline{uu} - \overline{vv}) \frac{U}{R}}_{\text{co-ordinate rotation}} \quad \dots \dots 6.10$$

which can be rewritten as,

$$P_{(\overline{uv})} = (\overline{uu}) \left[\frac{\partial V}{\partial s} + 2 \frac{U}{R} \right] + (\overline{vv}) \left[\frac{\partial U}{\partial n} - \frac{U}{R} \right] \quad \dots \dots 6.11$$

When $W=0$, the other two shear stresses are zero.

6.2.2 Effects on Reynolds Stress Production

Using the above equations it is possible to assess the effect of streamline curvature and streamwise acceleration on the production terms in the Reynolds stress transport equations. By assuming that the co-ordinates are aligned with actual streamlines in the flow, the terms can be further simplified since the cross-stream velocity (V) and its streamwise derivative ($\partial V / \partial s$) are both zero.

Within a plane turbulent boundary layer with zero pressure gradient, the only significant strain rate is $\partial U / \partial n$. Thus, $P_{vv} = 0$ (Eq. 6.6) and Eq. 6.9 reduces to the same result as Eq. 6.4, i.e.,

$$P_{(k)} = P_{(\overline{uu}/2)} = (-\overline{uv}) \left[\frac{\partial U}{\partial n} \right] \quad \dots \dots 6.12$$

Thus it is apparent that turbulent kinetic energy production occurs only within the $\bar{u}\bar{u}$ normal stress component, as a result of the work done by the interaction of the shear stress ($-\bar{u}\bar{v}$) and the shear strain ($\partial U/\partial n$). The $\bar{v}\bar{v}$ and $\bar{w}\bar{w}$ normal stresses are not directly produced, but they exist by receiving energy from the $\bar{u}\bar{u}$ component via the velocity-pressure gradient interaction. Dissipation of energy from all three components prevents the magnitude of the normal stresses increasing under equilibrium conditions.

Shear stress is produced from the interaction of the cross-stream normal stress ($\bar{v}\bar{v}$) and the shear strain, i.e., Eq. 6.11 reduces to,

$$P_{(-\bar{u}\bar{v})} = (\bar{v}\bar{v}) \left[\frac{\partial U}{\partial n} \right] \quad \dots\dots 6.13$$

This is balanced by the velocity-pressure gradient interaction, since direct dissipation of shear stress is negligible (except in the near-wall region).

6.2.2.1 Streamline Curvature

In addition to the shear strain ($\partial U/\partial n$), the extra strain due to curvature (U/R) increases or decreases the production of the individual Reynolds stresses. Thus Eq. 6.4 becomes,

$$P_{(\bar{u}\bar{u}/2)} = (-\bar{u}\bar{v}) \left[\frac{\partial U}{\partial n} - \frac{U}{R} \right] \quad \dots\dots 6.14$$

and Eq. 6.6 becomes,

$$P_{(\bar{v}\bar{v}/2)} = (-\bar{u}\bar{v}) \left[2 \frac{U}{R} \right] \quad \dots\dots 6.15$$

These combine, as in Eq. 6.9, to give,

$$P_{(k)} = (-\bar{u}\bar{v}) \left[\frac{\partial U}{\partial n} + \frac{U}{R} \right] \quad \dots\dots 6.16$$

Finally, the shear stress production (Eq. 6.11) becomes,

$$P_{(-\bar{u}\bar{v})} = (\bar{v}\bar{v}) \left[\frac{\partial U}{\partial n} \right] + (2\bar{u}\bar{u} - \bar{v}\bar{v}) \left[\frac{U}{R} \right] \quad \dots\dots 6.17$$

which can be rewritten as,

$$P_{(-\bar{uv})} = (\bar{vv}) \left[\frac{\partial U}{\partial n} + \left\{ 2 \frac{\bar{uu}}{\bar{vv}} - 1 \right\} \frac{U}{R} \right] \quad \dots \dots 6.18$$

In general, the significance of the extra terms depends on the magnitude of U/R in comparison to $\partial U / \partial n$. However, it can be seen that within a typical turbulent boundary layer, where $\bar{uu} > \bar{vv} > |\bar{uv}|$, the extra term in the shear stress production will be the most significant of all.

Irrotational Curved Flow

In a curved flow away from solid surfaces, the shear strain ($\partial U / \partial n$) and the extra strain (U/R) both exist, although, for irrotational flow, they will be equal such that the vorticity is zero, i.e.,

$$\frac{\partial U}{\partial n} = \frac{U}{R} \quad \dots \dots 6.19$$

Thus, it is apparent (Eq. 6.14) that $P_{\bar{uu}} = 0$. However, turbulent kinetic energy production occurs within the \bar{vv} component (Eq. 6.15) so that Eq. 6.16 becomes,

$$P_{(k)} = (-\bar{uv}) \left[2 \frac{U}{R} \right] \quad \dots \dots 6.20$$

and Eq. 6.11 shows that shear stress is produced by,

$$P_{(-\bar{uv})} = (\bar{uu}) \left[2 \frac{U}{R} \right] \quad \dots \dots 6.21$$

6.2.2.2 Streamwise Acceleration

In addition to the shear strain ($\partial U / \partial n$), the extra strain due to acceleration ($\partial U / \partial s$) increases or decreases the production of the individual Reynolds stresses. However, in this case, only the normal stresses and turbulent kinetic energy are directly affected. Thus Eq. 6.4 becomes,

$$P_{(\bar{uu}/2)} = (-\bar{uv}) \left[\frac{\partial U}{\partial n} \right] - (\bar{uu}) \left[\frac{\partial U}{\partial s} \right] \quad \dots \dots 6.22$$

and Eq. 6.6 becomes,

$$P_{(\bar{vv}/2)} = (\bar{vv}) \left[\frac{\partial U}{\partial s} \right] \quad \dots \dots 6.23$$

These combine, as in Eq. 6.9, to give,

$$P_{(k)} = (-\bar{uv}) \left[\frac{\partial U}{\partial n} \right] - (\bar{uu} - \bar{vv}) \left[\frac{\partial U}{\partial s} \right] \quad 6.24$$

Again, the significance of the extra terms depends on the magnitude of $\partial U / \partial s$ in comparison to $\partial U / \partial n$.

6.2.3 Assessment of the Effects

The Reynolds stress transport equations are rate equations, that is the various terms on the right hand side affect the rate of change ($D\bar{u}_i\bar{u}_j/Dt$) of a particular Reynolds stress. For a steady flow, $D\bar{u}_i\bar{u}_j/Dt$ reduces to the convection term ($U_k \partial \bar{u}_i \bar{u}_j / \partial x_k$), which in a streamline oriented co-ordinate system becomes $U \partial \bar{u}_i \bar{u}_j / \partial s$. Under equilibrium conditions there is no variation of flow properties in the streamwise direction, which implies that the convection term for each quantity is zero. To balance the budget, therefore, the sum of the other terms (production, dissipation, etc.) must be zero.

In order to assess the effect of extra strain on the Reynolds stresses, it is necessary to consider the instantaneous effect of increasing or decreasing the production. Relative to equilibrium conditions, this will produce a streamwise gradient in the Reynolds stresses. Assuming that the extra strain is sustained, the other quantities in the transport equation will adjust to produce new equilibrium conditions but, since these quantities are themselves governed by rate equations, there will be a finite delay, or lag, before this occurs. Thus, as the other quantities adjust, the streamwise gradient of the Reynolds stresses will eventually decay to zero.

Assuming, for example, that the Reynolds stresses \bar{uu} , \bar{vv} and $-\bar{uv}$ are all positive and that the shear strain ($\partial U / \partial n$) is predominantly positive, as in the inner wall boundary layer, the effect of extra strain can be examined.

6.2.3.1 Convex Curvature

In this case the extra strain (U/R) is negative and small in comparison to the large positive $\partial U / \partial n$ in the near-wall region. However, in the outer layer of the boundary layer $\partial U / \partial n$ is much smaller, becoming negative near the edge of the boundary layer and equal to U/R in the irrotational free stream, whilst U/R remains nearly constant. Thus the negative U/R together with the reduced, and sometimes negative, $\partial U / \partial n$ has a significant influence on the production of the Reynolds stresses in the outer layer.

Relative to a plane boundary layer in which the shear stress production (Eq. 6.13) is always positive, convex curvature reduces this (Eq. 6.18), giving rise to a significant

region of negative production over the outer edge of the boundary layer. The significance of this can be estimated by considering the strain rates (Fig. 78) derived from the mean velocity measurements. For example, within the inner wall region at $x/L = 0.125$, U/R is of the same order of magnitude as $\partial U/\partial n$ over a large proportion of the boundary layer. As an indication of the effect that this has on the production of shear stress, consider the position at which the production is zero. This can be determined from,

$$\frac{\partial U}{\partial n} = \left(2 \frac{\bar{u}\bar{u}}{\bar{v}\bar{v}} - 1 \right) \left[-\frac{U}{R} \right] \quad \dots\dots 6.25$$

The normal stress ratio $\bar{v}\bar{v}/\bar{u}\bar{u}$ (Fig. 47) is fairly constant throughout the boundary layer with $\bar{u}\bar{u}$ broadly $2-2\frac{1}{2}$ times $\bar{v}\bar{v}$. Thus production is zero when $\partial U/\partial n$ is about 3-4 times the magnitude of U/R , which in the present flow occurs at $n/\delta \approx 0.2$.

Under equilibrium conditions the positive shear stress production (P) is balanced, ignoring turbulent transport, by the negative velocity-pressure gradient interaction (Π), i.e.,

$$U \frac{\partial(-\bar{u}\bar{v})}{\partial s} = P_{(-\bar{u}\bar{v})} + \Pi_{(-\bar{u}\bar{v})} \quad \dots\dots 6.26$$

However, the reduced (and largely negative) production, arising from the application of convex curvature, initially results in a large negative streamwise shear stress gradient, since the negative Π will remain unaffected. This gradient would be sufficient to reduce the shear stress to zero in a streamwise distance of about $2\delta \sim 3\delta$. However, since the magnitude of Π also reduces in the streamwise direction, the streamwise gradient of shear stress will diminish. Providing the extra strain is sustained, the gradient will remain negative and so there is no reason why the shear stress cannot reduce to zero and subsequently change sign. In the present flow, however, the shear stress (Fig. 81) virtually disappears in the outer boundary layer over both convex surfaces, but there is no sign reversal since the extra strain rate begins to reduce before this is achieved, causing the shear stress to increase again.

Relative to a plane boundary layer, turbulent kinetic energy production (Eq. 6.16) appears to be reduced by the negative U/R . As with the shear stress, there is a region of negative production in the outer layer. However in this case, the region is much smaller and zero production occurs when the total strain ($\partial U/\partial n + U/R$) is zero. For example, within the inner wall region at $x/L = 0.125$, the total strain (Fig. 79) is zero at $n/\delta \approx 0.6$. Furthermore, according to the normal stress production terms, the extra strain

would tend to increase the streamwise component (Eq. 6.14) while the cross-stream component (Eq. 6.15) reduces, by twice as much, to give the net reduction in turbulent kinetic energy production. However, since the shear stress is very small (Fig. 81), the extra strain cannot promote a difference between the individual components. Thus, the dominant effect is an overall reduction in the turbulent kinetic energy (Fig. 45), due to the low shear stress reducing its production (Fig. 89).

In addition, since the normal stress to turbulent kinetic energy ratios (Figs. 51, 52 and 53) do not appear to be significantly affected by the convex curvature, the velocity-pressure gradient interaction, which is almost entirely due to the pressure-strain correlation, must continue to effectively redistribute the energy, ensuring that all the normal stresses are reduced equally. This behaviour is associated with the 'mean strain' component, that which redistributes the production, ensuring that all the normal stresses respond to the reduction of turbulent kinetic energy production. Moreover, under condition of sustained extra strain, in which there is little or no production of energy in any of the normal stress components, the 'return to isotropy' component of the pressure-strain would tend to equalise, or isotropise, the turbulence. This effect was seen in the experiments of Gillis and Johnston^[63], who suggested that strong convex curvature destroys the large scale turbulence in the outer layer, leaving only the fine scale debris of the upstream boundary layer, which decays to a nearly isotropic state as it moves downstream. In the present case, the extra strain was not present for long enough to affect the structure of the turbulence in this way.

6.2.3.2 Concave Curvature

In this case the extra strain (U/R) is positive (with respect to the positive stresses and shear strain considered by way of example). Again, U/R is small in comparison to the large positive $\partial U/\partial n$ in the near-wall region, but in the outer layer U/R is significant in comparison to $\partial U/\partial n$, as in the convex case. The only difference in this case is that $\partial U/\partial n$ remains positive as it reduces to the zero vorticity condition in the core region, which can be seen (Fig. 78), for example, in the inner wall region at $x/L = 0.875$.

The magnitude of the extra strains in the concave flow are slightly less than the equivalent convex case due, in general, to the smaller U and larger R in the concave regions. However, the shear stress production (Eq. 6.18) is significantly influenced by the extra strain which, with the factor of 3-4 resulting from the normal stress ratio, increases the production over a large proportion of the outer layer. For example, extra strain makes the largest contribution to the production over the outer one third of the boundary layer, and at $n/\delta \approx 0.2$ provides about a quarter of the total production.

The increase in production, arising from the application of concave curvature, initially creates an imbalance in the shear stress transport equation which gives rise to a large positive streamwise gradient. Naturally, the velocity-pressure gradient interaction follows behind, reducing the rate of increase of the shear stress. Eventually, if the extra strain was sustained, a new equilibrium state would be established, with higher shear stress. In the present case, however, the removal of the extra strain causes the shear stress to reduce again.

The turbulent kinetic energy production (Eq. 6.16) is also increased by concave curvature (Fig. 89) but, as in the convex case, this is mainly due to the modified shear stress (Fig. 81). In this case, however, the level of shear stress is much higher and so the extra strain is able to have a limited effect on the proportioning of the normal stresses. The production of the cross-stream component (Eq. 6.15) is increased, and the streamwise component (Eq. 6.14) reduced, giving rise to an increase in the ratio $\overline{vv}/\overline{uu}$ (Fig. 47) towards the end of the concave bends. This effect was seen in the strong concave boundary layer experiments of Barlow and Johnston^[10].

6.2.3.3 Irrotational Core Region

Throughout the core region, between the annulus wall boundary layers, the vorticity is zero (Fig. 79). Although the shear stress is also zero, the flow at inlet to the S-shaped duct contains a certain amount of turbulence, with a turbulent kinetic energy of about $0.000075 U_{Mean}^2$, which is very small in comparison to the levels reached within the boundary layers (Fig. 45). The existence of turbulence in the core region makes it possible for shear stress to be produced (Eq. 6.21). Within the first bend, U/R is negative and so the shear stress ($-\overline{uv}$) will reduce from zero to a negative value. The existence of shear stress then allows turbulent kinetic energy to be produced (Eq. 6.20) within the \overline{vv} component. Without any production, the turbulent kinetic energy will decay at a rate determined by the dissipation rate (ϵ), but, within the first bend, the finite positive production will offset the dissipation, and may lead to an increase of turbulent kinetic energy. Within the second bend, the positive U/R will lead to positive shear stress production, tending to return the shear stress back to zero, and, at the same time, the turbulent kinetic energy production will become negative, increasing the rate of decay of the turbulence. Although these effects are undetectable in the present experimental results, they can be seen in the numerical prediction using the Reynolds stress transport equation turbulence model (Fig. 144); albeit with extremely small magnitude.

6.2.3.4 Acceleration/Deceleration

In this case the extra strain ($\partial U / \partial s$) has no effect on the shear stress, and only a very limited effect on the normal stresses. The production of turbulent kinetic energy (Eq. 6.24) will tend to reduce when the flow is accelerating ($\partial U / \partial s > 0$) due to a decrease in the production of \bar{uu} (Eq. 6.22) and a lesser increase in the production of \bar{vv} (Eq. 6.23). For decelerating flow ($\partial U / \partial s < 0$) the exact opposite will occur. In comparison to the curvature extra strain (U/R) of the same magnitude, Irwin and Arnot Smith^[72] have shown theoretically that $\partial U / \partial s$ has a relatively weak effect on the Reynolds stresses. In the present case, the magnitude of $\partial U / \partial s$ (Fig. 78) is very small throughout the flow, reaching a maximum half way along the duct close to the inner wall, where the flow is decelerating, and the outer wall, where the flow is accelerating. In addition, $\partial U / \partial s$ can only have an effect near the edge of the boundary layer, where $\partial U / \partial n$ is small, but, in this region, the normal stresses are very small. Streamwise acceleration, therefore, has an insignificant effect on Reynolds stress production.

6.2.3.5 Summary of the Effects

The most significant extra strain affecting the production of the Reynolds stresses, in particular the shear stress, is due to streamline curvature. This arises because of the sensitivity of the shear stress production to U/R , together with the direct coupling between the production terms. The large change in $-\bar{uv}$ that occurs as a direct result of U/R , significantly affects the production of turbulent kinetic energy. This leads to a change in the magnitude of turbulent kinetic energy, and its components, which, in turn, affects the production of $-\bar{uv}$, and so on. Through the velocity-pressure gradient interaction, the normal stress components are mainly affected equally, although in the concave case, the extra strain leads to a proportionally larger increase in \bar{vv} than in the \bar{uu} component. In support of the present findings, Gibson et al.^[62] describe a similar mechanism by which the extra strain affects production in a flow with mild streamline curvature. However, as also seen by others (e.g., Moser and Moin^[108], Muck et al.^[109] and Hoffmann et al.^[69]), the overall effects are less pronounced in this case.

6.3 The Behaviour of the Modelled Reynolds Stress Equations

In complex flows, each Reynolds stress has a unique behaviour, which is described by its transport equation. Unfortunately, as seen in Section 6.1.3, this behaviour cannot be represented adequately by the eddy-viscosity model, which relates the stresses directly to the mean strain rates. This is particularly so in non-equilibrium flows, in which the complex strain field varies rapidly from one location to the next. For example, in the

flow through an S-shaped duct, not only is there a significant variation of the primary strain rate, brought about by the rapidly varying static pressure and the more slowly varying shear stress (which affect the streamwise acceleration as discussed in Section 4.2.4.5), but, in addition, the extra strain rate due to curvature is applied, reversed and removed within the length of the duct (as seen in Section 4.2.4.2). Since the strain rates affect the Reynolds stresses through their rate of production, their magnitude is best determined via the transport equations.

To understand the behaviour of the Reynolds stress transport equations, and in particular the Gibson and Launder^[59] modelled form of these (given in Sect. 5.2.2.2), it is necessary to simplify the equations. In doing so, the importance of the pressure-strain (ϕ_{ij}) model becomes apparent, and it can be seen how the numerical value of the constants in this model determine many of the important features of the predicted turbulent flow.

6.3.1 Simplified Modelled Equations

In this section, the high Reynolds number form of the modelled transport equations (Eq. 5.21) are simplified by assuming that the flow is a 2D ($\partial/\partial z = 0$) plane thin shear layer ($W = 0$, $V \ll U$, $\partial/\partial x \ll \partial/\partial y$). For free shear flow, these equations are relatively simple, but, for boundary layer flow, the inclusion of the near-wall component of the pressure-strain model complicates matters.

6.3.1.1 Free Shear Layer

For plane shear flow, the Reynolds stress transport equations become,

$$U \frac{\partial \bar{uv}}{\partial x} = (1 - C_2) P_{(\bar{uv})} - \epsilon C_1 \left(\frac{\bar{uv}}{k} \right) + T_{(\bar{uv})} \quad \dots \dots 6.27$$

$$U \frac{\partial \bar{uu}}{\partial x} = (2 - \frac{4}{3} C_2) P - \epsilon \left(\frac{2}{3} + C_1 \left(\frac{\bar{uu}}{k} - \frac{2}{3} \right) \right) + T_{(\bar{uu})} \quad \dots \dots 6.28$$

$$U \frac{\partial \bar{vv}}{\partial x} = \frac{2}{3} C_2 P - \epsilon \left(\frac{2}{3} + C_1 \left(\frac{\bar{vv}}{k} - \frac{2}{3} \right) \right) + T_{(\bar{vv})} \quad \dots \dots 6.29$$

$$U \frac{\partial \bar{ww}}{\partial x} = \frac{2}{3} C_2 P - \epsilon \left(\frac{2}{3} + C_1 \left(\frac{\bar{ww}}{k} - \frac{2}{3} \right) \right) + T_{(\bar{ww})} \quad \dots \dots 6.30$$

where,

$$P_{(\bar{uv})} = -\bar{vv} \frac{\partial U}{\partial y} \quad \dots\dots 6.31$$

$$P = -\bar{uv} \frac{\partial U}{\partial y} \quad \dots\dots 6.32$$

$$T_{(\bar{u_i u_j})} = \frac{\partial}{\partial y} \left(C_s \frac{k^2}{\varepsilon} \frac{\partial \bar{u_i u_j}}{\partial y} \right) \quad \dots\dots 6.33$$

In addition, the transport equation for turbulent kinetic energy becomes,

$$U \frac{\partial k}{\partial x} = P - \varepsilon + T_{(k)} \quad \dots\dots 6.34$$

and equation for its dissipation rate becomes,

$$U \frac{\partial \varepsilon}{\partial x} = \frac{\varepsilon}{k} (C_{\varepsilon 1} P - C_{\varepsilon 2} \varepsilon) + T_{(\varepsilon)} \quad \dots\dots 6.35$$

Equilibrium Flow and the Model Constants

When a flow is in equilibrium the convection terms in the momentum and Reynolds stress transport equations are all zero. By neglecting turbulent transport, since it may be assumed to be small in comparison to P and ε , the k -equation (Eq. 6.34) implies that $P = \varepsilon$, which can be used to simplify the other Reynolds stress transport equations (replacing ε with P). Thus, by neglecting $T_{(\bar{uv})}$, Eq. 6.27 reduces to,

$$\left(\frac{\bar{uv}}{k} \right)^2 = C \left(\frac{\bar{vv}}{k} \right) \quad \dots\dots 6.36$$

where,

$$C = \frac{(1 - C_2)}{C_1} \quad \dots\dots 6.37$$

and the normal stress equations reduce to,

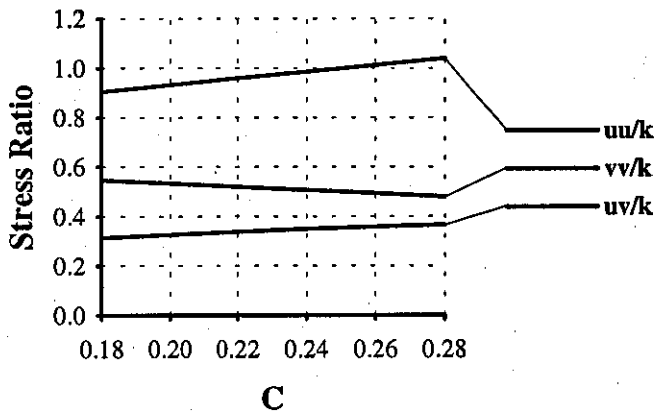
$$\frac{\bar{uu}}{k} = \frac{2}{3} (1 + 2C) \quad \dots\dots 6.38$$

$$\frac{\bar{vv}}{k} = \frac{\bar{ww}}{k} = \frac{2}{3} (1 - C) \quad \dots\dots 6.39$$

Substituting for \bar{vv}/k in Eq. 6.36 gives,

$$\frac{\overline{uv}}{k} = \pm \sqrt{\frac{2}{3} C(1-C)} \quad 6.40$$

The above analysis has been carried out by many workers (e.g., Launder et al.^[92] and Gibson and Launder^[59]), and shows that the numerical value of the constant C (i.e., C_1 and C_2 together) determines the stress ratios for equilibrium free shear flow, e.g.,



Variation of Reynolds Stress Ratios with Constant C

As noted by Launder^[89], nearly all have adopted $C \approx 0.23$; although, since this can be achieved with any suitable combination of C_1 and C_2 , there are some differences between the chosen values of C_1 and C_2 . Most workers have taken $C_2 \approx 0.6$, since it is exactly 0.6 in rapidly distorted isotropic turbulence.

Gibson and Launder^[59] determined the best value of C to meet experimentally measured values of the stress ratios in equilibrium free shear flow, which they gave as,

$$\frac{\overline{uv}}{k} = -0.34, \quad \frac{\overline{uu}}{k} = 0.96 \quad \text{and} \quad \frac{\overline{vv}}{k} = \frac{\overline{ww}}{k} = 0.52 \quad 6.41$$

The optimum constant is $C=0.22$, reproducing the measured ratios almost exactly. Gibson and Launder^[59] set $C_2=0.6$, which requires $C_1=1.818$ to give $C=0.22$. Thus, $C_1=1.8$ was recommended.

6.3.1.2 The Near-wall Region

For boundary layer flow, the wall contribution to the pressure-strain model ($\phi_{ij}^{(w)}$) must be included. The modelled transport equations for plane 2D flow (with $\underline{n}=\{0,1,0\}$) reduce to,

$$U \frac{\partial \bar{uv}}{\partial x} = (1 - C_2 + \frac{3}{2} C_2 C'_2) P_{(\bar{uv})} - \epsilon (C_1 + \frac{3}{2} C'_1) \left(\frac{\bar{uv}}{k} \right) + T_{(\bar{uv})} \quad \dots \dots 6.42$$

$$U \frac{\partial \bar{uu}}{\partial x} = (2 - \frac{4}{3} C_2 + \frac{2}{3} C_2 C'_2) P - \epsilon \left(\frac{2}{3} + C_1 \left(\frac{\bar{uu}}{k} - \frac{2}{3} \right) - C'_1 \left(\frac{\bar{vv}}{k} \right) \right) + T_{(\bar{uu})} \quad \dots \dots 6.43$$

$$U \frac{\partial \bar{vv}}{\partial x} = (\frac{2}{3} C_2 - \frac{4}{3} C_2 C'_2) P - \epsilon \left(\frac{2}{3} + C_1 \left(\frac{\bar{vv}}{k} - \frac{2}{3} \right) + 2 C'_1 \left(\frac{\bar{vv}}{k} \right) \right) + T_{(\bar{vv})} \quad \dots \dots 6.44$$

$$U \frac{\partial \bar{ww}}{\partial x} = (\frac{2}{3} C_2 + \frac{2}{3} C_2 C'_2) P - \epsilon \left(\frac{2}{3} + C_1 \left(\frac{\bar{ww}}{k} - \frac{2}{3} \right) - C'_1 \left(\frac{\bar{vv}}{k} \right) \right) + T_{(\bar{ww})} \quad \dots \dots 6.45$$

Equilibrium Flow and the Model Constants

For zero convection and by neglecting turbulent transport, and with the use of $P = \epsilon$, Eq. 6.42 reduces to,

$$\left(\frac{\bar{uv}}{k} \right)^2 = \left(\frac{\bar{vv}}{k} \right) \left(\frac{2(1 - C_2) + 3C_2 C'_2}{2C_1 + 3C'_1} \right) \quad \dots \dots 6.46$$

and the normal stress equations reduce to,

$$\frac{\bar{uu}}{k} = \frac{2}{3} \left(\frac{C_1(C_1 + 2(1 - C_2) + C_2 C'_2) + 3C'_1(C_1 + (1 - C_2))}{C_1(C_1 + 2C'_1)} \right) \quad \dots \dots 6.47$$

$$\frac{\bar{vv}}{k} = \frac{2}{3} \left(\frac{C_1 - (1 - C_2) - 2C_2 C'_2}{C_1 + 2C'_1} \right) \quad \dots \dots 6.48$$

$$\frac{\bar{ww}}{k} = 2 - \frac{\bar{uu}}{k} - \frac{\bar{vv}}{k} \quad \dots \dots 6.49$$

Substituting for \bar{vv}/k in Eq. 6.46 gives,

$$\frac{\bar{uv}}{k} = \pm \sqrt{\frac{2}{3} \left(\frac{C_1 - (1 - C_2) - 2C_2 C'_2}{C_1 + 2C'_1} \right) \left(\frac{2(1 - C_2) + 3C_2 C'_2}{2C_1 + 3C'_1} \right)} \quad \dots \dots 6.50$$

Note that these equations have been obtained by many workers (e.g., Lien and Leschziner^[97]), and it can be seen that they reduce to the equivalent free shear layer equations when C'_1 and C'_2 are set to zero. It is apparent, therefore, that these constants act to modify (or correct) the free shear layer stress ratios in the vicinity of a solid

boundary. Remember, also, that the correction is applied gradually, through the use of a wall-distance based function, which only takes full effect in the near-wall region.

Gibson and Launder^[59] determined the best values for the constants C'_1 and C'_2 , in their $\phi_{ij}^{(w)}$ model, to match experimentally measured near-wall stress ratios, obtained from equilibrium boundary layer flow, which they gave as,

$$\frac{\overline{uv}}{k} = -0.26, \frac{\overline{uu}}{k} = 1.10, \frac{\overline{vv}}{k} = 0.25 \text{ and } \frac{\overline{ww}}{k} = 0.65 \quad \dots\dots 6.51$$

With $C_1 = 1.8$ and $C_2 = 0.6$, these ratios are almost exactly reproduced with $C'_1 = 0.472$ and $C'_2 = 0.309$. However, Gibson and Launder^[59] recommended $C'_1 = 0.5$ and $C'_2 = 0.3$, which have been adopted as the standard model constants. With these, the resulting stress ratios become,

$$\frac{\overline{uv}}{k} = -0.255, \frac{\overline{uu}}{k} = 1.098, \frac{\overline{vv}}{k} = 0.248 \text{ and } \frac{\overline{ww}}{k} = 0.654 \quad \dots\dots 6.52$$

6.3.2 Limitations of the Modelled Equations

Whilst solution of the modelled Reynolds stress transport equations provides a much better prediction of complex flow, it must be remembered that the models, included to facilitate closure of the equations, may still lead to errors in the prediction of the Reynolds stresses. However, any inaccuracies introduced at second order level have a much smaller effect on the momentum equations than a first order closure model such as the eddy-viscosity assumption, leading to a much more accurate prediction.

For progress to be made, it is necessary to examine the limitations of the existing models. In comparison to the present experimental data, the prediction using the standard Gibson and Launder^[59] model and constants has shown that it incorrectly reproduces several of the important features of the S-shaped duct flow (see Section 6.1). It has already been seen (in Sect. 6.3.1) how the constants in the pressure-strain (ϕ_{ij}) model (C_1 , C_2 , C'_1 and C'_2) effectively determine the anisotropy of the Reynolds stresses, and here it is shown that the chosen values could be largely responsible for the limitations of the model. However, other factors are also discussed.

6.3.2.1 Assessment of the Model Constants

According to the present measurements, the cross-stream normal stress component (\overline{vv}) predicted by the standard model is too small (Fig. 134). In particular, at the upstream station ($x/L = -0.4$), where the flow is effectively in equilibrium, it is most surprising

that the predicted \overline{vv} does not agree with the experimental data. (Remember that a separate parallel annular duct calculation, using exactly the same turbulence model, was used to set the inlet conditions for the S-shaped duct.) Since the predicted turbulent kinetic energy is in reasonable agreement with the data (Fig. 137), the failure of the prediction to reproduce the correct level of \overline{vv} is due entirely to the near-wall component of the pressure-strain model. In Section 6.3.1.2, it was shown that the level of \overline{vv}/k in the near-wall region of an equilibrium boundary layer depends on the value of the various model constants (Eq. 6.48). Since the wall functions, in effect, ensure that this value is achieved at all the wall-adjacent grid points, the model constants must be responsible for the discrepancy. Furthermore, at the outer edge of the boundary layer, the predicted \overline{vv} (Fig. 134) is still being influenced by the presence of the wall, with values below \overline{ww} (Fig. 135), whereas the experimental values are similar in this region (like a free shear layer). This suggests that the wall component of the pressure-strain is affecting the prediction over too much of the boundary layer.

Thus, it would appear that the standard constants overly suppress the \overline{vv} normal stress adjacent to the wall, and the influence of the wall correction is being felt too far away from the wall. Since the pressure-strain effectively determines the distribution of the normal stress components, giving rise to the turbulent kinetic energy, the under prediction of \overline{vv} must be accompanied by an over prediction of the other two components (Figs. 133 & 135). In general, therefore, the level of anisotropy given by the standard model is too large (Figs. 140, 141, 142 & 143); with a_{22} below the measured data and, to a lesser extent, a_{11} and a_{33} above. Thus, by modifying the numerical value of the constants in the pressure-strain model, it should be possible to improve the level of anisotropy, at least for equilibrium flow.

Reassessment of the Constants

A numerical optimisation technique was used to determine new values for the constants C'_1 and C'_2 , based on the following values suggested by the stress ratios (Figs. 50, 51, 52 & 53) in the near-wall region,

$$\frac{\overline{uv}}{k} = -0.28, \quad \frac{\overline{uu}}{k} = 1.05, \quad \frac{\overline{vv}}{k} = 0.35 \text{ and } \frac{\overline{ww}}{k} = 0.60 \quad \dots\dots 6.53$$

Using this technique, the optimum values of the constants were determined by an algorithm which automatically varied the numerical value of the constants so as to minimise the difference between the calculated stress ratios, implied by a particular set of constants (i.e., Eqs. 6.47, 6.48, 6.49 and 6.50), and the required values (Eq. 6.53). Thus, with only C_2 fixed at 0.6, excellent agreement was obtained with $C_1 = 1.778$,

$C'_1=0.298$ and $C'_2=0.109$, and with the additional constraint of $C_1=1.8$, good agreement was obtained with $C'_1=0.301$ and $C'_2=0.116$.

It seems, therefore, that the coefficients $C_1=1.8$, $C_2=0.6$, $C'_1=0.3$ and $C'_2=0.1$ represent a better set than the standard values. However, it should be emphasised that these are based on the present experimental data only, and there is no evidence that this alternative set of constants would perform better in general. It is of interest, though, to note how sensitive the model constants are to the experimental data used to determine their values (i.e., Eq. 6.53 compared with Eq. 6.52).

6.3.2.2 Response of the Modelled Equations

In solving the Reynolds stress transport equations, it appears that the modelled form of the equations gives rise to an error in the predicted shear stress (Fig. 136). This is most noticeable in the convex regions, where the rapid reduction in the magnitude of the shear stress overshoots the minimum level reached by the experimental data, leading to a change of sign before increasing again. Similarly, in the concave regions, the increasing shear stress magnitude overshoots the largest level reached by the data.

As far as the effect of curvature is concerned, it was shown in Section 6.2.3 that the extra strain due to curvature (U/R) affects the production of the Reynolds stresses, and that the shear stress production (Eq. 6.18) was particularly sensitive to U/R . However, it appears that the modelled shear stress equation is too sensitive to curvature. This has been previously observed on several occasions (e.g., Gibson et al.^[60], Rodi and Scheuerer^[128], Gibson and Rodi^[61]), and, although it appears to be poorly understood, is effectively a characteristic of the standard Gibson and Launder^[59] model. The possible reasons for this behaviour can be determined by considering the predominant terms in the modelled shear stress transport equation (Eq. 6.27), for this case of flow along a curved streamline, i.e.,

$$U \frac{\partial \bar{uv}}{\partial s} = (1 - C_2) P_{(\bar{uv})} - \epsilon C_1 \left(\frac{\bar{uv}}{k} \right) \quad 6.54$$

where the shear stress production (Eq. 6.18) is rewritten as,

$$P_{(\bar{uv})} = -\bar{vv} \left(\frac{\partial U}{\partial n} + \left\{ 2 \frac{\bar{uu}}{\bar{vv}} - 1 \right\} \frac{U}{R} \right) \quad 6.55$$

One of the possible reasons for the exaggerated behaviour of \bar{uv} has already been discussed in Section 6.3.2.1. Here it was shown that the standard model constants give rise to a low value of \bar{vv} across the whole of the boundary layer, and so the stress ratio

$\overline{vv}/\overline{uu}$ predicted by the model is also lower than that suggested by the experimental data (Fig. 139). Consequently, the shear stress production term (Eq. 6.55) becomes more sensitive to extra strain, with a factor of about 5-6 multiplying U/R . Thus, as curvature is applied, the imbalance in Eq. 6.54 is larger than it should be, leading to a more rapid rate of change of \overline{uv} in the streamwise direction, which means that \overline{uv} increases or decreases by more than it should in a given streamwise distance.

By the same reasoning, the value of the constants (C_1 and C_2) in Eq. 6.54 may be partly responsible for the discrepancy, in that they effectively determine the size of the terms on the right hand side. It was shown in Section 6.3.1.1 that when these terms are equal and opposite, as in equilibrium free shear flow, the Reynolds stress ratios are dependant only on the ratio $C = (1 - C_2)/C_1$. However, when out of balance, the magnitude of the constants also influences the magnitude of the convection term, i.e., the rate at which the shear stress changes in the streamwise direction. For example, if C_1 was reduced to 1.35 (75% of 1.8) and C_2 was changed to 0.7 to maintain C then, regardless of the magnitude of the production or dissipation rates, the magnitude of any imbalance would be 75% of its usual value, and the change of shear stress in a given streamwise distance would be reduced by the same proportion.

The final possibility, suggested by Gibson et al.^[60], is that ϵ responds too slowly to the imposition of U/R in the curved regions. The changing magnitude of ϵ ensures that the streamwise gradient of \overline{uv} gradually reduces, following a change in the strain rate, such that the flow tends towards equilibrium. Therefore, if ϵ does not change quickly enough, the streamwise gradient of \overline{uv} will be sustained at too high a level for too long, resulting in an excessive change in the shear stress. However, in the same way, ϵ is responsible for controlling the rate of change of the turbulent kinetic energy in the streamwise direction (Eq. 6.34), as its production rate (Eq. 6.16) changes with U/R . Since there is good agreement between the measured and predicted turbulent kinetic energy (Fig. 137), it would appear that the behaviour of ϵ is reasonably correct and cannot, by itself, explain the excessive behaviour of the shear stress.

6.3.2.3 Wall Functions

At the solid boundaries, equilibrium wall functions have been used to determine the boundary conditions for the Reynolds stresses and dissipation rate, and it is worthwhile considering the effect that these might be having on the predictions. Primarily, it is assumed that the shear stress (magnitude) is given by U_τ^2 , where U_τ is obtained from the streamwise velocity at the first grid point using the log-law method described in Chapter 3 (Sect. 3.2.4.2), and the dissipation rate is obtained from $U_\tau^3/\kappa n$. Moreover, the use of equilibrium wall functions leads to the near-wall stress ratios, determined by

the various constants in the pressure-strain model (Sect. 6.3.1.2), effectively being achieved at all the wall-adjacent grid points.

In applying wall functions, it is necessary to ensure that the first grid point is located in the linear log-law region of the boundary layer. Considering the complexity of the annular S-shaped duct flow, the mean velocity exhibits a surprisingly large amount of linear log-law behaviour in the near-wall region (see Section 4.2.4.1). For the inner wall boundary layer (Fig. 74), there is excellent agreement everywhere, up to $n^+ = 100$, despite the curvature and severe adverse pressure gradient. Along the outer wall (Fig. 75), however, the strong favourable pressure gradient completely changes the mean velocity behaviour. The increase in the velocity close to the wall gives rise to an increase in the wall shear stress, and, in addition, the total shear stress (τ) reduces away from the wall in order to balance the pressure gradient. At the start of the favourable pressure gradient, these changes occur within the laminar sublayer but, subsequently, the Reynolds stresses are also affected, since a higher rate of production occurs as a result of the increased strain rate. In strong favourable pressure gradient, therefore, the rapidly varying shear stress (Fig. 81) seems to affect the mean velocity in such a way that the usual linear log-law behaviour is lost. As such, the mean velocity cannot be used to determine the wall shear stress, since a different U_τ value would be obtained at every position. However, even though the U_τ values will not correspond to the true wall shear stress, the consequences of using these lower values at the first grid point are not too severe, since the shear stress is reducing rapidly anyway. Overall, the predicted shear stress in the near-wall region appears to be reasonably good at every location (Fig. 136).

As far as the normal stresses (Figs. 133, 134 & 135) are concerned, the wall functions do not severely limit the accuracy of the prediction. Apart from the problem with the low $\bar{v}v$ level, produced by the choice of constants in the pressure-strain model (discussed in Section 6.3.2.1), a reasonably acceptable prediction of the normal stresses and the turbulent kinetic energy (Fig. 137) is achieved. Since the structure parameters (discussed in Section 4.2.3.2) remain fairly constant throughout the flow, the wall functions, which effectively impose certain stress ratios in the near-wall region, exhibit reasonable behaviour in this case.

6.3.2.4 Turbulent Transport

In the modelled Reynolds stress transport equations, turbulent transport was obtained using a simple gradient diffusion model for the triple velocity correlations, with an isotropic diffusion coefficient based on k^2/ϵ . In complex flows, the validity of this assumption is questionable, but, in comparison to the assumptions made in deriving the pressure-strain model, its effect on the predicted Reynolds stresses is likely to be small.

Nevertheless, as improvements are made in the pressure-strain model, it will become necessary to consider the turbulent transport model in more detail.

During the present investigation, all ten independent triple velocity correlations were obtained from the 3D LDA measurements (see Section 4.2.3.3), four of which are nominally zero, since the flow is 2D with $W=0$. Of particular interest are \overline{uvv} (Fig. 58) and $\overline{q^2v}$ (Fig. 66), since their cross-stream gradients form the predominant turbulent transport terms in the shear stress and turbulent kinetic energy equations. (Note that $\overline{q^2v}$, obtained from the sum $\overline{uuv} + \overline{vvv} + \overline{wwv}$, is actually twice the correlation \overline{kv} appearing in the k -equation.) In addition, the transport velocity V_q (Fig. 67) has been obtained as $\sqrt{\overline{q^2v}/\overline{q^2}}$, where $\overline{q^2}$ is twice the turbulent kinetic energy (Fig. 45), since this provides a further indication of the behaviour of the triple correlations. In general, the predominant Reynolds stress transport is away from the wall towards the edge of the boundary layer, providing the mechanism by which the boundary layer grows.

Overall, it is clear that turbulent transport is strongly affected by curvature. Along the inner wall, the initial convex curvature reduces \overline{uvv} to zero and $\overline{q^2v}$ to a very low level over the outer layer of the boundary layer, effectively destroying the large-scale shear-stress-containing turbulent motion. Since this does not recover for a considerable distance, the existing Reynolds stresses in the near-wall region are effectively trapped, since they cannot be transported to the edge of the boundary layer, thereby diminishing its growth rate. Downstream of the convex bend, however, the strong adverse pressure gradient gives rise to large variations in both \overline{uvv} and $\overline{q^2v}$, but only over a narrow region close to the wall. Although, as discussed in Section 4.2.4.5, this region of elevated Reynolds stresses mainly moves away from the wall because of the way that the strain rate (and therefore Reynolds stress production) is increased on the outer edge of the elevated region, the outward movement is also aided by the increased turbulent transport. Moreover, as separation is approached, there is some transport of the Reynolds stresses towards the wall. In the outer wall boundary layer, the concave curvature greatly increases \overline{uvv} and $\overline{q^2v}$, giving rise to large cross-stream gradients ($\partial\overline{uvv}/\partial n$ and $\partial\overline{kv}/\partial n$). These tend to increase the shear stress and turbulent kinetic energy over the outer part of the boundary layer, and reduce them in the near-wall region. Downstream of the concave bend, Reynolds stress production is dramatically reduced in the outer layer, due to the reduced strain rate, and therefore the turbulent transport becomes significant. However, the subsequent convex curvature virtually, but not completely, destroys the turbulent motion in the outer layer.

To assess the validity of a gradient diffusion model for the triple velocity correlations, consider the cross-stream shear stress gradient $\partial \bar{u}v/\partial n$ (Fig. 84) which, in the model, will give rise to $\bar{u}v v$ (Fig. 58). In very simple terms, there is a noticeable similarity between these quantities. When the variation of k^2/ϵ is also considered, which reacts to curvature in a similar manner to k (Fig. 45), the data would suggest that the behaviour of the turbulent transport model is reasonable. Of course, it will not be perfect, since the triple correlations are, themselves, governed by transport equations, and will behave independently of the shear stress gradients, especially in complex flows. Nevertheless, it is suggested that, for the present predictions at least, the gradient diffusion model provides acceptable representation of actual Reynolds stress turbulent transport. Note that the extra transport terms, such as $\bar{u}v v/R$, appearing in the Reynolds stress equations in curvilinear co-ordinates (Appendix 4), were not present in the coded form of the model. Considering the other simplifications, this was more than justified since they are an order of magnitude smaller than the actual gradients $\partial \bar{u}v v/\partial n$.

In the modelled dissipation rate transport equation, turbulent transport is also obtained using a simple gradient diffusion model with an isotropic diffusion coefficient. The constant (C_ϵ) in this model is determined by considering the behaviour of the equation in near-wall equilibrium flow, for which the log-law applies. In this region, $k = U_\tau^2/a$ and $\epsilon = U_\tau^3/\kappa n$, which can be differentiated to give an expression for $T_{(\epsilon)}$. With $P=\epsilon$ in Eq. 6.35, it is easily shown that,

$$C_\epsilon = \frac{a^3}{\kappa^2} (C_{\epsilon 2} - C_{\epsilon 1}) \quad \dots\dots 6.56$$

In the present predictions, the value of C_ϵ was derived by assuming $C_{\epsilon 1} = 1.45$, $C_{\epsilon 2} = 1.90$ and $a^3/\kappa^2 = 0.0986$, which gave $C_\epsilon = 0.044$. Moreover, it should be noted that the modified pressure-strain model constants suggested in Section 6.3.2.1 require a different C_ϵ value. In using these new constants, the value of 'a' increases from 0.255 to 0.28 (i.e., $a^3/\kappa^2 = 0.1306$), and, therefore, $C_\epsilon = 0.059$ would be needed with the same $C_{\epsilon 1}$ and $C_{\epsilon 2}$ values.

The one real concern, regarding the gradient diffusion model used in the Reynolds stress equations, is the value chosen for the constant (C_s). For the present prediction, a value of 0.058 was used (which is approximately $1.3 \times C_\epsilon$ as in the $k-\epsilon$ model). Based on the present experimental data this value was found to be too low, especially for shear stress transport. This was established by deriving the turbulent diffusion coefficients for the transport of turbulent kinetic energy and shear stress, which were then compared to the turbulent viscosity (v_t) which is, of course, the turbulent diffusion coefficient for the

transport of momentum. Using the data obtained in the equilibrium turbulent boundary layers at the end of the inlet length ($x/L = -0.75$), v_t was obtained from \bar{uv} (Fig. 81) and $\partial U/\partial n$ (Fig. 80) as the ratio $\bar{uv}/(\partial U/\partial n)$. For turbulent kinetic energy, the diffusion coefficient was obtained from $\bar{q^2 v}$ (Fig. 66) and $\partial \bar{q^2}/\partial n$ (derived from the k distribution, Fig. 45) as the ratio $\bar{q^2 v}/(\partial \bar{q^2}/\partial n)$ and found to be about $1.5 \times v_t$. For shear stress, however, the diffusion coefficient was obtained from \bar{uvv} (Fig. 58) and $\partial \bar{uv}/\partial n$ (Fig. 84) as $\bar{uvv}/(\partial \bar{uv}/\partial n)$ and found to be about $5 \times v_t$, significantly higher. For equilibrium flow in which $P = \epsilon$, the eddy-viscosity assumption gives $v_t = a^2 k^2 / \epsilon$. With $a = 0.28$, this implies that $C_s = 0.12$ is required for turbulent kinetic energy and $C_s = 0.39$ for shear stress.

Regardless of the fact that the different requirements could never be properly satisfied with an isotropic model, it is clear that the value used in the present prediction was too low. The use of the tensor based model of Daly and Harlow^[41] would be no better either, since the dominant term is proportional to $\bar{vv}k/\epsilon$. Since, in overall terms, the ratio \bar{vv}/k (Fig. 52) is fairly constant, this is effectively the same as using k^2/ϵ ; with an appropriate adjustment of the constant. The more sophisticated tensor based model of Hanjalic and Launder^[66] does effectively provide different diffusion coefficient for each of the Reynolds stresses, even in simple shear flow, but it is not obvious whether this would meet the above requirements.

6.3.2.5 Overcoming the Limitations

It is apparent that the pressure-strain model is responsible for the error in the predicted cross-stream normal stress, and probably the incorrect shear stress behaviour as well. Primarily, the fault lies with the over-simplistic near-wall component which, with the standard values for the constants, leads to the incorrect level of anisotropy. This undoubtedly contributes to the over-sensitive behaviour of the shear stress, although other factors may also be involved. Improvements are clearly possible by adjusting the constants as indicated in Section 6.3.2.1, but, to overcome the fundamental weaknesses of pressure-strain models of this kind, recent developments have tended to use transport equations in the low Reynolds number near-wall region (see So et al.^[149] for an overview).

Even though most of the low Reynolds number formulations revert to the Gibson and Launder^[59] (or Launder et al.^[92]) pressure-strain model at high Reynolds number, improvements in the modelling of the velocity-pressure gradient interaction and the dissipation rate in the near-wall region have led to improvements in the overall

behaviour of the predicted Reynolds stresses. For example, Shima^[140] has developed a model which has been able to capture the large reduction in shear stress brought about by strong convex curvature, without the excessive overshoot typical of the Gibson and Launder^[59] model. Another promising low Reynolds number approach, developed by Durbin^[50], has successfully demonstrated its ability to predict flow with strong curvature, and has the advantage of not using any wall-distance or turbulent Reynolds number based functions, typical of the other models.

Apart from the suggested changes to the constants of the existing model, which ought to be at least assessed, it is strongly recommended that the present annular S-shaped duct flow should be predicted using one of the more recently developed low Reynolds number turbulence models. Not only is the flow sufficiently complex for this to be an exacting test of the various models, but there is sufficient experimental data with which to judge the accuracy of the models.

CONCLUSIONS

A detailed investigation into the aerodynamic behaviour of an annular S-shaped duct has been completed. Initially, a new test rig was designed and constructed, and a data acquisition system developed, to allow measurements to be obtained using a 5-hole probe and a 3-component LDA system. The comprehensive data acquired has led to a thorough understanding of the physical behaviour of the flow (Chapter 4), and allowed the accuracy of standard numerical prediction methods to be assessed (Chapter 6).

The mean velocity and turbulence data show that the 2D axisymmetric flow through an S-shaped duct is complex, with the rapidly varying streamwise pressure gradients and streamline curvature having a significant effect on the flow behaviour. Along with the primary shear strain rate, the extra strain rate due to streamline curvature was seen to affect Reynolds stress production. This significantly affects the shear stress distribution, which, together with the pressure gradient, affects the mean velocity distribution. Whilst the strong adverse pressure gradient along the inner wall reduced the wall shear stress, boundary layer separation did not occur.

The total pressure variation was derived from the shear stress gradient, and found to be in excellent agreement with the directly measured data. The overall total pressure loss through the duct was relatively low, and some regions of increasing total pressure were observed. Moreover, the rate at which the total pressure reduces in the streamwise direction was found to be lower downstream of the S-shaped duct.

The axisymmetric flow through the S-shaped duct was predicted using standard $k-\epsilon$ and Reynolds stress transport equation turbulence models. In order to predict the physical behaviour of flow adequately, the Reynolds stresses must be obtained from transport equations, and not from an eddy-viscosity model. Even then, the modelling assumptions contained in the Reynolds stress transport equations, particularly the pressure-strain model, limit the accuracy of the prediction.

With a single stage compressor upstream of the S-shaped duct, the presence of the blade wakes has a beneficial effect on the flow. Within the first bend, there is a relatively large movement of wake fluid towards the inner wall, which helps prevent the boundary layer from separating. Moreover, the total pressure loss within the boundary layers is not increased substantially by the wakes.

RECOMMENDATIONS

Given the detail and quality of the experimental data, it is suggested that this annular S-shaped duct be used as a standard test case for CFD methods. In the 2D axisymmetric case, the flow is complex, with rapidly varying pressure gradients and curvature strongly affecting the behaviour, and the accurate prediction of this is a challenge for any turbulence model. Having reassessed the value of constants in the standard Gibson and Launder^[59] pressure-strain model (Sect. 6.3.2.1), further predictions could be carried out using the new values. Moreover, as discussed in Section 6.3.2.5, the recently developed low Reynolds number transport equation turbulence models could be assessed, and, in addition, it would be very interesting to use LES to predict this flow. Another aspect for further investigation, is the prediction of the 3D flow downstream of the compressor. With the stator exit conditions fully defined, there is a need to predict the development of stator blade wakes within the S-shaped duct.

To make further use of the test rig, there are several ways in which the present work could be extended. One possibility is to investigate the behaviour of the S-shaped duct with swirling flow, which could be achieved by removing the stator blade row of the compressor. Another option would be to investigate the effect of struts within the S-shaped duct, since these are often necessary within a gas turbine engine, and, by producing lift, these could be used in place of a stator blade row. Alternatively, a shorter, more highly loaded S-shaped duct could be designed and tested, which, since it is more difficult to predict flow close to separation, would provide an even more demanding test case for assessing the performance of CFD methods.

In the present investigation, it has not been possible to establish the extent to which streamline curvature influences the growth of the inner wall boundary layer. Although the convex curvature upstream of the strong adverse pressure gradient suppresses the shear stress in the outer part of the boundary layer, it is possible that this helps to promote the growth of a region of elevated shear stress adjacent to the inner wall, which actually helps to reduce the deceleration of the near-wall flow, and thereby delay separation. The mechanism by which the pressure and shear stress gradients combine to generate this region was described in Section 4.2.4.5, but it is not clear how significant the shear stress reduction due to curvature is in this process. It would be interesting, therefore, to investigate turbulent boundary layer flow along a straight wall with a pressure distribution matching that of the S-shaped duct, which could be induced by profiling the opposite wall.

REFERENCES

1. Adenubi, S. O., "Performance and Flow Regime of Annular Diffusers with Axial Turbomachine Discharge Inlet Conditions", Transactions of the ASME, Journal of Fluids Engineering, Vol. 98, pp. 236-243, 1976.
2. Alving, A. E., Smits, A. J. and Watmuff, J. H., "Turbulent Boundary Layer Relaxation from Convex Curvature", Journal of Fluid Mechanics, Vol. 211, pp. 529-556, 1990.
3. Amann, C. A., Nordenson, G. E. and Razinsky, E. H., "The Turbine Interstage Diffuser", Emissions Research Department Report GMR-1083, General Motors, 1971.
4. Bailey, D. W., Britchford, K. M., Carrotte, J. F. and Stevens, S. J., "Performance Assessment of an Annular S-shaped Duct", Transactions of the ASME, Journal of Turbomachinery, Vol. 119, pp. 149-156, 1997.
5. Bailey, D. W. and Carrotte, J. F., "The Influence of Inlet Swirl on the Flow Within an Annular S-shaped Duct", ASME Paper No. 96-GT-60, 1996.
6. Baldwin, B. S. and Lomax, H., "Thin Layer Approximation and Algebraic Stress Model for Separated Turbulent Flows", AIAA Paper No. 78-257, 1978.
7. Baldwin, B. S. and Barth, T. J., "A One-equation Turbulence Transport Model for High Reynolds Number Wall-bounded Flows", NASA TM 102847, 1990.
8. Bandyopadhyay, P. R. and Ahmed, A., "Turbulent Boundary Layers Subjected to Multiple Curvatures and Pressure Gradients", Journal of Fluid Mechanics, Vol. 246, pp. 503-527, 1993.
9. Bansod, P. and Bradshaw, P., "The Flow in S-shaped Ducts", Aeronautical Quarterly, Vol. 23, pp. 131-140, 1972.
10. Barlow, R. S. and Johnston, J. P., "Structure of a Turbulent Boundary Layer on a Concave Surface", Journal of Fluid Mechanics, Vol. 191, pp. 137-176, 1988.
11. Barlow, R. S. and Johnston, J. P., "Local Effects of Large-scale Eddies on Bursting in a Concave Boundary Layer", Journal of Fluid Mechanics, Vol. 191, pp. 177-195, 1988.
12. Baskaran, V., Smits, A. J. and Joubert, P. N., "A Turbulent Flow over a Curved Hill. Part 1. Growth of an Internal Boundary Layer", Journal of Fluid Mechanics, Vol. 182, pp. 47-83, 1987.

References

13. Baskaran, V., Smits, A. J. and Joubert, P. N., "A Turbulent Flow over a Curved Hill. Part 2. Effects of Streamline Curvature and Streamwise Pressure Gradient", Journal of Fluid Mechanics, Vol. 232, pp. 377-402, 1991.
14. Blackwelder, R. F. and Kovasznay, L. S. G., "Large-scale Motion of a Turbulent Boundary Layer During Relaminarization", Journal of Fluid Mechanics, Vol. 53, pp. 61-83, 1972.
15. Bradshaw, P., Ferriss, D. H. and Atwell, N. P., "Calculation of Boundary-layer Development Using the Turbulent Energy Equation", Journal of Fluid Mechanics, Vol. 28, pp. 593-616, 1967.
16. Bradshaw, P., "The Turbulence Structure of Equilibrium Boundary Layers", Journal of Fluid Mechanics, Vol. 29, pp. 625-645, 1967.
17. Bradshaw, P., "The Analogy Between Streamline Curvature and Buoyancy in Turbulent Shear Flow", Journal of Fluid Mechanics, Vol. 36, pp. 177-191, 1969.
18. Bradshaw, P., "Effects of Streamline Curvature on Turbulent Flow", AGARD AG-169, 1973.
19. Bradshaw, P., "Review - Complex Turbulent Flows", Transactions of the ASME, Journal of Fluids Engineering, Vol. 97, pp. 146-154, 1975.
20. Bradshaw, P., "An Introduction to Turbulence and its Measurement", Pergamon Press, 1975.
21. Bradshaw, P., Editor, "Turbulence", Springer-Verlag Berlin Heidelberg, 1976.
22. Bradshaw, P., "Complex Strain Fields", Proceedings of the 1980-81 AFOSR-HTTM-STANFORD Conference on Complex Turbulent Flows, eds. S. J. Kline et al., Thermosciences Division, Mechanical Engineering Department, Stanford University, pp. 700-712, 1981.
23. Bradshaw, P. and Huang, G. P., "The Law of the Wall in Turbulent Flow", Osborne Reynolds Centenary Symposium, Manchester, England, 1994.
24. Britchford, K. M., Manners, A. P., McGuirk, J. J. and Stevens, S. J., "Measurement and Prediction of Flow in Annular S-shaped Ducts", Engineering Turbulence Modelling and Experiments 2, eds. W. Rodi and F. Martelli, Elsevier Science Publishers B. V., pp. 785-794, 1993.
25. Britchford, K. M., Carrotte, J. F., Stevens, S. J., and McGuirk, J. J. "The Development of the Mean Flow and Turbulence Structure in an Annular S-shaped Duct", ASME Paper No. 94-GT-457, 1994.

References

26. Burrill, K. F. and Barnes, R. W., "Complex Annular Ducts for use in Gas Turbine Engines -Current Problem Areas in their Design", Paper No. 20, 1970.
27. Carrotte, J. F., Britchford, K. M. and Wray, A. P., "Three Component LDA Measurements of Annulus Wall Boundary Layers Upstream of an Annular S-shaped Duct", Proceedings of the Fifth International Conference on Laser Anemometry Advance and Applications, Veldhoven, The Netherlands, pp. 111-118, 1993.
28. Carrotte, J. F. and Britchford, K. M., "The Effect of Laser Beam Orientation on the Accuracy of 3D LDA Measurements Within an Annular Test Facility", Proceedings of the Seventh International Symposium on Applications of Laser Techniques to Fluid Mechanics, Lisbon, Portugal, pp. 17.3.1-17.3.8, 1994.
29. Castro, I. P. and Bradshaw, P., "The Turbulence Structure of a Highly Curved Mixing Layer", Journal of Fluid Mechanics, Vol. 73, pp. 265-304, 1976.
30. Cebeci, T. and Smith, A. M. O., "Analysis of Turbulent Boundary Layers", Academic Press, 1974.
31. Cebeci, T. and Bradshaw, P., "Momentum Transfer in Boundary Layers", Hemisphere Publishing Corporation, 1977.
32. Chen, H. C. and Patel, V. C., "Near-wall Turbulence Models for Complex Flows Including Separation", AIAA Journal, Vol. 26, pp. 641-648, 1988.
33. Cheng, G. C. and Farokhi, S., "On Turbulent Flows Dominated by Curvature Effects", Transactions of the ASME, Journal of Fluids Engineering, Vol. 114, pp. 52-57, 1992.
34. Chiwanga, S. C. and Ramaprian, B. R., "The Effect of Convex Wall Curvature on the Large-scale Structure of the Turbulent Boundary Layer", Engineering Turbulence Modelling and Experiments, eds. W. Rodi and E. N. Ganic, Elsevier Science Publishing Co., pp. 553-562, 1990.
35. Chou, P. Y., "On Velocity Correlations and the Solution of the Equations of Turbulent Flow", Quarterly Applied Mathematics, Vol. 3, pp. 38-54, 1945.
36. Chung, M. K., Park, S. W. and Kim, K. C., "Curvature Effects on Third-order Velocity Correlations and Its Model Representation", The Physics of Fluids, Vol. 30, pp. 626-628, 1987.
37. Clauser, F. H., "Turbulent Boundary Layers in Adverse Pressure Gradients", Journal of the Aeronautical Sciences, Vol. 21, pp. 91-108, 1954.

References

38. Coles, D., "The Law of the Wake in the Turbulent Boundary Layer", *Journal of Fluid Mechanics*, Vol. 1, pp. 191-226, 1956.
39. Cohen, H., Rogers, G. F. C. and Saravanamuttoo, H. I. H., "Gas Turbine Theory", Second Edition, Longman, 1972
40. Craft, T. J. and Launder, B. E., "New Wall-reflection Model Applied to the Turbulent Impinging Jet", *AIAA Journal*, Vol. 30, pp. 2970-2972, 1992.
41. Daly, B. J. and Harlow, F. H., "Transport Equations in Turbulence", *The Physics of Fluids*, Vol. 13, pp. 2634-2649, 1970.
42. Dantec, "57N10 Burst Spectrum Analyser", User Manual, Dantec Elektronic, Denmark, 1991.
43. Davidov, B. I., "On the Statistical Dynamics of an Incompressible Turbulent Fluid", *Dokl. Akad. Nauk S.S.R.*, Vol. 136, pp. 47-50, 1961, also Vol. 127, pp. 768-770, 1959.
44. De Henau, V., Raithby, G. D. and Thompson, B. E., "Prediction of Flows with Strong Curvature and Pressure Gradient Using k- ϵ Turbulence Model", *Transactions of the ASME, Journal of Fluids Engineering*, Vol. 112, pp. 40-47, 1992.
45. Dengel, P. and Fernholz, H. H., "An experimental Investigation of a Turbulent Boundary Layer in the Vicinity of Separation", *Journal of Fluid Mechanics*, Vol. 212, pp. 615-636, 1990.
46. Dianat, M. and Castro, I. P., "Measurements in Separating Boundary Layers", *AIAA Journal*, Vol. 27, pp. 719-724, 1989.
47. Dianat, M. and Castro, I. P., "Turbulence in Separated Boundary Layer", *Journal of Fluid Mechanics*, Vol. 226, pp. 91-123, 1991.
48. Dominy, R. G. and Kirkham, D. A., "The Influence of Blade Wakes on the Performance of Inter-turbine Diffusers", *ASME Paper No. 94-GT-207*, 1994.
49. Driver, D. M., "Reynolds Shear Stress Measurements in a Separated Boundary Layer", *AIAA Paper No. 91-1787*, 1991.
50. Durbin, P. A., "A Reynolds Stress Model for Near-wall Turbulence", *Journal of Fluid Mechanics*, Vol. 249, pp. 465-498, 1993.
51. Edwards, R. V., Editor, "Report of the Special Panel on Statistical Particle Bias Problems in Laser Anemometry", *Transactions of the ASME, Journal of Fluids Engineering*, Vol. 109, pp. 89-93, 1987.

References

52. Eghlima, A. and Kleinstreuer, C., "Numerical Analysis of Attached Turbulent Boundary Layers along Strongly Curved Surfaces", AIAA Journal, Vol. 23, pp. 177-184, 1985.
53. Ellis, L. B. and Joubert, P. N., "Turbulent Shear Flow in a Curved Duct", Journal of Fluid Mechanics, Vol. 62, pp. 65-84, 1974.
54. Eskinazi, S. and Yeh, H., "An Investigation on Fully Developed Turbulent Flows in a Curved Channel", Journal of the Aeronautical Sciences, Vol. 23, pp. 23-34&75, 1956.
55. Eskinazi, S. and Erian, F. F., "Energy Reversal in Turbulent Flows", The Physics of Fluids, Vol. 12, pp. 1988-1998, 1969.
56. Evans, R. L., "Freestream Turbulence Effects on Turbulent Boundary Layers in an Adverse Pressure Gradient", AIAA Journal, Vol. 23, pp. 1814-1816, 1985.
57. Fu, S, Launder, B. E. and Tselepidakis, D. P., "Accommodating the Effects of High Strain Rates in Modelling the Pressure-strain Correlation", Report No. TFD/87/5, UMIST, 1987.
58. Gibson, M. M., "An Algebraic Stress and Heat-flux Model for Turbulent Shear Flow with Streamline Curvature", International Journal of Heat and Mass Transfer, Vol. 21, pp. 1609-1617, 1978.
59. Gibson, M. M. and Launder, B. E., "Ground Effects on Pressure Fluctuations in the Atmospheric Boundary Layer", Journal of Fluid Mechanics, Vol. 86, pp. 491-511, 1978.
60. Gibson, M. M., Jones, W. P. and Younis, B. A., "Calculation of Turbulent Boundary Layers on Curved Surfaces", The Physics of Fluids, Vol. 24, pp. 386-395, 1981.
61. Gibson, M. M. and Rodi, W., "A Reynolds-stress Closure Model of Turbulence Applied to the Calculation of a Highly Curved Mixing Layer", Journal of Fluid Mechanics, Vol. 103, pp. 161-182, 1981.
62. Gibson, M. M., Verriopoulos, C. A. and Vlachos, N. S., "Turbulent Boundary Layer on a Mildly Curved Convex Surface", Experiments in Fluids, Vol. 2, pp. 17-24, 1984.
63. Gillis, J. C. and Johnston, J. P., "Turbulent Boundary Layer Flow and Structure on a Convex Wall and its Redevelopment on a Flat Wall", Journal of Fluid Mechanics, Vol. 135, pp. 123-153, 1983.

References

64. Goldberg, P., "Upstream History and Apparent Stress in Turbulent Boundary Layers", Gas Turbine Laboratory Report No. 85, Massachusetts Institute of Technology, 1966.
65. Hanjalic, K., "Advanced Turbulence Closure Models: A view of Current Status and Future Prospects", International Journal of Heat and Fluid Flow, Vol. 15, pp. 178-203, 1994.
66. Hanjalic, K. and Launder, B. E., "A Reynolds Stress Model of Turbulence and Its Application to Thin Shear Layers", Journal of Fluid Mechanics, Vol. 52, pp. 609-638, 1972.
67. Hanjalic, K. and Launder, B. E., "Sensitizing the Dissipation Equation to Irrotational Strains", Transactions of the ASME, Journal of Fluids Engineering, Vol. 102, pp. 34-40, 1980.
68. Hinze, J. O., "Turbulence", McGraw-Hill, 1959.
69. Hoffmann, P. H., Muck, K. C. and Bradshaw, P., "The Effect of Concave Surface Curvature on Turbulent Boundary Layers", Journal of Fluid Mechanics, Vol. 161, pp. 371-403, 1985.
70. Hong, S. K. and Murthy, S. N. B., "Pressure-strain Correlations in Curved Wall Boundary Layers", AIAA Journal, Vol. 24, pp. 971-978, 1986.
71. Hunt, I. A. and Joubert, P. N., "Effects of Small Streamline Curvature on Turbulent Duct Flow", Journal of Fluid Mechanics, Vol. 91, pp. 633-659, 1979.
72. Irwin, H. P. A. H. and Arnot Smith, P., "Prediction of the Effect of Curvature on Turbulence", The Physics of Fluids, Vol. 18, pp. 624-630, 1975.
73. Japikse, D. and Pampreen, R., "Annular Diffuser Performance for an Automotive Gas Turbine", Transactions of the ASME, Journal of Engineering for Power, Vol. 101, pp. 358-372, 1979.
74. Johansson, A. V. and Hallbäck, M., "Modelling of Rapid Pressure-strain in Reynolds-stress Closures", Journal of Fluid Mechanics, Vol. 269, pp. 143-168, 1994.
75. Johansson, T. G. and Karlsson, R. I., "The Energy Budget in the Near-wall Region of a Turbulent Boundary Layer", Applications of Laser Anemometry to Fluid Mechanics, eds. R. J. Adrian et al., Springer-Verlag Berlin Heidelberg, pp. 3-22, 1989.

References

76. Johnson, A. E. and Hancock, P. E., "The Effect of Extra Strain Rates of Streamline Curvature and Divergence on Mixing Layers", *Turbulent Shear Flows 7*, Springer-Verlag Berlin Heidelberg, pp. 253-267, 1991.
77. Johnson, D. A. and King, L. S., "A Mathematically Simple Turbulence Closure Model for Attached and Separated Turbulent Boundary Layers", *AIAA Journal*, Vol. 23, pp. 1684-1692, 1985.
78. Jones, W. P. and Launder, B. E., "The Prediction of Laminarization with a Two-equation Model of Turbulence", *International Journal of Heat and Mass Transfer*, Vol. 15, pp. 301-314, 1972.
79. Jones, W. P. and Launder, B. E., "The Calculation of Low-Reynolds-number Phenomena with a Two-equation Model of Turbulence", *International Journal of Heat and Mass Transfer*, Vol. 16, pp. 1119-1130, 1973.
80. Jones, W. P. and Marquis, A. J., "Calculation of Axisymmetric Recirculating Flows with a Second-order Turbulence Model", *Proceedings of the Fifth Symposium on Turbulent Shear Flows*, Cornell, USA, pp. 20.1-20.4, 1985.
81. Jones, W. P. and Manners, A. P., "The Calculation of the Flow Through a Two-dimensional Faired Diffuser", *Turbulent Shear Flows 6*, Springer-Verlag Berlin Heidelberg, pp. 18-31, 1989.
82. Karlsson, R. I., "Near-wall Measurements of Turbulence Structure in Boundary Layers and Wall Jets", *Proceedings of the International Conference on Near-wall Turbulent Flows*, Tempe, Arizona, USA, pp. 423-432, 1993.
83. Kim, J., Moin, P. and Moser, R., "Turbulence Statistics in a Fully Developed Channel Flow at Low Reynolds Number", *Journal of Fluid Mechanics*, Vol. 177, pp. 133-166, 1987.
84. Klebanoff, P. S., "Characteristics of Turbulence in a Boundary Layer with Zero Pressure Gradient", NACA Report No. 1247, 1955. (superseding NACA TN 3178, 1954.)
85. Klein, A., "Review: Effects of Inlet Conditions on Conical-diffuser Performance", *Transactions of the ASME, Journal of Fluids Engineering*, Vol. 103, pp. 250-257, 1981.
86. Kline, S. J., Cantwell, B. J. and Lilley, G. M., "The 1980-81 AFOSR-HTTM-STANFORD Conference on Complex Turbulent Flows", Thermosciences Division, Mechanical Engineering Department, Stanford University, 1981.

87. Kline, S. J., Bardina, J. G. and Strawn, R. C., "Correlation of the Detachment of Two-dimensional Turbulent Boundary Layers", AIAA Journal, Vol. 21, pp. 68-73, 1983.
88. Launder, B. E., "Second-moment Closure: Present... and Future?", International Journal of Heat and Mass Transfer, Vol. 10, pp. 282-300, 1989.
89. Launder, B. E., "Second-moment Closure and its Use in Modelling Turbulent Industrial Flows", International Journal for Numerical Methods in Fluids, Vol. 9, pp. 963-985, 1989.
90. Launder, B. E., "On the Modelling of Turbulent Industrial Flows", Computational Methods in Applied Sciences, Ed. Ch. Hirsch, Elsevier Science Publishers B. V., pp. 91-102, 1992.
91. Launder, B. E., Priddin, C. H. and Sharma, B. I., "The Calculation of Turbulent Boundary Layers on Spinning and Curved Surfaces", Transactions of the ASME, Journal of Fluids Engineering, Vol. 99, pp. 231-239, 1977.
92. Launder, B. E., Reece, G. and Rodi, W., "Progress in the Development of a Reynolds Stress Turbulence Closure", Journal of Fluid Mechanics, Vol. 68, pp. 537-566, 1975.
93. Launder, B. E. and Spalding, D. B., "The Numerical Computation of Turbulent Flows", Computer Methods in Applied Mechanics and Engineering, Vol. 3, pp. 269-289, 1974.
94. Launder, B. E. and Tselepidakis, D. P., "Progress and Paradoxes in Modelling Near-wall Turbulence", Proceedings of the Eighth Symposium on Turbulent Shear Flows, Munich, Germany, pp. 29.1.1-29.1.6, 1991.
95. Leschziner, M. A., "Modelling Engineering Flow with Reynolds Stress Turbulence Closure", Journal of Wind Engineering and Industrial Aerodynamics, Vol. 35, pp. 21-47, 1990.
96. Leung, A. W. C. and Squire, L. C., "A Comparison of Several Eddy Viscosity Turbulence Models in Two and Three Dimensional Boundary Layer Flows", Aeronautical Journal, Vol. 98, pp. 73-82, 1994.
97. Lien, F. S. and Leschziner, M. A., "Assessment of Turbulence-transport Models Including Non-linear RNG Eddy-viscosity Formulation and Second-moment Closure for Flow Over a Backward-facing Step", Institute of Science and Technology Report No. TFD/93/09, University of Manchester, 1993.
98. Little, A. R. and Manners, A. P., "Predictions of the Pressure Losses in 2D and 3D Model Dump Diffusers", ASME Paper No. 93-GT-184, 1993.

References

99. Ludwieg, H. and Tillmann, W., "Investigation of the Wall Shearing Stress in Turbulent Boundary Layers", NACA TM 1285, 1950.
100. Manners, A. P., "The Calculation of the Flows in Gas Turbine Combustion Systems", Ph.D. Thesis, University of London, 1988.
101. Manners, A. P. and King, R. A., "Grid Generation and Flow Calculation for Complex Gas Turbine Combustion Systems", New Techniques in Mathematics and Computational Modelling of Turbulent Diffusion and Mixing in Industrial and Environmental Problems, Loughborough, 1991.
102. Mansour, N. N., Kim, J. and Moin, P., "Reynolds-stress and Dissipation-rate Budgets in a Turbulent Channel Flow", Journal of Fluid Mechanics, Vol. 194, pp. 15-44, 1988.
103. Marvin, J. G., "Turbulence Modelling for Computational Aerodynamics", AIAA Journal, Vol. 21, pp. 941-955, 1983.
104. Md. Abdalla, H. A., "Swirling Flow in Curved Wall Annuli", Ph.D. Thesis, Department of Mechanical Engineering, Indian Institute of Science, 1988.
105. Menter, F. R., "Performance of Popular Turbulence Models for Attached and Separated Adverse Pressure Gradient Flows", AIAA Paper No. 91-1784, 1991.
106. Meroney, R. N. and Bradshaw, P., "Turbulent Boundary Layer Growth over a Longitudinally Curved Surface", AIAA Journal, Vol. 13, pp. 1448-1453, 1975.
107. Moin, P. and Kim, J., "Numerical Investigation of Turbulent Channel Flow", Journal of Fluid Mechanics, Vol. 118, pp. 341-377, 1982.
108. Moser, R. D. and Moin, P., "The Effect of Curvature in Wall-bounded Turbulent Flows", Journal of Fluid Mechanics, Vol. 175, pp. 479-510, 1987.
109. Muck, K. C., Hoffmann, P. H. and Bradshaw, P., "The Effect of Convex Surface Curvature on Turbulent Boundary Layers", Journal of Fluid Mechanics, Vol. 161, pp. 347-369, 1985.
110. Murlis, J., Tsai, H. M. and Bradshaw, P., "The Structure of Turbulent Boundary Layers at Low Reynolds Numbers", Journal of Fluid Mechanics, Vol. 122, pp. 13-56, 1982.
111. Nakayama, A., "Curvature and Pressure-gradient Effects on a Small-defect Wake", Journal of Fluid Mechanics, Vol. 175, pp. 215-246, 1987.
112. Narasimha, R. and Screenivasan, K. R., "Relaminarization in Highly Accelerated Turbulent Boundary Layers", Journal of Fluid Mechanics, Vol. 61, pp. 417-447, 1973.

References

113. Park, S. W. and Chung, M. K., "Curvature-dependant Two-equation Model for Prediction of Turbulent Recirculating Flows", AIAA Journal, Vol. 27, pp. 340-344, 1989.
114. Patankar, S. V. and Spalding, D. B., "A Calculation Procedure for Heat, Mass and Momentum Transfer in Three-dimensional Parabolic Flows", International Journal of Heat and Mass Transfer, Vol. 15, pp. 1787-1806, 1972
115. Patel, V. C., "Calibration of the Preston Tube and Limitations on its Use in Pressure Gradients", Journal of Fluid Mechanics, Vol. 23, pp. 185-208, 1965.
116. Patel, V. C., "The Effects of Curvature on the Turbulent Boundary Layer", Aeronautical Research Council, Reports and Memoranda No. 3599, 1968.
117. Patel, V. C., "Measurement of Secondary Flow in the Boundary Layers of a 180 degree Channel", Aeronautical Research Council, Current Paper No. 1043, 1969.
118. Patel, V. C. and Head, M. R., "Reversion of Turbulent to Laminar Flow", Journal of Fluid Mechanics, Vol. 34, pp. 371-392, 1968.
119. Pearson, W. E, Manners, A. P. and Passmore, M. A., "Prediction of the Flow Around a Bluff Body in Close Proximity to the Ground", Proceedings of the Royal Aeronautical Society Two Day Conference on Vehicle Aerodynamics, Loughborough, England, pp. 29.1-29.12, 1994.
120. Ramaprian, B. R. and Shivaprasad, B. G., "Mean Flow Measurements in Turbulent Boundary Layers along Mildly Curved Surfaces", AIAA Journal, Vol. 15, pp. 189-196, 1977.
121. Ramaprian, B. R. and Shivaprasad, B. G., "The Structure of Turbulent Boundary Layers along Mildly Curved Surfaces", Journal of Fluid Mechanics, Vol. 85, pp. 273-303, 1978.
122. Ramaprian, B. R. and Shivaprasad, B. G., "The Instantaneous Structure of Mildly Curved Turbulent Boundary Layers", Journal of Fluid Mechanics, Vol. 115, pp. 39-58, 1982.
123. Rastogi, A. K. and Whitelaw, J. H., "Procedure for Predicting the Influence of Longitudinal Curvature on Boundary Layer Flows", ASME Paper No. 71-WA/FE-37, 1971.
124. Rayleigh, J. W. S., Lord, "On the Dynamics of Revolving Fluids", Proceedings of the Royal Society of London, Series A, Vol. 6, pp. 148-154, 1916.
125. Reynolds, W. C., "Computation of Turbulent Flows", Annual Review of Fluid Mechanics, eds. Van Dyke, M. et al., Vol. 8, pp. 183-208, 1976.

References

126. Rhee, C. M. and Chow, W. L., "A Numerical Study of the Turbulent Flow Past an Isolated Airfoil", AIAA Journal, Vol. 21, pp. 1525-1532, 1982.
127. Richmond, M. C. and Patel, V. C., "Convex and Concave Surface Curvature Effects in Wall-bounded Turbulent Flows", AIAA Journal, Vol. 29, pp. 895-902, 1991.
128. Rodi, W. and Scheuerer, G., "Calculation of Curved Shear Layers with Two-equation Turbulence Models", Physics of Fluids, Vol. 26, pp. 1422-1436, 1983.
129. Rodi, W. and Scheuerer, G., "Scrutinizing the k- ϵ Turbulence Model Under Adverse Pressure Gradient Conditions", Transactions of the ASME, Journal of Fluids Engineering, Vol. 108, pp. 174-179, 1986.
130. Rolls-Royce, "Various Internal Reports", Private Communication.
131. Rotta, J. C., "Statistische Theorie Nichthomogener Turbulenz", Zeitschrift für Physik, Vol. 129, pp. 547-572, also Vol. 131, pp. 51-77, 1951.
132. Rotta, J. C., "Turbulent Boundary Layers in Incompressible Flow", Progress in Aeronautical Science, Vol. 2, pp. 1-219, eds. A. Ferri et al., Pergamon Press, 1962.
133. Ryhming, I. L., Truong, T. V. and Lindberg, P. A., "Summary and Conclusions for the Test Case T1", Numerical Simulation of Unsteady Flows and Transition to Turbulence, eds. O. Pironneau et al., Cambridge University Press, pp. 197-243, 1992.
134. Samuel, A. E. and Joubert, P. N., "A Boundary Layer Developing in an Increasingly Adverse Pressure Gradient", Journal of Fluid Mechanics, Vol. 66, pp. 481-505, 1974.
135. Schlichting, H., "Boundary Layer Theory", McGraw-Hill Book Company, 1968.
136. Schmidbauer, H., "Behaviour of Turbulent Boundary Layers on Curved Convex Walls", NACA TM 791, 1936.
137. Schubauer, G. B. and Klebanoff, P. S., "Investigation of Separation of the Turbulent Boundary Layer", NACA Report No. 1030, 1951.
138. Shih, T. H. and Lumley, J. L., "Critical Comparison of Second-order Closures with Direct Numerical Simulations of Homogeneous Turbulence", AIAA Journal, Vol. 31, pp. 663-670, 1993.

References

139. Shiloh, K., Shivaprasad, B. G. and Simpson, R. L., "The Structure of a Separating Turbulent Boundary Layer. Part 3. Transverse Velocity Measurements", *Journal of Fluid Mechanics*, Vol. 113, pp. 75-90, 1981.
140. Shima, N., "Prediction of Turbulent Boundary Layers with a Second-moment Closure: Part II - Effects of Streamline Curvature and Spanwise Rotation", *Transactions of the ASME, Journal of Fluids Engineering*, Vol. 115, pp. 64-69, 1993.
141. Shir, C. C., "A preliminary Numerical Study of Atmospheric Turbulent Flows in the Idealised Planetary Boundary Layer", *Journal of Atmospheric Science*, Vol. 30, pp. 1327-1339, 1973.
142. Shivaprasad, B. G. and Ramaprian, B. R., "Turbulence Measurements in Boundary Layers along Mildly Curved Surfaces", *Transactions of the ASME, Journal of Fluids Engineering*, Vol. 100, pp. 37-46, 1978.
143. Shizawa, T. and Homani, S., "Experiment on Turbulent Boundary Layers over a Concave Surface - Effects of Introduction of Curvature", *Fourth Symposium on Turbulent Shear Flows*, Karlsruhe, Germany, pp. 6.38-6.43, 1983.
144. Simpson, R. L., Strickland, J. H. and Barr, P. W., "Features of a Separating Turbulent Boundary Layer in the Vicinity of Separation", *Journal of Fluid Mechanics*, Vol. 79, pp. 553-594, 1977.
145. Simpson, R. L., Chew, Y.-T. and Shivaprasad, B. G., "The Structure of a Separating Turbulent Boundary Layer. Part 1. Mean Flow and Reynolds Stresses", *Journal of Fluid Mechanics*, Vol. 113, pp. 23-51, 1981.
146. Simpson, R. L., Chew, Y.-T. and Shivaprasad, B. G., "The Structure of a Separating Turbulent Boundary Layer. Part 2. Higher Order Turbulence Results", *Journal of Fluid Mechanics*, Vol. 113, pp. 53-73, 1981.
147. Smits, A. J., Young, S. T. B. and Bradshaw, P., "The Effect of Short Regions of High Surface Curvature on Turbulent Boundary Layers", *Journal of Fluid Mechanics*, Vol. 94, pp. 209-242, 1979.
148. Smits, A. J., Eaton, J. A. and Bradshaw, P., "The Response of a Turbulent Boundary Layer to Lateral Divergence", *Journal of Fluid Mechanics*, Vol. 94, pp. 243-268, 1979.
149. So, R. M. C., Lai, Y. G., Zhang, H. S. and Hwang, B. C., "Second-order Near-wall Turbulence Closures: A Review", *AIAA Journal*, Vol. 29, pp. 1819-1835, 1991.

References

150. So, R. M. C. and Mellor, G. L., "An Experimental Investigation of Turbulent Boundary Layers along Curved Surfaces", NASA CR-1940, 1972.
151. So, R. M. C. and Mellor, G. L., "Experiment on Convex Curvature Effects in Turbulent Boundary Layers", Journal of Fluid Mechanics, Vol. 60, pp. 43-62, 1973.
152. So, R. M. C. and Mellor, G. L., "Experiment on Turbulent Boundary Layers on a Concave Wall", Aeronautical Quarterly, Vol. 26, pp. 25-40, 1975.
153. So, R. M. C. and Mellor, G. L., "Turbulent Boundary Layers with Large Streamline Curvature Effects", Journal of Applied Mathematics and Physics, Vol. 29, pp. 54-74, 1978.
154. Sovran, G. and Klomp, E. D., "Experimentally Determined Optimum Geometries for Rectilinear Diffusers with Rectangular, Conical or Annular Cross-section", Fluid Dynamics of Internal Flow, ed. G. Sovran, Elsevier Publishing Co., 1967.
155. Spalart, P. R., "Numerical Study of Sink-flow Boundary Layers", Journal of Fluid Mechanics, Vol. 172, pp. 307-328, 1986.
156. Spalart, P. R., "Direct Simulation of a Turbulent Boundary Layer up to $R_0 = 1410$ ", Journal of Fluid Mechanics, Vol. 187, pp. 61-98, 1988.
157. Spalart, P. R. and Watmuff, J. H., "Experimental and Numerical Study of a Turbulent Boundary Layer with Pressure Gradients", Journal of Fluid Mechanics, Vol. 249, pp. 337-371, 1993.
158. Spalding, D. B., "A Novel Finite-difference Formulation for Differential Expressions Involving Both First and Second Derivatives", International Journal of Numerical Methods in Engineering, Vol. 4, pp. 551-559, 1972.
159. Speziale, C. G., "Analytical Methods for the Development of Reynolds-stress Closures in Turbulence", Annual Review of Fluid Mechanics, Vol. 23, pp. 107-157, 1991.
160. Speziale, C. G., Sarkar, S. and Gatski, T. B., "Modelling the Pressure-strain Correlation of Turbulence: An Invariant Dynamical Systems Approach", Journal of Fluid Mechanics, Vol. 227, pp. 245-272, 1991.
161. Speziale, C. G. and Gatski, T. B., "Assessment of Second-order Closure Models in Turbulent Flows", AIAA Journal, Vol. 32, pp. 2113-2115, 1994.

References

162. Stevens, S. J. and Eccleston, B., "The Performance of Combustion Chamber Annular Diffusers", Department of Transport Technology Report No. TT 69 R 02, Loughborough University, 1969.
163. Stevens, S. J. and Fry, P., "Measurement of Boundary Layer Growth in Annular Diffusers", Journal of Aircraft, Vol. 10, pp. 73-80, 1973.
164. Stevens, S. J. and Williams, G. J., "The Performance of Annular Diffusers", Department of Transport Technology Report No. TT 69 14, Loughborough University, 1969.
165. Stevens, S. J. and Williams, G. J., "The Influence of Initial Conditions on the Performance of Annular Diffusers", Transactions of the ASME, Journal of Fluids Engineering, Vol. 102, pp. 357-363, 1980.
166. Stevens, S. J. and Wray, A. P., "The Influence of Blade Wakes on the Performance of Outwardly Curved Combustor Pre-diffusers", AIAA Paper No. 85-1291, 1985.
167. Stock, H. W. and Haase, W., "Determination of Length Scales in Algebraic Turbulence Models for Navier-Stokes Methods", AIAA Journal, Vol. 27, pp. 5-14, 1989.
168. Sucharov, L. J. P. H., "An Analysis of Flow in a Swan Necked Duct", M.Sc. Thesis, Department of Mechanical Engineering, Cranfield Institute of Technology, 1971.
169. Sung, H. J., Jang, H. C. and Cho, C. H., "Curvature-dependent Two-equation Model for Recirculating Flows", Engineering Turbulence Modelling and Experiments, eds. W. Rodi and E. N. Ganic, Elsevier Science Publishing Co., pp. 33-42, 1990.
170. Tani, I., "Production of Longitudinal Vortices in the Boundary Layer along a Concave Wall", Journal of Geographical Research, Vol. 67, pp. 3075-3080, 1962.
171. Tennekes, H. and Lumley, J. L., "A First Course in Turbulence", MIT Press, 1972.
172. Thayer, E. B., "Evaluation of Curved-wall Annular Diffusers", ASME Paper No. 71-WA/FE-35, 1971.
173. Townsend, A. A., "The Development of Turbulent Boundary Layers with Negligible Wall Stress", Journal of Fluid Mechanics, Vol. 8, pp. 143-155, 1960.

References

174. Townsend, A. A., "The Behaviour of a Turbulent Boundary Layer Near Separation", *Journal of Fluid Mechanics*, Vol. 12, pp. 536-554, 1962.
175. Townsend, A. A., "The Structure of Turbulent Shear Flow", Cambridge University Press, 1976.
176. Tsuji, Y. and Morikawa, Y., "Turbulent Boundary Layer with Pressure Gradient Alternating in Sign", *Aeronautical Quarterly*, Vol. 27, pp. 15-28, 1976.
177. Von Kármán, T., "Some Aspects of the Turbulence Problem", *Proceedings of the Fourth International Congress of Applied Mechanics*, Cambridge, p. 54, 1934.
178. Wattendorf, F. L., "A Study of the Effect of Curvature on Fully Developed Turbulent Flow", *Proceedings of the Royal Society of London, Series A*, Vol. 148, pp. 565-598, 1935.
179. Wheeler, A. J. and Johnston, J. P., "An Assessment of Three-dimensional Turbulent Boundary Layer Prediction Methods", *Transactions of the ASME, Journal of Fluids Engineering*, Vol. 95, pp. 415-421, 1973.
180. Wilcken, H., "Effect of Curved Surfaces on Turbulent Boundary Layers", NASA TT-F-11421, 1967. Translation of "Turbulente Grenzschichten an gewoelbten Flächen", Berlin, Vol. 1, pp. 357-376, 1930.
181. Wilcox, D. C., "Reassessment of the Scale-determining Equation for Advanced Turbulence Models", *AIAA Journal*, Vol. 26, pp. 1299-1310, 1988.
182. Wray, A. P., "The Analysis of 5-Hole Probe Data using Generalised Computer Software", Department of Transport Technology Report No. TT 86 R06, Loughborough University, 1986.
183. Wray, A. P., Carrotte, J. F. and Wilson, C. W., "The Development of a Large Annular Facility for the Testing Gas Turbine Combustor Diffuser Systems", *AIAA Paper No. 93-2546*, 1993.

TABLES

- 1 S-shaped Duct Geometry
- 2 Traverse Geometry
- 3 Rotor Aerodynamic Parameters
- 4 Rotor Profile Parameters
- 5 Stator Aerodynamic Parameters
- 6 Stator Profile Parameters
- 7 Optical Configuration
- 8 Boundary Layer Integral Properties
- 9 Wall Pressure Gradient
- 10 Wall Geometrical Curvature
- 11 Shape Parameters
- 12 Effective Curvature and Wall Potential Velocity
- 13 Wall Shear Stress
- 14 Wall Shear Stress based on Wall Potential Velocity

Inner Wall				Outer Wall			
x/L	r (m)	r' (-)	r'' (m ⁻¹)	x/L	r (m)	r' (-)	r'' (m ⁻¹)
0.000	0.2845	0.000	-8.18	0.000	0.3556	0.000	-4.30
0.039	0.2841	-0.075	-8.04	0.060	0.3551	-0.062	-4.23
0.078	0.2831	-0.151	-7.47	0.120	0.3538	-0.122	-4.03
0.118	0.2812	-0.223	-6.69	0.179	0.3516	-0.180	-3.69
0.159	0.2787	-0.291	-5.73	0.237	0.3487	-0.232	-3.25
0.201	0.2754	-0.352	-4.65	0.294	0.3452	-0.277	-2.73
0.245	0.2713	-0.405	-3.56	0.350	0.3412	-0.314	-2.14
0.290	0.2667	-0.447	-2.48	0.405	0.3368	-0.342	-1.49
0.337	0.2614	-0.477	-1.46	0.459	0.3322	-0.360	-0.82
0.384	0.2559	-0.492	-0.50	0.510	0.3277	-0.367	-0.13
0.432	0.2500	-0.493	0.39	0.560	0.3232	-0.364	0.59
0.483	0.2441	-0.479	1.23	0.609	0.3189	-0.350	1.32
0.535	0.2381	-0.452	1.99	0.657	0.3150	-0.327	2.06
0.589	0.2325	-0.413	2.68	0.703	0.3115	-0.296	2.77
0.644	0.2273	-0.364	3.26	0.748	0.3084	-0.259	3.41
0.702	0.2226	-0.307	3.70	0.791	0.3059	-0.217	3.90
0.760	0.2187	-0.247	3.98	0.834	0.3039	-0.173	4.20
0.819	0.2156	-0.184	4.12	0.876	0.3024	-0.128	4.30
0.879	0.2134	-0.122	4.16	0.918	0.3013	-0.084	4.28
0.940	0.2120	-0.061	4.15	0.959	0.3007	-0.042	4.21
1.000	0.2116	0.000	4.14	1.000	0.3005	0.000	4.15

Table 1 S-shaped Duct Geometry

Tables

Traverse	x_m/L	r_m (m)	ϕ ($^{\circ}$)	x_i/L	r_i (m)	x_o/L	r_o (m)
W1	-0.7487	0.32005	0.0	-0.749	0.2847	-0.749	0.3554
W2	-0.5459	0.32005	0.0	-0.546	0.2847	-0.546	0.3554
A1	0.0000	0.32005	0.0	0.000	0.2847	0.000	0.3554
N1	0.0199	0.32005	-1.8	0.015	0.2847	0.024	0.3554
A2	0.1237	0.31755	-9.3	0.099	0.2826	0.148	0.3525
A3	0.2477	0.31025	-17.2	0.203	0.2756	0.292	0.3449
B1	0.3718	0.29925	-20.8	0.314	0.2640	0.430	0.3346
A4	0.4959	0.28655	-22.2	0.433	0.2499	0.559	0.3232
B2	0.6208	0.27430	-19.7	0.563	0.2349	0.680	0.3137
A5	0.7469	0.26435	-13.2	0.702	0.2223	0.792	0.3064
B3	0.8730	0.25805	-5.9	0.850	0.2137	0.896	0.3024
A6	1.0256	0.25600	0.0	1.026	0.2116	1.026	0.3005
A7	1.3896	0.25600	0.0	1.390	0.2116	1.390	0.3005
A8	1.7577	0.25600	0.0	1.758	0.2116	1.758	0.3005

Table 2 Traverse Geometry

Tables

SEC	r (m)	\hbar (-)	α_1 (°)	α_2 (°)	INC (°)	DEV (°)	LOSS (-)
1	0.2862	0.0254	57.64	45.21	-1.44	8.23	0.0544
2	0.2896	0.0729	57.94	45.97	-1.45	7.99	0.0515
3	0.2930	0.1203	58.23	46.71	-1.45	7.75	0.0487
4	0.2964	0.1678	58.51	47.42	-1.46	7.51	0.0457
5	0.2998	0.2153	58.80	48.10	-1.46	7.29	0.0432
6	0.3066	0.3103	59.36	49.39	-1.47	6.87	0.0397
7	0.3133	0.4052	59.91	50.58	-1.47	6.51	0.0378
8	0.3201	0.5002	60.45	51.69	-1.47	6.18	0.0370
9	0.3269	0.5951	60.98	52.72	-1.47	5.87	0.0380
10	0.3337	0.6900	61.50	53.67	-1.48	5.58	0.0405
11	0.3404	0.7848	62.00	54.55	-1.48	5.36	0.0458
12	0.3438	0.8321	62.25	54.97	-1.48	5.27	0.0493
13	0.3471	0.8794	62.50	55.38	-1.48	5.19	0.0532
14	0.3505	0.9267	62.74	55.77	-1.48	5.11	0.0570
15	0.3538	0.9739	62.97	56.16	-1.49	5.04	0.0608

Table 3 Rotor Aerodynamic Parameters

SEC	C _{AX} (mm)	C (mm)	S/C (-)	T/C (-)	R _{le} /T (-)	R _{te} /T (-)	α' ₁ (°)	α' ₂ (°)	ξ (°)	θ (°)
1	32.0	47.62	0.878	0.080	0.0600	0.0600	59.08	36.98	48.03	22.10
2	31.8	47.92	0.883	0.078	0.0630	0.0630	59.38	37.99	48.68	21.40
3	31.6	48.22	0.888	0.076	0.0660	0.0660	59.68	38.96	49.32	20.71
4	31.4	48.51	0.893	0.074	0.0690	0.0690	59.97	39.91	49.94	20.06
5	31.2	48.80	0.898	0.072	0.0720	0.0720	60.26	40.81	50.54	19.45
6	30.8	49.34	0.908	0.068	0.0780	0.0780	60.83	42.51	51.67	18.32
7	30.4	49.85	0.918	0.064	0.0840	0.0840	61.38	44.07	52.73	17.31
8	30.0	50.32	0.929	0.060	0.0900	0.0900	61.93	45.51	53.72	16.42
9	29.6	50.77	0.941	0.056	0.0960	0.0960	62.45	46.84	54.66	15.61
10	29.2	51.18	0.952	0.052	0.1020	0.1020	62.98	48.09	55.53	14.89
11	28.8	51.53	0.965	0.048	0.1080	0.1080	63.49	49.19	56.34	14.30
12	28.6	51.68	0.972	0.046	0.1110	0.1110	63.73	49.70	56.72	14.03
13	28.4	51.83	0.978	0.044	0.1140	0.1140	63.98	50.19	57.09	13.79
14	28.2	51.96	0.985	0.042	0.1170	0.1170	64.22	50.66	57.44	13.56
15	28.0	52.10	0.992	0.040	0.1200	0.1199	64.46	51.12	57.79	13.34

Table 4 Rotor Profile Parameters

Tables

SEC	r (m)	\bar{h} (-)	α_3 (°)	α_4 (°)	INC (°)	DEV (°)	LOSS (-)
1	0.2864	0.0261	30.34	0.00	0.44	5.72	0.0576
2	0.2898	0.0740	29.92	0.00	0.44	5.74	0.0552
3	0.2932	0.1217	29.50	0.00	0.45	5.75	0.0529
4	0.2966	0.1695	29.09	0.00	0.45	5.77	0.0505
5	0.2999	0.2172	28.71	0.00	0.46	5.80	0.0483
6	0.3067	0.3122	28.07	0.00	0.46	5.86	0.0447
7	0.3134	0.4070	27.55	0.00	0.44	5.96	0.0421
8	0.3202	0.5015	27.11	0.00	0.44	6.06	0.0409
9	0.3268	0.5956	26.81	0.00	0.45	6.15	0.0414
10	0.3335	0.6895	26.63	0.00	0.44	6.26	0.0426
11	0.3402	0.7831	26.64	0.00	0.44	6.39	0.0452
12	0.3435	0.8299	26.70	0.00	0.44	6.47	0.0469
13	0.3468	0.8767	26.80	0.00	0.45	6.55	0.0488
14	0.3502	0.9234	26.90	0.00	0.44	6.63	0.0507
15	0.3535	0.9702	27.00	0.00	0.45	6.72	0.0527

Table 5 Stator Aerodynamic Parameters

SEC	C _{AX} (mm)	C (mm)	S/C (-)	T/C (-)	R _{le} /T (-)	R _{te} /T (-)	α' ₃ (°)	α' ₄ (°)	ξ (°)	θ (°)
1	50.0	51.16	0.567	0.060	0.1245	0.0799	29.90	-5.72	12.28	35.62
2	50.0	51.11	0.574	0.060	0.1245	0.0799	29.48	-5.74	12.06	35.22
3	50.0	51.08	0.582	0.060	0.1245	0.0799	29.05	-5.75	11.85	34.80
4	50.0	51.04	0.589	0.060	0.1245	0.0799	28.63	-5.77	11.64	34.40
5	50.0	51.00	0.596	0.060	0.1245	0.0799	28.25	-5.80	11.44	34.05
6	50.0	50.94	0.610	0.060	0.1245	0.0799	27.60	-5.86	11.08	33.46
7	50.0	50.89	0.624	0.060	0.1244	0.0798	27.10	-5.96	10.78	33.06
8	50.0	50.85	0.638	0.060	0.1244	0.0798	26.67	-6.06	10.51	32.73
9	50.0	50.82	0.652	0.060	0.1243	0.0798	26.36	-6.15	10.31	32.52
10	50.0	50.80	0.665	0.060	0.1243	0.0799	26.18	-6.26	10.17	32.44
11	50.0	50.78	0.679	0.060	0.1243	0.0799	26.20	-6.39	10.10	32.59
12	50.0	50.78	0.686	0.060	0.1243	0.0799	26.26	-6.47	10.10	32.73
13	50.0	50.78	0.692	0.060	0.1243	0.0799	26.35	-6.55	10.10	32.90
14	50.0	50.78	0.699	0.060	0.1243	0.0799	26.46	-6.63	10.11	33.09
15	50.0	50.78	0.705	0.060	0.1243	0.0799	26.55	-6.72	10.12	33.27

Table 6 Stator Profile Parameters

Tables

Stn.	x_m/L	α ($^{\circ}$)	β ($^{\circ}$)	γ_g ($^{\circ}$)	γ_b ($^{\circ}$)
1	-0.75	22.6	-19.9	45.0	-45.0
2	0.02	-47.4	-9.4	44.0	-45.4
3	0.125	-24.9	17.7	44.3	-45.2
4	0.25	25.2	-17.1	46.5	-43.8
5	0.375	25.0	-17.3	46.4	-45.3
6	0.5	25.2	-17.1	47.0	-45.0
7	0.625	25.4	-16.6	46.2	-46.0
8	0.75	25.2	-17.1	46.2	-43.9
9	0.875	-22.4	17.8	45.0	-45.0
10	1.0	-22.4	17.8	44.4	-45.9
11	1.39	-25.0	17.8	45.2	-45.2
12	1.76	25.4	-17.0	45.3	-44.7

Table 7 Optical Configuration

Tables

Stn.	x_m/L	Inner Wall					Outer Wall				
		δ/h_{in}	δ^*/h_{in}	δ^{**}/h_{in}	θ/h_{in}	H	δ/h_{in}	δ^*/h_{in}	δ^{**}/h_{in}	θ/h_{in}	H
1	-0.55	0.239	0.0338	0.0591	0.0254	1.33	0.239	0.0338	0.0591	0.0254	1.33
2	0.0	0.218	0.0239	0.0429	0.0190	1.26	0.288	0.0492	0.0837	0.0344	1.43
3	0.125	0.214	0.0232	0.0415	0.0183	1.27	0.292	0.0520	0.0892	0.0372	1.40
4	0.25	0.236	0.0274	0.0485	0.0211	1.30	0.294	0.0471	0.0823	0.0352	1.34
5	0.375	0.271	0.0429	0.0731	0.0302	1.42	0.293	0.0387	0.0689	0.0302	1.28
6	0.5	0.319	0.0612	0.1007	0.0395	1.55	0.298	0.0323	0.0584	0.0261	1.24
7	0.625	0.366	0.0844	0.1358	0.0515	1.64	0.305	0.0309	0.0563	0.0254	1.22
8	0.75	0.412	0.1027	0.1645	0.0619	1.66	0.316	0.0316	0.0576	0.0259	1.22
9	0.875	0.424	0.1055	0.1710	0.0655	1.61	0.327	0.0352	0.0635	0.0284	1.24
10	1.0	0.408	0.0816	0.1386	0.0570	1.43	0.345	0.0422	0.0752	0.0330	1.28
11	1.39	0.387	0.0654	0.1149	0.0495	1.32	0.380	0.0534	0.0933	0.0399	1.34
12	1.76	0.401	0.0675	0.1190	0.0515	1.31	0.401	0.0555	0.0970	0.0415	1.34

Table 8 Boundary Layer Integral Properties

Tables

Stn.	x_m/L	Inner Wall							Outer Wall						
		s/h_{in}	C_p	$\frac{\partial C_p}{\partial(s/h_{in})}$	δ^*/h_{in}	$10^3 C_f$	β	$10^2 \chi$	s/h_{in}	C_p	$\frac{\partial C_p}{\partial(s/h_{in})}$	δ^*/h_{in}	$10^3 C_f$	β	$10^2 \chi$
1	-0.55	-1.86	0.03	0.0	0.034	3.84	0.0	0.0	-1.86	0.03	0.0	0.034	3.84	0.0	0.0
2	0.0	0.0	-0.23	-0.30	0.024	5.92	-1.21	-0.67	0.0	0.14	0.09	0.049	2.60	1.70	0.69
3	0.125	0.34	-0.33	-0.04	0.023	6.24	-0.15	-0.08	0.50	0.18	0.0	0.052	2.40	0.0	0.0
4	0.25	0.71	-0.25	0.29	0.027	5.18	1.54	0.79	1.00	0.14	-0.10	0.047	3.08	-1.53	-0.60
5	0.375	1.12	-0.11	0.33	0.043	2.20	6.44	3.26	1.50	0.08	-0.20	0.039	5.26	-1.47	-0.53
6	0.5	1.57	0.03	0.27	0.061	1.44	11.47	5.04	1.96	-0.05	-0.29	0.032	7.64	-1.23	-0.44
7	0.625	2.05	0.15	0.17	0.084	1.00	14.35	5.48	2.40	-0.18	-0.26	0.031	9.02	-0.89	-0.31
8	0.75	2.56	0.20	0.06	0.103	1.02	6.04	1.88	2.79	-0.26	-0.09	0.032	8.10	-0.35	-0.13
9	0.875	3.08	0.21	-0.06	0.105	1.30	-4.87	-1.30	3.15	-0.25	0.18	0.035	6.16	1.03	0.38
10	1.0	3.68	0.12	-0.17	0.082	2.40	-5.78	-1.47	3.59	-0.11	0.25	0.042	4.36	2.42	0.89
11	1.39	4.92	0.00	0.0	0.065	3.42	0.0	0.0	4.83	-0.02	0.0	0.053	3.24	0.0	0.0
12	1.76	6.17	-0.02	0.0	0.068	3.60	0.0	0.0	6.08	-0.02	0.0	0.056	3.02	0.0	0.0

Table 9 Wall Pressure Gradient

Tables

Stn.	x_m/L	Inner Wall				Outer Wall			
		s/h_{in}	h_{in}/R	δ/h_{in}	δ/R	s/h_{in}	h_{in}/R	δ/h_{in}	δ/R
1	-0.55	-1.86	0.0	0.239	0.0	-1.86	0.0	0.239	0.0
2	0.0	0.0	-0.22	0.218	-0.048	0.0	-0.18	0.288	-0.052
3	0.125	0.34	-0.50	0.214	-0.107	0.50	-0.28	0.292	-0.082
4	0.25	0.71	-0.38	0.236	-0.090	1.00	-0.20	0.294	-0.059
5	0.375	1.12	-0.14	0.271	-0.038	1.50	-0.08	0.293	-0.023
6	0.5	1.57	0.04	0.319	0.013	1.96	0.06	0.298	0.018
7	0.625	2.05	0.17	0.366	0.062	2.40	0.17	0.305	0.052
8	0.75	2.56	0.25	0.412	0.103	2.79	0.26	0.316	0.082
9	0.875	3.08	0.28	0.424	0.119	3.15	0.28	0.327	0.092
10	1.0	3.68	0.10	0.408	0.041	3.59	0.10	0.345	0.035
11	1.39	4.92	0.0	0.387	0.0	4.83	0.0	0.380	0.0
12	1.76	6.17	0.0	0.401	0.0	6.08	0.0	0.401	0.0

Table 10 Wall Geometrical Curvature

Tables

Stn.	x_m/L	Inner Wall				Outer Wall			
		s/h_{in}	H	U_r/U_{p_w}	G	s/h_{in}	H	U_r/U_{p_w}	G
1	-0.55	-1.86	1.33	0.0410	6.05	-1.86	1.33	0.0410	6.05
2	0.0	0.0	1.26	0.0456	4.53	0.0	1.43	0.0368	8.17
3	0.125	0.34	1.27	0.0455	4.68	0.50	1.40	0.0361	7.92
4	0.25	0.71	1.30	0.0420	5.50	1.00	1.34	0.0403	6.30
5	0.375	1.12	1.42	0.0290	10.2	1.50	1.28	0.0499	4.38
6	0.5	1.57	1.55	0.0253	14.0	1.96	1.24	0.0556	3.48
7	0.625	2.05	1.64	0.0220	17.7	2.40	1.22	0.0571	3.16
8	0.75	2.56	1.66	0.0231	17.2	2.79	1.22	0.0512	3.52
9	0.875	3.08	1.61	0.0261	14.5	3.15	1.24	0.0447	4.33
10	1.0	3.68	1.43	0.0337	8.93	3.59	1.28	0.0397	5.51
11	1.39	4.92	1.32	0.0375	6.46	4.83	1.34	0.0365	6.95
12	1.76	6.17	1.31	0.0384	6.17	6.08	1.34	0.0352	7.21

Table 11 Shape Parameters

Tables

Stn.	x_m/L	Passage		Inner Wall			Outer Wall		
		$h_{in}K_{eff}$	U_m/U_{Mean}	n_w/h_{in}	U_{p_w}/U_m	U_{p_w}/U_{Mean}	n_w/h_{in}	U_{p_w}/U_m	U_{p_w}/U_{Mean}
1	-0.55	0.0	1.069	-0.497	1.0	1.069	0.497	1.0	1.069
2	0.0	0.199	1.076	-0.495	1.109	1.194	0.495	0.910	0.980
3	0.125	0.249	1.078	-0.494	1.140	1.229	0.494	0.891	0.960
4	0.25	0.213	1.080	-0.510	1.122	1.212	0.510	0.902	0.974
5	0.375	0.100	1.082	-0.530	1.056	1.142	0.530	0.950	1.028
6	0.5	-0.043	1.085	-0.557	0.977	1.060	0.557	1.024	1.111
7	0.625	-0.128	1.090	-0.578	0.931	1.015	0.578	1.080	1.177
8	0.75	-0.199	1.093	-0.606	0.892	0.975	0.606	1.137	1.243
9	0.875	-0.192	1.095	-0.621	0.893	0.978	0.621	1.135	1.243
10	1.0	-0.107	1.097	-0.624	0.938	1.029	0.624	1.071	1.175
11	1.39	0.0	1.102	-0.623	1.0	1.102	0.623	1.0	1.102
12	1.76	0.0	1.105	-0.620	1.0	1.105	0.620	1.0	1.105

Table 12 Effective Curvature and Wall Potential Velocity

Tables

Stn.	x_m/L	Inner Wall				Outer Wall			
		θ/h_{in}	R_θ	U_τ/U_{Mean}	$10^3 C_f$	θ/h_{in}	R_θ	U_τ/U_{Mean}	$10^3 C_f$
1	-0.55	0.0254	3513	0.0438	3.84	0.0254	3513	0.0438	3.84
2	0.0	0.0190	2635	0.0544	5.92	0.0344	4782	0.0360	2.60
3	0.125	0.0183	2537	0.0559	6.24	0.0372	5172	0.0346	2.40
4	0.25	0.0211	2928	0.0509	5.18	0.0352	4879	0.0393	3.08
5	0.375	0.0302	4196	0.0332	2.20	0.0302	4196	0.0513	5.26
6	0.5	0.0395	5465	0.0268	1.44	0.0261	3611	0.0618	7.64
7	0.625	0.0515	7124	0.0224	1.00	0.0254	3513	0.0672	9.02
8	0.75	0.0619	8588	0.0226	1.02	0.0259	3611	0.0636	8.10
9	0.875	0.0655	9076	0.0255	1.30	0.0284	3903	0.0555	6.16
10	1.0	0.0570	7904	0.0346	2.40	0.0330	4587	0.0467	4.36
11	1.39	0.0495	6831	0.0413	3.42	0.0399	5562	0.0402	3.24
12	1.76	0.0515	7124	0.0424	3.60	0.0415	5855	0.0389	3.02

Table 13 Wall Shear Stress

Tables

Stn.	x_m/L	Inner Wall				Outer Wall			
		U_{p_w}/U_{Mean}	R'_θ	U_v/U_{p_w}	$10^3 C'_f$	U_{p_w}/U_{Mean}	R'_θ	U_v/U_{p_w}	$10^3 C'_f$
1	-0.55	1.069	3756	0.0410	3.36	1.069	3756	0.0410	3.36
2	0.0	1.194	3145	0.0456	4.16	0.980	4684	0.0368	2.71
3	0.125	1.229	3118	0.0455	4.13	0.960	4965	0.0361	2.60
4	0.25	1.212	3548	0.0420	3.53	0.974	4753	0.0403	3.25
5	0.375	1.142	4793	0.0290	1.69	1.028	4313	0.0499	4.98
6	0.5	1.060	5792	0.0253	1.29	1.111	4013	0.0556	6.18
7	0.625	1.015	7230	0.0220	0.97	1.177	4135	0.0571	6.51
8	0.75	0.975	8376	0.0231	1.07	1.243	4488	0.0512	5.24
9	0.875	0.978	8879	0.0261	1.36	1.243	4853	0.0447	3.99
10	1.0	1.029	8130	0.0337	2.27	1.175	5390	0.0397	3.16
11	1.39	1.102	7528	0.0375	2.81	1.102	6130	0.0365	2.67
12	1.76	1.105	7872	0.0384	2.95	1.105	6470	0.0352	2.47

Table 14 Wall Shear Stress based on Wall Potential Velocity

FIGURES

- 1 Gas Turbine Schematic
- 2 Rig General Arrangement
- 3 Working Section and Traverse Locations
- 4 LDA Optical Arrangement
- 5 Five Hole Probe Calibration
- 6 Compressor Characteristics
- 7 Wall Static Pressure Distribution
- 8 Static Pressure Distribution
- 9 Streamwise Velocity Distribution
- 10 Velocity Vectors throughout S-shaped Duct
- 11 Flow Streamlines
- 12 Distribution of Streamwise Velocity Ratio vs. Height - 5HP Data with Boundary Layer Thickness Indicated
- 13 Distribution of Streamwise Velocity Ratio vs. Stream Function - 5HP Data with Boundary Layer Thickness Indicated
- 14 Streamwise Velocity Distribution - Comparison of LDA and 5HP Data
- 15 Cross-stream Velocity Distribution - Comparison of LDA and 5HP Data
- 16 Circumferential Velocity Distribution - Comparison of LDA and 5HP Data
- 17 Radial Velocity Distribution - Comparison of LDA and 5HP Data
- 18 Potential velocity Distribution - Comparison of LDA and 5HP Data
- 19 Streamwise Velocity Ratio Distribution - Comparison of LDA and 5HP Data
- 20 Axial Variation of Mean Pressure Coefficient
- 21 Axial Variation of Kinetic Energy Flux Coefficient
- 22 Axial Variation of Displacement Thickness - Experiment (LDA & 5HP) Clean
- 23 Axial Variation of Momentum Thickness - Experiment (LDA & 5HP) Clean
- 24 Axial Variation of Boundary Layer Shape Parameter - Experiment (LDA & 5HP) Clean
- 25 Axial Variation of Friction Velocity - Experiment (LDA & 5HP) Clean
- 26 Axial Variation of Wall Potential Velocity - Experiment (LDA & 5HP) Clean vs. Inviscid Calculation
- 27 Axial Variation of Boundary Layer Thickness (δ , δ^* , θ)
- 28 Axial Variation of Boundary Layer Thickness (δ^* , θ)
- 29 Axial Variation of Boundary Layer Shape Parameter
- 30 Axial Variation of Skin Friction Coefficient

Figures

- 31 Skin Friction vs. Reynolds Number - (Up_w based)
- 32 Axial Variation of Skin Friction Coefficient -
Experiment vs. Ludwieg-Tillmann
- 33 Skin Friction Coefficient vs. Shape Parameter -
Experiment vs. Ludwieg-Tillmann
- 34 Pressure Gradient Parameter vs. Wall Curvature Parameter
- 35 Clauser Parameter vs. Pressure Gradient Parameter
- 36 Clauser Parameter vs. Wall Curvature Parameter
- 37 Shape Parameter vs. Pressure Gradient Parameter
- 38 Skin Friction Coefficient vs. Pressure Gradient Parameter
- 39 Variation of Streamwise Normal Stress (\overline{uu})
- 40 Variation of Cross-stream Normal Stress (\overline{vv})
- 41 Variation of Circumferential Normal Stress (\overline{ww})
- 42 Variation of Reynolds Shear Stress (\overline{uv})
- 43 Variation of Reynolds Shear Stress (\overline{uw})
- 44 Variation of Reynolds Shear Stress (\overline{vw})
- 45 Variation of Turbulent Kinetic Energy
- 46 Variation of Shear Stress Correlation Coefficient
- 47 Variation of Reynolds Stress Ratio ($\overline{vv}/\overline{uu}$)
- 48 Variation of Reynolds Stress Ratio ($\overline{uv}/\overline{uu}$)
- 49 Variation of Reynolds Stress Ratio ($\overline{uv}/\overline{vv}$)
- 50 Variation of Reynolds Stress Ratio (\overline{uv}/k)
- 51 Variation of Reynolds Stress Ratio (\overline{uu}/k)
- 52 Variation of Reynolds Stress Ratio (\overline{vv}/k)
- 53 Variation of Reynolds Stress Ratio (\overline{ww}/k)
- 54 Measured Reynolds Stress Anisotropy
- 55 Variation of Triple Velocity Correlation (\overline{uuu})
- 56 Variation of Triple Velocity Correlation (\overline{uuv})
- 57 Variation of Triple Velocity Correlation (\overline{uuw})
- 58 Variation of Triple Velocity Correlation (\overline{uvv})
- 59 Variation of Triple Velocity Correlation (\overline{uvw})
- 60 Variation of Triple Velocity Correlation (\overline{uww})
- 61 Variation of Triple Velocity Correlation (\overline{vvv})
- 62 Variation of Triple Velocity Correlation (\overline{vww})
- 63 Variation of Triple Velocity Correlation (\overline{vww})
- 64 Variation of Triple Velocity Correlation (\overline{www})
- 65 Variation of Triple Velocity Correlation ($\overline{q^2 u}$)
- 66 Variation of Triple Velocity Correlation ($\overline{q^2 v}$)

Figures

- 67 Turbulent Kinetic Energy Transport Velocity (V_q)
- 68 Variation of U-skewness
- 69 Variation of V-skewness
- 70 Variation of W-skewness
- 71 Variation of U-intermittency
- 72 Variation of V-intermittency
- 73 Variation of W-intermittency
- 74 Measured Inner Wall Streamwise Velocity - Log-law Co-ordinates
- 75 Measured Outer Wall Streamwise Velocity - Log-law Co-ordinates
- 76 Measured Reynolds Shear Stress Profiles - Inner Wall -
(Non-dimensionalised by Local Parameters)
- 77 Measured Reynolds Shear Stress Profiles - Outer Wall -
(Non-dimensionalised by Local Parameters)
- 78 Mean Strain Rate Distribution
- 79 Strain Rate and Vorticity Distribution
- 80 Cross-Stream Gradient of Streamwise Velocity
- 81 Measured Reynolds Shear Stress Profiles
with 'Best Fit' Interpretation and Wall Values
- 82 Total Shear Stress Distribution vs. Height -
'Best Fit' Interpretation of Measured Reynolds Shear Stress Profiles
- 83 Total Shear Stress Distribution vs. Stream Function -
'Best Fit' Interpretation of Measured Reynolds Shear Stress Profiles
- 84 Variation of Shear Stress Gradient ($\partial \bar{u}v / \partial n$) vs. Stream Function
- 85 Variation of Shear Stress Gradient ($U \partial \bar{u}v / \partial n$) vs. Height
- 86 Regions of Positive and Negative Shear Stress Gradient
- 87 Comparison of Measured and Derived Total Pressure
- 88 Axial Variation of Loss Coefficient -
Experiment (5HP) vs. Shear Stress Derived Value (LDA)
- 89 Variation of Turbulent Kinetic Energy Production
- 90 Mean Energy Redistribution and Loss
- 91 Variation of Streamwise Pressure Gradient (cf. Shear Stress Gradient)
- 92 Streamwise Acceleration (cf. Stress Gradient minus Pressure Gradient)
- 93 Streamwise Velocity Profiles vs. Height - (Clean Inlet - 5HP)
- 94 Streamwise Velocity Profiles vs. Stream Function - (Clean Inlet - 5HP)
- 95 Total Pressure Distribution vs. Height - (Clean Inlet - 5HP)
- 96 Total Pressure Distribution vs. Stream Function - (Clean Inlet - 5HP)
- 97 Total Pressure Distribution vs. Fractional Distance from Wall -
(Clean Inlet - 5HP)

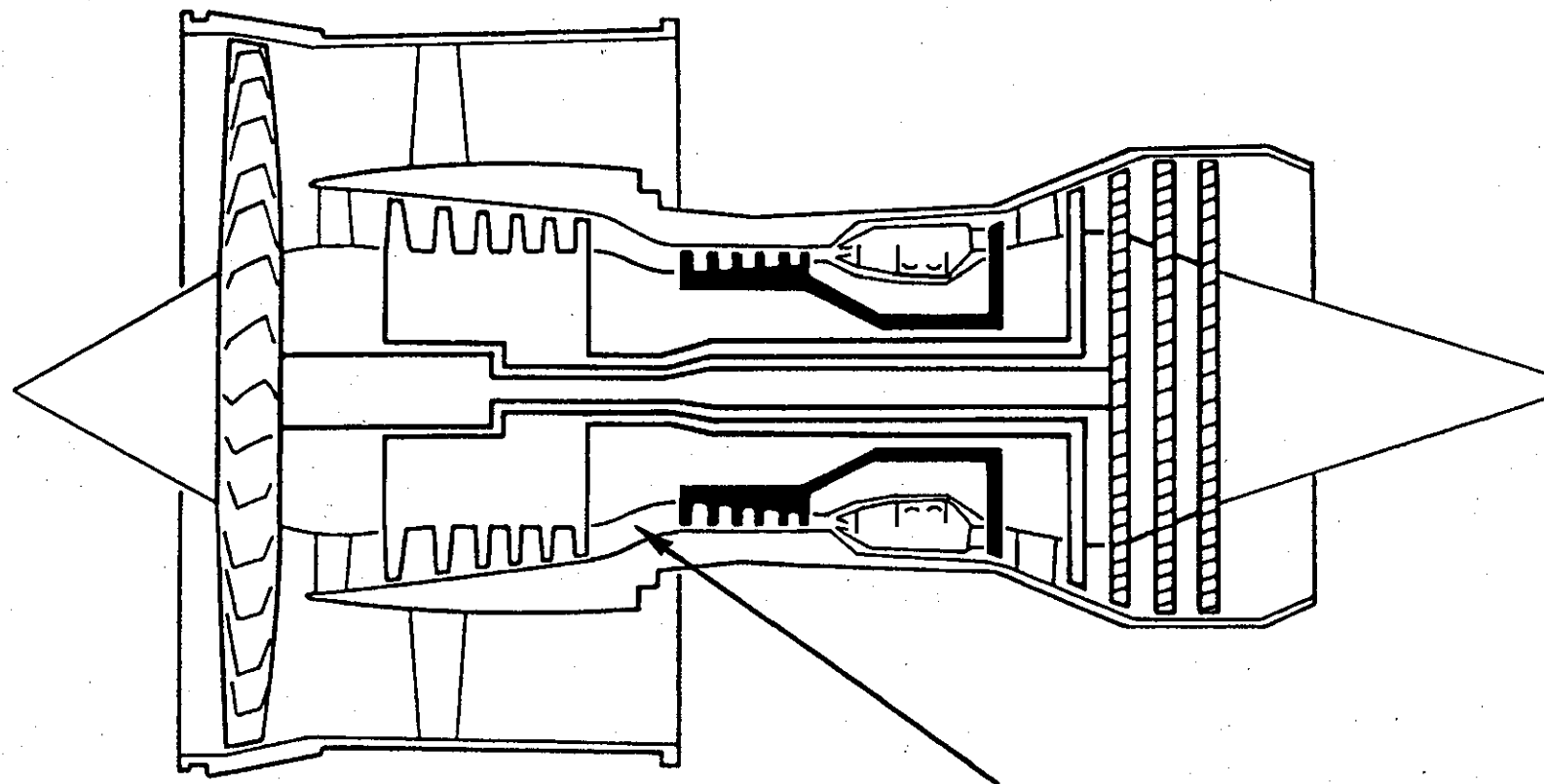
Figures

- 98 Total Pressure Distribution vs. Fractional Mass Flow from Wall -
(Clean Inlet - 5HP)
- 99 Total Pressure Distribution vs. Fractional Distance from Wall -
(Clean Inlet - Derived from LDA $\bar{u}\bar{v}$ Measurements)
- 100 Total Pressure Distribution vs. Fractional Mass Flow from Wall -
(Clean Inlet - Derived from LDA $\bar{u}\bar{v}$ Measurements)
- 101 Experimental Measurement Mesh
- 102 Contours of Streamwise Velocity (S-duct Inlet - $x/L = 0.0$)
- 103 Contours of Radial Velocity (S-duct Inlet - $x/L = 0.0$)
- 104 Contours of Circumferential Velocity (S-duct Inlet - $x/L = 0.0$)
- 105 Secondary Velocity Vectors (S-duct Inlet - $x/L = 0.0$)
- 106 Contours of Total Pressure Coefficient (S-duct Inlet - $x/L = 0.0$)
- 107 Measured Contours of Total Pressure Coefficient
- 108 Mean and Wall Static Pressure Distribution With the Compressor
- 109 Comparison of the Static Pressure Distribution With and Without
the Compressor - (Pitch-averaged 5HP Measurements)
- 110 Comparison of Streamwise Velocity Profiles With and Without
the Compressor - (Pitch-averaged 5HP Measurements)
- 111 Streamwise Velocity Profiles vs. Height - (Compressor at Inlet - 5HP)
- 112 Streamwise Velocity Profiles vs. Stream Function - (Compressor at Inlet - 5HP)
- 113 Total Pressure Distribution vs. Height - (Compressor at Inlet - 5HP)
- 114 Total Pressure Distribution vs. Stream Function - (Compressor at Inlet - 5HP)
- 115 Axial Variation of Boundary Layer Shape Parameter With and Without
the Compressor
- 116 Secondary Velocity Vectors ($x/L = 0.25$)
- 117 Contours of Turbulent Kinetic Energy (S-duct Inlet - $x/L = 0.02$)
- 118 Contours of $\bar{u}\bar{u}$ Normal Stress (S-duct Inlet - $x/L = 0.02$)
- 119 Contours of $\bar{v}\bar{v}$ Normal Stress (S-duct Inlet - $x/L = 0.02$)
- 120 Contours of $\bar{w}\bar{w}$ Normal Stress (S-duct Inlet - $x/L = 0.02$)
- 121 Contours of $\bar{u}\bar{w}$ Shear Stress (S-duct Inlet - $x/L = 0.02$)
- 122 Contours of $\bar{v}\bar{w}$ Shear Stress (S-duct Inlet - $x/L = 0.02$)
- 123 Contours of $\bar{u}\bar{v}$ Shear Stress (S-duct Inlet - $x/L = 0.02$)
- 124 CFD Calculation Grid
- 125 Axial Variation of Boundary Layer Displacement Thickness -
(CFD vs. Experiment)
- 126 Axial Variation of Boundary Layer Momentum Thickness -
(CFD vs. Experiment)
- 127 Axial Variation of Boundary Layer Shape Parameter - (CFD vs. Experiment)

Figures

- 128 Axial Variation of Friction Velocity - (CFD vs. Experiment)
- 129 Comparison of Measured (LDA) and Predicted Streamwise Velocity Profiles
- 130 Comparison of Measured (SHP) and Predicted Streamwise Velocity Profiles
- 131 Comparison of Measured (LDA) and Predicted Radial Velocity Profiles
- 132 Comparison of Measured (SHP) and Predicted Radial Velocity Profiles
- 133 Comparison of Measured and Predicted
Streamwise Normal Stress Profiles (\overline{uu})
- 134 Comparison of Measured and Predicted
Cross-stream Normal Stress Profiles (\overline{vv})
- 135 Comparison of Measured and Predicted
Circumferential Normal Stress Profiles (\overline{ww})
- 136 Comparison of Measured and Predicted Reynolds Shear Stress Profiles (\overline{uv})
- 137 Comparison of Measured and Predicted Turbulent Kinetic Energy Profiles
- 138 Predicted Turbulent Kinetic Energy Dissipation Rate Profiles
- 139 Comparison of Measured and Predicted Normal Stress Ratio ($\overline{vv}/\overline{uu}$)
- 140 Comparison of Measured and Predicted Anisotropy Tensor Component a_{11}
- 141 Comparison of Measured and Predicted Anisotropy Tensor Component a_{22}
- 142 Comparison of Measured and Predicted Anisotropy Tensor Component a_{33}
- 143 Comparison of Measured and Predicted Anisotropy Tensor Component a_{12}
- 144 Predicted Reynolds Stresses in Core Region
- 145 Predicted Turbulent Kinetic Energy in Core Region
- 146 Predicted Shear Stress in Core Region

Gas Turbine Schematic



Annular S-shaped Duct

Rig General Arrangement

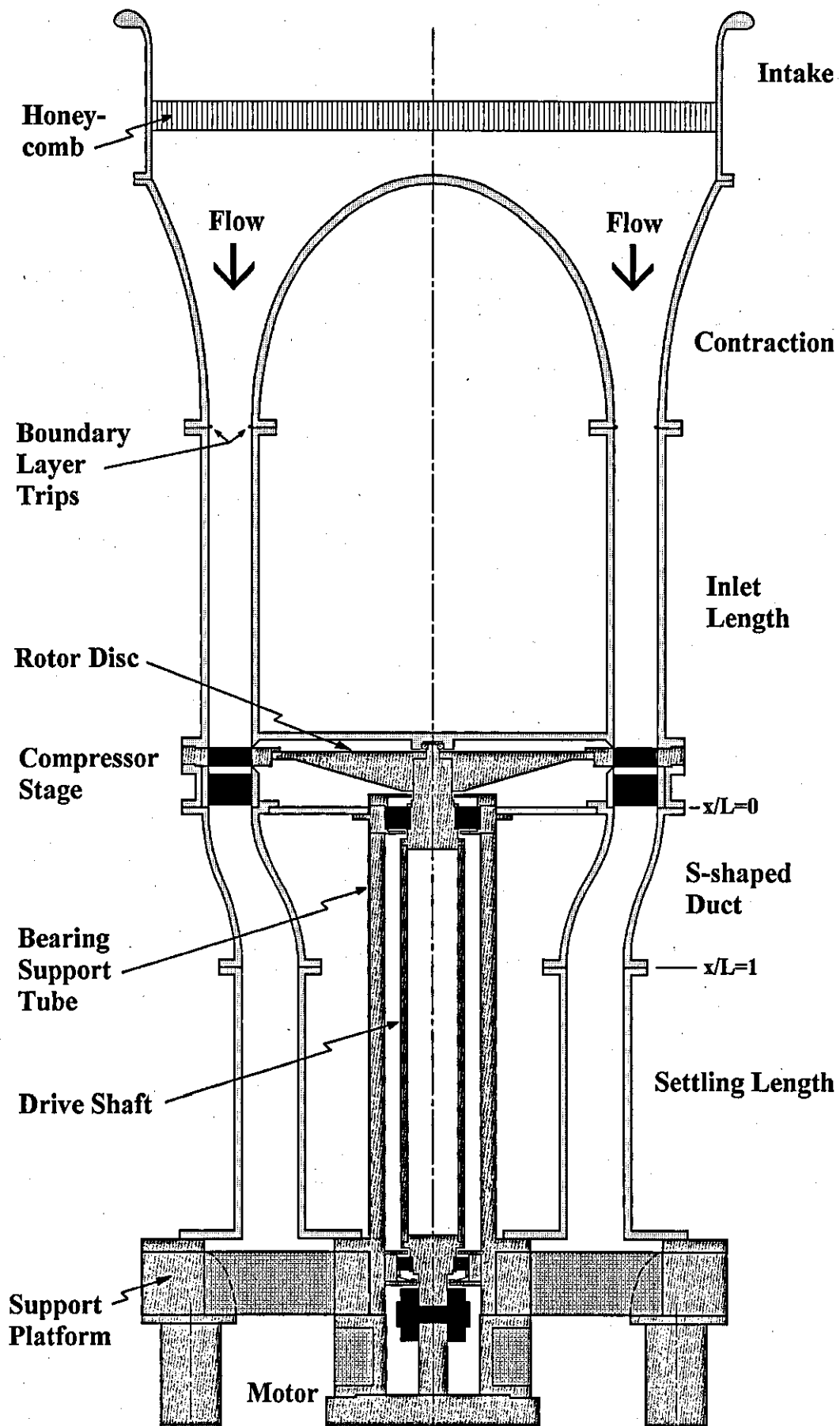


Figure 3

Working Section and Traverse Locations

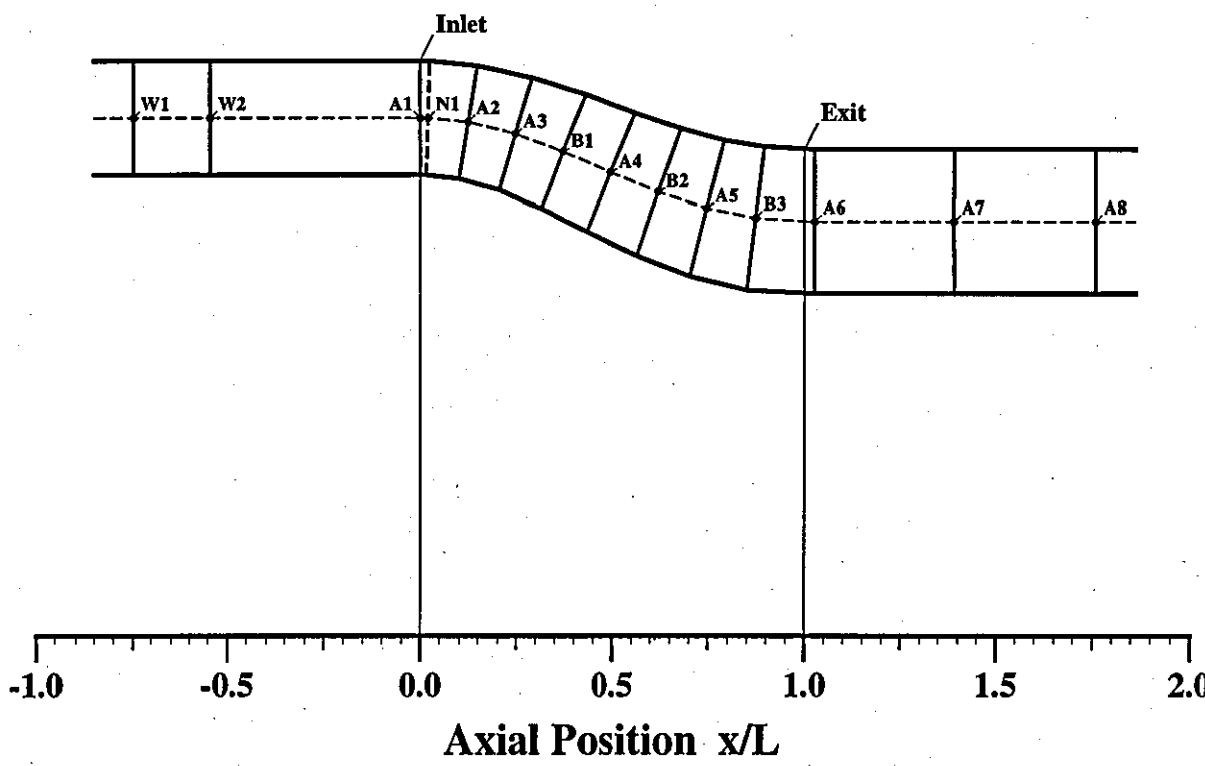
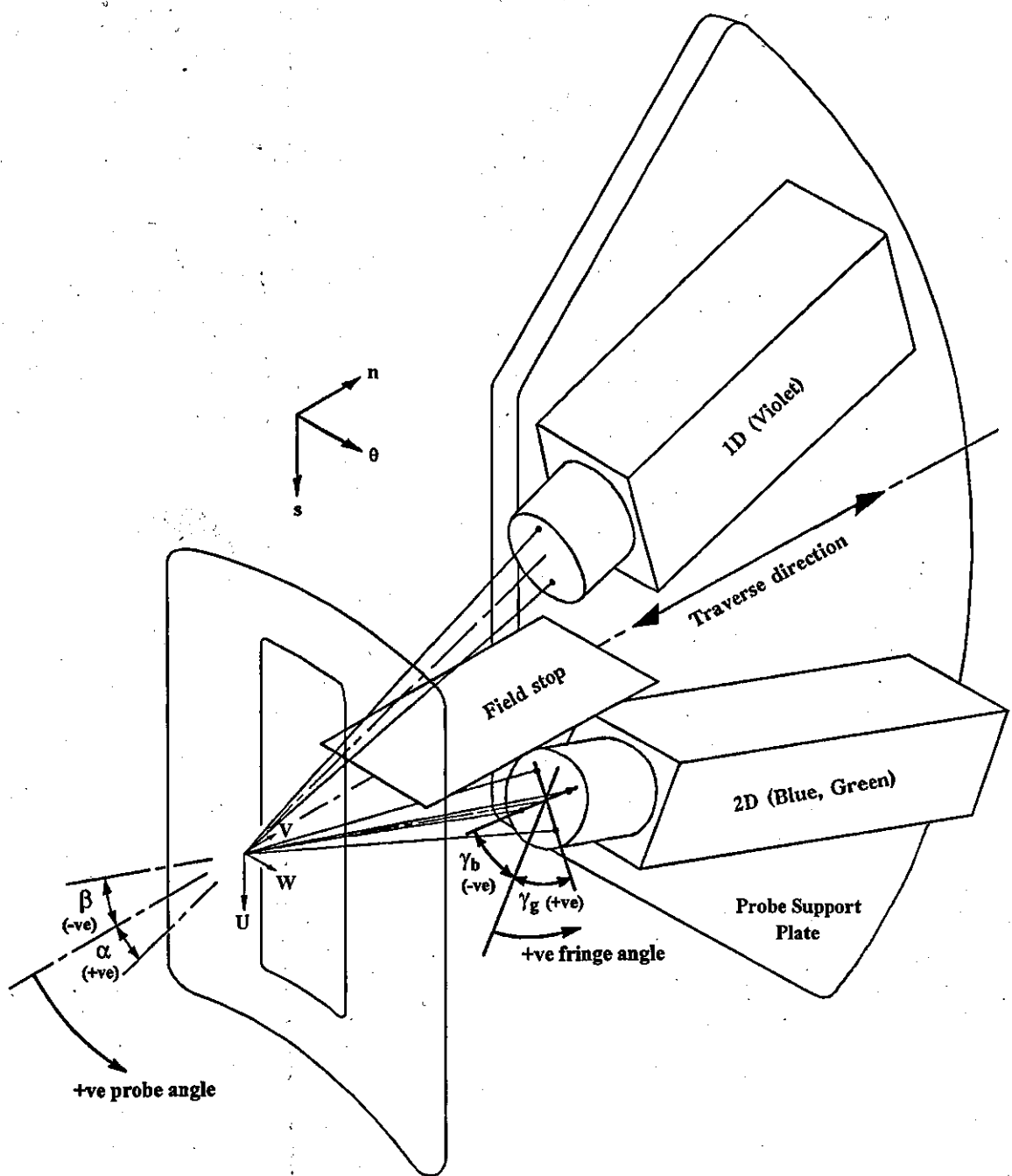


Figure 4

LDA Optical Arrangement



Five Hole Probe Calibration

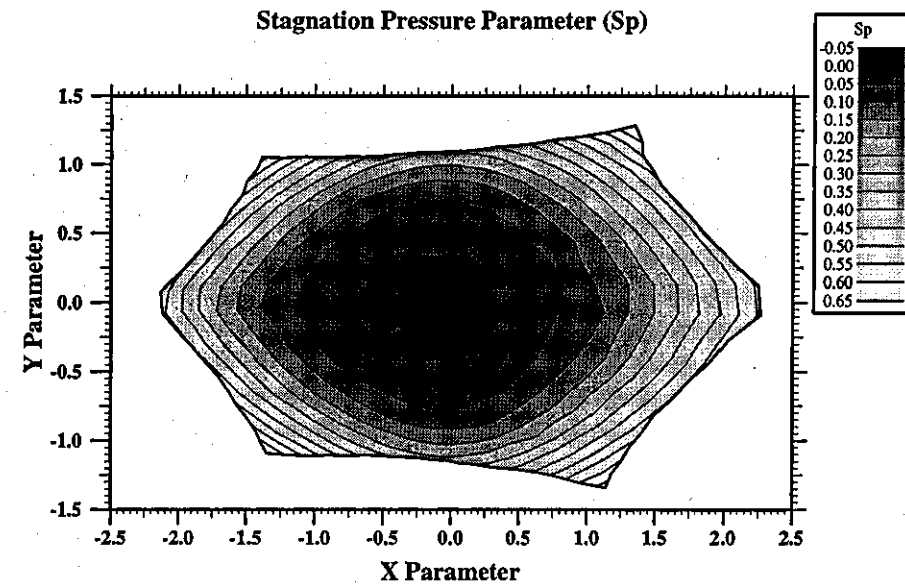
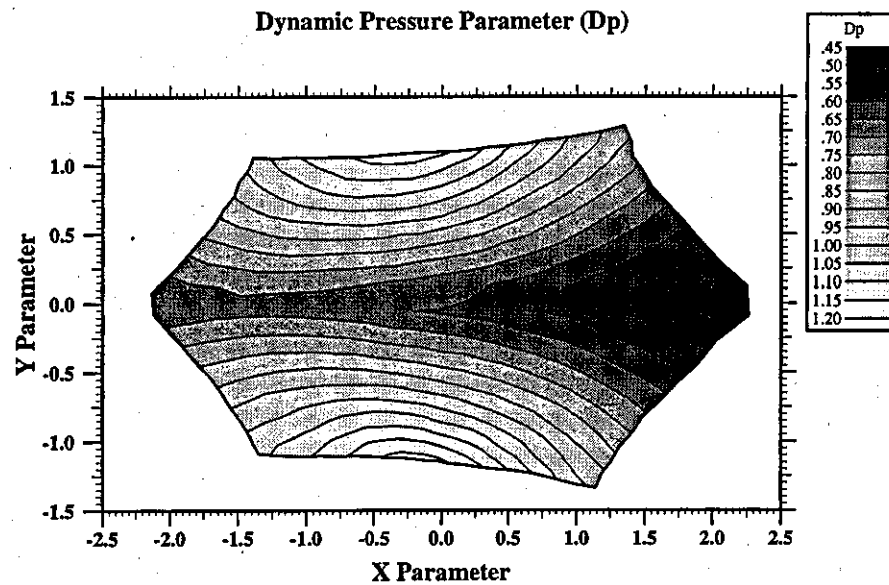
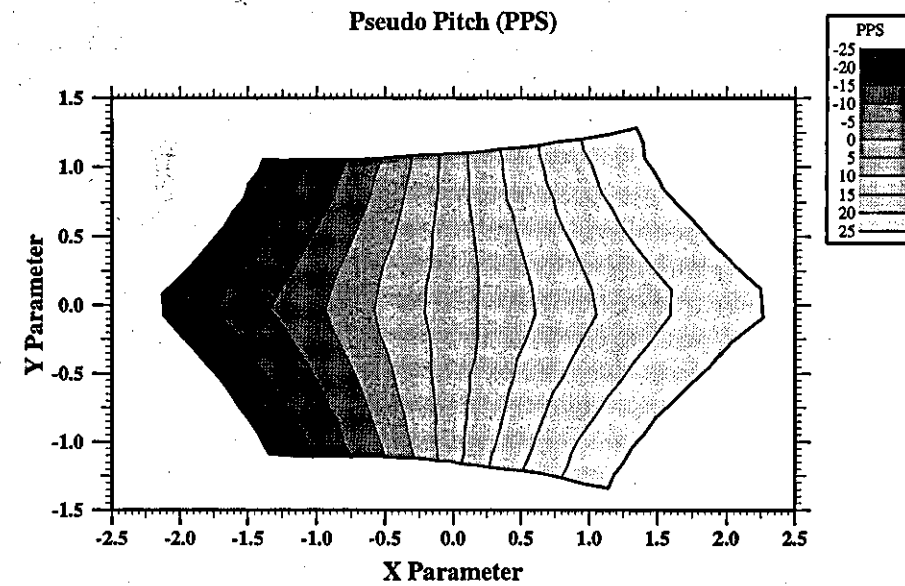
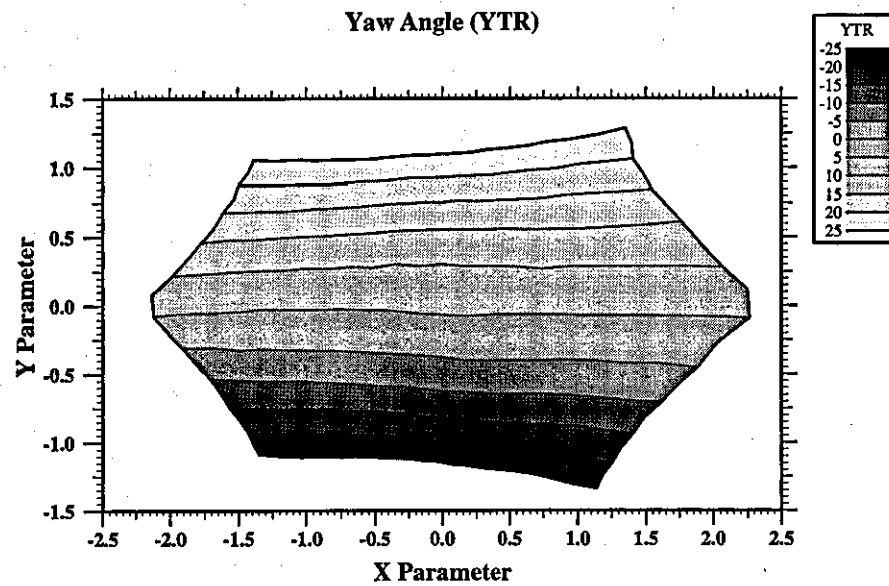
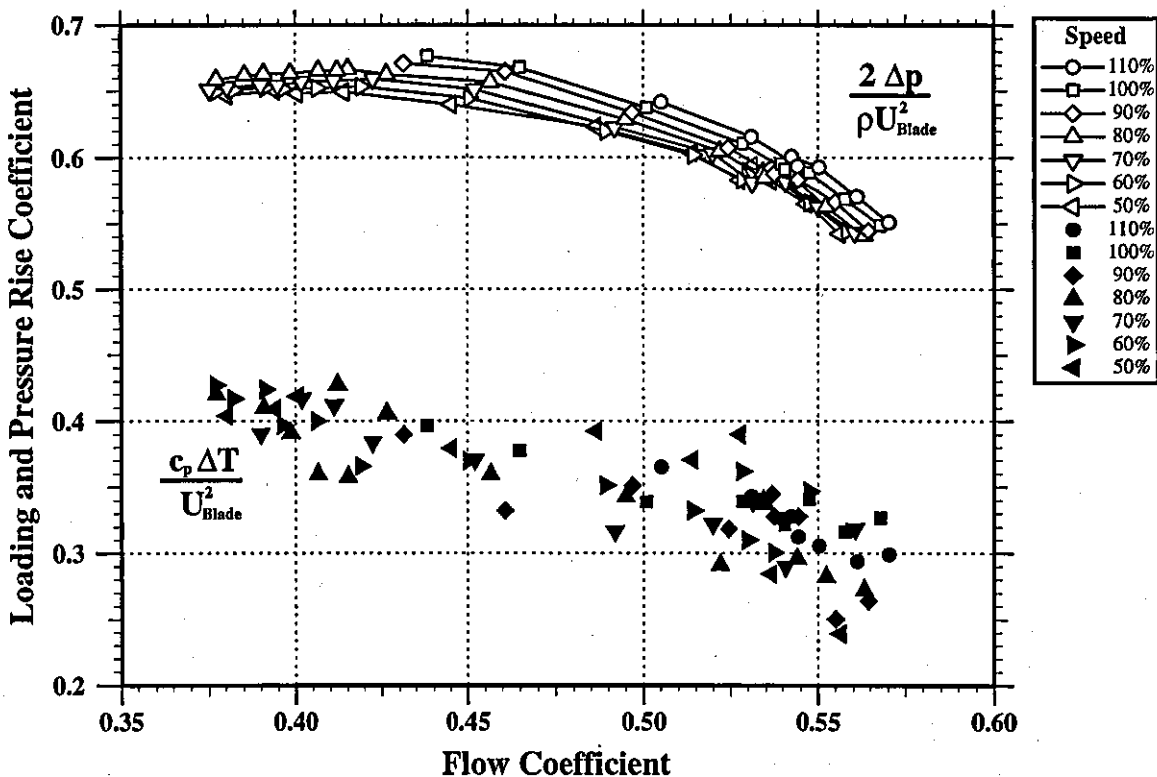
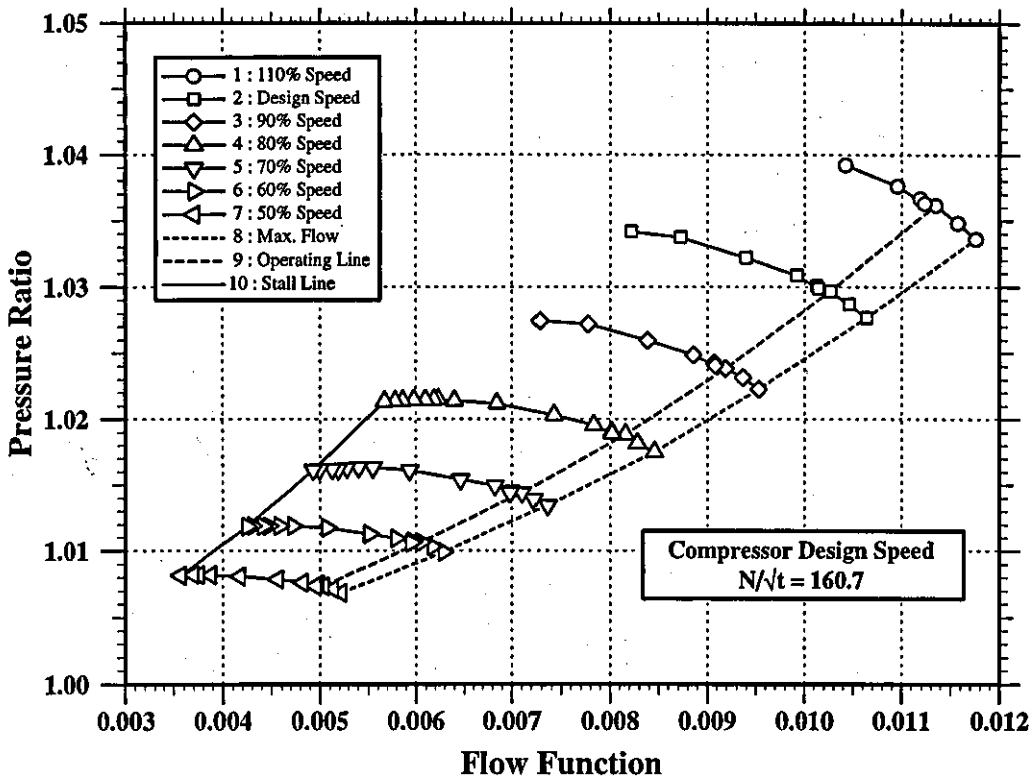


Figure 5

Figure 6

Compressor Characteristics



Wall Static Pressure Distribution

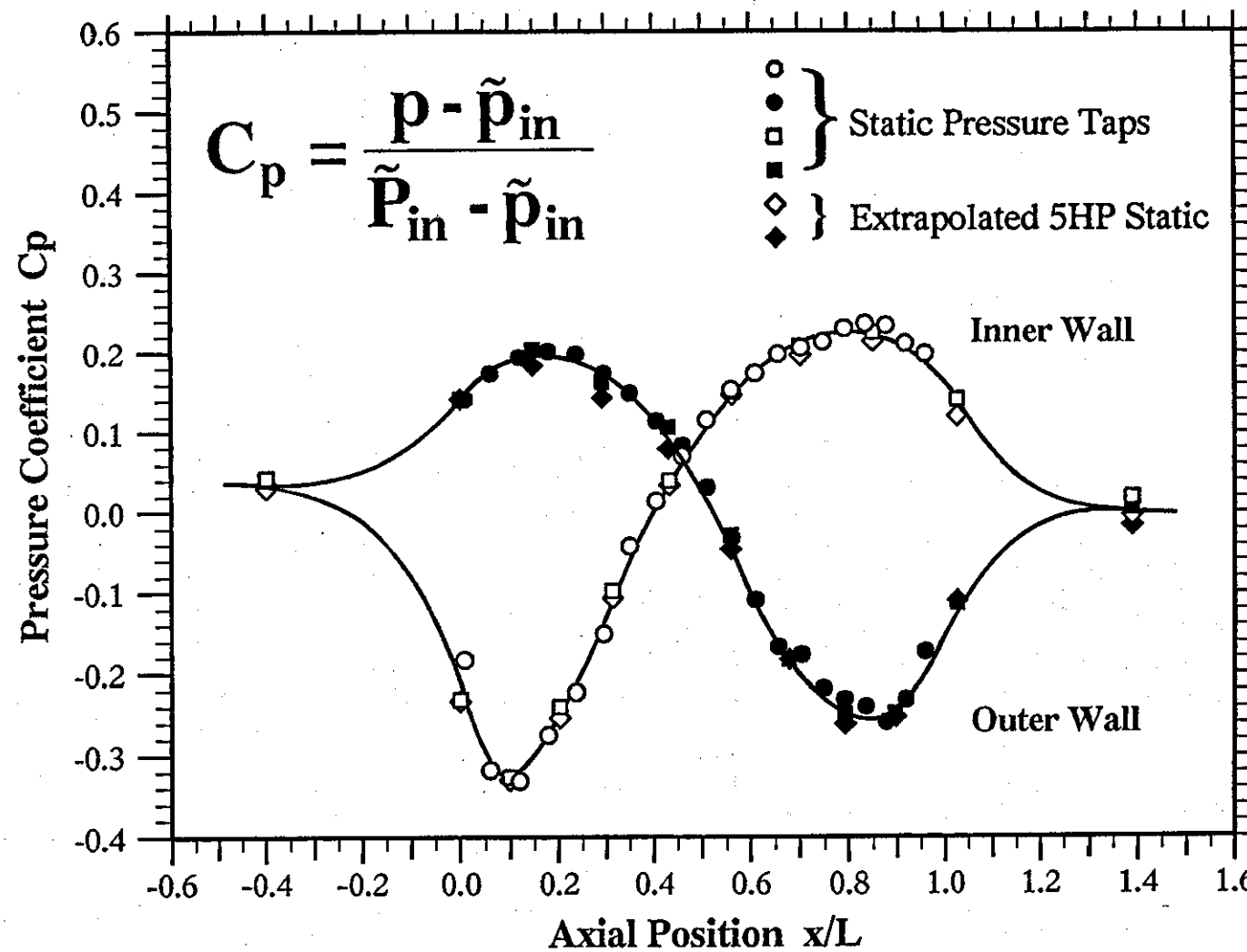


Figure 7

Figure 8

Measured Static Pressure Distribution

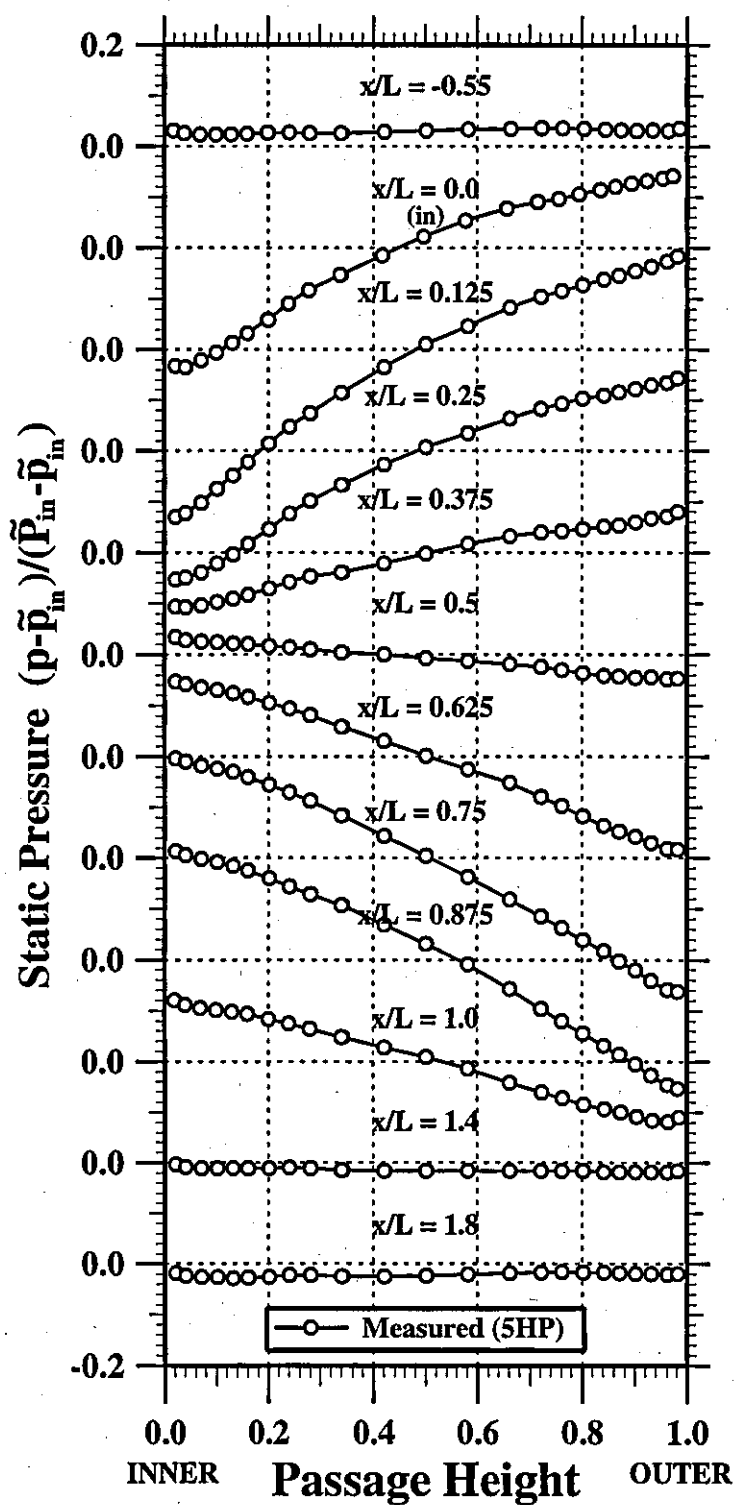


Figure 9

Measured Streamwise Velocity Distribution

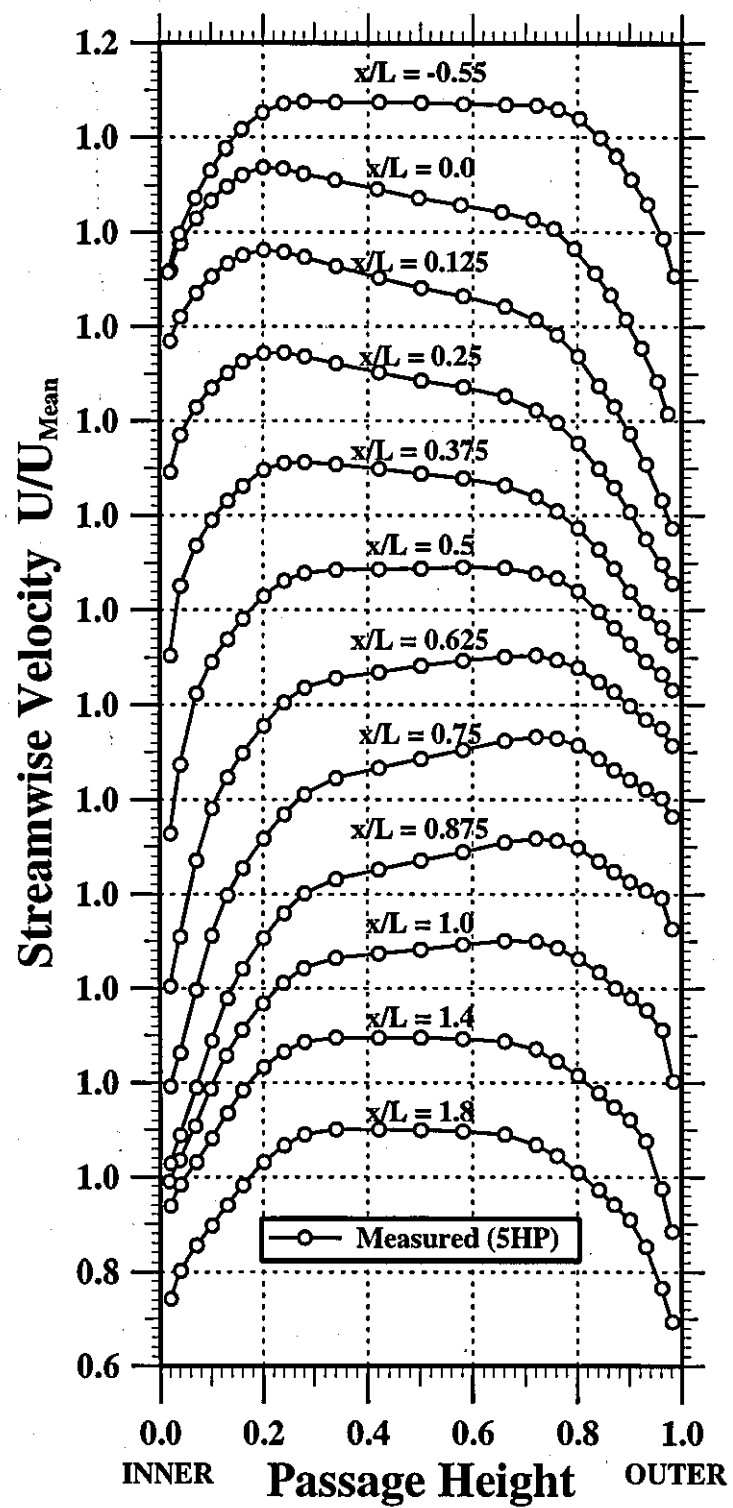


Figure 10

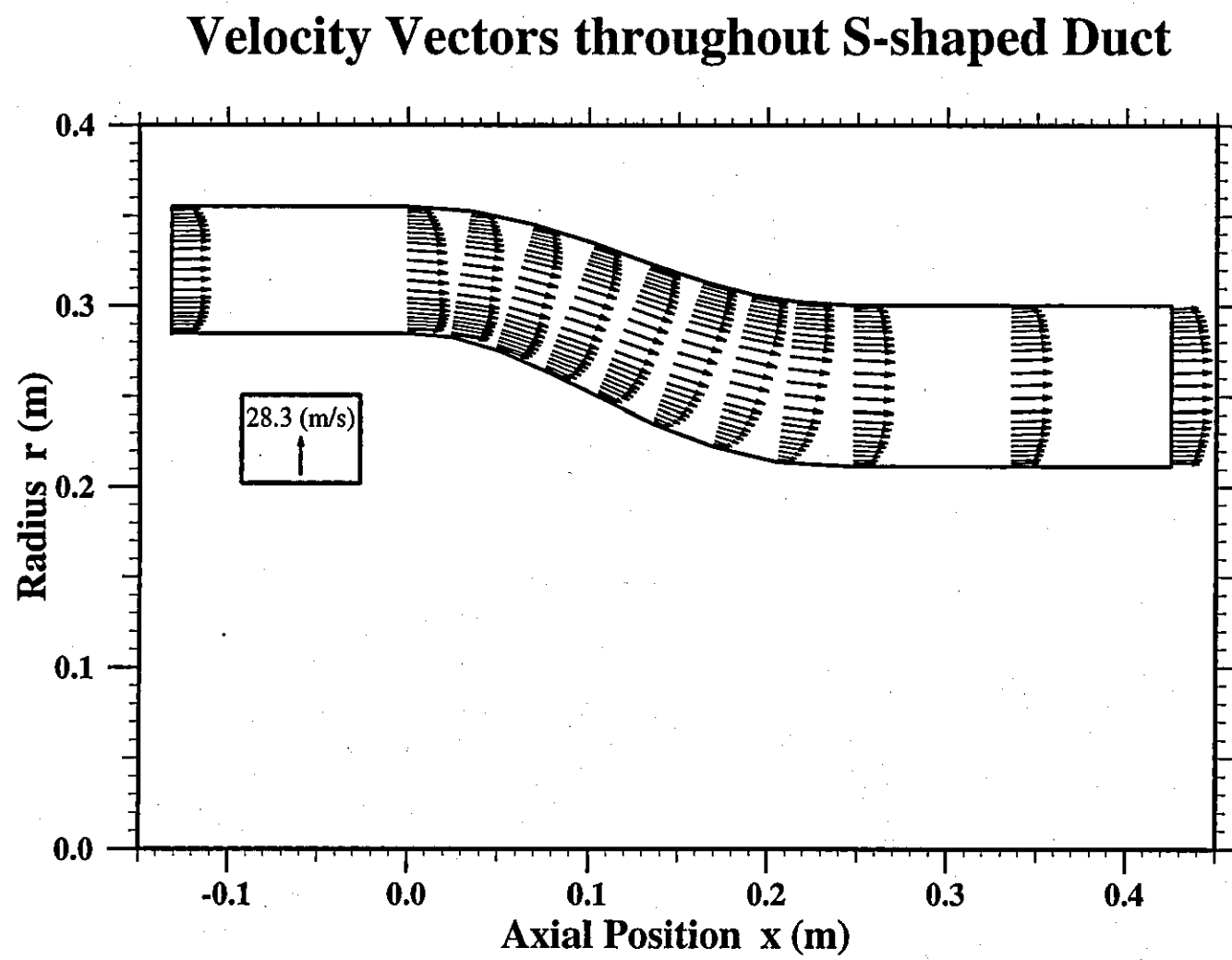


Figure 11

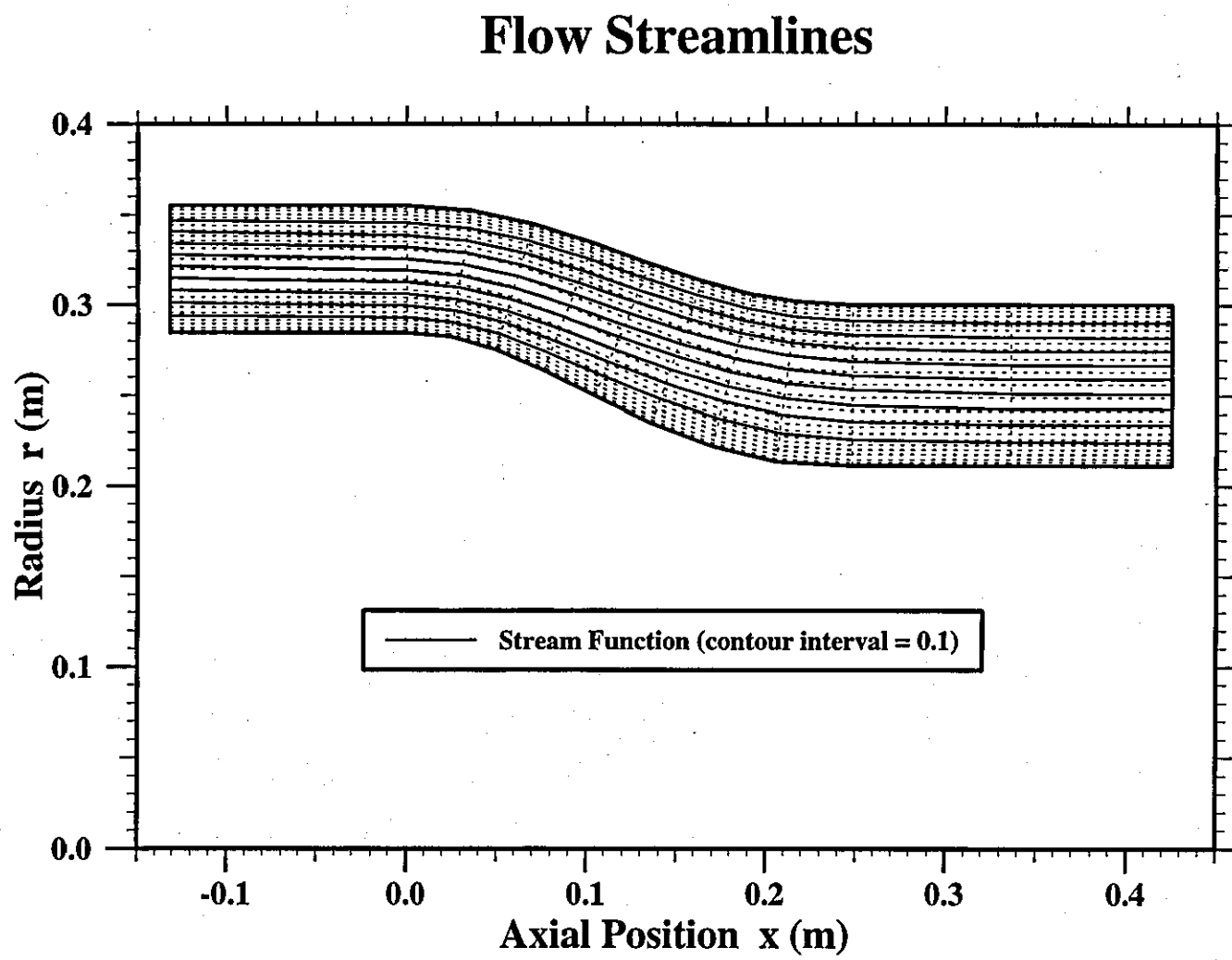


Figure 12

Distribution of Streamwise Velocity Ratio SHP Data with Boundary Layer Thickness Indicated

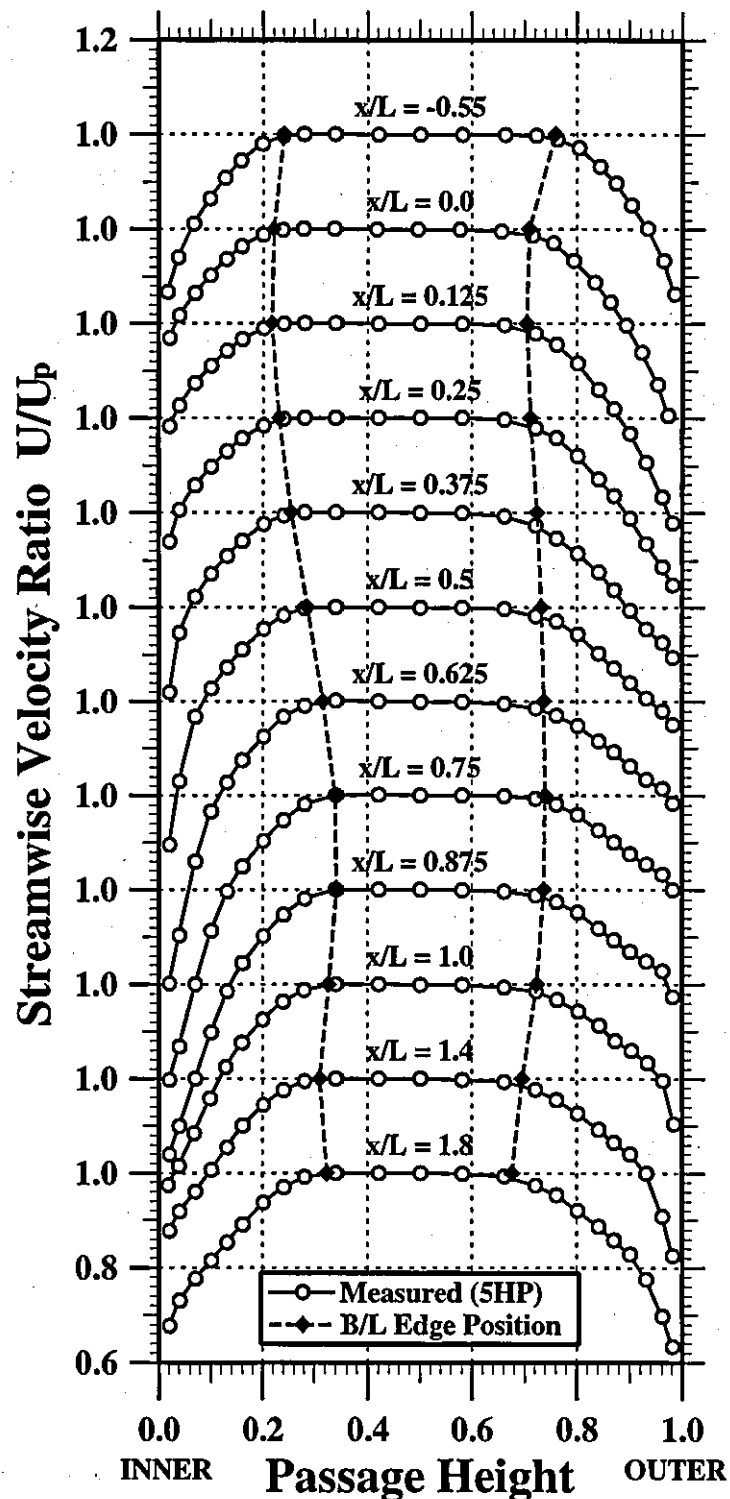


Figure 13

Distribution of Streamwise Velocity Ratio SHP Data with Boundary Layer Thickness Indicated

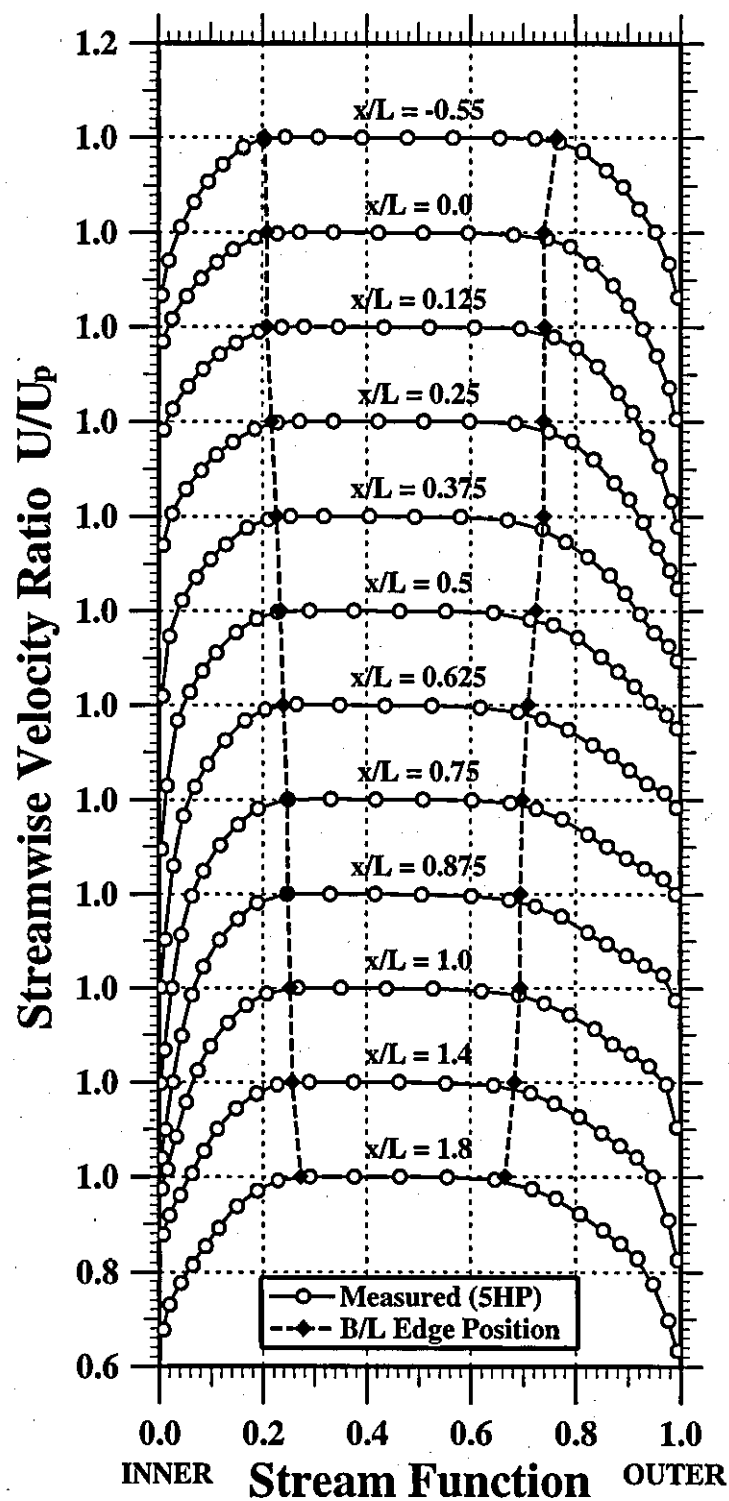


Figure 14

Streamwise Velocity Distribution Comparison of LDA and 5HP Data

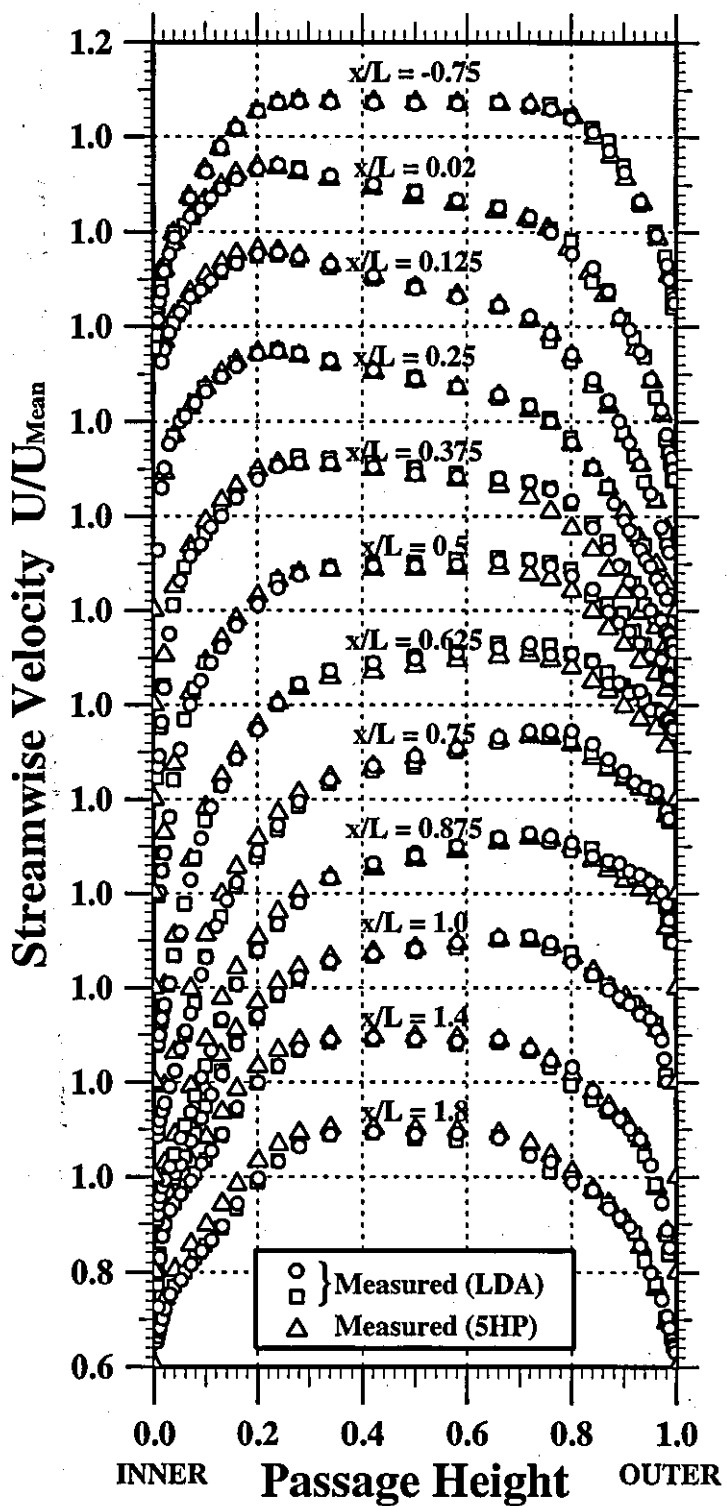


Figure 15

Cross-stream Velocity Distribution Comparison of LDA and 5HP Data

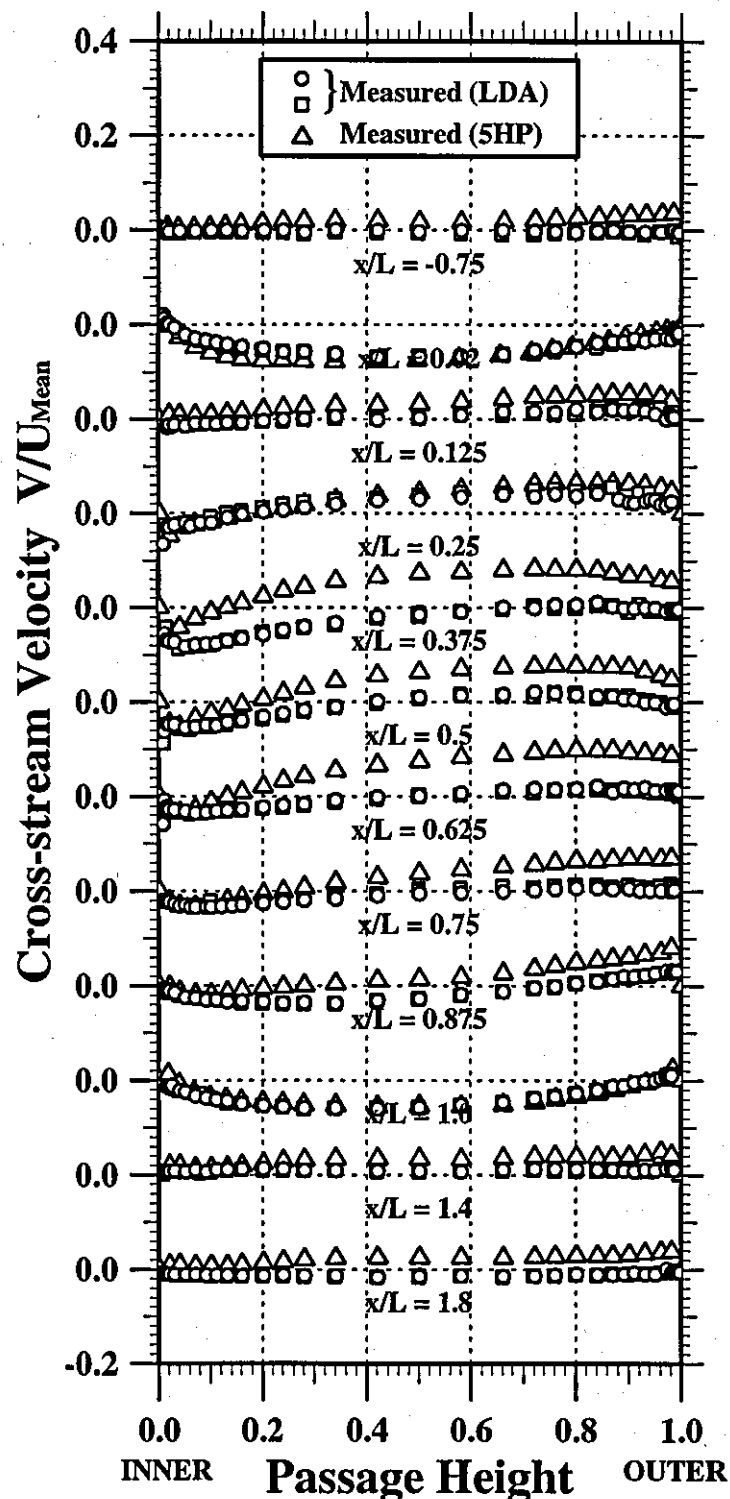


Figure 16

Circumferential Velocity Distribution Comparison of LDA and 5HP Data

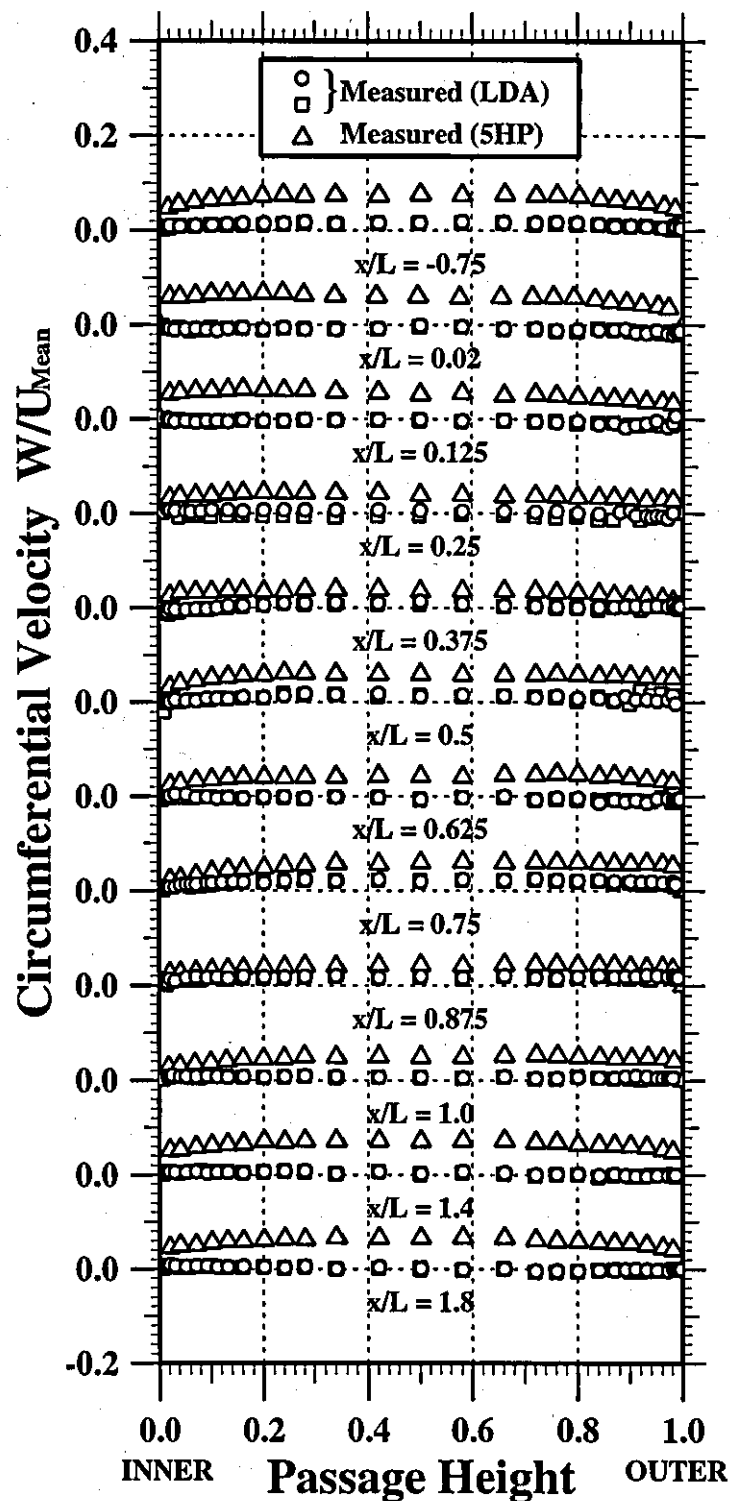


Figure 17

Radial Velocity Distribution Comparison of LDA and 5HP Data

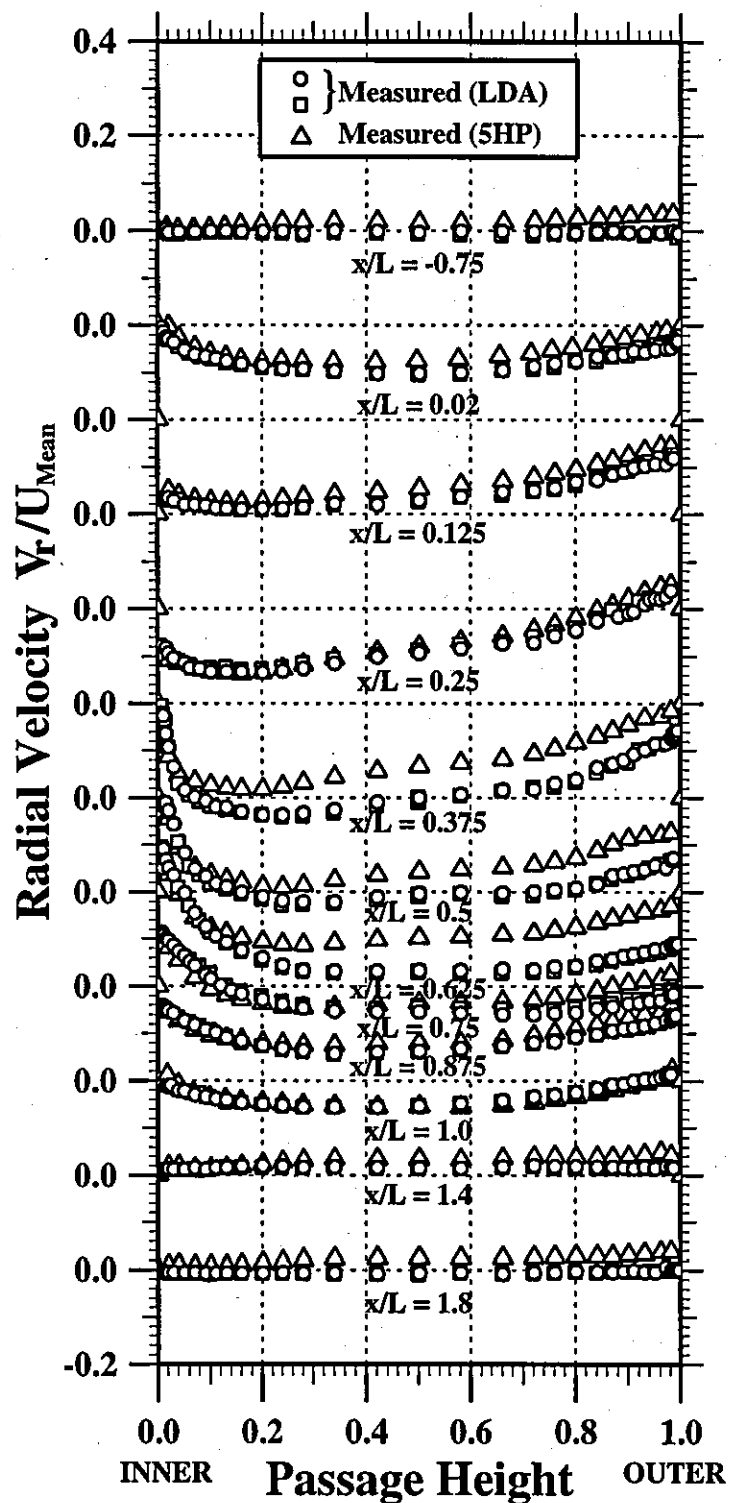


Figure 18

Potential Velocity Distribution Comparison of LDA and 5HP Data

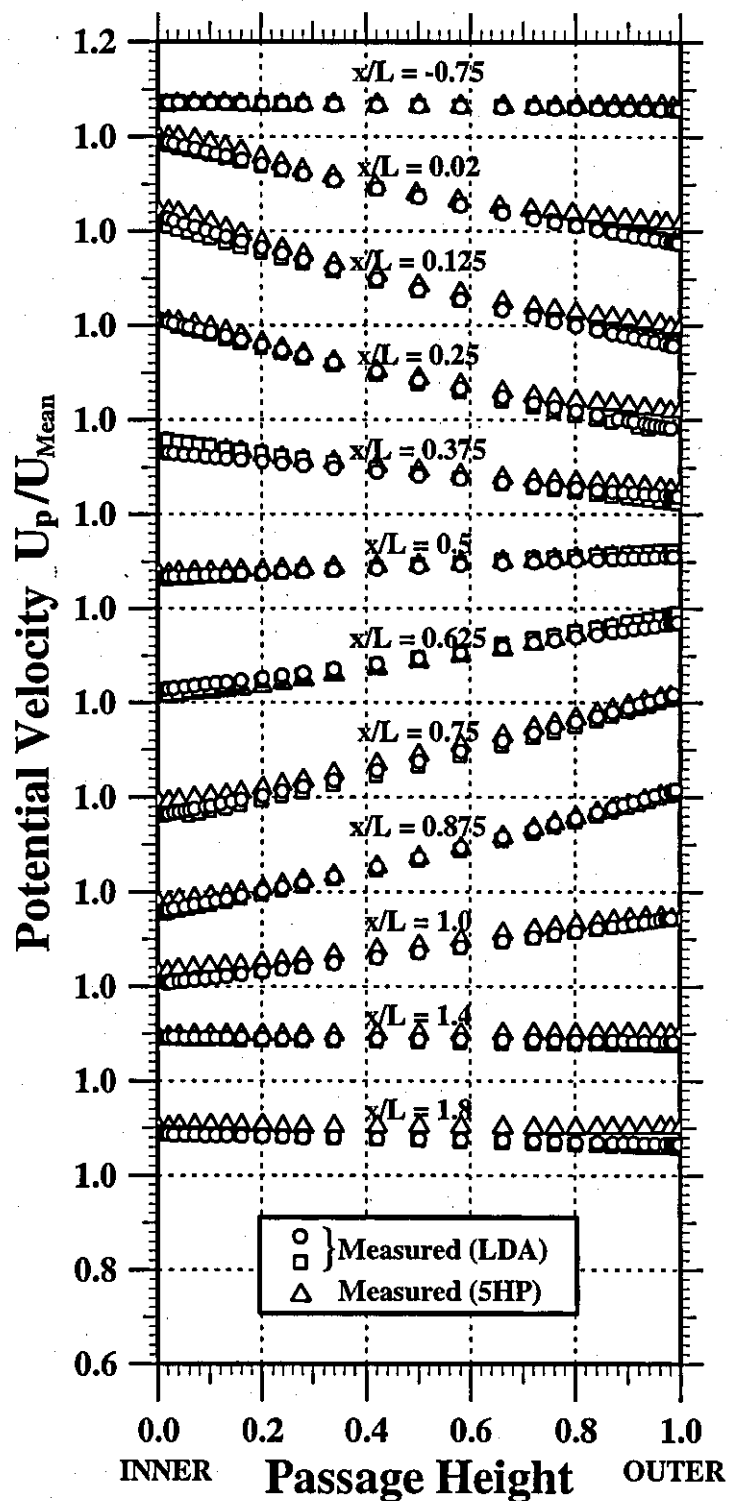


Figure 19

Streamwise Velocity Ratio Distribution Comparison of LDA and 5HP Data

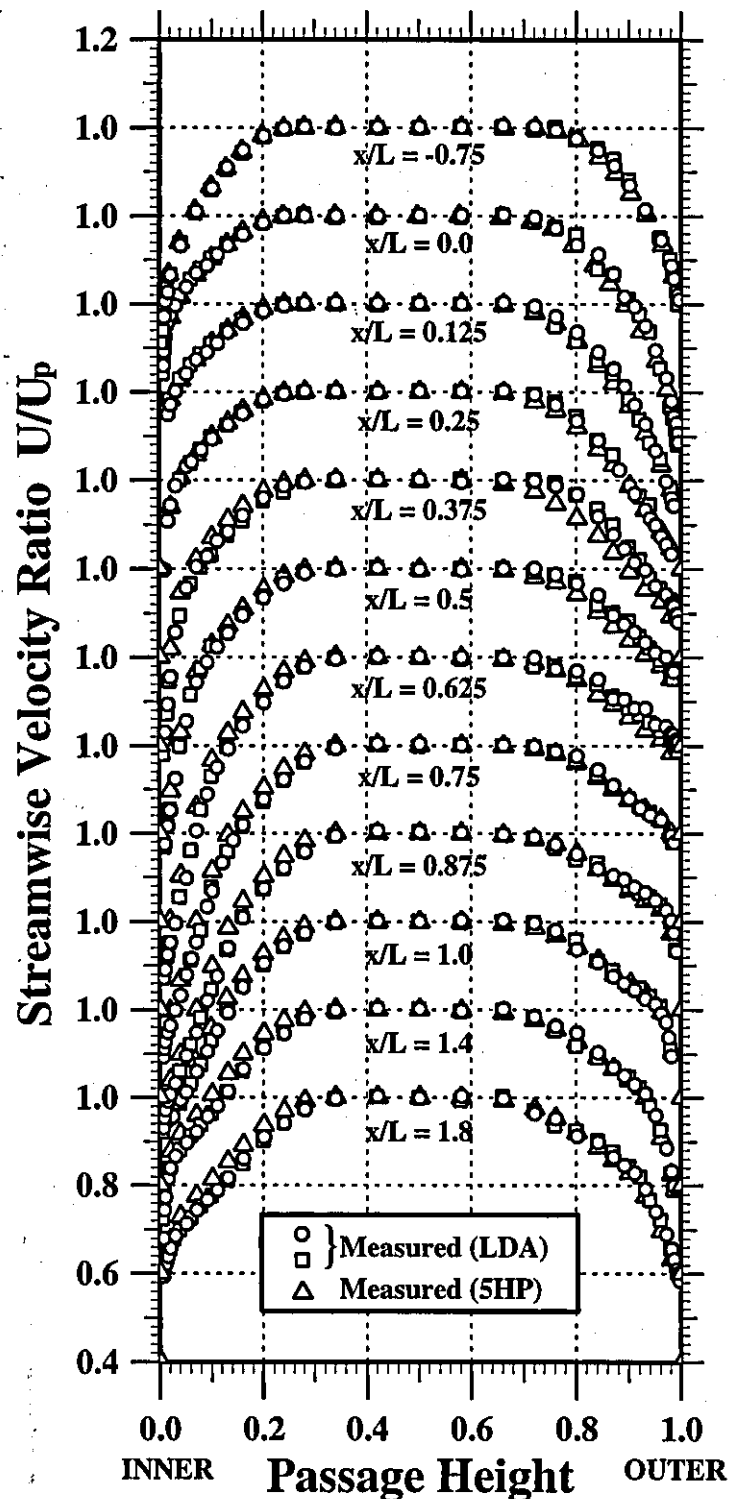


Figure 20

Axial Variation of Mean Pressure Coefficient

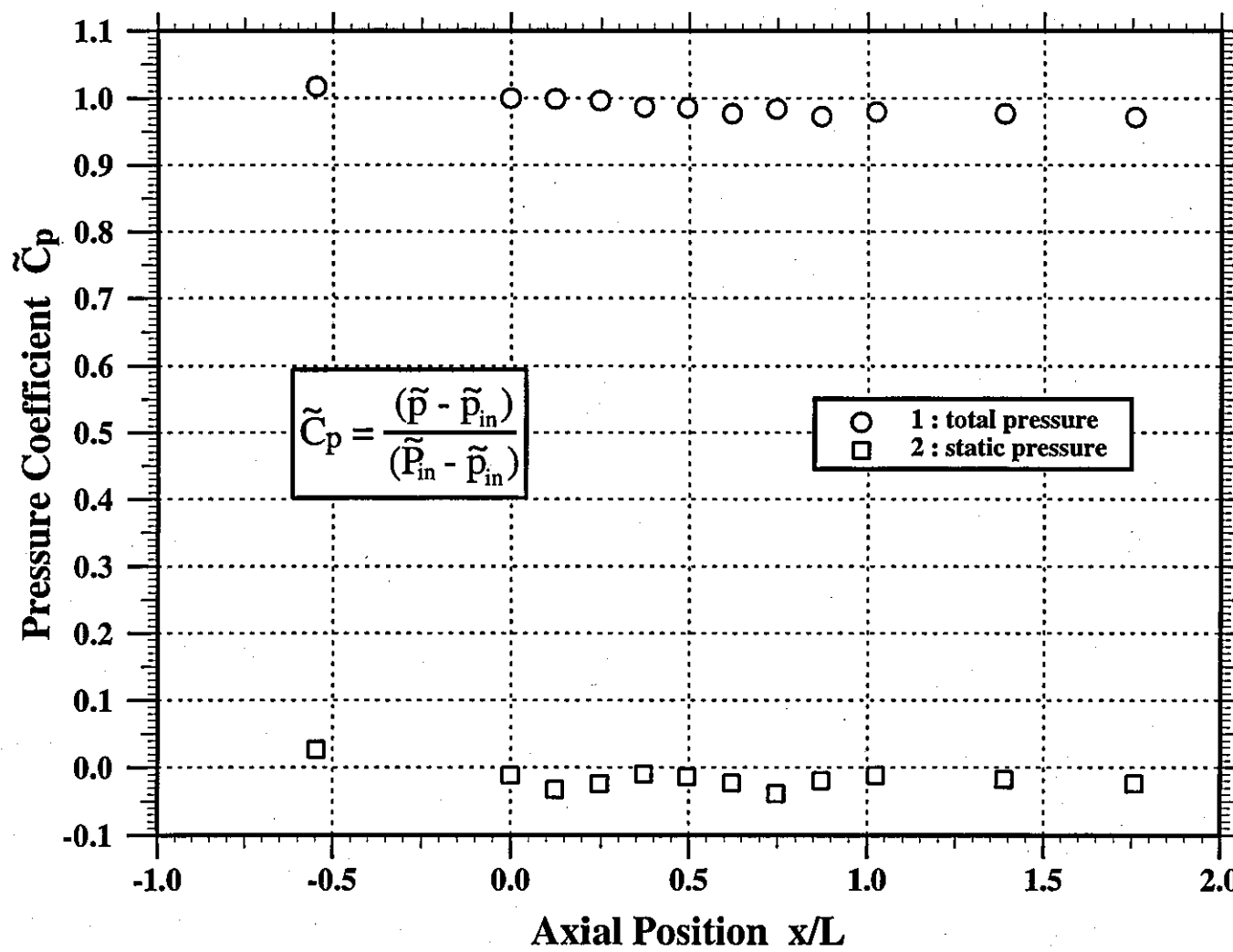


Figure 21

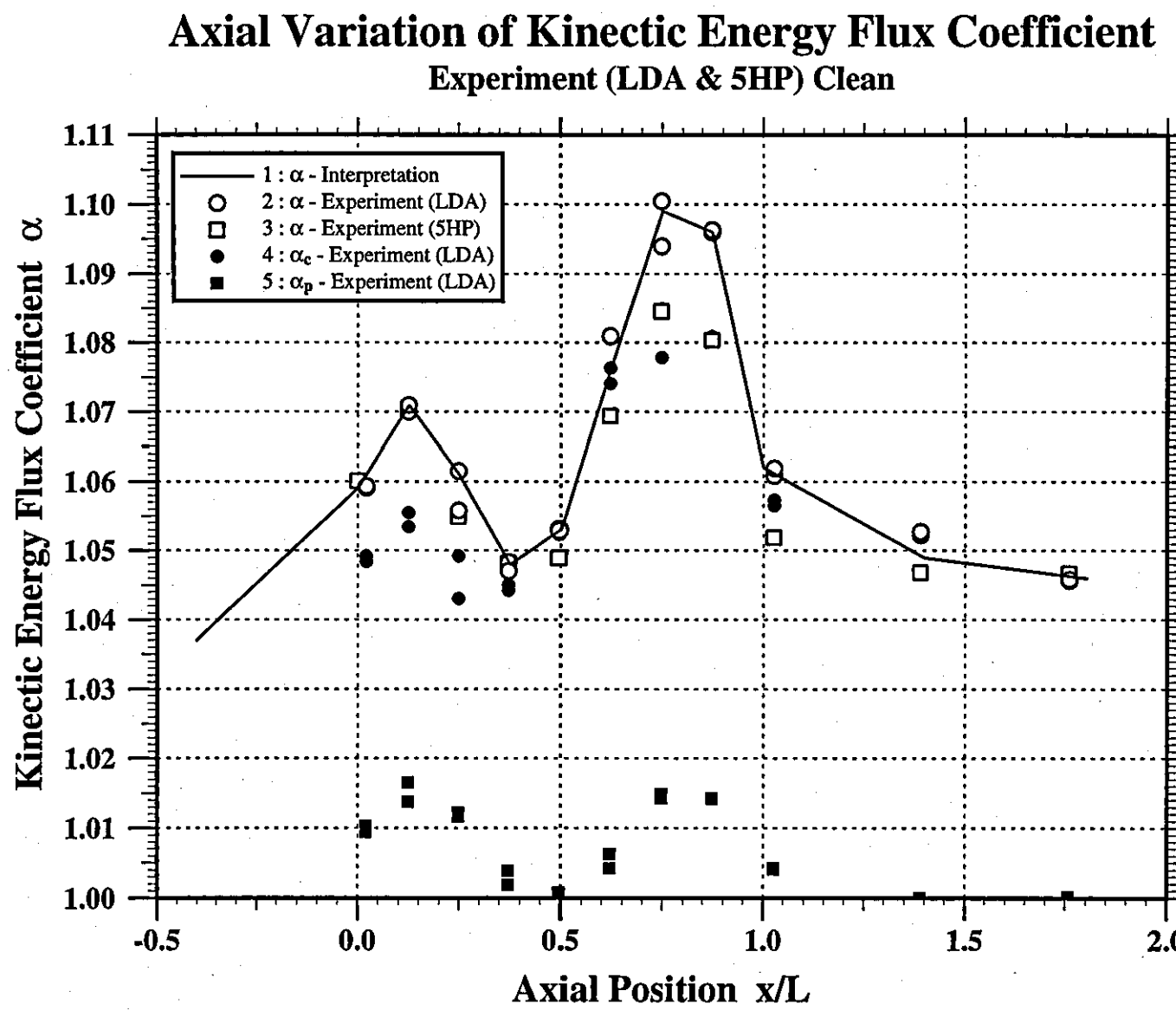


Figure 22

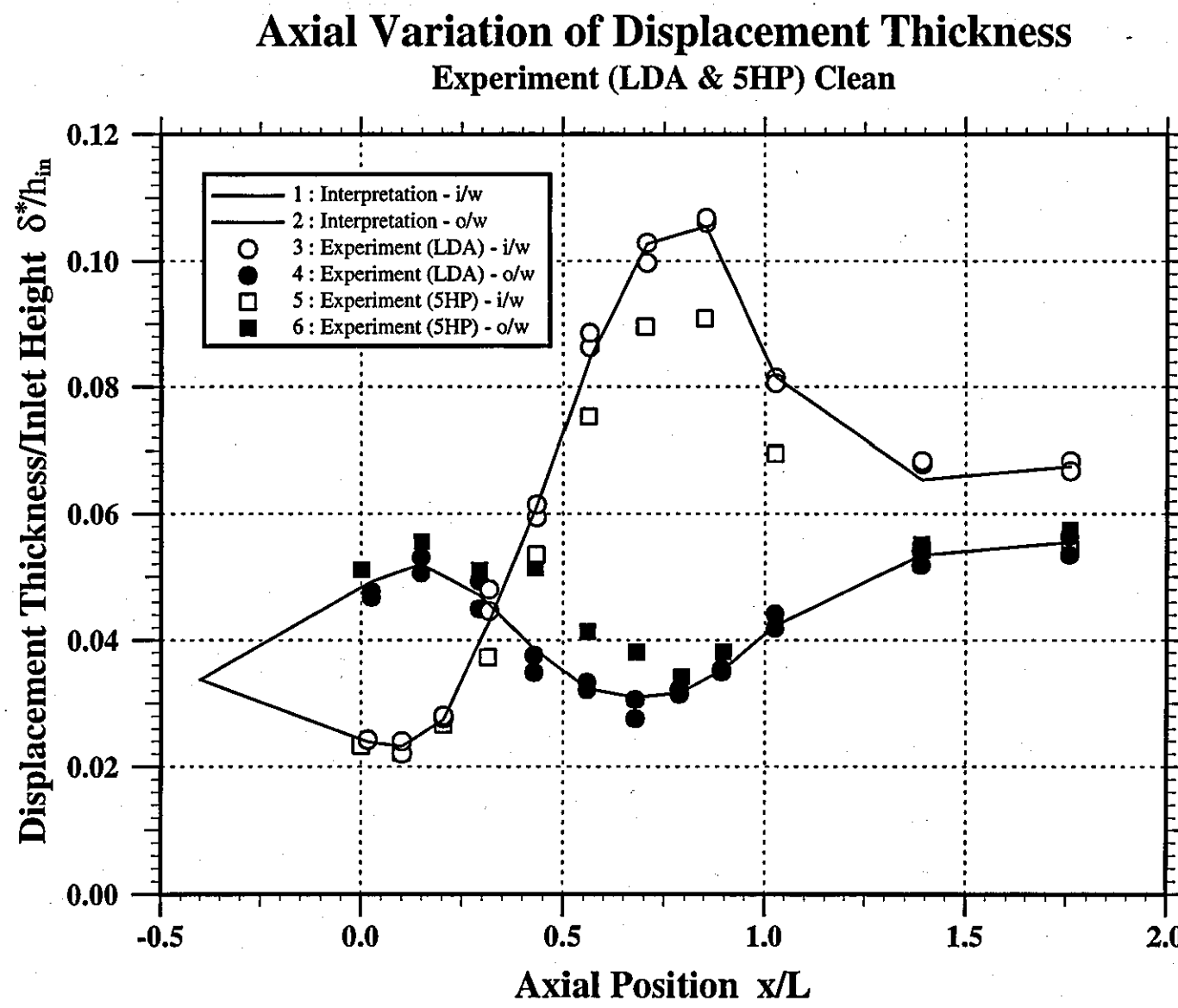


Figure 23

Axial Variation of Momentum Thickness

Experiment (LDA & 5HP) Clean

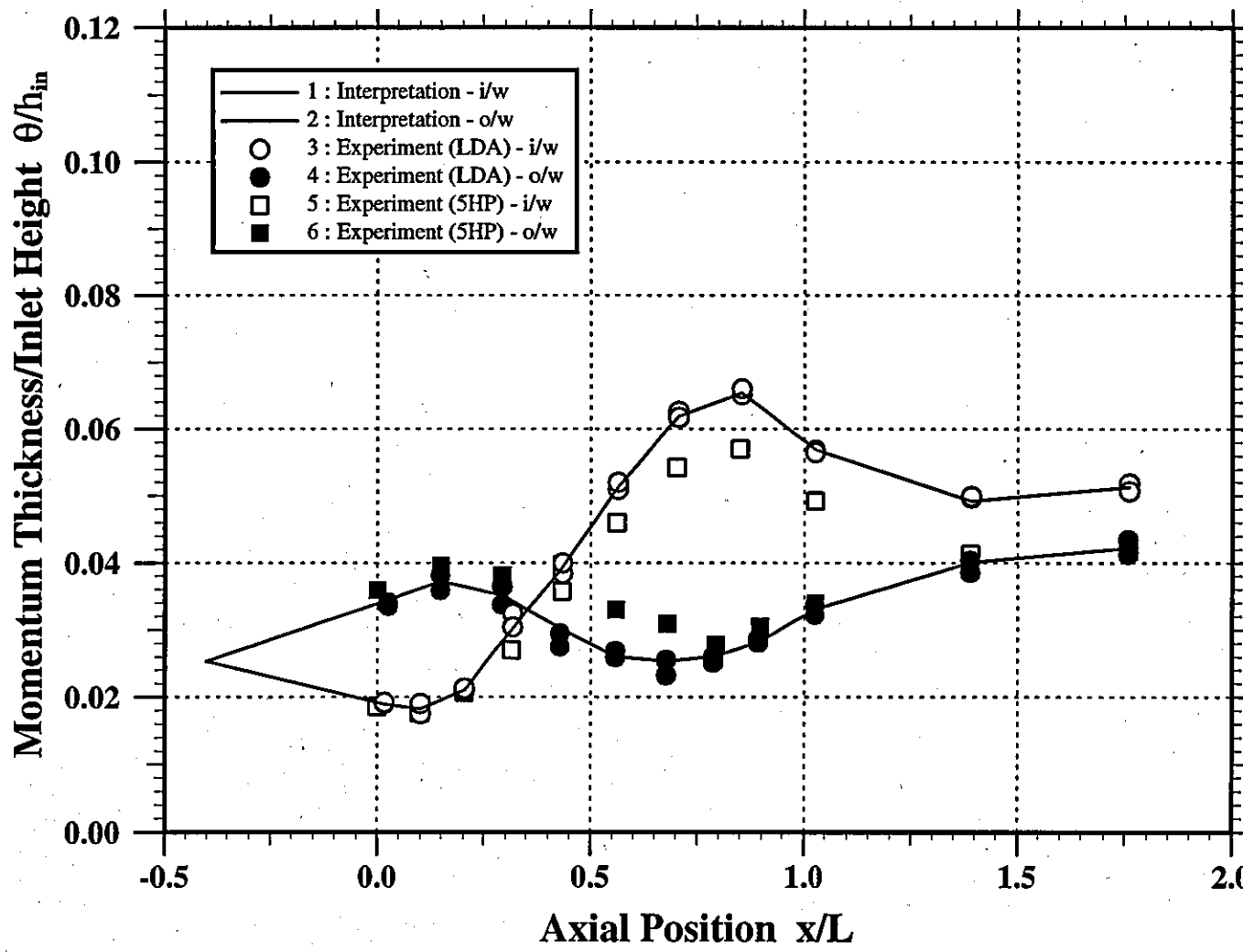


Figure 24

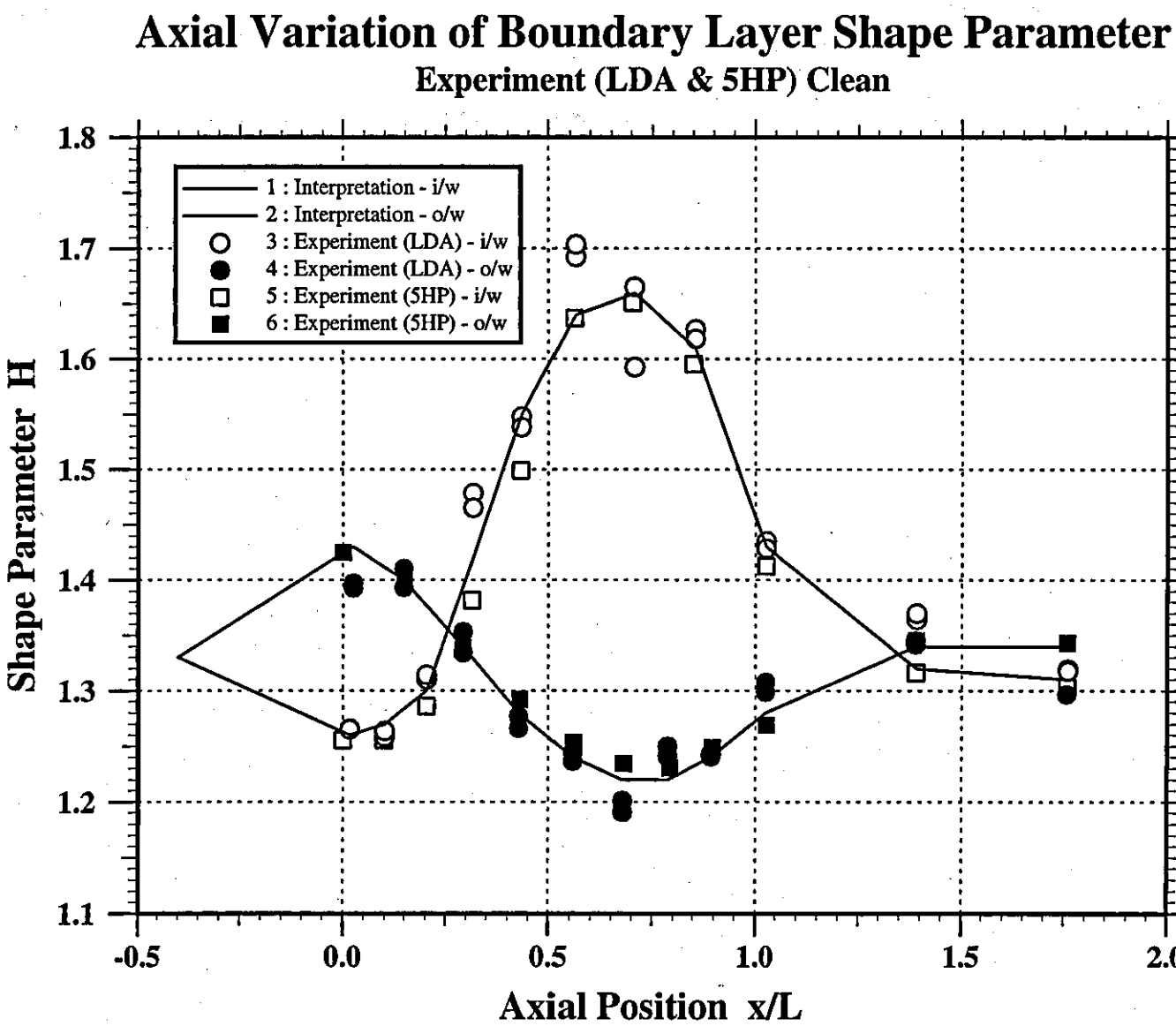
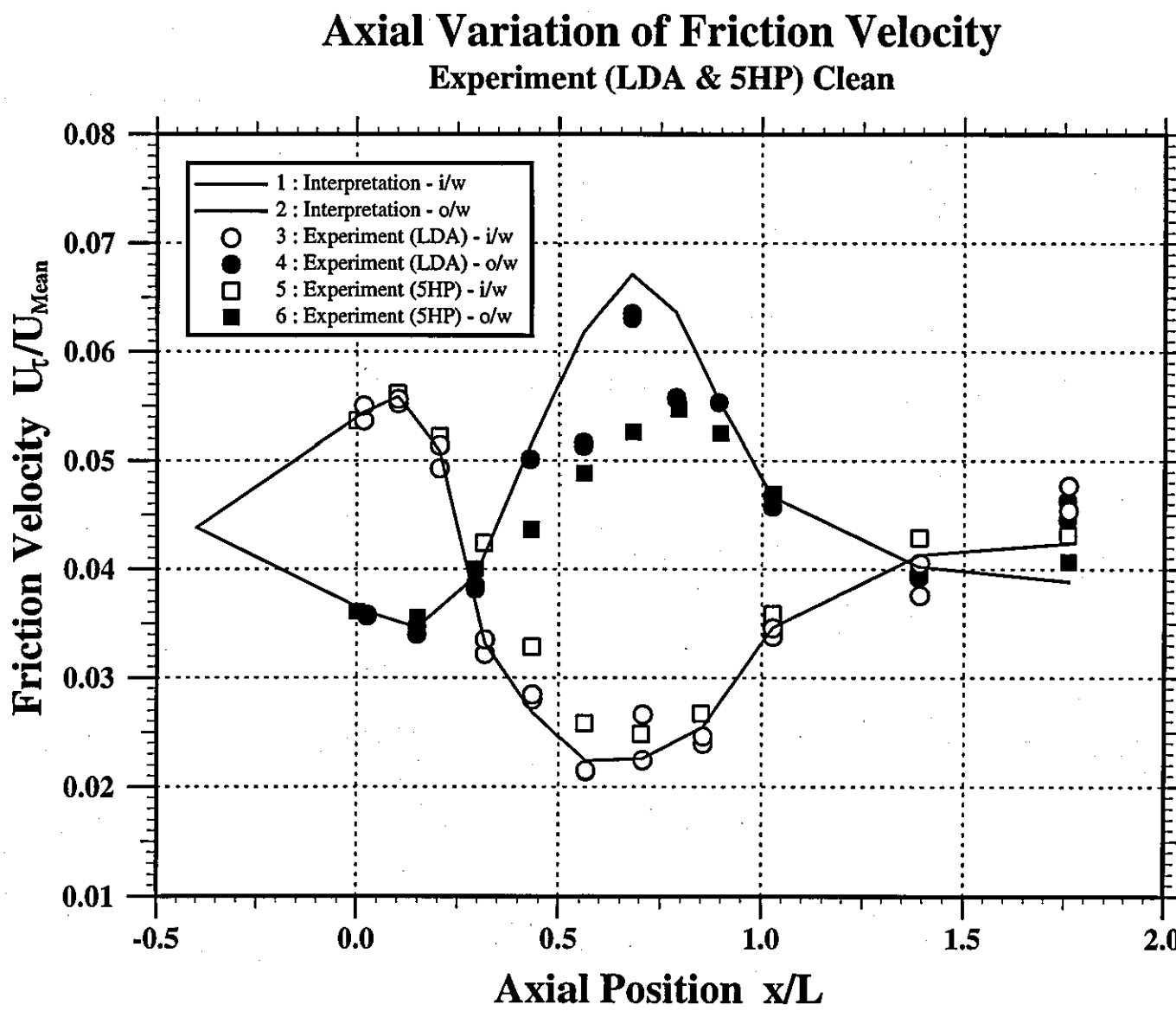


Figure 25



Axial Variation of Wall Potential Velocity Experiment (LDA & 5HP) Clean vs. Inviscid Calculation

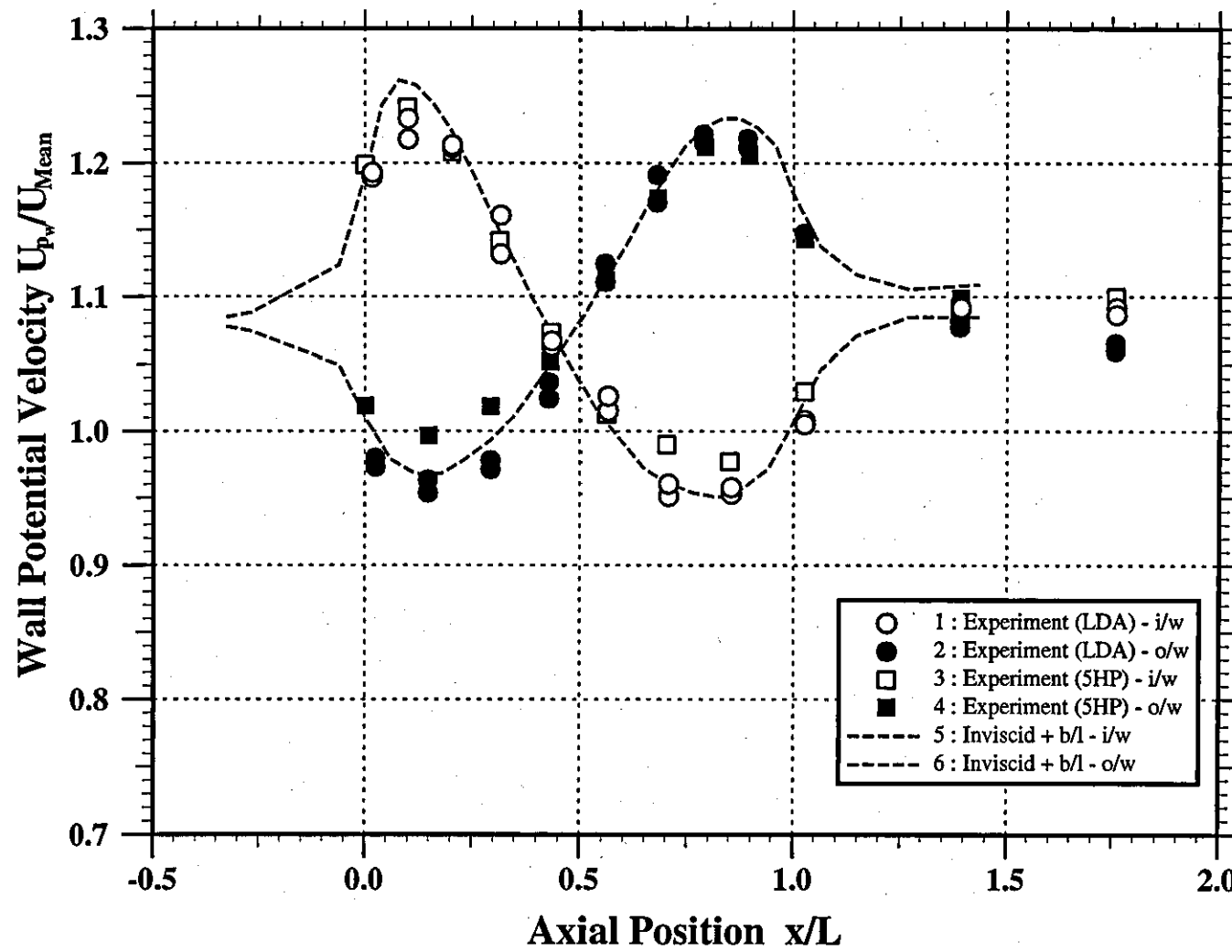


Figure 26

Figure 27

Axial Variation of Boundary Layer Thickness

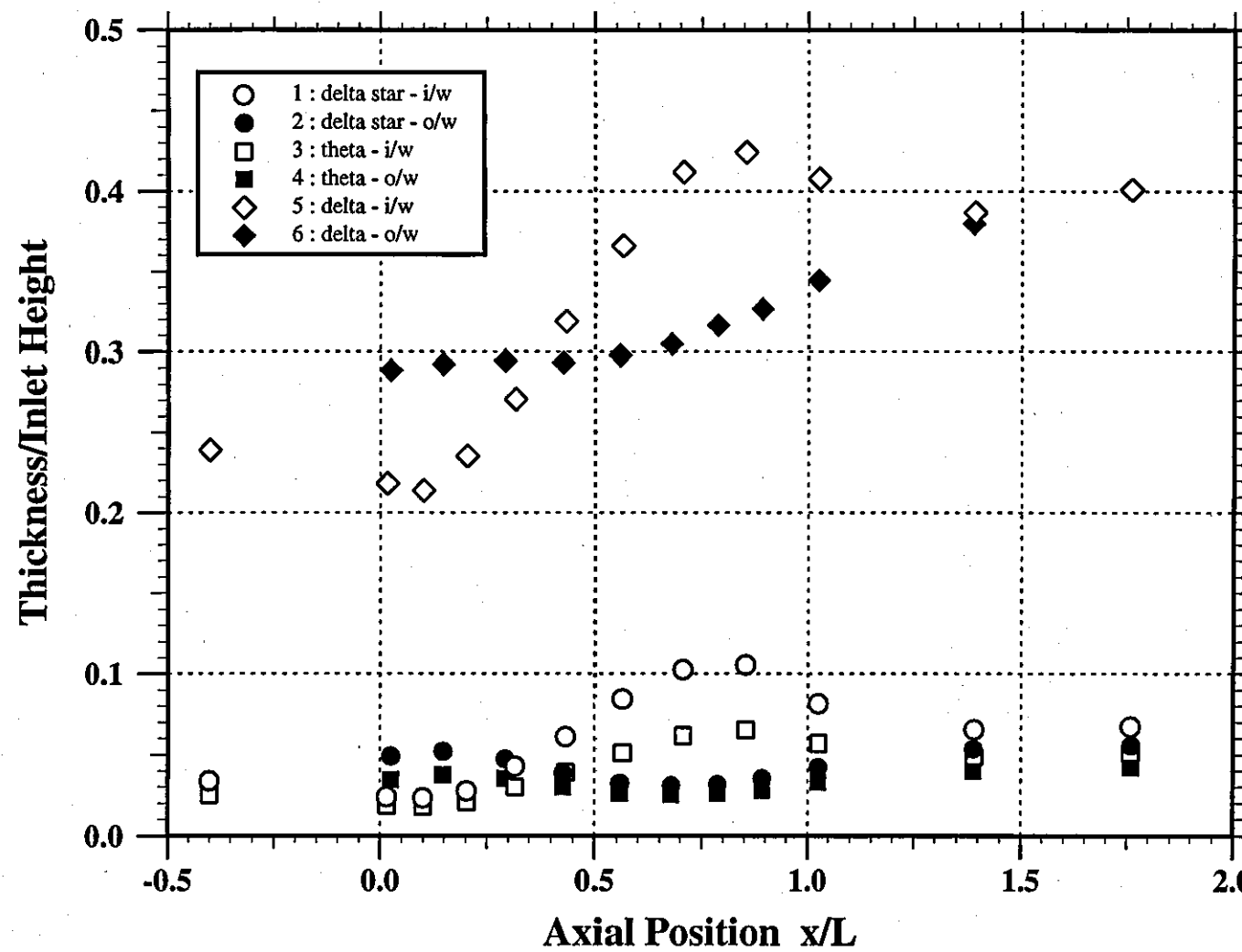
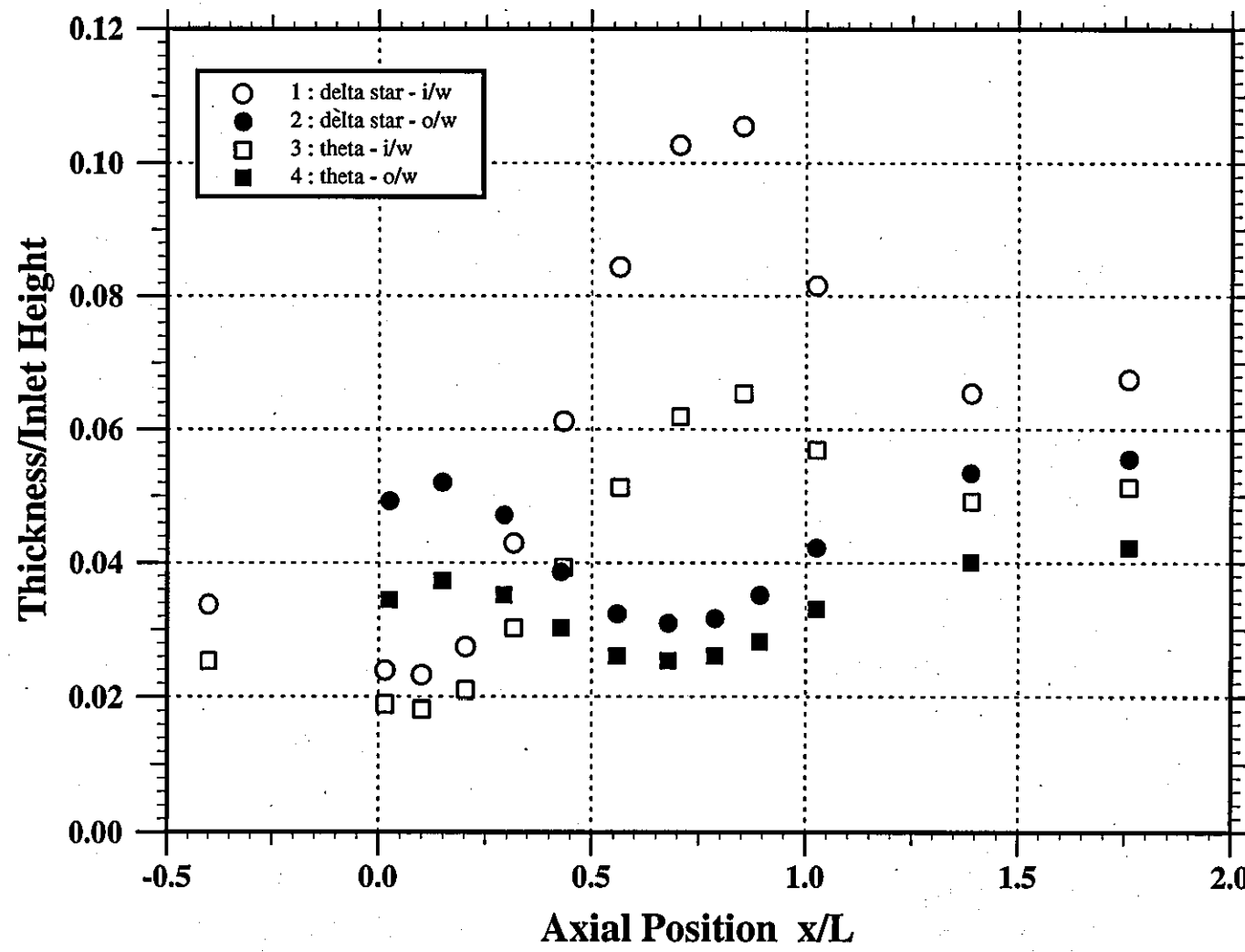


Figure 28

Axial Variation of Boundary Layer Thickness



Axial Variation of Boundary Layer Shape Parameter

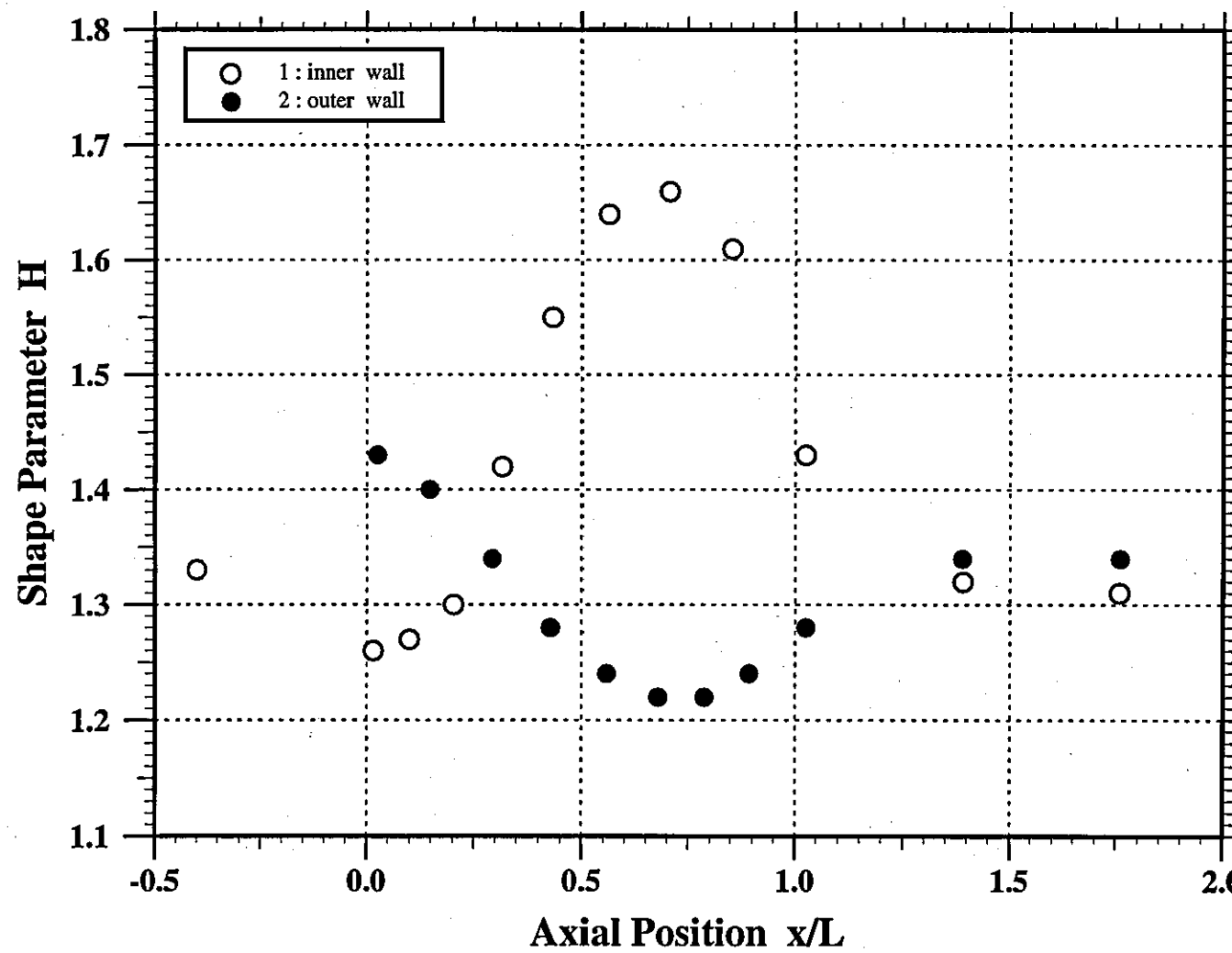
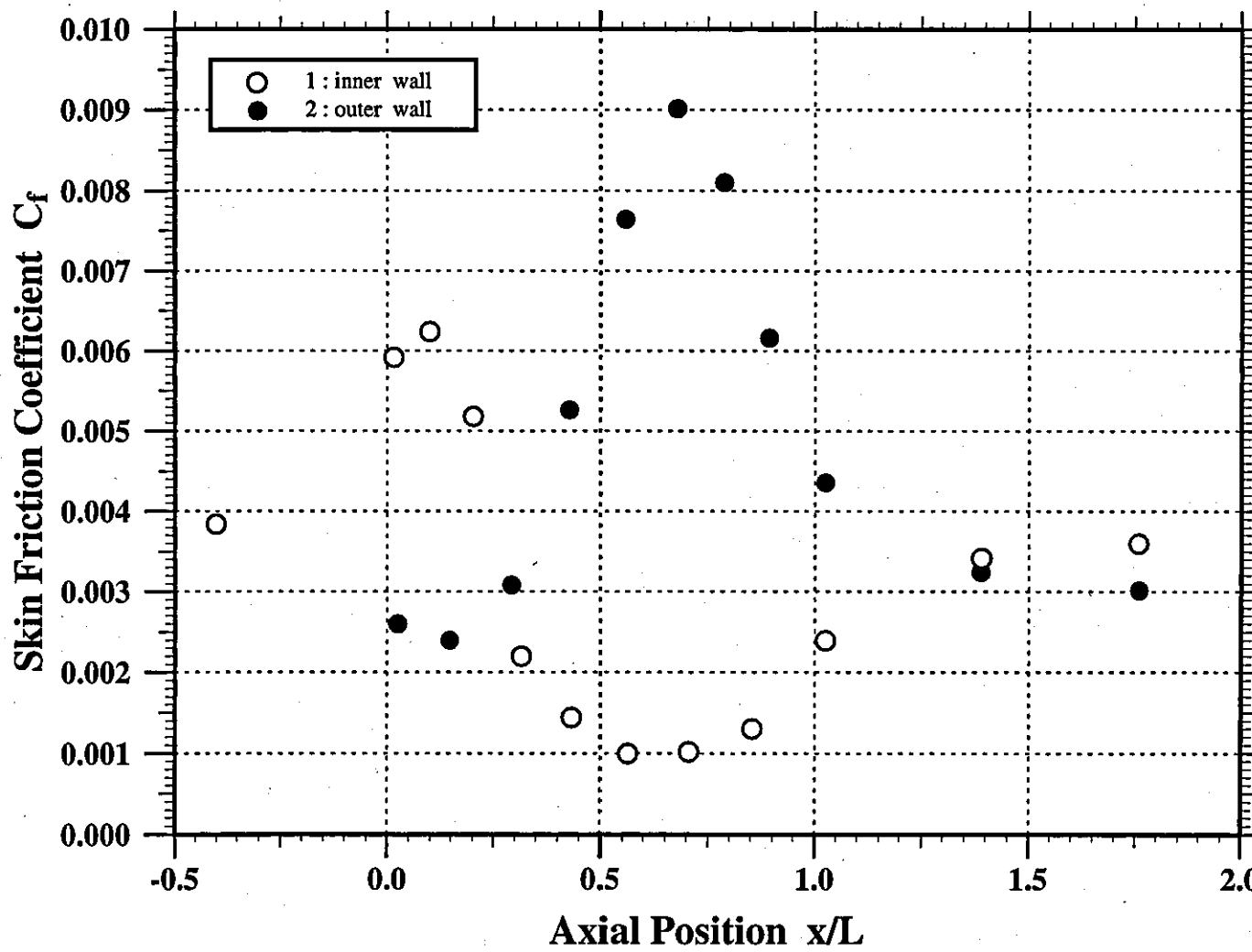


Figure 29

Figure 30

Axial Variation of Skin Friction Coefficient



Skin Friction vs. Reynolds Number (U_{Pw} Based)

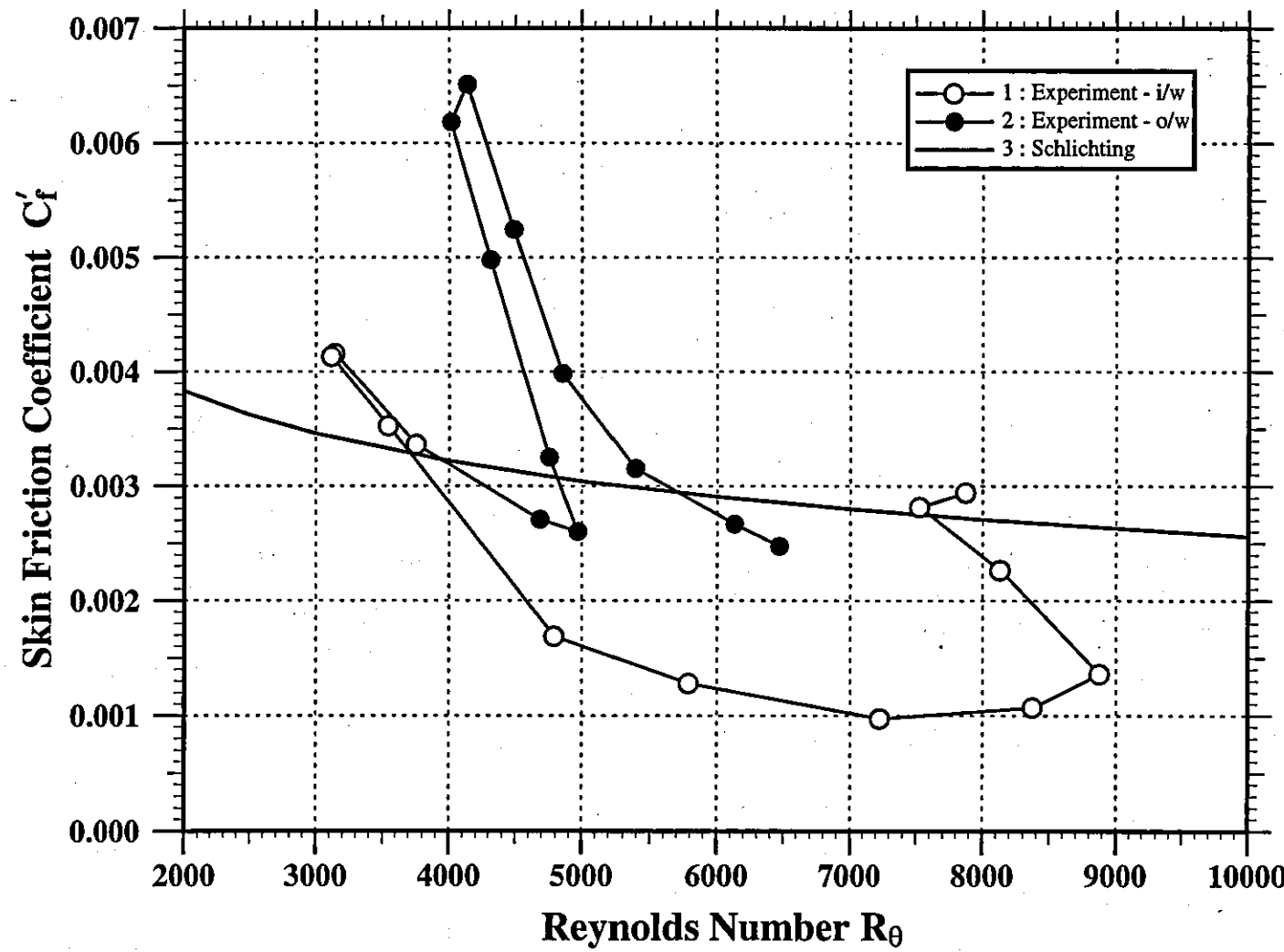


Figure 31

Figure 32

Axial Variation of Skin Friction Coefficient Experiment vs. Ludwig-Tillmann

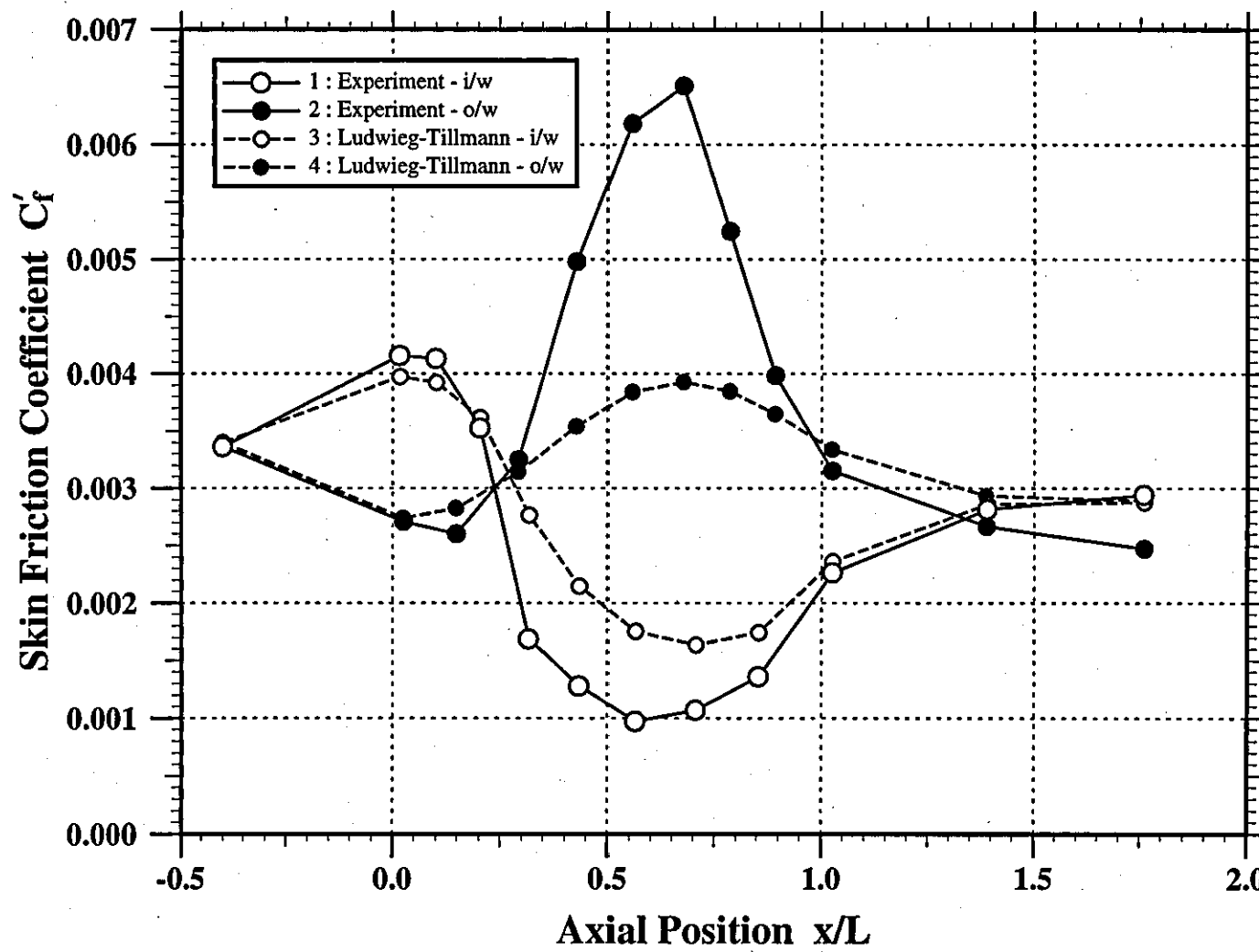


Figure 33

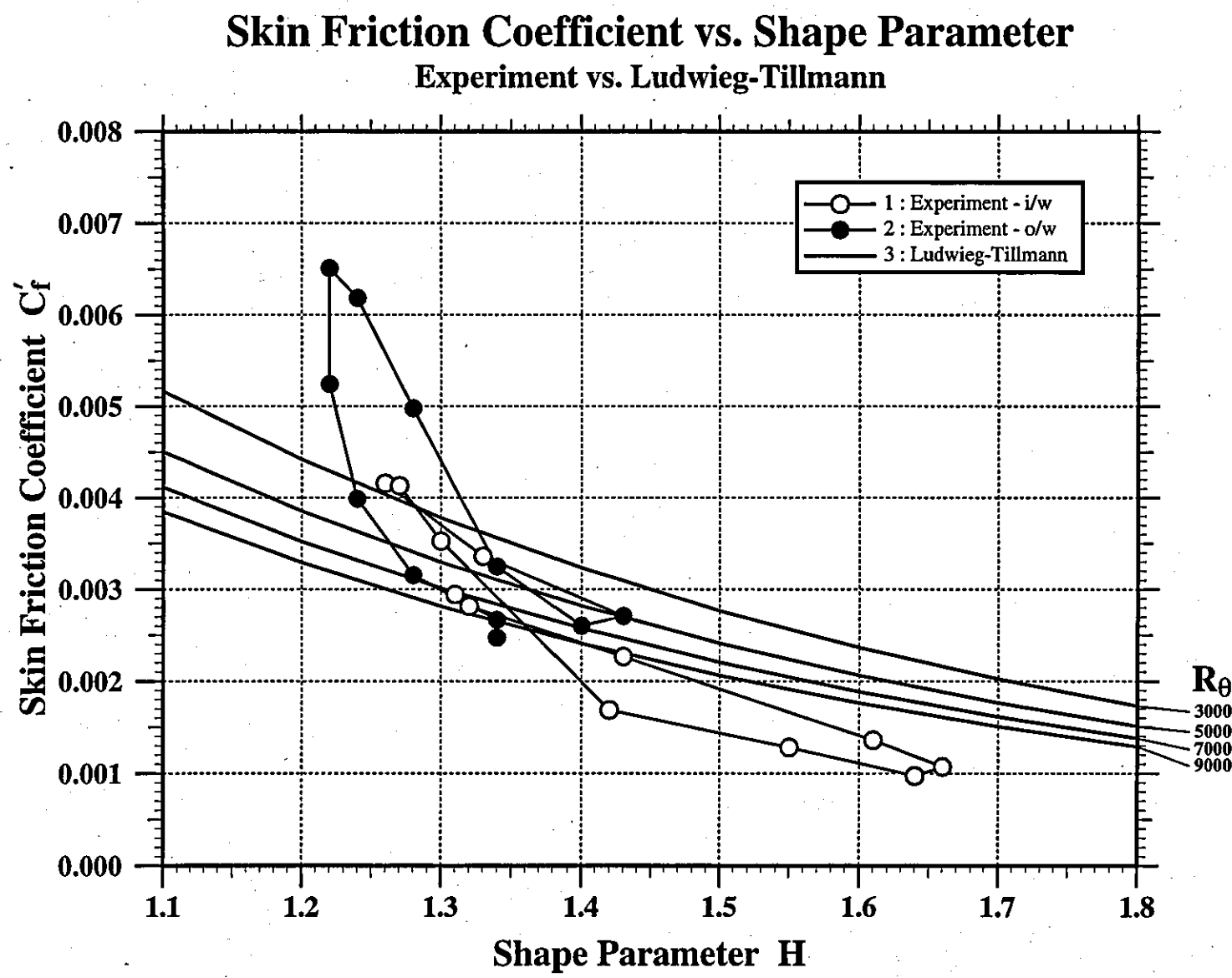
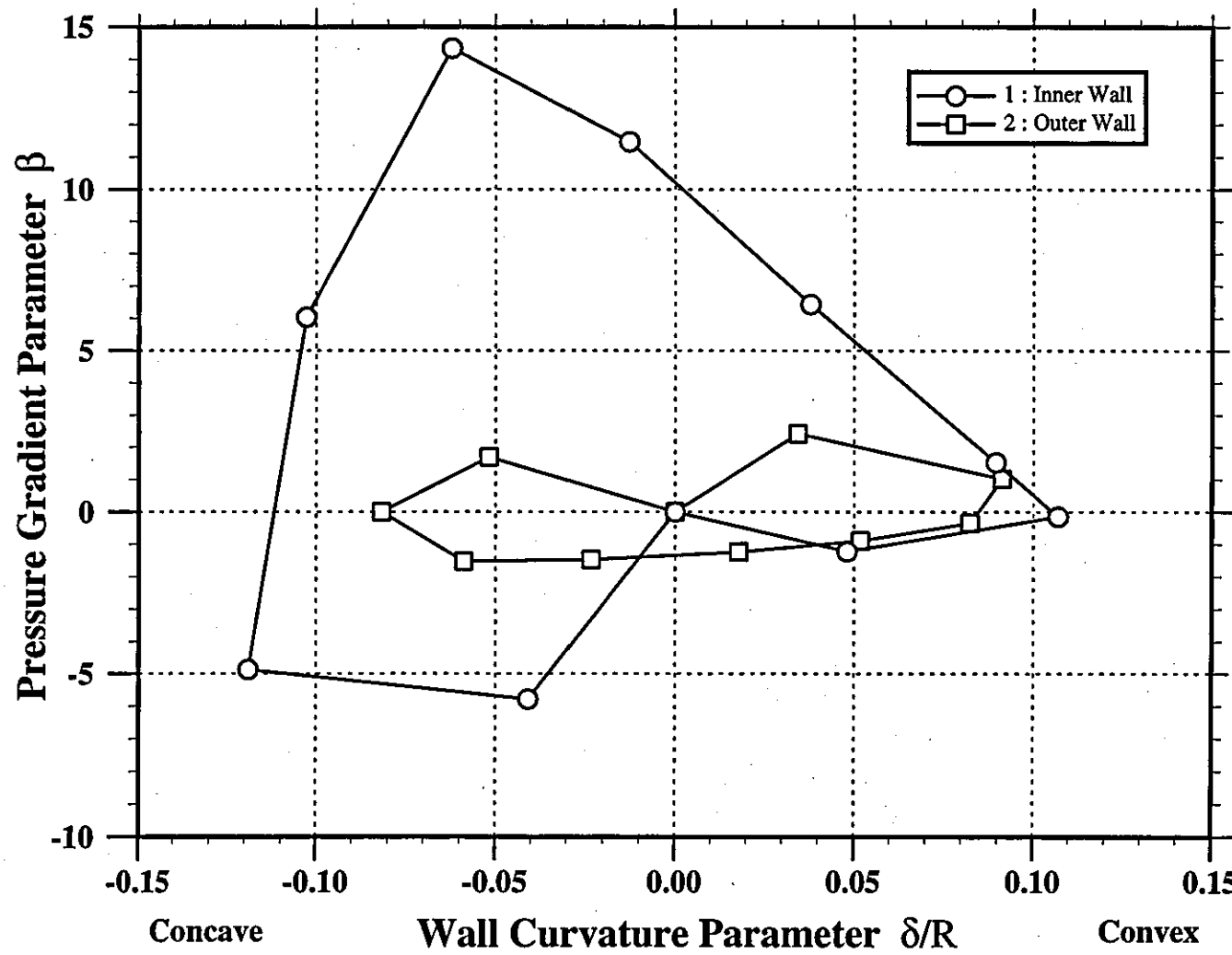


Figure 34

Pressure Gradient Parameter vs. Wall Curvature Parameter



Clauser Parameter vs. Pressure Gradient Parameter

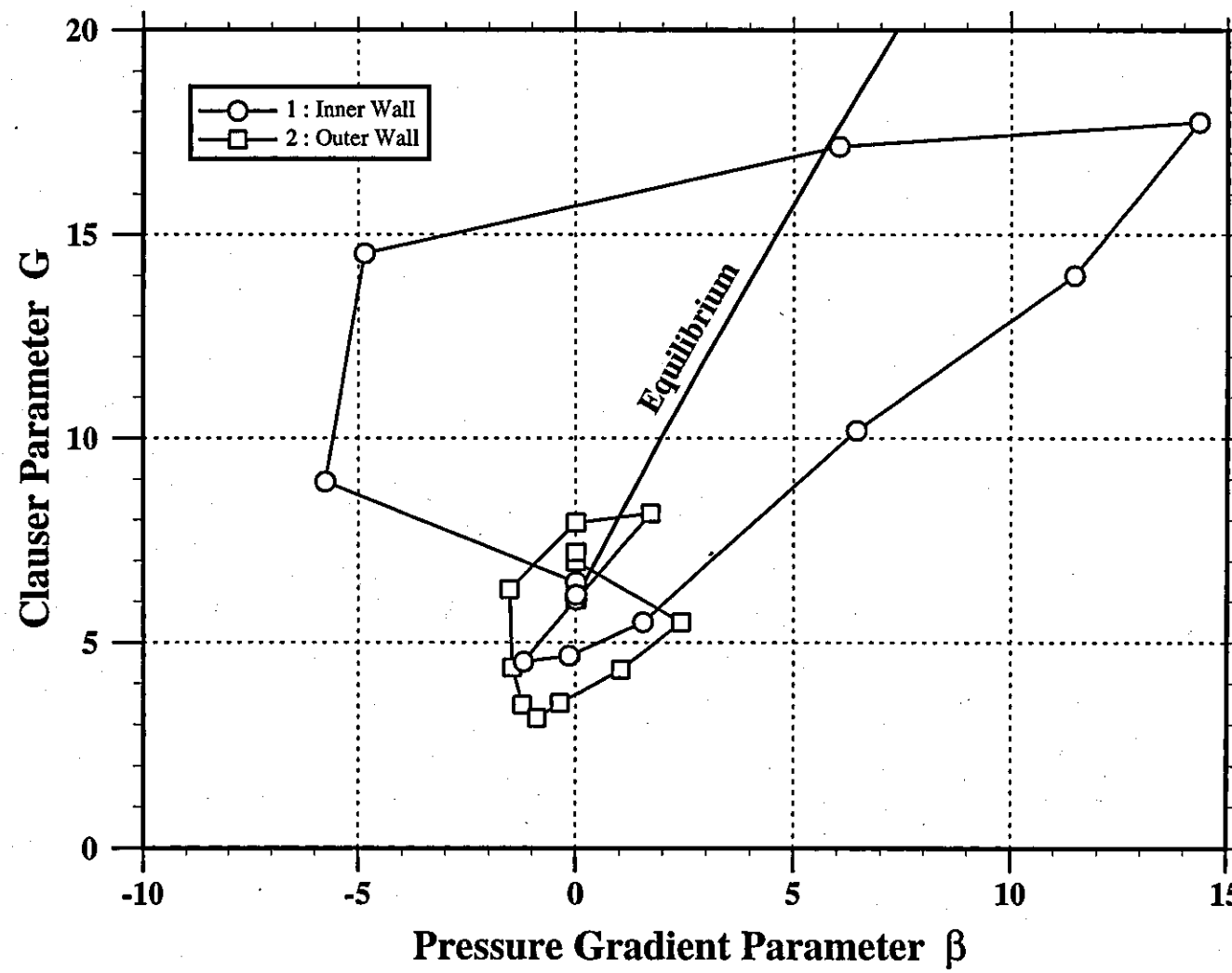
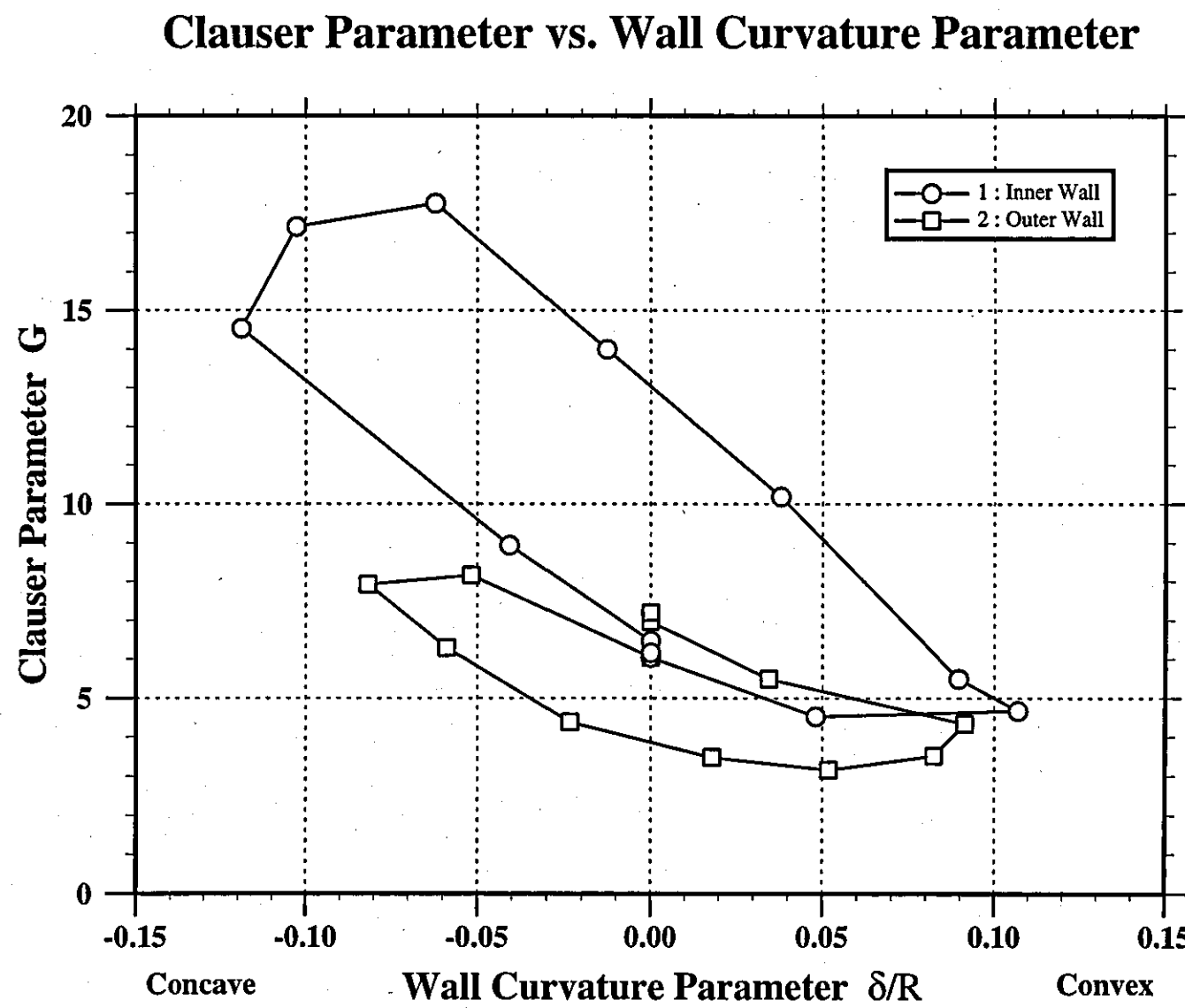


Figure 35

Figure 36



Shape Parameter vs. Pressure Gradient Parameter

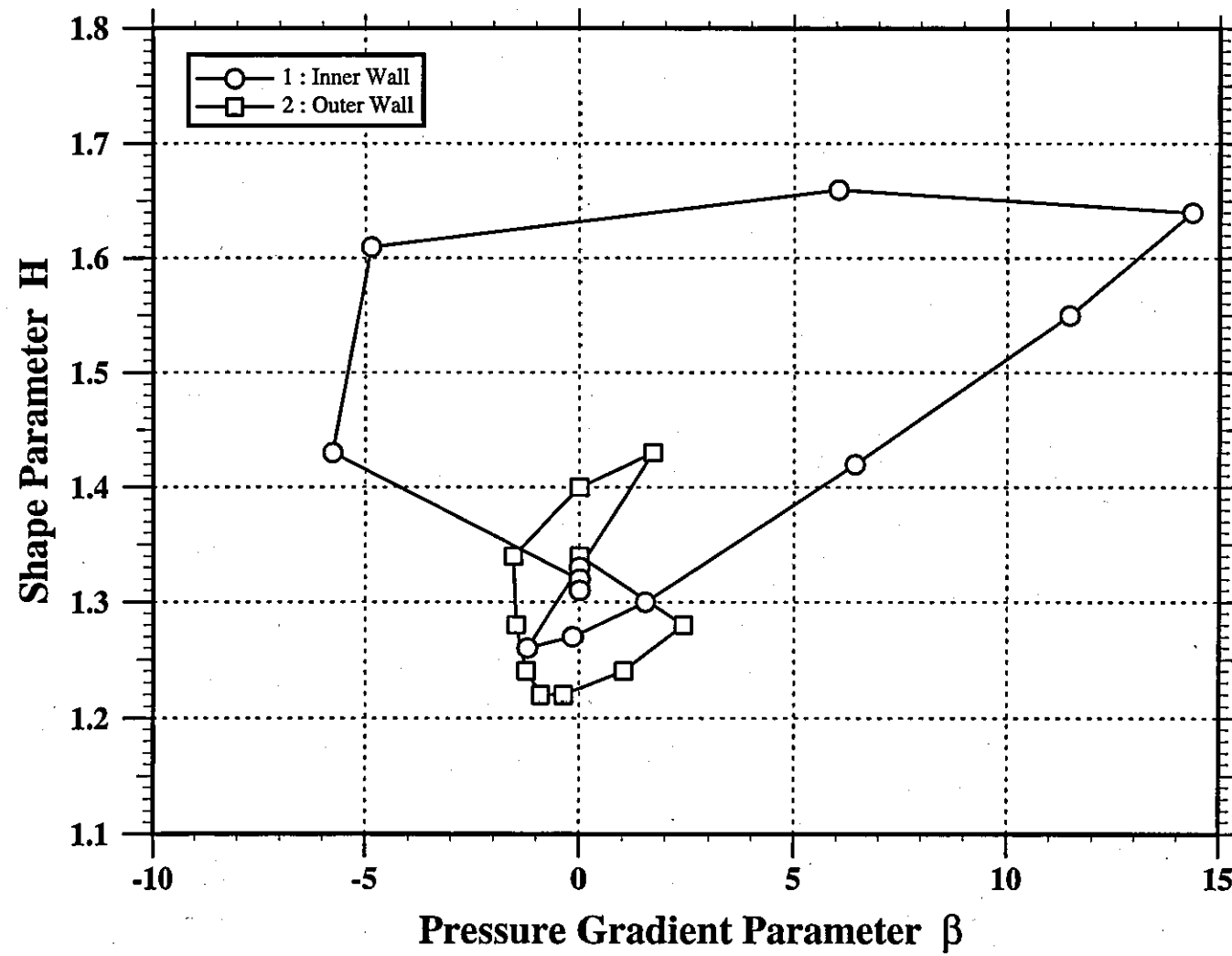


Figure 37

Skin Friction Coefficient vs. Pressure Gradient Parameter

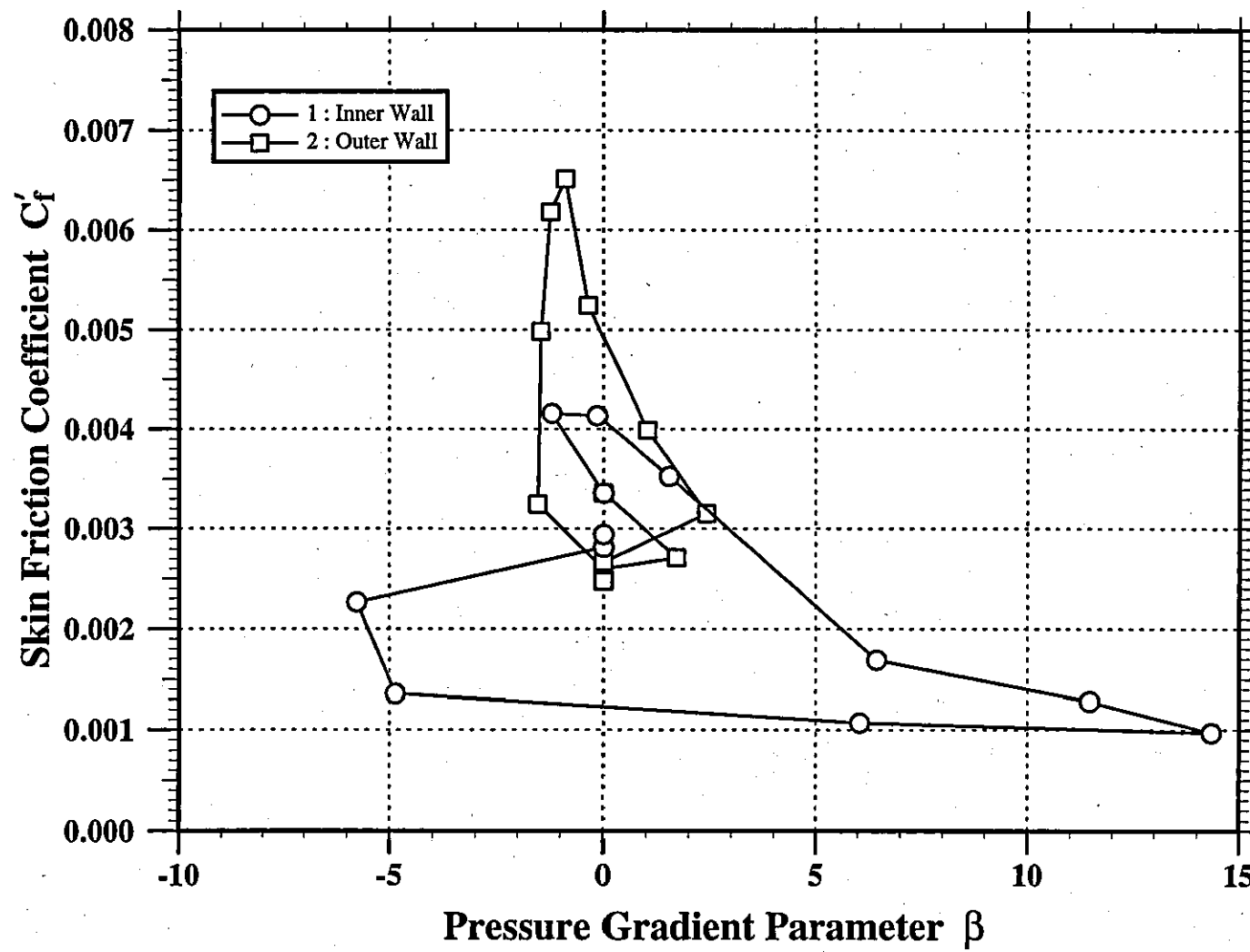


Figure 38

Variation of Streamwise Normal Stress ($\bar{u}u$)

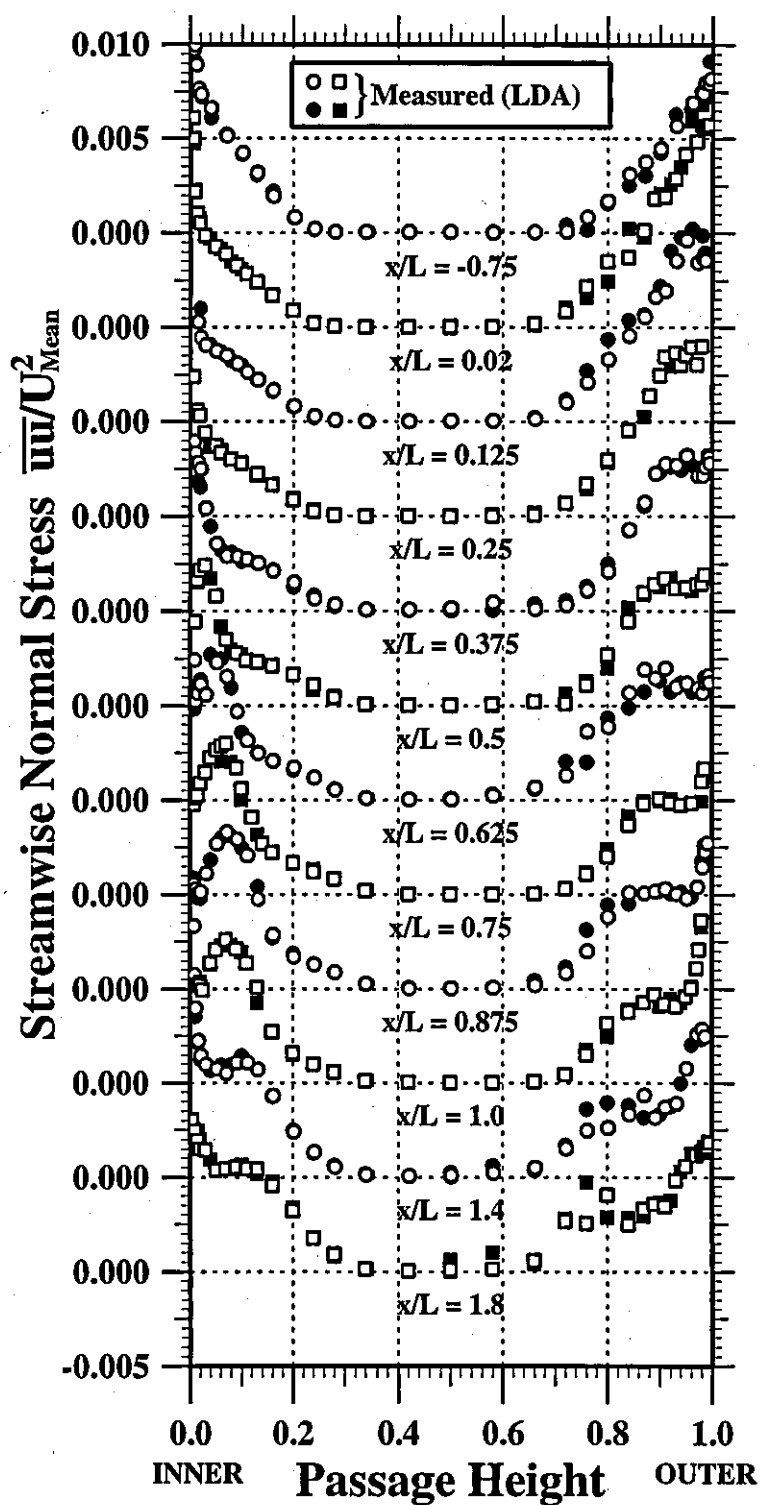


Figure 40

Variation of Cross-stream Normal Stress ($\bar{v}v$)

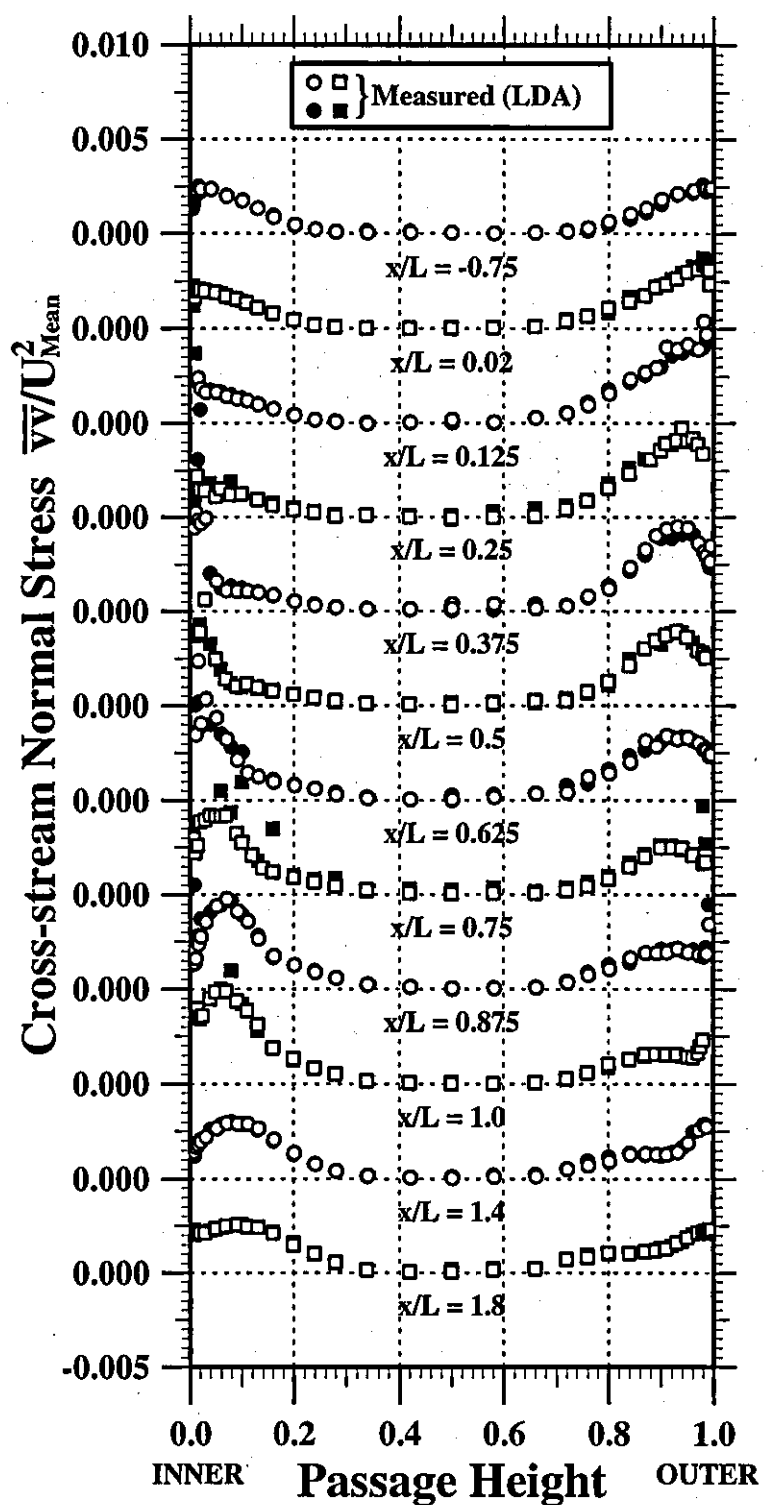


Figure 41

Variation of Circumferential Normal Stress ($\overline{w}w$)

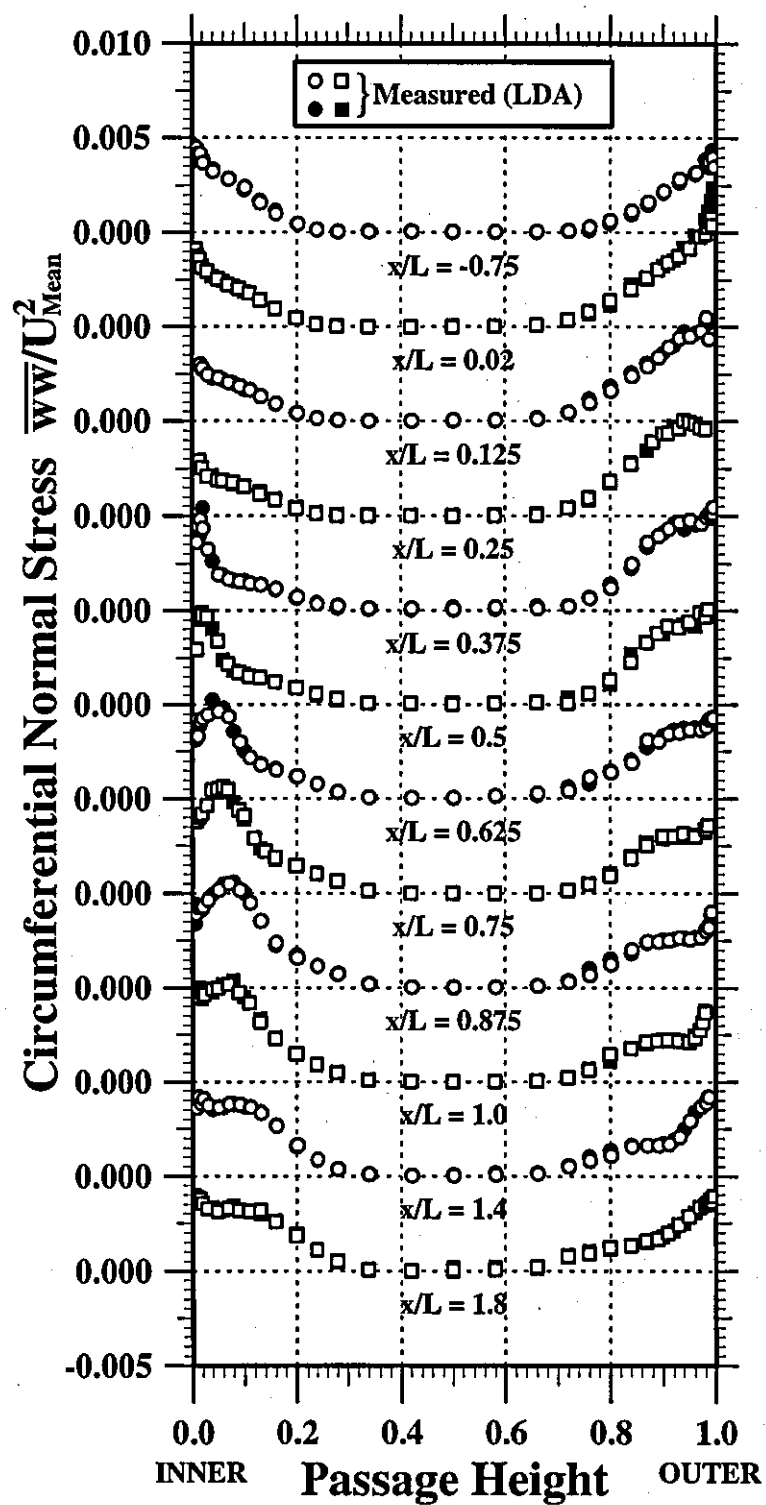


Figure 42

Variation of Reynolds Shear Stress ($\bar{u}v$)

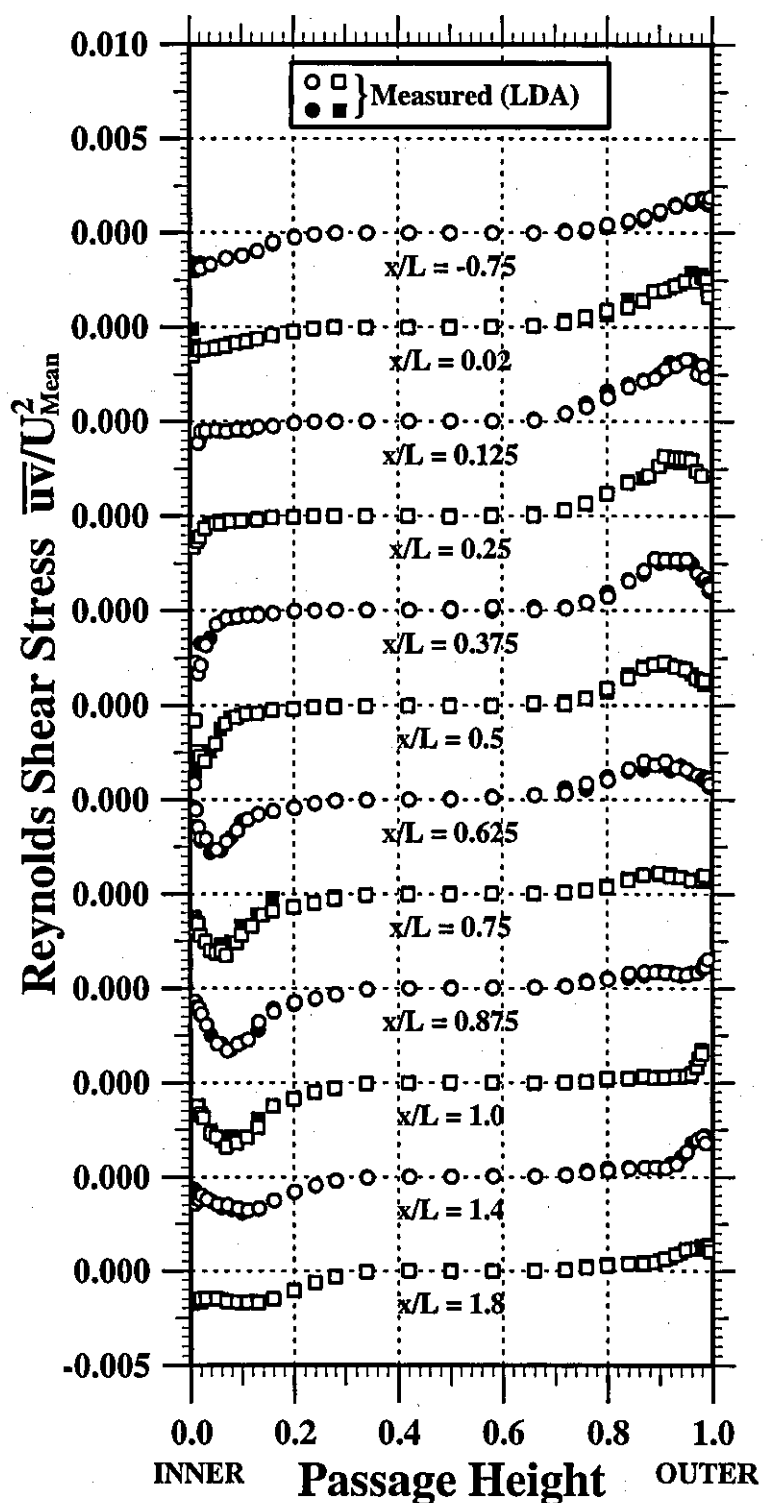
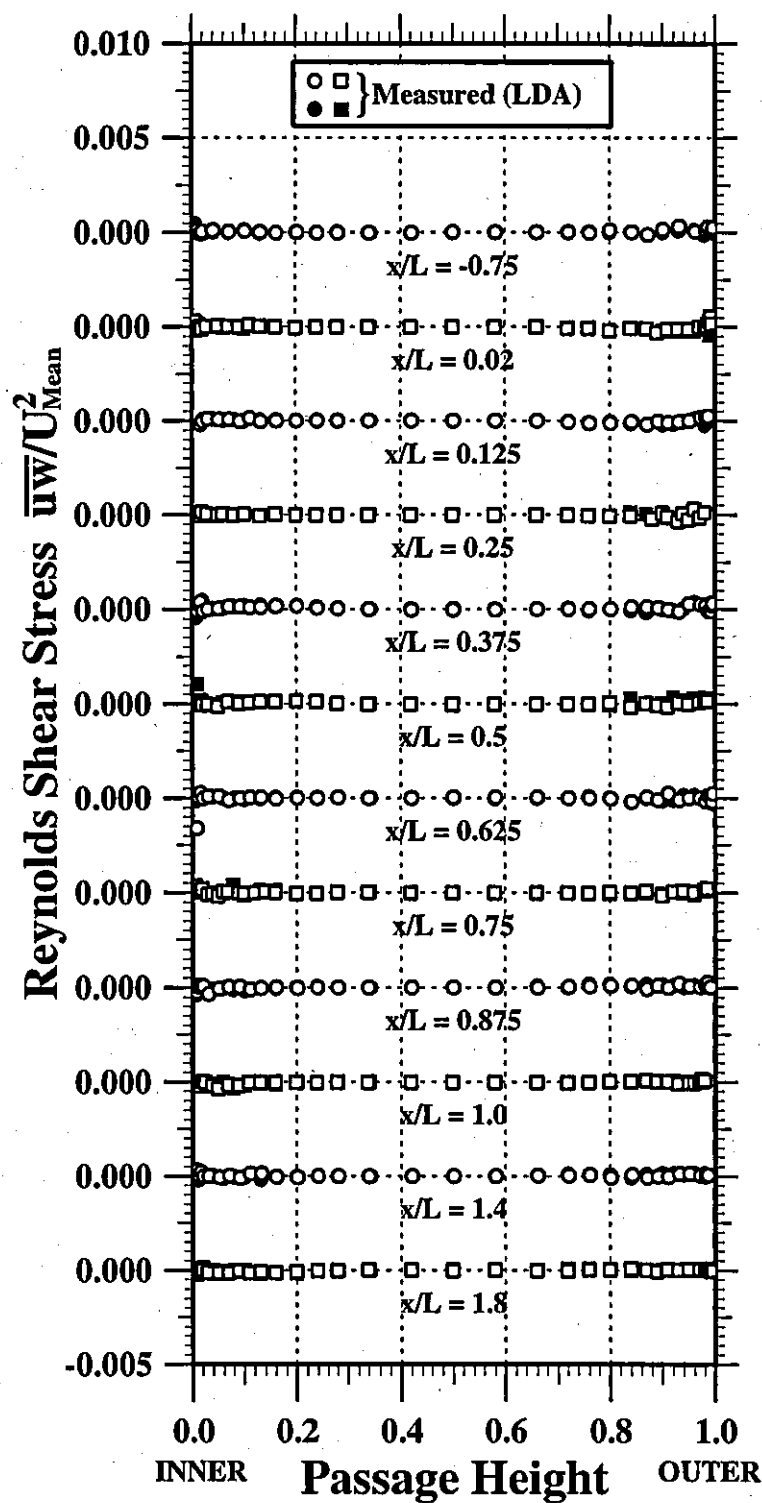


Figure 43

Variation of Reynolds Shear Stress (\bar{uw})



Variation of Reynolds Shear Stress (\overline{vw})

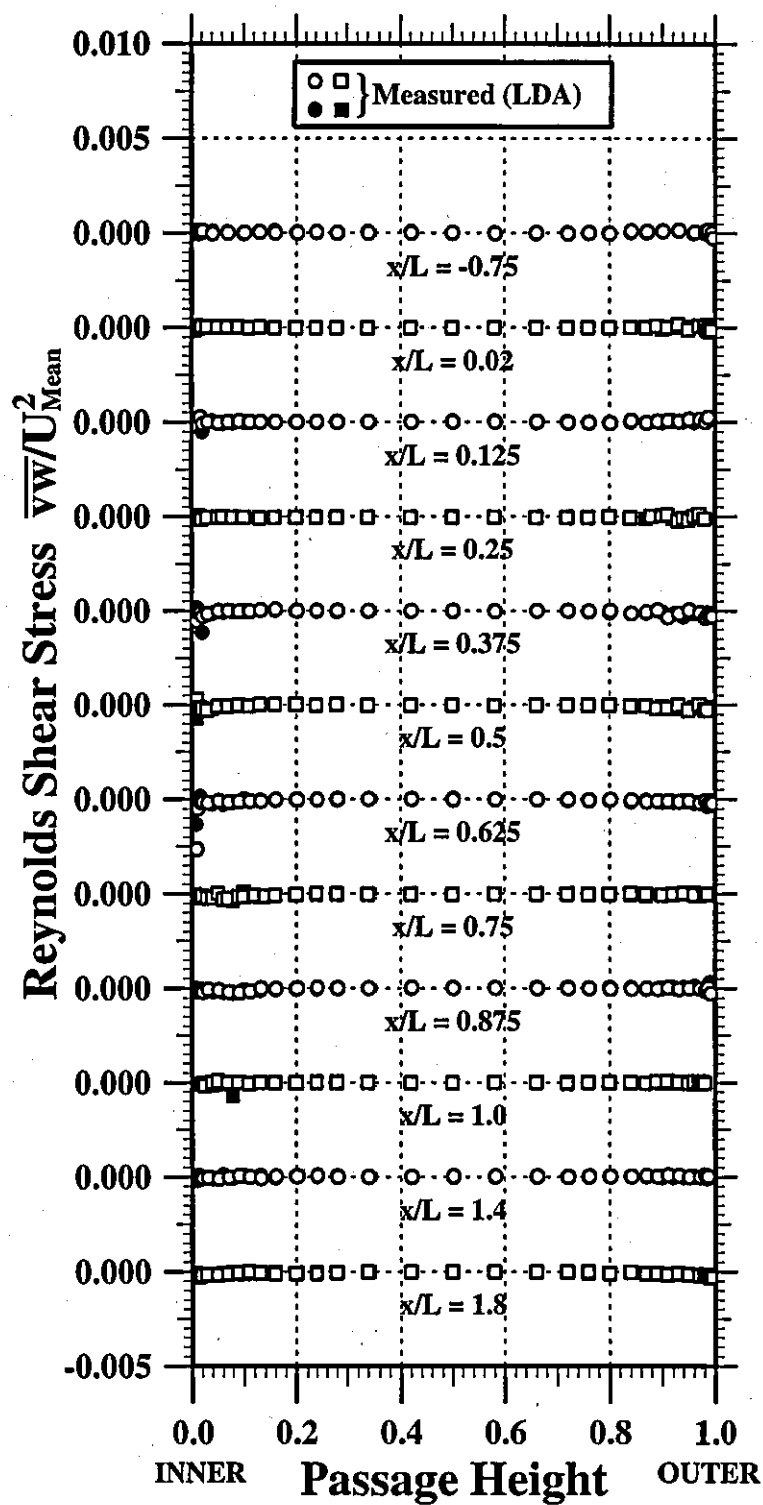
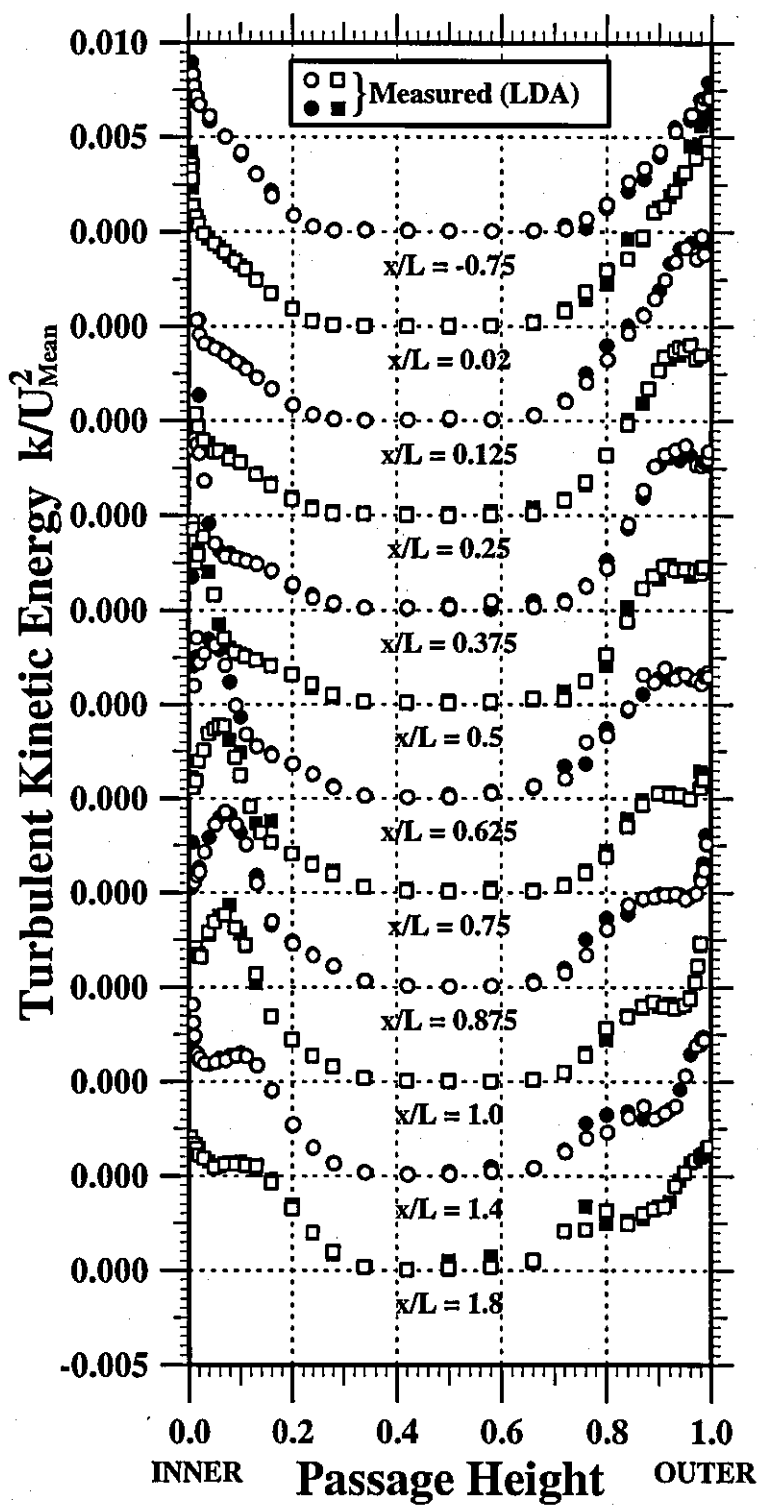


Figure 45

Variation of Turbulent Kinetic Energy



Variation of Shear Stress Correlation Coefficient

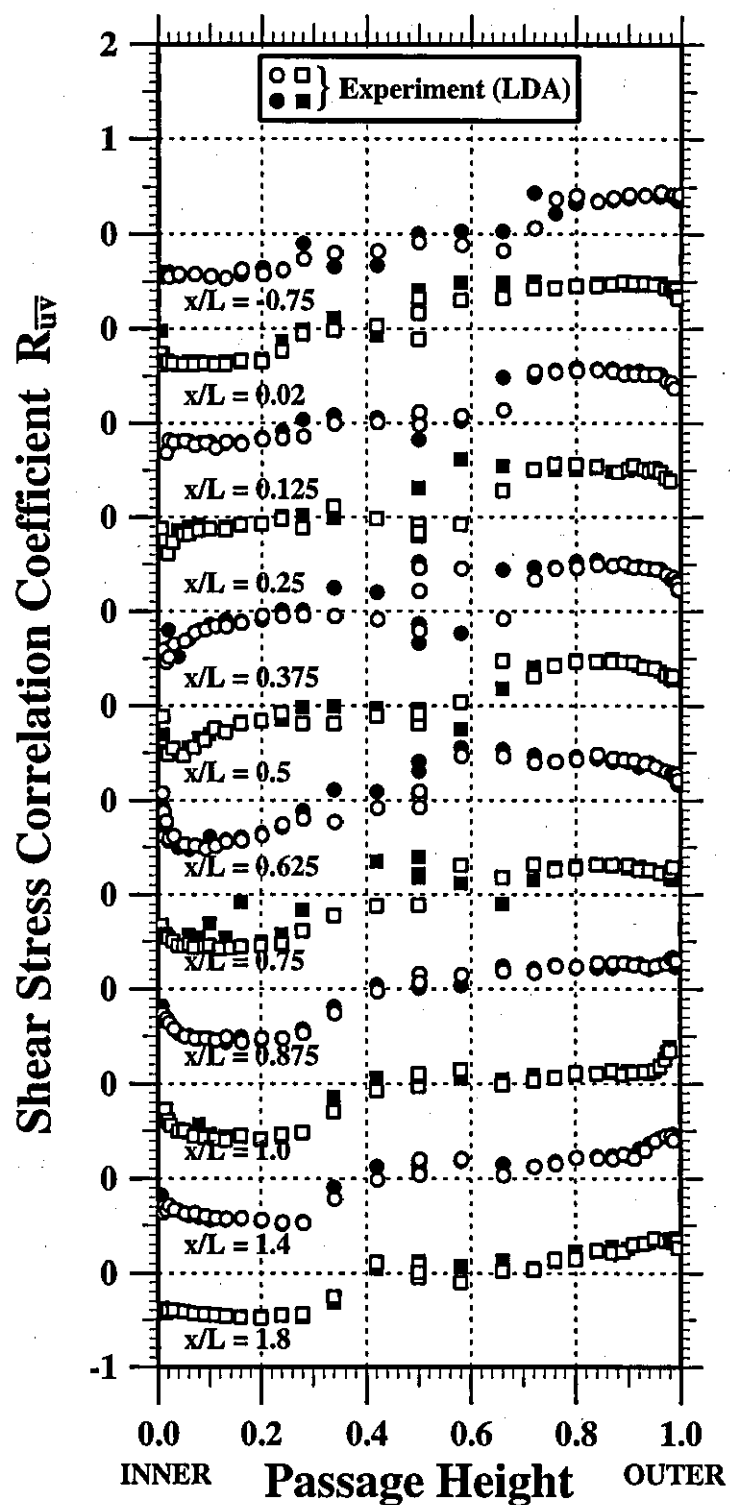


Figure 47

Variation of Reynolds Stress Ratio ($\overline{vv}/\overline{uu}$)

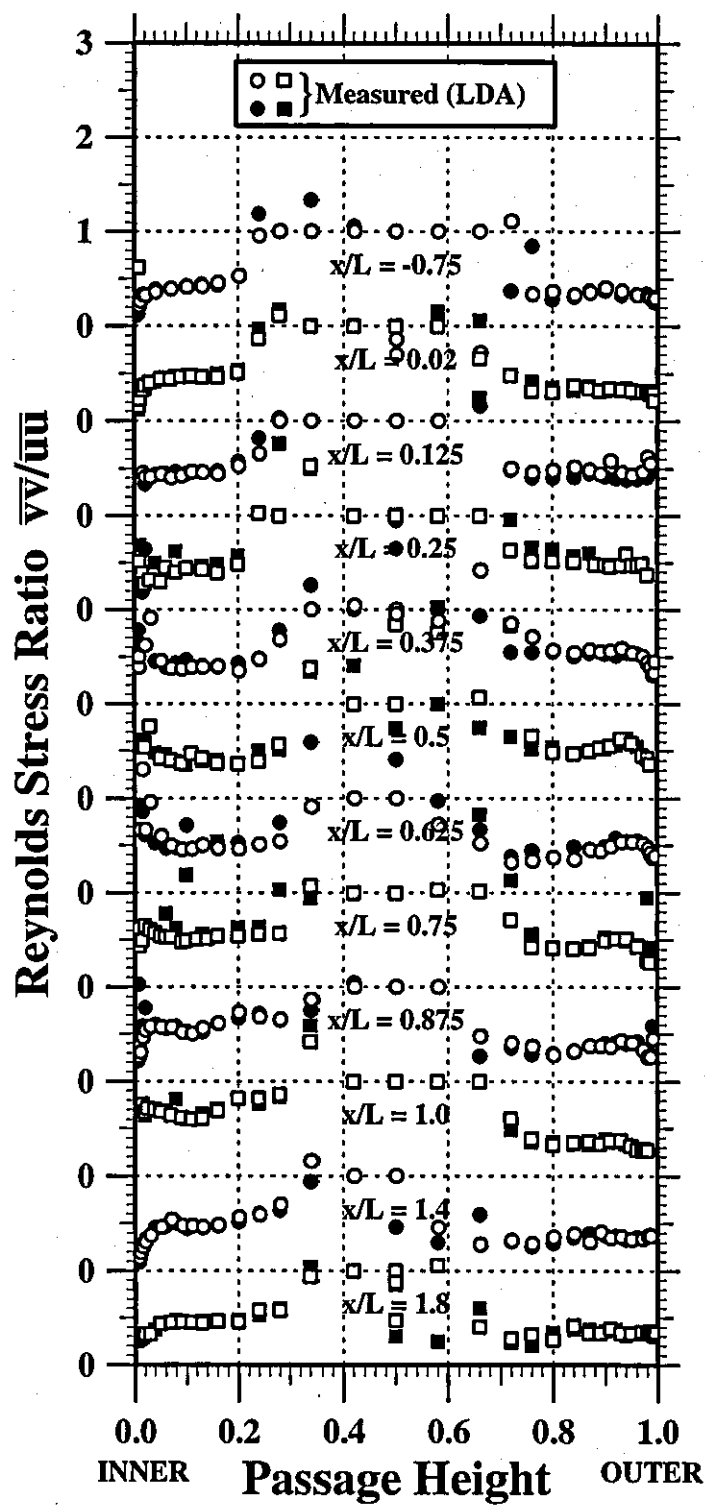


Figure 48

Variation of Reynolds Stress Ratio (\bar{uv}/\bar{uu})

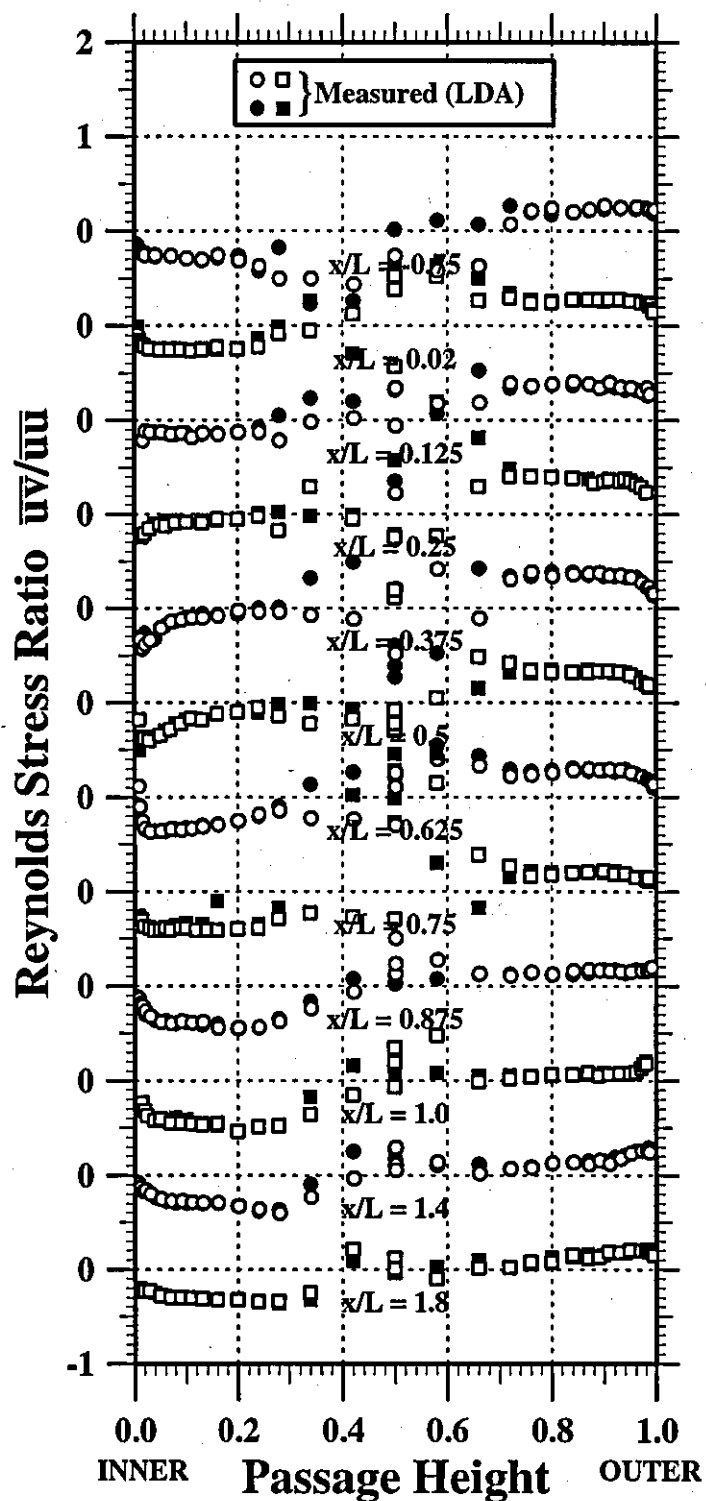


Figure 49

Variation of Reynolds Stress Ratio (\bar{uv}/\bar{vv})

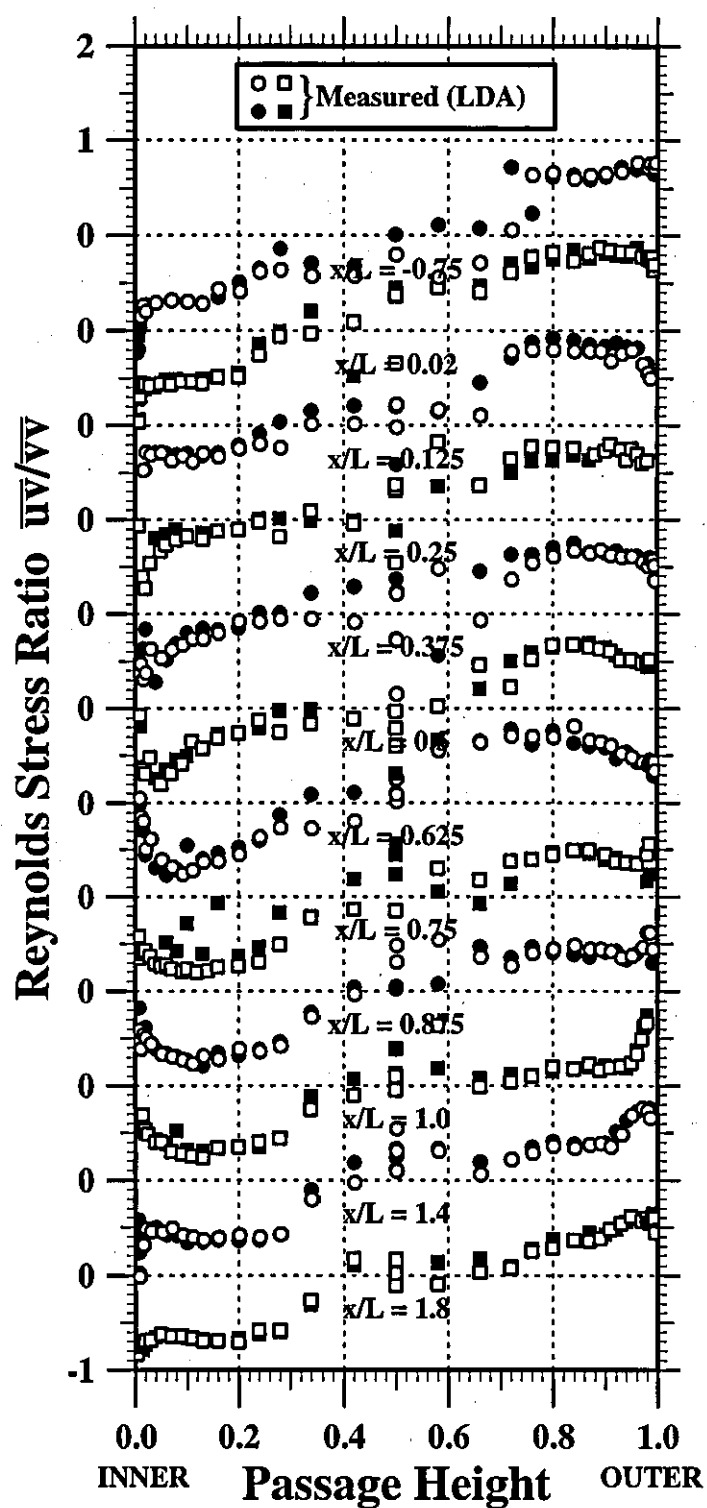


Figure 50

Variation of Reynolds Stress Ratio ($\bar{u}v/k$)

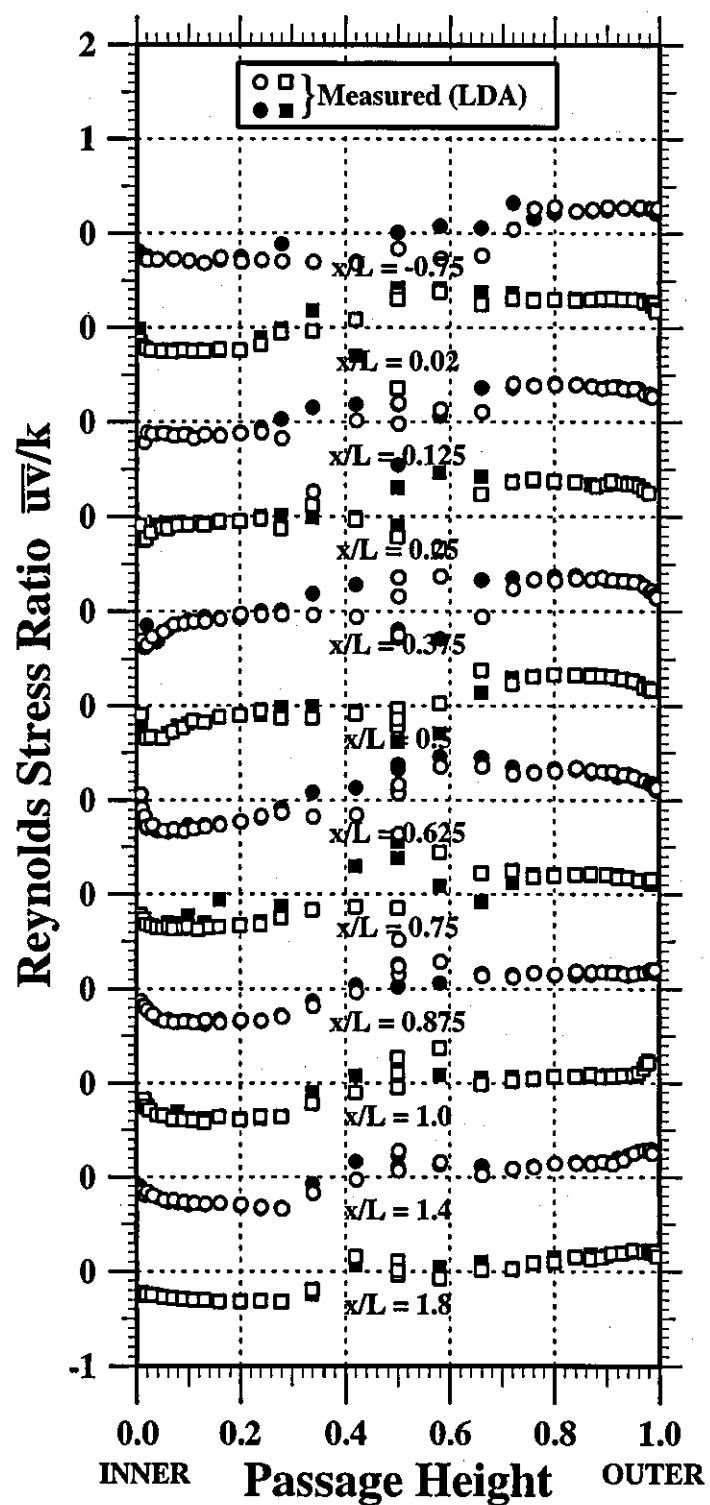


Figure 51

Variation of Reynolds Stress Ratio ($\bar{u}\bar{u}/k$)

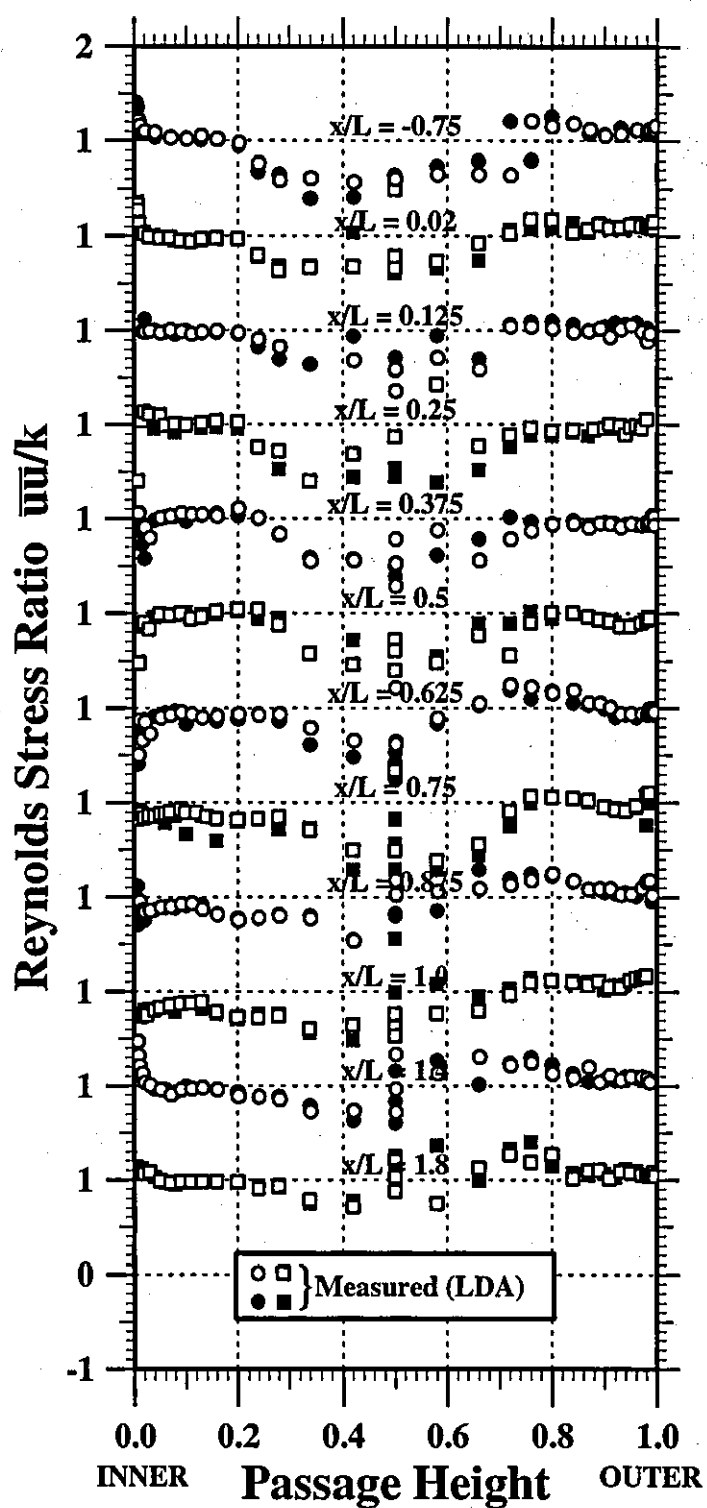


Figure 52

Variation of Reynolds Stress Ratio ($\bar{v}v/k$)

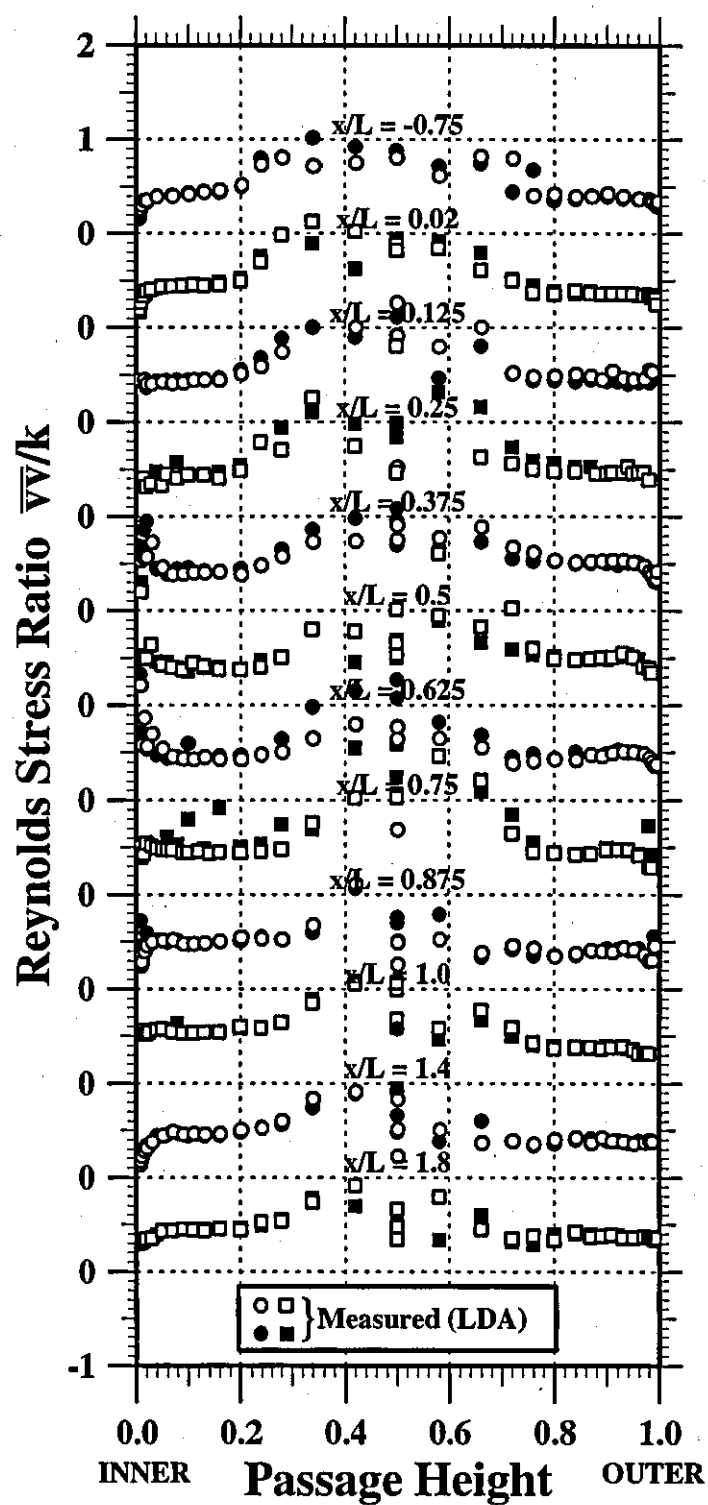


Figure 53

Variation of Reynolds Stress Ratio ($\overline{w w}/k$)

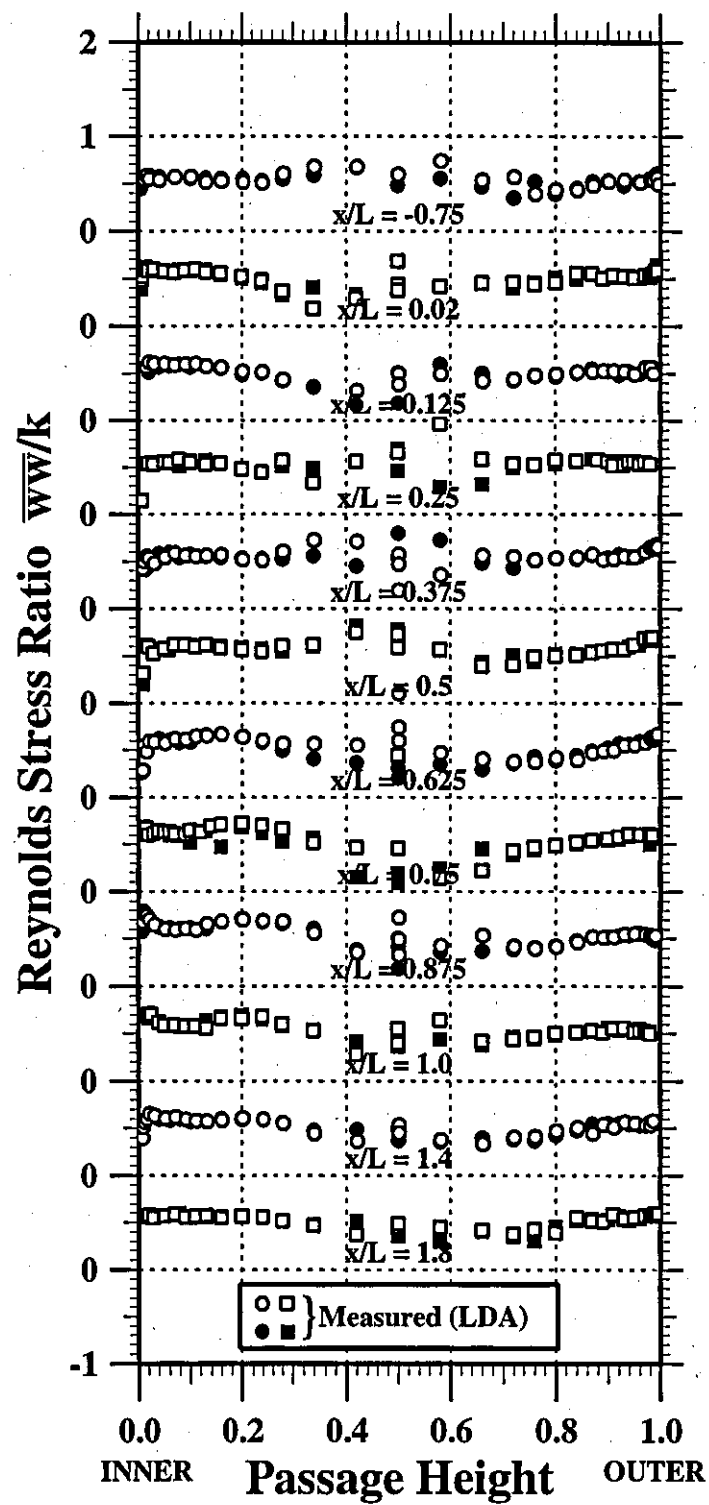


Figure 54

Measured Reynolds Stress Anisotropy

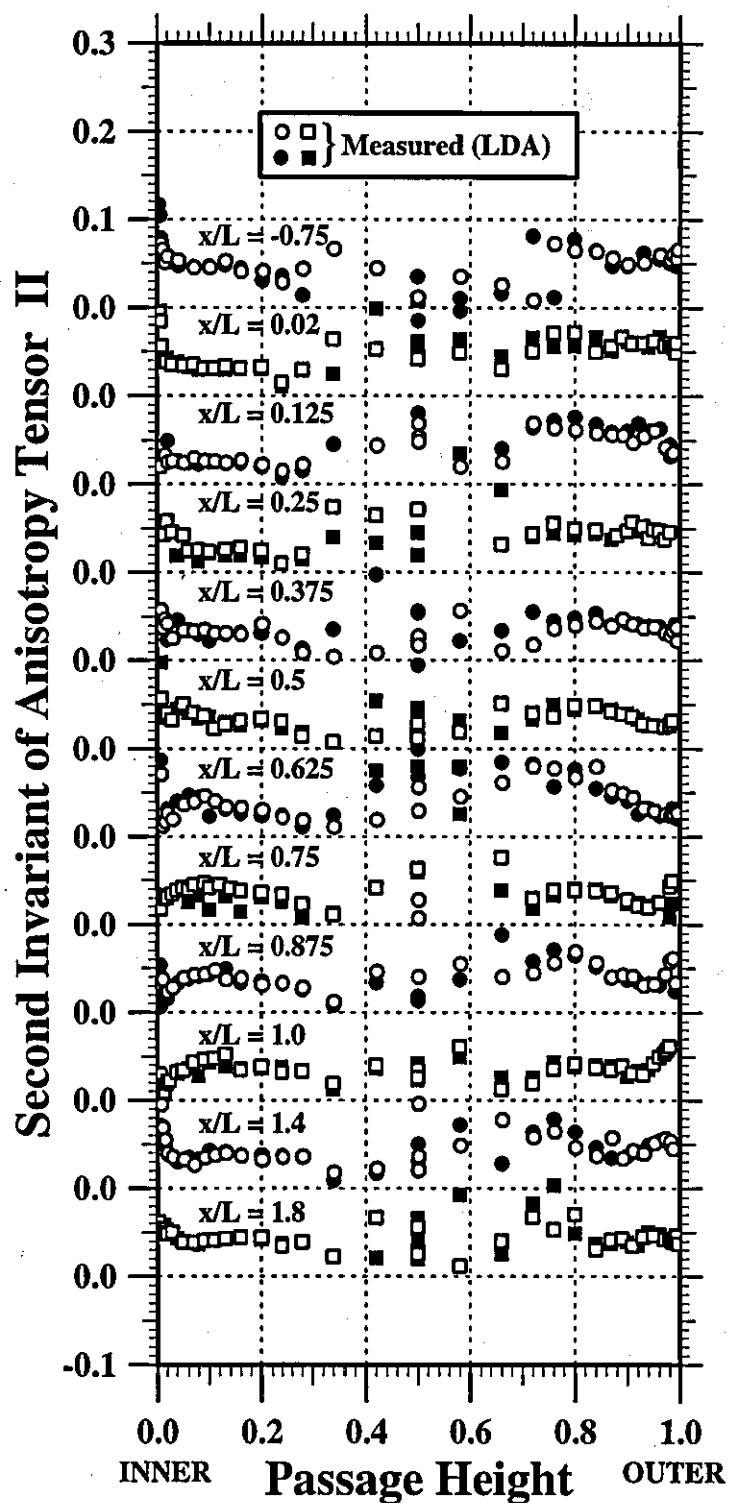


Figure 55

Variation of Triple Velocity Correlation (\overline{uuu})

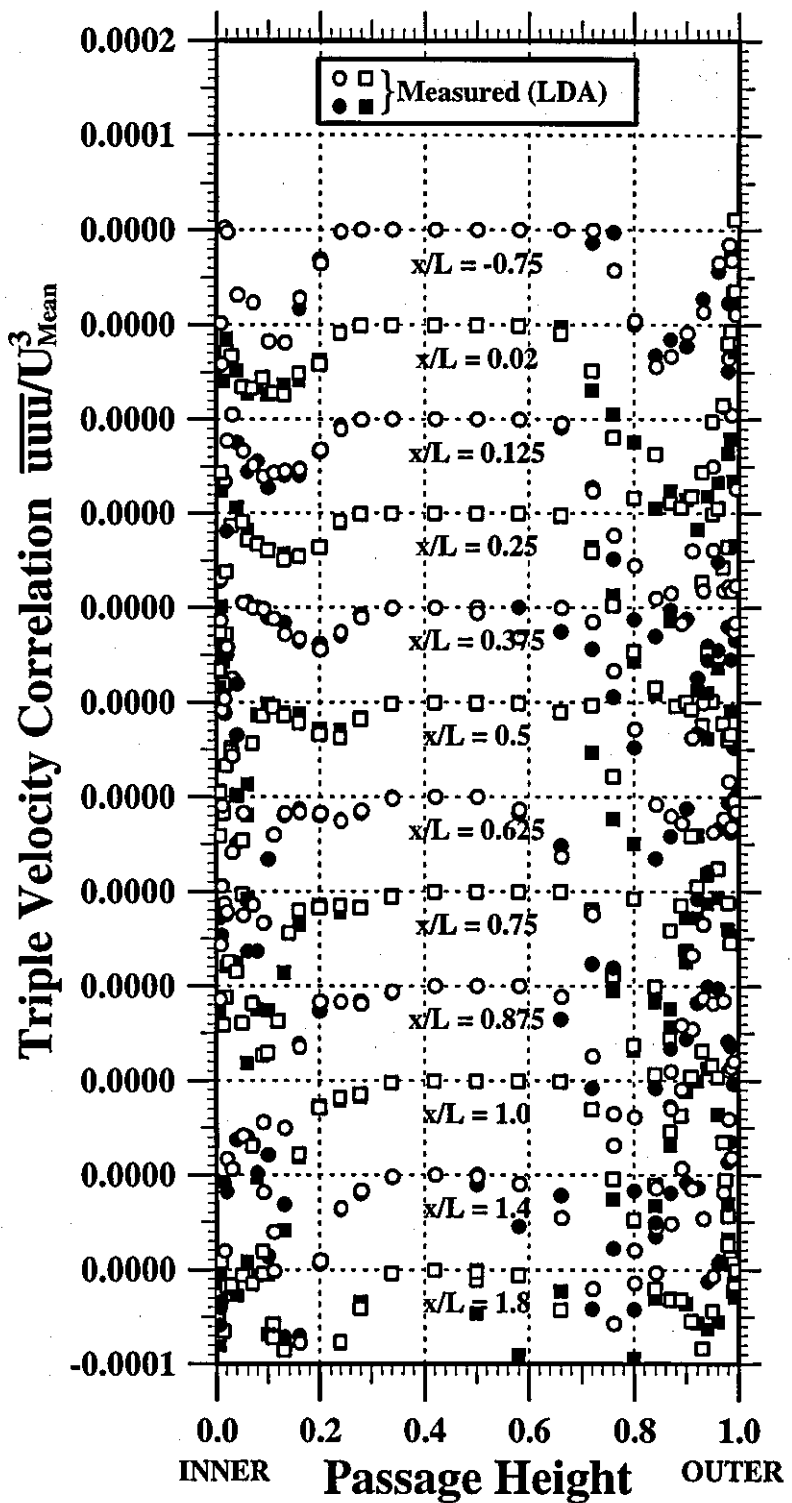


Figure 56

Variation of Triple Velocity Correlation (\overline{uuv})

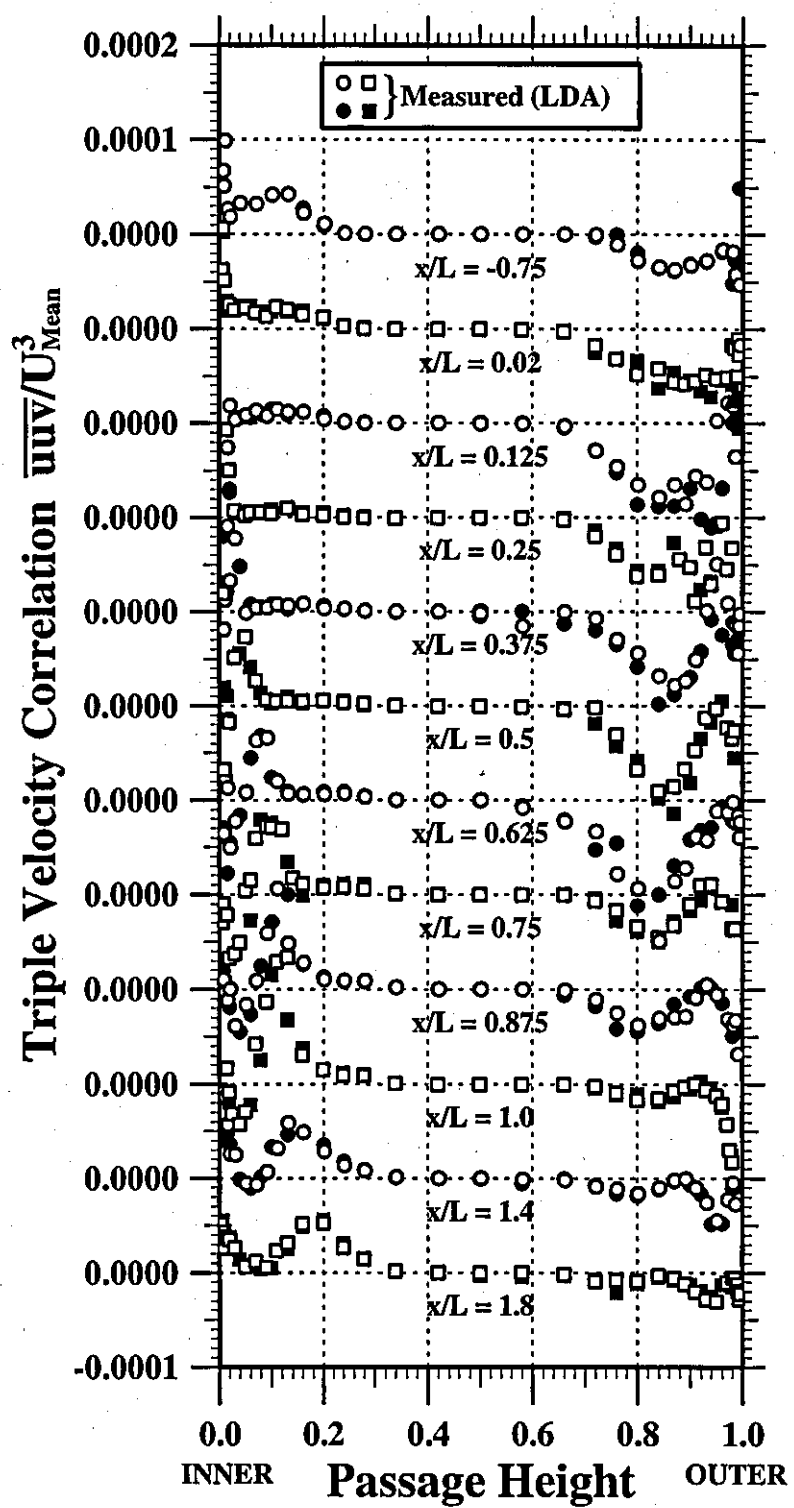
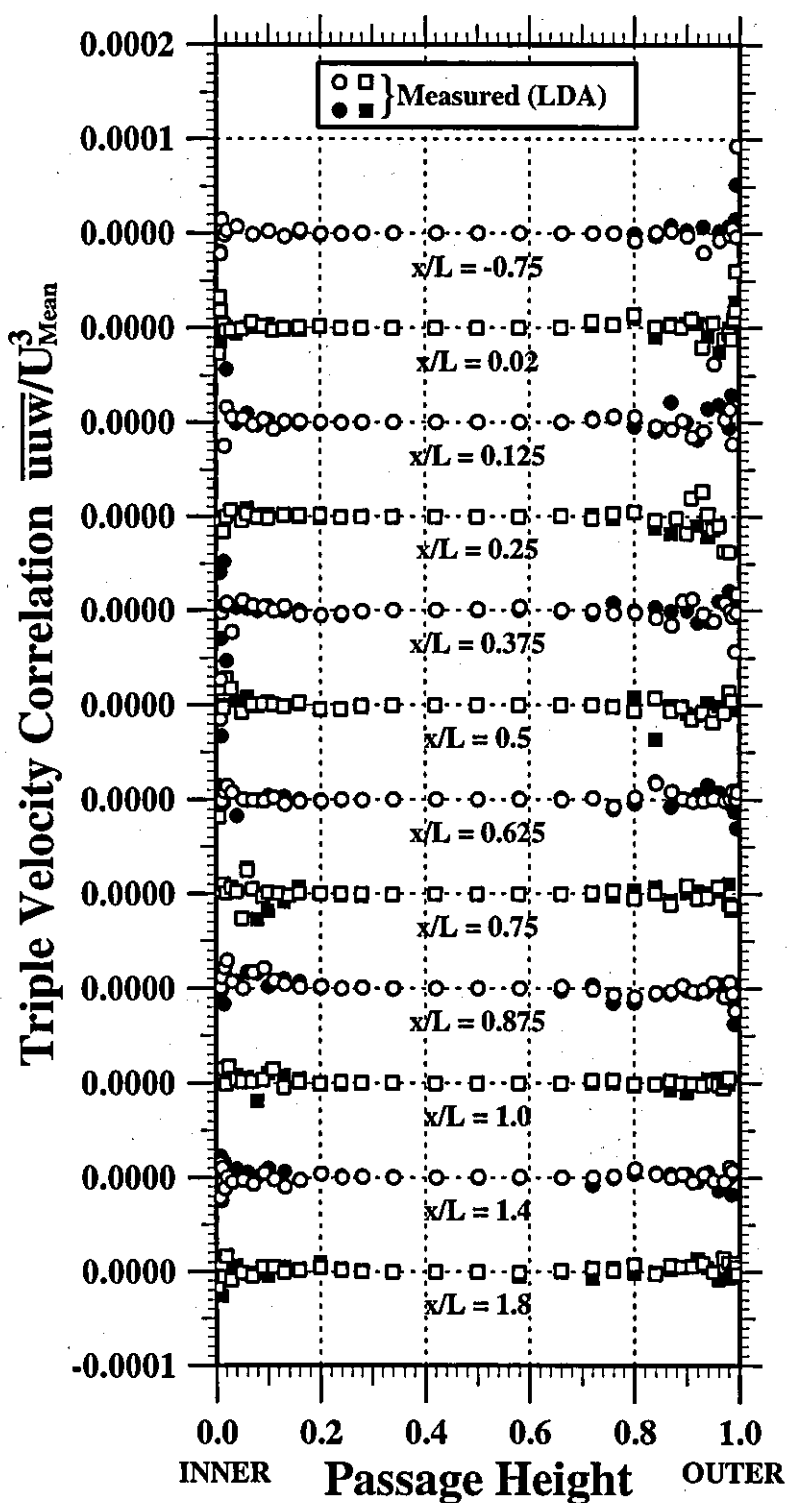
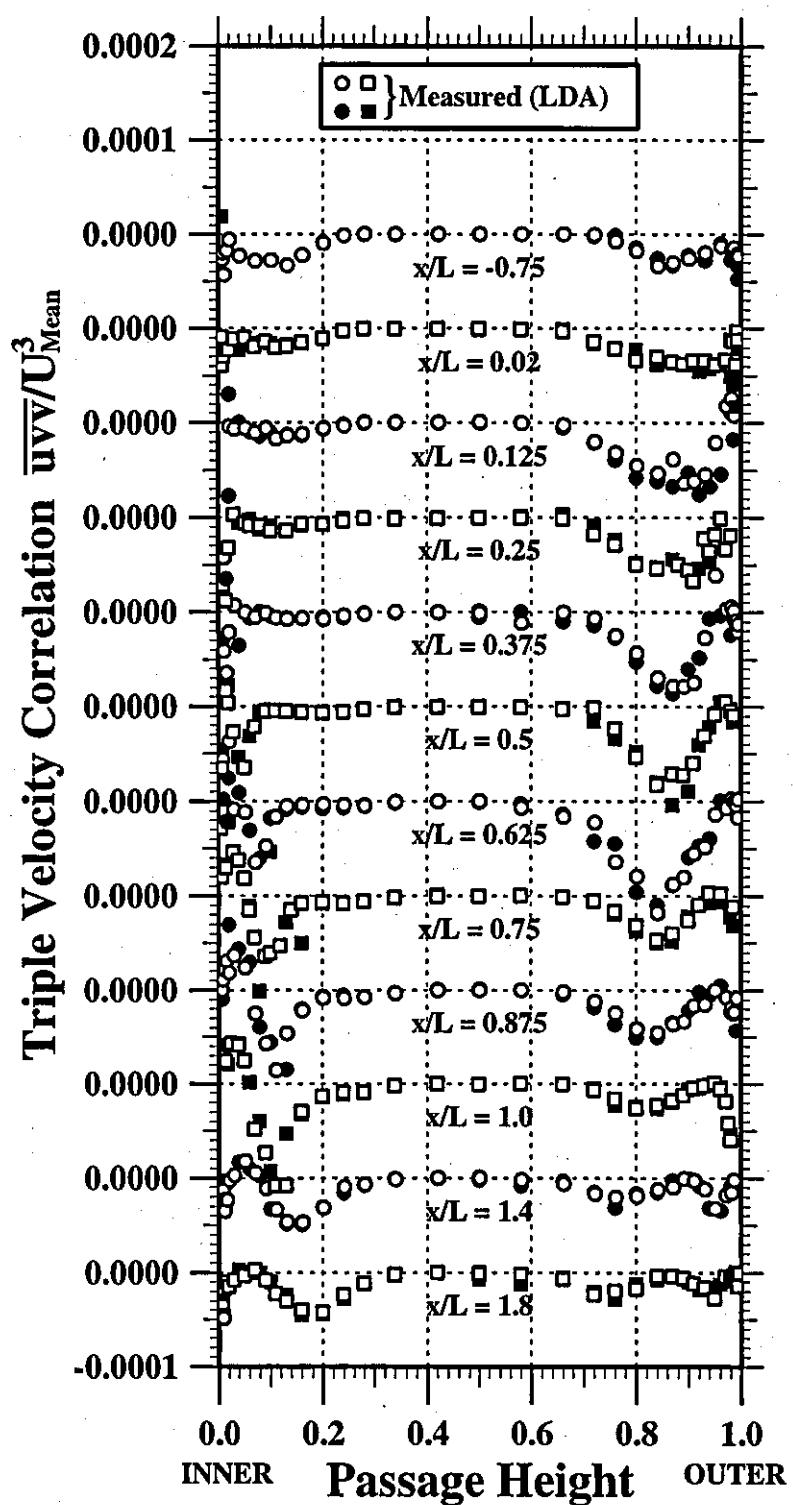


Figure 57

Variation of Triple Velocity Correlation (\overline{uuw})



Variation of Triple Velocity Correlation (\overline{uvw})



Variation of Triple Velocity Correlation (\bar{uvw})

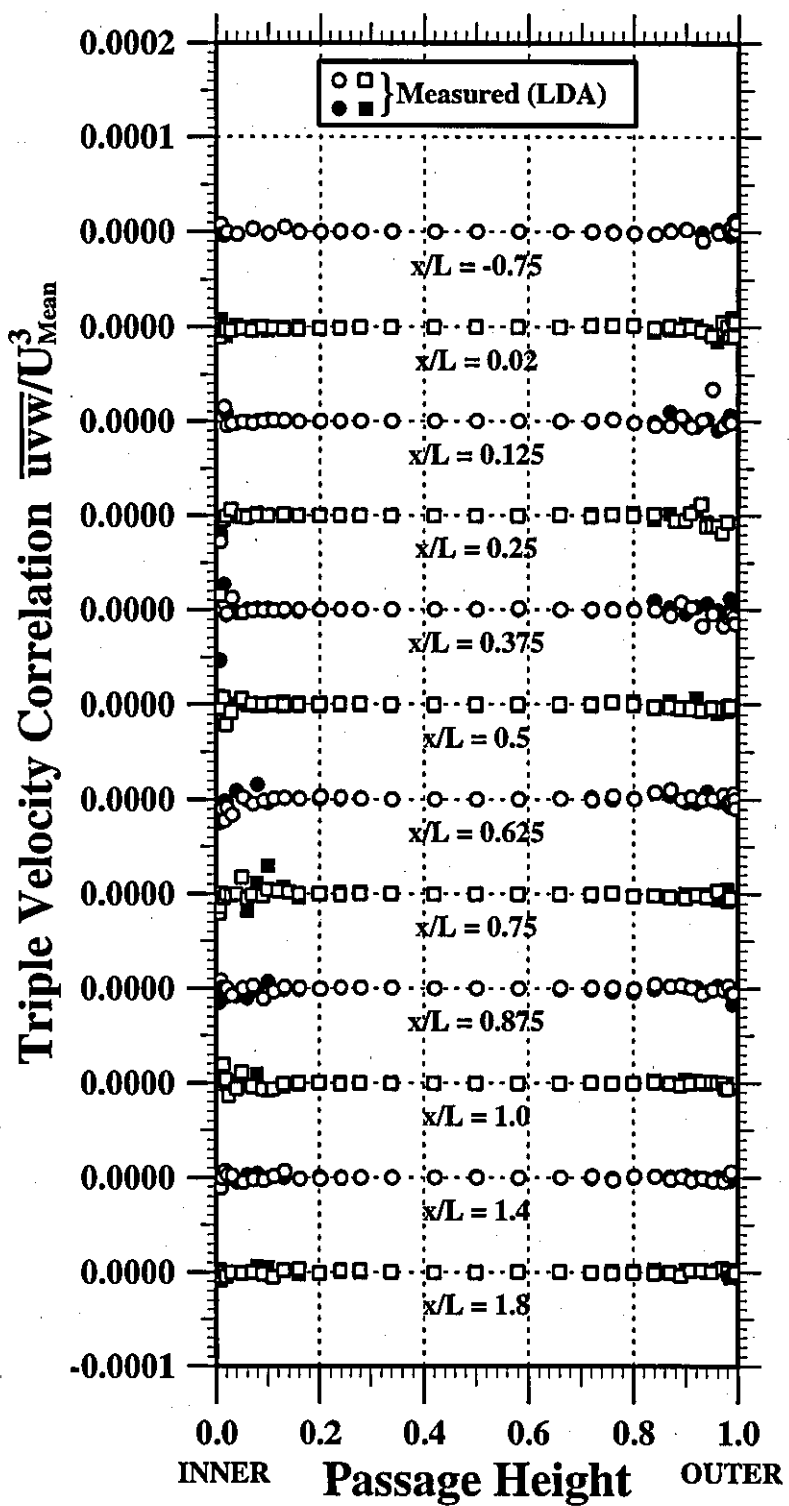


Figure 60

Variation of Triple Velocity Correlation ($\overline{uvw}/U_{\text{Mean}}^3$)

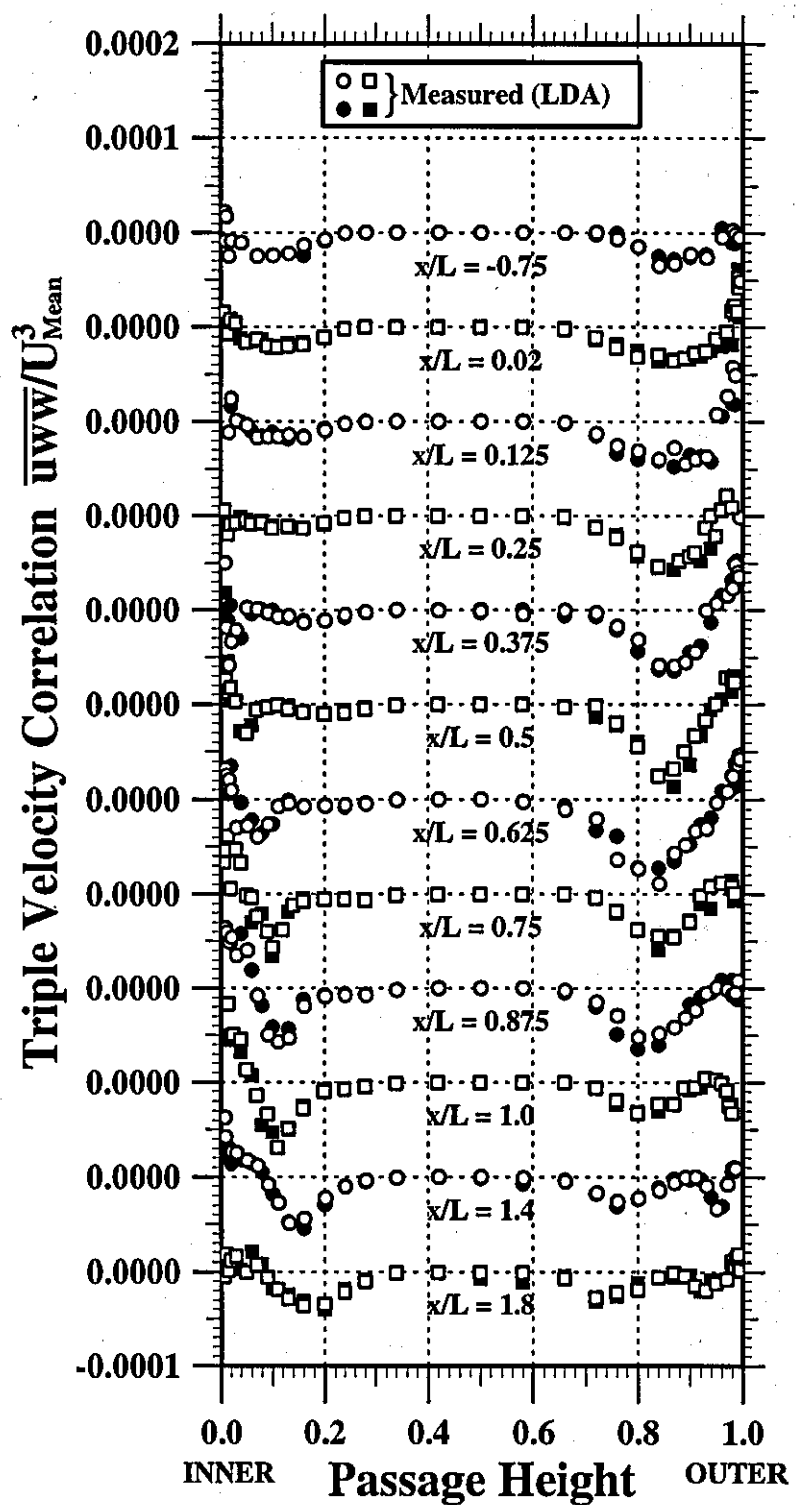


Figure 61

Variation of Triple Velocity Correlation (\overline{vvv})

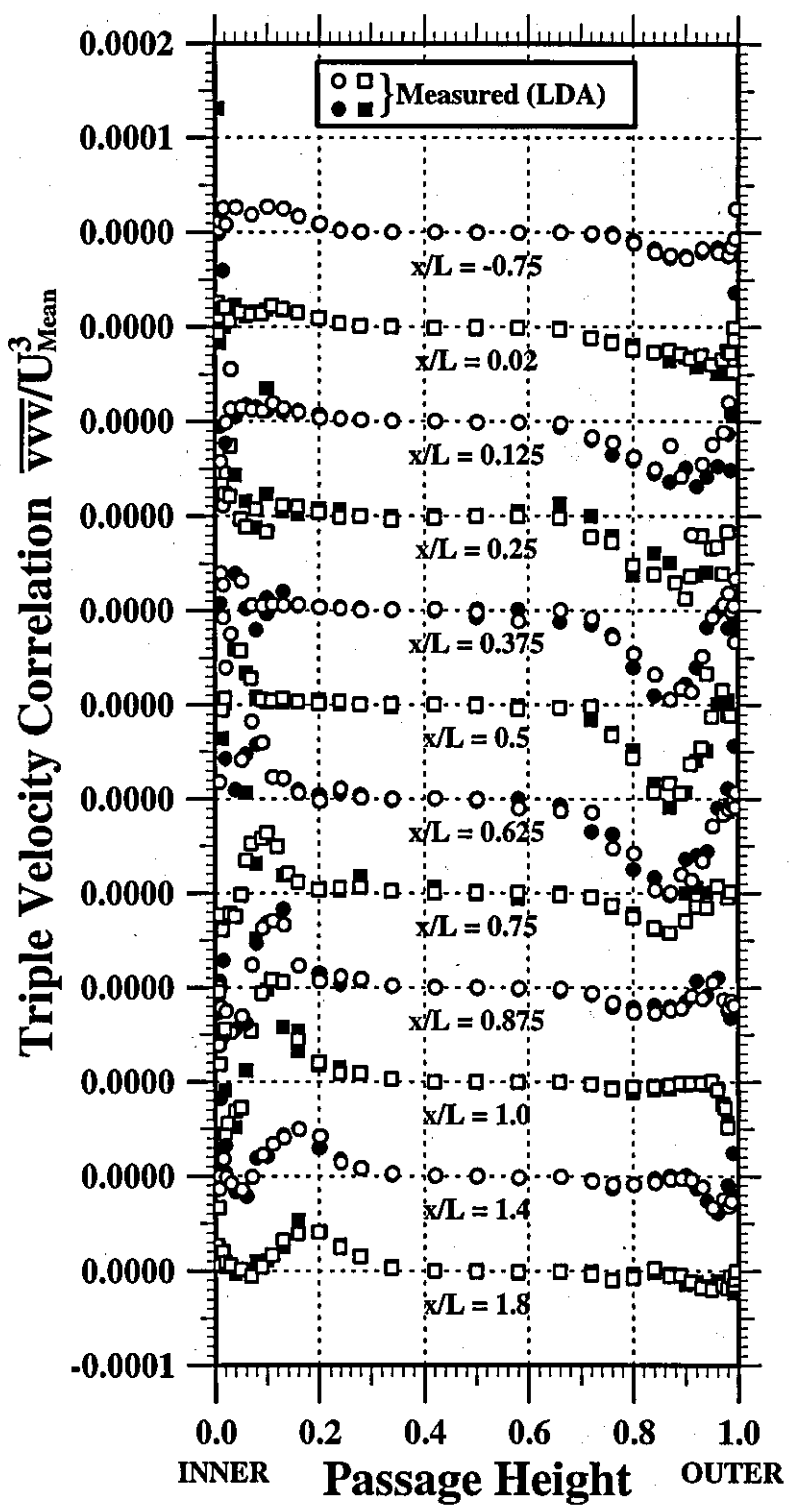


Figure 62

Variation of Triple Velocity Correlation (\overline{vvw})

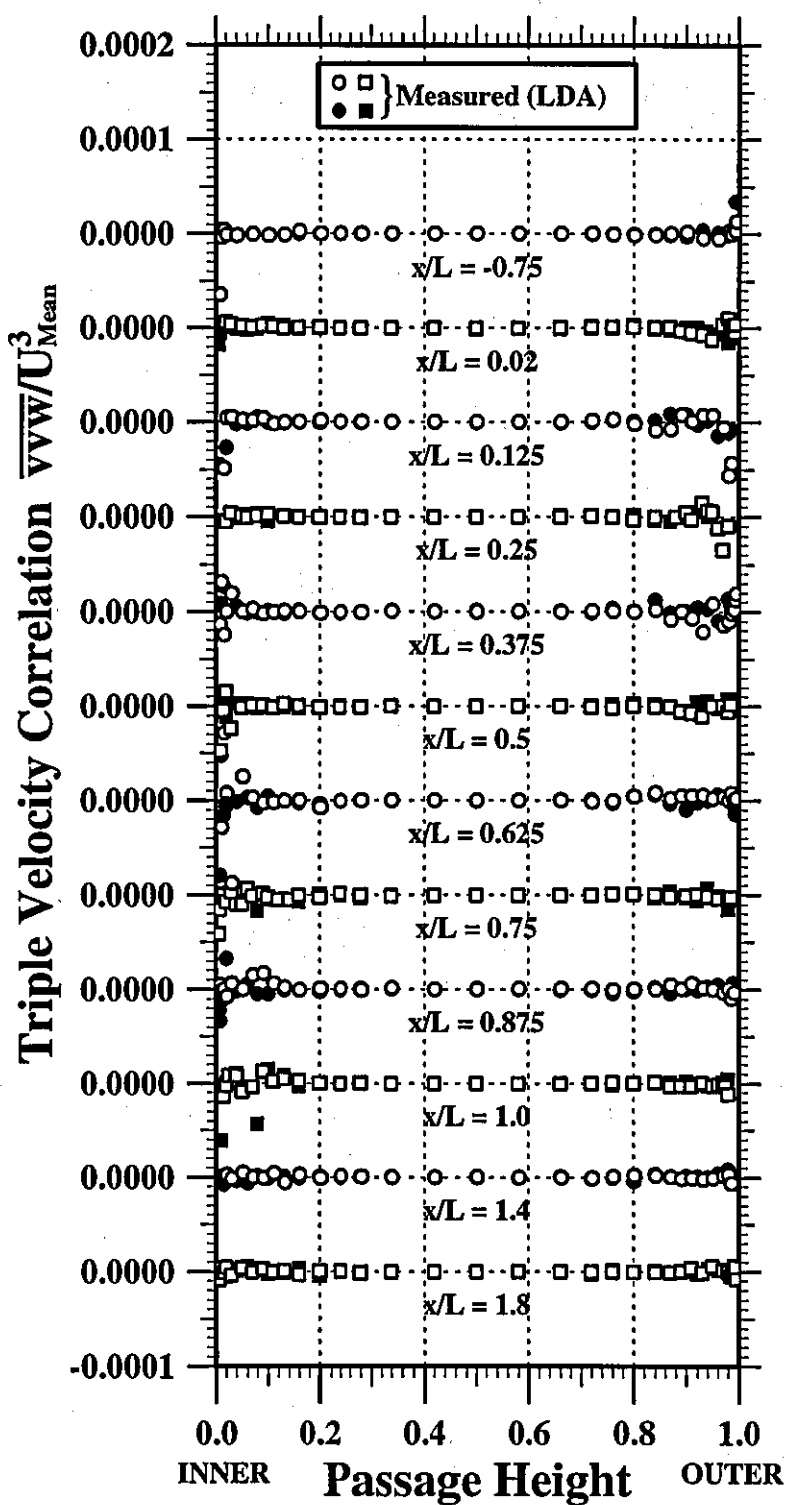


Figure 63

Variation of Triple Velocity Correlation ($\overline{vww}/U_{\text{Mean}}^3$)

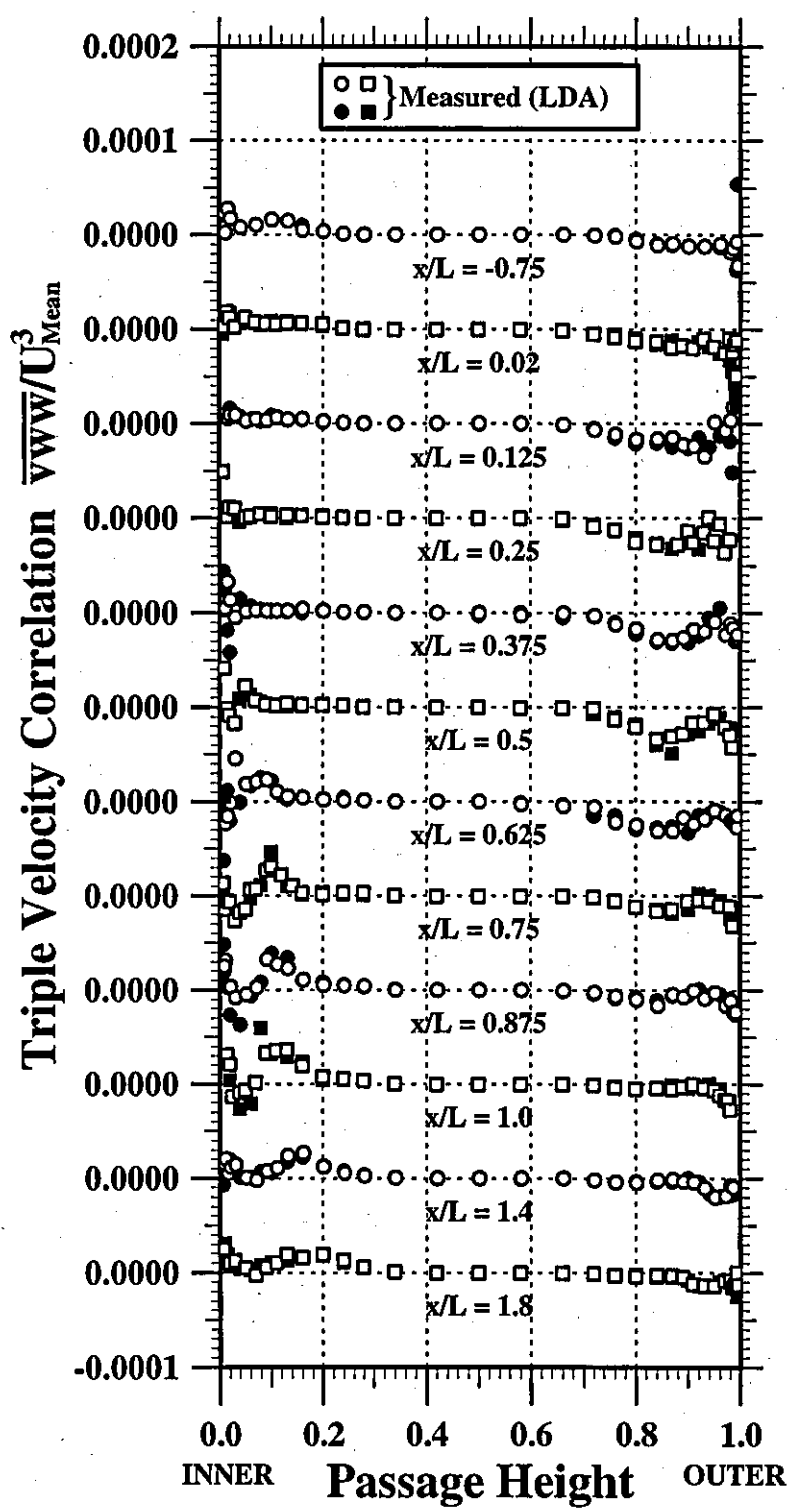


Figure 64

Variation of Triple Velocity Correlation ($\overline{www}/U_{\text{Mean}}^3$)

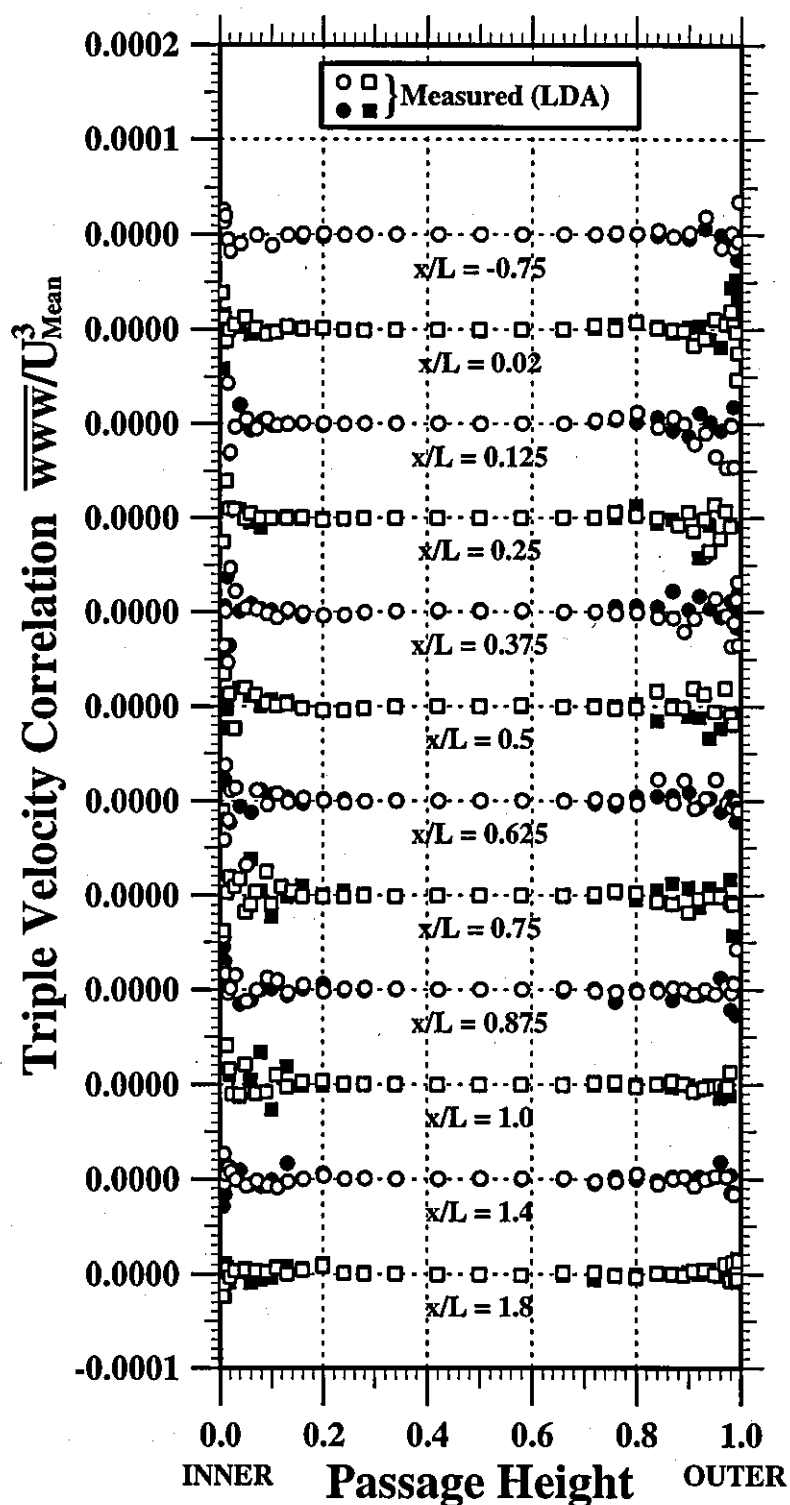


Figure 65

Variation of Triple Velocity Correlation ($\bar{q}\bar{q}\bar{u}$)

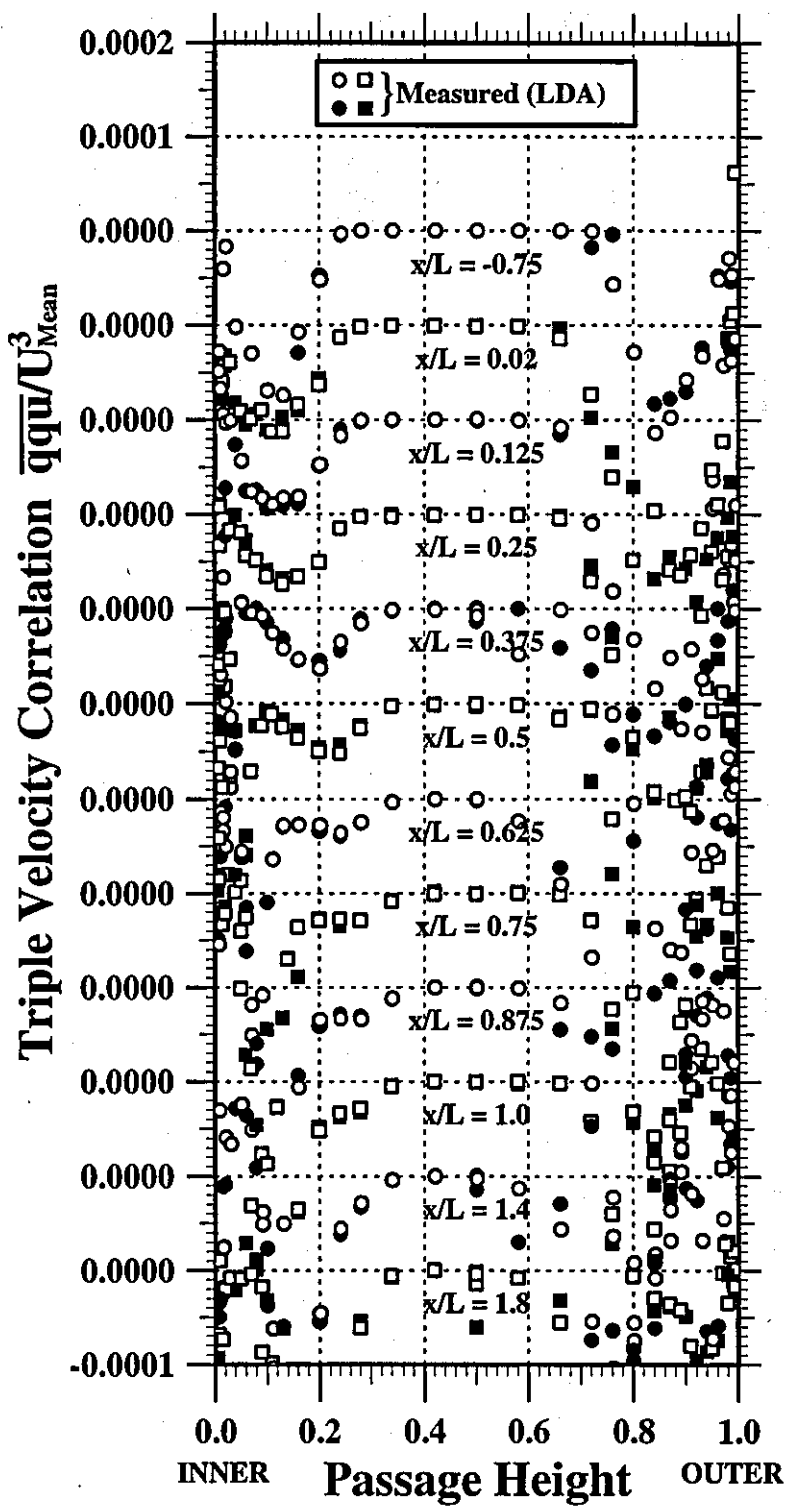
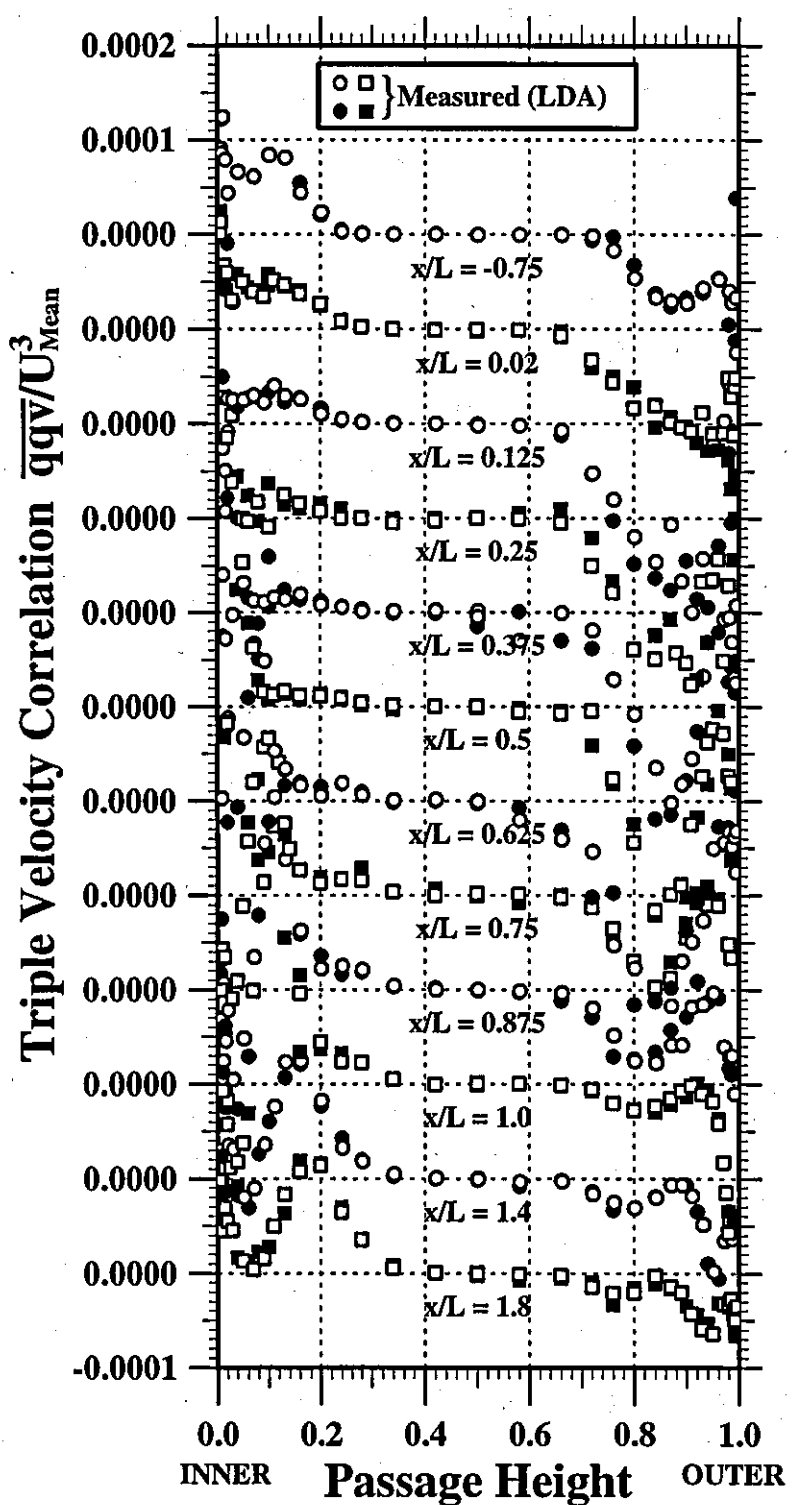


Figure 66

Variation of Triple Velocity Correlation (\overline{qqv})



Turbulent Kinetic Energy Transport Velocity (V_q)

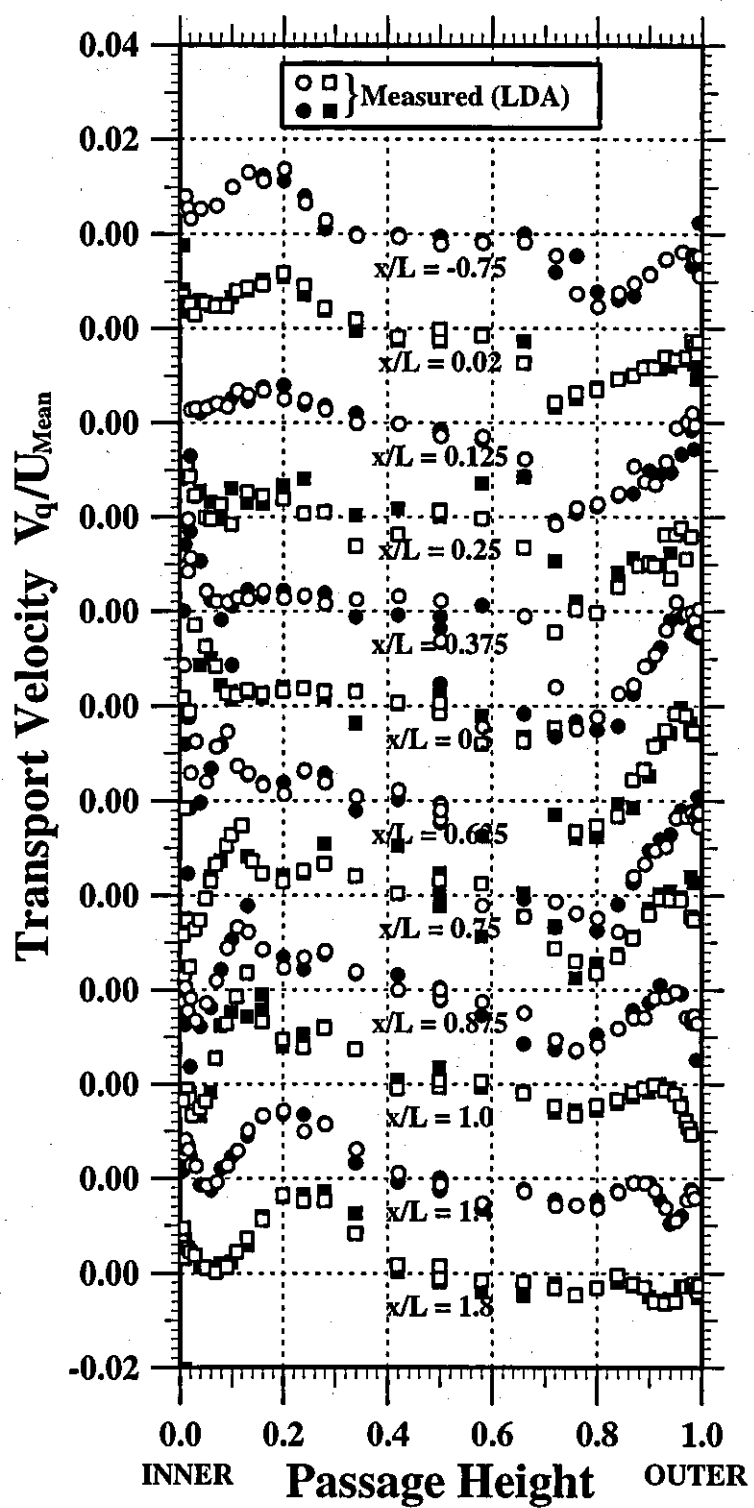


Figure 68

Variation of U-skewness

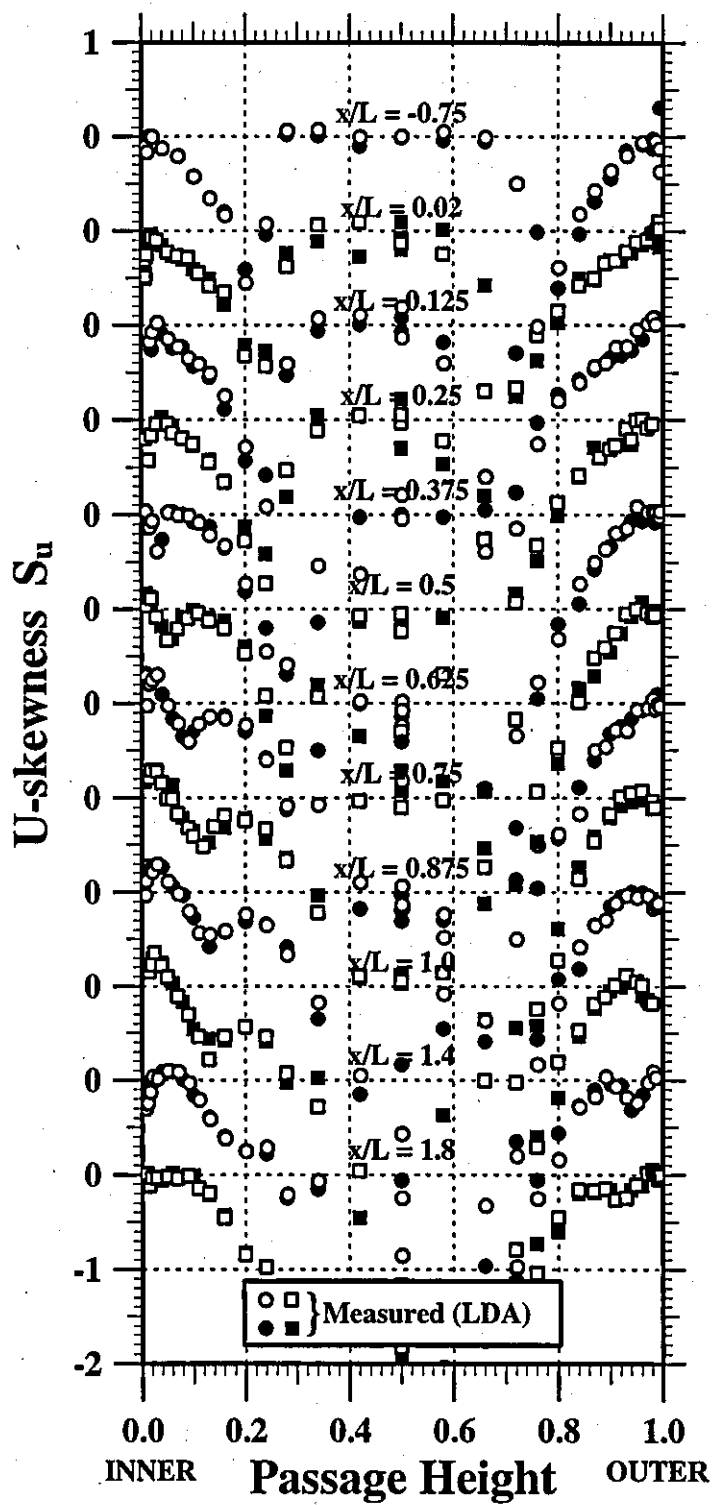


Figure 69

Variation of V-skewness

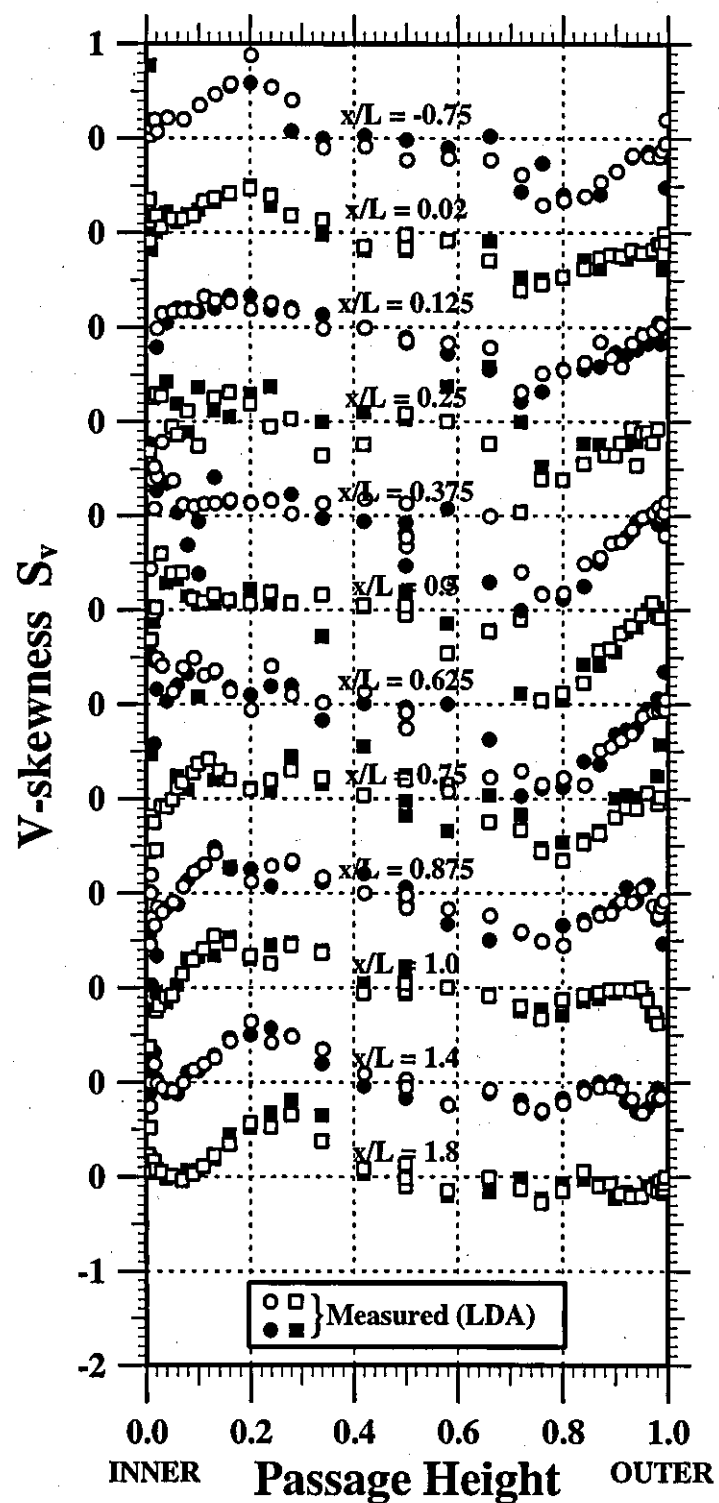


Figure 70

Variation of W-skewness

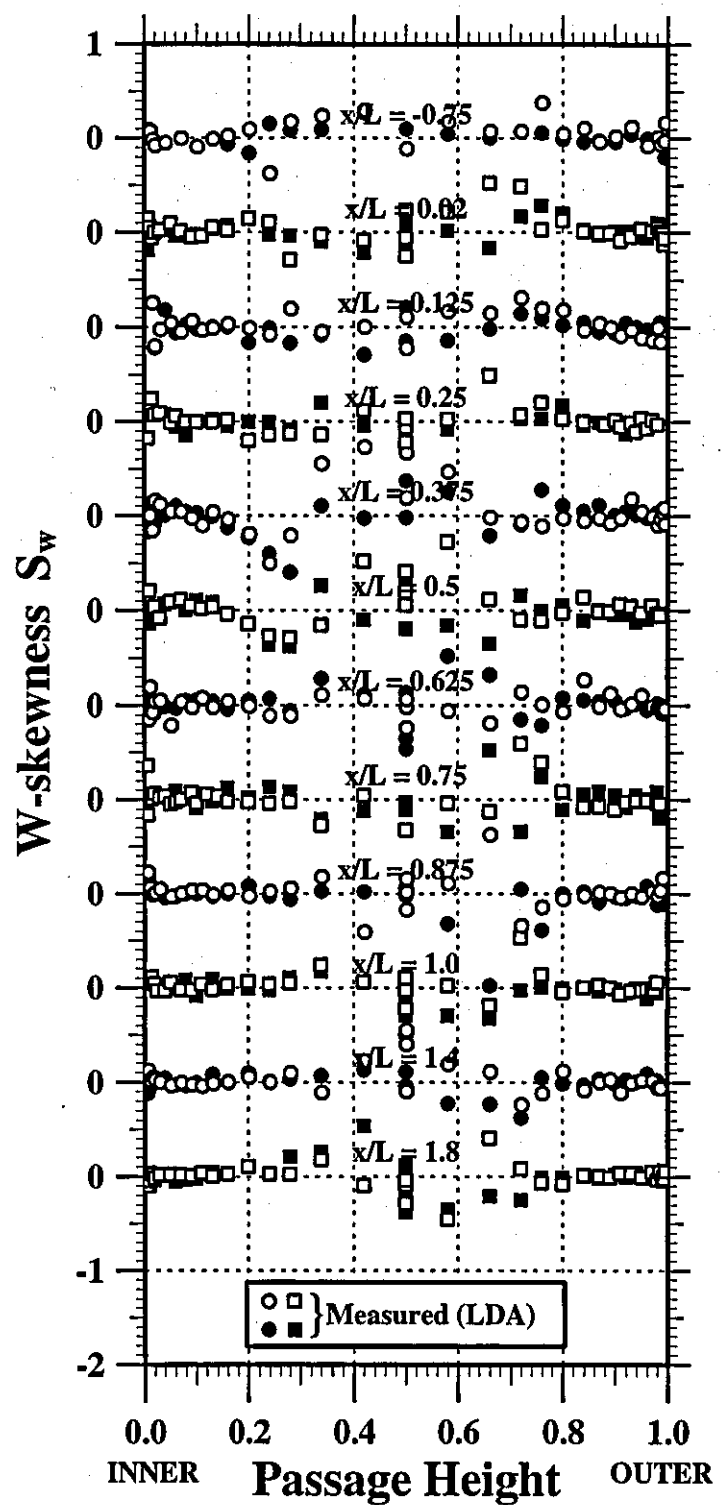


Figure 71

Variation of U-intermittency

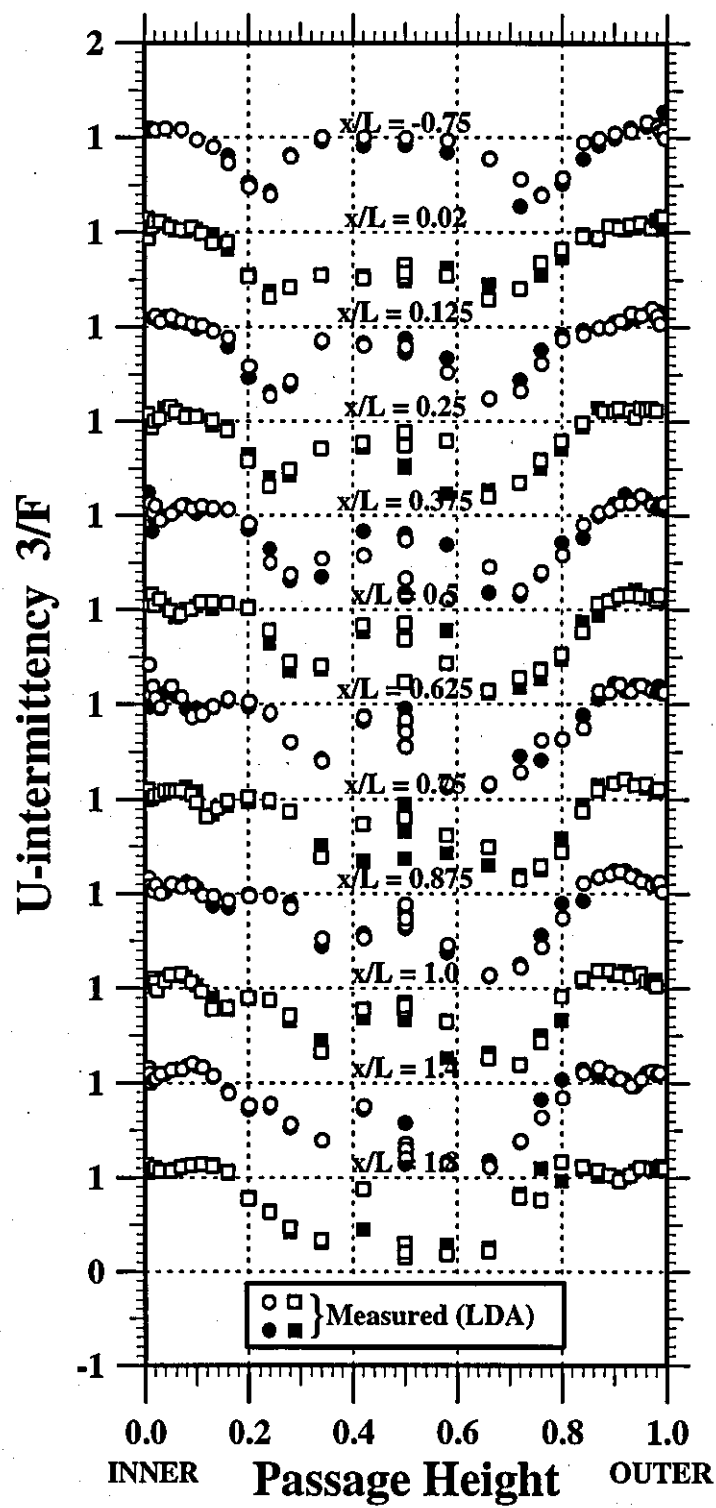


Figure 72

Variation of V-intermittency

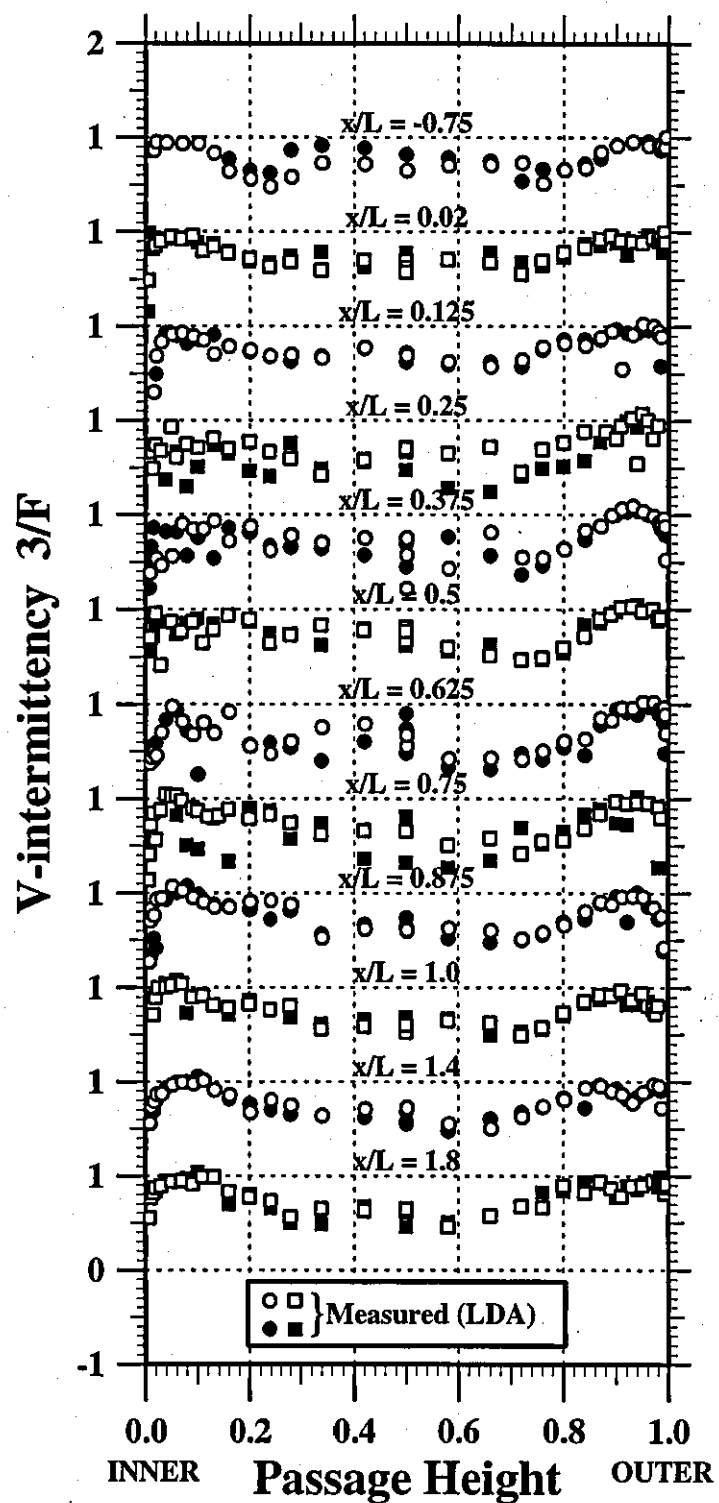


Figure 73

Variation of W-intermittency

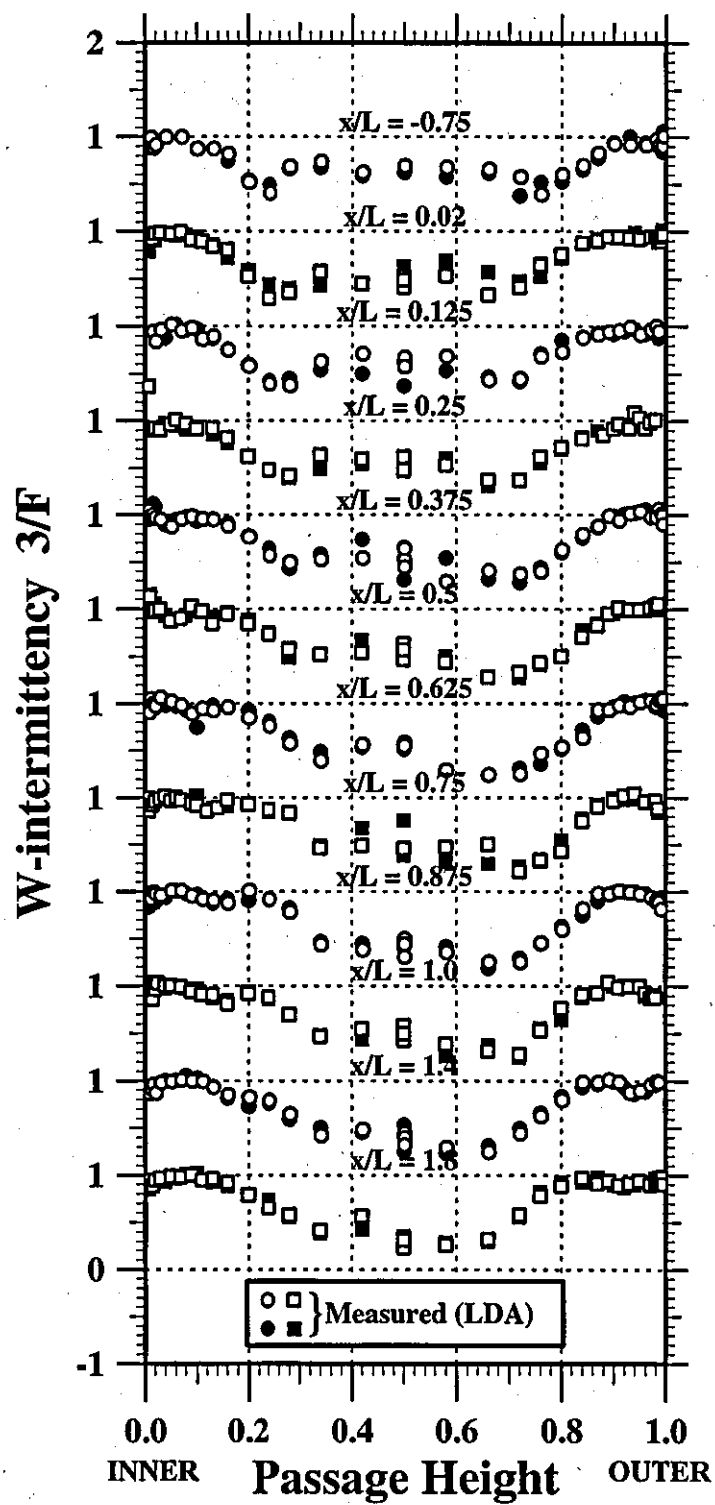


Figure 74

Measured Inner Wall Streamwise Velocity Log-law Co-ordinates

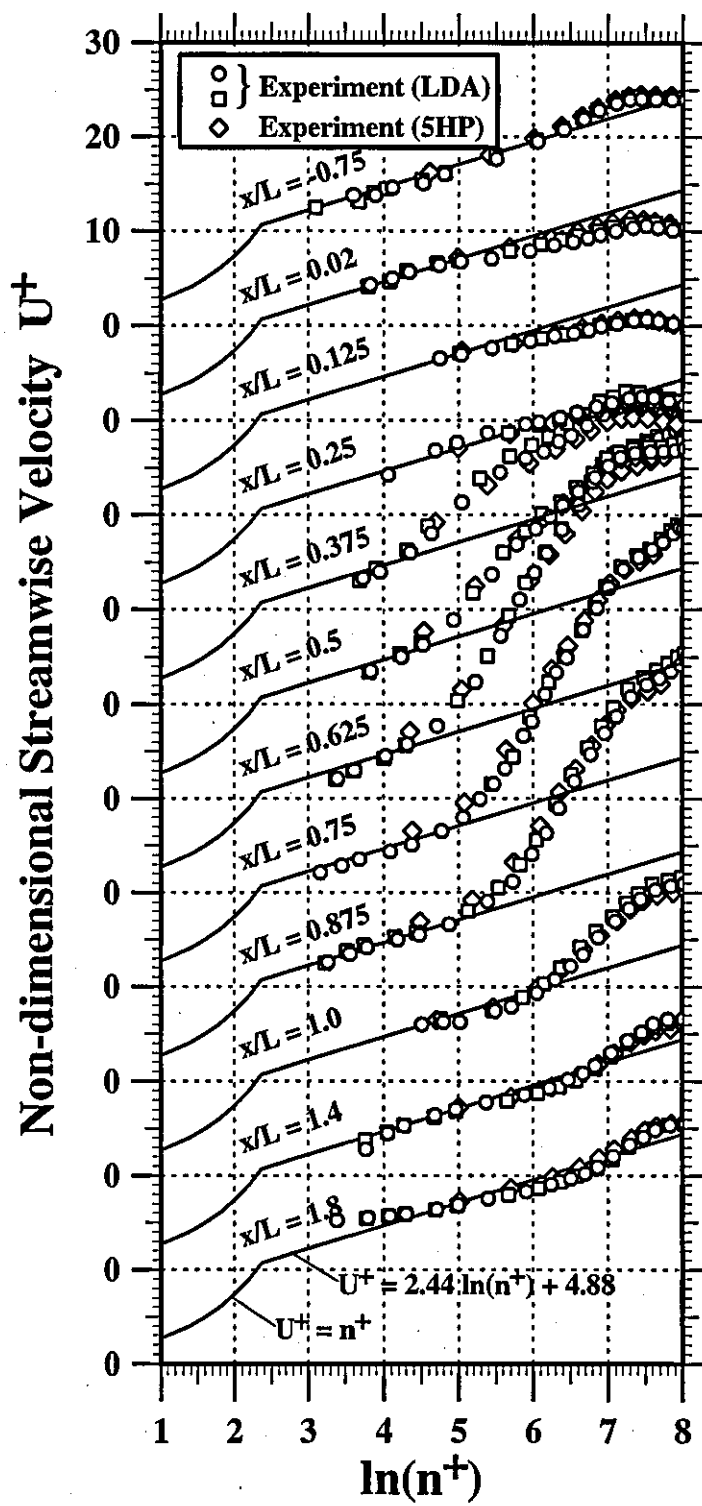


Figure 75

Measured Outer Wall Streamwise Velocity Log-law Co-ordinates

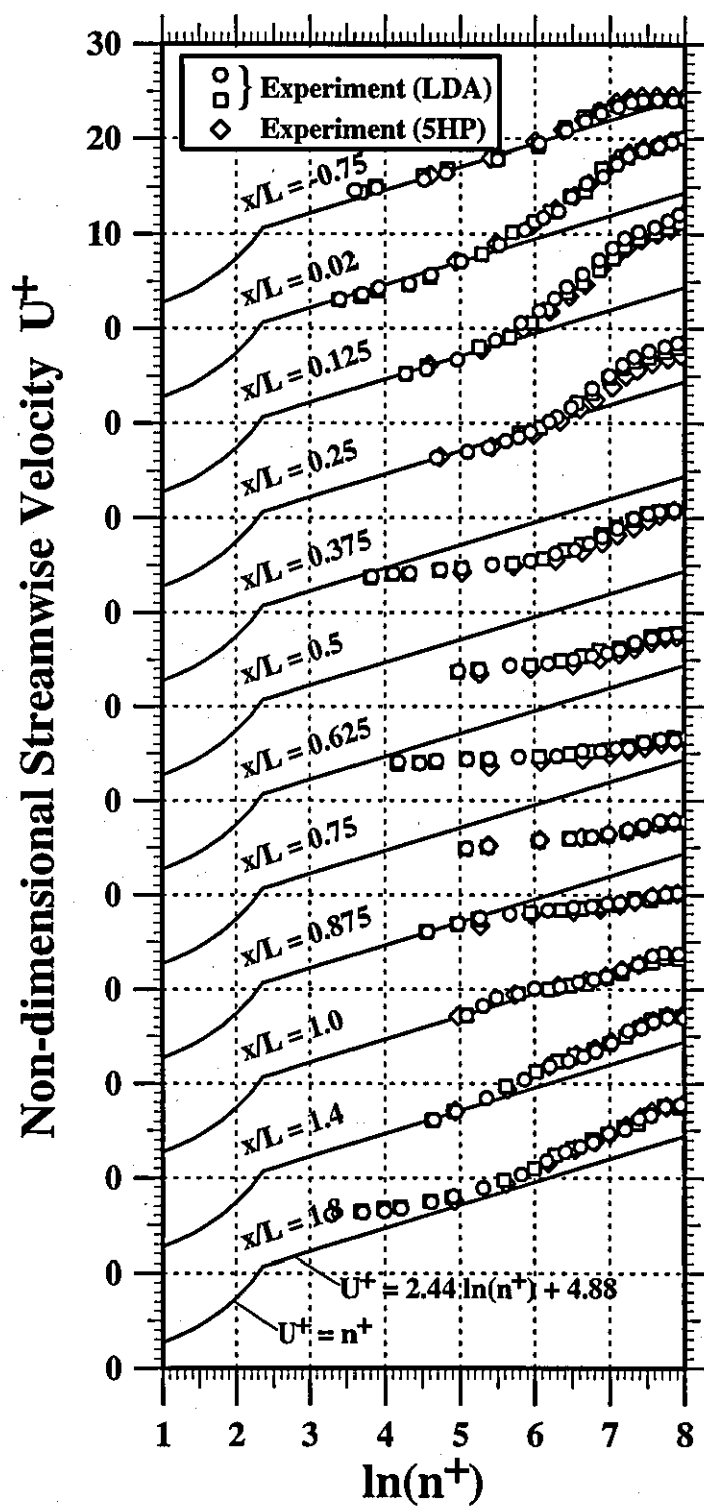
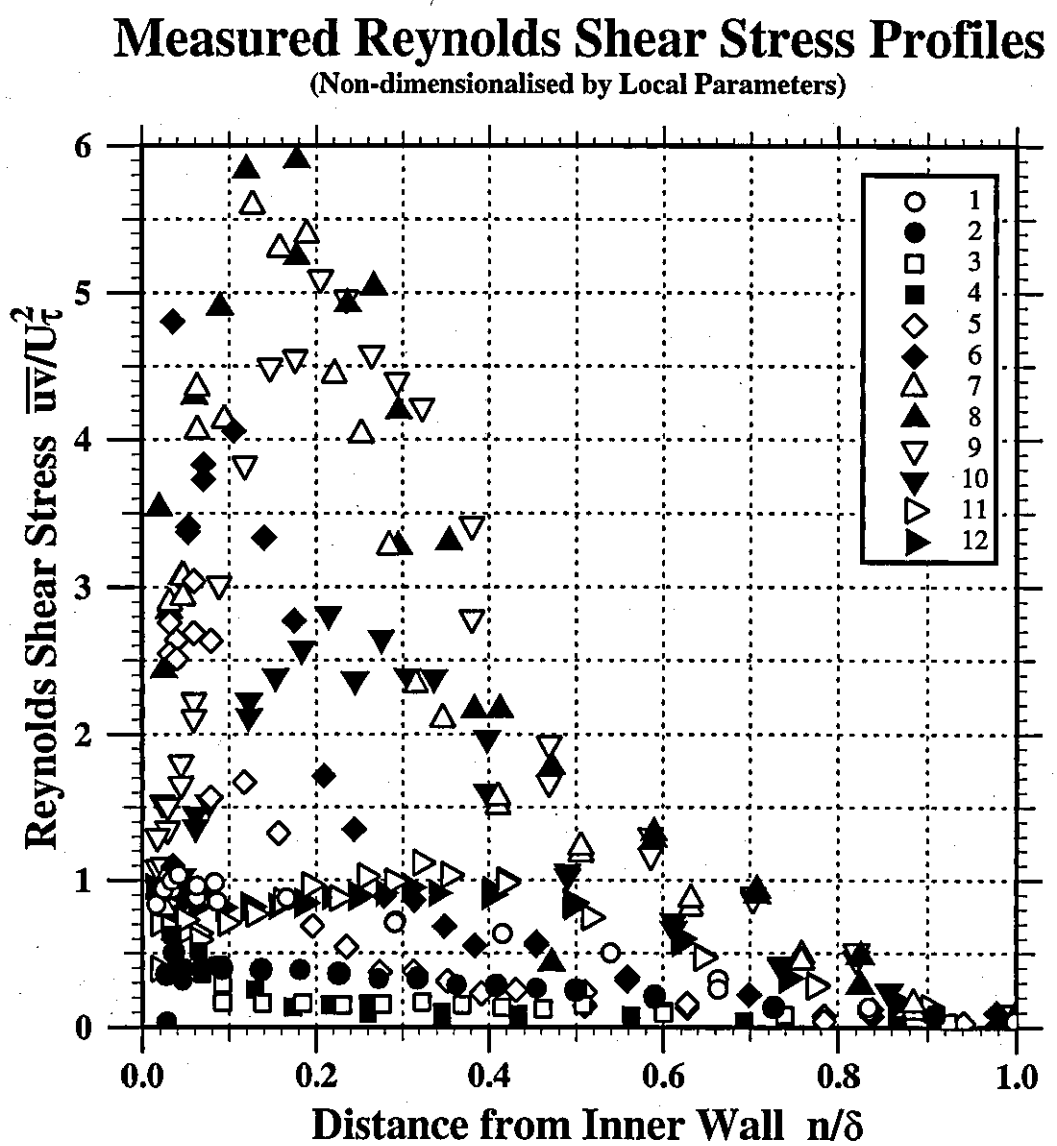
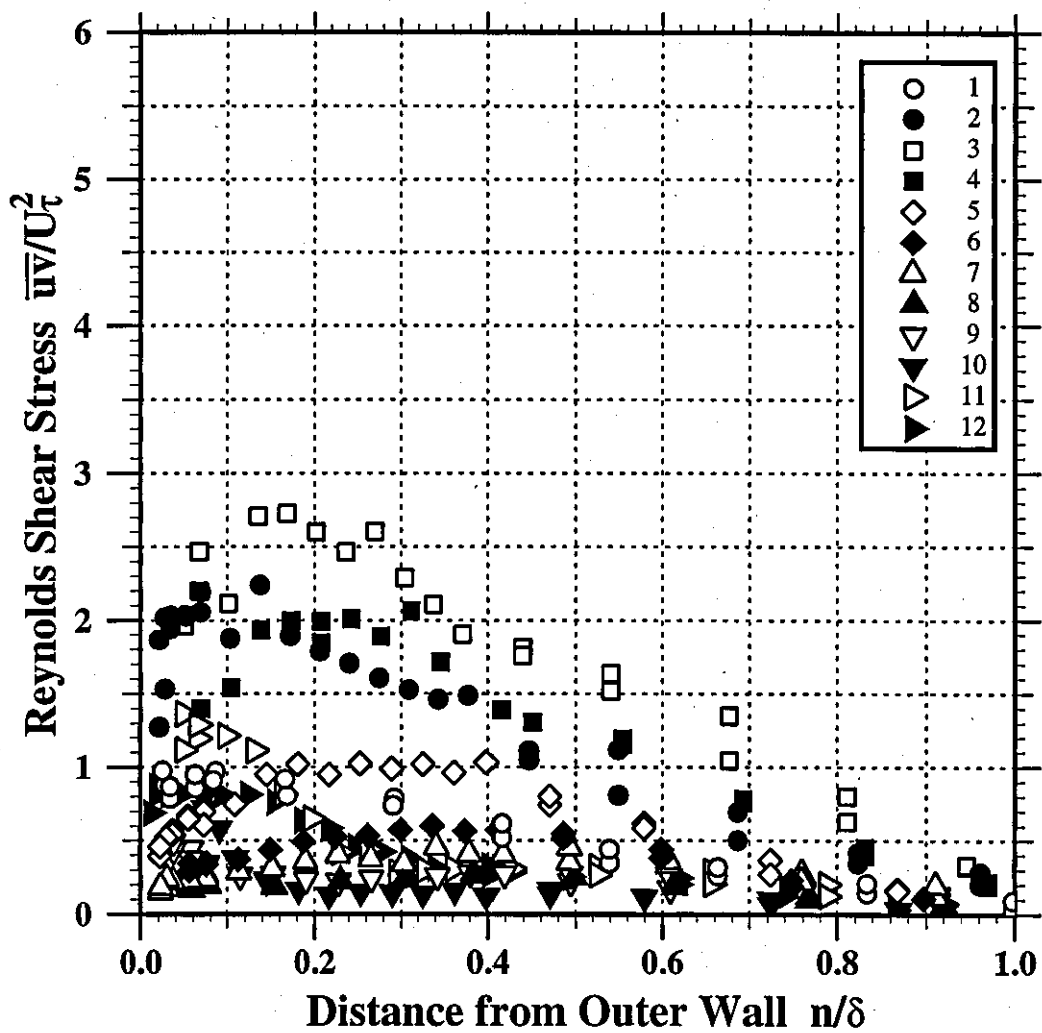


Figure 76



Measured Reynolds Shear Stress Profiles

(Non-dimensionalised by Local Parameters)



Mean Strain Rate Distribution

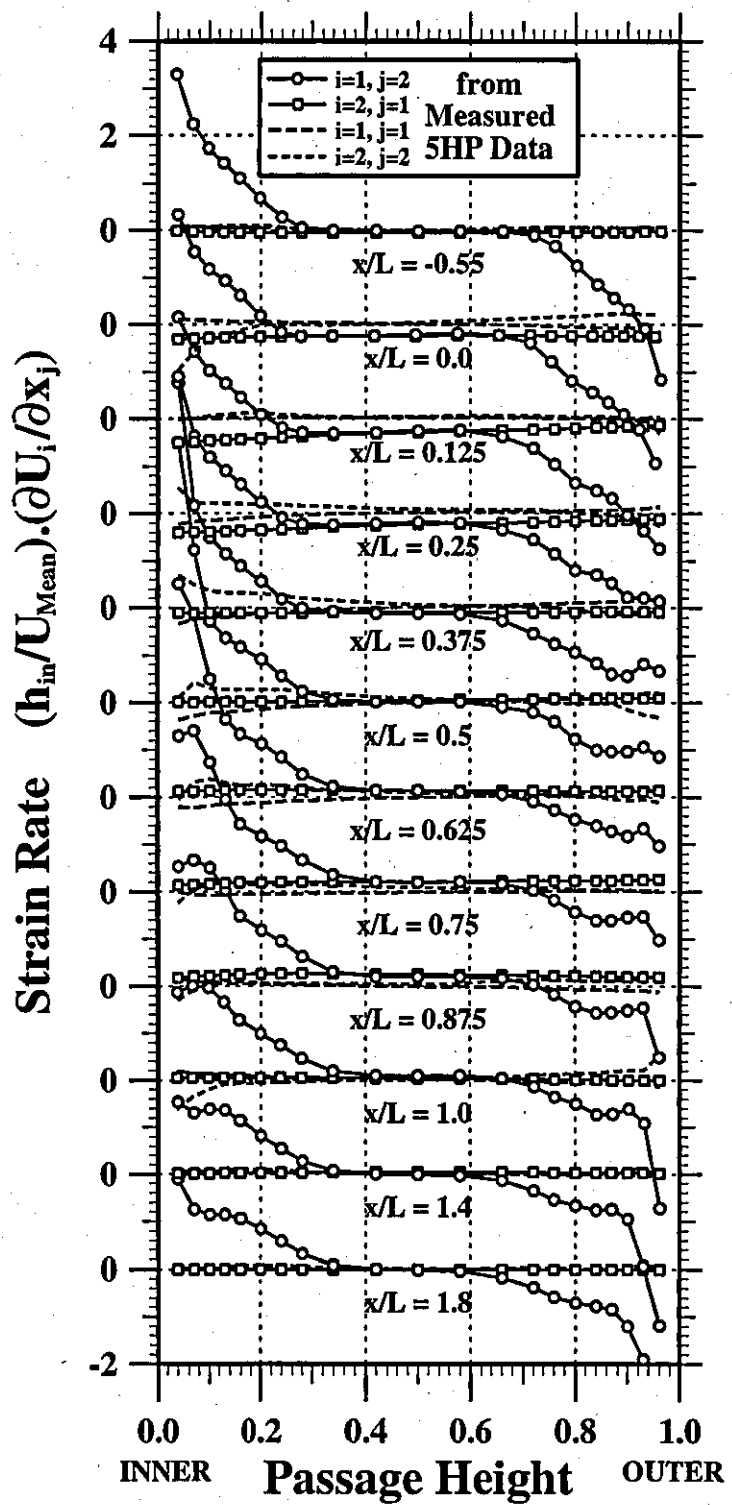


Figure 79

Strain Rate and Vorticity Distribution

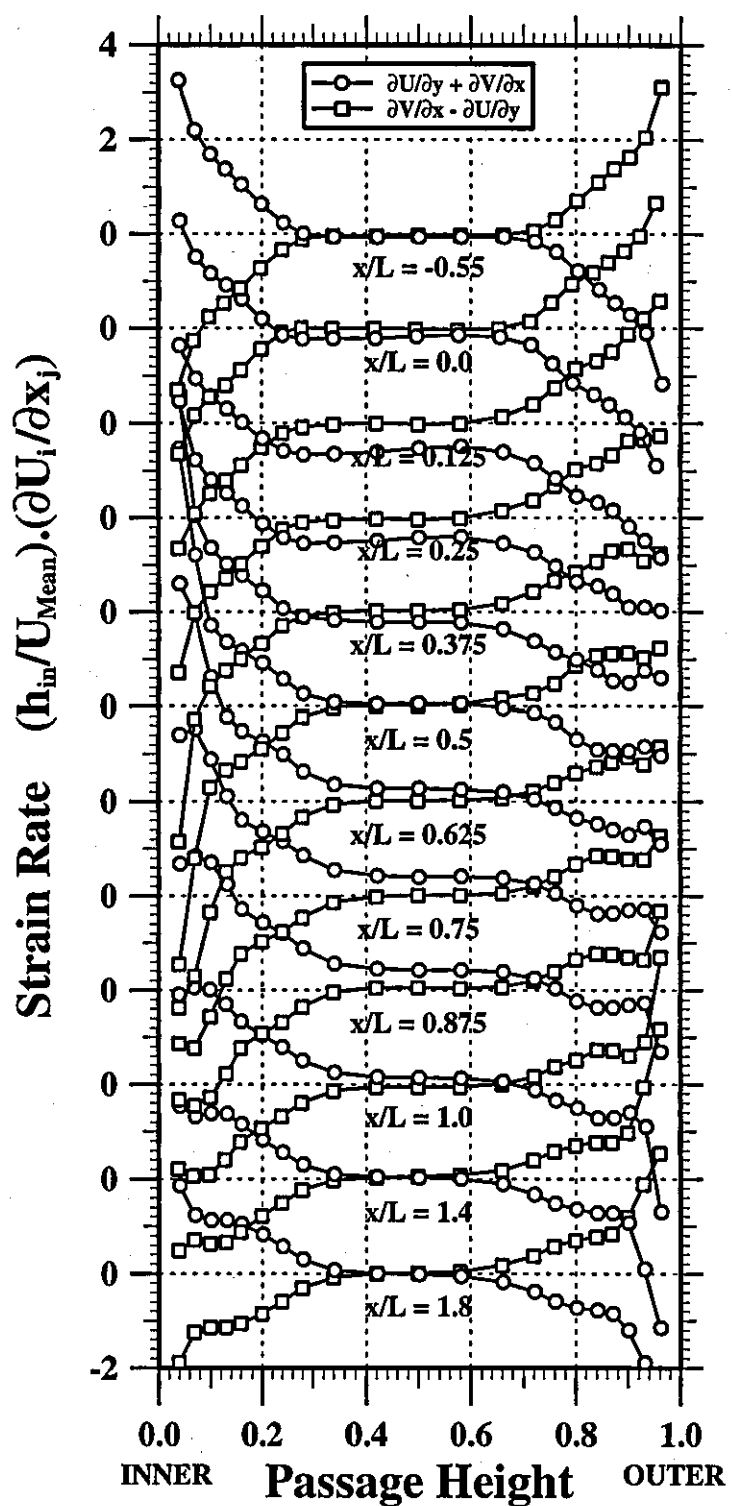
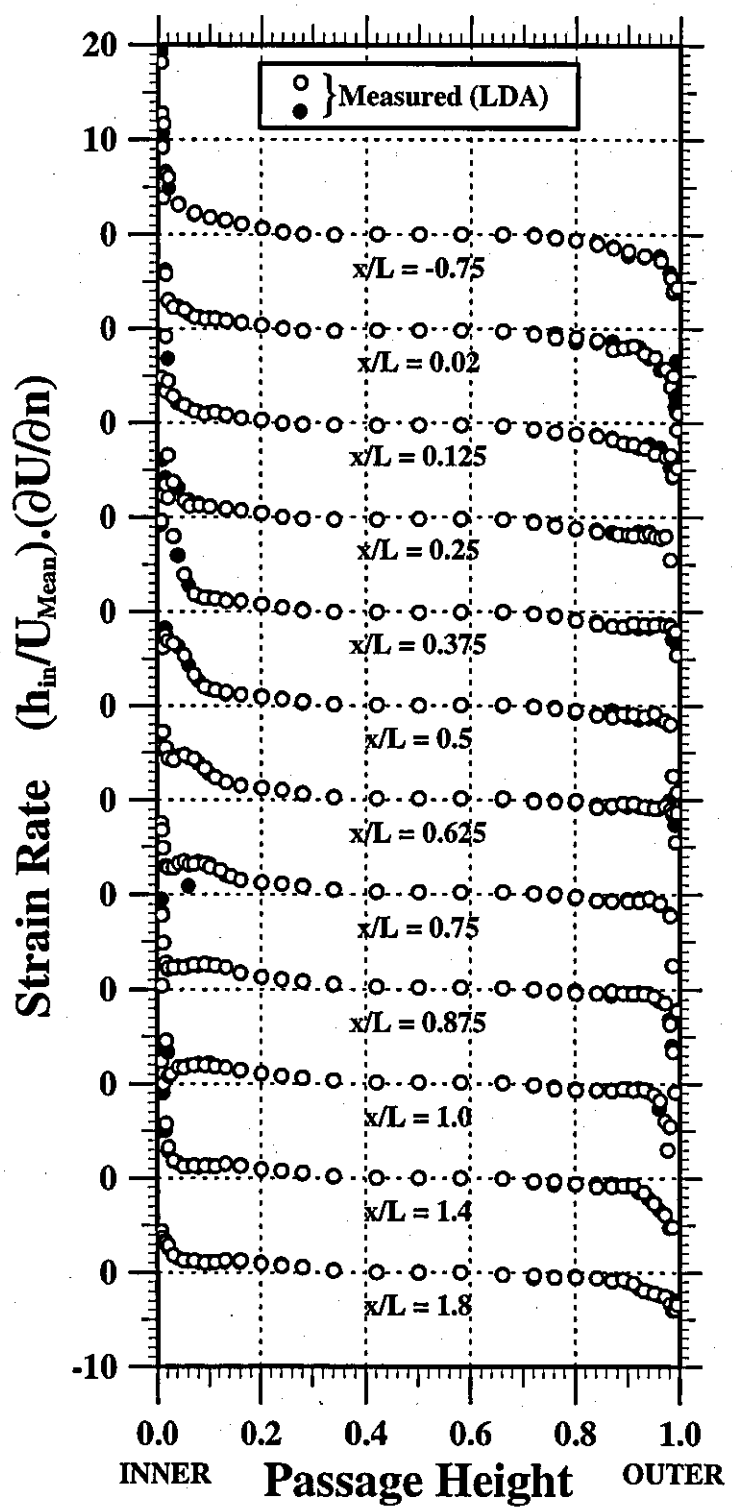


Figure 80

Cross-stream Gradient of Streamwise Velocity



Measured Reynolds Shear Stress Profiles with 'Best Fit' Interpretation and Wall Values

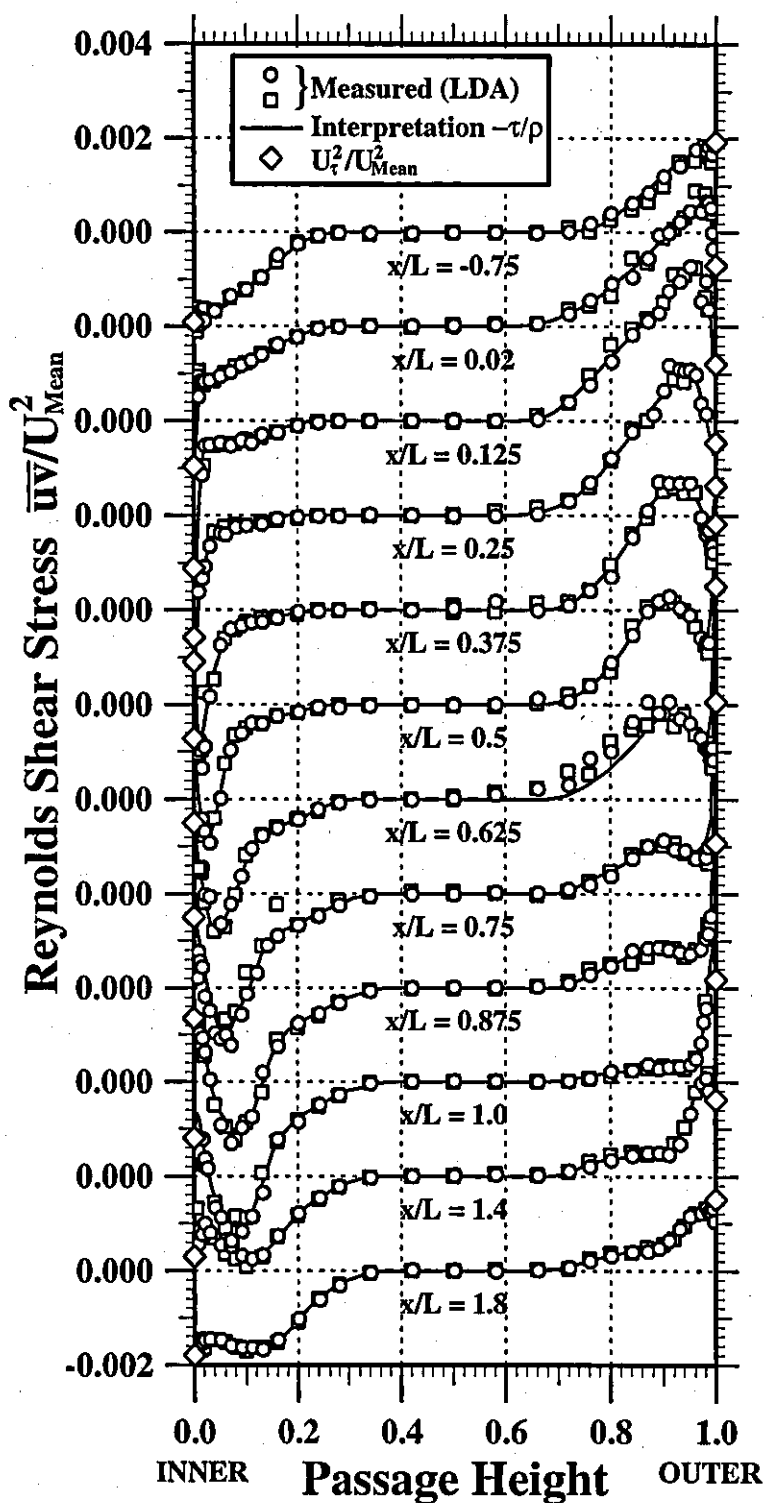


Figure 82

Total Shear Stress Distribution

'Best Fit' Interpretation of Measured Reynolds Shear Stress Profiles

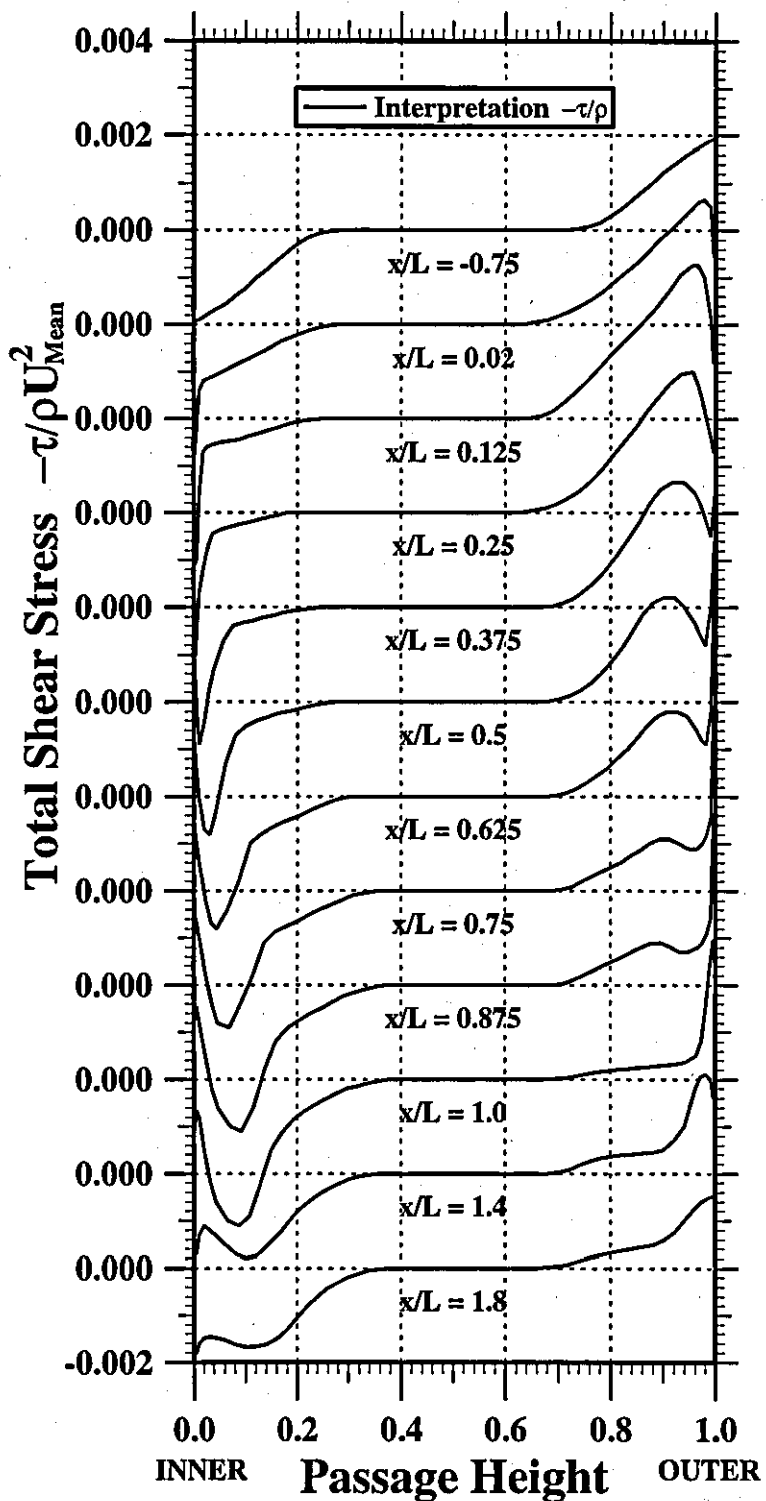


Figure 83

Total Shear Stress Distribution

'Best Fit' Interpretation of Measured Reynolds Shear Stress Profiles

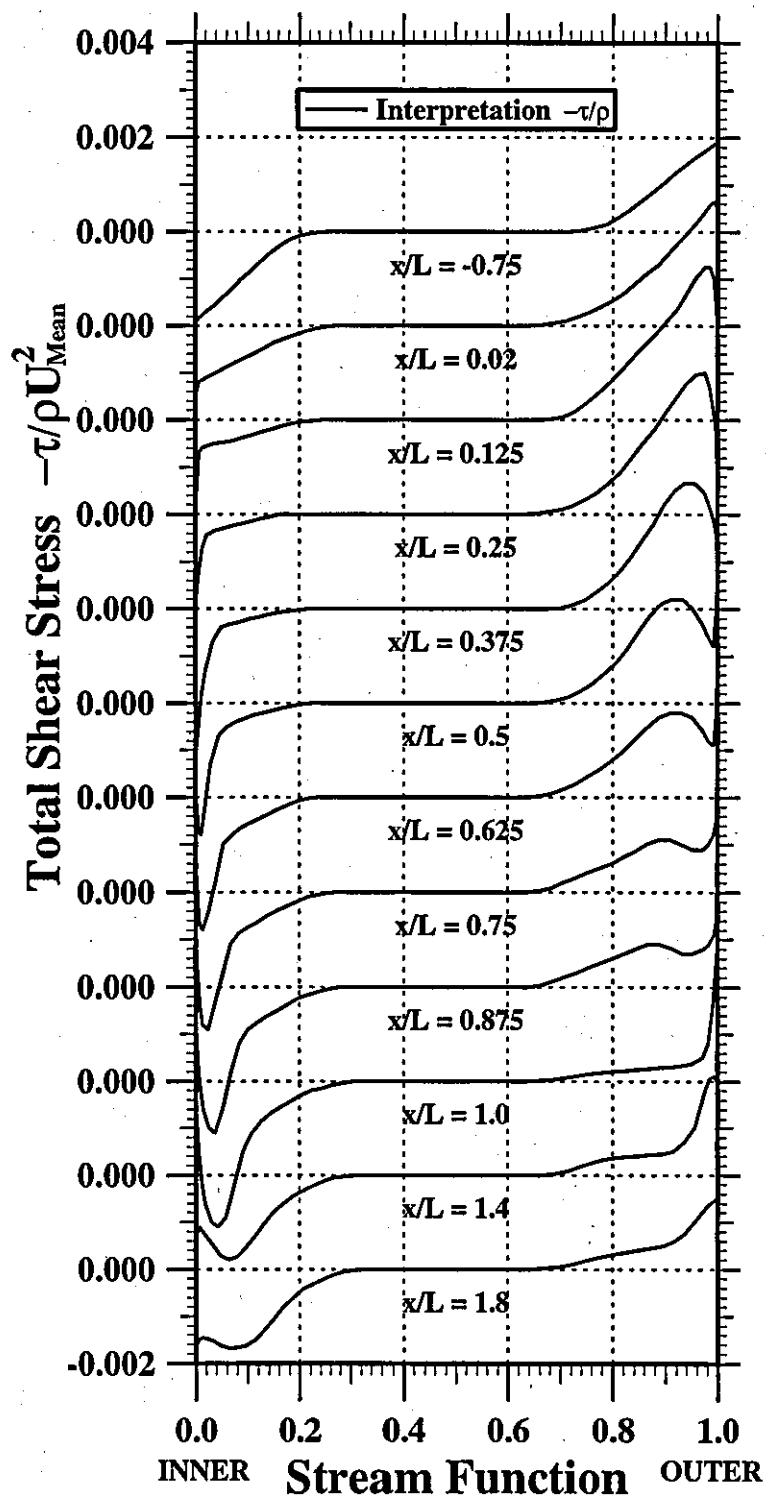


Figure 84

Variation of Shear Stress Gradient $(\partial \bar{u}v / \partial n)$

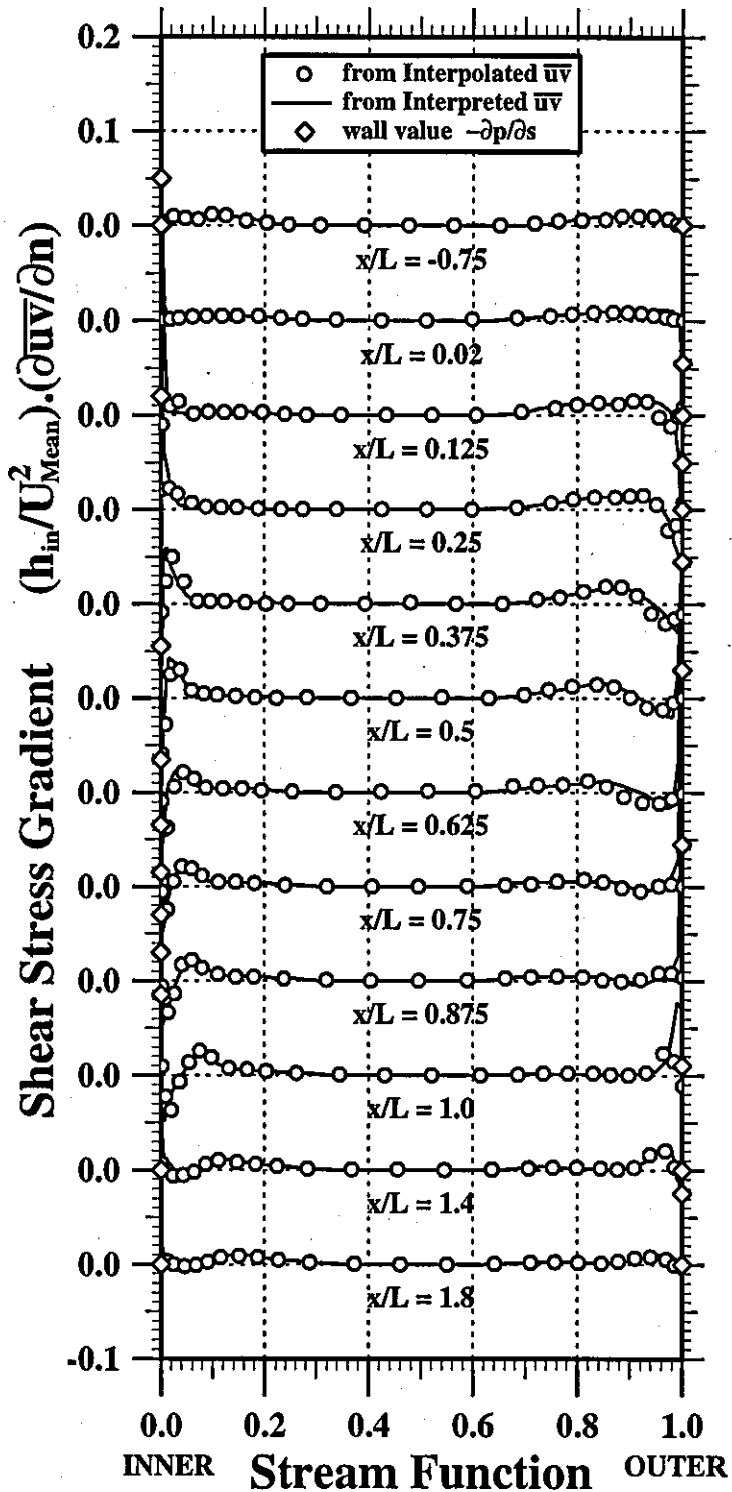
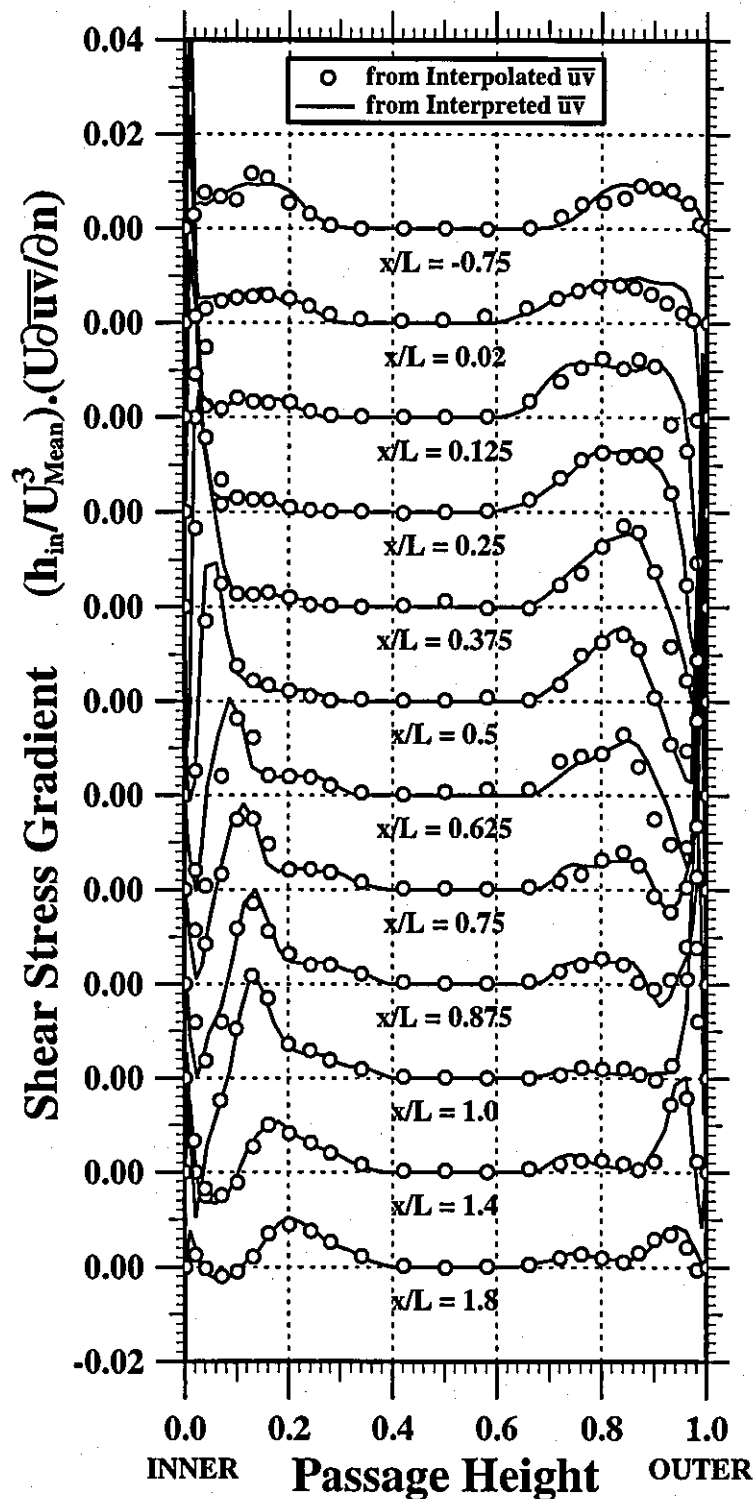


Figure 85

Variation of Shear Stress Gradient ($U\partial\bar{u}\bar{v}/\partial n$)



Regions of Positive and Negative Shear Stress Gradient

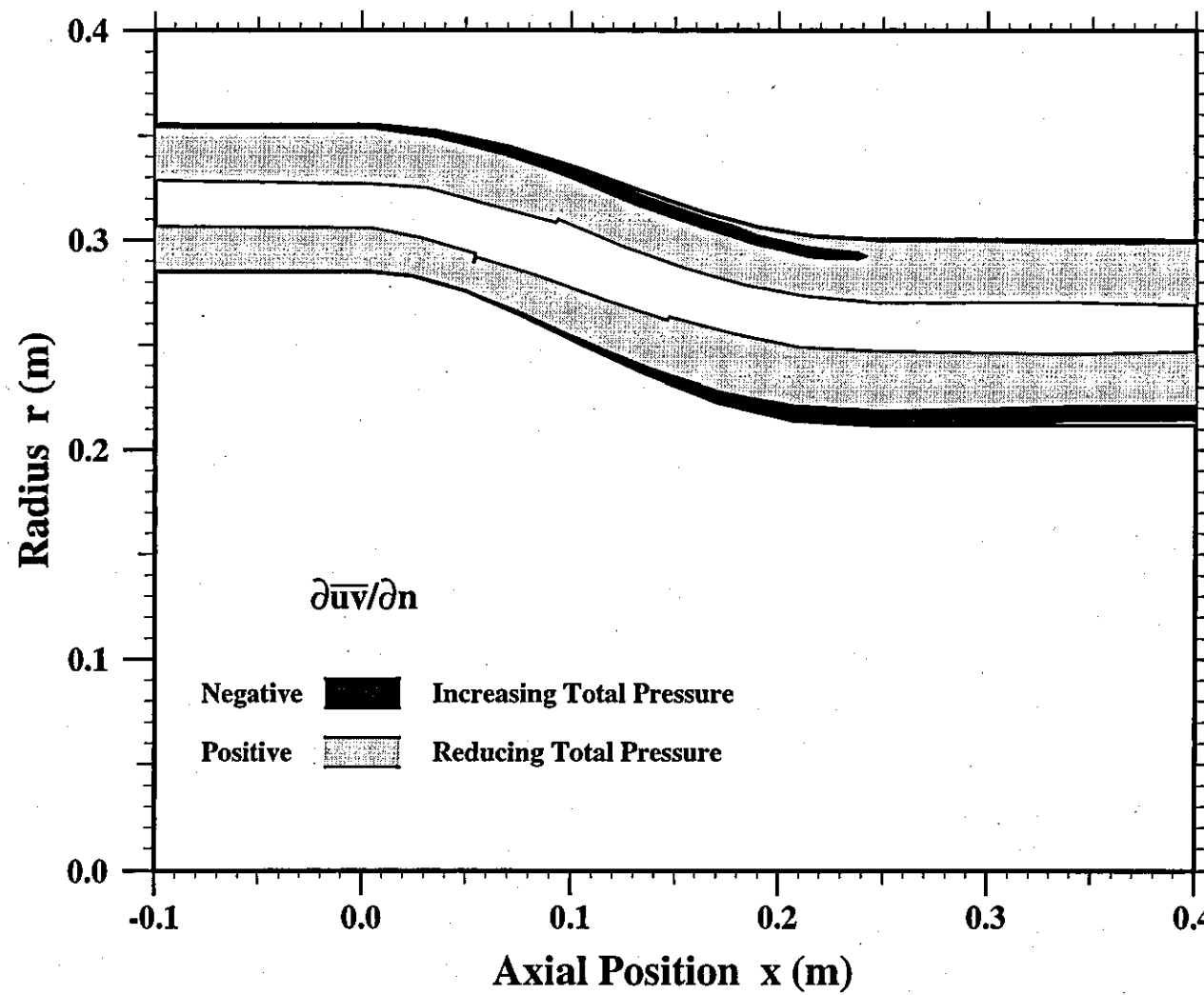


Figure 86

Figure 87

Comparison of Measured and Derived Total Pressure

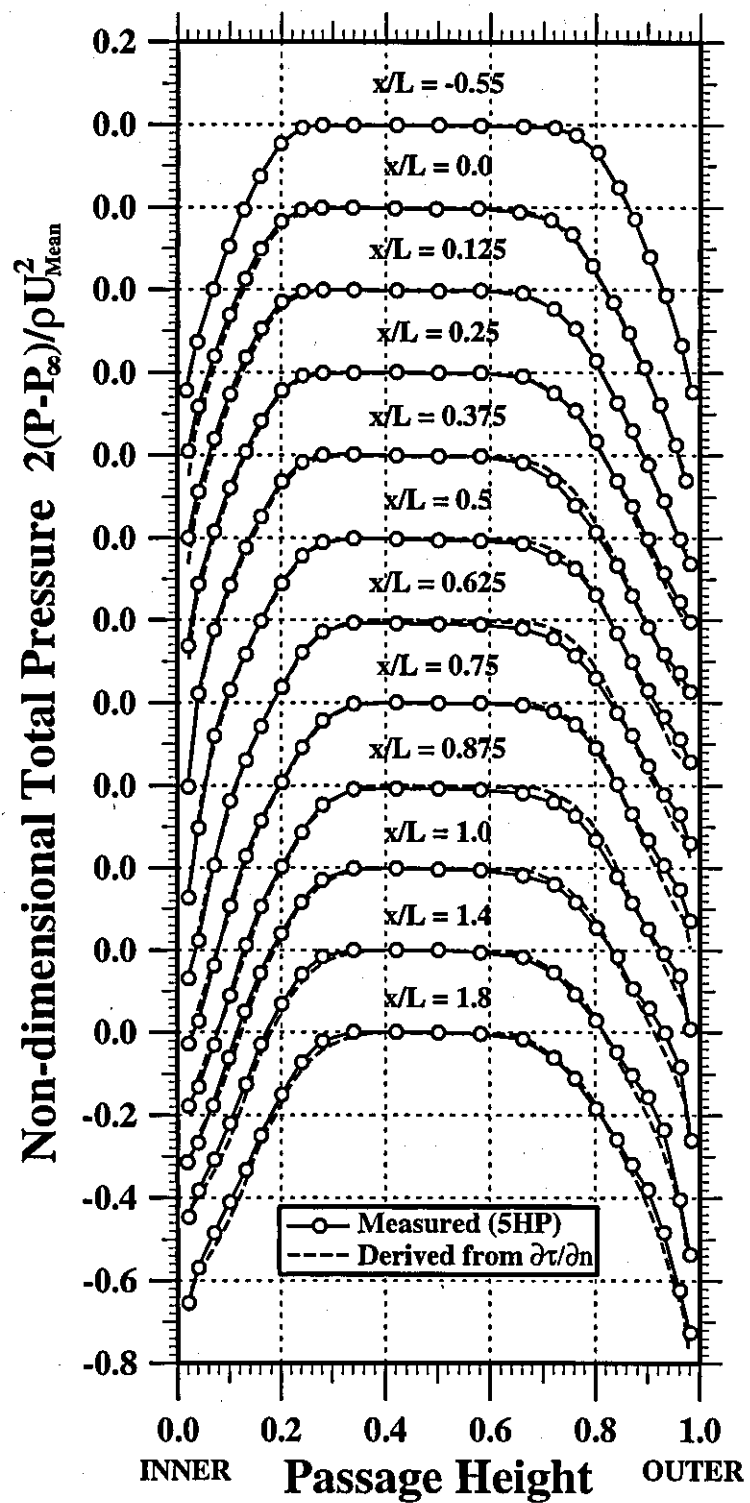


Figure 88

Axial Variation of Loss Coefficient Experiment (5HP) vs Shear Stress Derived Value (LDA)

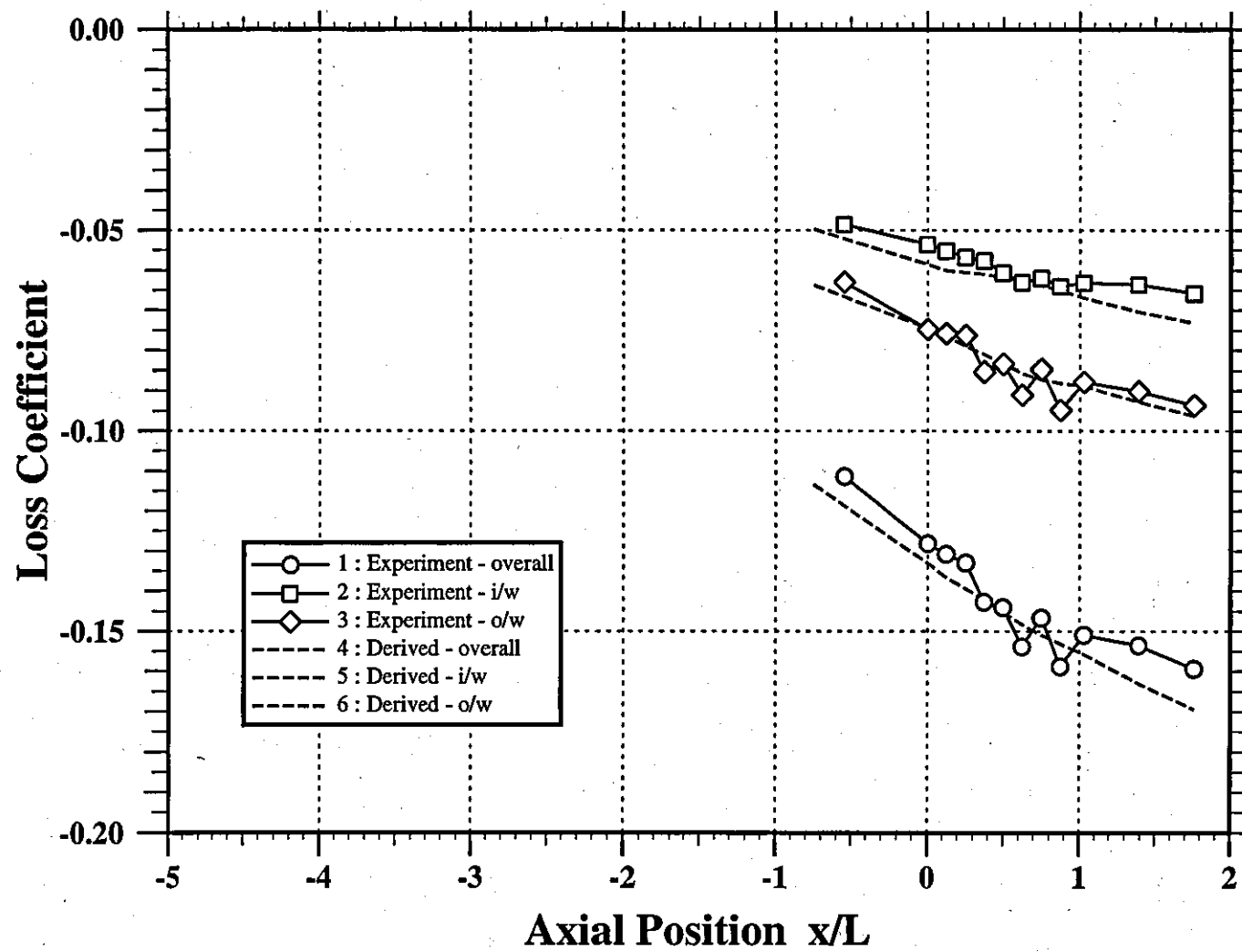


Figure 89

Variation of Turbulent Kinetic Energy Production

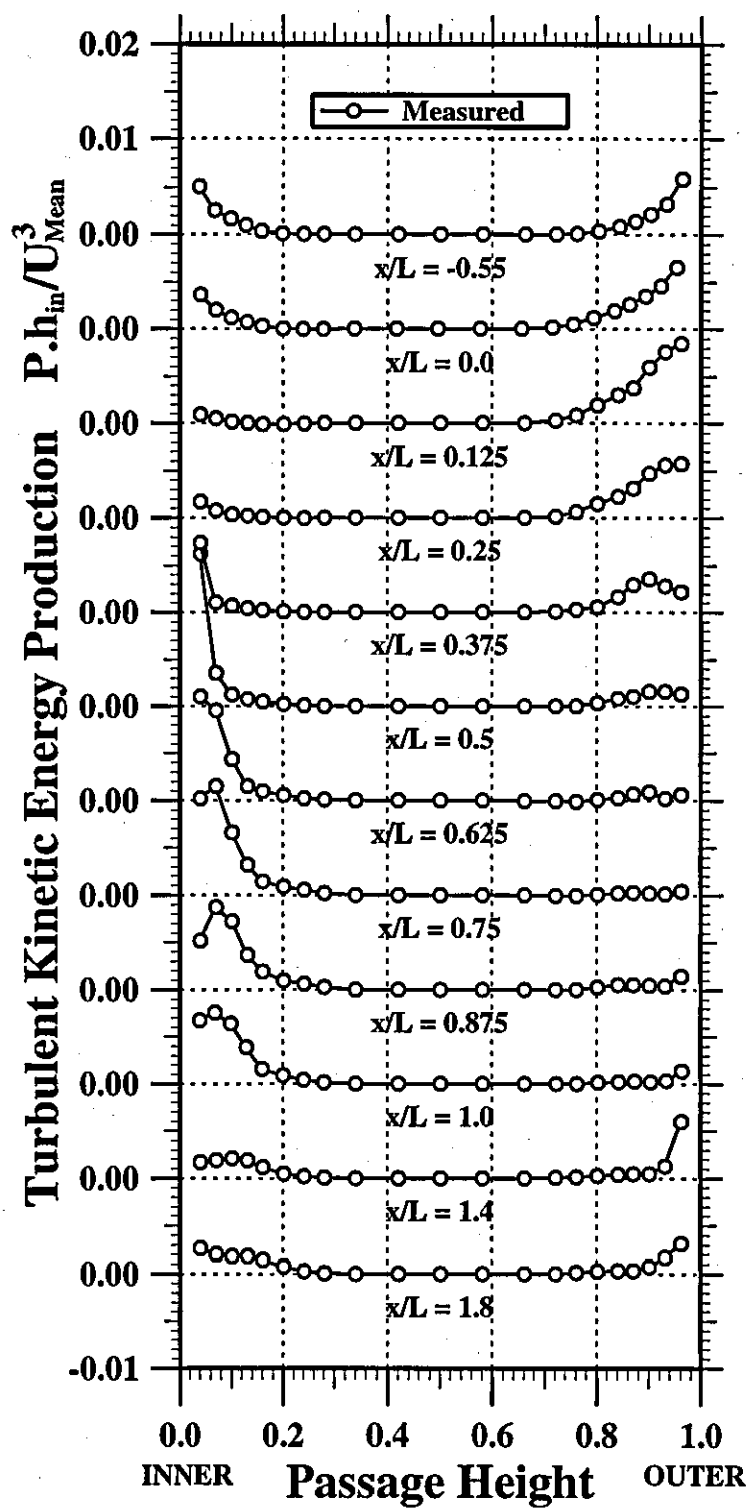


Figure 90

Mean Energy Redistribution and Loss

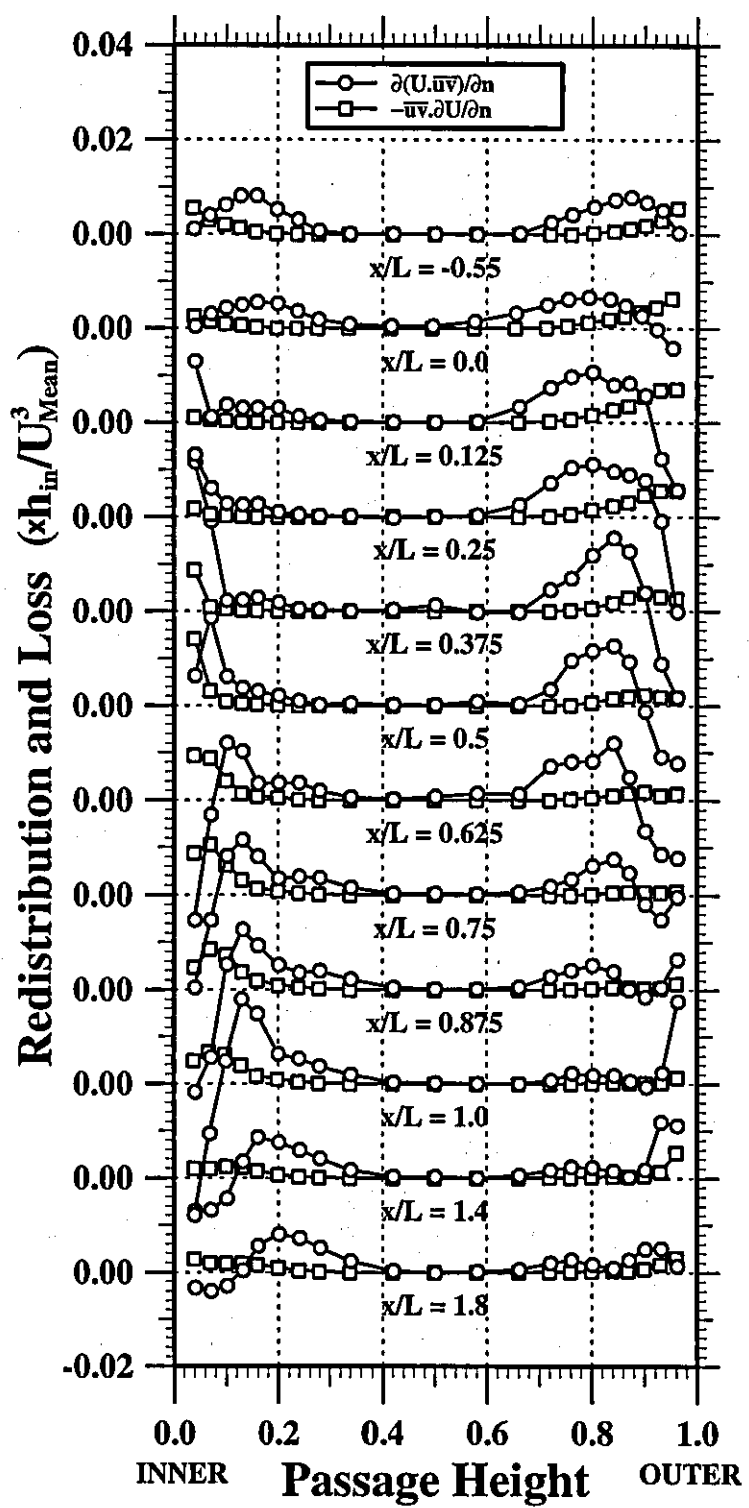


Figure 91

Variation of Streamwise Pressure Gradient (and Shear Stress Gradient)

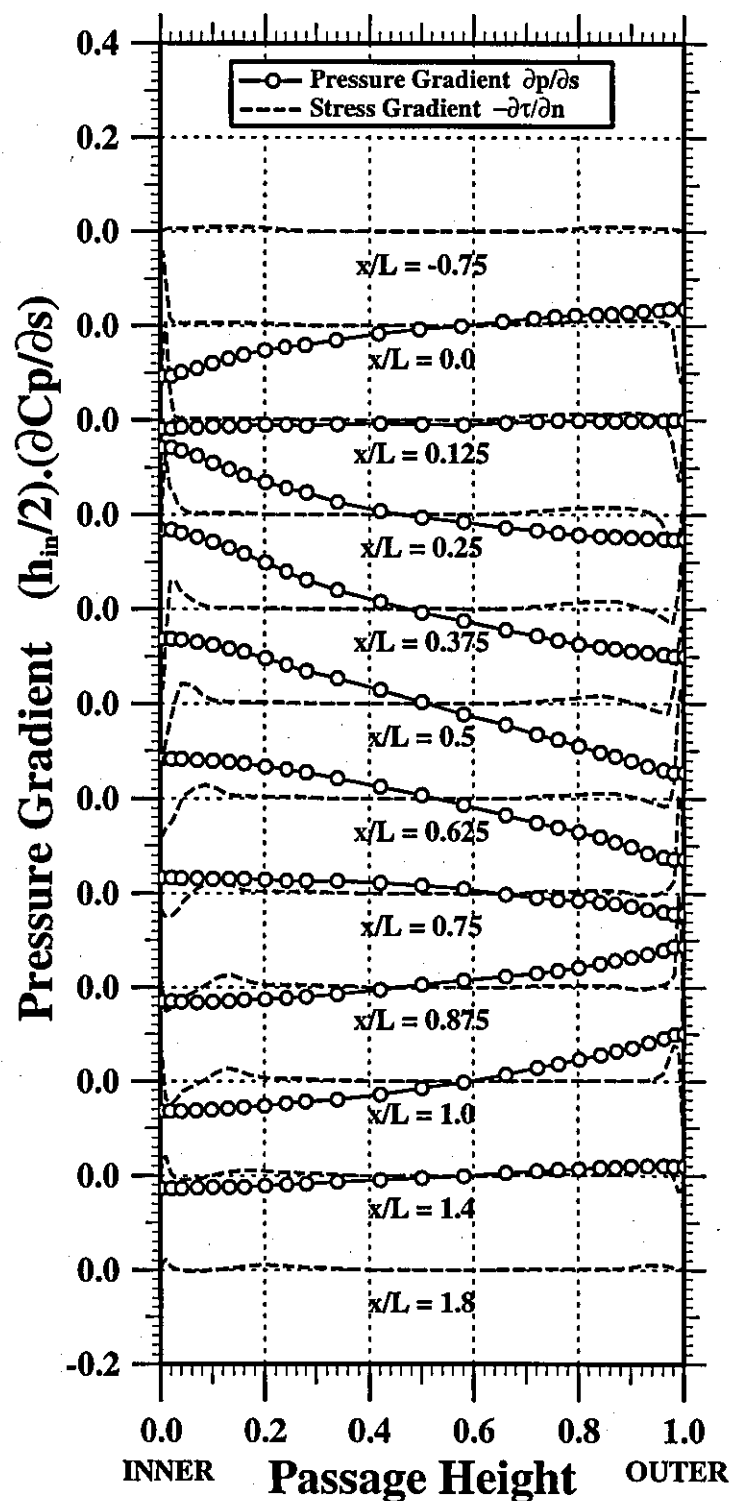
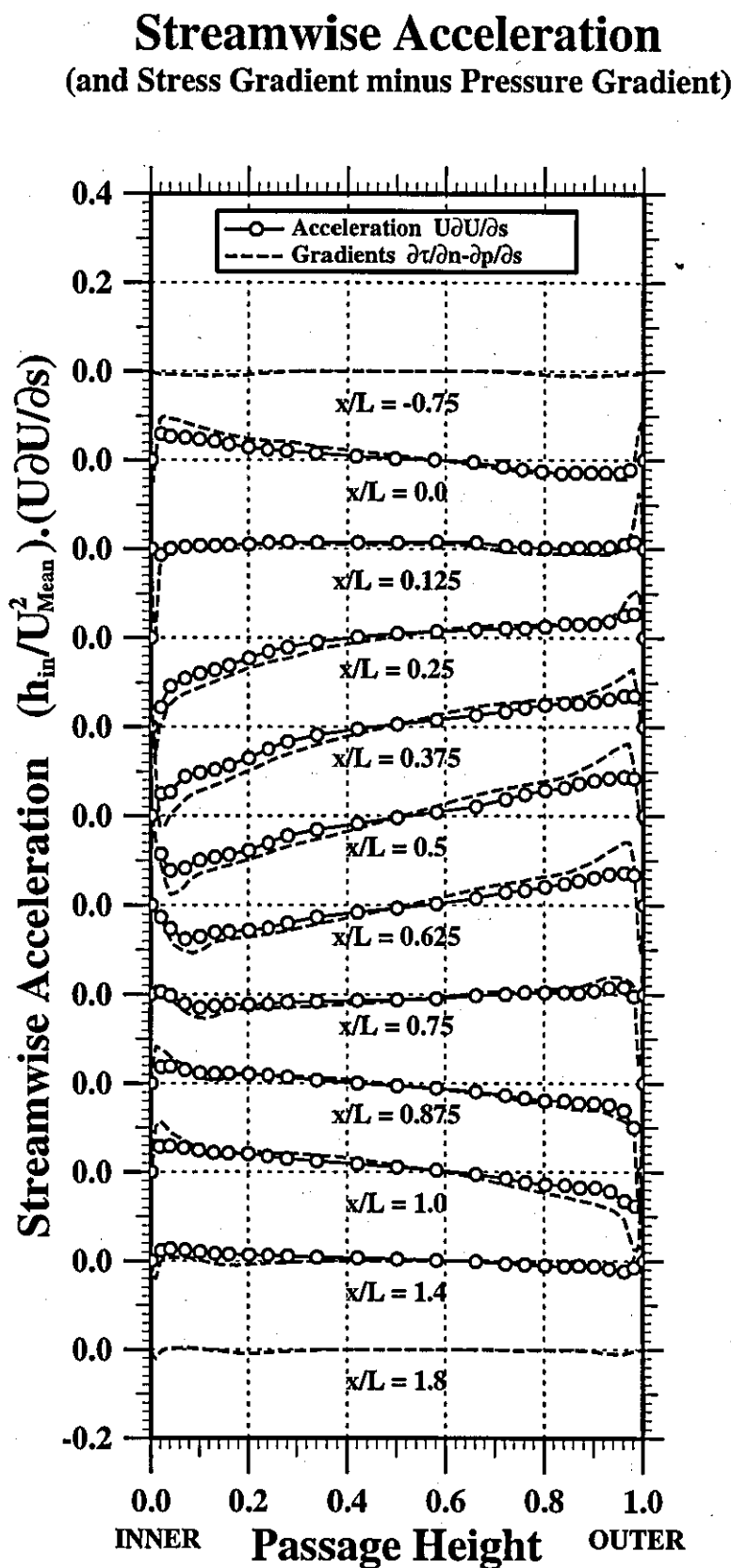
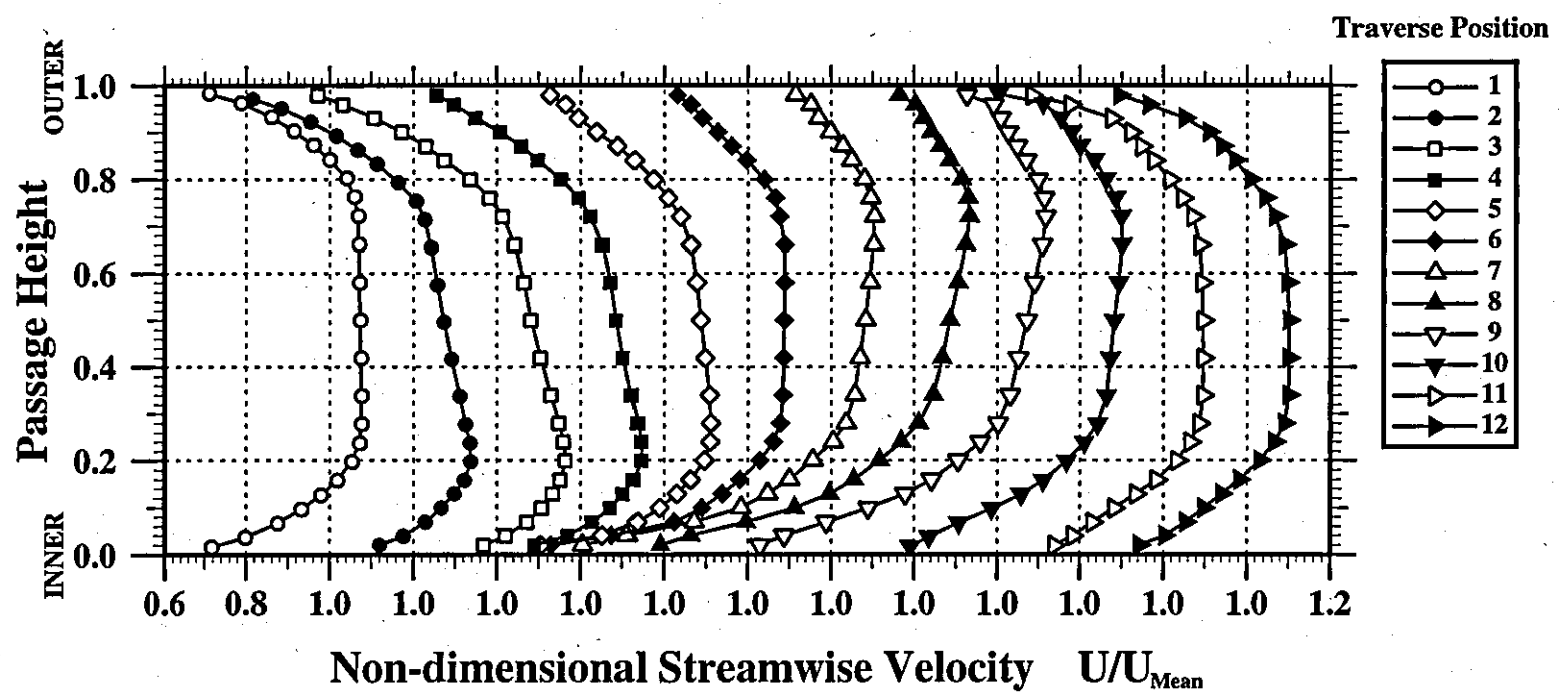


Figure 92

Streamwise Velocity Profiles (Clean Inlet - 5HP)



Streamwise Velocity Profiles (Clean Inlet - 5HP)

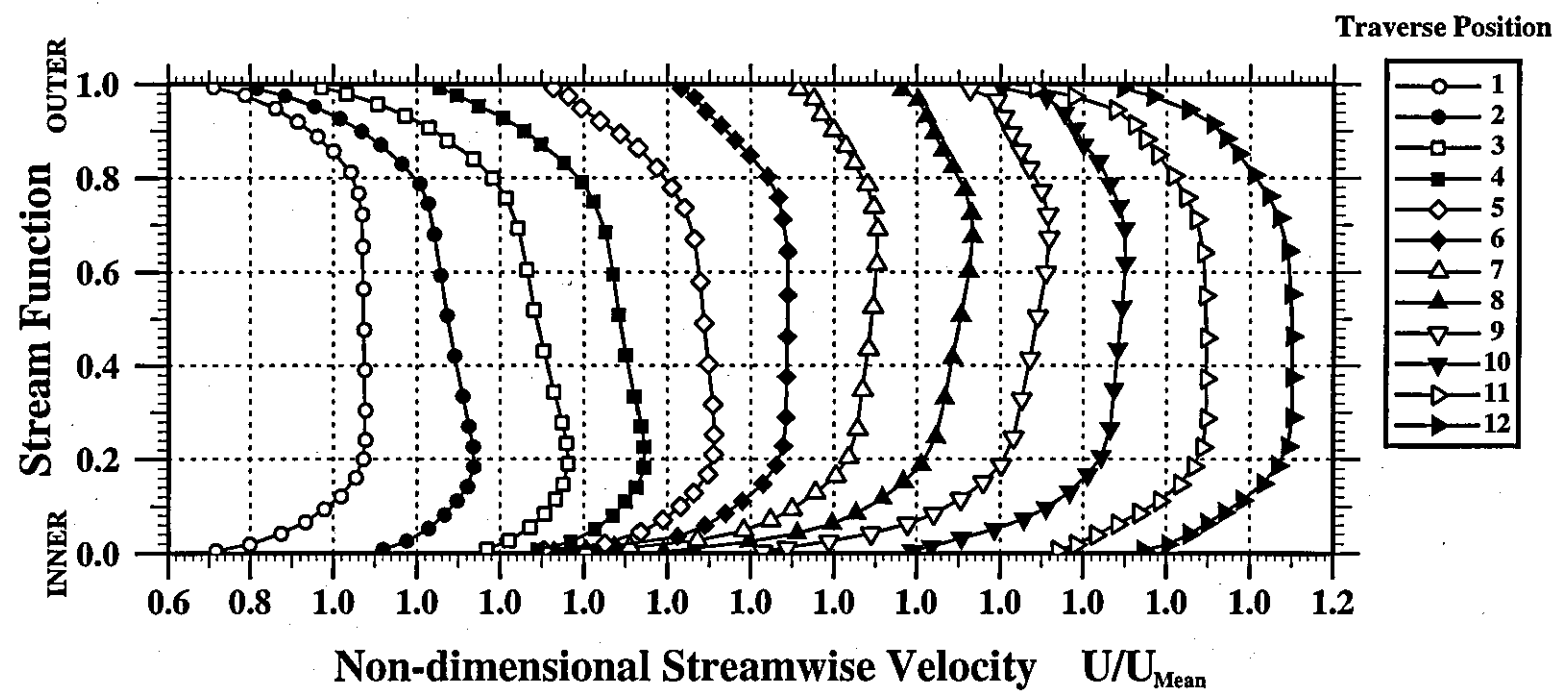


Figure 94

Total Pressure Distribution (Clean Inlet - 5HP)

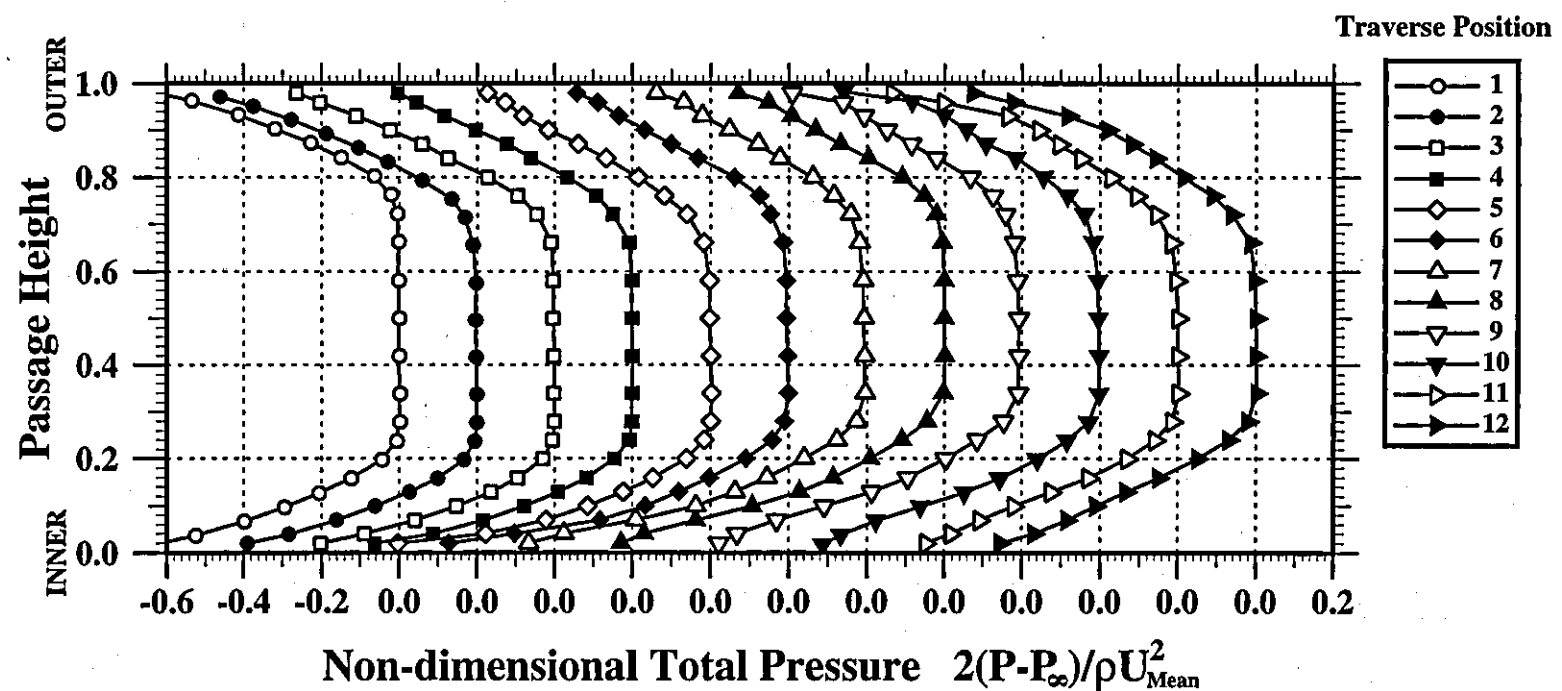


Figure 95

Total Pressure Distribution (Clean Inlet - 5HP)

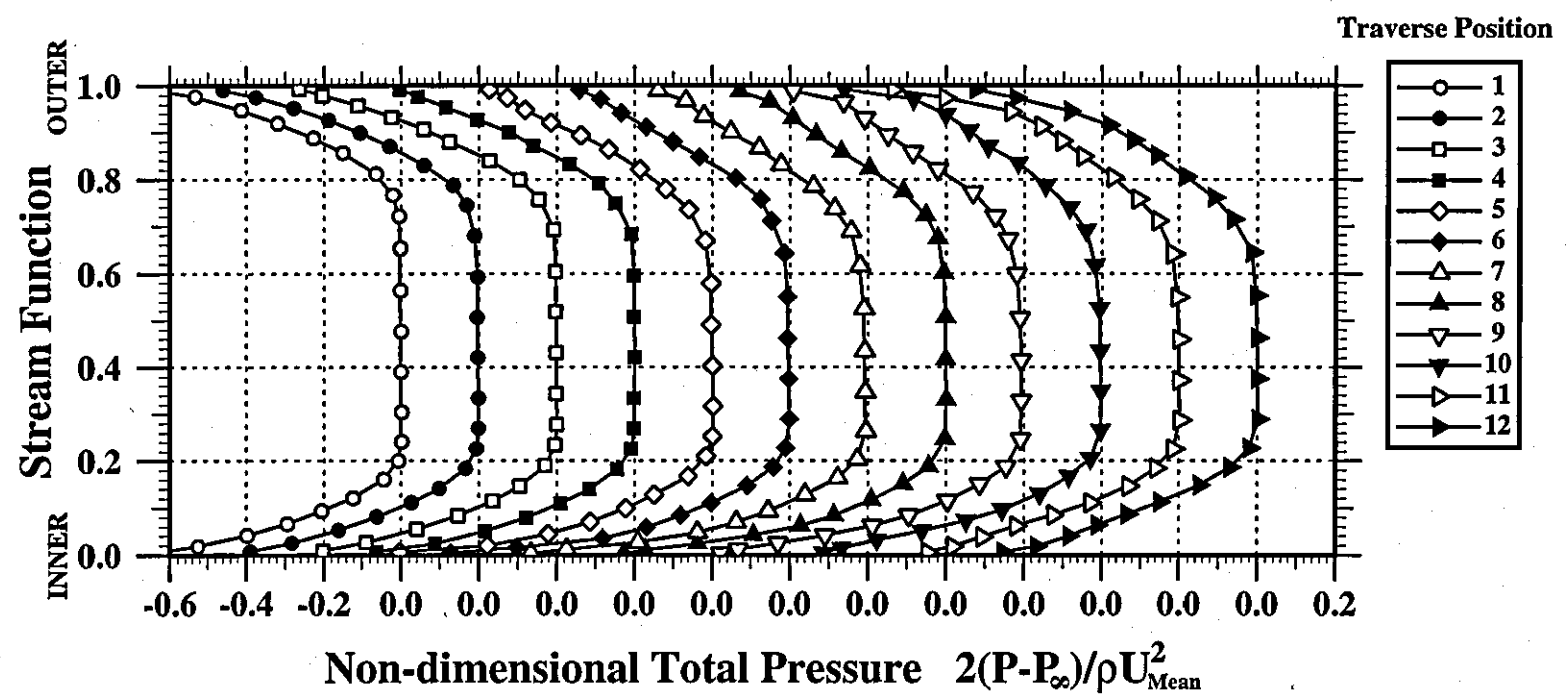


Figure 96

Total Pressure Distribution (Clean Inlet - 5HP)

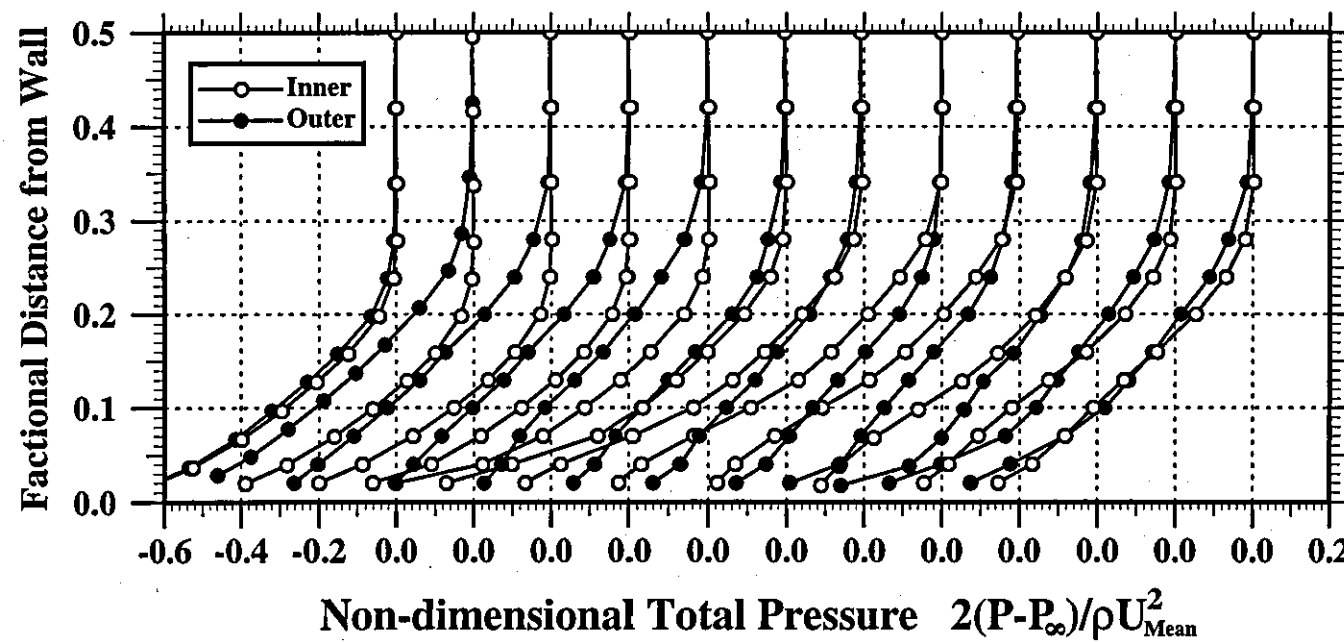
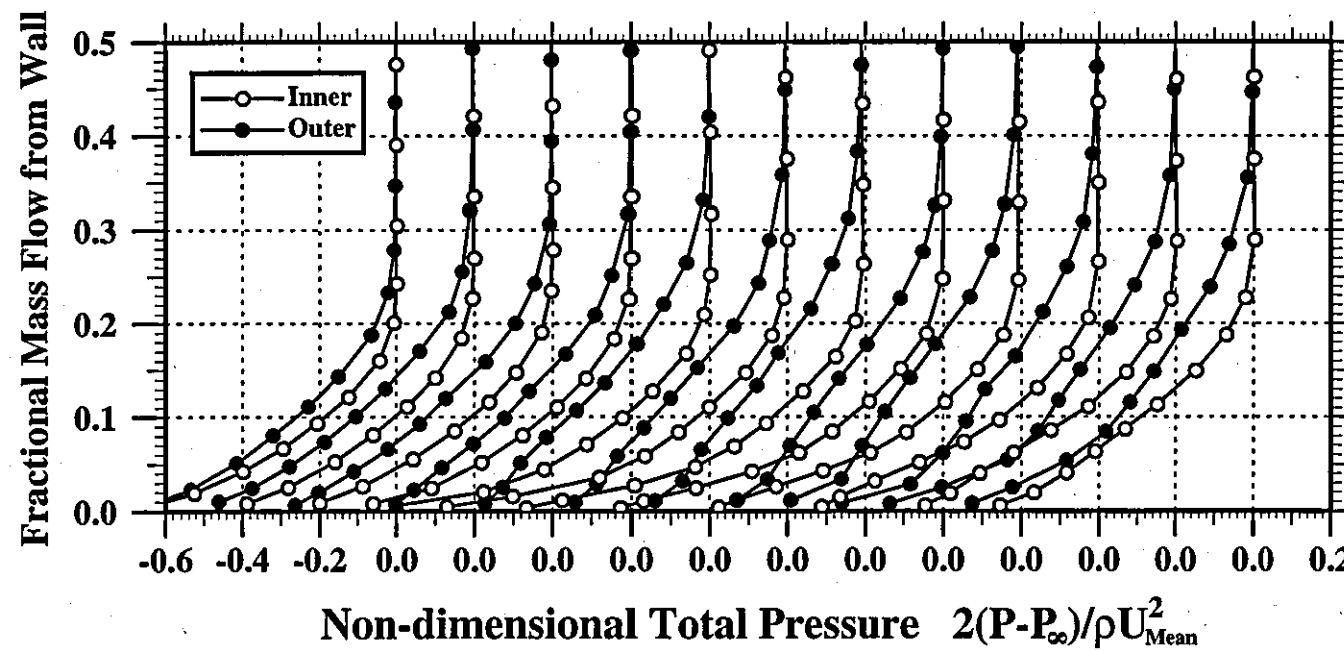
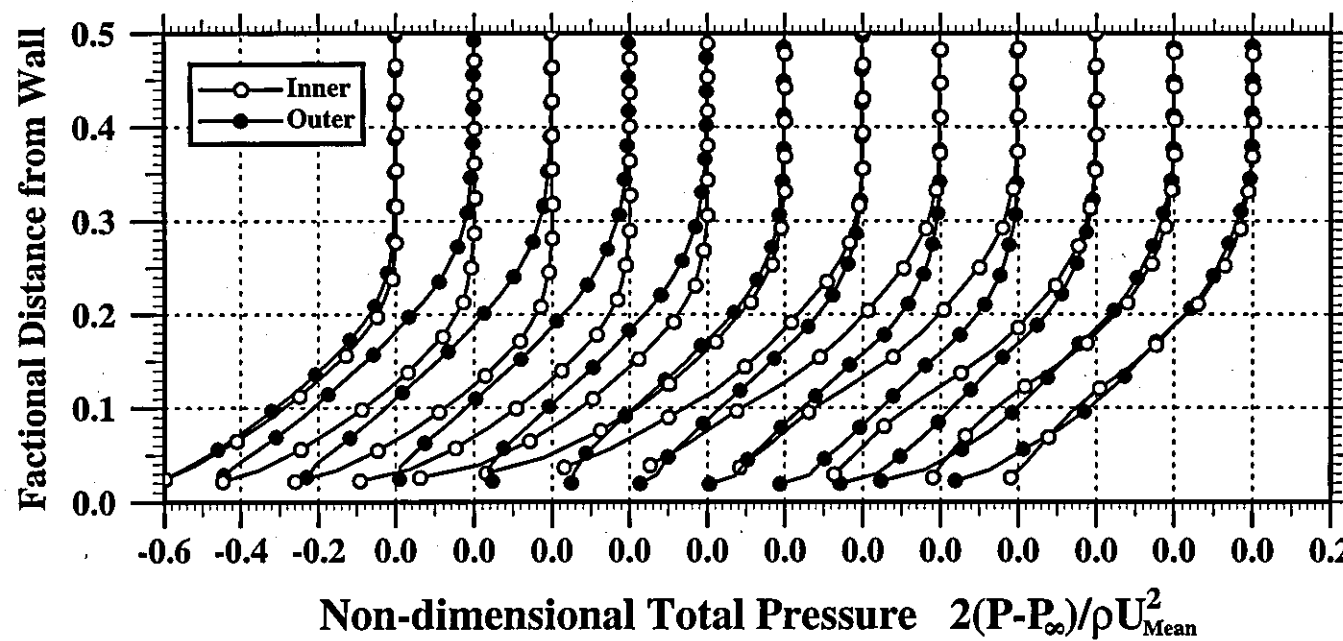


Figure 97

Total Pressure Distribution (Clean Inlet - 5HP)



Total Pressure Distribution (Clean Inlet - Derived from LDA $\bar{u}\bar{v}$ Measurements)



Total Pressure Distribution (Clean Inlet - Derived from LDA $\bar{u}\bar{v}$ Measurements)

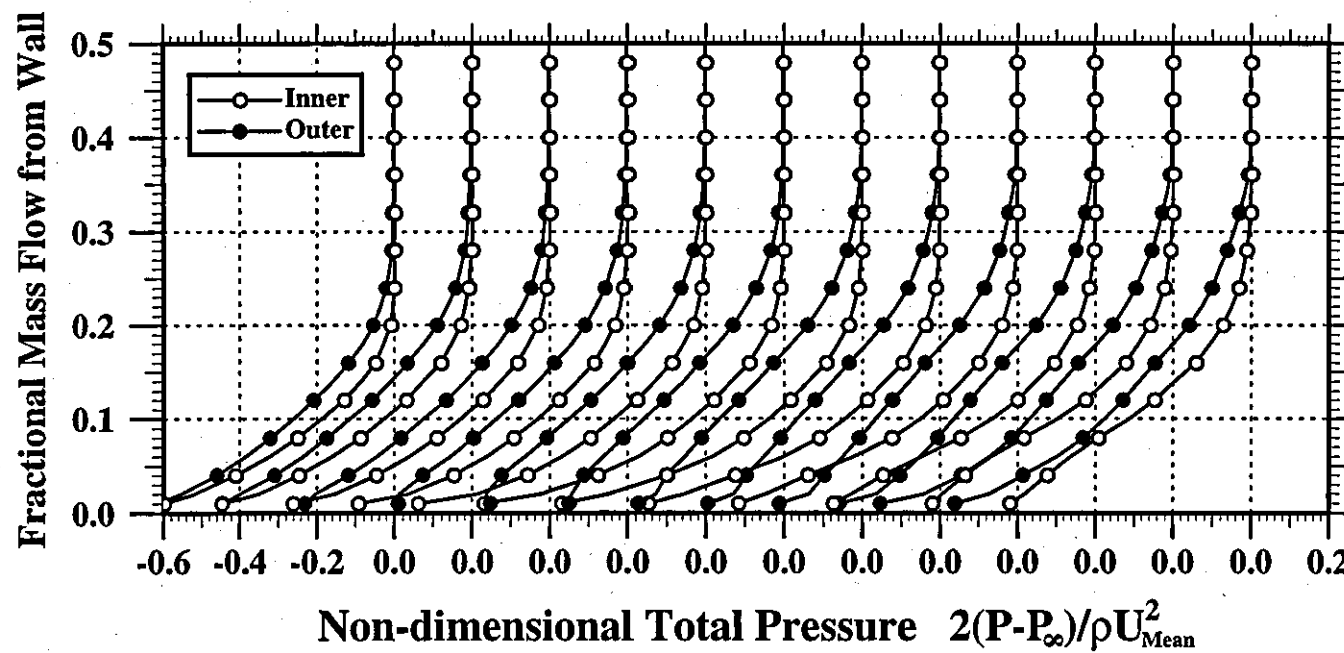


Figure 100

Experimental Measurement Mesh

(11 axial x 25 radial x 21 circumferential)

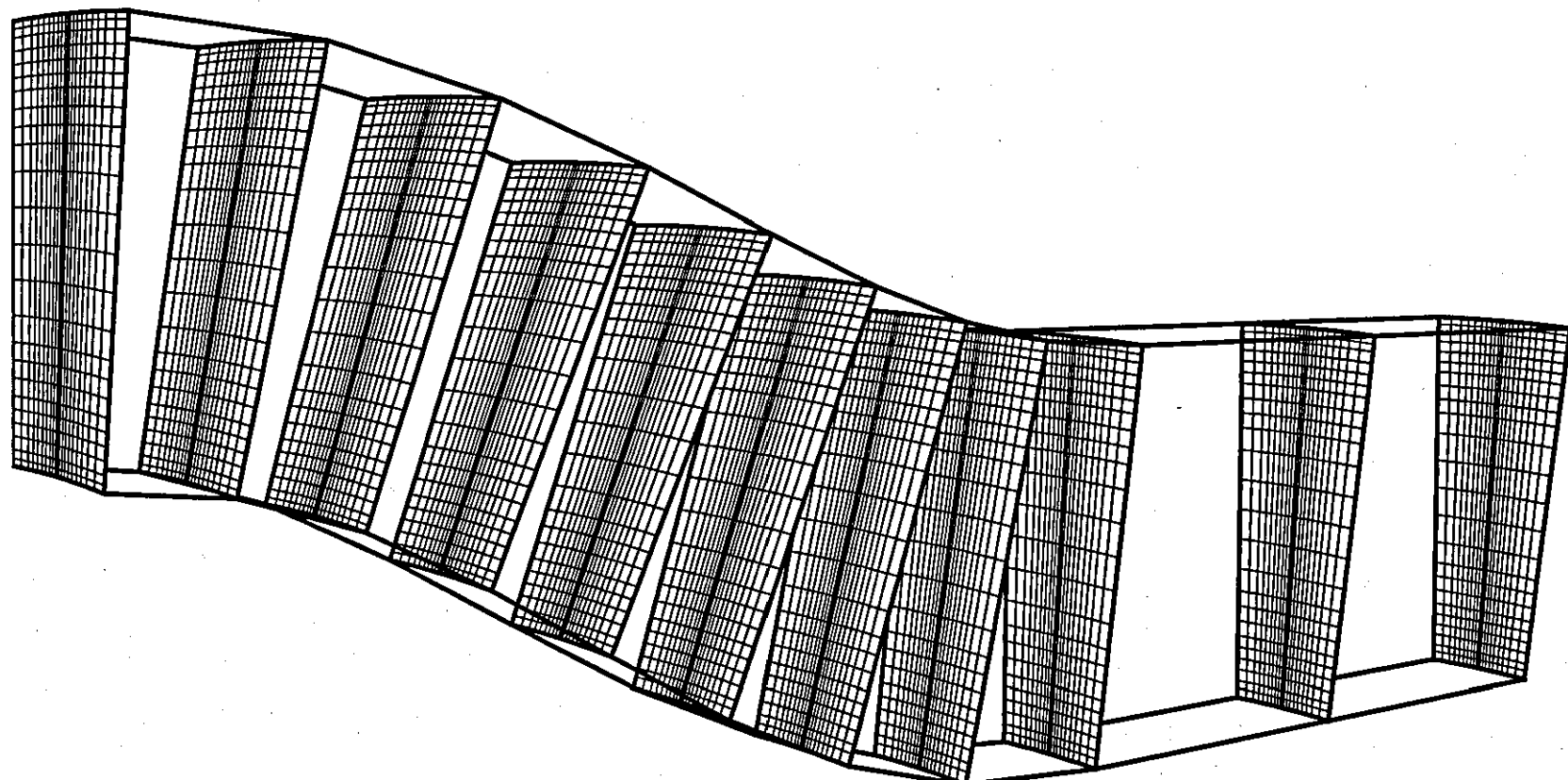


Figure 101

Figure 102

Contours of Streamwise Velocity (S-duct Inlet - $x/L=0.0$)

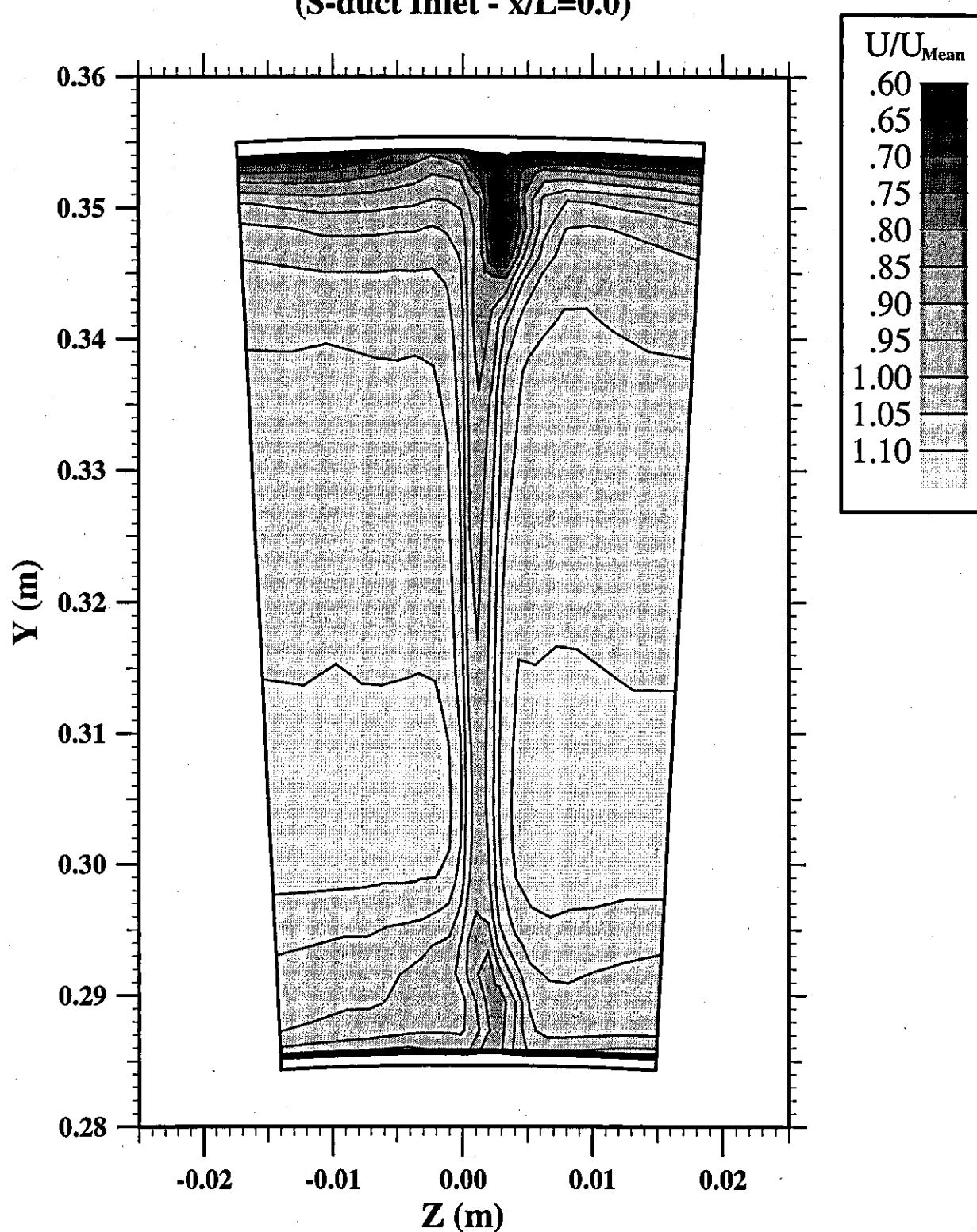


Figure 103

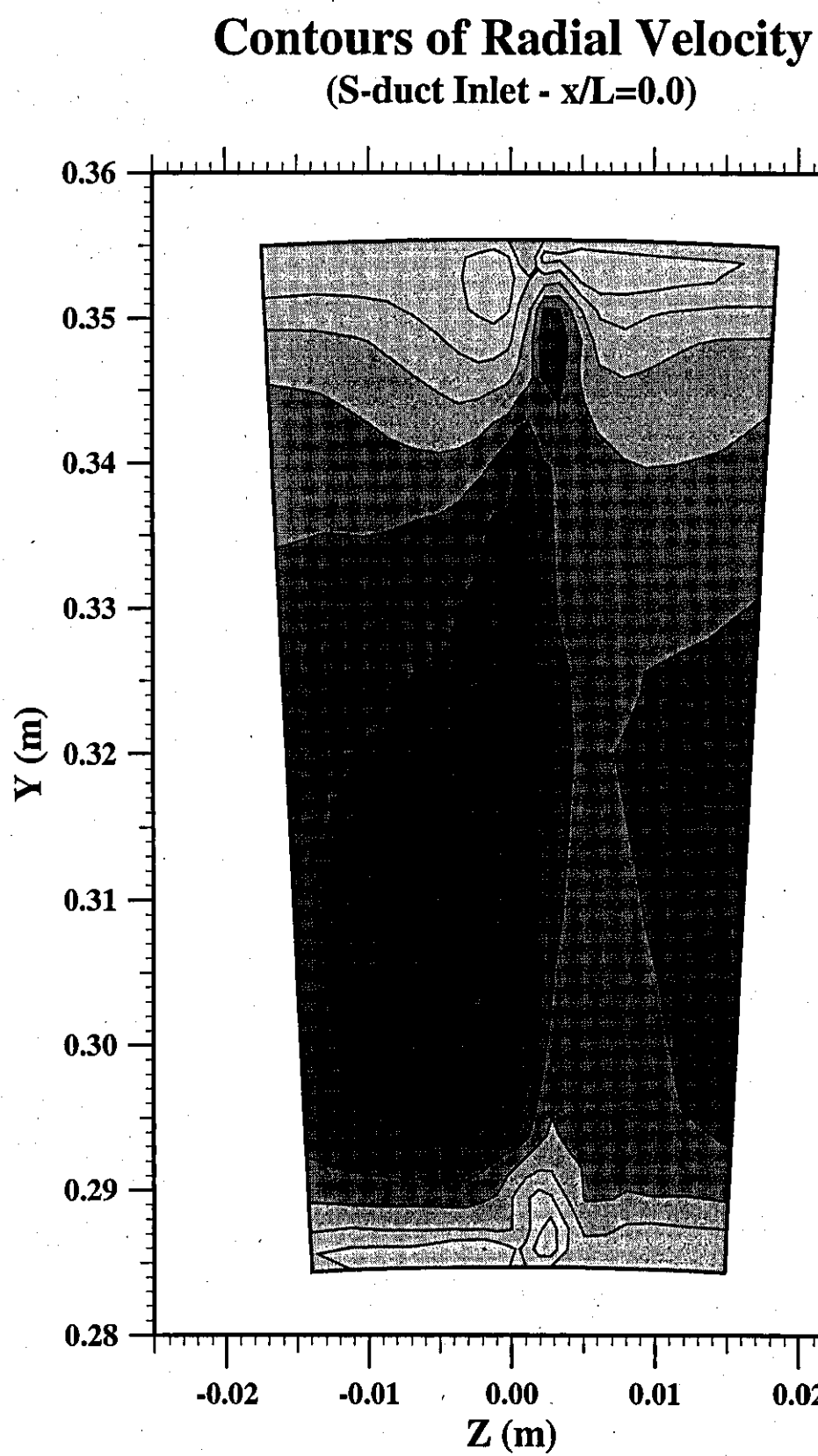


Figure 104

Contours of Circumferential Velocity (S-duct Inlet - $x/L=0.0$)

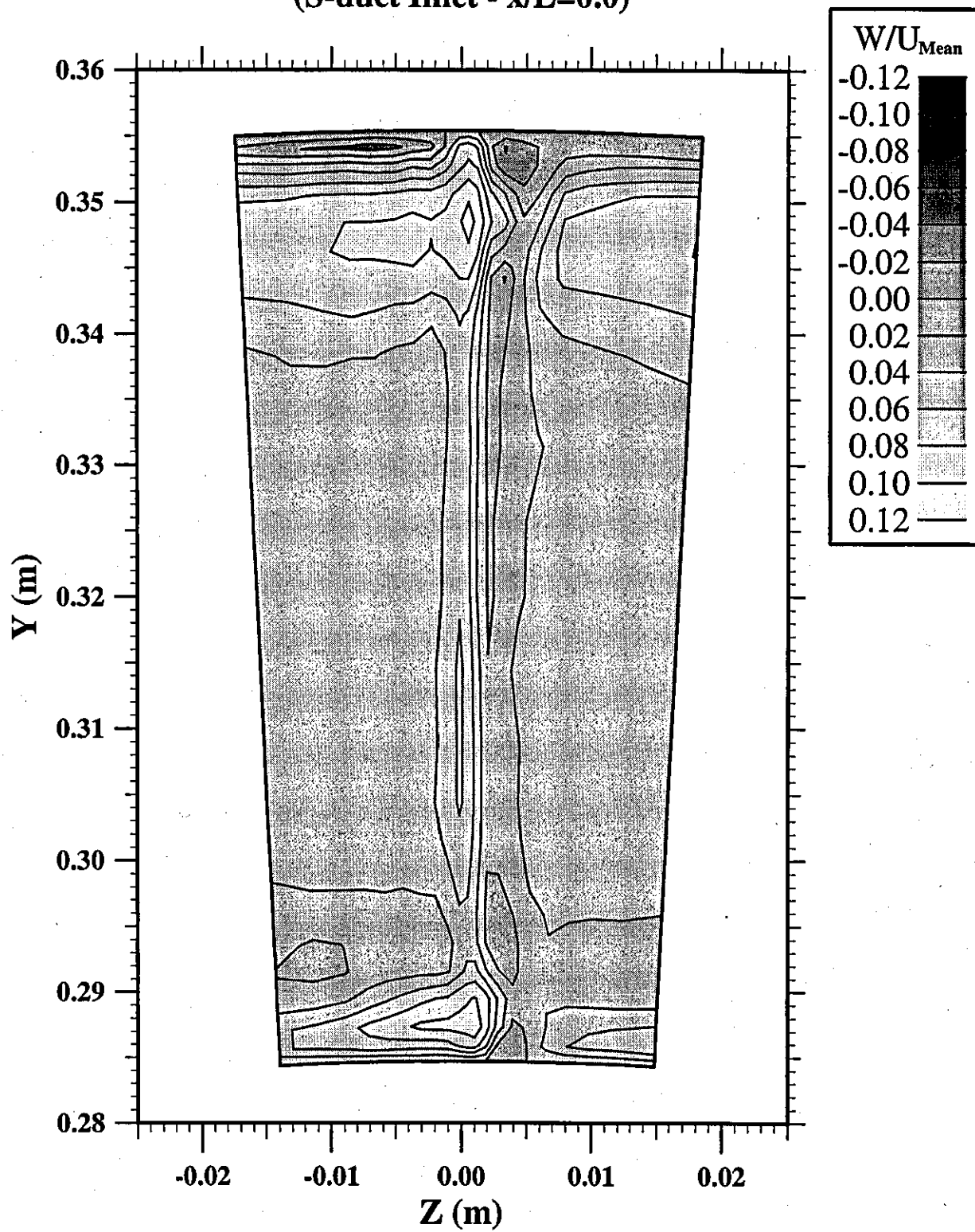


Figure 105

Secondary Velocity Vectors (S-duct Inlet - $x/L=0.0$)

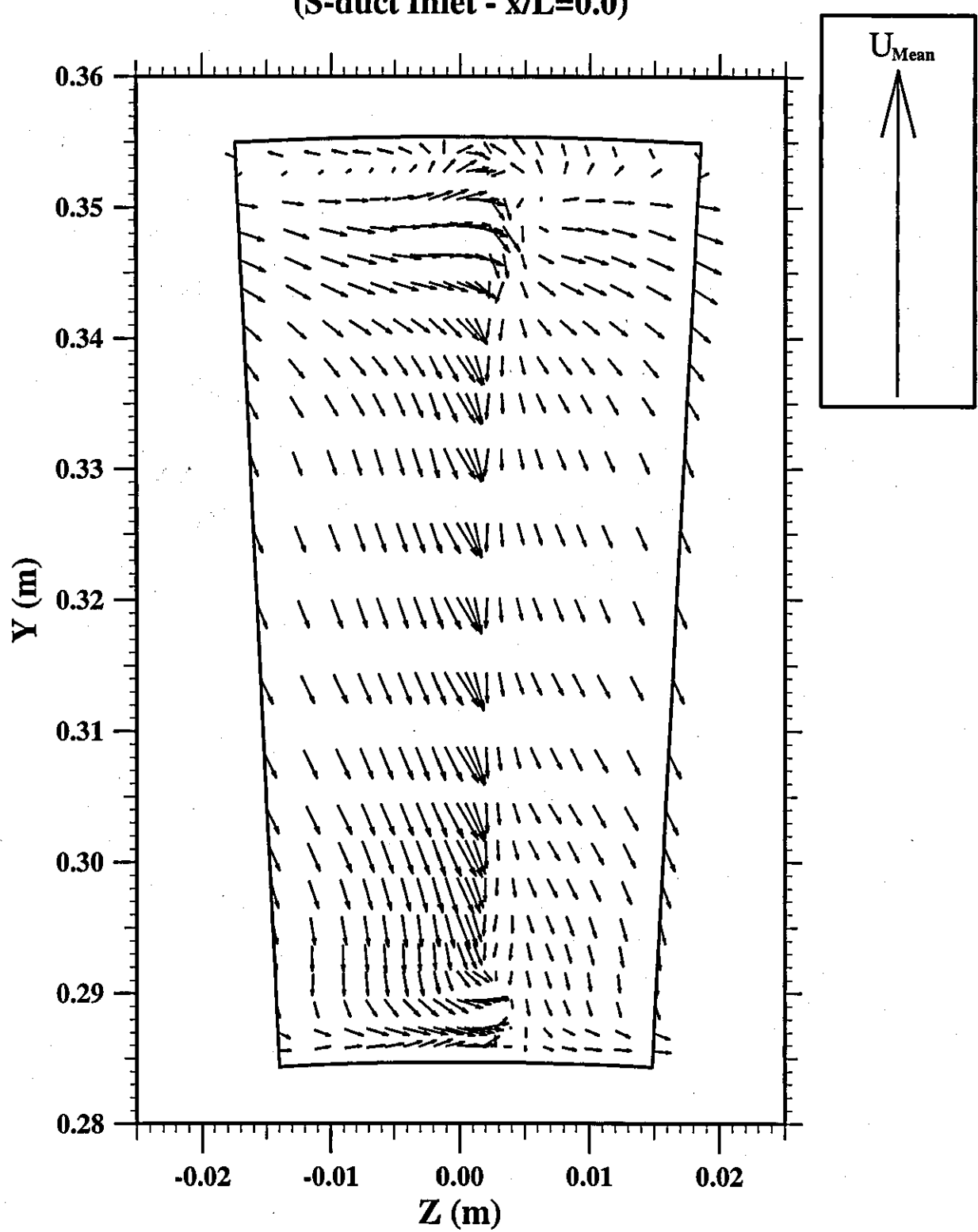
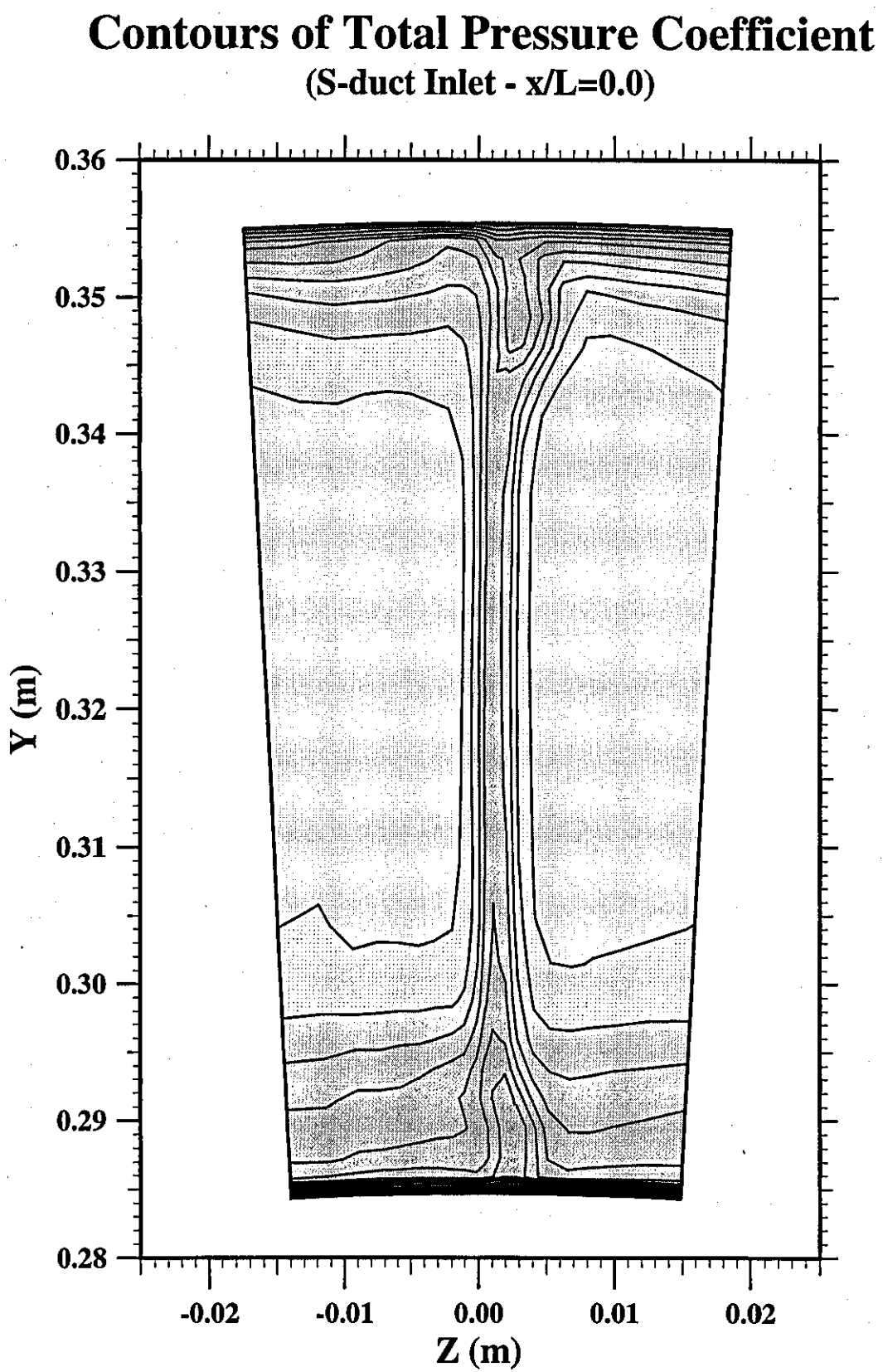
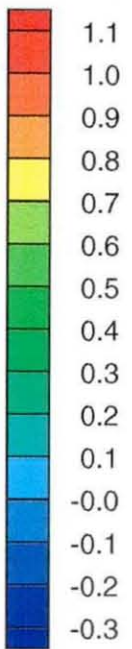


Figure 106





Contours of Total Pressure Coefficient

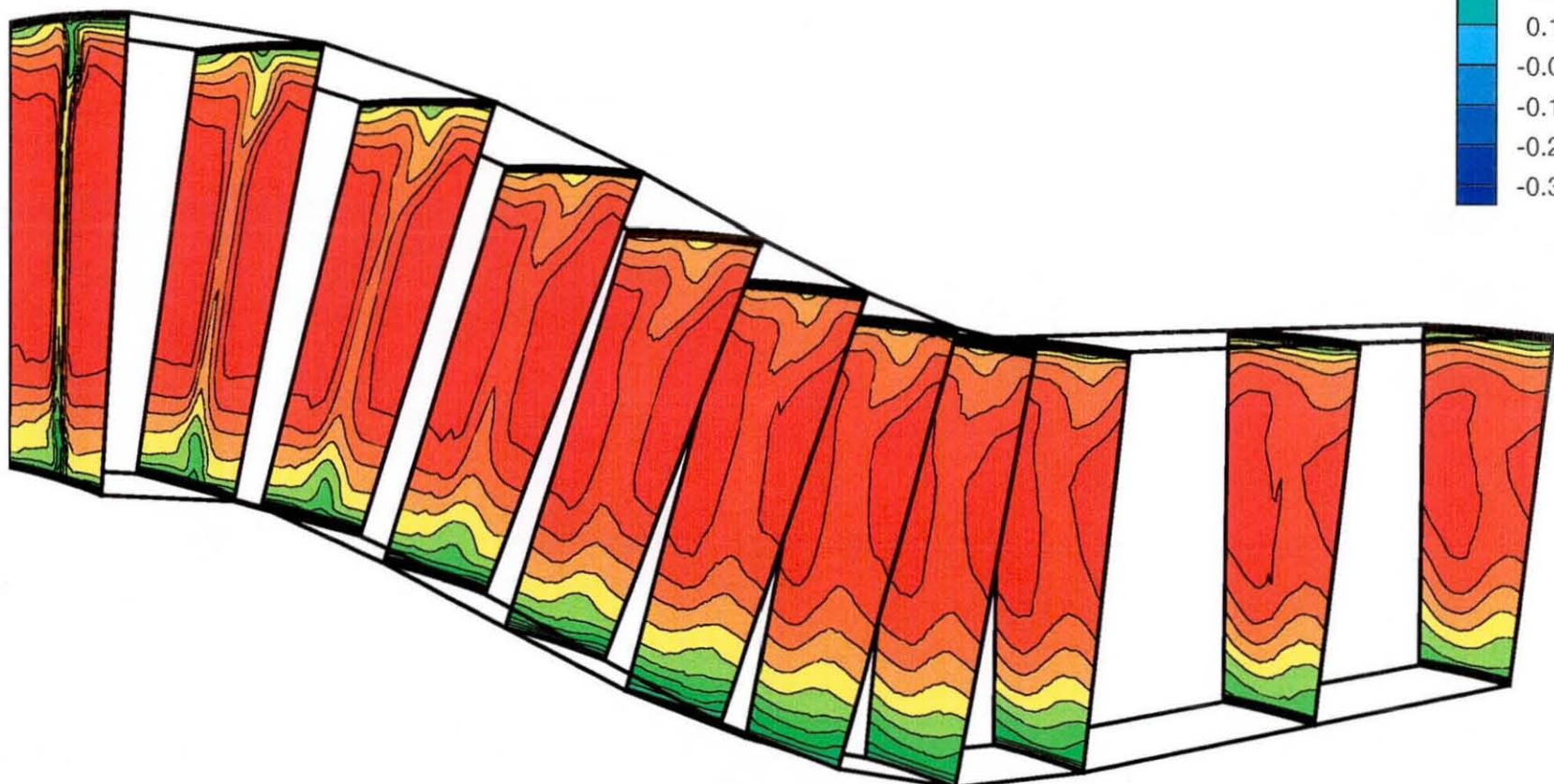


Figure 107

Mean and Wall Static Pressure Distribution

With the Compressor

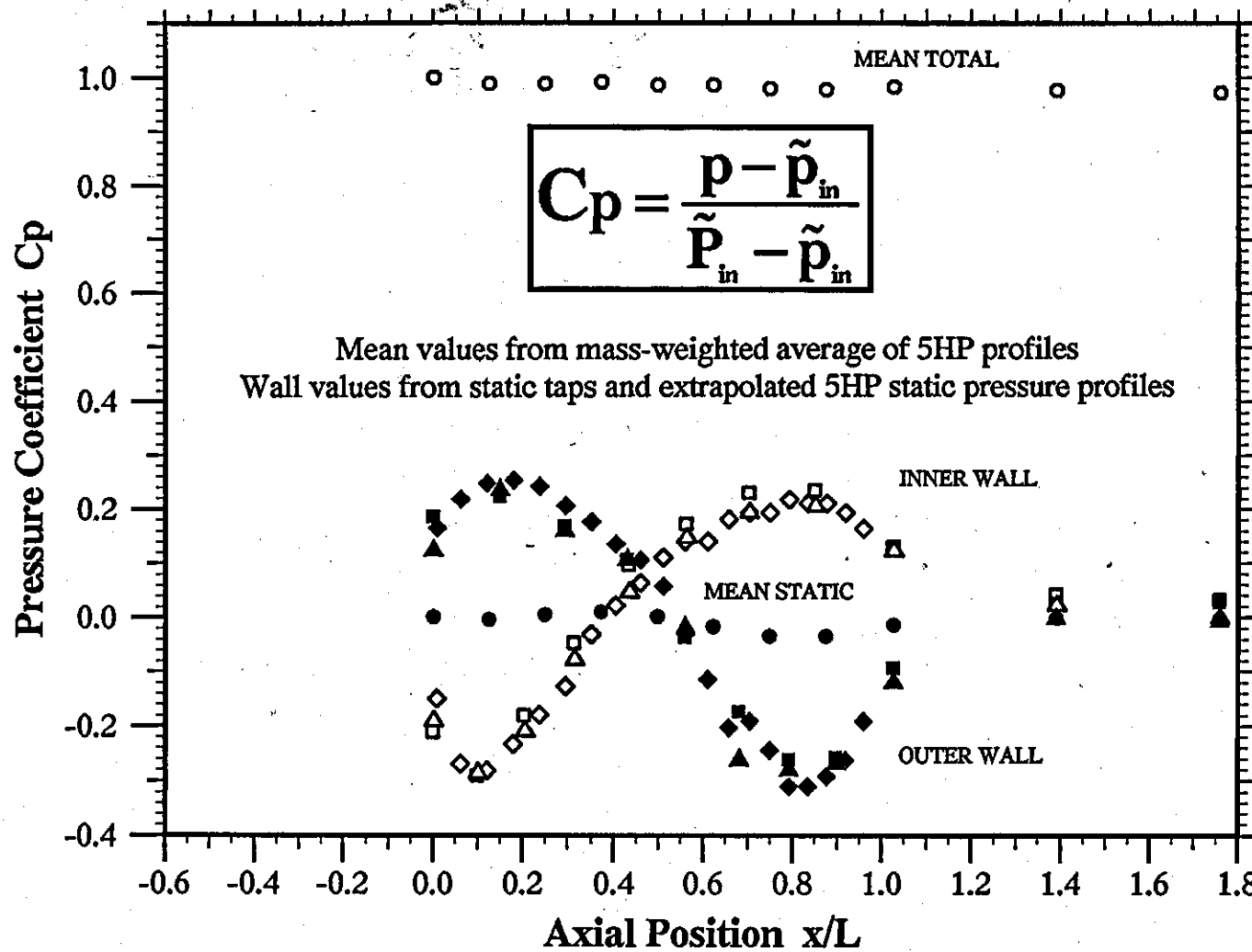


Figure 109

Comparison of the Static Pressure Distribution With and Without the Compressor

(Pitch-averaged 5HP Measurements)

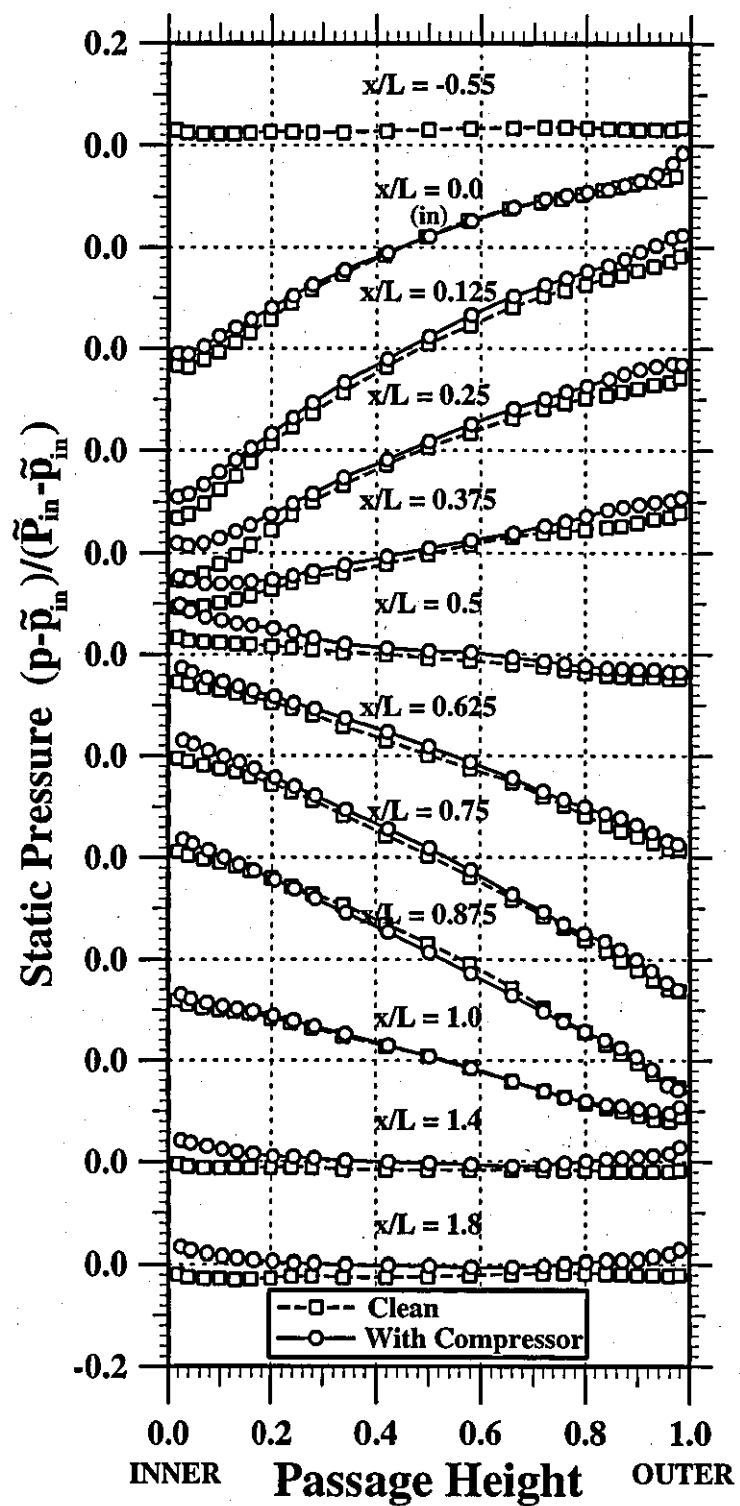
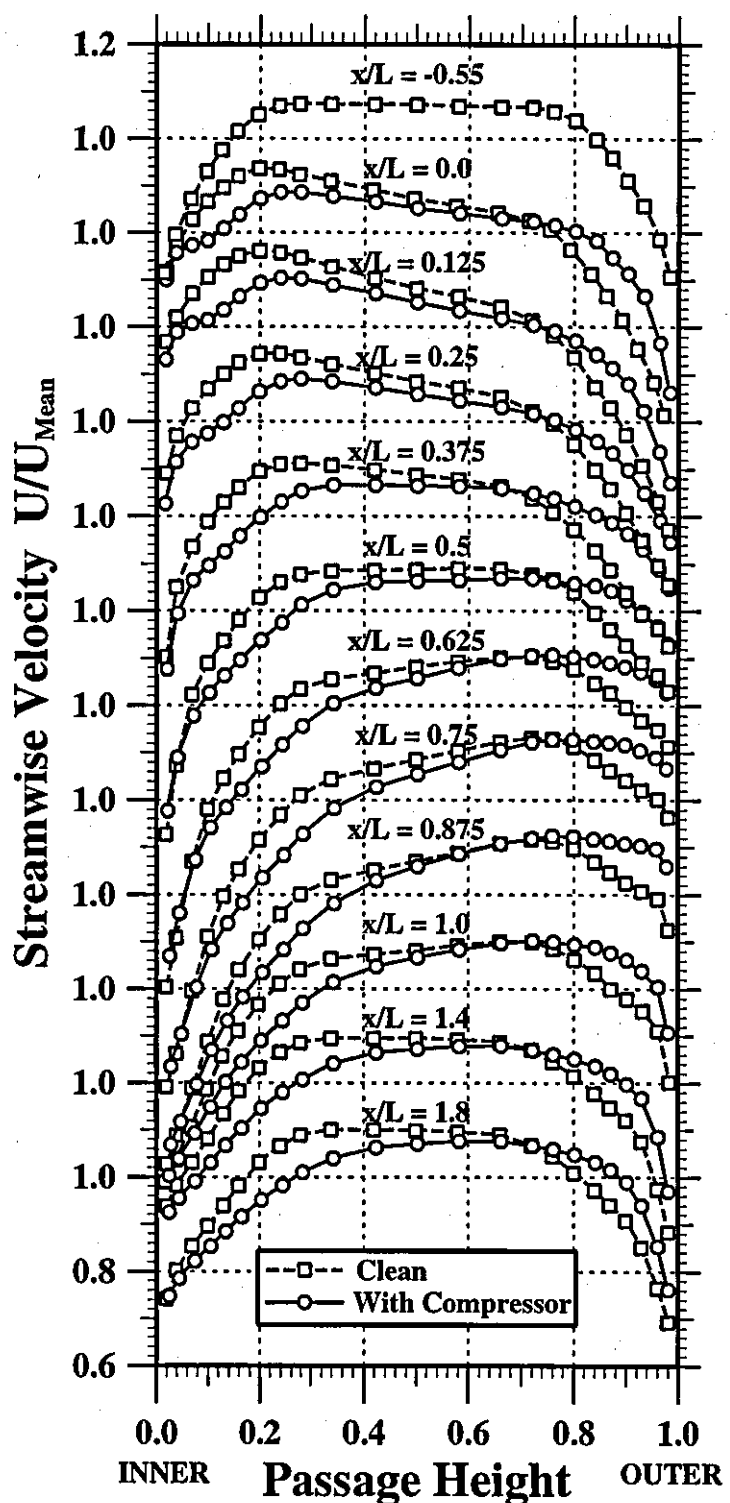


Figure 110

Comparison of Streamwise Velocity Profiles With and Without the Compressor (Pitch-averaged 5HP Measurements)



Streamwise Velocity Profiles

(Compressor at Inlet - 5HP)

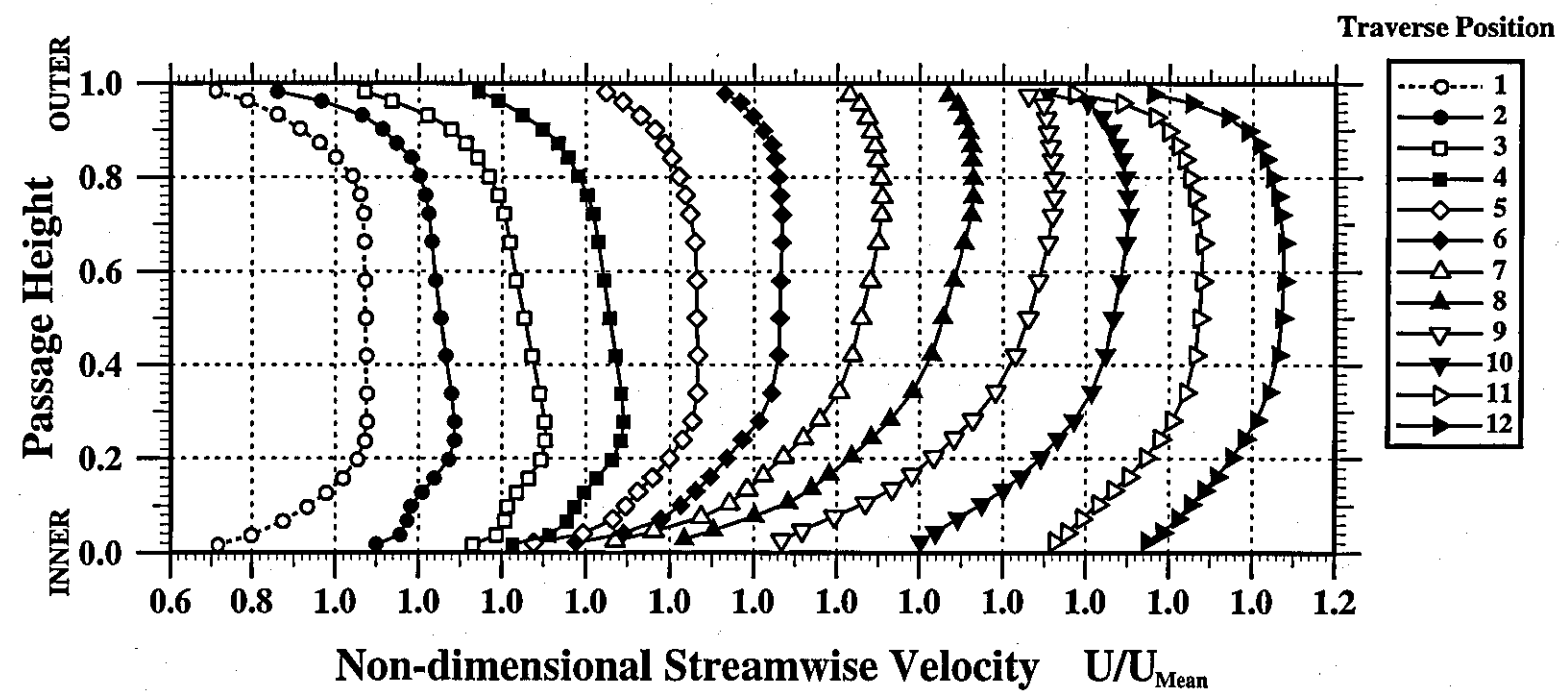
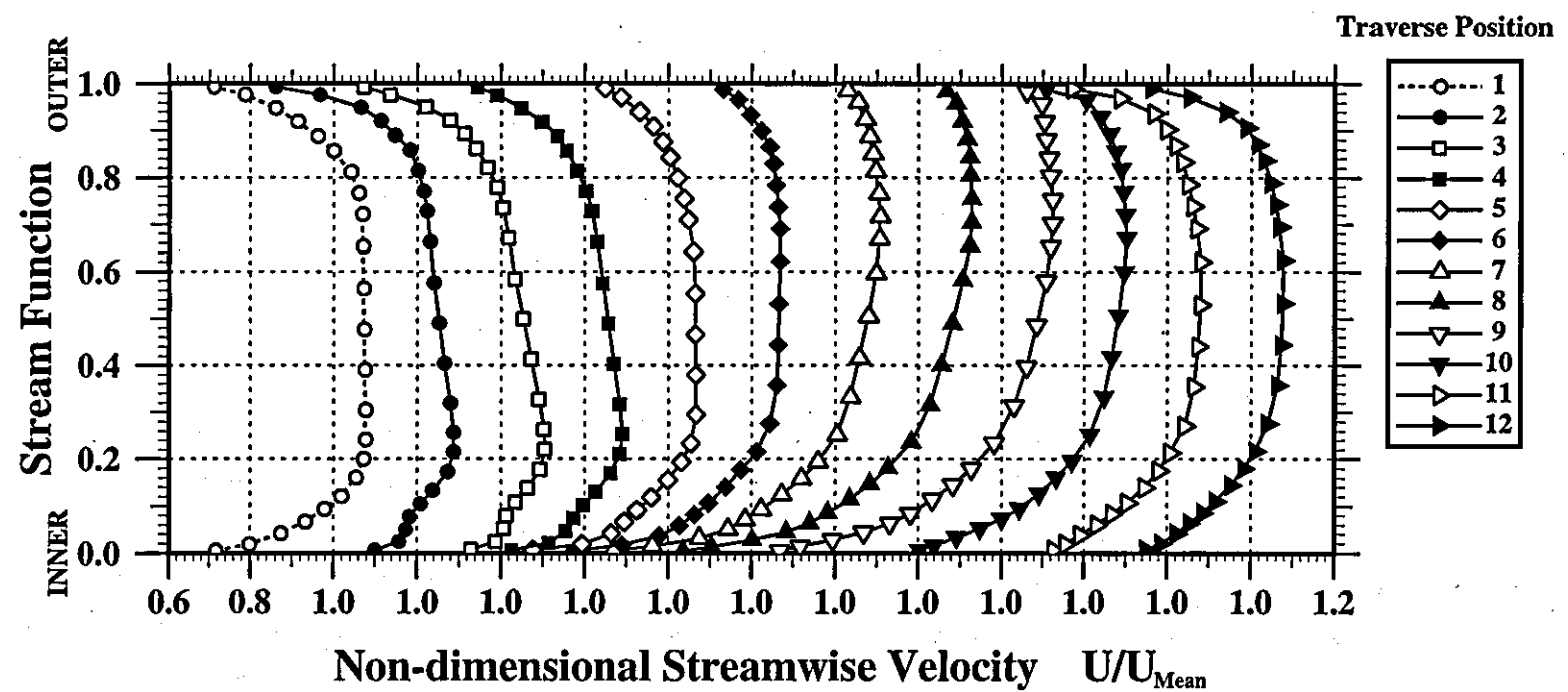


Figure III

Figure 112

Streamwise Velocity Profiles (Compressor at Inlet - 5HP)



Total Pressure Distribution (Compressor at Inlet - 5HP)

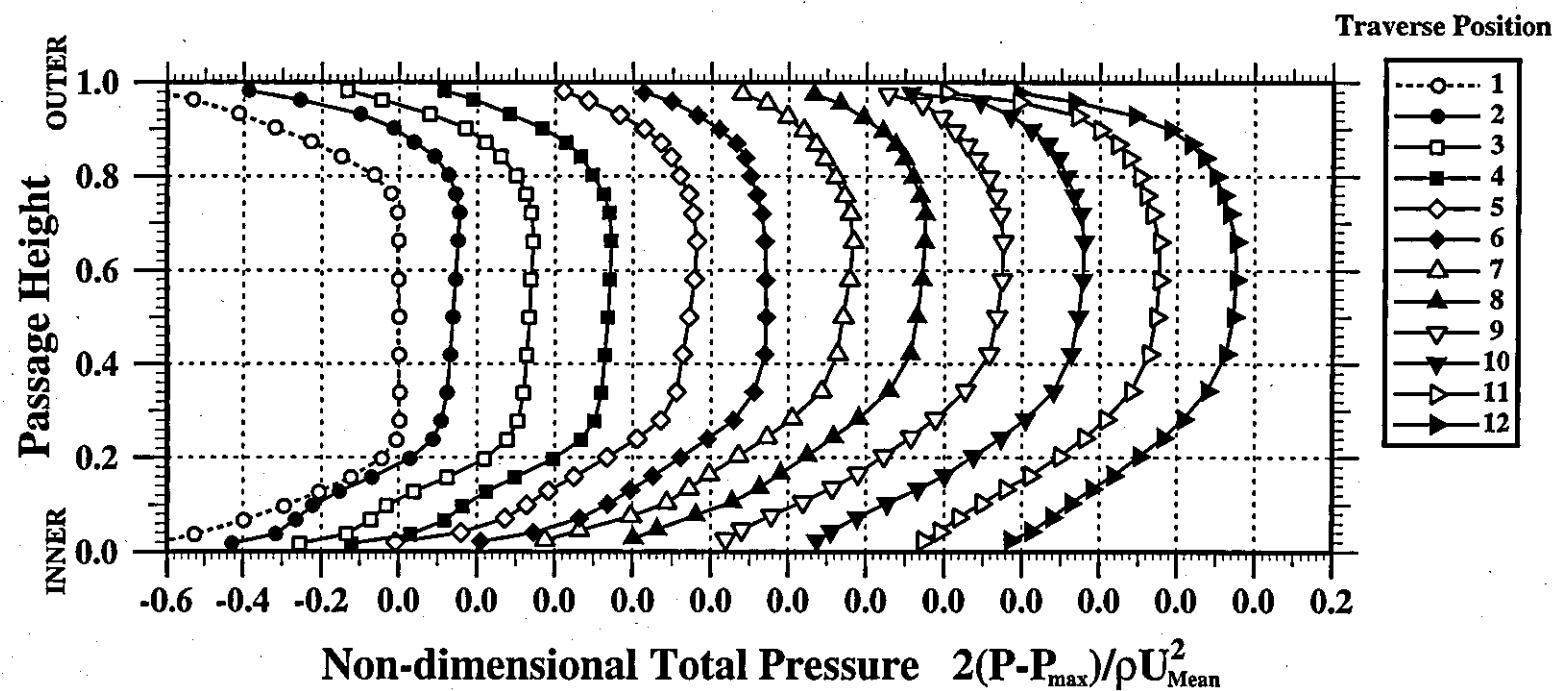


Figure 113

Total Pressure Distribution (Compressor at Inlet - 5HP)

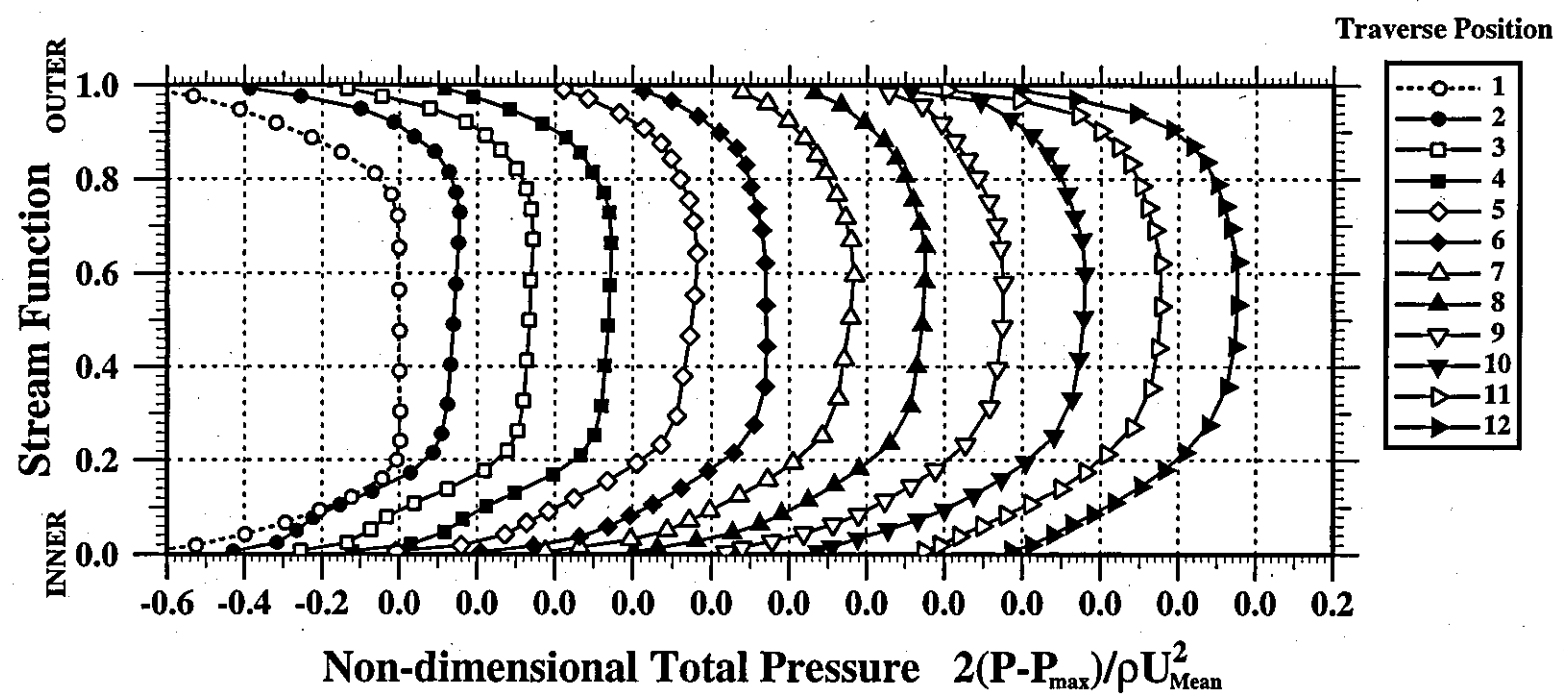


Figure 114

Axial Variation of Boundary Layer Shape Parameter With and Without the Compressor

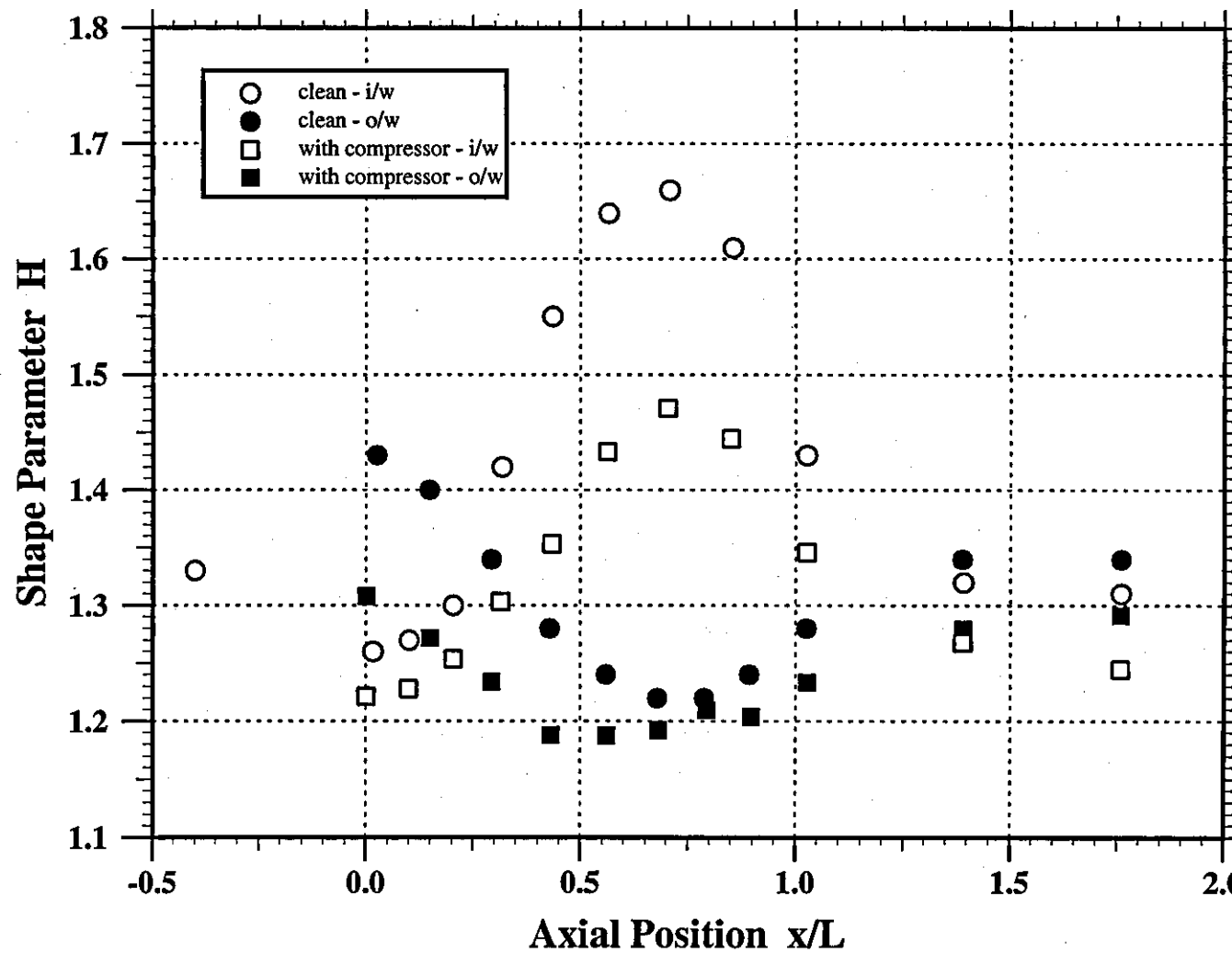


Figure 115

Figure 116

Secondary Velocity Vectors ($x/L=0.25$)

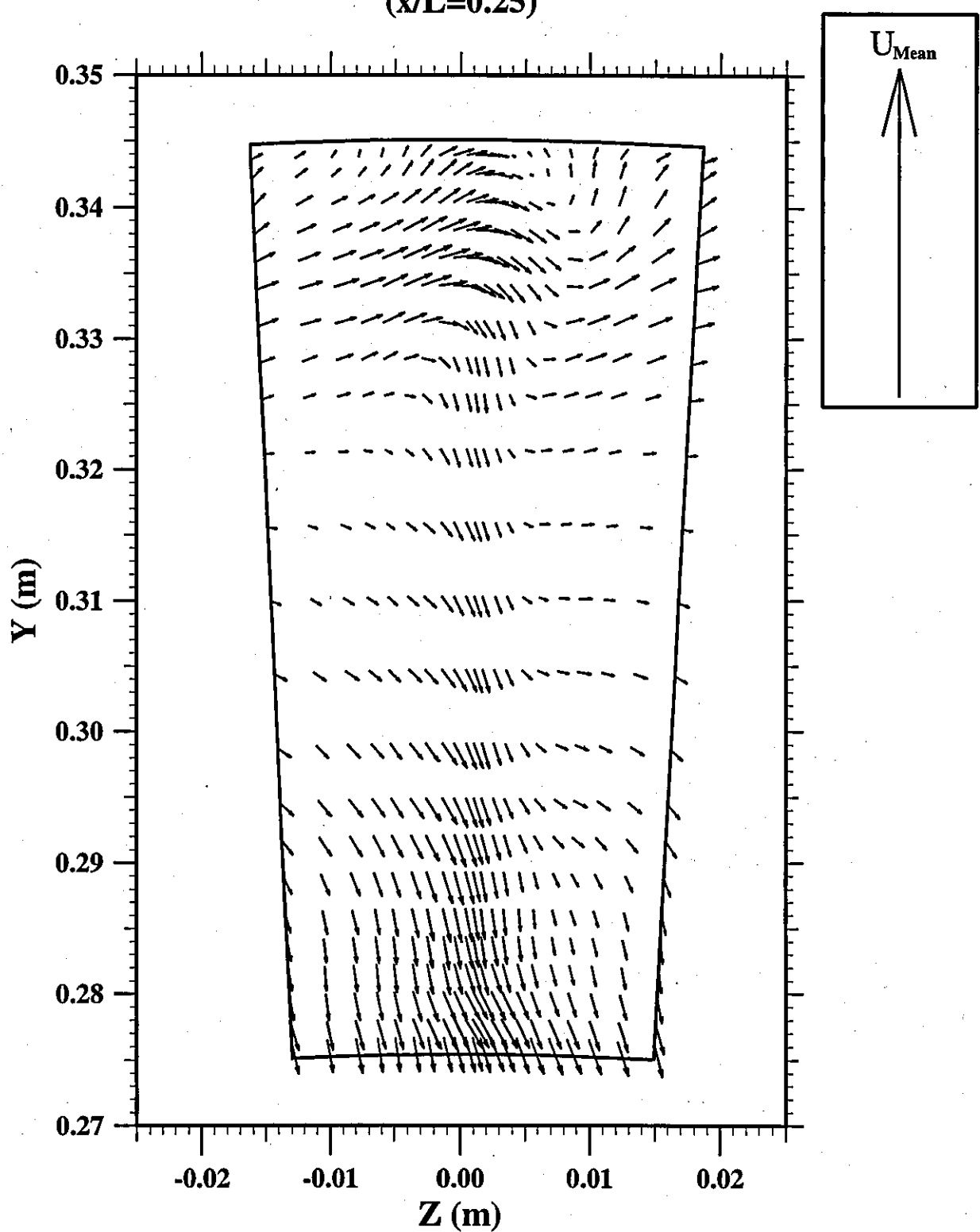


Figure 117

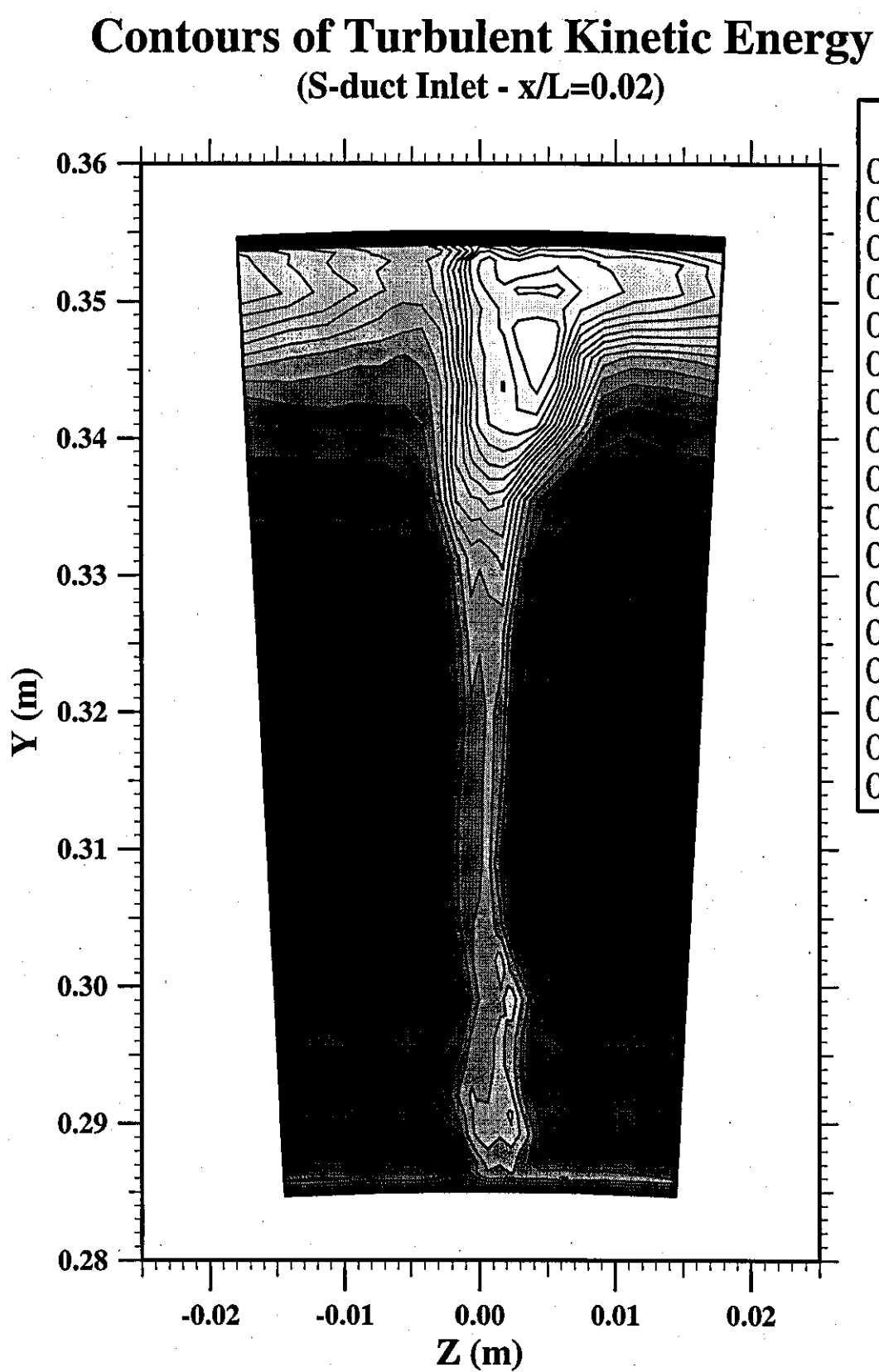


Figure 118

Contours of $\bar{u}\bar{u}$ Normal Stress
(S-duct Inlet - $x/L=0.02$)

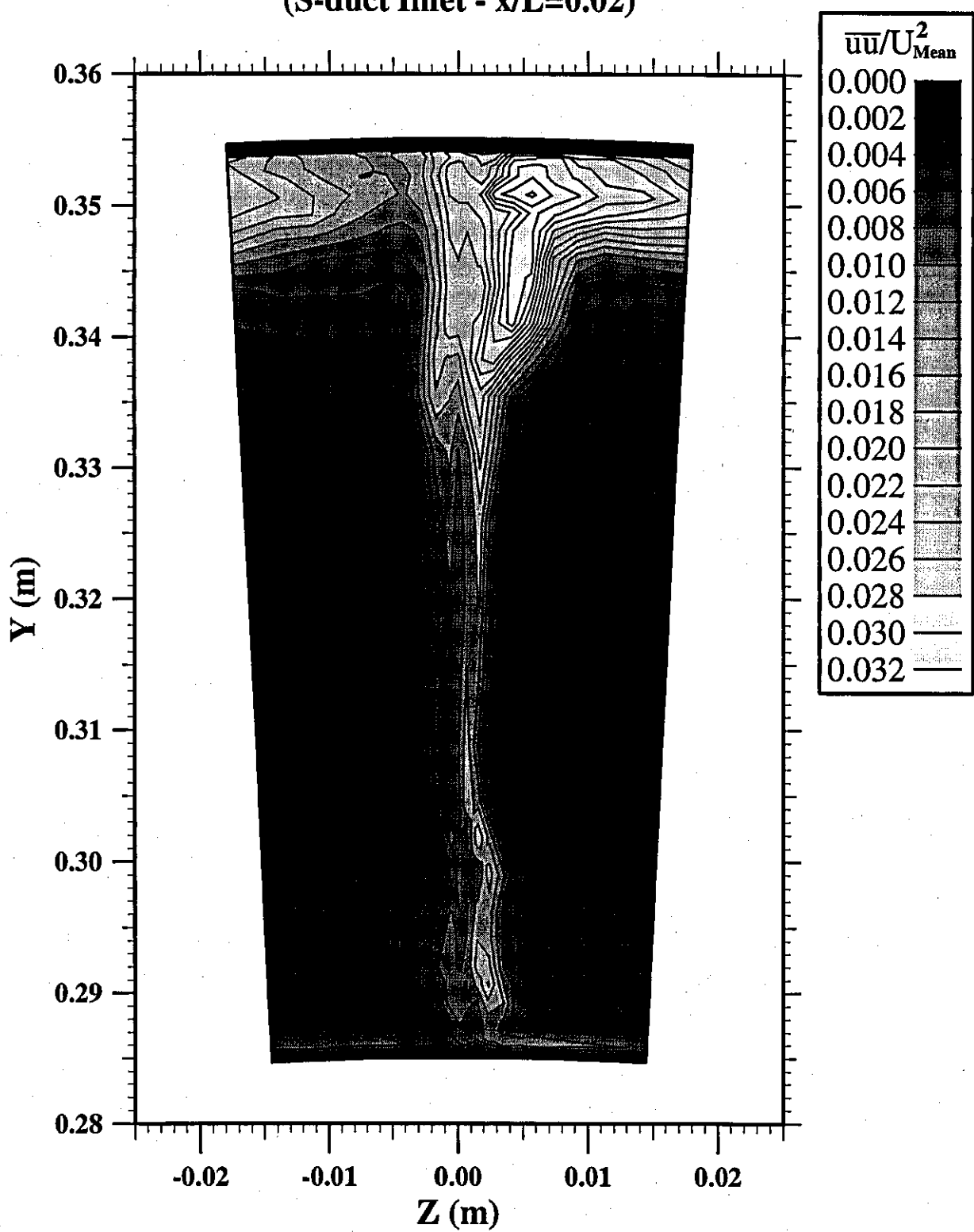


Figure 119

**Contours of $\bar{v}\bar{v}$ Normal Stress
(S-duct Inlet - $x/L=0.02$)**

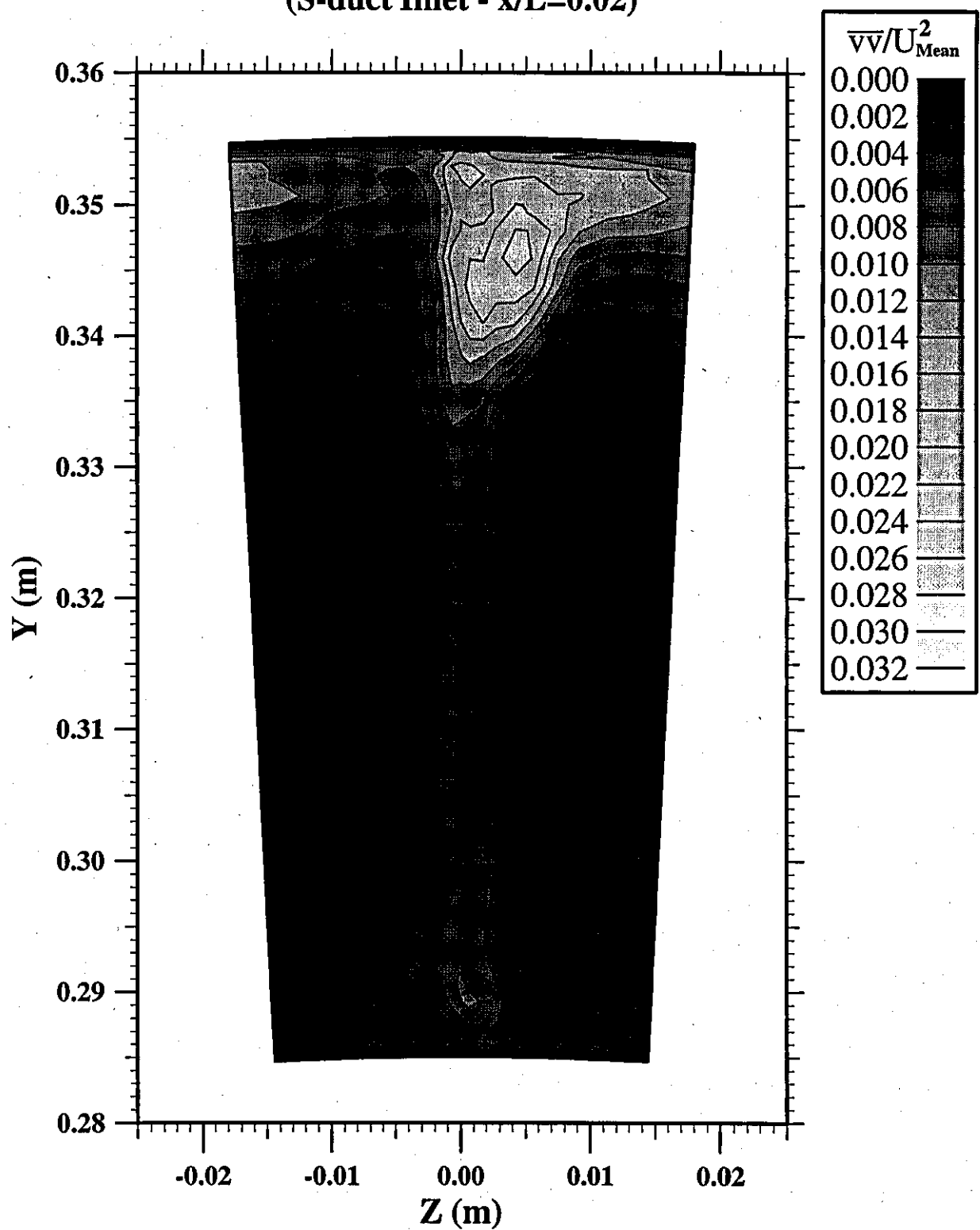


Figure 120

Contours of $\overline{w w}$ Normal Stress (S-duct Inlet - $x/L=0.02$)

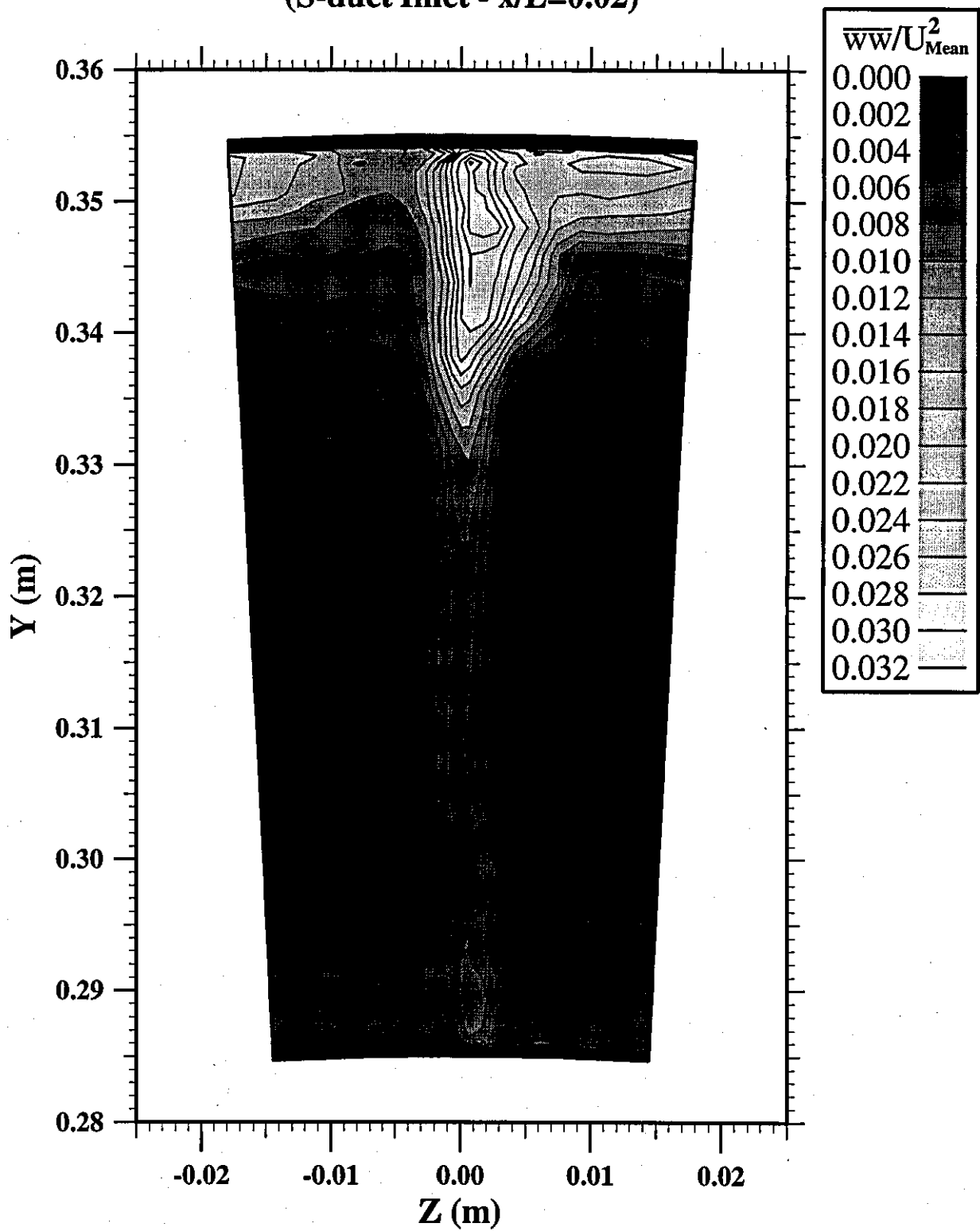


Figure 121

Contours of $\bar{u}w$ Shear Stress
(S-duct Inlet - $x/L=0.02$)

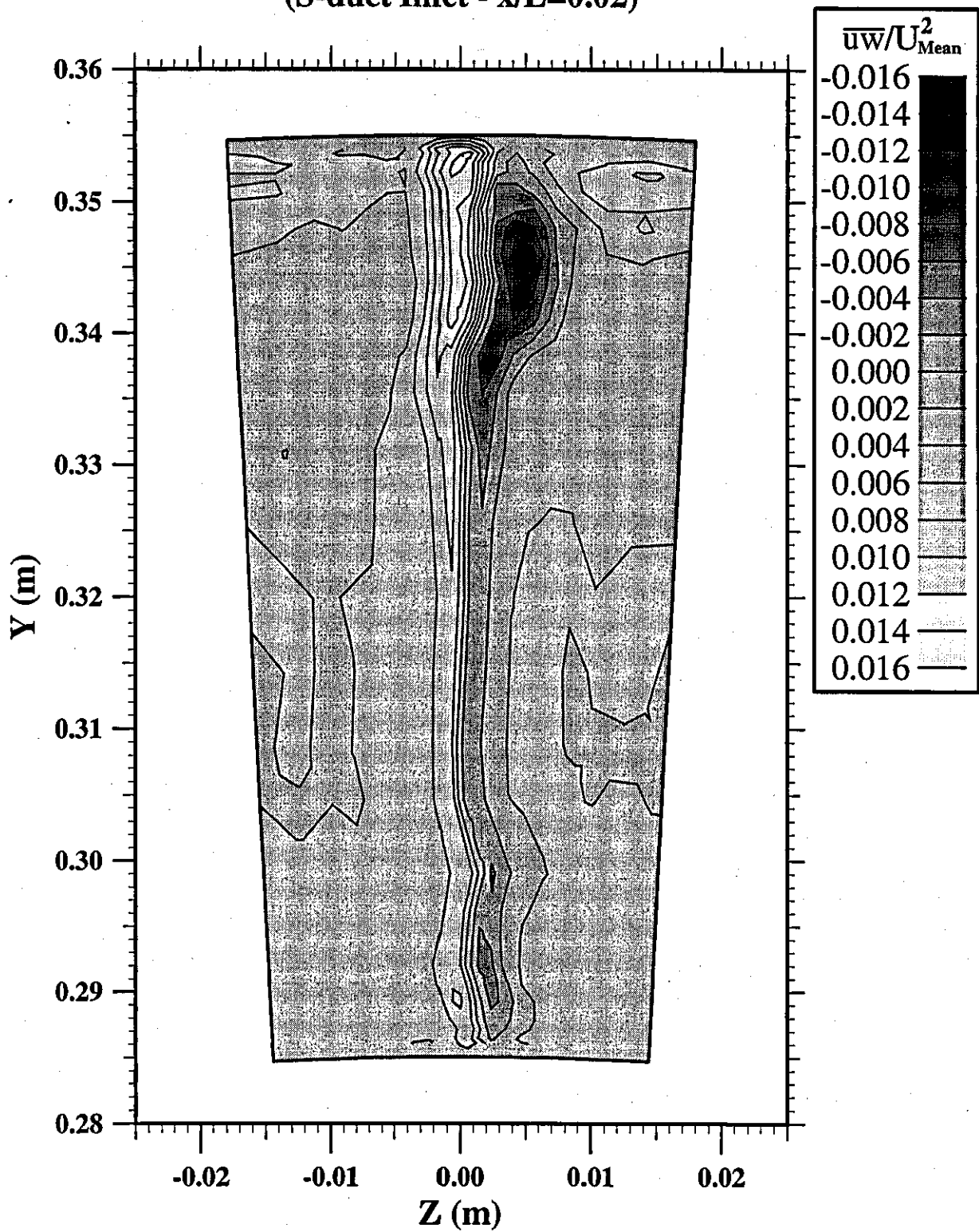


Figure 122

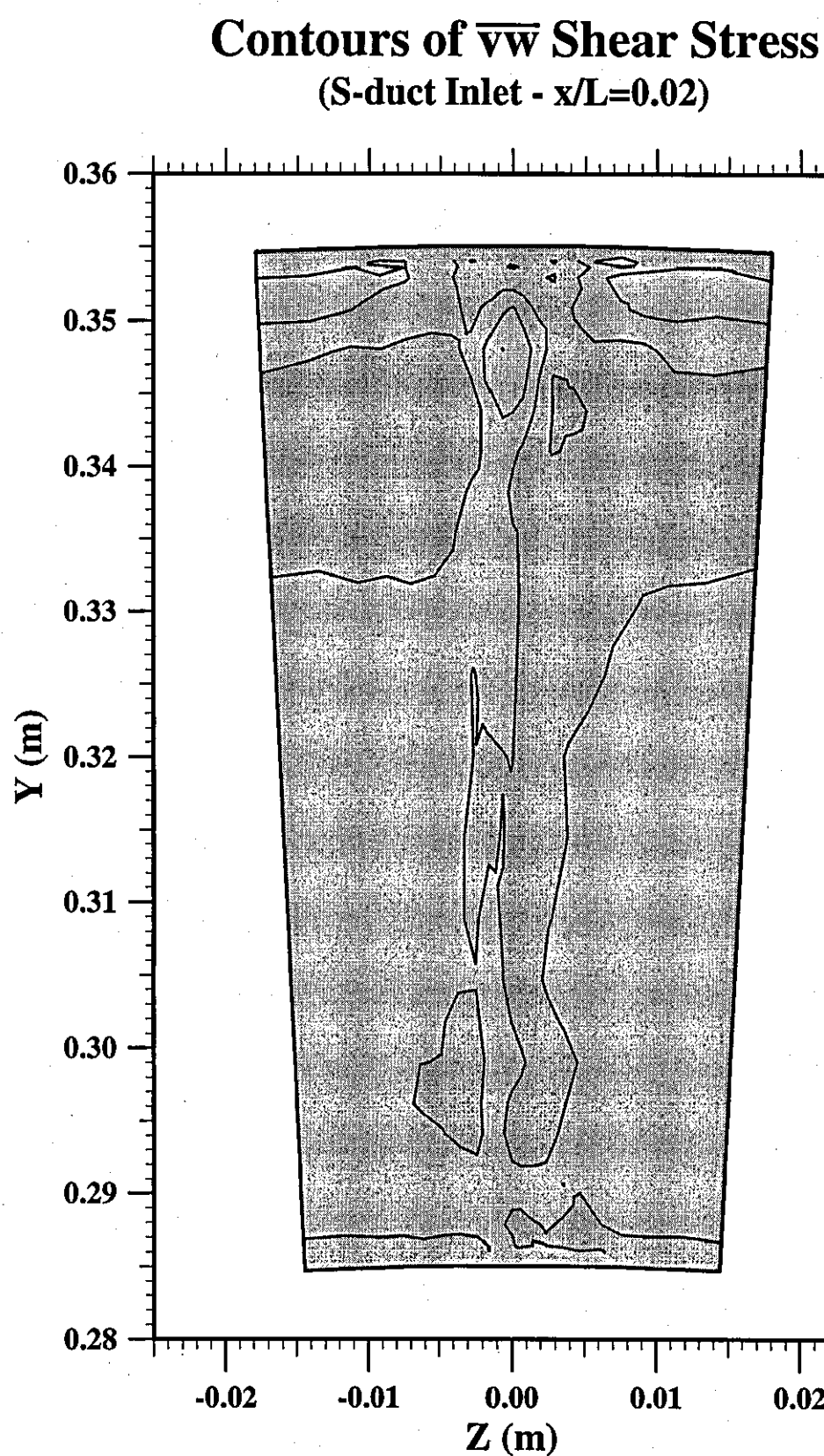
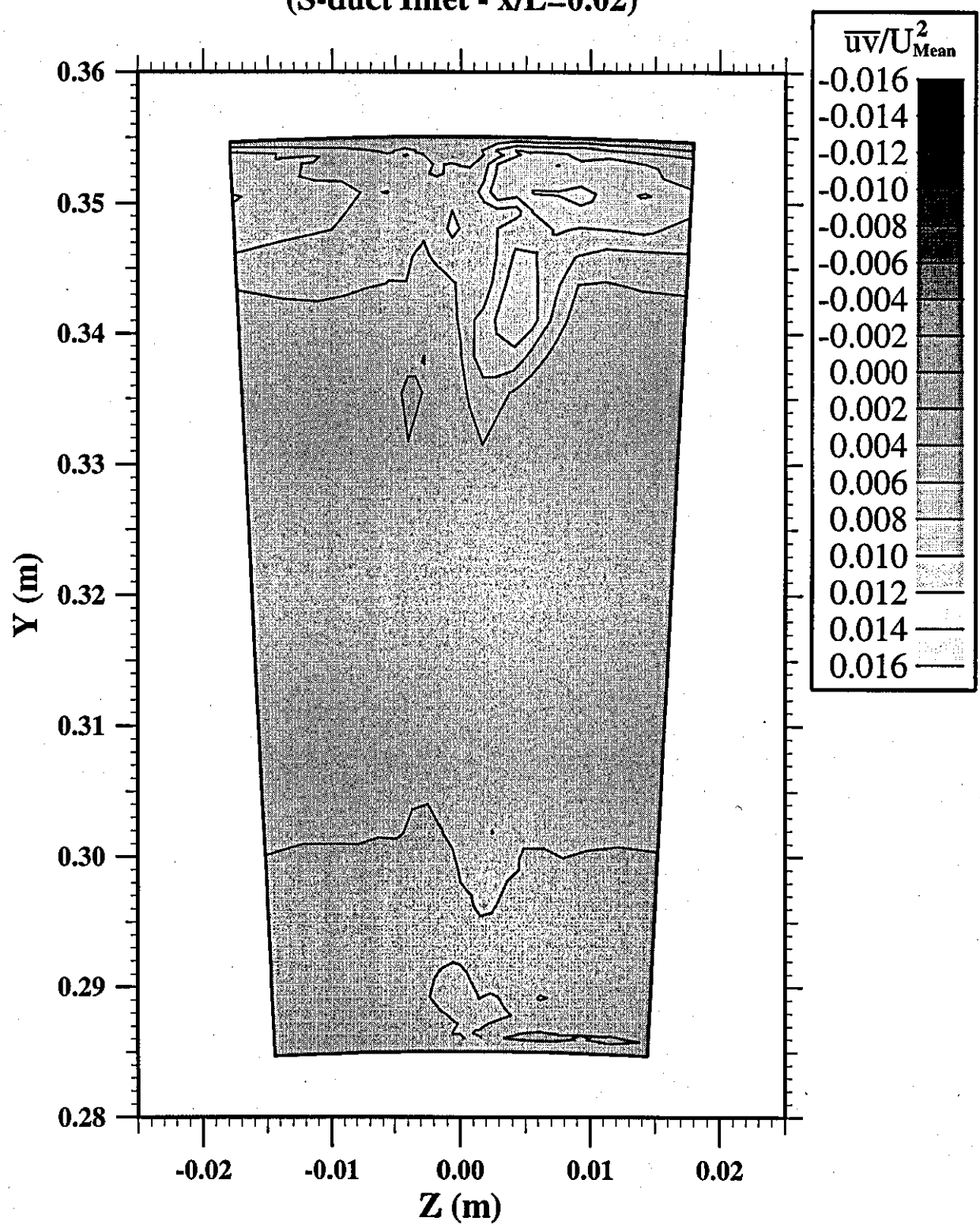


Figure 123

Contours of $\bar{u}\bar{v}$ Shear Stress (S-duct Inlet - $x/L=0.02$)



CFD Calculation Grid

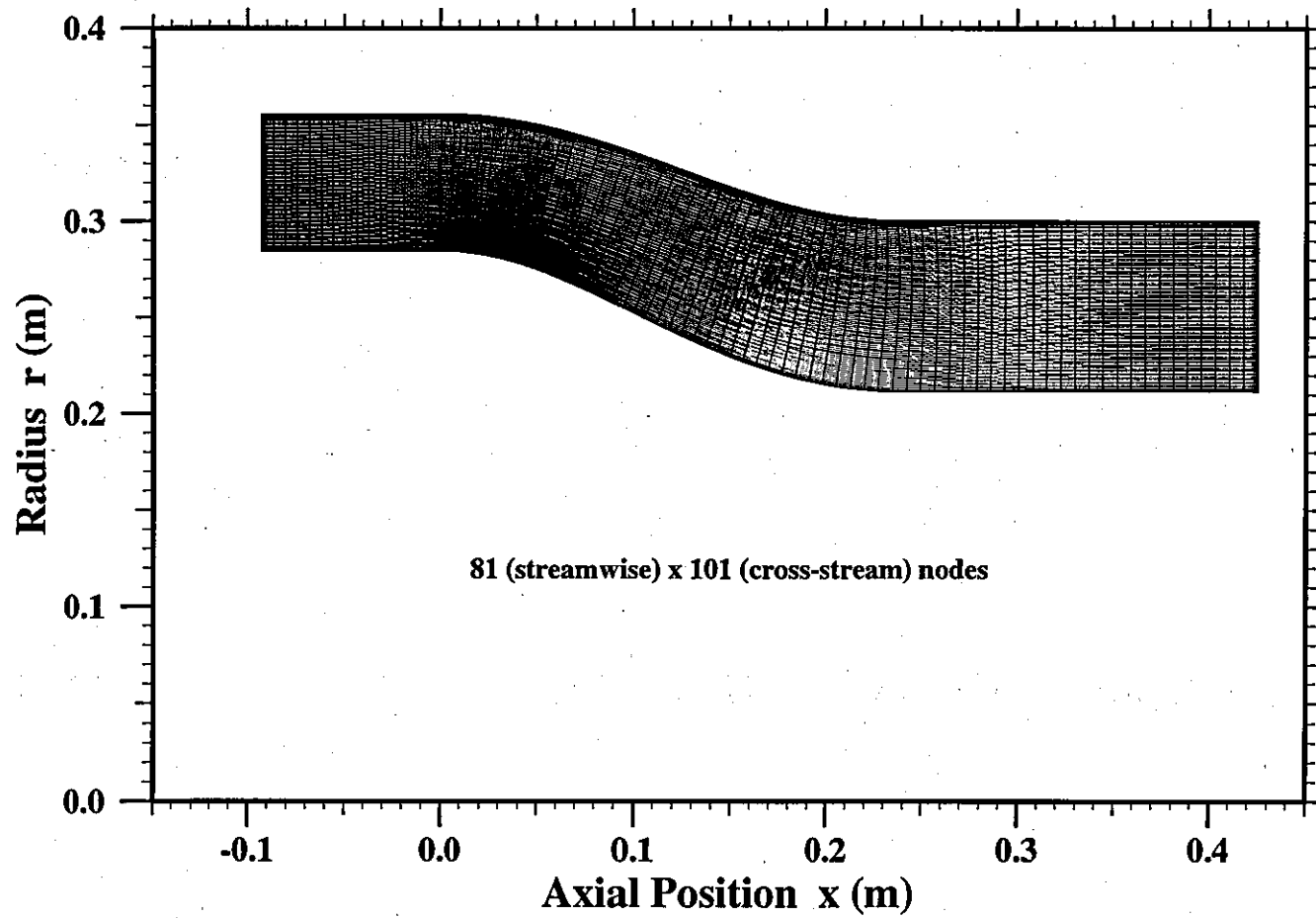


Figure 124

Axial Variation of Displacement Thickness (CFD vs. Experiment)

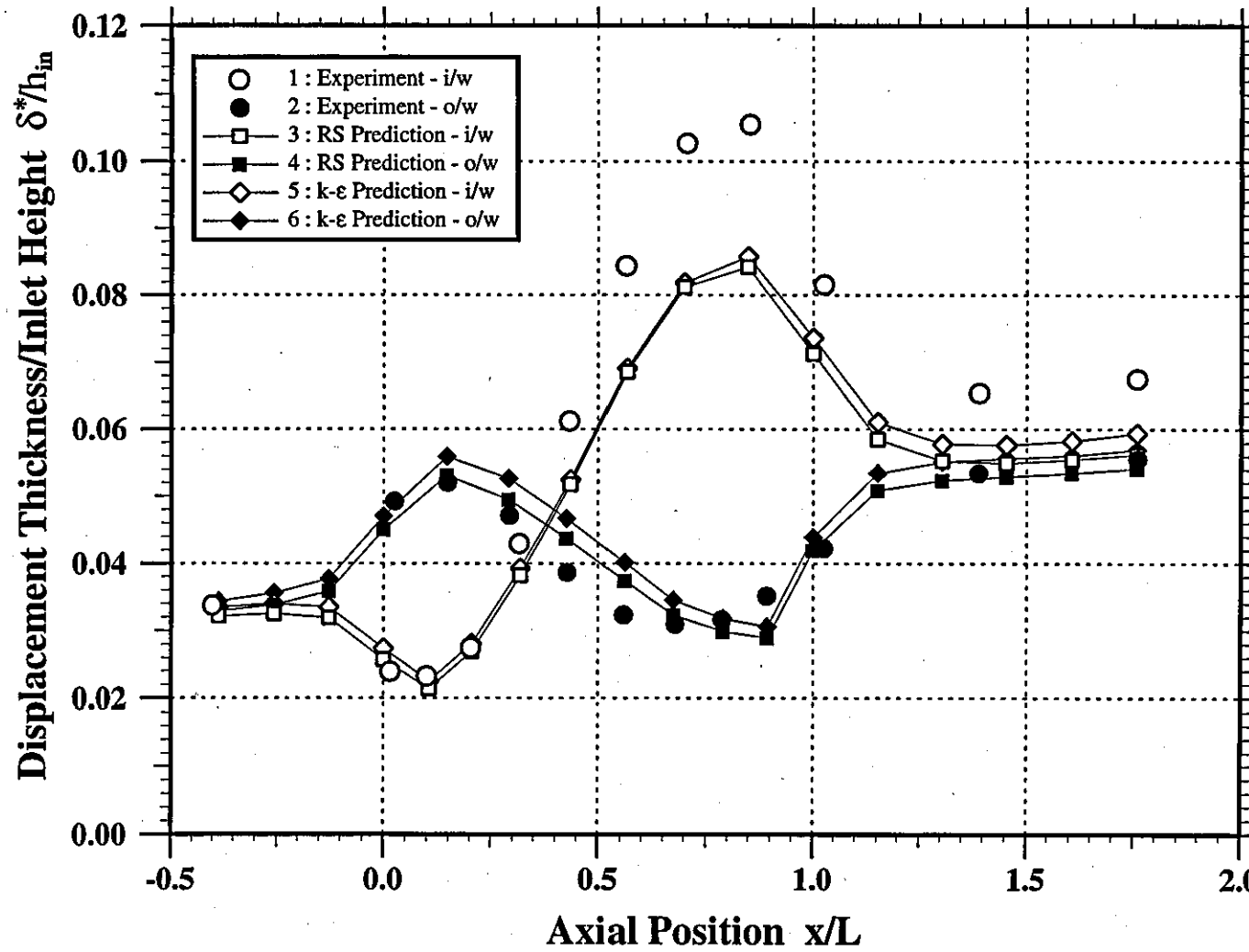


Figure 125

Axial Variation of Momentum Thickness (CFD vs. Experiment)

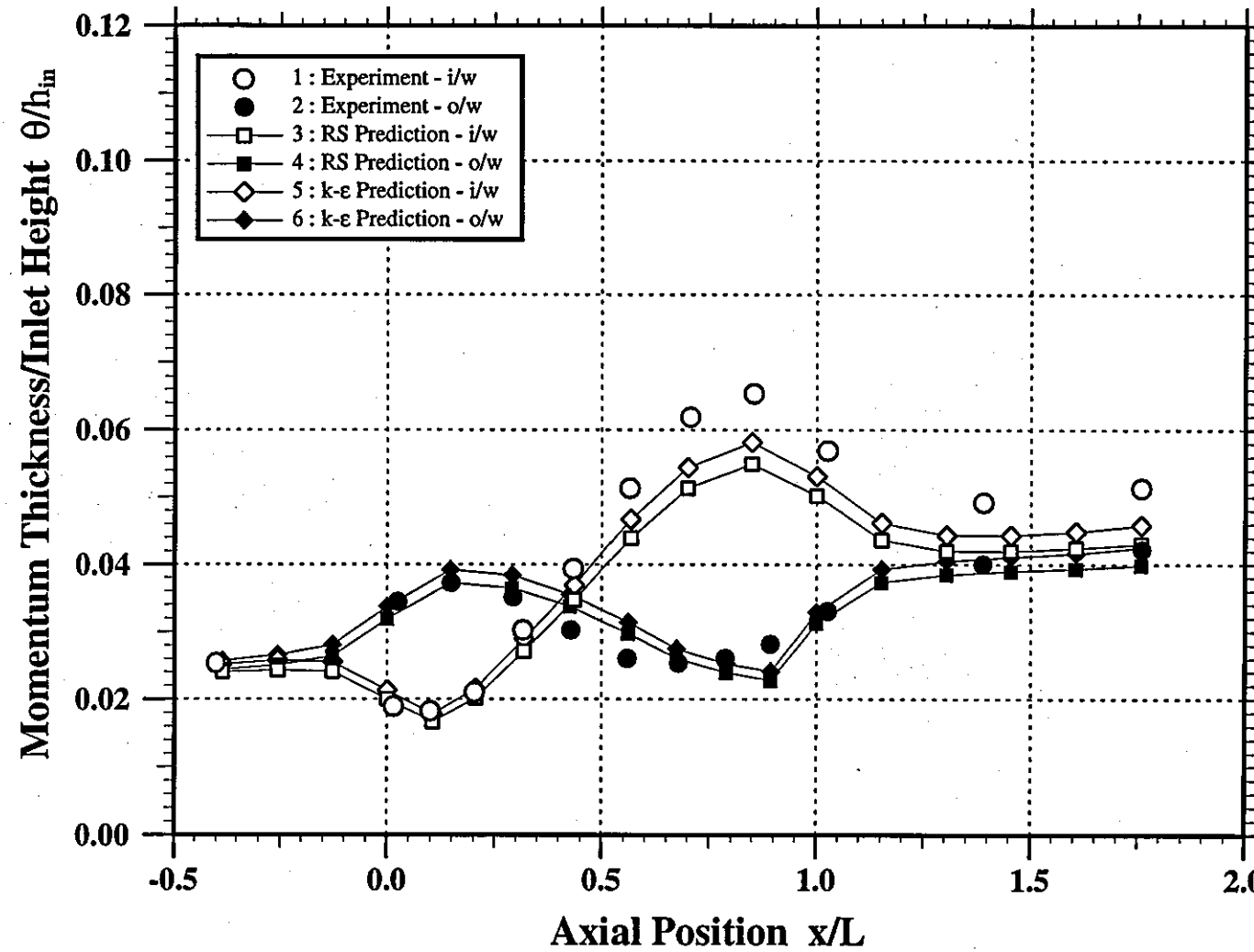


Figure 126

Axial Variation of Boundary Layer Shape Parameter (CFD vs. Experiment)

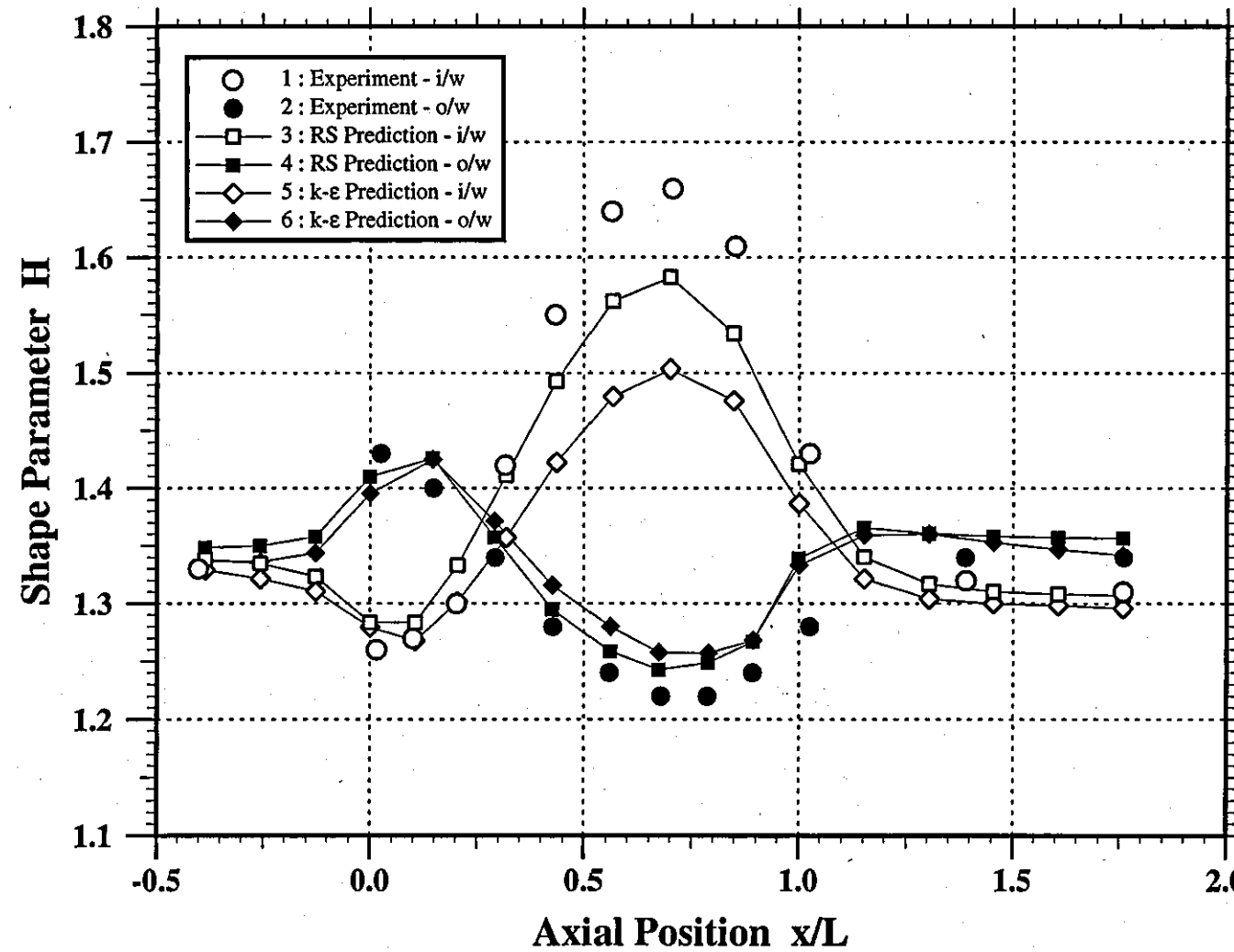


Figure 127

Axial Variation of Friction Velocity (CFD vs. Experiment)

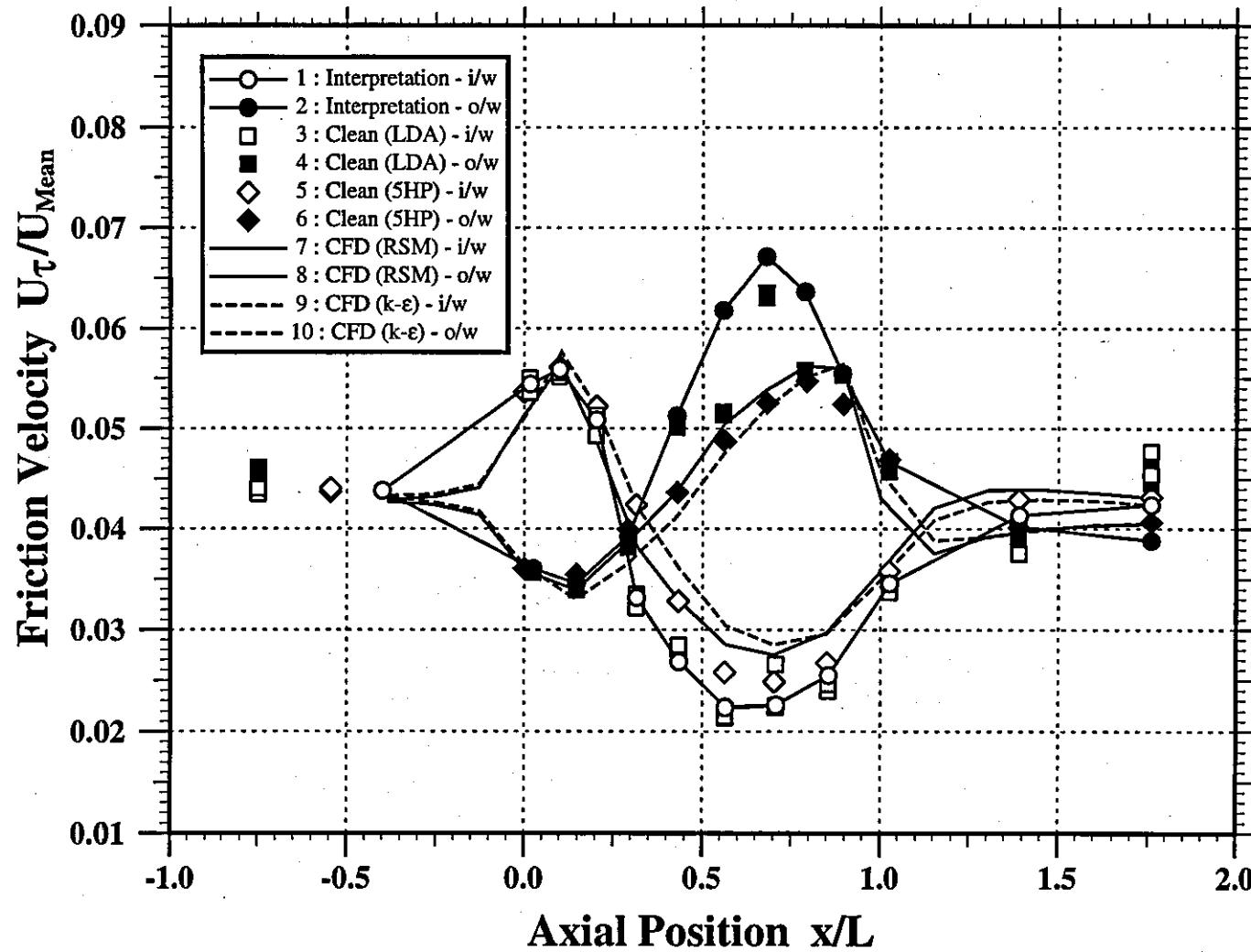


Figure 128

Figure 129

Comparison of Measured and Predicted Streamwise Velocity Profiles

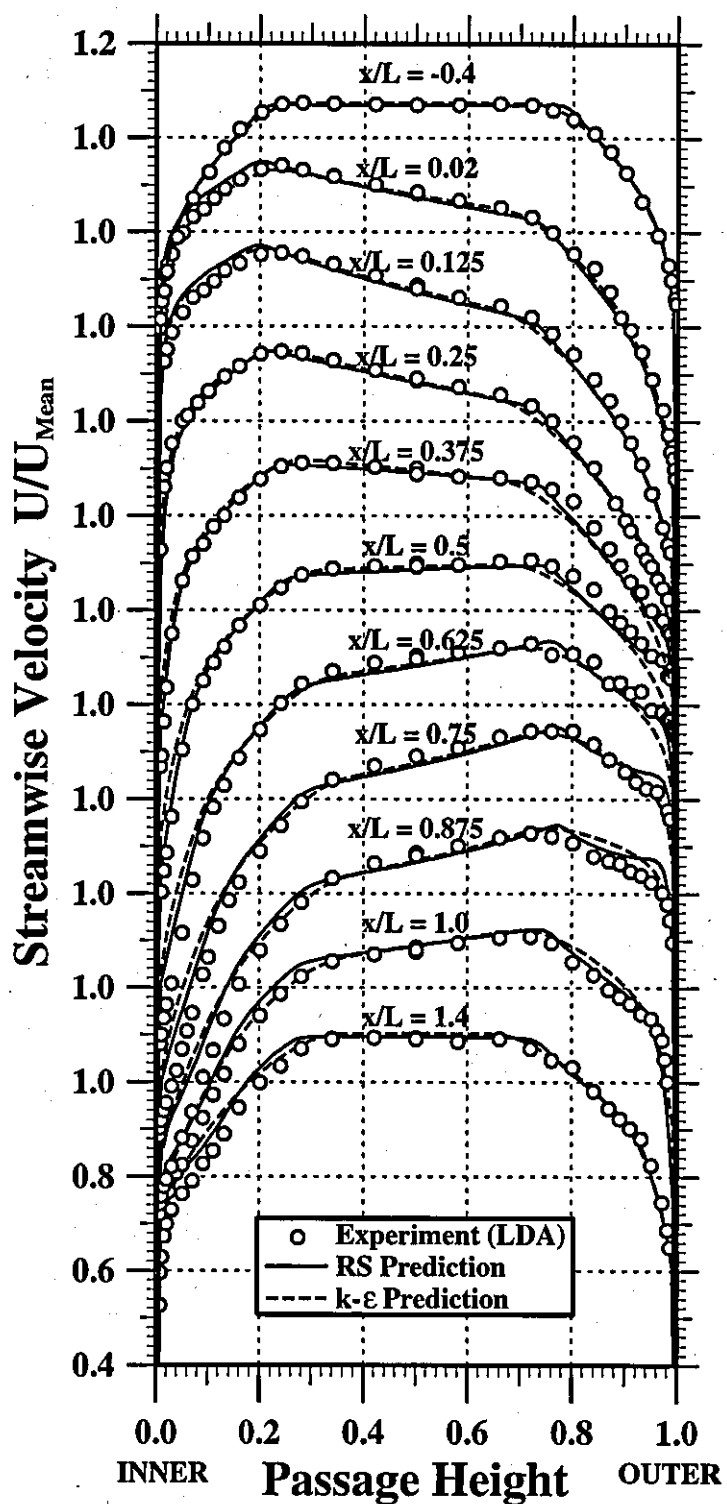


Figure 130

Comparison of Measured and Predicted Streamwise Velocity Profiles

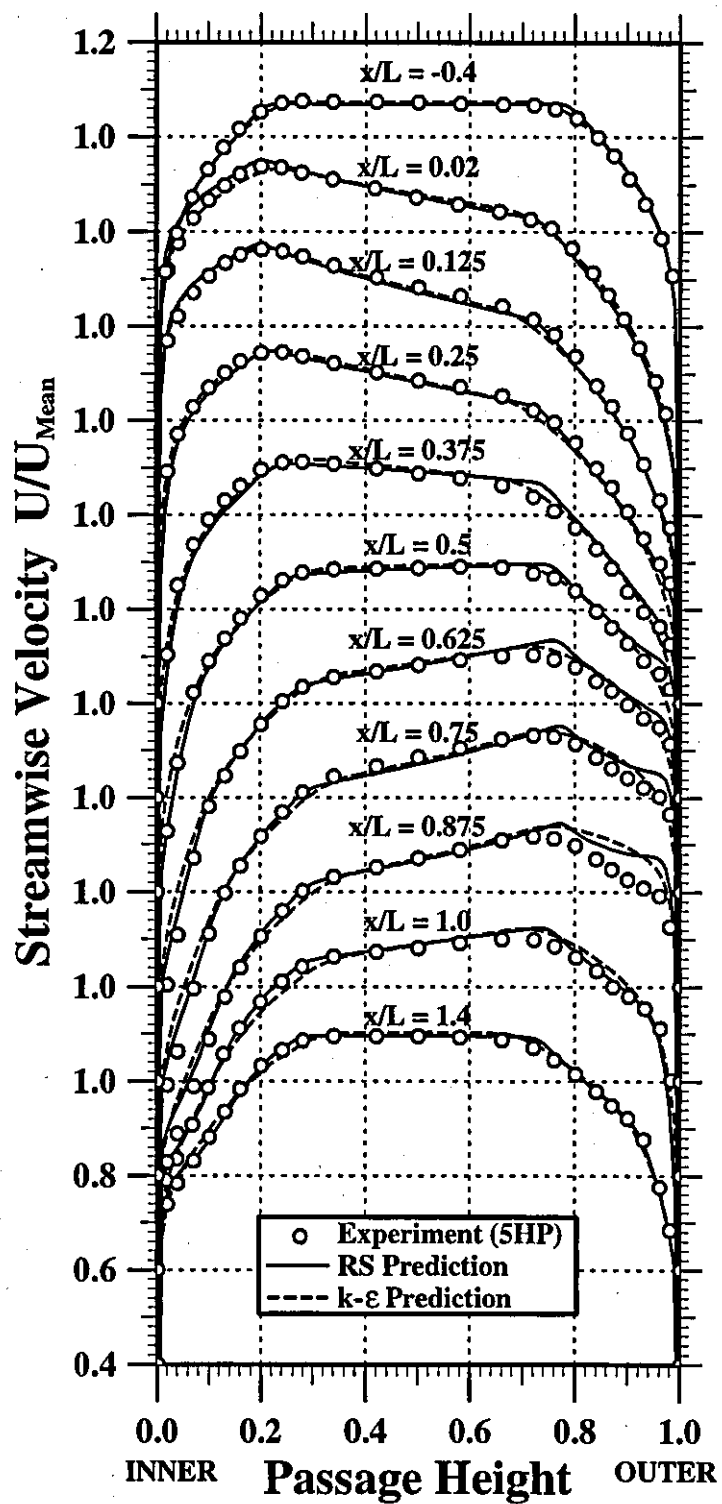


Figure 131

Comparison of Measured and Predicted Radial Velocity Profiles

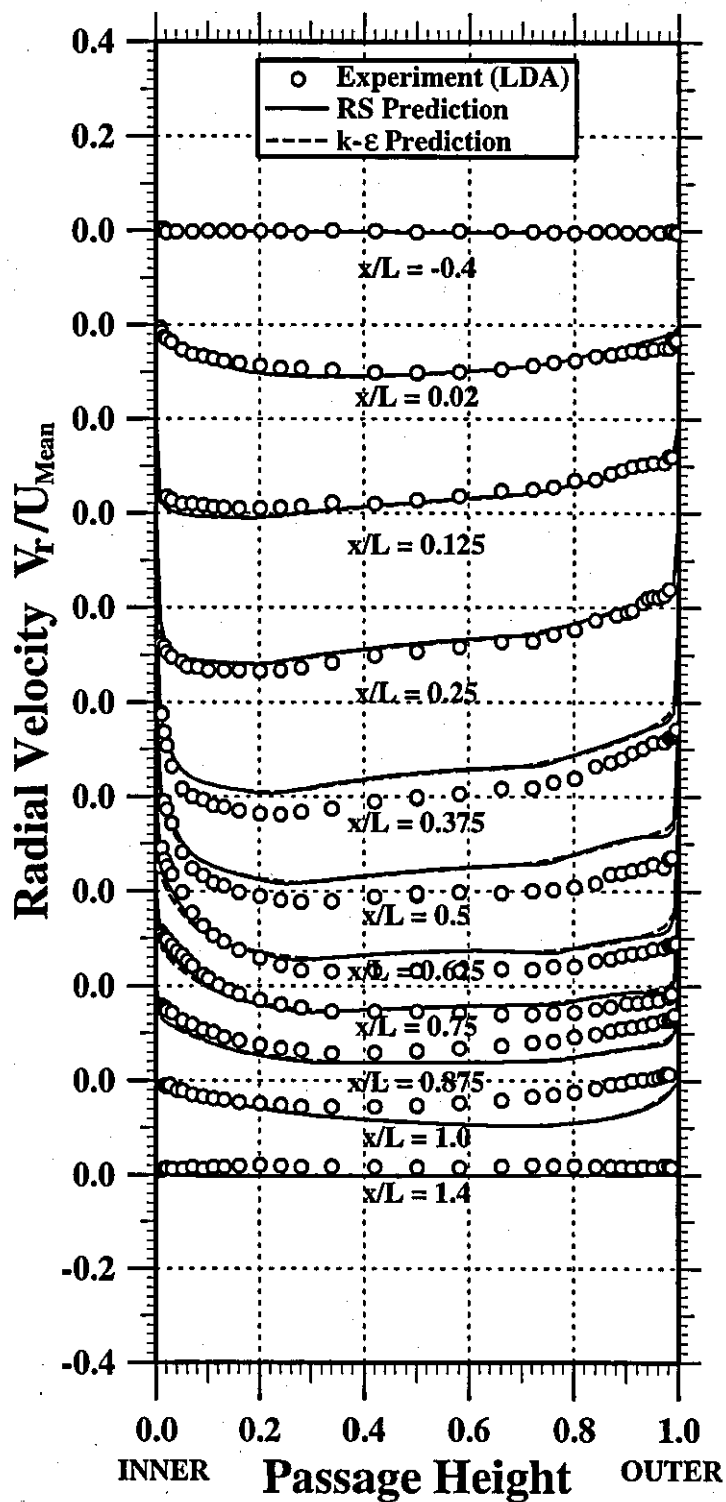


Figure 132

Comparison of Measured and Predicted Radial Velocity Profiles

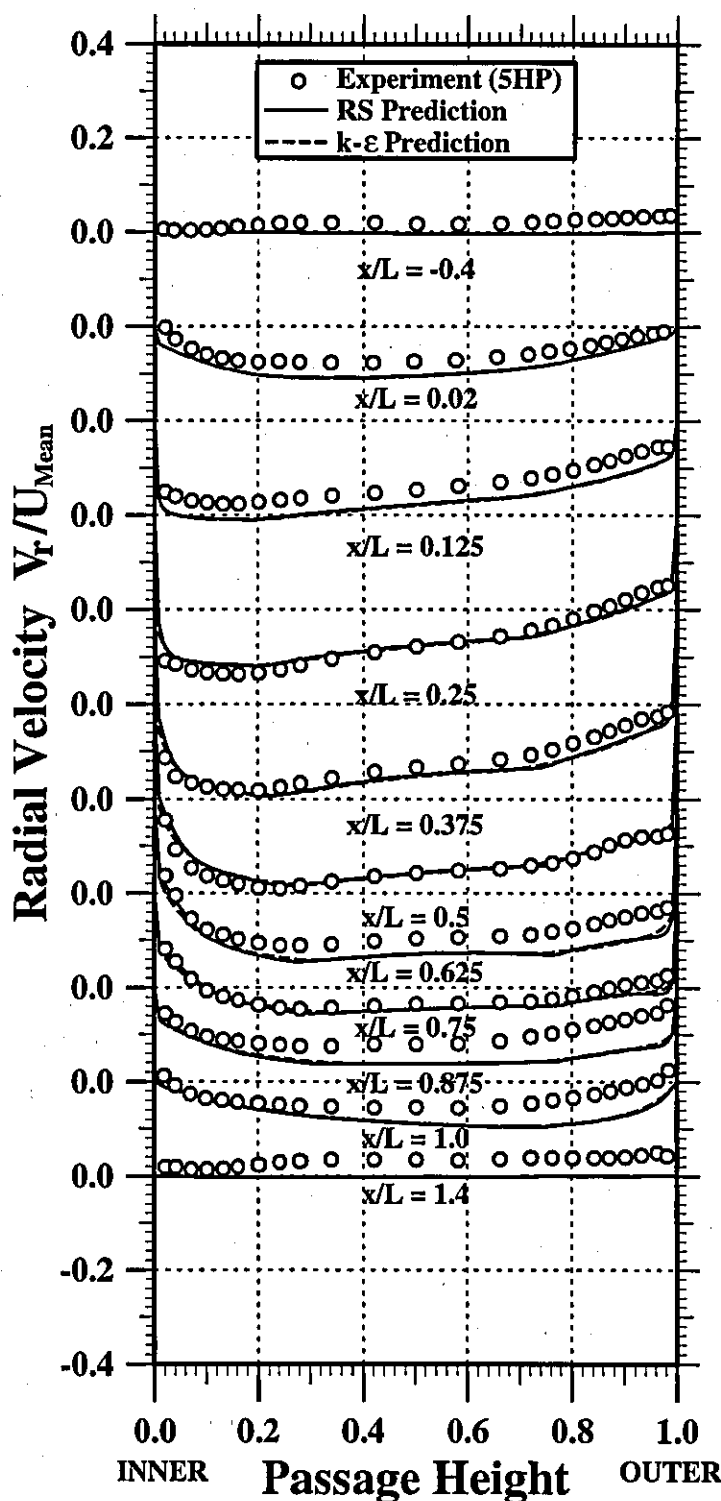


Figure 155

Comparison of Measured and Predicted Streamwise Normal Stress Profiles

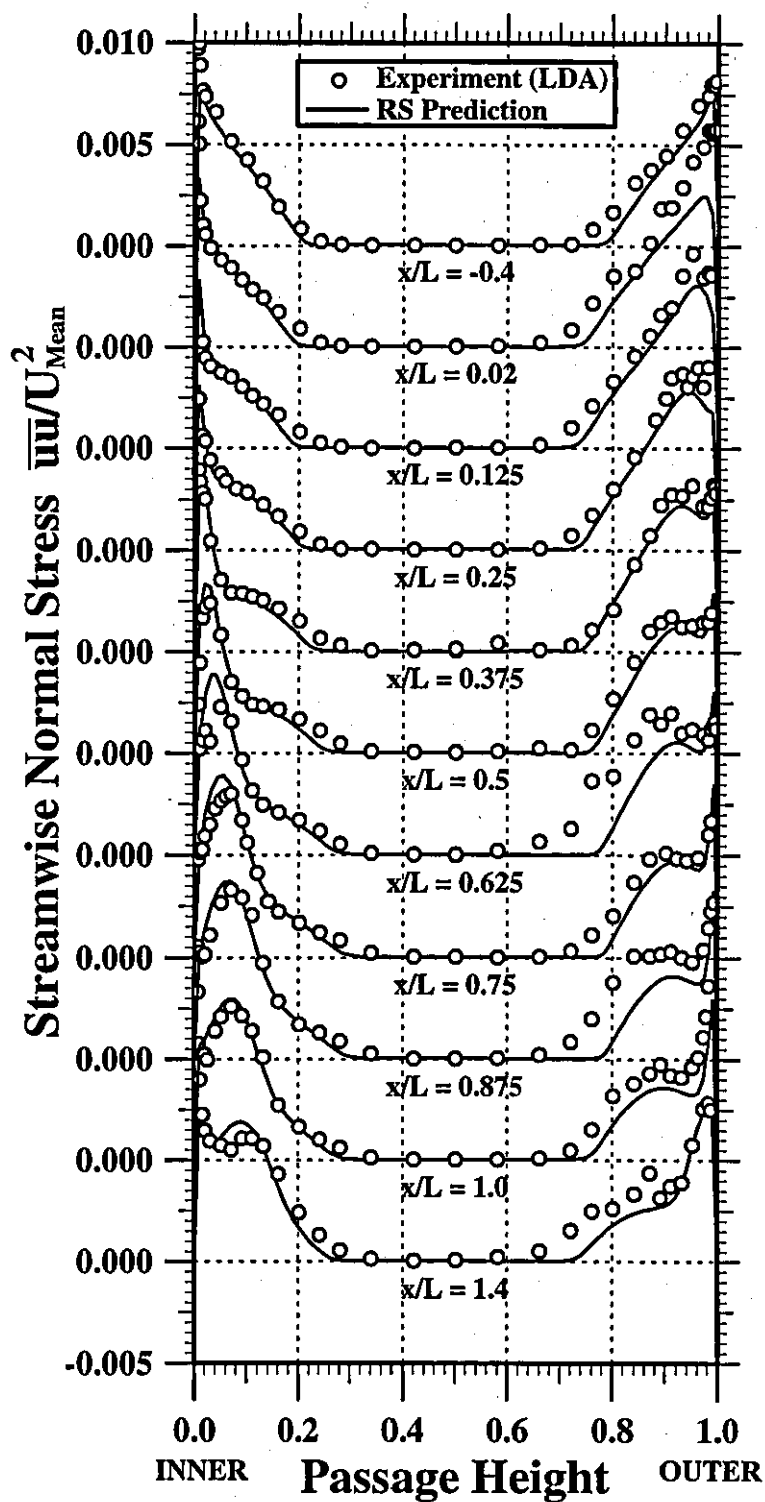


Figure 134

Comparison of Measured and Predicted Cross-stream Normal Stress Profiles

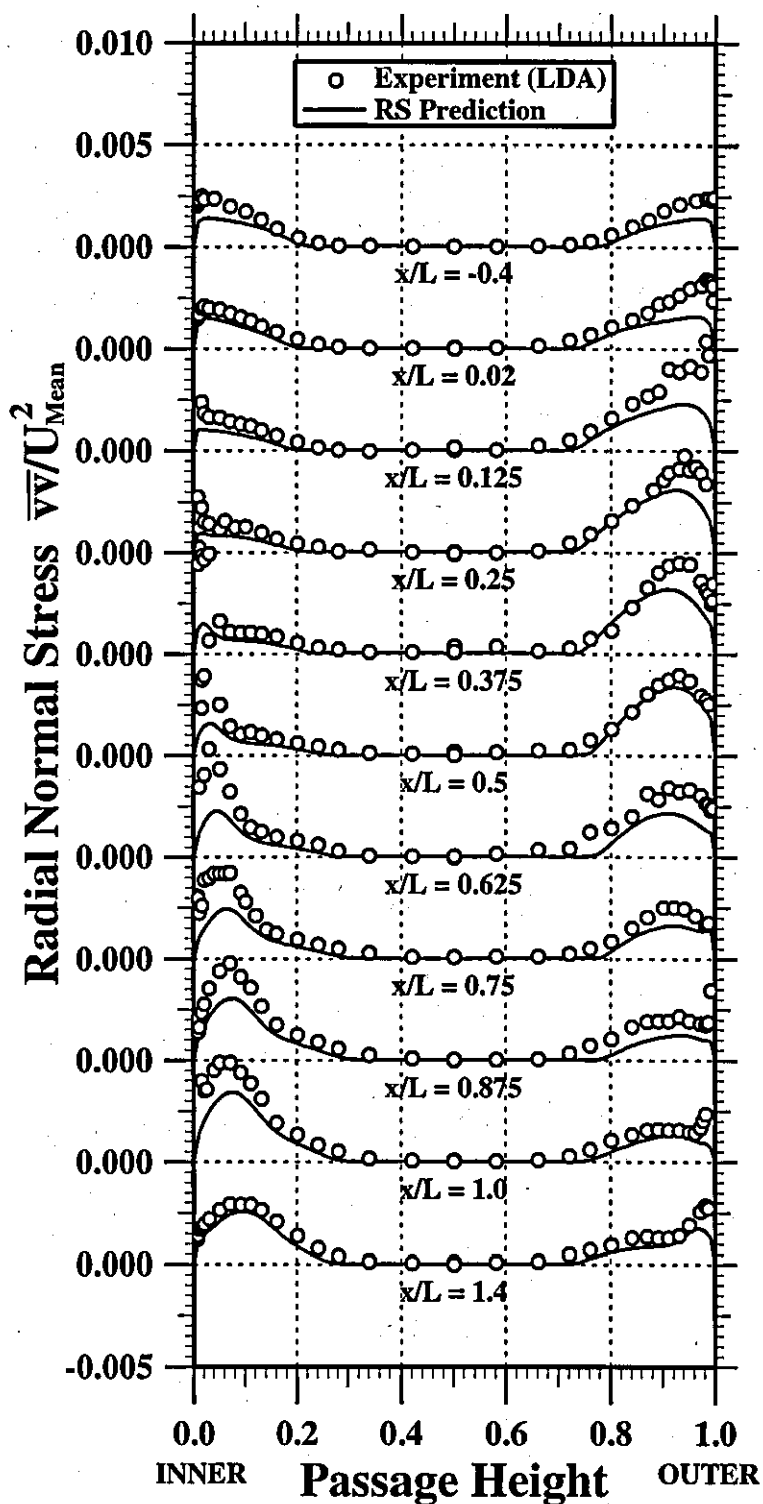


Figure 135

Comparison of Measured and Predicted Circumferential Normal Stress Profiles

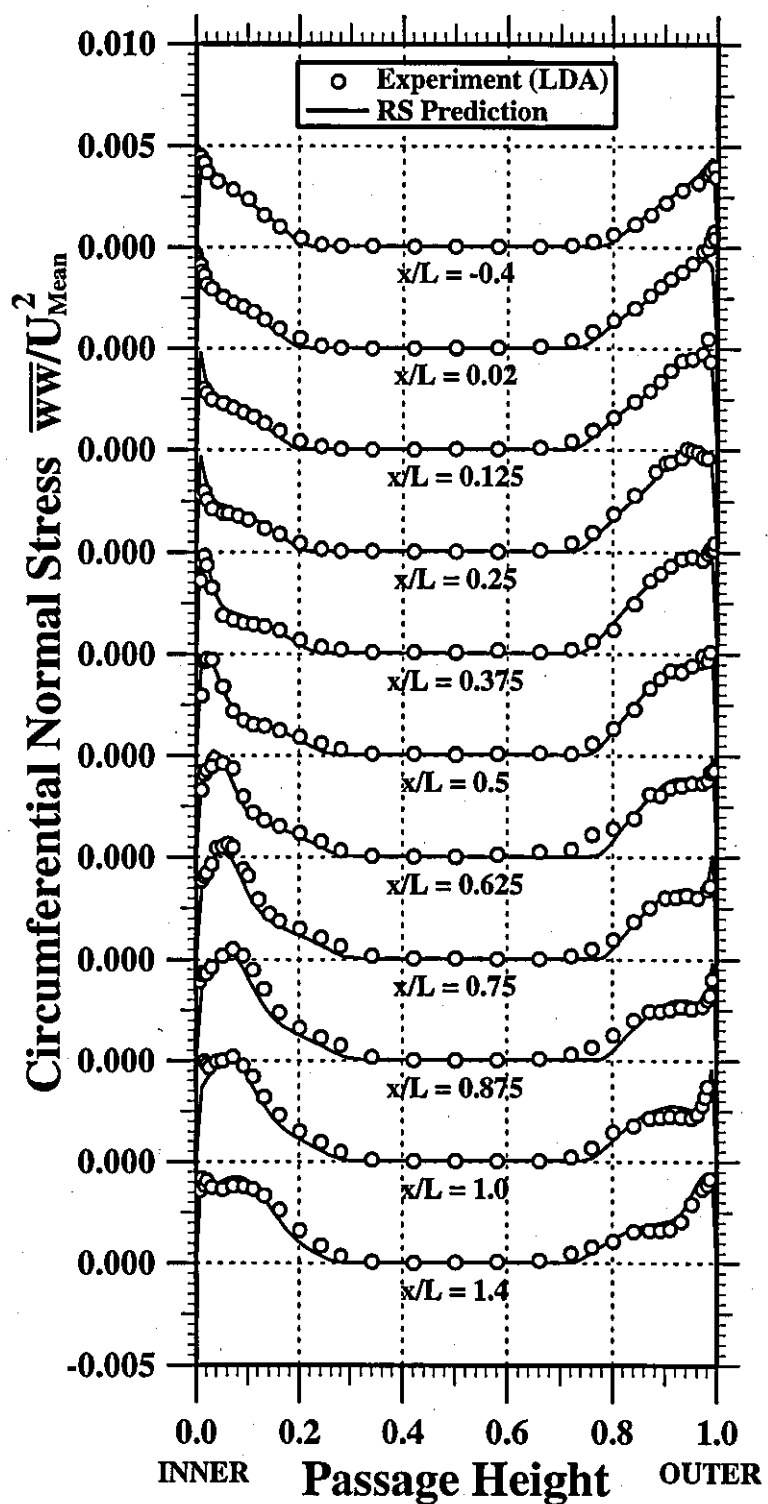


Figure 136

Comparison of Measured and Predicted Reynolds Shear Stress Profiles

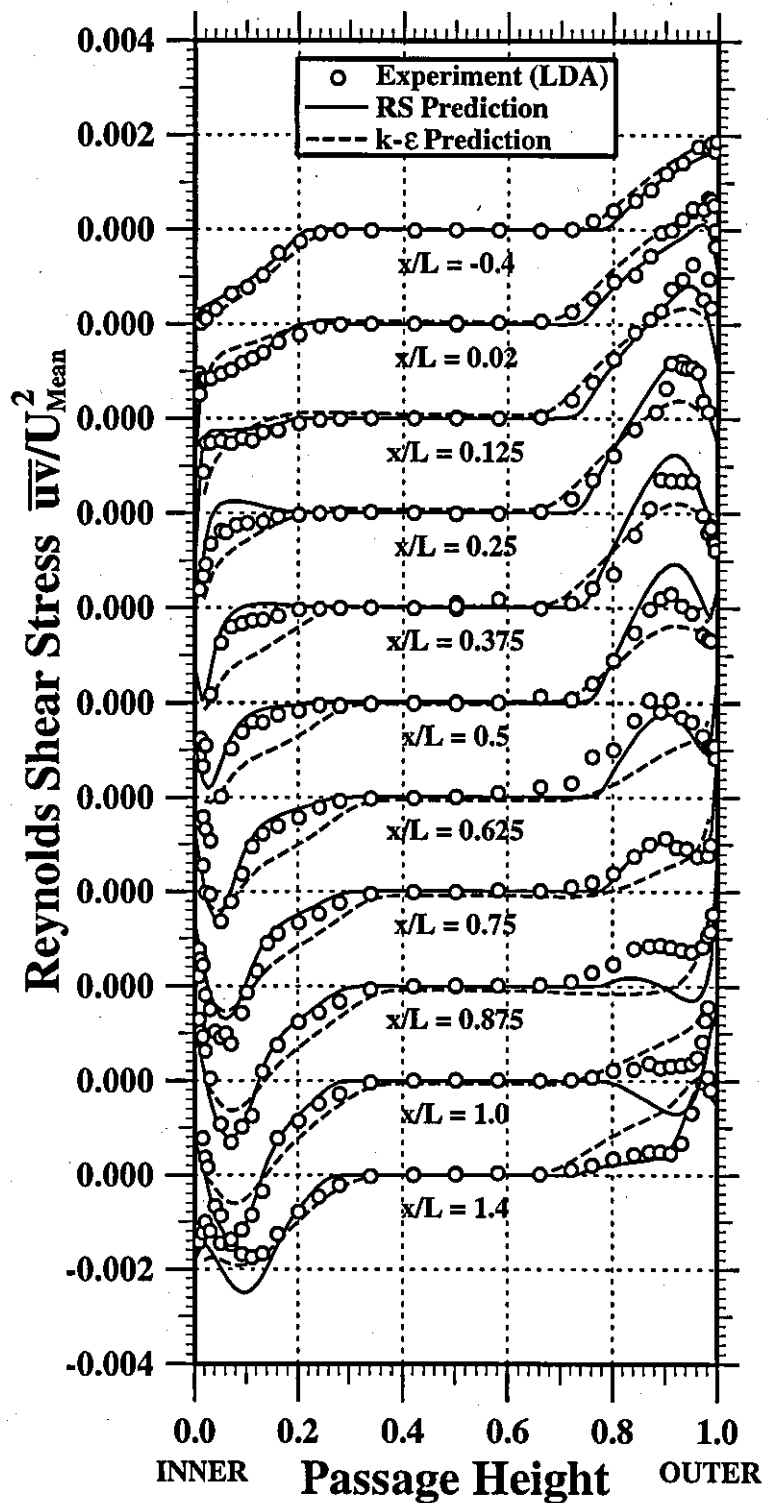


Figure 137

Comparison of Measured and Predicted Turbulent Kinetic Energy Profiles

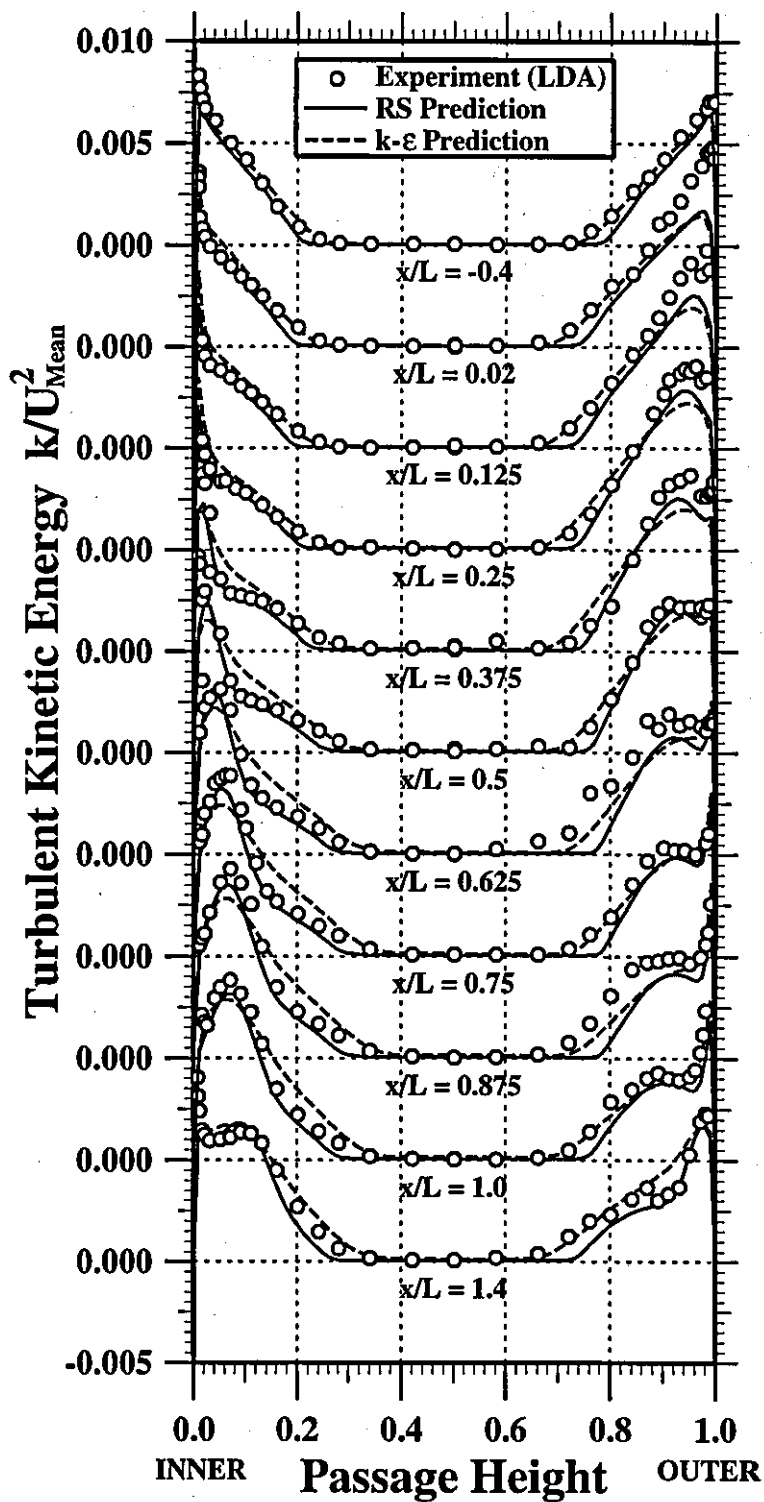


Figure 138

Comparison of Predicted Dissipation Rate of Turbulent Kinetic Energy Profiles

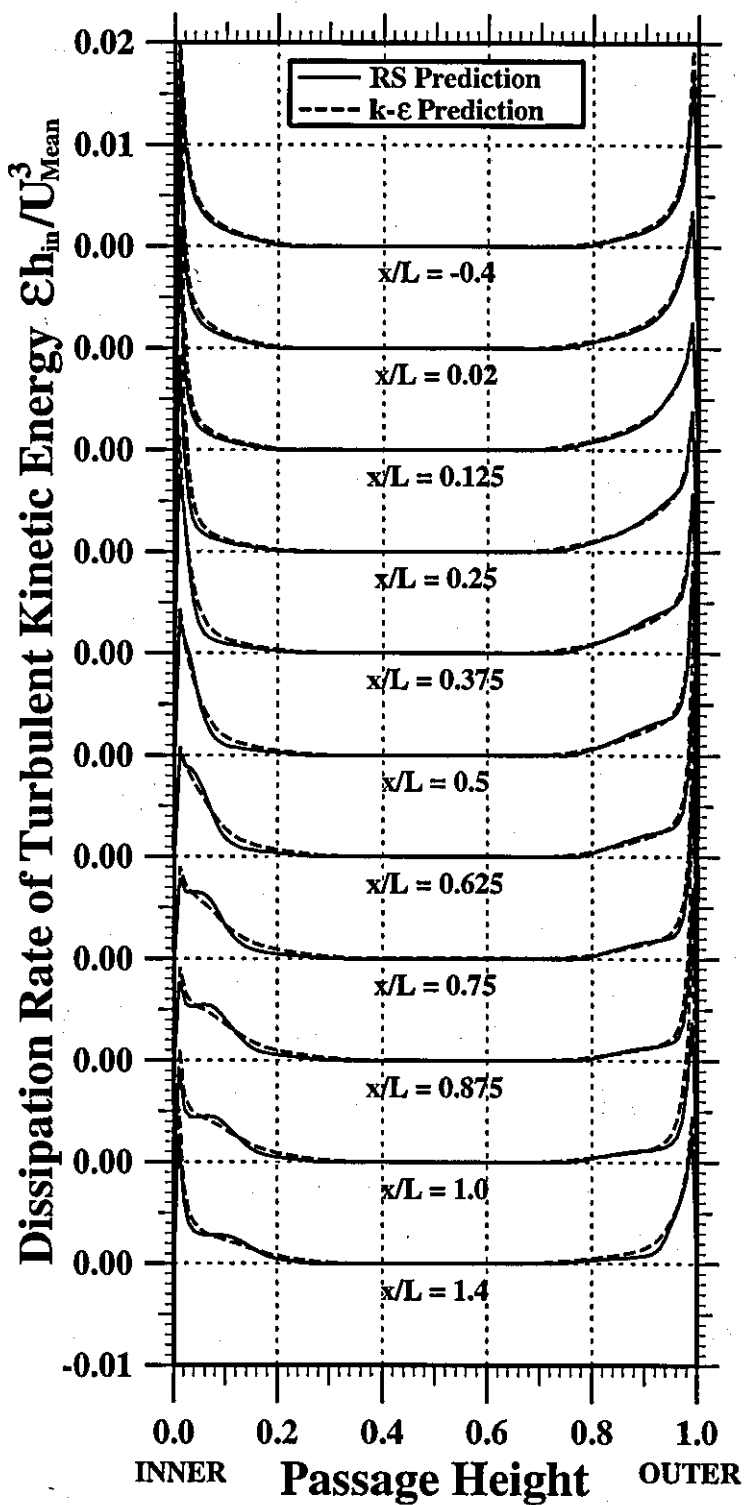


Figure 139

Comparison of Measured and Predicted Normal Stress Ratio ($\bar{v}v/\bar{u}u$)

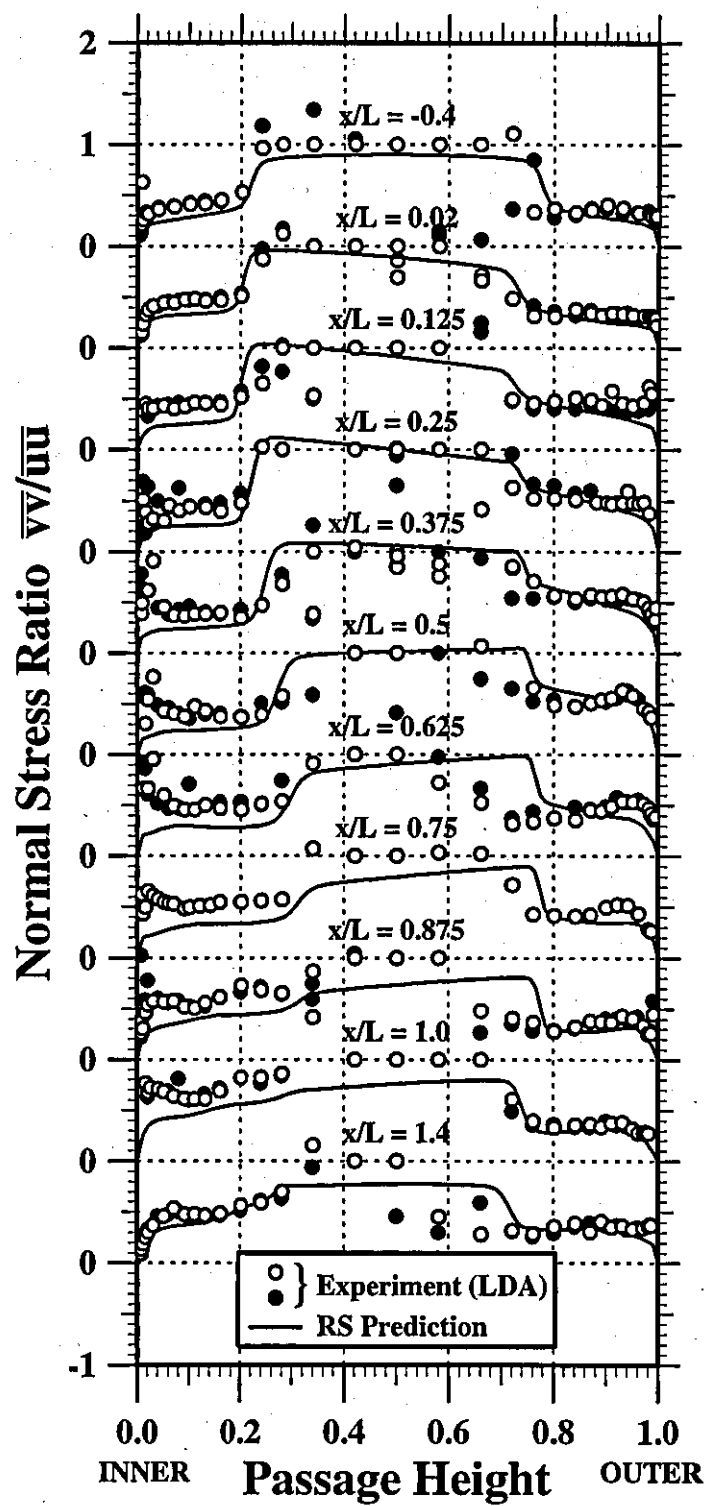
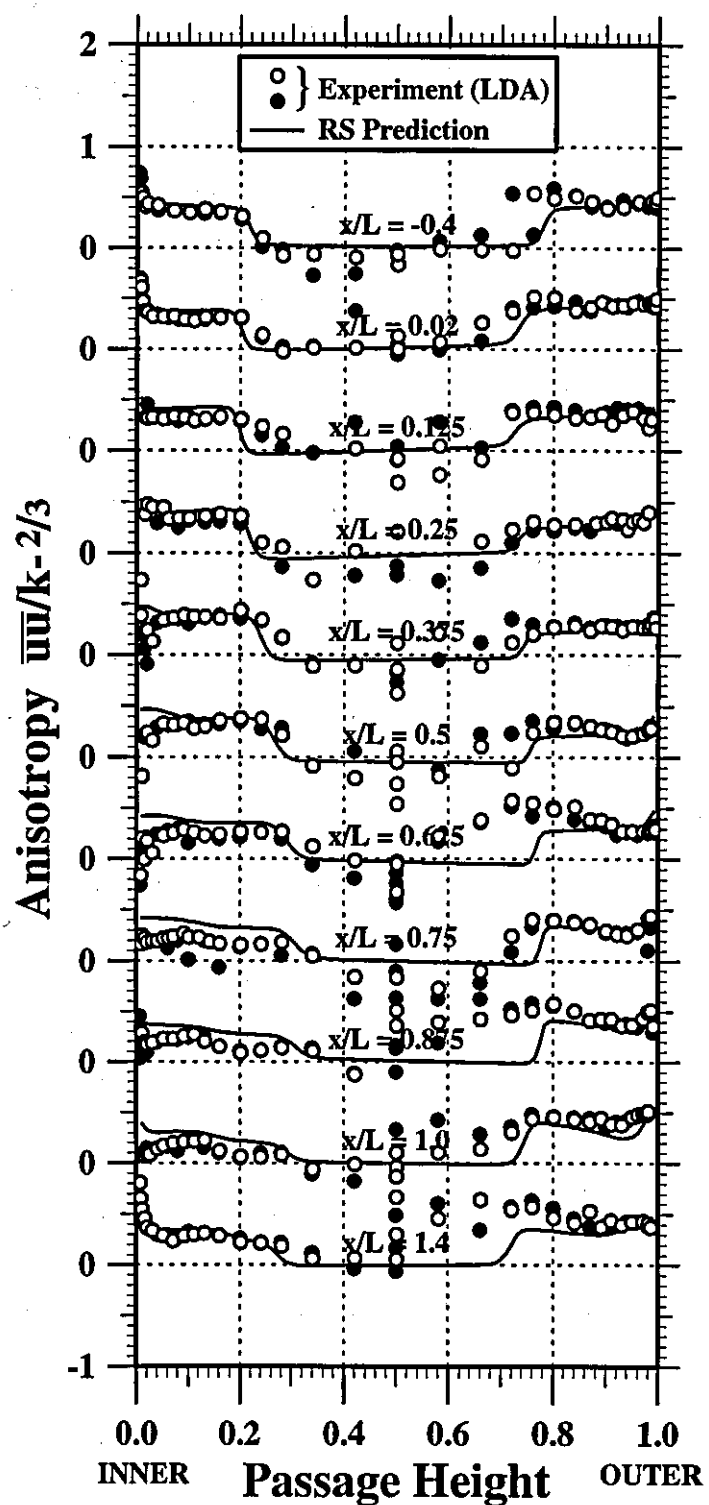


Figure 140

Comparison of Measured and Predicted Anisotropy Tensor Component a_{11}



Comparison of Measured and Predicted Anisotropy Tensor Component a_{22}

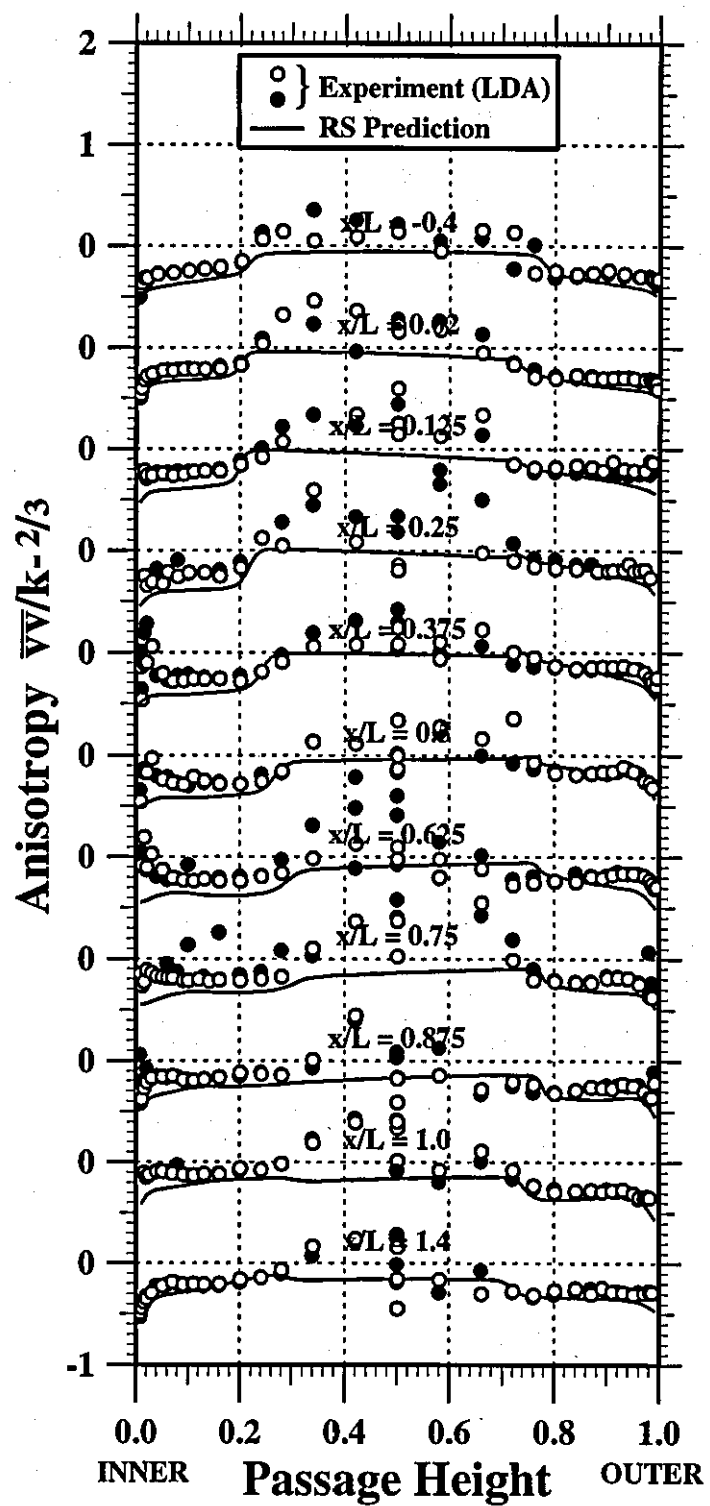


Figure 142

Comparison of Measured and Predicted Anisotropy Tensor Component a_{33}

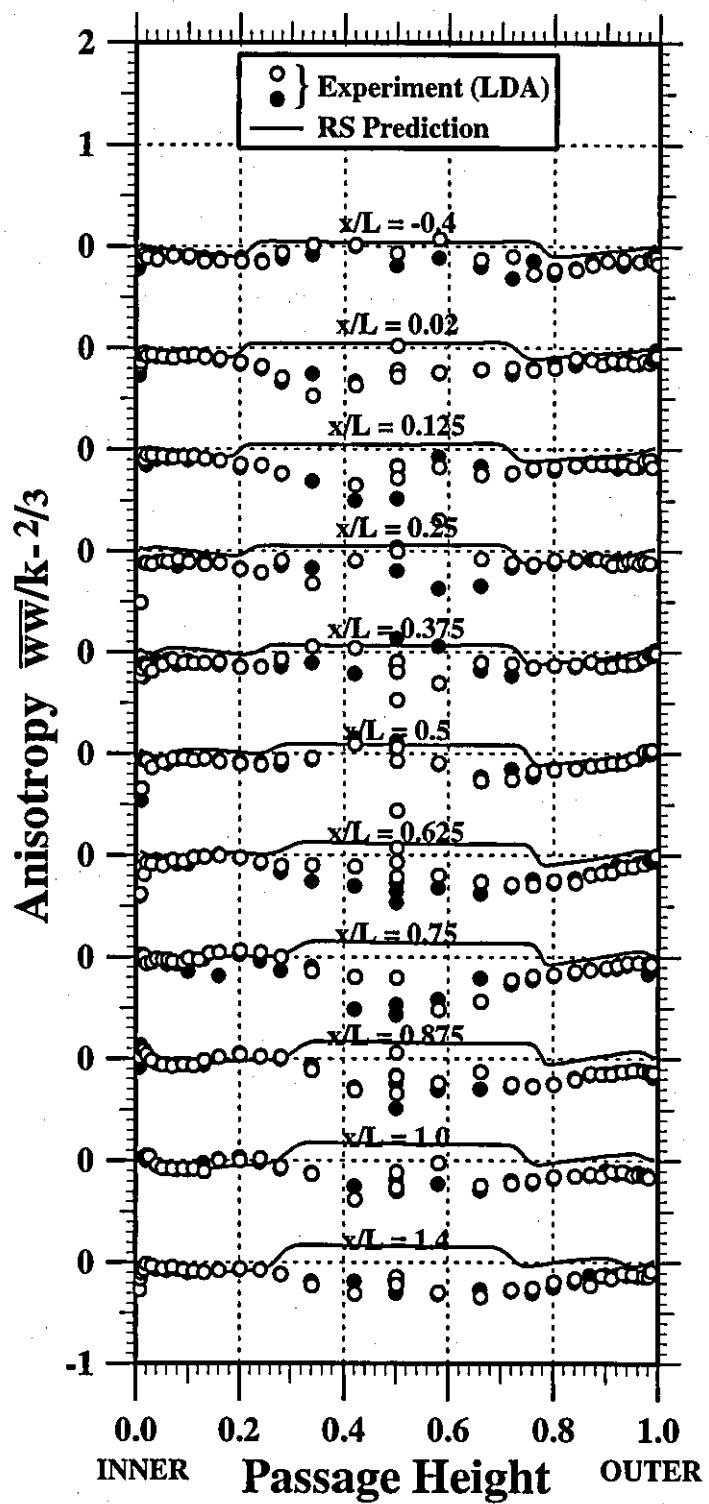


Figure 143

Comparison of Measured and Predicted Anisotropy Tensor Component a_{12}

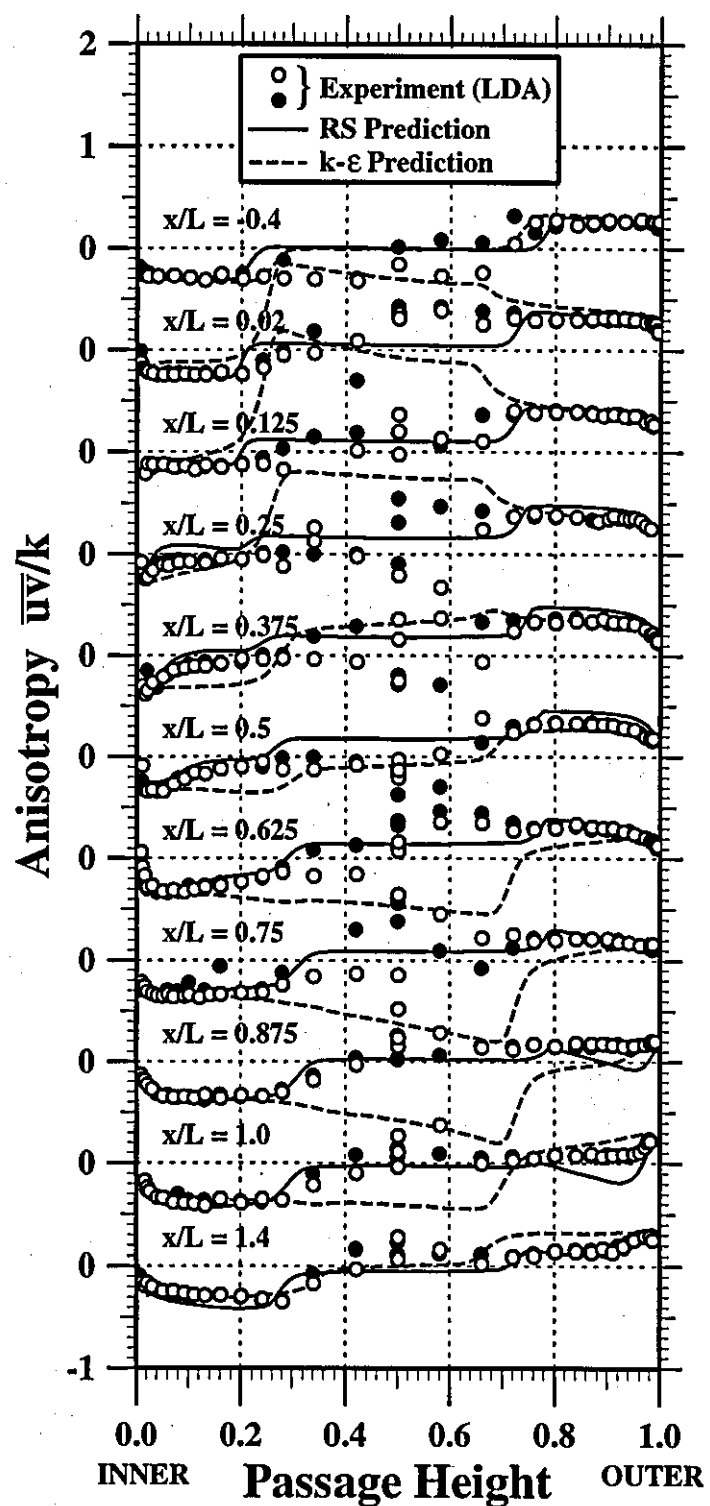
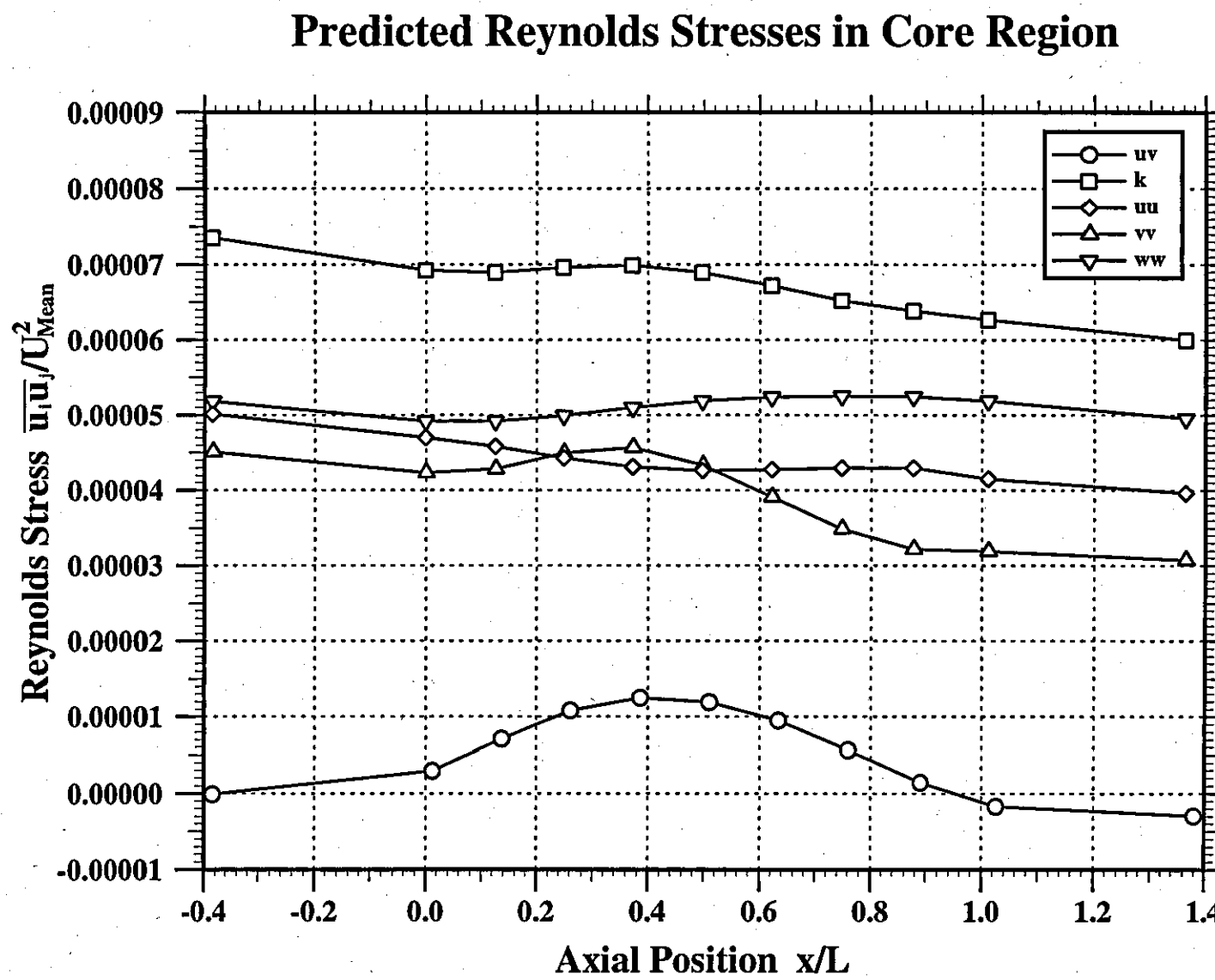


Figure 144



Predicted Turbulent Kinetic Energy in Core Region

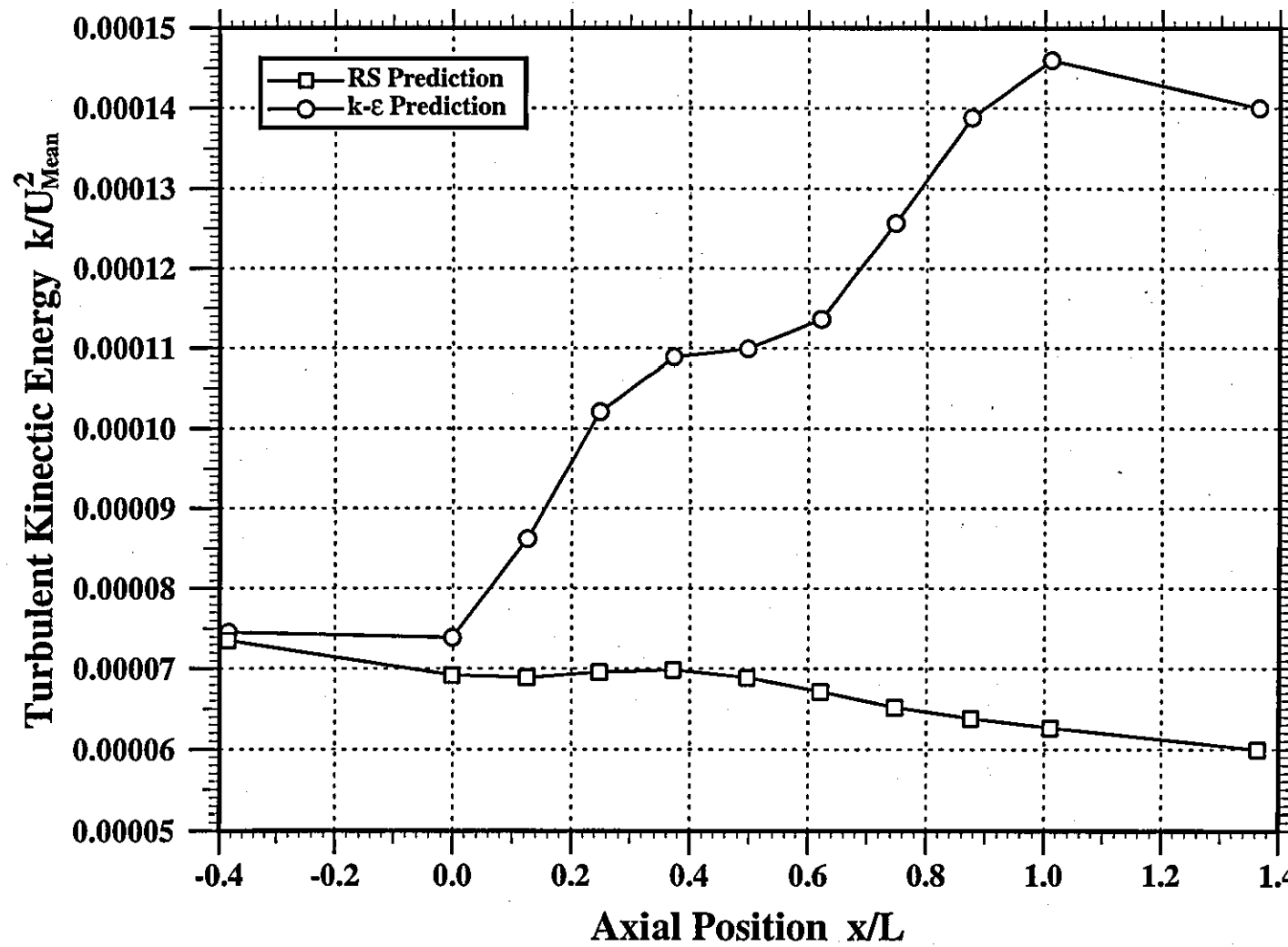


Figure 145

Predicted Shear Stress in Core Region

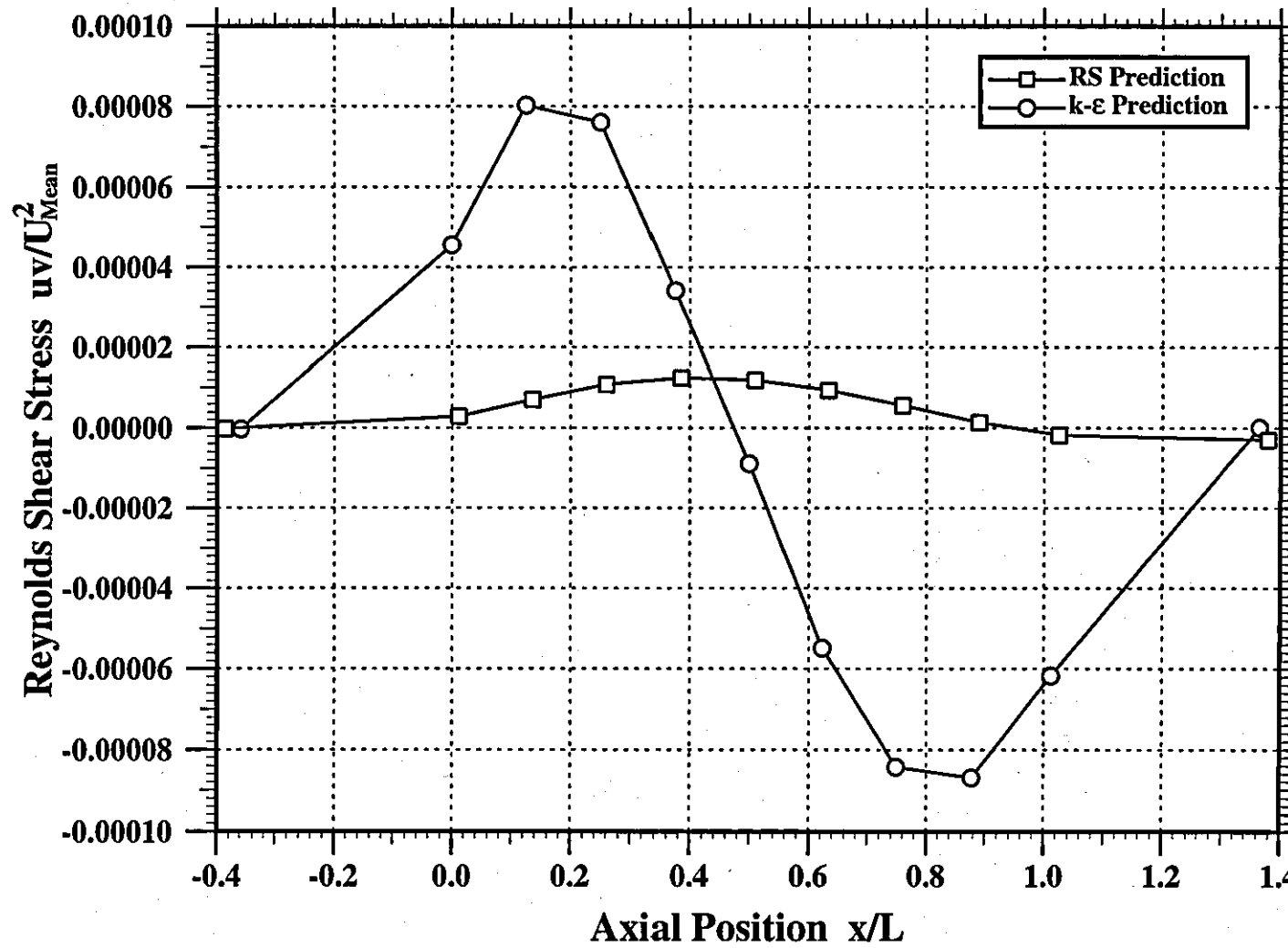
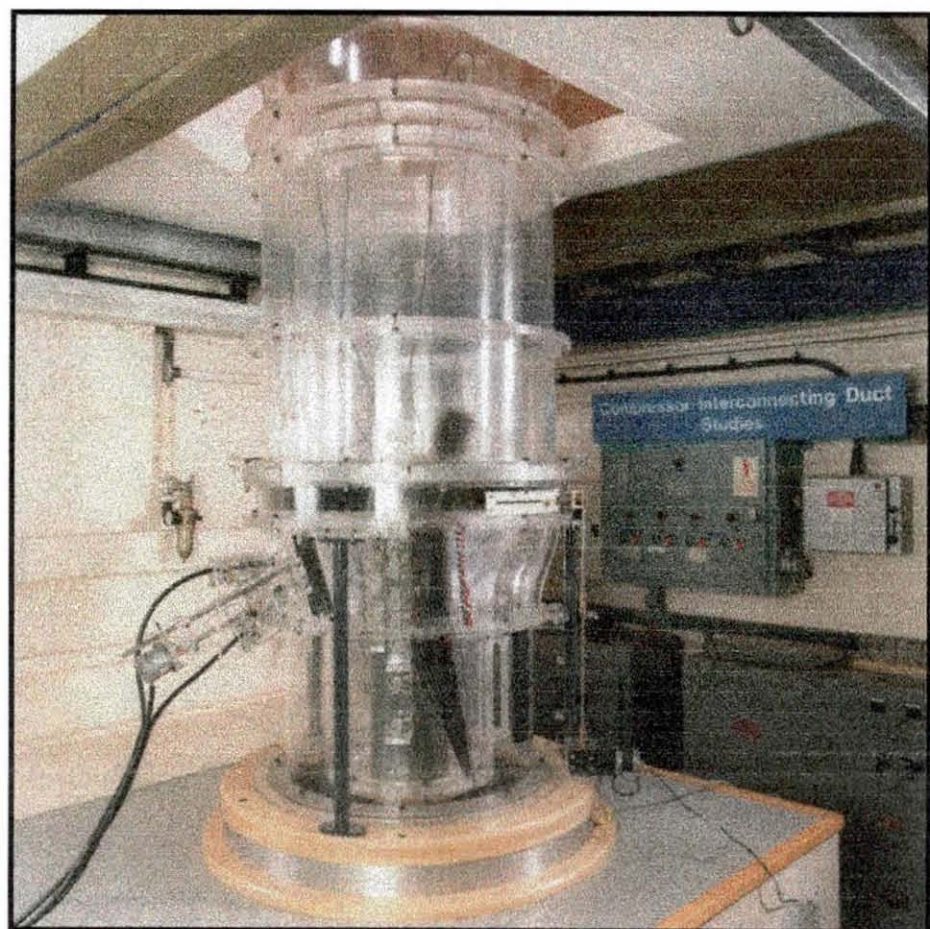


Figure 146

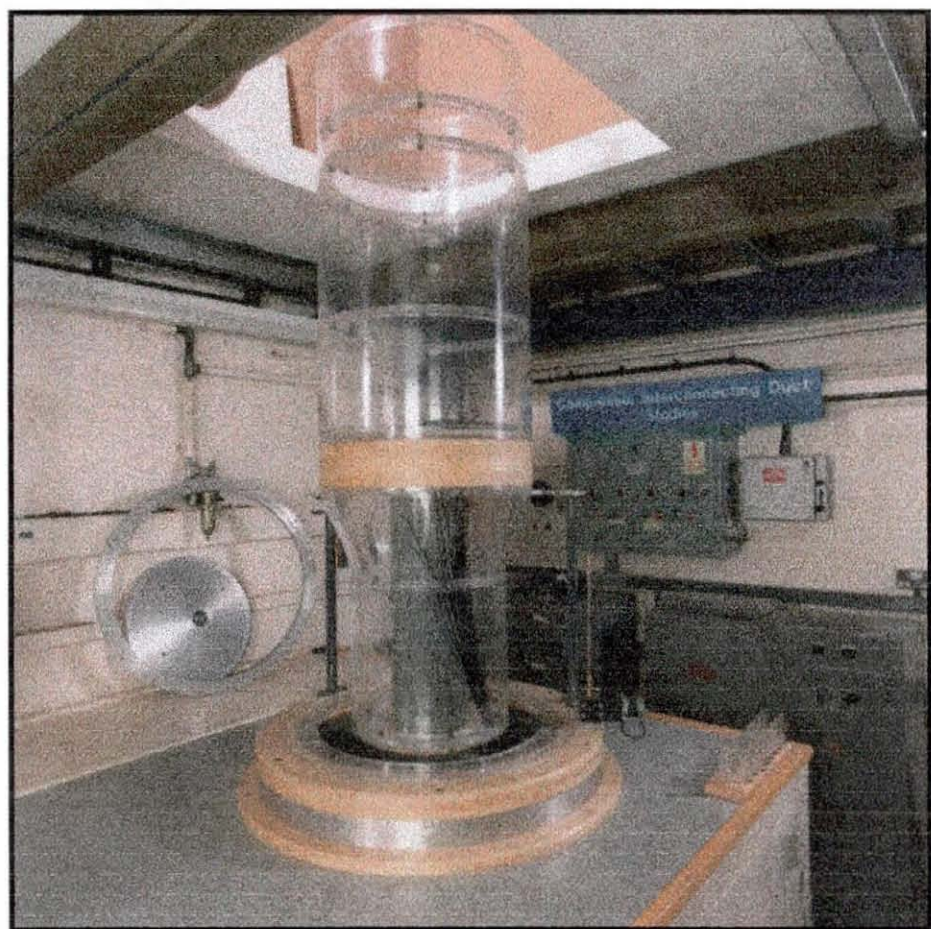
PHOTOGRAPHS

- 1 Overall View of Test Rig**
- 2 Rig Inner Wall**
- 3 Air Intake**
- 4 Compressor Rotor**
- 5 Compressor Stator**
- 6 Test Section**
- 7 LDA Optical Arrangement and Traverse**
- 8 Laser and Data Acquisition System**

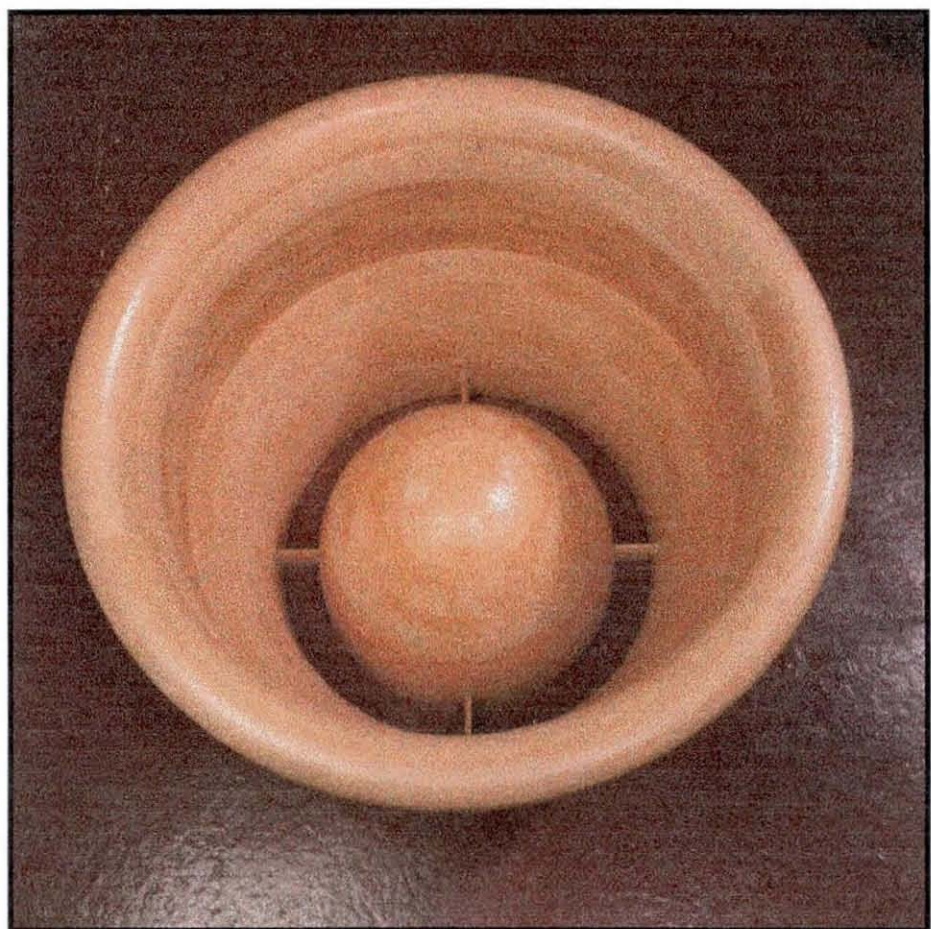


Photograph 1 Overall View of Test Rig

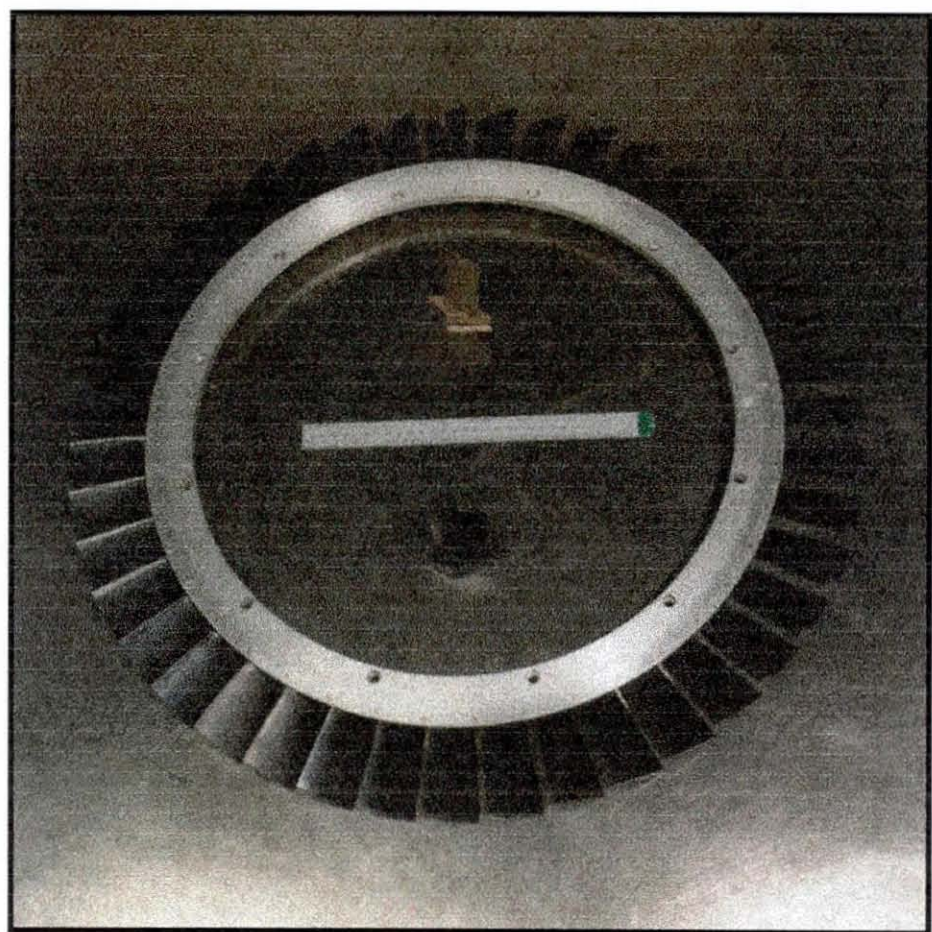
Photographs



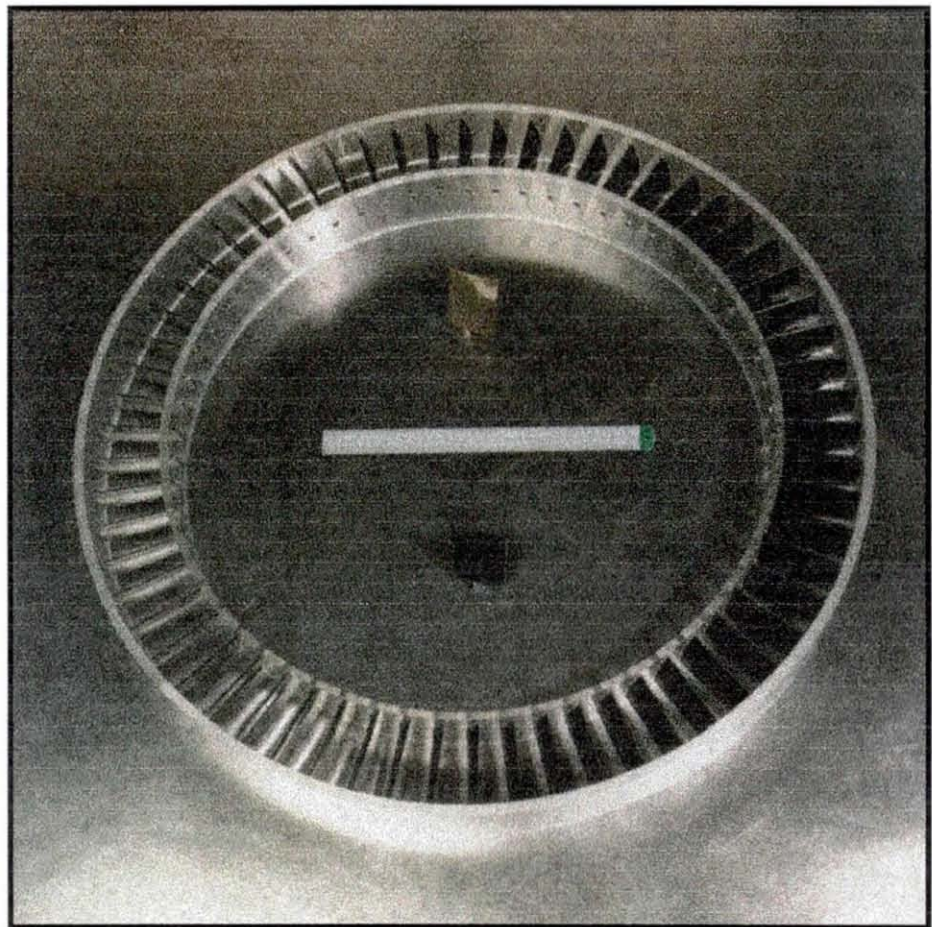
Photograph 2 Rig Inner Wall



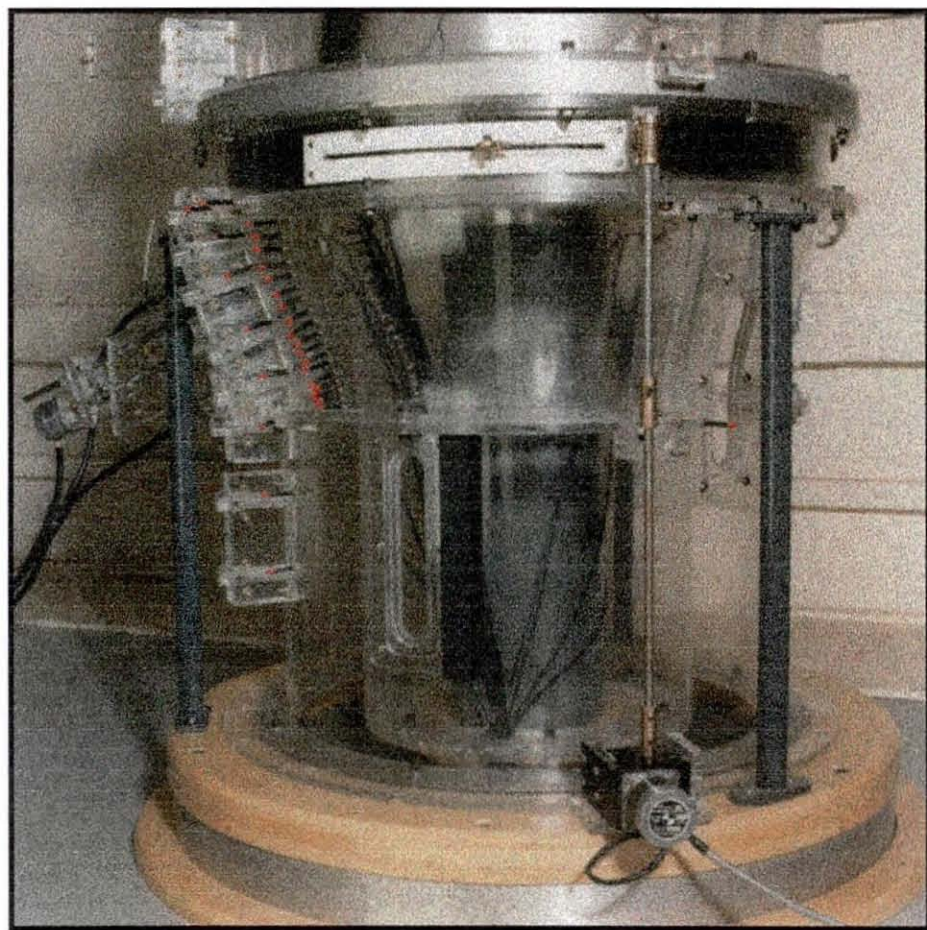
Photograph 3 Air Intake



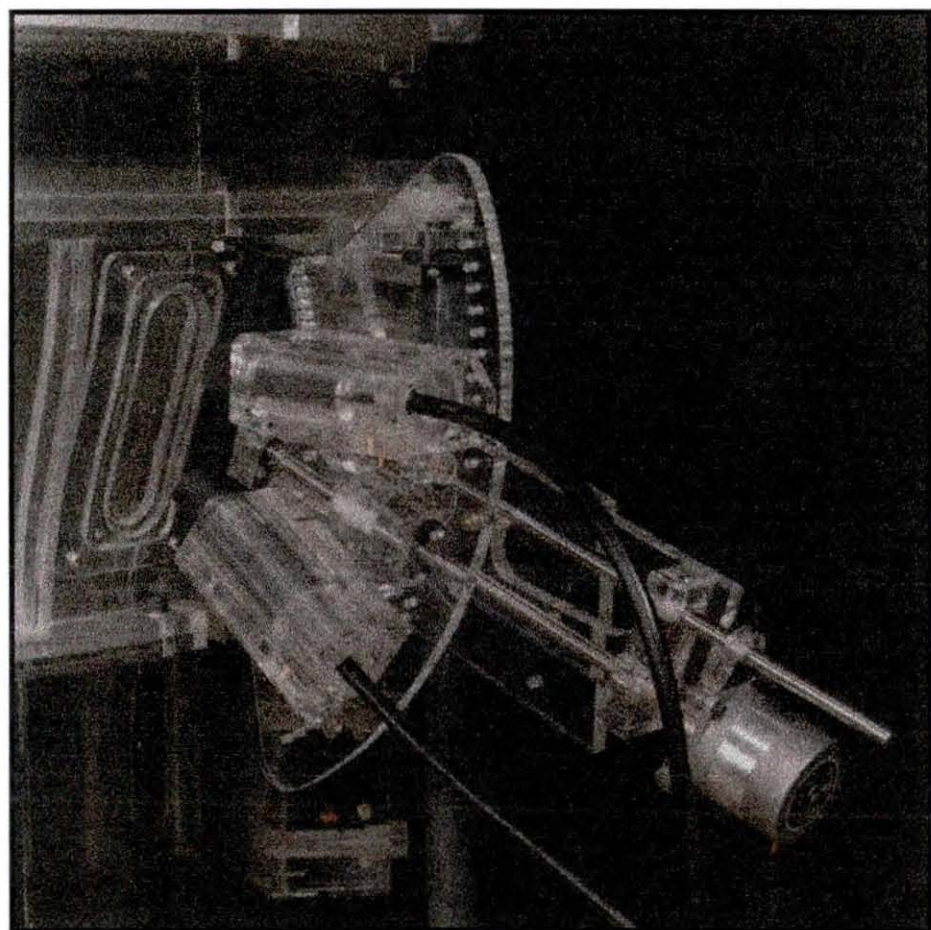
Photograph 4 Compressor Rotor



Photograph 5 Compressor Stator



Photograph 6 Test Section



Photograph 7 LDA Optical Arrangement and Traverse



Photograph 8 Laser and Data Acquisition System

APPENDIX 1 SINGLE STAGE AXIAL COMPRESSOR DESIGN

In order to specify a suitable blade geometry, it was first necessary to estimate the radial variation of aerodynamic conditions that would arise at the inlet and exit of each blade row. To assist in this, a 2D (axisymmetric) through-flow inviscid (streamline curvature) calculation method was used, which could include a specified change in conditions across a nominal blade row (or rows). The calculation grid was based on the known dimensions of the compressor annulus and S-shaped duct, but the axial location and chord of the compressor blade rows had to be estimated initially. A true blade chord of about 50 mm was required in order to attain a Reynolds number (based on chord) of $\sim 2.0 \times 10^5$ for the stator ($V_3 = 57.4$ m/s from mid-height velocity triangles); which was considered to be the minimum acceptable value to avoid the possibility of laminar separation. A similar chord was chosen for the rotor, such that the aspect ratio of both blades was comparable, giving a Reynolds number of 3.6×10^5 because of the higher inlet velocity ($V_1 = 104.8$ m/s) relative to the blade.

The through-flow analysis program was run with basic aerodynamic conditions corresponding to the design point. The inlet total pressure and temperature were assumed constant, and equal to standard day conditions. In addition, the radial variation of conditions across the blades were specified as constant stage pressure ratio (1.026), constant stator exit swirl angle (0.0) and an estimated loss coefficient distribution for each blade row. In calculating the aerodynamic conditions, it was important to include the S-shaped duct in the analysis, since its presence was found to affect the velocity and air angle distributions of the stator.

To achieve the calculated aerodynamic conditions, the necessary blade geometry had to be determined. Initially, the mid-height blade geometry was estimated; blade inlet and exit angle, space-chord ratio, thickness-chord ratio, etc. This was then analysed using a 2D blade-to-blade inviscid calculation method, with coupled integral boundary layer, giving an estimate of the loss and exit air angle produced by the blade passage, for the inlet conditions specified by the through-flow calculation. Therefore, in a iterative manner, it was possible to revise the mid-height blade geometry, until the conditions produced by the blade passage were acceptable; low loss and an exit air angle which matched that of the through-flow calculation.

One of the key parameters at this stage was the space-chord ratio. For a given chord, this is determined by the number of blades, and, since the aerodynamic performance of the blade passage is strongly affected by the space-chord ratio, it was important to

determine the required number of rotor and stator blades. Clearly, the minimum number of blades is required, consistent with a blade-passage that will operate satisfactorily over a range of conditions; not just at the design point. Assuming that the relative swirl angle produced by the rotor remains approximately constant, it is apparent from the velocity triangles that, as the axial velocity is reduced (by throttling the compressor), the stator incidence and static pressure rise increase more rapidly than for the rotor. Therefore, despite a lower static pressure rise through the stator at the design condition, the space-chord ratio of the stator had to be less than the rotor, in order for the compressor to have a reasonable stall range. As such, 43 rotor and 62 stator blades were chosen.

With the blade numbers fixed, it was necessary to determine the chord, and position, of both blade rows. By specifying the axial chord distribution of both blades, the radial distribution of chord and space-chord ratio were dependant on the blade stagger, which was determined by the blade angles. The stator was very simply given a constant axial chord of 50 mm, giving rise to a true chord of approximately 51 mm, and the axial chord of the rotor was set to vary linearly from 32 mm at the root to 28 mm at the tip, giving an approximately constant true chord of 50 mm. At the same time, the locations of the rotor and stator blade rows were decided. Upstream of the S-shaped duct inlet ($x = 0$), the mid-chord position of the rotor blade was located at -0.093 m and the mid-chord position of the stator blade at -0.040 m , giving a inter-blade gap of 13 mm (at mid-height) and an axial distance of 15 mm between the stator trailing edge and the S-shaped duct.

In addition, the thickness of the blades was considered. The thickness-chord ratio distribution of the stator was chosen to be a constant 6%, typical of gas turbine stator blades, but, for the rotor, the distribution had to taper. Due to the centripetal acceleration and aerodynamic load, the root is subjected to a higher mechanical stress than the tip, so therefore the root of the rotor blade needed to be thicker than the tip. Although a full stress analysis was not undertaken, it was thought that, by using values typical of metal rotor blades in real compressors, the fairly low speed, lightly loaded, plastic rig blades would operate satisfactorily; which previous experience of similar blades had shown to be the case. Therefore, the thickness-chord ratio was made to vary linearly from 8% at the root to 3% at the tip. Furthermore, by using standard aerofoil types, the chordwise thickness distribution was predetermined. For the rotor, a double-circular arc profile was used, for which the suction and pressure surfaces are formed by circular arcs whose centres are adjusted to give the required maximum thickness at the mid-chord position. For the stator, a standard C4 profile was used, for which a known thickness distribution is added to a circular arc camber-line, achieving

the required maximum thickness at 40% chord. In addition, the leading and trailing edge thickness was specified for both blades.

All that remained to generate a complete blade geometry was the radial distribution of inlet and exit blade angles. These were determined by calculating the 2D flow through the blade passage, for a number of sections obtained by intersecting the blade with pseudo stream-surfaces. For each section, the blade exit angle was adjusted, by iteration, until the predicted exit air angle matched that of the through-flow calculation. In addition, the inlet blade angle, initially set to give zero incidence, was adjusted to improve the predicted velocity distribution around the leading edge. Having obtained a preliminary blade, for which a radial distribution of loss coefficient had been predicted by the 2D blade-to-blade calculation, the through-flow calculation was updated with more realistic values. As well as the predicted profile loss, a secondary loss rule was applied ($0.03(3h^2 - 3h + 1.5)/\text{aspect ratio}$) which increased the loss towards the walls and, for the rotor, an estimated tip clearance loss was also included. In addition, the presence of annulus wall boundary layers was accounted for by using a coupled integral boundary layer calculation, in which the displacement thickness was added to the walls. A blockage of 5% was obtained at compressor inlet and so the mass flow was reduced to 8.52 kg/s to maintain the same velocity at mid-height. With a revised estimate of the inlet and exit flow conditions, the blade angles were given a final adjustment, using the same iterative technique, until each blade row produced the desired behaviour.

APPENDIX 2 IDEAL BEHAVIOUR OF A CURVED FLOW

Within the annulus wall turbulent boundary layers, the mean velocity must reduce to zero at the wall giving rise to viscous and turbulent stresses. To determine the extent to which the mean velocity distribution is affected by these stresses, it is necessary to establish the ideal behaviour of the flow by assuming that it is inviscid. Moreover, in a curved flow this ideal velocity will not remain constant and, therefore, its variation needs to be determined.

A2.1 The Exact Inviscid Behaviour

For inviscid flow the Euler equations are applicable. In s-n-z co-ordinates, assuming 2D ($\partial/\partial z = 0$) flow with $W = 0$, these are,

$$\frac{\partial U}{\partial s} + \frac{\partial V}{\partial n} - \frac{V}{R} = 0 \quad \dots\dots \text{A2.1}$$

$$U \frac{\partial U}{\partial s} + V \frac{\partial U}{\partial n} - \frac{UV}{R} = -\frac{1}{\rho} \frac{\partial p}{\partial s} \quad \dots\dots \text{A2.2}$$

$$U \frac{\partial V}{\partial s} + V \frac{\partial V}{\partial n} + \frac{U^2}{R} = -\frac{1}{\rho} \frac{\partial p}{\partial n} \quad \dots\dots \text{A2.3}$$

where R is the geometric radius of curvature. These can be combined to give a mean energy equation,

$$\frac{U}{\rho} \frac{\partial P}{\partial s} + \frac{V}{\rho} \frac{\partial P}{\partial n} = 0 \quad \dots\dots \text{A2.4}$$

where the total pressure (P) is defined as,

$$P = p + \frac{1}{2} \rho (U^2 + V^2) \quad \dots\dots \text{A2.5}$$

and U and V are the mean velocity components in the streamwise (s) and cross-stream (n) directions (U_s and V_n with the subscripts dropped for convenience).

With the appropriate boundary conditions, the Euler equations could be solved to give the ideal variation of streamwise velocity. However, for flow through a relatively simple geometry, a full solution is unnecessary since, by considering the flow along streamlines ($\psi = \text{constant}$), the equations can be simplified with $V = 0$ and $\partial V/\partial s = 0$.

The mean energy equation shows that the total pressure remains constant along a streamline, i.e., $\partial P/\partial s = 0$ with $P = p + \frac{1}{2}\rho U^2$. Note that integration of the simplified streamwise momentum equation leads to same result.

The cross-stream momentum equation reduces to,

$$\frac{U^2}{R} = -\frac{1}{\rho} \frac{\partial p}{\partial n} \quad \dots\dots \text{A2.6}$$

which gives a simple relationship between pressure and velocity. Allowing for the definition of R with respect to $s-n$ co-ordinates, it shows that for a rotating flow the pressure must increase away from the centre of rotation (in order to support the centripetal acceleration) and for a plane flow ($R \rightarrow \infty$) $\partial p/\partial n = 0$.

Since $\rho U^2 = 2(P - p)$, Eq. A2.6 reduces to an ordinary differential equation,

$$\frac{dp}{dn} = \frac{-2(P - p)}{R} \quad \dots\dots \text{A2.7}$$

which applies at any streamwise location within the flow. With $P (= f(n))$ specified, this can be integrated to obtain a solution for $p (= f(n))$, provided that the radius of curvature of the streamlines (R) is known at all positions across the flow. However, this is not usually the case, especially when an arbitrary total pressure distribution is specified; although, as it will be seen, it is sometimes possible to approximate the variation of R with a simple analytical function.

In general, R is dependant on the velocity distribution ($U = f(s, n)$) which, in turn, is dependant on the pressure field; which must satisfy Eq. A2.7 at every streamwise location. Since Eq. A2.7 is dependant on R , an iterative solution is necessary. This forms the basis of the streamline curvature method of solving the Euler equations for duct flow, in which a series of streamlines are used to determine R . These are calculated from the velocity distribution, which must also satisfy continuity by ensuring the required total mass flow is achieved at every streamwise location. Equation A2.7 is then used to update the pressure field, and hence the velocity distribution, so that the streamlines can be recalculated; and so on until convergence is reached. Although total pressure is constant along a streamline, there is no restriction on the cross-stream distribution of total pressure, which simply becomes an inlet boundary condition along with the total mass flow.

A particular case of interest is that of constant inlet total pressure ($\partial P/\partial n = 0$). Providing there is no streamline curvature through the inlet plane ($1/R = 0$), the velocity

will be constant ($\partial U / \partial n = 0$). Consequently, the inlet flow will have zero vorticity since the z-component of vorticity (in s-n-z co-ordinates) is given by,

$$\Omega_z = \frac{\partial V}{\partial s} - \frac{\partial U}{\partial n} + \frac{U}{R} \quad \dots\dots A2.8$$

Further, a transport equation for the z-component of vorticity can be obtained from the Euler equations as,

$$U \frac{\partial \Omega_z}{\partial s} + V \frac{\partial \Omega_z}{\partial n} = 0 \quad \dots\dots A2.9$$

which shows that vorticity will remain constant along a streamline ($\partial \Omega_z / \partial s = 0$).

Hence with zero vorticity at inlet, the whole inviscid flow field can be considered as irrotational ($\Omega_z = 0$, everywhere). Thus, with the assumption that $\partial V / \partial s = 0$, Eq. A2.8 reduces to an ordinary differential equation,

$$\frac{dU}{dn} = \frac{U}{R} \quad \dots\dots A2.10$$

which applies at any streamwise location within the flow. This can be integrated to obtain a solution for $U (= f(n))$; again provided that the variation of R across the flow is known.

A2.2 Derivation of an Approximate Velocity Distribution

In order to obtain a simple analytical expression for the ideal variation of streamwise velocity across a curved (inviscid) flow, it is necessary to use a simple analytical function to approximate the variation of the streamline radius of curvature ($R = f(n)$). By assuming that all streamlines rotate about the same centre, and that at mid-height ($n = 0$) the effective radius of curvature is R_{eff} , the radius of curvature of any streamline is given by $R_{eff} + n$. Thus, the geometric radius of curvature (defined with respect to s-n co-ordinates) can be approximated by $R = -(R_{eff} + n)$.

With this approximation, the cross-stream variation of static pressure can be established by integration of Eq. A2.7, i.e.,

$$\int \frac{dp}{(P - p)} = \int \frac{2dn}{(R_{eff} + n)} \quad \dots\dots A2.11$$

For the case of constant inlet total pressure ($\partial P/\partial n = 0$), which also implies that the flow is irrotational, this integral expression can be evaluated analytically to give,

$$- \ln(P - p) = 2 \ln(R_{\text{eff}} + n) + \text{constant} \quad \dots\dots \text{A2.12}$$

therefore,

$$(P - p)(R_{\text{eff}} + n)^2 = C \quad \dots\dots \text{A2.13}$$

but $p = p_m$ when $n = 0$, therefore $C = (P - p_m)R_{\text{eff}}^2$ giving,

$$\frac{(P - p)}{(P - p_m)} = \left(\frac{R_{\text{eff}}}{R_{\text{eff}} + n} \right)^2 = \frac{1}{(1 + n K_{\text{eff}})^2} \quad \dots\dots \text{A2.14}$$

where the K_{eff} is the effective curvature ($= 1/R_{\text{eff}}$).

Since $U = \sqrt{2(P - p)/\rho}$ and $U = U_m$ when $n = 0$, the potential velocity (U_p) for irrotational flow can be approximated by,

$$U_p = \frac{U_m}{(1 + n K_{\text{eff}})} \quad \dots\dots \text{A2.15}$$

The same result can be obtained by integration of Eq. A2.10, which only applies to irrotational flow. In this case, the integral expression can be evaluated analytically to give,

$$U(R_{\text{eff}} + n) = C \quad \dots\dots \text{A2.16}$$

Since $U = U_m$ when $n = 0$, $C = U_m R_{\text{eff}}$, and the same result (Eq. A2.15) is obtained for the potential velocity. Of course, this analysis gives rise to the expected result (Eq. A2.16) for irrotational (free-vortex) flow, in that the variation of U is inversely proportional to the radius from the centre of rotation.

It must be remembered that the radius of curvature variation used to derive Eq. A2.15, given by $R = -(R_{\text{eff}} + n)$, is only an approximation. Even if this is considered reasonable, Eq. A2.15 cannot be used to predict the behaviour of inviscid flow through a curved duct, since U_m and K_{eff} are unknown. Although it might be possible to approximate these in some way, the only way of obtaining the exact variation is through iterative solution of the Euler equations. More importantly, however, Eq. A2.15 is particularly useful for the analysis of curved flow boundary layers.

APPENDIX 3 THE EXACT EQUATIONS OF MOTION

The various equations governing flow behaviour are presented in this appendix. These are the Reynolds-averaged Navier-Stokes equations for steady, incompressible, isothermal flow, the exact Reynolds stress transport equations, from which the turbulent kinetic energy transport equation is obtained, and the turbulent kinetic energy dissipation rate transport equation. For simplicity, all equations are presented here in Cartesian tensor notation, with the various terms identified. In Appendix 4, however, their fully expanded forms are given in Cartesian, curvilinear and polar co-ordinates.

A3.1 Continuity Equation

The continuity equation for steady, incompressible flow is,

$$\frac{\partial U_i}{\partial x_i} = 0 \quad \dots\dots A3.1$$

A3.2 Momentum Equations

The momentum equations for steady, incompressible, viscous flow are,

$$\underbrace{\frac{\partial}{\partial x_j}(U_j U_i)}_A = \underbrace{-\frac{1}{\rho} \frac{\partial p}{\partial x_i}}_B - \underbrace{\frac{\partial}{\partial x_j}(\bar{u}_i u_j)}_C + \underbrace{\frac{\partial}{\partial x_j} \left(v \left\{ \frac{\partial U_i}{\partial x_j} + \frac{\partial U_j}{\partial x_i} \right\} \right)}_D \quad \dots\dots A3.2$$

where the various terms are described as,

- A - convection
- B - static pressure gradient
- C - turbulent transport
- D - viscous diffusion

Alternatively, these can be written as,

$$U_j \frac{\partial U_i}{\partial x_j} = -\frac{1}{\rho} \frac{\partial p}{\partial x_i} - \frac{\partial}{\partial x_j} (\bar{u}_i u_j) + v \frac{\partial^2 U_i}{\partial x_j^2} \quad \dots\dots A3.3$$

In laminar flow, of course, the Reynolds stresses ($\bar{u}_i u_j$) are zero.

A3.3 Mean Energy Equation

The mean kinetic energy equation is given by the sum of $U_i \times U_i$ -momentum equation (Eq. A3.3), i.e.,

$$\frac{U_i}{\rho} \frac{\partial P}{\partial x_i} = -U_i \frac{\partial}{\partial x_j} (\bar{u}_i \bar{u}_j) + U_i \frac{\partial}{\partial x_j} \left(v \left\{ \frac{\partial U_i}{\partial x_j} + \frac{\partial U_j}{\partial x_i} \right\} \right) \quad \dots\dots \text{A3.4}$$

which can be rewritten as,

$$\underbrace{\frac{1}{\rho} \frac{\partial}{\partial x_i} (U_i P)}_{\text{A}} = \underbrace{\bar{u}_i \bar{u}_j \frac{\partial U_i}{\partial x_j}}_{\text{B}} - \underbrace{v \left\{ \frac{\partial U_i}{\partial x_j} + \frac{\partial U_j}{\partial x_i} \right\} \frac{\partial U_i}{\partial x_j}}_{\text{C}} \\ - \underbrace{\frac{\partial}{\partial x_j} (U_i \bar{u}_i \bar{u}_j)}_{\text{D}} + \underbrace{\frac{\partial}{\partial x_j} \left(U_i v \left\{ \frac{\partial U_i}{\partial x_j} + \frac{\partial U_j}{\partial x_i} \right\} \right)}_{\text{E}} \quad \dots\dots \text{A3.5}$$

where,

- A - convection
- B - turbulent dissipation (equal to turbulent kinetic energy production)
- C - viscous (or direct) dissipation
- D - turbulent transport
- E - viscous diffusion

A3.4 Reynolds Stress Transport Equations

The exact transport equations for the Reynolds stresses ($\bar{u}_i \bar{u}_j$) are,

$$\underbrace{\frac{\partial}{\partial x_k} (U_k \bar{u}_i \bar{u}_j)}_{\text{A}} = - \underbrace{\left(\bar{u}_i \bar{u}_k \frac{\partial U_j}{\partial x_k} + \bar{u}_j \bar{u}_k \frac{\partial U_i}{\partial x_k} \right)}_{\text{B}} \\ - \underbrace{\frac{\partial}{\partial x_k} (\bar{u}_i \bar{u}_j \bar{u}_k)}_{\text{C}} + \underbrace{\frac{\partial}{\partial x_k} \left(v \frac{\partial}{\partial x_k} (\bar{u}_i \bar{u}_j) \right)}_{\text{D}} \quad \dots\dots \text{A3.6} \\ - \underbrace{\frac{1}{\rho} \left(\bar{u}_i \frac{\partial p'}{\partial x_j} + \bar{u}_j \frac{\partial p'}{\partial x_i} \right)}_{\text{E}} - 2v \underbrace{\frac{\partial u_i}{\partial x_k} \frac{\partial u_j}{\partial x_k}}_{\text{F}}$$

where,

- A - convection (C_{ij})

- B - production (P_{ij})
- C - turbulent transport (T_{ij})
- D - viscous diffusion (V_{ij})
- E - velocity-pressure gradient interaction (Π_{ij})
- F - dissipation (ϵ_{ij})

N.B.,

$$\frac{\partial}{\partial x_k} \left(U_k \overline{u_i u_j} \right) \equiv U_k \frac{\partial \overline{u_i u_j}}{\partial x_k}$$

At high Reynolds number term D becomes insignificant.

A3.5 Turbulent Kinetic Energy Transport Equation

The exact transport equation for turbulent kinetic energy (k) is obtained as half the sum of the normal stress transport equations since $k = \frac{1}{2} \overline{u_k u_k}$, i.e.,

$$\underbrace{\frac{\partial}{\partial x_i} (U_i k)}_A = \underbrace{- \left(\overline{u_i u_j} \frac{\partial U_i}{\partial x_j} \right)}_B - \underbrace{\frac{\partial}{\partial x_i} (\overline{k u_i})}_C + \underbrace{\frac{\partial}{\partial x_i} \left(v \frac{\partial k}{\partial x_i} \right)}_D \\ - \underbrace{\frac{1}{\rho} \left(u_i \frac{\partial p'}{\partial x_i} \right)}_E - \underbrace{v \frac{\partial u_i}{\partial x_j} \frac{\partial u_i}{\partial x_j}}_F \quad \dots\dots A3.7$$

where,

- A - convection (C)
- B - production (P)
- C - turbulent transport (T)
- D - viscous diffusion (V)
- E - velocity-pressure gradient interaction (Π)
- F - dissipation (ϵ)

N.B.,

$$\frac{\partial}{\partial x_i} (U_i k) \equiv U_i \frac{\partial k}{\partial x_i}$$

At high Reynolds number term D becomes insignificant. In this equation, term E only represents pressure transport (since the pressure-strain has zero trace) which is insignificant, except in the near-wall region.

A3.6 Turbulent Kinetic Energy Dissipation Rate Equation

The exact transport equation for the dissipation rate of turbulent kinetic energy (ϵ) is;

$$\frac{\partial}{\partial x_k} (U_k \epsilon) = \underbrace{-\frac{\partial}{\partial x_k} \left(v u_k \frac{\partial u_i}{\partial x_j} \frac{\partial u_i}{\partial x_j} \right)}_{A} - \underbrace{\frac{\partial}{\partial x_k} \left(\frac{2v}{\rho} \frac{\partial p'}{\partial x_i} \frac{\partial u_k}{\partial x_i} \right)}_{B} + \underbrace{\frac{\partial}{\partial x_k} \left(v \frac{\partial \epsilon}{\partial x_k} \right)}_{C} \\ - \underbrace{2v \frac{\partial U_i}{\partial x_k} \left(\frac{\partial u_i}{\partial x_j} \frac{\partial u_k}{\partial x_j} + \frac{\partial u_j}{\partial x_i} \frac{\partial u_j}{\partial x_k} \right)}_{E} - \underbrace{2v u_k \frac{\partial u_i}{\partial x_j} \frac{\partial^2 U_i}{\partial x_j \partial x_k}}_{F} \\ - \underbrace{2v \frac{\partial u_i}{\partial x_j} \frac{\partial u_i}{\partial x_k} \frac{\partial u_k}{\partial x_j}}_{G} - \underbrace{2v^2 \frac{\partial^2 u_i}{\partial x_j \partial x_k} \frac{\partial^2 u_i}{\partial x_j \partial x_k}}_{H} \quad \dots \dots A3.8$$

where,

- A - convection (C_ϵ)
- B - turbulent transport (T_ϵ)
- C - pressure transport (Π_ϵ)
- D - viscous diffusion (V_ϵ)
- E - creation by interaction of turbulence and the mean flow ($P_\epsilon^{(1)}$)
- F - creation by interaction of turbulence and the mean flow ($P_\epsilon^{(2)}$)
- G - creation by turbulence ($P_\epsilon^{(3)}$)
- H - viscous destruction ($-P_\epsilon^{(4)}$)

N.B.,

$$\frac{\partial}{\partial x_k} (U_k \epsilon) \equiv U_k \frac{\partial \epsilon}{\partial x_k}$$

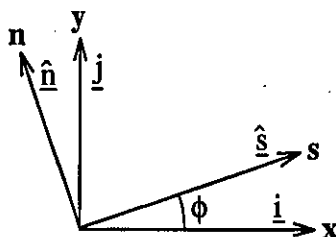
At high Reynolds number term D becomes insignificant.

APPENDIX 4 TRANSFORMATION OF THE EQUATIONS OF MOTION TO CURVILINEAR AND POLAR CO-ORDINATES

The continuity, momentum and Reynolds stress transport equations are usually derived in a Cartesian co-ordinate system and written in tensor notation (see Appendix 3). However, to investigate the behaviour of the flow within an annular S-shaped duct it was desirable to use a curvilinear co-ordinate system, approximately aligned with the mean flow direction. In this appendix, the method by which the Cartesian equations were transformed into s-n-z co-ordinates is described and the resultant equations are given in full. In addition, the equations of motion in polar ($x-r-\theta$) co-ordinates are presented.

A4.1 Method of Transformation

A4.1.1 Curvilinear (s-n-z) Co-ordinates



Definition of Co-ordinates

For a simple rotation about the z-axis, the unit vectors in the s and n directions are given by,

$$\hat{s} = \cos \phi \underline{i} + \sin \phi \underline{j} \quad \dots \dots \text{A4.1}$$

$$\hat{n} = \underline{k} \otimes \hat{s} = -\sin \phi \underline{i} + \cos \phi \underline{j} \quad \dots \dots \text{A4.2}$$

and, given a velocity vector $\underline{U} = U\underline{i} + V\underline{j} + W\underline{k}$, the velocity components in the s-n-z directions are obtained from, $U_s = \underline{U} \bullet \hat{s}$, $V_n = \underline{U} \bullet \hat{n}$ and $W_z = W$, giving,

Transformation of the Equations of Motion

$$\underline{U}^{sn} = \begin{Bmatrix} U_s \\ V_n \\ W_z \end{Bmatrix} = \begin{bmatrix} \cos\phi & \sin\phi & 0 \\ -\sin\phi & \cos\phi & 0 \\ 0 & 0 & 1 \end{bmatrix} \begin{Bmatrix} U \\ V \\ W \end{Bmatrix} = [T] \underline{U} \quad \dots\dots A4.3$$

where $[T]$ is the transformation matrix with components T_{ij} . Thus, in tensor notation,

$$U_i^{sn} = T_{ij} U_j \quad \dots\dots A4.4$$

i.e.,

$$U_s = \cos\phi U + \sin\phi V \quad \dots\dots A4.4a$$

$$V_n = -\sin\phi U + \cos\phi V \quad \dots\dots A4.4b$$

$$W_z = W \quad \dots\dots A4.4c$$

Further, the components of the Reynolds stress tensor are obtained as,

$$\overline{u_i^{sn} u_j^{sn}} = T_{ik} T_{jl} \overline{u_k u_l} \quad \dots\dots A4.5$$

i.e.,

$$\overline{u_s u_s} = \cos^2\phi \overline{uu} + \sin^2\phi \overline{vv} + \sin 2\phi \overline{uv} \quad \dots\dots A4.5a$$

$$\overline{v_n v_n} = \sin^2\phi \overline{uu} + \cos^2\phi \overline{vv} - \sin 2\phi \overline{uv} \quad \dots\dots A4.5b$$

$$\overline{w_z w_z} = \overline{ww} \quad \dots\dots A4.5c$$

$$\overline{u_s v_n} = -\frac{1}{2} \sin 2\phi \overline{uu} + \frac{1}{2} \sin 2\phi \overline{vv} + \cos 2\phi \overline{uv} \quad \dots\dots A4.5d$$

$$\overline{u_s w_z} = \cos\phi \overline{uw} + \sin\phi \overline{vw} \quad \dots\dots A4.5e$$

$$\overline{v_n w_z} = -\sin\phi \overline{uw} + \cos\phi \overline{vw} \quad \dots\dots A4.5f$$

Thus, the momentum equations in s-n-z co-ordinates are obtained using Eq. A4.4, i.e., the U_i^{sn} momentum equation is obtained as the sum ($j = 1, 3$) of T_{ij} multiplied by the U_j momentum equation, e.g., the U_s equation is given by $\cos\phi$ times the U equation plus $\sin\phi$ times the V equation.

Similarly, the Reynolds stress equations are obtained using Eq. A4.5, i.e., the $\overline{u_i^{sn} u_j^{sn}}$ Reynolds stress transport equation is obtained by adding together a number of Cartesian Reynolds stress transport equations, each multiplied by the appropriate function of ϕ .

A4.1.1.1 Transformation of the Cartesian Variables

Before transformation of the equations can take place, the various terms in the Cartesian equations have to, themselves, be converted into s-n-z variables. This is achieved by using the inverse transformation $[T']$, which has components T'_{ij} , i.e.,

$$[T'] = [T]^{-1} = [T]^T = \begin{bmatrix} \cos \phi & -\sin \phi & 0 \\ \sin \phi & \cos \phi & 0 \\ 0 & 0 & 1 \end{bmatrix} \quad \dots\dots A4.6$$

Thus, the Cartesian velocities are replaced by,

$$U_i = T'_{ij} U_j^{sn} \quad \dots\dots A4.7$$

the Reynolds stresses by,

$$\overline{u_i u_j} = T'_{ik} T'_{jl} \overline{u_k^{sn} u_l^{sn}} \quad \dots\dots A4.8$$

and the triple velocity correlations by,

$$\overline{u_i u_j u_k} = T'_{il} T'_{jm} T'_{kn} \overline{u_l^{sn} u_m^{sn} u_n^{sn}} \quad \dots\dots A4.9$$

In addition, the Cartesian derivatives need to be converted into derivatives in the s-n-z directions using,

$$\frac{\partial}{\partial x_i} = T'_{ij} \frac{\partial}{\partial x_j^{sn}} \quad \dots\dots A4.10$$

For scalar quantities, the derivative transformation is straight forward. However, for derivatives of velocities, Reynolds stresses or triple velocity correlations, it is necessary to apply the transformation to these before taking the derivative. For example, the strain rate transformation would become,

$$\frac{\partial U_i}{\partial x_j} = T'_{jl} \frac{\partial (T'_{ik} U_k^{sn})}{\partial x_j^{sn}} = T'_{jl} \left\{ T'_{ik} \frac{\partial U_k^{sn}}{\partial x_j^{sn}} + U_k^{sn} \frac{\partial T'_{ik}}{\partial x_j^{sn}} \right\} \quad \dots\dots A4.11$$

By splitting the derivative in this way, it is clear that the derivatives of the transformation components ($\partial T'_{ik}/\partial x_j^{sn}$) must be obtained and included.

In general, ϕ varies in the s direction only and so derivatives of ϕ in the n and z directions are zero. Further, $\partial \phi / \partial s$ is, by definition, equal to the geometric curvature ($1/R$). Thus, for any function $f(\phi)$ operated on by Eq. A4.10,

$$\frac{\partial f(\phi)}{\partial s} = \frac{\partial f(\phi)}{\partial \phi} \frac{\partial \phi}{\partial s} = \frac{f'(\phi)}{R} \quad \dots\dots A4.12$$

and $f'(\phi)$ can be readily obtained. This, of course, is the origin of the 'extra' terms appearing in the transformed equations.

By way of further example, consider the normal strain rates which form the continuity equation. These can be obtained from Eq. A4.11 as,

$$\begin{aligned} \frac{\partial U}{\partial x} &= \cos^2 \phi \frac{\partial U_s}{\partial s} - \sin \phi \cos \phi \frac{U_s}{R} - \sin \phi \cos \phi \frac{\partial V_n}{\partial s} - \cos^2 \phi \frac{V_n}{R} \\ &\quad - \sin \phi \cos \phi \frac{\partial U_s}{\partial n} + \sin^2 \phi \frac{\partial V_n}{\partial n} \end{aligned} \quad \dots\dots A4.13$$

$$\begin{aligned} \frac{\partial V}{\partial y} &= \sin^2 \phi \frac{\partial U_s}{\partial s} + \sin \phi \cos \phi \frac{U_s}{R} + \sin \phi \cos \phi \frac{\partial V_n}{\partial s} - \sin^2 \phi \frac{V_n}{R} \\ &\quad + \sin \phi \cos \phi \frac{\partial U_s}{\partial n} + \cos^2 \phi \frac{\partial V_n}{\partial n} \end{aligned} \quad \dots\dots A4.14$$

$$\frac{\partial W}{\partial z} = \frac{\partial W_z}{\partial z} \quad \dots\dots A4.15$$

which when added together give,

$$\frac{\partial U}{\partial x} + \frac{\partial V}{\partial y} + \frac{\partial W}{\partial z} = \frac{\partial U_s}{\partial s} + \frac{\partial V_n}{\partial n} + \frac{\partial W_z}{\partial z} - \frac{V_n}{R} \quad \dots\dots A4.16$$

A4.1.1.2 Transformation of the Cartesian Equations

The processes of transforming the Cartesian momentum and Reynolds stress transport equations involves several steps. Firstly, for a given term, the Cartesian variables are replaced by s-n-z variables using Eq. A4.10 in combination with Eq. A4.7, Eq. A4.8 or Eq. A4.9, taking care to ensure that the derivatives of the transformation components are included. This has to be carried out for the same term in each of the Cartesian equations before the equivalent term in the transformed equations can be determined from Eq. A4.4 or Eq. A4.5. For example, the convection term in the U_i^{sn} momentum equation is determined from,

$$C_{U_i^{sn}} = T_{ij} \left\{ U_k \frac{\partial U_j}{\partial x_k} \right\} = T_{ij} \left\{ \left(T'_{kl} U_l^{sn} \right) T'_{km} \frac{\partial (T'_{jn} U_n^{sn})}{\partial x_m} \right\} \quad \dots\dots A4.17$$

For each new l, m, n term ($U_l^{sn} \partial U_n^{sn} / \partial x_m^{sn}$ or $U_l^{sn} U_n^{sn} / R$), the transformation coefficients are summed over j, k and simplify to either zero or an integer value. In practice, for the

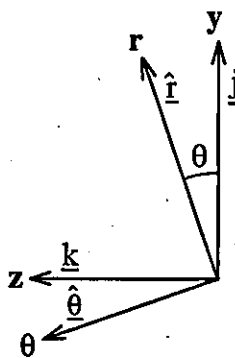
s-n-z transformation, a large number of the terms are zero, because of the zero coefficients in the transformation, and do not have to be considered. For the others, the algebraic manipulation is relatively simple and the coefficients rapidly reduce to indicate which extra terms arise alongside those that resemble the original Cartesian terms.

For the Reynolds stress transport equations even more terms are involved in determining the transformed equations. For example, the production term in the $\overline{u_i^{sn} u_j^{sn}}$ transport equation is obtained from,

$$\begin{aligned} P_{\overline{u_i^{sn} u_j^{sn}}} &= -T_{ik} T_{jl} \left\{ \overline{u_k u_m} \frac{\partial U_l}{\partial x_m} + \overline{u_l u_m} \frac{\partial U_k}{\partial x_m} \right\} \\ &= -T_{ik} T_{jl} \left\{ \left(T'_{kn} T'_{mo} \overline{u_n^{sn} u_o^{sn}} \right) T'_{mp} \frac{\partial (T'_{lq} U_q^{sn})}{\partial x_p^{sn}} + \left(T'_{ln} T'_{mo} \overline{u_n^{sn} u_o^{sn}} \right) T'_{mp} \frac{\partial (T'_{kq} U_q^{sn})}{\partial x_p^{sn}} \right\} \quad \dots \dots \text{A4.18} \end{aligned}$$

In this case, for each new n, o, p, q term ($\overline{u_n^{sn} u_o^{sn}} \partial U_q^{sn} / \partial x_p^{sn}$ or $\overline{u_n^{sn} u_o^{sn}} U_q^{sn} / R$) the transformation coefficients are summed over k, l and m. Fortunately, a large number of the terms are again zero and do not have to be considered. For the others, the algebraic manipulation of the coefficients indicates which terms remain.

A4.1.2 Polar (x-r-θ) Co-ordinates



Definition of Co-ordinates

Transformation to polar co-ordinates is identical to the s-n-z case just considered, except that rotation now occurs about the x-axis. For this case, the unit vectors in the r and θ directions are given by,

Transformation of the Equations of Motion

$$\hat{\underline{r}} = \cos\theta \underline{j} + \sin\theta \underline{k} \quad \dots\dots \text{A4.19}$$

$$\hat{\underline{\theta}} = \underline{i} \otimes \hat{\underline{r}} = -\sin\theta \underline{j} + \cos\theta \underline{k} \quad \dots\dots \text{A4.20}$$

and the velocity components in the $x-r-\theta$ directions are obtained from, $\underline{V}_a = \underline{U}$, $V_r = \underline{U} \bullet \hat{\underline{r}}$ and $V_\theta = \underline{U} \bullet \hat{\underline{\theta}}$, giving,

$$\underline{U}^{tr} = \begin{Bmatrix} V_a \\ V_r \\ V_\theta \end{Bmatrix} = \begin{bmatrix} 1 & 0 & 0 \\ 0 & \cos\theta & \sin\theta \\ 0 & -\sin\theta & \cos\theta \end{bmatrix} \begin{Bmatrix} U \\ V \\ W \end{Bmatrix} = [T]\underline{U} \quad \dots\dots \text{A4.21}$$

The technique by which the polar equations of motion are obtained is identical to that described in Section A4.1.1.2, except that the polar transformation coefficients are now used. In addition, since θ only varies in the θ -direction, derivatives of the coefficients are given by $f'(\theta)/r$ since $\partial\theta = r\partial\theta$.

In practice, the process of transforming the equations to polar co-ordinates was relatively simple, having been through the algebraic manipulation necessary for the $s-n-z$ equations, and the terms could be determined by careful consideration of the appropriate change of variable and orientation of the $x-r-\theta$ system.

A4.2 Comparison of the Equations of Motion in Cartesian (x-y-z), Curvilinear (s-n-z) and Polar (x-r-θ) Co-ordinates

A4.2.1 Continuity Equation

x-y-z

$$\frac{\partial U}{\partial x} + \frac{\partial V}{\partial y} + \frac{\partial W}{\partial z} = 0 \quad \dots\dots \text{A4.22}$$

s-n-z

$$\frac{\partial U_s}{\partial s} + \frac{\partial V_n}{\partial n} + \frac{\partial W_z}{\partial z} - \frac{V_n}{R} = 0 \quad \dots\dots \text{A4.23}$$

x-r-θ

$$\frac{\partial V_a}{\partial x} + \frac{\partial V_r}{\partial r} + \frac{1}{r} \frac{\partial V_\theta}{\partial \theta} + \frac{V_r}{r} = 0 \quad \dots\dots \text{A4.24}$$

or,

$$\frac{\partial V_a}{\partial x} + \frac{1}{r} \frac{\partial}{\partial r} (r V_r) + \frac{1}{r} \frac{\partial V_\theta}{\partial \theta} = 0 \quad \dots\dots \text{A4.25}$$

A4.2.2 Momentum Equations

A4.2.2.1 U-equation

x-y-z

$$U \frac{\partial U}{\partial x} + V \frac{\partial U}{\partial y} + W \frac{\partial U}{\partial z} = - \frac{1}{\rho} \frac{\partial p}{\partial x} \\ - \left(\frac{\partial \overline{uv}}{\partial x} + \frac{\partial \overline{uw}}{\partial y} + \frac{\partial \overline{vw}}{\partial z} \right) \\ + v \left(\frac{\partial^2 U}{\partial x^2} + \frac{\partial^2 U}{\partial y^2} + \frac{\partial^2 U}{\partial z^2} \right) \quad \dots\dots A4.26$$

NB,

$$U \frac{\partial U}{\partial x} + V \frac{\partial U}{\partial y} + W \frac{\partial U}{\partial z} \equiv \frac{\partial UU}{\partial x} + \frac{\partial UV}{\partial y} + \frac{\partial UW}{\partial z}$$

s-n-z

$$U_s \frac{\partial U_s}{\partial s} + V_n \frac{\partial U_s}{\partial n} + W_z \frac{\partial U_s}{\partial z} - \frac{U_s V_n}{R} = - \frac{1}{\rho} \frac{\partial p}{\partial s} \\ - \left(\frac{\partial \overline{u_s u_s}}{\partial s} + \frac{\partial \overline{u_s v_n}}{\partial n} + \frac{\partial \overline{u_s w_z}}{\partial z} - 2 \frac{\overline{u_s v_n}}{R} \right) \\ + v \left(\frac{\partial^2 U_s}{\partial s^2} + \frac{\partial^2 U_s}{\partial n^2} + \frac{\partial^2 U_s}{\partial z^2} - \frac{1}{R} \frac{\partial U_s}{\partial n} - \frac{2}{R} \frac{\partial V_n}{\partial s} - \frac{U_s}{R^2} \right) \quad \dots\dots A4.27$$

NB,

$$U_s \frac{\partial U_s}{\partial s} + V_n \frac{\partial U_s}{\partial n} + W_z \frac{\partial U_s}{\partial z} - \frac{U_s V_n}{R} \equiv \frac{\partial U_s U_s}{\partial s} + \frac{\partial U_s V_n}{\partial n} + \frac{\partial U_s W_z}{\partial z} - 2 \frac{U_s V_n}{R}$$

x-r-theta

$$V_a \frac{\partial V_a}{\partial x} + V_r \frac{\partial V_a}{\partial r} + \frac{V_\theta}{r} \frac{\partial V_a}{\partial \theta} = - \frac{1}{\rho} \frac{\partial p}{\partial x} \\ - \left(\frac{\partial \overline{v_a v_a}}{\partial x} + \frac{\partial \overline{v_a v_r}}{\partial r} + \frac{1}{r} \frac{\partial \overline{v_a v_\theta}}{\partial \theta} + \frac{\overline{v_a v_r}}{r} \right) \\ + v \left(\frac{\partial^2 V_a}{\partial x^2} + \frac{\partial^2 V_a}{\partial r^2} + \frac{1}{r^2} \frac{\partial^2 V_a}{\partial \theta^2} + \frac{1}{r} \frac{\partial V_a}{\partial r} \right) \quad \dots\dots A4.28$$

or,

Transformation of the Equations of Motion

$$\begin{aligned}
 V_a \frac{\partial V_a}{\partial x} + V_r \frac{\partial V_a}{\partial r} + \frac{V_\theta}{r} \frac{\partial V_a}{\partial \theta} &= -\frac{1}{\rho} \frac{\partial p}{\partial x} \\
 - \left(\frac{\partial v_a v_a}{\partial x} + \frac{1}{r} \frac{\partial}{\partial r} \{ r v_a v_r \} + \frac{1}{r} \frac{\partial v_a v_\theta}{\partial \theta} \right) \\
 + v \left(\frac{\partial^2 V_a}{\partial x^2} + \frac{1}{r} \frac{\partial}{\partial r} \left\{ r \frac{\partial V_a}{\partial r} \right\} + \frac{1}{r^2} \frac{\partial^2 V_a}{\partial \theta^2} \right)
 \end{aligned} \quad \dots\dots A4.29$$

NB,

$$\begin{aligned}
 V_a \frac{\partial V_a}{\partial x} + V_r \frac{\partial V_a}{\partial r} + \frac{V_\theta}{r} \frac{\partial V_a}{\partial \theta} &\equiv \frac{\partial V_a V_a}{\partial x} + \frac{\partial V_a V_r}{\partial r} + \frac{1}{r} \frac{\partial V_a V_\theta}{\partial \theta} + \frac{V_a V_r}{r} \\
 &\equiv \frac{\partial V_a V_a}{\partial x} + \frac{1}{r} \frac{\partial}{\partial r} \{ r V_a V_r \} + \frac{1}{r} \frac{\partial V_a V_\theta}{\partial \theta}
 \end{aligned}$$

A4.2.2.2 V-equation

x-y-z

$$U \frac{\partial V}{\partial x} + V \frac{\partial V}{\partial y} + W \frac{\partial V}{\partial z} = - \frac{1}{\rho} \frac{\partial p}{\partial y}$$

$$- \left(\frac{\partial \bar{uv}}{\partial x} + \frac{\partial \bar{vv}}{\partial y} + \frac{\partial \bar{vw}}{\partial z} \right) \quad \dots\dots A4.30$$

$$+ v \left(\frac{\partial^2 V}{\partial x^2} + \frac{\partial^2 V}{\partial y^2} + \frac{\partial^2 V}{\partial z^2} \right)$$

NB,

$$U \frac{\partial V}{\partial x} + V \frac{\partial V}{\partial y} + W \frac{\partial V}{\partial z} \equiv \frac{\partial UV}{\partial x} + \frac{\partial VV}{\partial y} + \frac{\partial VW}{\partial z}$$

s-n-z

$$U_s \frac{\partial V_n}{\partial s} + V_n \frac{\partial V_n}{\partial n} + W_z \frac{\partial V_n}{\partial z} + \frac{U_s U_s}{R} = - \frac{1}{\rho} \frac{\partial p}{\partial n}$$

$$- \left(\frac{\partial \bar{u}_s \bar{v}_n}{\partial s} + \frac{\partial \bar{v}_n \bar{v}_n}{\partial n} + \frac{\partial \bar{v}_n \bar{w}_z}{\partial z} + \frac{(\bar{u}_s \bar{u}_s - \bar{v}_n \bar{v}_n)}{R} \right) \quad \dots\dots A4.31$$

$$+ v \left(\frac{\partial^2 V_n}{\partial s^2} + \frac{\partial^2 V_n}{\partial n^2} + \frac{\partial^2 V_n}{\partial z^2} - \frac{1}{R} \frac{\partial V_n}{\partial n} + \frac{2}{R} \frac{\partial U_s}{\partial s} - \frac{V_n}{R^2} \right)$$

NB,

$$U_s \frac{\partial V_n}{\partial s} + V_n \frac{\partial V_n}{\partial n} + W_z \frac{\partial V_n}{\partial z} + \frac{U_s U_s}{R} \equiv \frac{\partial U_s V_n}{\partial s} + \frac{\partial V_n V_n}{\partial n} + \frac{\partial V_n W_z}{\partial z} + \frac{(U_s U_s - V_n V_n)}{R}$$

x-r-theta

$$V_r \frac{\partial V_r}{\partial x} + V_r \frac{\partial V_r}{\partial r} + \frac{V_\theta}{r} \frac{\partial V_r}{\partial \theta} - \frac{V_\theta V_\theta}{r} = - \frac{1}{\rho} \frac{\partial p}{\partial r}$$

$$- \left(\frac{\partial \bar{v}_r \bar{v}_r}{\partial x} + \frac{\partial \bar{v}_r \bar{v}_r}{\partial r} + \frac{1}{r} \frac{\partial \bar{v}_r \bar{v}_\theta}{\partial \theta} + \frac{(\bar{v}_r \bar{v}_r - \bar{v}_\theta \bar{v}_\theta)}{r} \right) \quad \dots\dots A4.32$$

$$+ v \left(\frac{\partial^2 V_r}{\partial x^2} + \frac{\partial^2 V_r}{\partial r^2} + \frac{1}{r^2} \frac{\partial^2 V_r}{\partial \theta^2} + \frac{1}{r} \frac{\partial V_r}{\partial r} - \frac{2}{r^2} \frac{\partial V_\theta}{\partial \theta} - \frac{V_r}{r^2} \right)$$

or,

Transformation of the Equations of Motion

$$\begin{aligned}
 & V_a \frac{\partial V_r}{\partial x} + V_r \frac{\partial V_r}{\partial r} + \frac{V_\theta}{r} \frac{\partial V_r}{\partial \theta} - \frac{V_\theta V_\theta}{r} = -\frac{1}{\rho} \frac{\partial p}{\partial r} \\
 & - \left(\frac{\partial v_a v_r}{\partial x} + \frac{1}{r} \frac{\partial}{\partial r} \{ r v_r v_r \} + \frac{1}{r} \frac{\partial v_r v_\theta}{\partial \theta} - \frac{v_\theta v_\theta}{r} \right) \quad \dots\dots A4.33 \\
 & + v \left(\frac{\partial^2 V_r}{\partial x^2} + \frac{1}{r} \frac{\partial}{\partial r} \left\{ r \frac{\partial V_r}{\partial r} \right\} + \frac{1}{r^2} \frac{\partial^2 V_r}{\partial \theta^2} - \frac{2}{r^2} \frac{\partial V_\theta}{\partial \theta} - \frac{V_r}{r^2} \right)
 \end{aligned}$$

NB,

$$\begin{aligned} V_a \frac{\partial V_r}{\partial x} + V_r \frac{\partial V_r}{\partial r} + \frac{V_\theta}{r} \frac{\partial V_r}{\partial \theta} - \frac{V_\theta V_\theta}{r} &\equiv \frac{\partial V_a V_r}{\partial x} + \frac{\partial V_r V_r}{\partial r} + \frac{1}{r} \frac{\partial V_r V_\theta}{\partial \theta} + \frac{(V_r V_r - V_\theta V_\theta)}{r} \\ &\equiv \frac{\partial V_a V_r}{\partial x} + \frac{1}{r} \frac{\partial}{\partial r} \{r V_r V_r\} + \frac{1}{r} \frac{\partial V_r V_\theta}{\partial \theta} - \frac{V_\theta V_\theta}{r} \end{aligned}$$

A4.2.2.3 W-equation

x-y-z

$$U \frac{\partial W}{\partial x} + V \frac{\partial W}{\partial y} + W \frac{\partial W}{\partial z} = - \frac{1}{\rho} \frac{\partial p}{\partial z}$$

$$- \left(\frac{\partial \overline{uw}}{\partial x} + \frac{\partial \overline{vw}}{\partial y} + \frac{\partial \overline{ww}}{\partial z} \right) \quad \dots\dots A4.34$$

$$+ v \left(\frac{\partial^2 W}{\partial x^2} + \frac{\partial^2 W}{\partial y^2} + \frac{\partial^2 W}{\partial z^2} \right)$$

NB,

$$U \frac{\partial W}{\partial x} + V \frac{\partial W}{\partial y} + W \frac{\partial W}{\partial z} \equiv \frac{\partial UW}{\partial x} + \frac{\partial VW}{\partial y} + \frac{\partial WW}{\partial z}$$

s-n-z

$$U_s \frac{\partial W_z}{\partial s} + V_n \frac{\partial W_z}{\partial n} + W_z \frac{\partial W_z}{\partial z} = - \frac{1}{\rho} \frac{\partial p}{\partial z}$$

$$- \left(\frac{\partial \overline{u_s w_z}}{\partial s} + \frac{\partial \overline{v_n w_z}}{\partial n} + \frac{\partial \overline{w_z w_z}}{\partial z} - \frac{\overline{v_n w_z}}{R} \right) \quad \dots\dots A4.35$$

$$+ v \left(\frac{\partial^2 W_z}{\partial s^2} + \frac{\partial^2 W_z}{\partial n^2} + \frac{\partial^2 W_z}{\partial z^2} - \frac{1}{R} \frac{\partial W_z}{\partial n} \right)$$

NB,

$$U_s \frac{\partial W_z}{\partial s} + V_n \frac{\partial W_z}{\partial n} + W_z \frac{\partial W_z}{\partial z} \equiv \frac{\partial U_s W_z}{\partial s} + \frac{\partial V_n W_z}{\partial n} + \frac{\partial W_z W_z}{\partial z} - \frac{V_n W_z}{R}$$

x-r-theta

$$V_a \frac{\partial V_\theta}{\partial x} + V_r \frac{\partial V_\theta}{\partial r} + \frac{V_\theta}{r} \frac{\partial V_\theta}{\partial \theta} + \frac{V_r V_\theta}{r} = - \frac{1}{\rho} \frac{1}{r} \frac{\partial p}{\partial \theta}$$

$$- \left(\frac{\partial \overline{v_a v_\theta}}{\partial x} + \frac{\partial \overline{v_r v_\theta}}{\partial r} + \frac{1}{r} \frac{\partial \overline{v_\theta v_\theta}}{\partial \theta} + 2 \frac{\overline{v_r v_\theta}}{r} \right) \quad \dots\dots A4.36$$

$$+ v \left(\frac{\partial^2 V_\theta}{\partial x^2} + \frac{\partial^2 V_\theta}{\partial r^2} + \frac{1}{r^2} \frac{\partial^2 V_\theta}{\partial \theta^2} + \frac{1}{r} \frac{\partial V_\theta}{\partial r} + \frac{2}{r^2} \frac{\partial V_r}{\partial \theta} - \frac{V_\theta}{r^2} \right)$$

or,

Transformation of the Equations of Motion

$$\begin{aligned}
 V_a \frac{\partial V_\theta}{\partial x} + V_r \frac{\partial V_\theta}{\partial r} + \frac{V_\theta}{r} \frac{\partial V_\theta}{\partial \theta} + \frac{V_r V_\theta}{r} &= -\frac{1}{\rho} \frac{1}{r} \frac{\partial p}{\partial \theta} \\
 -\left(\frac{\partial \overline{v_a v_\theta}}{\partial x} + \frac{1}{r} \frac{\partial}{\partial r} \left\{ r \overline{v_r v_\theta} \right\} + \frac{1}{r} \frac{\partial \overline{v_\theta v_\theta}}{\partial \theta} + \frac{\overline{v_r v_\theta}}{r} \right) \\
 + v \left(\frac{\partial^2 V_\theta}{\partial x^2} + \frac{1}{r} \frac{\partial}{\partial r} \left\{ r \frac{\partial V_\theta}{\partial r} \right\} + \frac{1}{r^2} \frac{\partial^2 V_\theta}{\partial \theta^2} + \frac{2}{r^2} \frac{\partial V_r}{\partial \theta} - \frac{V_\theta}{r^2} \right)
 \end{aligned} \quad \dots\dots A4.37$$

NB,

$$\begin{aligned}
 V_a \frac{\partial V_\theta}{\partial x} + V_r \frac{\partial V_\theta}{\partial r} + \frac{V_\theta}{r} \frac{\partial V_\theta}{\partial \theta} + \frac{V_r V_\theta}{r} &\equiv \frac{\partial V_a V_\theta}{\partial x} + \frac{\partial V_r V_\theta}{\partial r} + \frac{1}{r} \frac{\partial V_\theta V_\theta}{\partial \theta} + 2 \frac{V_r V_\theta}{r} \\
 &\equiv \frac{\partial V_a V_\theta}{\partial x} + \frac{1}{r} \frac{\partial}{\partial r} \left\{ r V_r V_\theta \right\} + \frac{1}{r} \frac{\partial V_\theta V_\theta}{\partial \theta} + \frac{V_r V_\theta}{r}
 \end{aligned}$$

A4.2.3 Mean Energy Equation

For 2D mean flow ($\partial/\partial z=0$), neglecting viscous terms.

x-y-z

$$\begin{aligned} \frac{U}{\rho} \frac{\partial P}{\partial x} + \frac{V}{\rho} \frac{\partial P}{\partial y} &= -U \left(\frac{\partial \bar{u}u}{\partial x} + \frac{\partial \bar{u}v}{\partial y} \right) \\ &\quad - V \left(\frac{\partial \bar{u}v}{\partial x} + \frac{\partial \bar{v}v}{\partial y} \right) \\ &\quad - W \left(\frac{\partial \bar{u}w}{\partial x} + \frac{\partial \bar{v}w}{\partial y} \right) \end{aligned} \quad \dots\dots A4.38$$

s-n-z

$$\begin{aligned} \frac{U_s}{\rho} \frac{\partial P}{\partial s} + \frac{V_n}{\rho} \frac{\partial P}{\partial n} &= -U_s \left(\frac{\partial \bar{u}_s u_s}{\partial s} + \frac{\partial \bar{u}_s v_n}{\partial n} - 2 \frac{\bar{u}_s v_n}{R} \right) \\ &\quad - V_n \left(\frac{\partial \bar{u}_s v_n}{\partial s} + \frac{\partial \bar{v}_n v_n}{\partial n} + \frac{(\bar{u}_s u_s - \bar{v}_n v_n)}{R} \right) \\ &\quad - W_z \left(\frac{\partial \bar{u}_s w_z}{\partial s} + \frac{\partial \bar{v}_n w_z}{\partial n} - \frac{\bar{v}_n w_z}{R} \right) \end{aligned} \quad \dots\dots A4.39$$

x-r-theta

$$\begin{aligned} \frac{V_a}{\rho} \frac{\partial P}{\partial x} + \frac{V_r}{\rho} \frac{\partial P}{\partial r} &= -V_a \left(\frac{\partial \bar{v}_a v_a}{\partial x} + \frac{\partial \bar{v}_a v_r}{\partial r} + \frac{\bar{v}_a v_r}{r} \right) \\ &\quad - V_r \left(\frac{\partial \bar{v}_a v_r}{\partial x} + \frac{\partial \bar{v}_r v_r}{\partial r} + \frac{(\bar{v}_r v_r - \bar{v}_\theta v_\theta)}{r} \right) \\ &\quad - V_\theta \left(\frac{\partial \bar{v}_a v_\theta}{\partial x} + \frac{\partial \bar{v}_r v_\theta}{\partial r} + 2 \frac{\bar{v}_r v_\theta}{r} \right) \end{aligned} \quad \dots\dots A4.40$$

or,

$$\begin{aligned} \frac{V_a}{\rho} \frac{\partial P}{\partial x} + \frac{V_r}{\rho} \frac{\partial P}{\partial r} &= -V_a \left(\frac{\partial \bar{v}_a v_a}{\partial x} + \frac{1}{r} \frac{\partial}{\partial r} \{ r \bar{v}_a v_r \} \right) \\ &\quad - V_r \left(\frac{\partial \bar{v}_a v_r}{\partial x} + \frac{1}{r} \frac{\partial}{\partial r} \{ r \bar{v}_r v_r \} - \frac{\bar{v}_\theta v_\theta}{r} \right) \\ &\quad - V_\theta \left(\frac{\partial \bar{v}_a v_\theta}{\partial x} + \frac{1}{r} \frac{\partial}{\partial r} \{ r \bar{v}_r v_\theta \} + \frac{\bar{v}_r v_\theta}{r} \right) \end{aligned} \quad \dots\dots A4.41$$

A4.2.4 Reynolds Stress Transport Equations

For 2D mean flow ($\partial/\partial z=0$).

A4.2.4.1 \overline{uu} -equation

x-y-z

$$U \frac{\partial \overline{uu}}{\partial x} + V \frac{\partial \overline{uu}}{\partial y} = -2 \left(\overline{uu} \frac{\partial U}{\partial x} + \overline{uv} \frac{\partial U}{\partial y} \right) \\ - \left(\frac{\partial \overline{uuu}}{\partial x} + \frac{\partial \overline{uuv}}{\partial y} \right) + v \left(\frac{\partial^2 \overline{uu}}{\partial x^2} + \frac{\partial^2 \overline{uu}}{\partial y^2} \right) \\ - \frac{2}{\rho} \overline{u} \frac{\partial p'}{\partial x} - 2v \left(\left(\frac{\partial u}{\partial x} \right)^2 + \left(\frac{\partial u}{\partial y} \right)^2 + \left(\frac{\partial u}{\partial z} \right)^2 \right) \quad \dots\dots A4.42$$

s-n-z

$$U_s \frac{\partial \overline{u_s u_s}}{\partial s} + V_n \frac{\partial \overline{u_s u_s}}{\partial n} - 2 \frac{\overline{U_s u_s v_n}}{R} = \\ -2 \left(\overline{u_s u_s} \frac{\partial U_s}{\partial s} + \overline{u_s v_n} \frac{\partial U_s}{\partial n} - \overline{u_s u_s} \frac{V_n}{R} \right) \\ - \left(\frac{\partial \overline{u_s u_s u_s}}{\partial s} + \frac{\partial \overline{u_s u_s v_n}}{\partial n} - 3 \frac{\overline{u_s u_s v_n}}{R} \right) \\ + v \left(\frac{\partial^2 \overline{u_s u_s}}{\partial s^2} + \frac{\partial^2 \overline{u_s u_s}}{\partial n^2} - \frac{1}{R} \left(4 \frac{\partial \overline{u_s v_n}}{\partial s} + \frac{\partial \overline{u_s u_s}}{\partial n} \right) - 2 \frac{(\overline{u_s u_s} - \overline{v_n v_n})}{R^2} \right) \\ - \frac{2}{\rho} \overline{u_s} \frac{\partial p'}{\partial s} - (\text{dissipation terms}) \quad \dots\dots A4.43$$

x-r-th

$$V_a \frac{\partial \overline{v_a v_a}}{\partial x} + V_r \frac{\partial \overline{v_a v_a}}{\partial r} = \\ -2 \left(\overline{v_a v_a} \frac{\partial V_a}{\partial x} + \overline{v_a v_r} \frac{\partial V_a}{\partial r} \right) \\ - \left(\frac{\partial \overline{v_a v_a v_a}}{\partial x} + \frac{\partial \overline{v_a v_a v_r}}{\partial r} + \frac{\overline{v_a v_a v_r}}{r} \right) \\ + v \left(\frac{\partial^2 \overline{v_a v_a}}{\partial x^2} + \frac{\partial^2 \overline{v_a v_a}}{\partial r^2} + \frac{1}{r} \frac{\partial \overline{v_a v_a}}{\partial r} \right) \\ - \frac{2}{\rho} \overline{v_a} \frac{\partial p'}{\partial x} - (\text{dissipation terms}) \quad \dots\dots A4.44$$

A4.2.4.2 $\bar{v}\bar{v}$ -equation

x-y-z

$$\begin{aligned}
 U \frac{\partial \bar{v}\bar{v}}{\partial x} + V \frac{\partial \bar{v}\bar{v}}{\partial y} = & -2 \left(\bar{u}\bar{v} \frac{\partial V}{\partial x} + \bar{v}\bar{v} \frac{\partial V}{\partial y} \right) \\
 & - \left(\frac{\partial \bar{u}\bar{v}\bar{v}}{\partial x} + \frac{\partial \bar{v}\bar{v}\bar{v}}{\partial y} \right) + V \left(\frac{\partial^2 \bar{v}\bar{v}}{\partial x^2} + \frac{\partial^2 \bar{v}\bar{v}}{\partial y^2} \right) \\
 & - \frac{2}{\rho} \bar{v} \frac{\partial p'}{\partial y} - 2V \left(\left(\frac{\partial v}{\partial x} \right)^2 + \left(\frac{\partial v}{\partial y} \right)^2 + \left(\frac{\partial v}{\partial z} \right)^2 \right)
 \end{aligned} \quad \dots\dots A4.45$$

s-n-z

$$\begin{aligned}
 U_s \frac{\partial \bar{v}_n \bar{v}_n}{\partial s} + V_n \frac{\partial \bar{v}_n \bar{v}_n}{\partial n} + 2 \frac{U_s \bar{u}_s \bar{v}_n}{R} = & \\
 -2 \left(\bar{u}_s \bar{v}_n \frac{\partial V_n}{\partial s} + \bar{v}_n \bar{v}_n \frac{\partial V_n}{\partial n} + \bar{u}_s \bar{v}_n \frac{U_s}{R} \right) & \\
 - \left(\frac{\partial \bar{u}_s \bar{v}_n \bar{v}_n}{\partial s} + \frac{\partial \bar{v}_n \bar{v}_n \bar{v}_n}{\partial n} + 2 \frac{\bar{u}_s \bar{u}_s \bar{v}_n}{R} - \frac{\bar{v}_n \bar{v}_n \bar{v}_n}{R} \right) & \dots\dots A4.46 \\
 + V \left(\frac{\partial^2 \bar{v}_n \bar{v}_n}{\partial s^2} + \frac{\partial^2 \bar{v}_n \bar{v}_n}{\partial n^2} + \frac{1}{R} \left(4 \frac{\partial \bar{u}_s \bar{v}_n}{\partial s} - \frac{\partial \bar{v}_n \bar{v}_n}{\partial n} \right) + 2 \frac{(\bar{u}_s \bar{u}_s - \bar{v}_n \bar{v}_n)}{R^2} \right) & \\
 - \frac{2}{\rho} \bar{v}_n \frac{\partial p'}{\partial n} - (\text{dissipation terms}) &
 \end{aligned}$$

x-r-theta

$$\begin{aligned}
 V_a \frac{\partial \bar{v}_r \bar{v}_r}{\partial x} + V_r \frac{\partial \bar{v}_r \bar{v}_r}{\partial r} - 2 \frac{V_\theta \bar{v}_r \bar{v}_\theta}{r} = & \\
 -2 \left(\bar{v}_a \bar{v}_r \frac{\partial V_r}{\partial x} + \bar{v}_r \bar{v}_r \frac{\partial V_r}{\partial r} - \bar{v}_r \bar{v}_\theta \frac{V_\theta}{r} \right) & \\
 - \left(\frac{\partial \bar{v}_a \bar{v}_r \bar{v}_r}{\partial x} + \frac{\partial \bar{v}_r \bar{v}_r \bar{v}_r}{\partial r} - 2 \frac{\bar{v}_r \bar{v}_\theta \bar{v}_\theta}{r} + \frac{\bar{v}_r \bar{v}_r \bar{v}_r}{r} \right) & \dots\dots A4.47 \\
 + V \left(\frac{\partial^2 \bar{v}_r \bar{v}_r}{\partial x^2} + \frac{\partial^2 \bar{v}_r \bar{v}_r}{\partial r^2} + \frac{1}{r} \frac{\partial \bar{v}_r \bar{v}_r}{\partial r} + 2 \frac{(\bar{v}_\theta \bar{v}_\theta - \bar{v}_r \bar{v}_r)}{r^2} \right) & \\
 - \frac{2}{\rho} \bar{v}_r \frac{\partial p'}{\partial r} - (\text{dissipation terms}) &
 \end{aligned}$$

A4.2.4.3 \overline{ww} -equation
x-y-z

$$\begin{aligned}
 U \frac{\partial \overline{ww}}{\partial x} + V \frac{\partial \overline{ww}}{\partial y} = & -2 \left(\overline{uw} \frac{\partial W}{\partial x} + \overline{vw} \frac{\partial W}{\partial y} \right) \\
 & - \left(\frac{\partial \overline{uvw}}{\partial x} + \frac{\partial \overline{vww}}{\partial y} \right) + V \left(\frac{\partial^2 \overline{ww}}{\partial x^2} + \frac{\partial^2 \overline{ww}}{\partial y^2} \right) \\
 & - \frac{2}{\rho} \overline{w} \frac{\partial p'}{\partial z} - 2V \left(\left(\frac{\partial w}{\partial x} \right)^2 + \left(\frac{\partial w}{\partial y} \right)^2 + \left(\frac{\partial w}{\partial z} \right)^2 \right)
 \end{aligned} \quad \dots\dots A4.48$$

s-n-z

$$\begin{aligned}
 U_s \frac{\partial \overline{w_z w_z}}{\partial s} + V_n \frac{\partial \overline{w_z w_z}}{\partial n} = & \\
 & -2 \left(\overline{u_s w_z} \frac{\partial W_z}{\partial s} + \overline{v_n w_z} \frac{\partial W_z}{\partial n} \right) \\
 & - \left(\frac{\partial \overline{u_s w_z w_z}}{\partial s} + \frac{\partial \overline{v_n w_z w_z}}{\partial n} - \frac{\overline{v_n w_z w_z}}{R} \right) \\
 & + V \left(\frac{\partial^2 \overline{w_z w_z}}{\partial s^2} + \frac{\partial^2 \overline{w_z w_z}}{\partial n^2} - \frac{1}{R} \frac{\partial \overline{w_z w_z}}{\partial n} \right) \\
 & - \frac{2}{\rho} \overline{w_z} \frac{\partial p'}{\partial z} - (\text{dissipation terms})
 \end{aligned} \quad \dots\dots A4.49$$

x-r-theta

$$\begin{aligned}
 V_a \frac{\partial \overline{v_\theta v_\theta}}{\partial x} + V_r \frac{\partial \overline{v_\theta v_\theta}}{\partial r} + 2 \frac{\overline{v_\theta v_r v_\theta}}{r} = & \\
 & -2 \left(\overline{v_a v_\theta} \frac{\partial V_\theta}{\partial x} + \overline{v_r v_\theta} \frac{\partial V_\theta}{\partial r} + \overline{v_\theta v_\theta} \frac{V_r}{r} \right) \\
 & - \left(\frac{\partial \overline{v_a v_\theta v_\theta}}{\partial x} + \frac{\partial \overline{v_r v_\theta v_\theta}}{\partial r} + 3 \frac{\overline{v_r v_\theta v_\theta}}{r} \right) \\
 & + V \left(\frac{\partial^2 \overline{v_\theta v_\theta}}{\partial x^2} + \frac{\partial^2 \overline{v_\theta v_\theta}}{\partial r^2} + \frac{1}{r} \frac{\partial \overline{v_\theta v_\theta}}{\partial r} - 2 \frac{(\overline{v_\theta v_\theta} - \overline{v_r v_r})}{r^2} \right) \\
 & - \frac{2}{\rho} \frac{\overline{v_\theta}}{r} \frac{\partial p'}{\partial \theta} - (\text{dissipation terms})
 \end{aligned} \quad \dots\dots A4.50$$

A4.2.4.4 $\bar{u}\bar{v}$ -equation

x-y-z

$$U \frac{\partial \bar{u}\bar{v}}{\partial x} + V \frac{\partial \bar{u}\bar{v}}{\partial y} = - \left(\bar{u}\bar{u} \frac{\partial V}{\partial x} + \bar{u}\bar{v} \left(\frac{\partial U}{\partial x} + \frac{\partial V}{\partial y} \right) + \bar{v}\bar{v} \frac{\partial U}{\partial y} \right) \\ - \left(\frac{\partial \bar{u}\bar{u}\bar{v}}{\partial x} + \frac{\partial \bar{u}\bar{v}\bar{v}}{\partial y} \right) + v \left(\frac{\partial^2 \bar{u}\bar{v}}{\partial x^2} + \frac{\partial^2 \bar{u}\bar{v}}{\partial y^2} \right) \\ - \frac{1}{\rho} \left(v \frac{\partial p'}{\partial x} + u \frac{\partial p'}{\partial y} \right) - 2v \left(\frac{\partial u}{\partial x} \frac{\partial v}{\partial x} + \frac{\partial u}{\partial y} \frac{\partial v}{\partial y} + \frac{\partial u}{\partial z} \frac{\partial v}{\partial z} \right) \quad \dots\dots A4.51$$

s-n-z

$$U_s \frac{\partial \bar{u}_s \bar{v}_n}{\partial s} + V_n \frac{\partial \bar{u}_s \bar{v}_n}{\partial n} + \frac{U_s (\bar{u}_s \bar{u}_s - \bar{v}_n \bar{v}_n)}{R} = \\ - \left(\bar{u}_s \bar{u}_s \frac{\partial V_n}{\partial s} + \bar{u}_s \bar{v}_n \left(\frac{\partial U_s}{\partial s} - \frac{V_n}{R} + \frac{\partial V_n}{\partial n} \right) + \bar{v}_n \bar{v}_n \frac{\partial U_s}{\partial n} + \bar{u}_s \bar{u}_s \frac{U_s}{R} \right) \\ - \left(\frac{\partial \bar{u}_s \bar{u}_s \bar{v}_n}{\partial s} + \frac{\partial \bar{u}_s \bar{v}_n \bar{v}_n}{\partial n} + \frac{\bar{u}_s \bar{u}_s \bar{u}_s}{R} - 2 \frac{\bar{u}_s \bar{v}_n \bar{v}_n}{R} \right) \\ + v \left(\frac{\partial^2 \bar{u}_s \bar{v}_n}{\partial s^2} + \frac{\partial^2 \bar{u}_s \bar{v}_n}{\partial n^2} + \frac{1}{R} \left(2 \frac{\partial}{\partial s} (\bar{u}_s \bar{u}_s - \bar{v}_n \bar{v}_n) - \frac{\partial \bar{u}_s \bar{v}_n}{\partial n} \right) - 4 \frac{\bar{u}_s \bar{v}_n}{R^2} \right) \\ - \frac{1}{\rho} \left(v_n \frac{\partial p'}{\partial s} + u_s \frac{\partial p'}{\partial n} \right) - (\text{dissipation terms}) \quad \dots\dots A4.52$$

x-r-theta

$$V_a \frac{\partial \bar{v}_a \bar{v}_r}{\partial x} + V_r \frac{\partial \bar{v}_a \bar{v}_r}{\partial r} - \frac{V_\theta \bar{v}_a \bar{v}_\theta}{r} = \\ - \left(\bar{v}_a \bar{v}_a \frac{\partial V_r}{\partial x} + \bar{v}_a \bar{v}_r \left(\frac{\partial V_a}{\partial x} + \frac{\partial V_r}{\partial r} \right) + \bar{v}_r \bar{v}_r \frac{\partial V_a}{\partial r} - \bar{v}_a \bar{v}_\theta \frac{V_\theta}{r} \right) \\ - \left(\frac{\partial \bar{v}_a \bar{v}_a \bar{v}_r}{\partial x} + \frac{\partial \bar{v}_a \bar{v}_r \bar{v}_r}{\partial r} + \frac{\bar{v}_a \bar{v}_r \bar{v}_r}{r} - \frac{\bar{v}_a \bar{v}_\theta \bar{v}_\theta}{r} \right) \\ + v \left(\frac{\partial^2 \bar{v}_a \bar{v}_r}{\partial x^2} + \frac{\partial^2 \bar{v}_a \bar{v}_r}{\partial r^2} + \frac{1}{r} \frac{\partial \bar{v}_a \bar{v}_r}{\partial r} - \frac{\bar{v}_a \bar{v}_r}{r^2} \right) \\ - \frac{1}{\rho} \left(v_r \frac{\partial p'}{\partial x} + v_a \frac{\partial p'}{\partial r} \right) - (\text{dissipation terms}) \quad \dots\dots A4.53$$

A4.2.4.5 \bar{uw} -equation

x-y-z

$$U \frac{\partial \bar{uw}}{\partial x} + V \frac{\partial \bar{uw}}{\partial y} = - \left(\bar{uu} \frac{\partial W}{\partial x} + \bar{uv} \frac{\partial W}{\partial y} + \bar{uw} \frac{\partial U}{\partial x} + \bar{vw} \frac{\partial U}{\partial y} \right) \\ - \left(\frac{\partial \bar{uuw}}{\partial x} + \frac{\partial \bar{uvw}}{\partial y} \right) + v \left(\frac{\partial^2 \bar{uw}}{\partial x^2} + \frac{\partial^2 \bar{uw}}{\partial y^2} \right) \\ - \frac{1}{\rho} \left(\bar{w} \frac{\partial p'}{\partial x} + \bar{u} \frac{\partial p'}{\partial z} \right) - 2v \left(\frac{\partial u}{\partial x} \frac{\partial w}{\partial x} + \frac{\partial u}{\partial y} \frac{\partial w}{\partial y} + \frac{\partial u}{\partial z} \frac{\partial w}{\partial z} \right) \quad \dots\dots A4.54$$

s-n-z

$$U_s \frac{\partial \bar{u_s w_z}}{\partial s} + V_n \frac{\partial \bar{u_s w_z}}{\partial n} - \frac{U_s \bar{v_n w_z}}{R} = \\ - \left(\bar{u_s u_s} \frac{\partial W_z}{\partial s} + \bar{u_s v_n} \frac{\partial W_z}{\partial n} + \bar{u_s w_z} \frac{\partial U_s}{\partial s} + \bar{v_n w_z} \frac{\partial U_s}{\partial n} - \frac{\bar{u_s w_z} V_n}{R} \right) \\ - \left(\frac{\partial \bar{u_s u_s w_z}}{\partial s} + \frac{\partial \bar{u_s v_n w_z}}{\partial n} - 2 \frac{\bar{u_s v_n w_z}}{R} \right) \quad \dots\dots A4.55 \\ + v \left(\frac{\partial^2 \bar{u_s w_z}}{\partial s^2} + \frac{\partial^2 \bar{u_s w_z}}{\partial n^2} - \frac{1}{R} \left(2 \frac{\partial \bar{v_n w_z}}{\partial s} + \frac{\partial \bar{u_s w_z}}{\partial n} \right) - \frac{\bar{u_s w_z}}{R^2} \right) \\ - \frac{1}{\rho} \left(\bar{w}_z \frac{\partial p'}{\partial s} + \bar{u}_s \frac{\partial p'}{\partial z} \right) - (\text{dissipation terms})$$

x-r-theta

$$V_a \frac{\partial \bar{v_a v_\theta}}{\partial x} + V_r \frac{\partial \bar{v_a v_\theta}}{\partial r} + \frac{\bar{V_\theta v_a v_r}}{r} = \\ - \left(\bar{v_a v_a} \frac{\partial V_\theta}{\partial x} + \bar{v_a v_r} \frac{\partial V_\theta}{\partial r} + \bar{v_a v_\theta} \frac{\partial V_a}{\partial x} + \bar{v_r v_\theta} \frac{\partial V_a}{\partial r} + \frac{\bar{v_a v_\theta} V_r}{r} \right) \\ - \left(\frac{\partial \bar{v_a v_a v_\theta}}{\partial x} + \frac{\partial \bar{v_a v_r v_\theta}}{\partial r} + 2 \frac{\bar{v_a v_r v_\theta}}{r} \right) \quad \dots\dots A4.56 \\ + v \left(\frac{\partial^2 \bar{v_a v_\theta}}{\partial x^2} + \frac{\partial^2 \bar{v_a v_\theta}}{\partial r^2} + \frac{1}{r} \frac{\partial \bar{v_a v_\theta}}{\partial r} - \frac{\bar{v_a v_\theta}}{r^2} \right) \\ - \frac{1}{\rho} \left(\bar{v_\theta} \frac{\partial p'}{\partial x} + \frac{\bar{v_a} \partial p'}{\partial \theta} \right) - (\text{dissipation terms})$$

A4.2.4.6 \bar{vw} -equation
x-y-z

$$\begin{aligned}
 U \frac{\partial \bar{vw}}{\partial x} + V \frac{\partial \bar{vw}}{\partial y} = & - \left(\bar{uv} \frac{\partial W}{\partial x} + \bar{vv} \frac{\partial W}{\partial y} + \bar{uw} \frac{\partial V}{\partial x} + \bar{vw} \frac{\partial V}{\partial y} \right) \\
 & - \left(\frac{\partial \bar{uvw}}{\partial x} + \frac{\partial \bar{vww}}{\partial y} \right) + v \left(\frac{\partial^2 \bar{vw}}{\partial x^2} + \frac{\partial^2 \bar{vw}}{\partial y^2} \right) \\
 & - \frac{1}{\rho} \left(w \frac{\partial p'}{\partial y} + v \frac{\partial p'}{\partial z} \right) - 2v \left(\frac{\partial v}{\partial x} \frac{\partial w}{\partial x} + \frac{\partial v}{\partial y} \frac{\partial w}{\partial y} + \frac{\partial v}{\partial z} \frac{\partial w}{\partial z} \right)
 \end{aligned} \quad \dots\dots A4.57$$

s-n-z

$$\begin{aligned}
 U_s \frac{\partial \bar{v_n w_z}}{\partial s} + V_n \frac{\partial \bar{v_n w_z}}{\partial n} + \frac{U_s \bar{u_s w_z}}{R} = & \\
 & - \left(\bar{u_s v_n} \frac{\partial W_z}{\partial s} + \bar{v_n v_n} \frac{\partial W_z}{\partial n} + \bar{u_s w_z} \frac{\partial V_n}{\partial s} + \bar{v_n w_z} \frac{\partial V_n}{\partial n} + \bar{u_s w_z} \frac{U_s}{R} \right) \\
 & - \left(\frac{\partial \bar{u_s v_n w_z}}{\partial s} + \frac{\partial \bar{v_n v_n w_z}}{\partial n} + \frac{\bar{u_s u_s w_z}}{R} - \frac{\bar{v_n v_n w_z}}{R} \right) \\
 & + v \left(\frac{\partial^2 \bar{v_n w_z}}{\partial s^2} + \frac{\partial^2 \bar{v_n w_z}}{\partial n^2} + \frac{1}{R} \left(2 \frac{\partial \bar{u_s w_z}}{\partial s} - \frac{\partial \bar{v_n w_z}}{\partial n} \right) - \frac{\bar{v_n w_z}}{R^2} \right) \\
 & - \frac{1}{\rho} \left(w_z \frac{\partial p'}{\partial n} + v_n \frac{\partial p'}{\partial z} \right) - (\text{dissipation terms})
 \end{aligned} \quad \dots\dots A4.58$$

x-r-theta

$$\begin{aligned}
 V_a \frac{\partial \bar{v_r v_\theta}}{\partial x} + V_r \frac{\partial \bar{v_r v_\theta}}{\partial r} - \frac{V_\theta (\bar{v_\theta v_\theta} - \bar{v_r v_r})}{r} = & \\
 & - \left(\bar{v_a v_r} \frac{\partial V_\theta}{\partial x} + \bar{v_r v_r} \frac{\partial V_\theta}{\partial r} + \bar{v_a v_\theta} \frac{\partial V_r}{\partial x} + \bar{v_r v_\theta} \frac{\partial V_r}{\partial r} + \bar{v_r v_\theta} \frac{V_r}{r} - \bar{v_\theta v_\theta} \frac{V_\theta}{r} \right) \\
 & - \left(\frac{\partial \bar{v_a v_r v_\theta}}{\partial x} + \frac{\partial \bar{v_r v_r v_\theta}}{\partial r} + 2 \frac{\bar{v_r v_r v_\theta}}{r} - \frac{\bar{v_\theta v_\theta v_\theta}}{r} \right) \\
 & + v \left(\frac{\partial^2 \bar{v_r v_\theta}}{\partial x^2} + \frac{\partial^2 \bar{v_r v_\theta}}{\partial r^2} + \frac{1}{r} \frac{\partial \bar{v_r v_\theta}}{\partial r} - 4 \frac{\bar{v_r v_\theta}}{r^2} \right) \\
 & - \frac{1}{\rho} \left(v_\theta \frac{\partial p'}{\partial r} + \frac{v_r}{r} \frac{\partial p'}{\partial \theta} \right) - (\text{dissipation terms})
 \end{aligned} \quad \dots\dots A4.59$$

A4.2.4.7 k-equation
x-y-z

$$U \frac{\partial k}{\partial x} + V \frac{\partial k}{\partial y} = - \left(\overline{uu} \frac{\partial U}{\partial x} + \overline{uv} \left(\frac{\partial U}{\partial y} + \frac{\partial V}{\partial x} \right) + \overline{vv} \frac{\partial V}{\partial y} + \overline{uw} \frac{\partial W}{\partial x} + \overline{vw} \frac{\partial W}{\partial y} \right) - \left(\frac{\partial \bar{ku}}{\partial x} + \frac{\partial \bar{kv}}{\partial y} \right) + v \left(\frac{\partial^2 k}{\partial x^2} + \frac{\partial^2 k}{\partial y^2} \right) - \frac{1}{\rho} \left(u \frac{\partial p'}{\partial x} + v \frac{\partial p'}{\partial y} + w \frac{\partial p'}{\partial z} \right) - \varepsilon \quad \dots \dots \text{A4.60}$$

where,

$$\varepsilon = v \left(\left(\frac{\partial u}{\partial x} \right)^2 + \left(\frac{\partial u}{\partial y} \right)^2 + \left(\frac{\partial u}{\partial z} \right)^2 + \left(\frac{\partial v}{\partial x} \right)^2 + \left(\frac{\partial v}{\partial y} \right)^2 + \left(\frac{\partial v}{\partial z} \right)^2 + \left(\frac{\partial w}{\partial x} \right)^2 + \left(\frac{\partial w}{\partial y} \right)^2 + \left(\frac{\partial w}{\partial z} \right)^2 \right)$$

s-n-z

$$U_s \frac{\partial k}{\partial s} + V_n \frac{\partial k}{\partial n} = - \left(\overline{u_s w_z} \frac{\partial W_z}{\partial s} + \overline{v_n w_z} \frac{\partial W_z}{\partial n} \right) - \left(\overline{u_s u_s} \left(\frac{\partial U_s}{\partial s} - \frac{V_n}{R} \right) + \overline{u_s v_n} \left(\frac{\partial U_s}{\partial n} + \frac{\partial V_n}{\partial s} + \frac{U_s}{R} \right) + \overline{v_n v_n} \frac{\partial V_n}{\partial n} \right) - \left(\frac{\partial \bar{k} u_s}{\partial s} + \frac{\partial \bar{k} v_n}{\partial n} - \frac{\bar{k} v_n}{R} \right) + v \left(\frac{\partial^2 k}{\partial s^2} + \frac{\partial^2 k}{\partial n^2} - \frac{1}{R} \frac{\partial k}{\partial n} \right) - \frac{1}{\rho} \left(\overline{u_s} \frac{\partial p'}{\partial s} + \overline{v_n} \frac{\partial p'}{\partial n} + \overline{w_z} \frac{\partial p'}{\partial z} \right) - (\text{dissipation terms}) \quad \dots \dots \text{A4.61}$$

x-r-theta

$$V_a \frac{\partial k}{\partial x} + V_r \frac{\partial k}{\partial r} = - \left(\overline{v_a v_\theta} \frac{\partial V_\theta}{\partial x} + \overline{v_r v_\theta} \frac{\partial V_\theta}{\partial r} \right) - \left(\overline{v_a v_a} \frac{\partial V_a}{\partial x} + \overline{v_a v_r} \left(\frac{\partial V_a}{\partial r} + \frac{\partial V_r}{\partial x} \right) + \overline{v_r v_r} \frac{\partial V_r}{\partial r} - \overline{v_r v_\theta} \frac{V_\theta}{r} + \overline{v_\theta v_\theta} \frac{V_r}{r} \right) - \left(\frac{\partial \bar{k} v_a}{\partial x} + \frac{\partial \bar{k} v_r}{\partial r} + \frac{\bar{k} v_r}{r} \right) + v \left(\frac{\partial^2 k}{\partial x^2} + \frac{\partial^2 k}{\partial r^2} + \frac{1}{r} \frac{\partial k}{\partial r} \right) - \frac{1}{\rho} \left(\overline{v_a} \frac{\partial p'}{\partial x} + \overline{v_r} \frac{\partial p'}{\partial r} + \frac{\overline{v_\theta}}{r} \frac{\partial p'}{\partial \theta} \right) - (\text{dissipation terms}) \quad \dots \dots \text{A4.62}$$

